Development of Modularly Assembled Synthetic Esterases

Olivia Matich

A thesis/research component submitted to
Auckland University of Technology
in fulfilment of the requirements for the degree of
Doctor of Philosophy

2026

School of Science

Abstract

This thesis describes the development of two conceptually distinct, modular artificial esterases based on cooperative catalysis. The first system exploits the self-assembly of amphiphiles bearing catalytically active head groups to form vesicular catalysts. The modular nature of this self-assembled system enables rapid catalyst discovery and optimisation by varying the identity and ratio of amphiphiles in solution, without the need for synthetic modification. Optimal activity was achieved using a 1:1:1 mixture of imidazole-, guanidine-, and di-(2-picolyl)amine-functionalised surfactants in the presence of Zn^{2+}. Mechanistic studies suggest nucleophilic catalysis by imidazole, transition-state stabilisation by guanidine via hydrogen bonding, and Zn^{2+}-mediated activation of a secondary nucleophile bound by di-(2-picolyl)amine, enabling catalyst turnover.

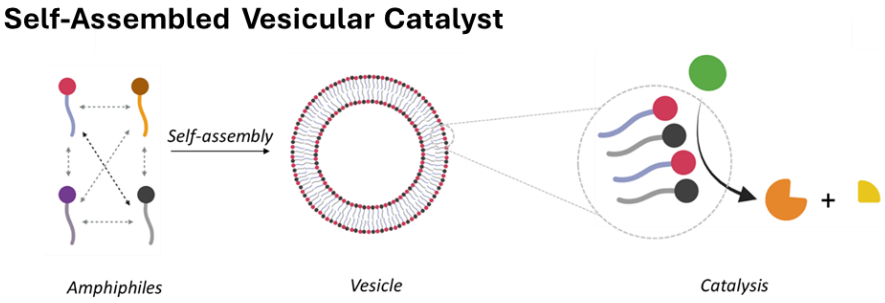

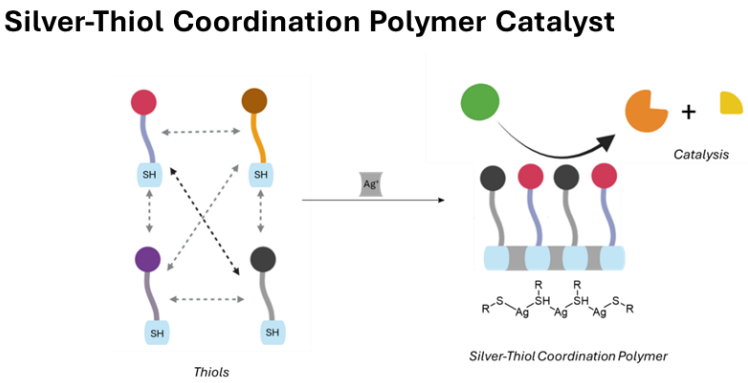

Comparison with reported artificial esterases revealed that more rigid and structurally defined systems typically display higher catalytic efficiencies. To address this limitation, a second catalytic platform was developed based on a silver-thiol coordination polymer, introducing structural rigidity while retaining modularity. These polymers were formed *in situ* from catalytically functionalised thiols, allowing systematic variation of active components. A 1:1:1 combination of imidazole-, guanidine-, and di-(2-picolyl)amine-

functionalised ligands produced the highest activity, notably in the absence of Zn^{2+}. Mechanistic analysis indicates that while the initial nucleophilic attack mirrors that of the vesicular system, the second catalytic step proceeds via the pyridine units of di-(2-picolyl)amine acting as either nucleophiles or general bases.

The silver-thiol polymer catalyst exhibited a 2.8-fold increase in catalytic efficiency relative to the vesicular system, underscoring the importance of rigidity and organisation in artificial enzyme design. Catalytic activity could be reversibly switched off and on by disrupting and reforming the silver-thiol coordination bonds using iodide and Ag^{+}, respectively, confirming their essential structural role. Overall, this work demonstrates how modular, self-assembled catalytic systems enable rapid optimisation of artificial esterases with minimal synthetic effort, while highlighting the critical role of cooperative interactions and structural organisation in achieving enzyme-like performance. These principles provide a foundation for the development of future artificial esterases for applications such as the hydrolytic degradation of ester-based plastics, including polyethylene terephthalate (PET).

Contents

List of Figures

List of Schemes

List of Tables

Abbreviations

δ	chemical shift
°C	degrees Celsius
μ	micro
μL	microlitre
μM	micromolar
Boc	*tert*-butyloxycarbonyl
CAC	critical aggregation concentration
CTAB	hexadecyltrimethylammonium bromide
d	doublet
dd	doublet of doublets
DEA	diethylamine
DIPEA	*N,N*-diisopropylethylamine
DLS	dynamic light scattering
DMF	*N,N*-dimethylformaldehyde
DMSO	dimethyl sulfoxide
DPH	1,6-diphenyl-1,3,5-hexatriene
ESI	electrospray ionisation
et al.	and others
EtOAc	ethyl acetate
EtOH	ethanol
eq.	equivalent
g	gram
HBTU	*N,N,N′,N′*-Tetramethyl-*O*-(1*H*-benzotriazol-1-yl)uronium hexafluorophosphate
HEPES	2-[4-(2-hydroxyethyl)poperazin-1-yl]ethanesulfonic acid
HPNPP	2-hydroxypropyl *p*-nitrophenyl phosphate
HRMS	high resolution mass spectrometry
Hz	hertz
IDA	indicator displacement assay
IR	infrared
J	coupling constant
m	multiplet

M	molar
MeCN	acetonitrile
MeOH	methanol
mg	milligram
mM	millimolar
mmol	millimole
mQ water	milli-Q water
m/z	mass to charge ratio
NMR	nuclear magnetic resonance
p	para
Pd/C	palladium on carbon
Ph	phenyl
PNP	*p*-nitrophenol
PNPB	*p*-nitrophenyl butyrate
ppm	parts per million
q	quartet
quant.	quantitative
quint	quintet
Rt	room temperature
s	singlet
SANS	small-angle neurtron scattering
SAXS	small-angle x-ray scattering
t	triplet
TACN	1,4,7-triazacyclononane
TCEP	tris(2-carboxyethyl)phosphine hydrochloride
TEM	transmission electron microscopy
TFA	trifluoroacetic acid
td	triplet of doublets
THF	tetrahydrofuran
TLC	thin layer chromatography
Ts	tosyl
TsCl	tosyl chloride
UV-vis	ultraviolet-visible

Attestation of Authorship

I hereby declare that this submission is my own work and that, to the best of my knowledge and belief, it contains no material previously published or written by another person (except where explicitly defined in the acknowledgements), nor used artificial intelligence tools or generative artificial intelligence tools (unless it is clearly stated, and referenced, along with the purpose of use), nor material which to a substantial extent has been submitted for the award of any other degree or diploma of a university or other institution of higher learning.

	20/12/2025
Signature	Date

Co-Authored Works

STUDENT AND SUPERVISOR APPROVALS

By signing you are confirming that the co-author contributions stated in the table(s) below are accurate.

Student Name	Olivia Matich	**Signature**		**Date**	23/01/26
Supervisor Nan	Jack Chen	**Signature**		**Date**	23/01/26

Chapter Number:	**2**
Manuscript Title:	**Development of Modularly Assembled Synthetic Esterases**
Publication Status:	**Published**
Reference if published:	**Matich, O.; Naiya, M. M.; Salam, J.; Tiban Anrango, B. A.; Chen, J. L.-Y. Modular Assembly and Optimization of an Artificial Esterase from Functionalised Matich Naiya 80% 10% Surfactants. ChemCatChem 2024, 16 https://doi.org/10.1002/cctc.202400945. (20), e202400945.**

AUTHOR SURNAME: (order as per manuscript)	**CONTRIBUTION**
Matich	**Formal analysis, investigation, writing**
Naiya	**Conceptualisation, writing, methodology**
Salam	**Investigation**
Tiban Anrango	**Investigation**
Chen	**Conceptualisation, formal analysis, writing**

Acknowledgements

Firstly, a huge thank you to my supervisor, Dr Jack L.-Y Chen, for all your help and support throughout the PhD. Thanks for talking me into doing a PhD in the first place and believing that I could do this even when I thought I could not. I have learnt so much from you over the last few years and have grown so much as a researcher with your guidance. Being a part of your research group has been a wonderful experience, from all the group meetings and problem sessions to helping out the newbies in the lab, I really enjoyed my time being back. You really pushed me throughout this PhD to be a better scientist both in and out of the lab. Thanks so much for having me back to do my PhD.

Secondly, a massive thank you to Dr Mohinder Maheshbhai Naiya for all your help in and out of the lab. You have been like a second supervisor to me and taught me so much. I learned so many lab skills from you and how to think more critically about the experimental conditions I was using for a particular reaction. I always enjoyed your stories about your past experiences in the lab and learning what not to do. Thanks for always being the person I could go to for any problems I had, whether they be big or small.

Thank you to AUT and the MacDiarmid Institute for the scholarships that enabled me to complete my PhD. Thanks to all the University staff who have helped me on this journey, including all the lab technicians. Thank you to the MacDiarmid Institute for the opportunity to go to conferences, symposia and research meetings where I got the opportunity to present my research and meet lots of wonderful researchers. Thanks to MESA for the chance to be a part of the committee for two years and for all the opportunities to meet and connect with other PhD students around the country. A special shout-out to Stephen and Nick, who accompanied me on the entire journey from different universities; it was always a treat to catch up again.

A huge thank you to all the amazing students that I have had the pleasure of working with in the lab over the last few years. In particular, thanks to Bronte, Jess and Rosie for being my big sisters in the lab. You always gave such good advice when I was feeling stressed and overwhelmed with everything. I also learned the best lab tips and tricks from you all. To our little chemistry gang: Andrés, Marc, Keer, Ben and Megan, thanks for all the good times both in and out of the lab. Can you believe I finally finished my PhD! Danielle,

Letitia and Paraminta, thanks for keeping me such good company in the lab during my last year. I love struggling alongside you guys on our respective projects. Lastly, to Marina, thanks for being the best write-up buddy a girl could ask for. You definitely kept me sane during these last few months.

To my best friend Tarsh, thanks for all the love and support throughout my PhD. You were always willing to listen to all my complaints about the lab and when things were not working, even though you do not know much about chemistry. I appreciate all the times we would catch up, and you would help distract me from the stress of my PhD.

Sophie, thanks for all the sisterly love in the form of joint rant sessions where we would trade stories about our respective degrees. Thanks for letting me harp on about what I was doing in the lab and pretending to listen to me. From all the times where we would go to the mall and get bubble tea or simply watch a favourite movie, thanks for keeping me company and distracting me from the PhD blues. Also, thanks for double-checking all my figures in my thesis.

Finally, to my parents, thanks for always being a shoulder to cry on when the PhD got too much. Thanks for believing in me and encouraging me to keep going even when things were not going well. For trying to problem solve and giving me ideas to try in the lab, even though you both know nothing about chemistry. I could not have gotten through this without your love and support. A special thanks to mum for double-checking all my compound numbers with me.

Chapter 1: Introduction and Literature Review

1.1 Enzymes

1.1.1 Biological catalysts

Enzymes are biological catalysts that can facilitate a variety of chemical reactions with very high catalytic efficiency and substrate specificity.[1] They are found in every living species, including mammals, plants, insects, yeast and bacteria.[2] Enzymes are referred to as biological catalysts due to their ability to accelerate chemical reactions without being used up themselves. They do this by lowering the activation energy of a biological reaction, which is the threshold energy that must be overcome for a reaction to occur.[3] Figure 1 shows that the presence of a catalyst can open up an alternative approach to the normal reaction pathway with lower activation energy, resulting in an increase in the rate of reaction. The multiple transition states and intermediate species that a catalytic pathway offers are depicted by several changes in energy during this pathway. Both the final result and the overall thermodynamics remain the same.[3] The lower activation energy is a result of the catalyst stabilising any transition state species in the reaction.[4] Enzymes are termed biological catalysts as they belong to a class of biological molecules called proteins.

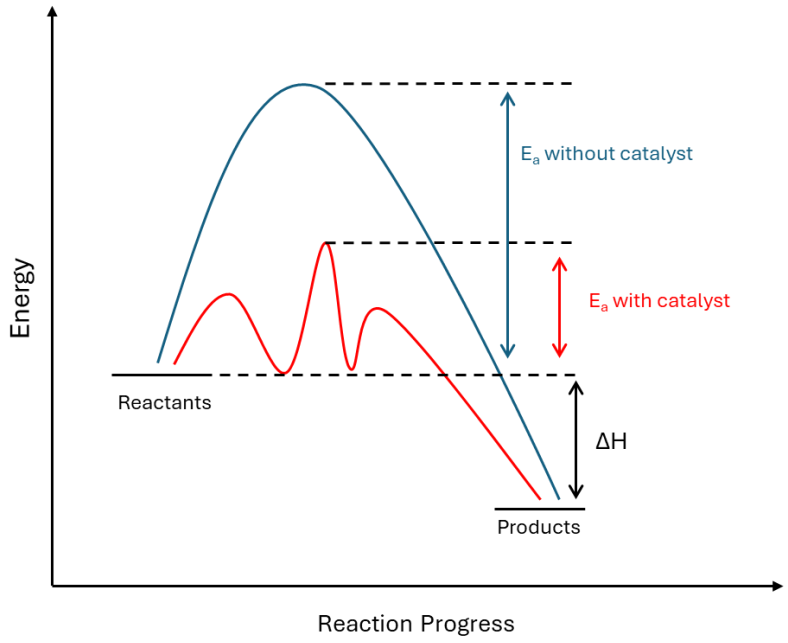

Figure 1: Energy profile diagram for reactions with and without a catalyst.

Enzymes are a type of protein and, therefore, are made up of a polypeptide chain of amino acids, which determine their structure and function.[5] This chain of amino acids can then fold itself into a three-dimensional structure held together by intermolecular forces such as hydrogen bonding, hydrophobic interactions, ionic bonding, covalent bonds and metal ion coordination (Figure 2). For globular proteins, this three-dimensional structure consists of a hydrophobic core, which gives the enzyme its specificity, and a hydrophilic shell, so the enzyme remains compatible with the aqueous environment of biological systems.[6] The microenvironments created from the protein structure can affect the reactivity of key catalytic groups, for example, shielding the active site from bulky solvents.[7] The folding of the polypeptide chain also gives rise to specific regions called binding sites, which play an important role in the enzyme's catalytic functions.

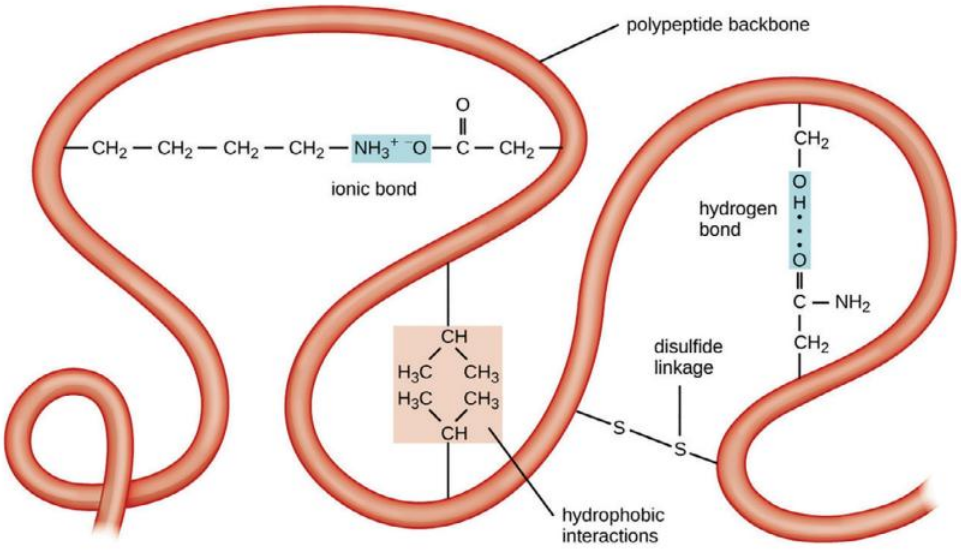

Figure 2: Tertiary protein structure. Source: Ref.[5]/Elsevier.

The amazing catalytic properties seen by enzymes are aided by the binding capabilities of these proteins.[8] Specific regions of the enzyme are designed to interact with other molecules. These sites can differ in their function and can bind different molecules.[9] A single enzyme can contain multiple binding sites. The active site of an enzyme is a binding site that directly facilitates catalysis. This active site consists of a catalytic site, which typically has two or more amino acid residues that are in close proximity to cooperatively catalyse a reaction.[9] Cooperative catalysis refers to a catalytic system that requires two or more functionalities working together to facilitate a chemical reaction. These cooperative interactions enhance the rate of reaction compared to the

functionalities working individually. This is one of the key features of enzymes that makes them such efficient catalysts. This type of catalysis is a key focus for this thesis and will be discussed throughout.

In addition to the catalytic site, the active site also consists of a substrate binding site. This part of the enzyme is capable of recognising the specific substrate molecule that the enzyme acts upon.[9] Substrate recognition is a unique feature of enzyme catalysis, which results in their high substrate specificity, with different enzymes having different target substrates. The binding site is also responsible for holding the substrate in place for the catalytic site during the chemical reaction. This allows the substrate to be in close proximity and in the correct orientation to the catalytic site, resulting in the acceleration of a chemical reaction.[6,8] The substrate binding site is another special feature of enzymes that contributes to their catalytic efficiency.

Though the active site is the primary part of the enzyme that facilitates catalysis, other areas of the enzyme may be involved. These include oxyanion holes, allosteric sites, and additional binding sites for either cofactors or coenzymes. While many types of binding sites are available on an enzyme, the focus of this thesis will be on the interactions at the active site.

In addition to amino acid residues, cofactors or coenzymes may also be involved in catalysing a reaction. Cofactors refer to molecules or ions that are covalently bound to the enzyme. These are essential for catalysis. For example, metal ions are found in metalloenzymes. Metals are bound to the enzyme through coordination bonds between the metal and amino acid residues. These metal ions can provide binding sites for substrates, electrophilic centres to aid in catalysis, and multiple oxidation states to facilitate redox reactions and electron transfer chemistry.[10] Other examples of cofactors include sulphate ions or organic groups such as flavin **1** or heme **2** (seen in Figure 3).

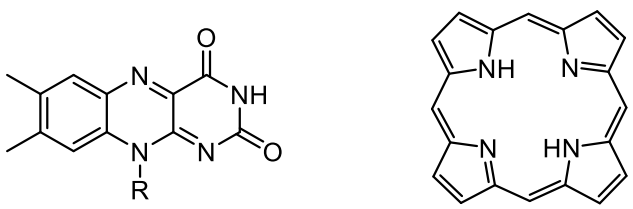

Flavin **1** Heme **2**

*Figure 3: Structure of enzyme cofactors flavin (**1**) and heme (**2**).*

Coenzymes are organic molecules that contain functionalities not found in proteins. The presence of these offers more functional groups and mechanisms for enzyme catalysis.[10] Coenzymes work in tandem with the enzyme, participating directly in catalysis. They are usually consumed during the reaction and will then be released from the active site.[9] Typically, coenzymes are not covalently bound to the enzyme; rather, they may be loosely associated with the enzyme or may be bound tightly, but not covalently, to the enzyme.[10] Examples of coenzymes include vitamins or the cellular energy carrier ATP.

1.1.2 Models of enzyme binding

Two key models have been proposed to account for the specificity of enzymes' binding at the active sites. These are the lock and key model by Emil Fischer and the induced fit model by Daniel Koshland.

The lock and key model, shown in Figure 4, proposes that the enzyme active site and the substrate are complementary geometric shapes to one another. This means that only substrates with the correct size and shape can fit into specific active sites, like how a key fits in a lock. This enzyme model nicely explains the specificity of enzymes; however, it does not account for the stabilisation of transition states by the enzyme.

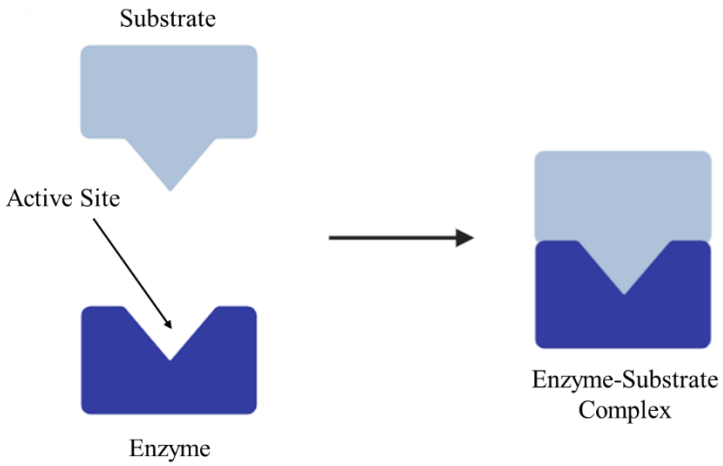

Figure 4: Schematic of the lock and key enzyme binding model.

The induced fit model (Figure 5) was proposed as a modified version of the lock and key model, which incorporated the flexibility of both enzymes and substrates. This model suggests that the active site is continuously changing shape due to interactions occurring between the substrate and the enzyme. Therefore, the substrate doesn’t bind a rigid active

site, but rather the amino acid residues making up the active site can move into the ideal position, allowing the enzyme to perform its catalytic function. The active site can then adjust its shape to fit the transition state of the reaction – something the lock and key method did not account for.

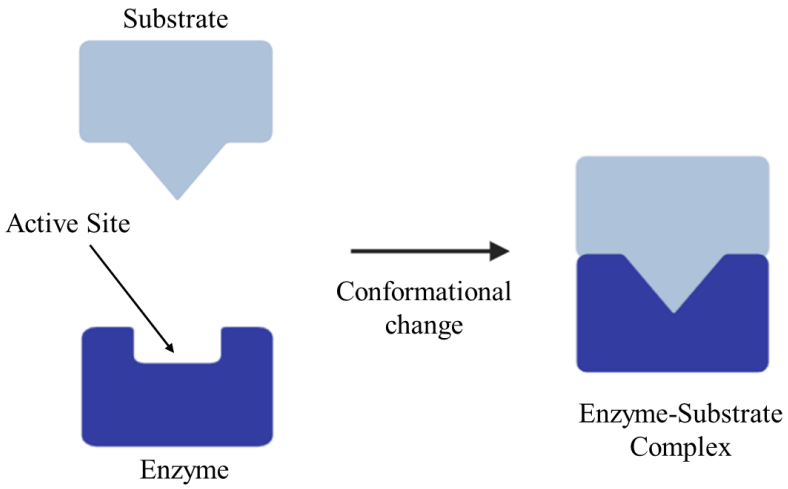

Figure 5: Schematic for the induced fit enzyme binding model.

Another important feature of enzymes is their dynamic nature. For a while now, scientists have understood that protein structures exist as an ensemble of interconverting conformations on all time scales (from femtoseconds to minutes).[11] These conformational changes can vary from small atom displacement to large-scale domain shifts.[11] At equilibrium, this group of protein structures interconvert between one another. For example, the protein ubiquitin has been found to exist in a variety of different conformations (see Figure 6). This dynamic nature is a result of the weak forces that hold together protein structures. Different protein structures may be involved in different parts of an enzyme's function. For example, different conformations of an enzyme may exist when a substrate is bound compared to when catalysis is occurring or even when the product is being released. This dynamic nature has led to an alternative binding model being proposed, called conformational selection. The model suggests that all protein conformations pre-exist, and that the substrate selects the most favourable one.[12] Since these conformations all exist at equilibrium, they will undergo a population shift, redistributing the conformational states.

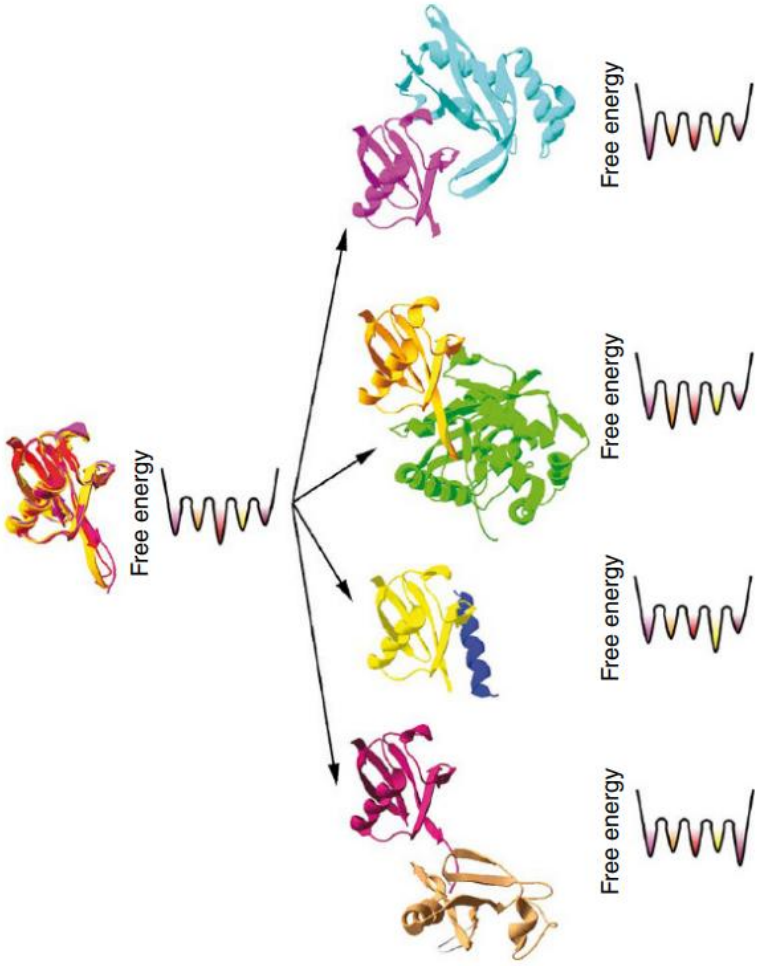

Figure 6: Example of some of the conformations of ubiquitin that exist in the conformational ensemble. Source: Reprinted from ref. [12] with permission. Copyright (2009) Springer Nature.

Scientists now believe that both conformational selection and the induced fit model play a part in enzyme binding. It is suggested that a conformational selection event occurs initially when the substrate is bound. This is then followed by the induced fit model, where remaining protein conformations optimise side chain and backbone interactions to induce the fit of the enzyme to the substrate.[12] A great example of this is seen with the protein ubiquitin. Ubiquitin is a small regulatory protein whose function involves binding other protein molecules, resulting in a change in that protein's function. NMR has been used to derive the conformational ensemble of ubiquitin. This suggests that all bound conformations exist in the absence of protein binding partners (see Figure 6). The free energy landscapes of these structures are yet to be determined, as the population of conformers in the ensemble and the energy barriers between them are unknown.[12]

However, these results highlight the dynamic nature of enzymes and their ability to adapt multiple conformations.

1.1.3 Michaelis-Menten kinetics

The efficiency of enzymatic systems can be determined using Michaelis-Menten kinetics. This concept was developed by Leonor Michaelis and Maud Menten to explain the kinetic rate enhancement of enzymes and to demonstrate how this enhancement is dependent on both enzyme and substrate concentrations. Michaelis-Menten kinetics offer an insight into the catalytic efficiency of the enzyme and the binding affinity of the substrate. It also provides a useful way to compare the catalytic efficiency between different enzymes.

Equation 1 describes the dependence of enzyme-catalysed reactions on substrate concentration using two parameters, V_{max} and K_M.[13] V_{max} is the maximum velocity; this refers to the maximum rate at which an enzyme can catalyse a reaction when its active site is saturated with substrate. K_M is the Michaelis-Menten constant, which is the substrate concentration at which the reaction rate is half of the V_{max}.[13] The K_M value can provide valuable insight into the affinity between the enzyme and the substrate, with a lower K_M value indicating stronger binding between the enzyme and substrate. These Michaelis-Menten parameters can be determined experimentally, as shown in Figure 7, by plotting the rate of reaction of an enzyme at increasing substrate concentrations. Here, V_{max} is the highest rate of catalysis, while K_M is the substrate concentration at half V_{max}.

$$V = \frac{V_{max}[S]}{K_M + [S]} \quad (1)$$

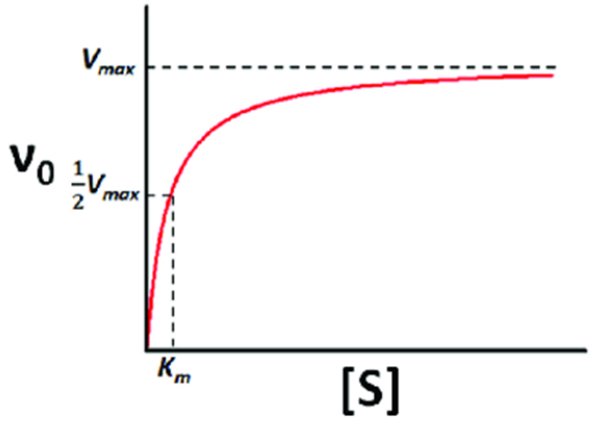

Figure 7: Michaelis-Menten plot to determine Vmax and KM. Source: Ref. [14]/Frontiers.

Another key parameter can be calculated, and this is the catalytic constant, k_{cat}. This determines the maximum rate of reaction at saturated substrate concentrations.[13] Equation 2 shows how to calculate this using the V_{max} and the total enzyme concentration. From this, the catalytic efficiency can be determined by looking at the ratio between k_{cat} and K_M, as shown in Equation 3. The greater this number, the more efficient the enzyme is.

$$k_{cat} = \frac{V_{max}}{[Enzyme]} \quad (2)$$

$$catalytic\ efficiency = \frac{k_{cat}}{K_M} \quad (3)$$

1.1.4 Hydrolase enzymes

Hydrolase enzymes are a class of enzymes that catalyse the hydrolysis of chemical bonds for a range of substrates, including lipids, sugars and peptides.[15] Serine proteases, such as α-chymotrypsin (Figure 8), are a type of hydrolase enzyme that have been heavily investigated for both their structure and catalytic mechanism.[16] These enzymes consist of a single protein unit with a single active site. The active site of these enzymes is called the catalytic triad, consisting of a serine, histidine and aspartic acid residue.[17] There is typically a region around this active site, called the binding pocket, which can attract and align the target substrate.[16] Amino acid residues close to the active site may participate in transition state binding, helping to stabilise the intermediate species; this is known as the oxyanion hole.[18]

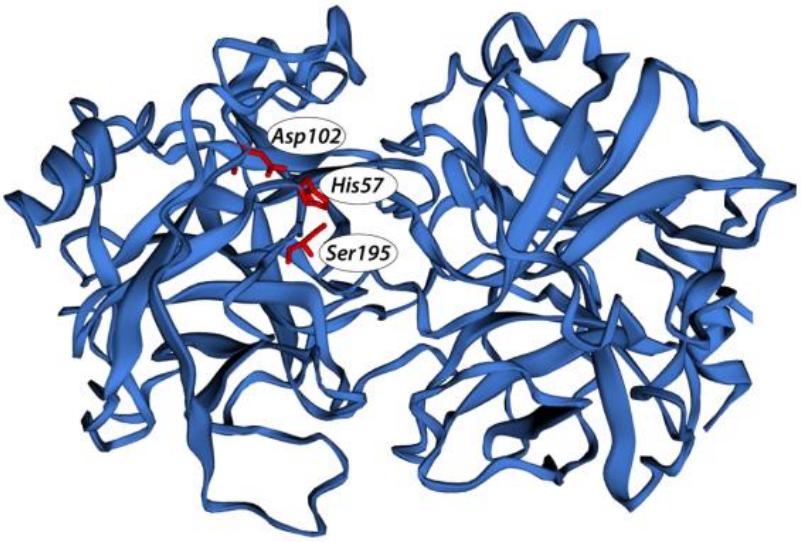

Figure 8: Structure of α-chymotrypsin. Source: Reprinted from ref. [16] with permission. Copyright (2019) American Chemical Society.

The catalytic mechanism for hydrolase enzymes, consisting of the serine, histidine, and aspartic acid catalytic triad, is shown below in Figure 9. Here, aspartic acid forms a hydrogen bond with the imidazole ring of histidine. This increases the pK_a of the imidazole nitrogen, allowing it to act as a strong general base. This imidazole nitrogen then deprotonates the alcohol on the serine molecule, allowing it to undergo nucleophilic attack of the substrate (in this case, an amide). A tetrahedral intermediate species is formed and stabilised by hydrogen bonding with nearby amino acid residues. The amine is then lost, and an ester is now formed between the substrate and the serine residue. The imidazole can once again act as a base, this time deprotonating a water molecule, for this to then undergo nucleophilic attack on the serine ester. This results in a second transition state before the carboxylic acid is lost and the original catalyst is regenerated. This specific mechanism has been found to occur in over 300 different hydrolase enzymes, including esterase enzymes.[16]

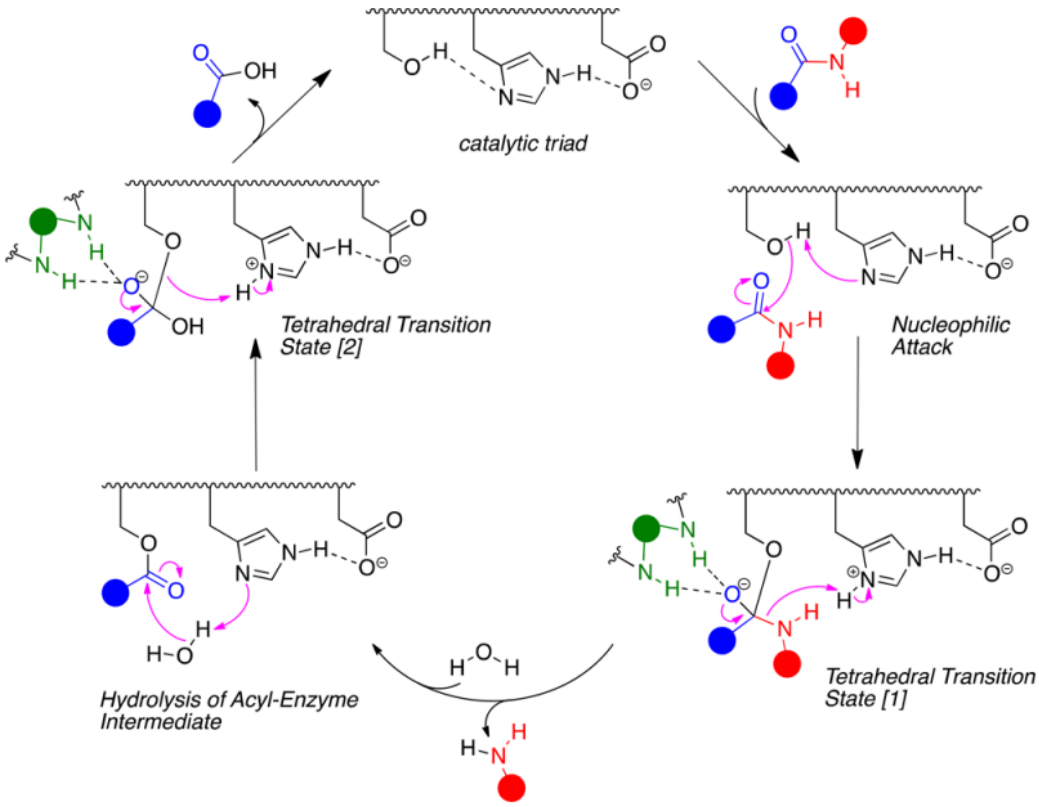

Figure 9: Mechanism of action for hydrolase enzymes with the catalytic triad present in the active site. Source: Reprinted from ref. [16] with permission. Copyright (2019) American Chemical Society.

Esterase enzymes are a subclass of hydrolytic enzymes that can catalyse the hydrolysis of ester bonds by the addition of a water molecule.[19] These typically display a broad substrate specificity with enzymes capable of cleaving thioesters, acetyl esters, carboxylic esters, phosphotriesters, cholesterol esters, acetylcholine, and dienelacetone.[19]

Carboxylic ester hydrolases catalyse the hydrolysis of esters into carboxylic acids and alcohols. These are found in all living organisms as they have important roles in metabolism, signal transduction and protein synthesis.[20] The active site of these types of enzymes consists of the catalytic triad serine, histidine and aspartic acid, which facilitate a cooperative mechanism previously shown in Figure 9.

1.1.5 Industrial applications of enzymes

Native enzymes have several applications in industrial processes due to their efficiency and sustainability compared with traditional chemical processes.[21] The pharmaceutical, food and beverage, detergent, textile, pulp and paper, leather, animal feed, personal care

and biofuel industries all currently utilise enzymes in their commercial processes.[21,22] Table 1 showcases the wide range of enzyme applications in these industries, ranging from simplifying chemical synthesis routes to improving process economics.[21] Enzymes typically offer milder operating conditions, high product selectivity and have a lower environmental impact as they reduce the consumption of energy and chemicals.[21,22]

Table 1: Industrial application of native enzymes. Source: Ref. [21]/MDPI.

Sector	Enzymes	Applications
Pharmaceuticals	Nitrile hydratase, transaminase, monoamine oxidase, lipase, penicillin acylase	Synthesis of intermediates for production of active pharmaceutical ingredients
Food Processing	Trypsin, amylase, glucose isomerase, papain, pectinase	Conversion of starch to glucose, production of high fructose corn syrup, production of prebiotics, debittering of fruit juice
Detergent	Protease, lipase, amylase, cellulase	Stain removal, removal of fats and oils, color retention,
Biofuels	Lipase, cellulase, xylanase	Production of fatty acid methyl esters, decomposition of lignocellulotic material for bioethanol production
Paper and Pulp	Lipase, cellulase, xylanase	Removal of lignin for improved bleaching, improvement in fiber properties

Esterase enzymes themselves have a wide range of industrial applications. They are used in the textile industry to aid in the uptake of chemical compounds by polyester fabrics.[23] Polyesterases are the enzymes responsible for this, and they can uptake dyes, anti-static, antistaining and antimicrobial agents into fabrics.[23] Esterases can also offer a promising new source of drugs, with some enzymes being found to have bactericidal activity on *Mycobacterium tuberculosis*.[24] In the food industry, esterases are used in various fruit juices to modify oils and fats, and to produce fragrances and flavours.[25] Esterase enzymes can also be found in a wide range of detergents due to their ability to break down fats and oils.[17]

Despite being really efficient catalysts, native enzymes have several drawbacks preventing their widespread industrial application.[2,22] Enzymes have a very narrow window of operating conditions (ideal pH and temperature range, for example); outside of these conditions, degradation can occur.[21] They also have poor substrate versatility and diversity due to their highly selective nature.[2,6] Preparation and purification of native enzymes is also quite costly, and they often require the use of cofactors or co-substrates,

which further increases production costs.[6] A variety of approaches have been tried to overcome these challenges, including screening enzymes from natural sources, genetic engineering, and immobilisation of the enzyme.[26]

One way to overcome these challenges is to immobilise enzymes onto a material with the desired physical, chemical, electrical and/or mechanical properties.[21] Immobilised enzymes can produce highly selective reaction outcomes under relatively mild conditions.[27] Methods for enzyme immobilisation are well documented in the literature; however, there are very few examples of these being utilised on an industrial scale. One of the biggest reasons for this is that the economic benefit of using immobilised enzymes is often not substantial compared with using the non-immobilised enzyme.[27]

Directed evolution is a process used to enhance the properties of a chosen native enzyme that can already facilitate the desired chemical reaction, with the steps for this shown in Figure 10. This method has been used to engineer enzymes for the production of biofuels, materials, fine chemicals and active pharmaceutical intermediates.[28] Here, the stability, activity or enantioselectivity can be enhanced by mimicking the natural selection process.[29] Random mutagenesis of one or more starting genes occurs, followed by a screening or selection step. This looks to isolate enzyme variants with desirable properties. The process can be repeated until the ideal level of change has been reached. Limitations of this method include the random nature of mutagenesis and the need for a high-throughput screening method to test the enzyme variants produced.[30]

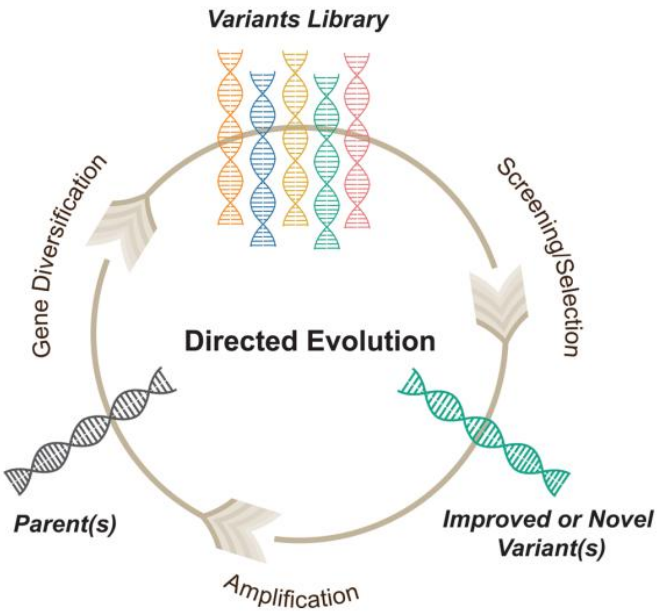

Figure 10: Process of directed evolution for enzyme enhancement. Source: Reprinted from ref. [28] with permission. Copyright (2021) American Chemical Society.

A potentially more promising alternative to enzyme immobilisation and directed evolution that researchers have been exploring in recent years is synthesising artificial catalysts inspired by enzymes.

1.2 Artificial catalysts inspired by enzymes

Scientists are now developing artificial catalysts inspired by enzymes with the hope of achieving similar or improved catalytic rates when compared to their native counterparts. Artificial catalysts have the advantage of tuneable structures and catalytic efficiencies because they can be optimised for a particular application.[6] They can have a wider substrate scope than native enzymes and have excellent tolerance to experimental conditions, as they are less sensitive and require less strict operating conditions compared to their native counterparts. Typically, these artificial catalyst systems have much simpler structures than their native enzyme counterparts.[17] A large majority of these artificial enzymes are inspired by the lock and key model of enzyme binding. Artificial enzymes typically designed have a rigid 'active site' that matches the structure of the desired substrate for catalysis to occur.

1.2.1 Design and synthesis

Artificial catalysts are typically synthesised based on cooperative catalysis, where two or more functional groups work together (cooperatively) to cleave the substrate. When working in this manner, higher rates of catalysis can be achieved compared to the sum of each functional group working independently.[31] Artificial catalysts aim to mimic the active catalytic centre of native enzymes. There are several methods to make an artificial catalyst, and these are shown in Figure 11. In these examples, pre-organisation of the catalytic functional groups helps to bring them close to one another in order to facilitate cooperative catalysis.[31] Here we have examples of the key catalytic groups attached onto molecular scaffolds, dendrimers, surfaces, or brought together by hydrogen bonding and hydrophobic interactions.

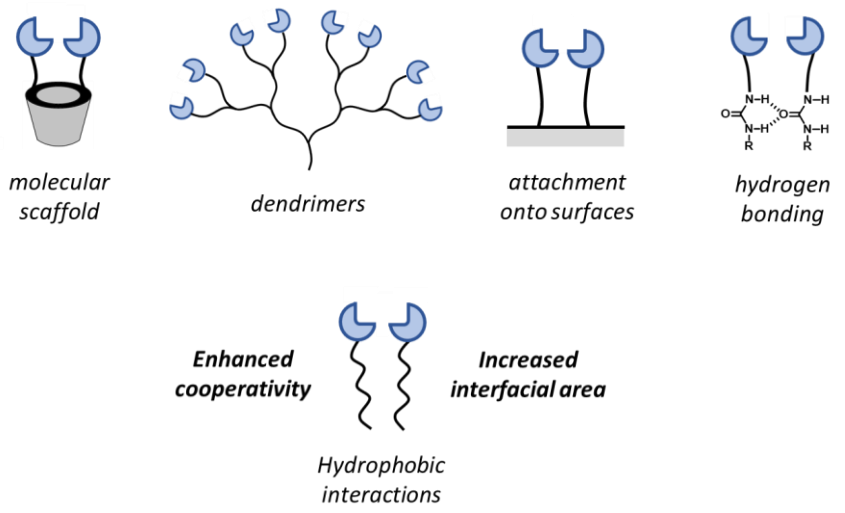

Figure 11: Methods to make an artificial catalyst. Source: Ref. [31]/Wiley-VCH.

1.2.2 Molecular scaffolds

There are many examples in the literature of artificial enzymes designed by attaching the key catalytic groups onto some type of molecular scaffold, such as cyclodextrins, cucurbiturils and cavitands. These types of systems create rigid catalytic structures, as the catalytic functionalities are fixed in place on the scaffold.

Cyclodextrins

Cyclodextrins are cyclic oligosaccharides capable of acting as artificial enzymes due to their ability to bind hydrophobic substrates within their cavity (Figure 12).[32] Hydroxyl

groups are located on the two rims of the scaffold. These can either react directly with the substrate or can be used to attach catalytic functional groups onto the scaffold.[1,32]

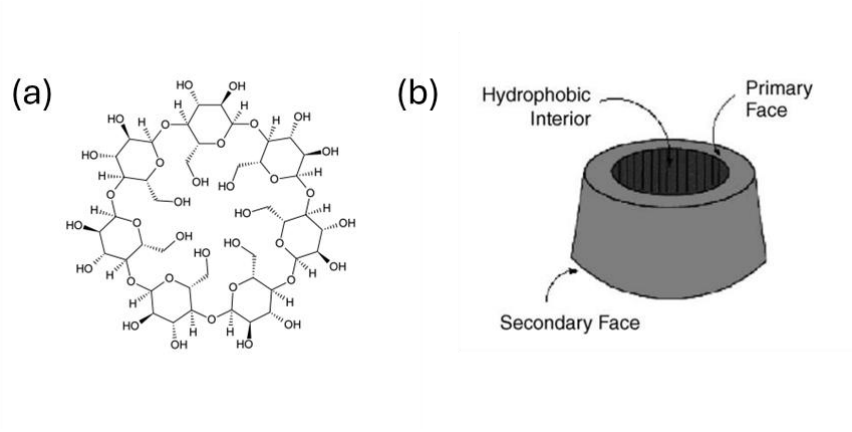

Figure 12: Structure of cyclodextrin scaffolds (a) chemical structure of beta-cyclodextrin, (b) representation of cyclodextrin as a molecular scaffold. Source: (b) Adapted from ref. [33] with permission. Copyright (2004) Elsevier.

The first step of the serine protease enzymatic mechanism can be mimicked by unfunctionalized cyclodextrins (Figure 13). Here, the hydroxyl groups in the rim can react with ester substrate **3**, cleaving the ester bond, resulting in acylation of the hydroxyl group.[32] Although this itself is not catalytic, it showed promise in using these types of structures as artificial enzymes.

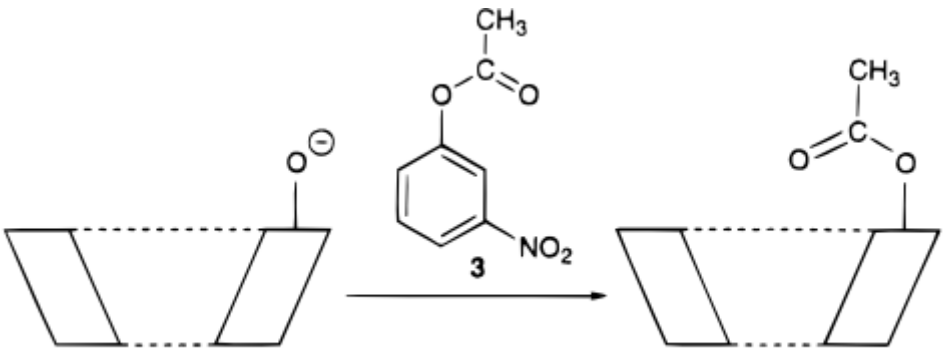

Figure 13: Cyclodextrin mimicking the first step of serine proteases. Source: Adapted from ref. [32] with permission. Copyright (1998) American Chemical Society.

An example of a cyclodextrin catalyst capable of facilitating ester hydrolysis is shown in Figure 14. Here, we have two cyclodextrin units linked by a bipyridyl group. This bipyridyl unit can bind a metal ion capable of facilitating hydrolysis. The two

cyclodextrin units act as binding sites for the enzyme, positioning the ester bond by the bipyridyl unit in order for catalysis to occur. In the presence of Cu^{2+}, several *p*-nitrophenyl esters can be hydrolysed with the catalyst, increasing the reaction rate by a factor of $10^4 - 10^5$.[34] Hydrolysis was found to decrease when only one cyclodextrin unit was present, indicating the importance of substrate binding interactions in catalysis.[34]

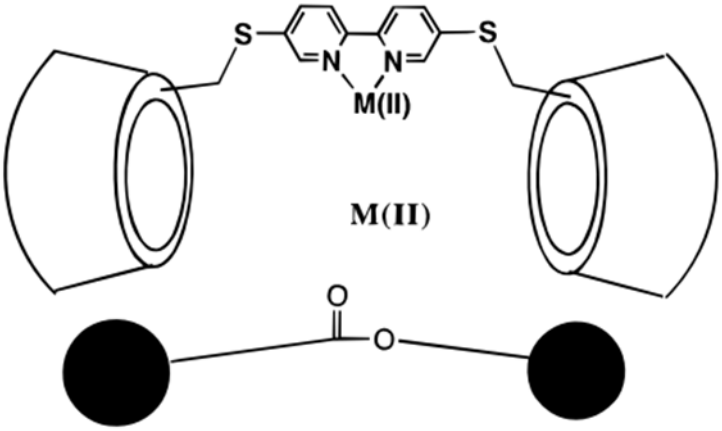

Figure 14: Cyclodextrin catalyst with bipyridyl linking unit. Source: Adapted from ref. [34] with permission. Copyright (1997) American Chemical Society.

Cucurbiturils

Cucurbiturils are a type of compound named after their resemblance to a pumpkin, the most well-known member of the *Cucurbitaceae* family (Figure 15).[35] This macrocyclic structure consists of six gycoluril units and twelve methylene bridges. The glycouril unit provides a hydrophobic pocket while the carbonyl groups at the top and bottom of the macrocycle add a polar component, allowing these structures to bind both polar and non-polar organic molecules.[36] These compounds are able to act as enzyme mimics due to their cation-receptor properties, as they tend to bind neutral and positively charged compounds within the macrocycle structure.[37]

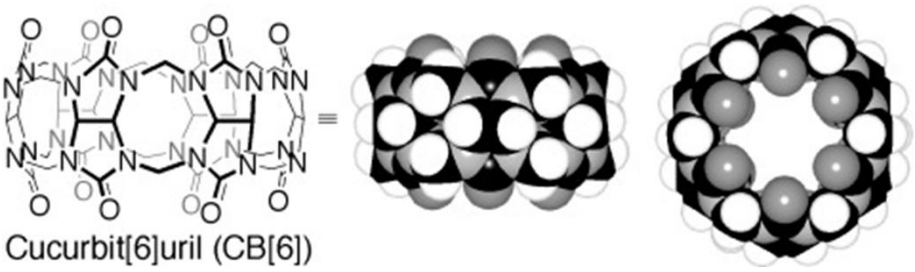

Figure 15: Structural formula, side and top views of a cucurbituril. Source: Reprinted from ref. [35] with permission. Copyright (2005) John Wiley and Sons.

Cucurbiturils have been shown to catalyse a wide range of different reactions, including cycloadditions, oxidations, and hydrolysis reactions.[38] Complexation with cucurbiturils can shift the pK_a of a substrate, allowing it to be protonated and therefore susceptible to hydrolysis. Therefore, acid-labile substrates can be catalysed by cucurbiturils if they contain specific anchoring groups that can bind strongly with the macrocycle.[37] This positions the reactive groups in the proximity of the cation receptor sites of the host (see Figure 16).[37] Klöck et al. were able to demonstrate an almost 300-fold rate enhancement of hydrolysis in the presence of their cucurbituril catalyst.[37]

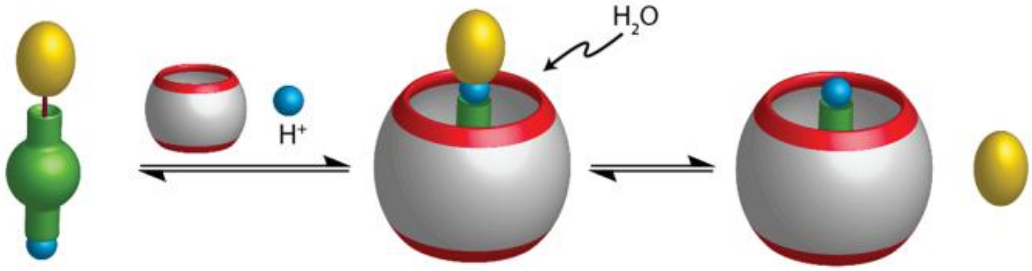

Figure 16: Schematic representation of how cucurbiturils can catalyse hydrolysis. Source: Reprinted from ref. [37] with permission. Copyright (2009) American Chemical Society.

Cavitands

Cavitands are another example of molecular scaffold systems that can be used for catalysis. Cavitands are container-shaped molecules that are designed to bind a target molecule within the structure (see Figure 17). These can be functionalised on the rim for catalysis. For example, a cavitand designed to facilitate aminolysis worked by selectively binding molecules with a trimethylammonium group.[39] This positioned the target near the catalytic functionality pyridine on the rim. Synergy between the recognition of the target

species in the cavity and the catalytic activity as a result of pyridine on the rim was observed.[39] The cavitand catalyst was shown to increase catalysis by 16 times compared with pyridine on its own.[39]

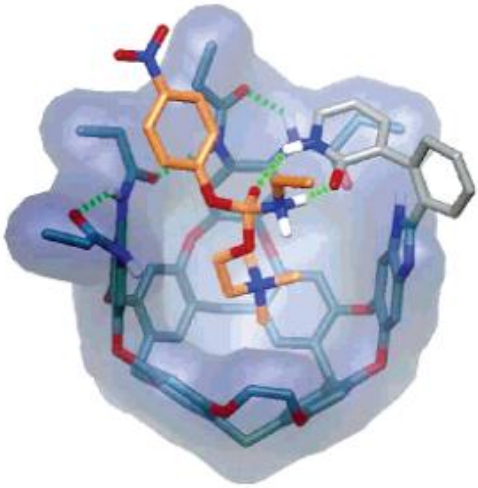

Figure 17: Structure of cavitand with target species bound. Source: Reprinted from ref. [39] with permission. Copyright (2004) American Chemical Society.

Cavitands have also been shown to catalyse the hydrolysis of choline carbonate through an enzyme-like mechanism (Figure 18).[40] This type of catalysis proceeds via three steps (Figure 19). First, the cavitand binds the substrate (choline carbonate **5**). Second, carbamoylation occurs with the carbamoyl group from the substrate attaching onto the cavitand's 2-aminobenzimidazole group to give compound **6**. This undergoes a rearrangement to form **7**, then the carbamate bond is hydrolysed in the third and final step to give back the catalysts **4** and the product **8**. The cavitand was found to have a much higher activity than individual 2-aminobenzimidazole units, highlighting the importance of substrate-catalyst binding, a feature of native enzymes that contributes to their exceptional catalytic activity.[40]

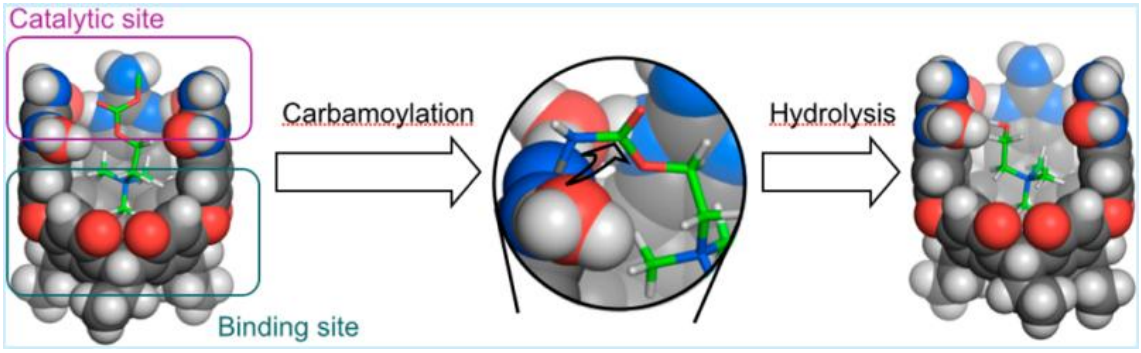

Figure 18: Cavitand for the hydrolysis of choline carbonate. Source: Reprinted from ref. [40] with permission. Copyright (2014) American Chemical Society.

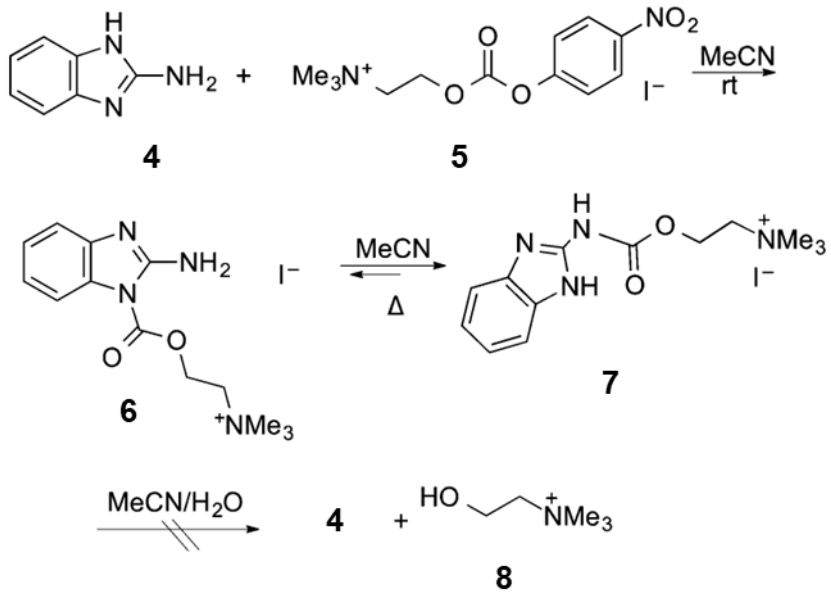

Figure 19: Steps for the catalysis of choline carbonate, starting with carbamoylation, rearrangement, then hydrolysis. Source: Adapted from ref. [40] with permission. Copyright (2014) American Chemical Society.

1.2.3 Dendrimers

Dendrimers are monodisperse, branched macromolecules that enable the formation of microenvironments, making them excellent artificial catalysts.[41] These structures can place the catalytic groups either at the dendritic core, on the branches or on the surface.

Dendritic architecture can be coupled with peptide sequencing to develop artificial catalysts that help combat the difficulty in predicting protein folding.[41] A dendritic peptide is forced to adopt a globular shape. This favours intramolecular interactions

between amino acids over intermolecular interactions, which lead to aggregations. A dendritic peptide **9** consisting of histidine amino acid residues, shown in Figure 20, was found to have a k_{cat}/k_{uncat} of 4000.[41] The histidine residues were found to be crucial for catalysis. Replacing just one of these residues would result in a 75% loss in activity, proving that cooperative catalysis was occurring between the residues in this dendrimer.[41]

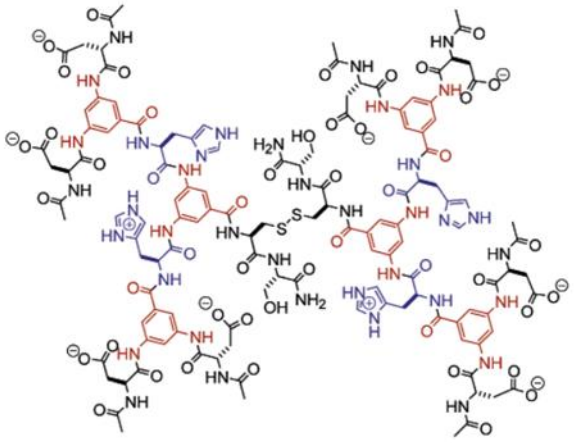

9

Figure 20: Initial dendritic peptide 9 synthesised by Darbre and Reymound. Source: Adapted from ref. [41] with permission. Copyright (2006) American Chemical Society.

An even larger dendritic peptide **10** was synthesised, consisting now of two amino acids in each branch (Figure 21) as opposed to one. This was found to have a k_{cat}/k_{uncat} of 90000 and a 20000-fold rate enhancement per catalytic site compared to 4-methylimidazole.[41] Here, it was proposed that the imidazole ring in the histidine residues acts as either a nucleophilic catalyst or as a general base catalyst for the activation of water as a nucleophile.[41]

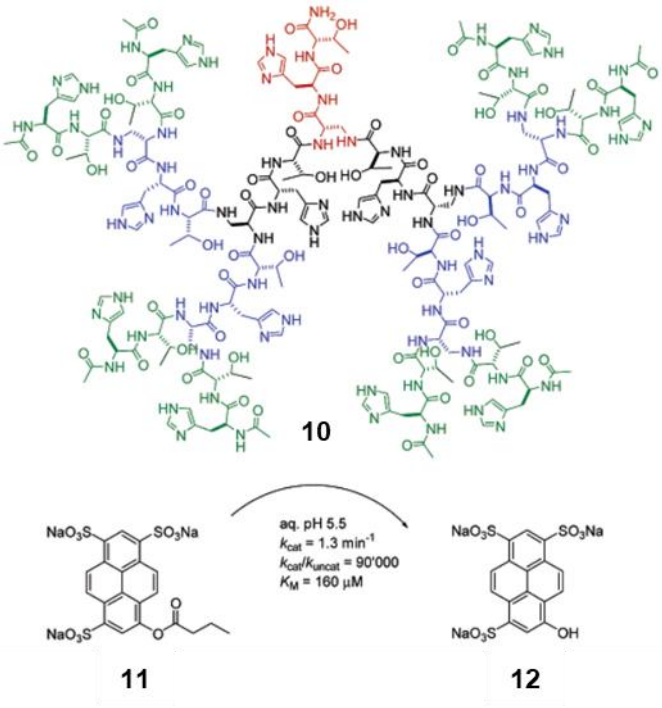

*Figure 21: Large histidine-containing dendritic peptide **10**. Source: Adapted from ref. [41] with permission. Copyright (2006) American Chemical Society.*

1.2.4 Attachment onto surfaces

Nanoparticle systems can often be used for catalysis, whereby the catalytic functional groups can be attached onto the surface of a nanoparticle to make a nanozyme. Gold nanoparticles can be functionalised with peptides containing one histidine, two arginine and one lysine residue, to create a nanozyme with esterase activity (Figure 22).[42] These amino acid residues have functional groups capable of facilitating nucleophilic, general-acid and/or base catalysis. In addition to this, they can help stabilise the negative charge of the transition state. Hydrophobic residues such as phenylalanine, tyrosine and leucine could be incorporated to enhance the hydrophobic nature of the reactive site, similar to what is seen around the active site of a native enzyme. This nanozyme was found to have a 3000-fold rate acceleration over that of the simple dipeptide, showing the advantage of attaching the key catalytic functional groups onto a surface to help promote cooperative catalysis.[42]

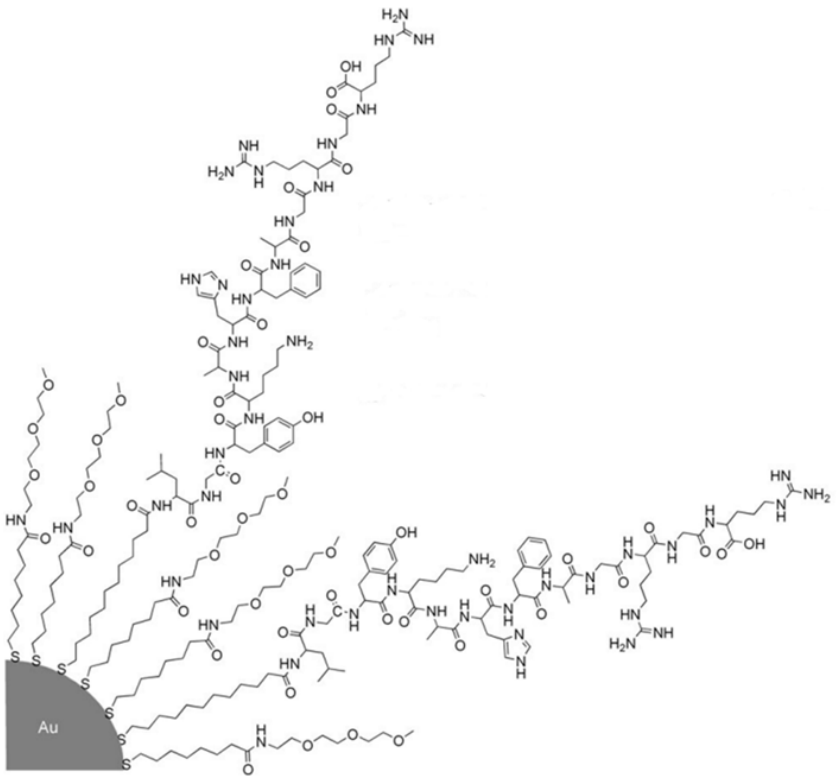

Figure 22: Structure of gold nanoparticle functionalised with peptides for esterase activity. Source: Ref. [42]/Wiley-VCH.

Another example of gold nanoparticles for esterase activity found the catalytic rate to be 30 times greater with the nanoparticles compared to the monomeric unit **13**.[43] Pasquato et al. functionalised the surface of the nanoparticles with long-chain (C12) thiols with an imidazole functionality for catalysis at the opposite end (see Figure 23). They deemed this increase in the rate to be due to the cooperativity experienced between neighbouring imidazole rings on the nanoparticle.[43] This cooperativity is not possible with the monomeric unit **13**.

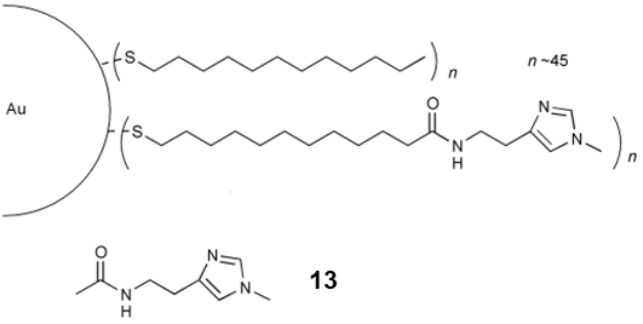

Figure 23: Gold nanoparticle functionalised with long-chain thiols containing imidazole rings and the imidazole monomeric unit (13). Source: Adapted from ref. [43] with permission. Copyright (2000) Royal Society of Chemistry.

1.2.5 Limitations of conventional catalysts

Molecular scaffolds, dendrimers or surface attachment examples just discussed focus on creating rigid binding pockets, along with restricting rotation of the bound substrate. These types of catalysts are effective enzyme mimics; however, challenges arise with the catalyst optimisation process. Any modifications to the functional groups used, or their position within the scaffold, require total synthesis of the entire catalyst to achieve. Therefore, the scaffolds mentioned above, and any artificial esterases made from these, are synthetically challenging to access. Many researchers are now looking to self-assembled catalytic systems to overcome these challenges.

1.2.6 Self-assembly

Self-assembly refers to the formation of supramolecular structures from smaller individual units via non-covalent interactions such as hydrogen bonding or hydrophobic interactions.[44] The advantages of a self-assembled system include its simplicity, low cost, dynamic nature and its ability to generate highly ordered structures.[44] These types of systems are comparable to native enzymes due to their dynamic structures, supramolecular forces driving substrate recognition, and their hydrophobic microenvironments for catalysis.[44] Self-assembled systems are also more synthetically accessible than catalysts attached onto molecular scaffolds, dendrimers or nanoparticles.[31] Exploring self-assembled catalytic systems for ester hydrolysis is one of the key focuses of this thesis, which will be explored in detail in Chapter 2.

1.3 Potential applications for artificial catalysts

Artificial catalysts could have the same industrial applications as native enzymes. In fact, the advantages that artificial catalysts offer in terms of stability and simplicity mean they could even be applied to industries where enzyme catalysts are not a good fit. Types of industries which could benefit from artificial catalysts include food and beverage, pharmaceutical, detergent, textile, and even recycling industries.

1.4 PETase

PETases are a new type of hydrolase enzyme that can break down PET plastic. These enzymes have been discovered in plastic-degrading microbes, capable of cleaving the ester bonds in PET.[45]

Polyethylene terephthalate (PET) is a thermoplastic polymer used in everything from food and drink packaging to polyester used in the textile industry, and even films used to make moulds for automotive and electrical parts. 27,653 million tons of PET are produced every year to meet this demand.[45] Though PET is a very useful material, these products typically have short life spans, leading to high consumption and disposal rates. This polymer is non-biodegradable, so disposal of PET has sparked serious environmental and economic concerns.[46] Recycling PET is the most viable waste treatment method, with the conventional recycling method shown in Figure 24. This starts with a water wash to remove any potential contaminants, followed by mechanical reprocessing to resize the plastic into flakes. These then undergo colouring/agglomeration followed by extrusion/palletisation before being remade into 'new' PET products.[47] The main advantage of mechanical recycling is the low cost when compared to other recycling methods. However, over time, this method can weaken the plastic and can result in decolouration of the final product.[46,47] Therefore, products made with recycled PET often also include new PET in order to retain the desired properties.

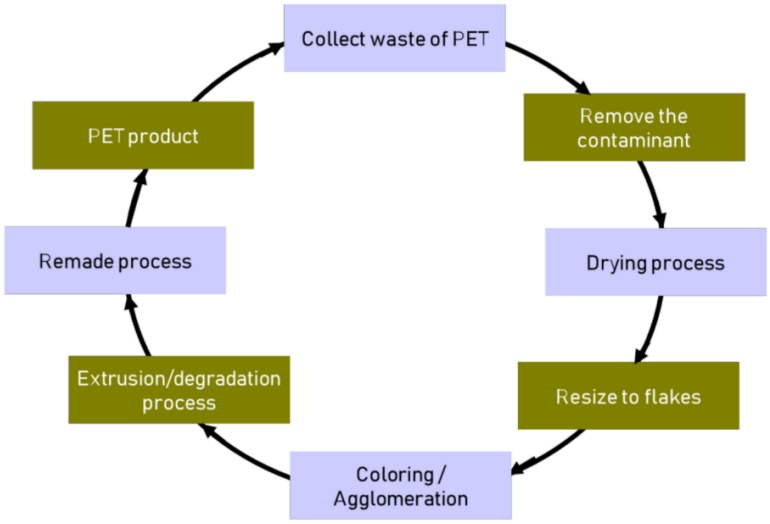

Figure 24: Flowchart of the conventional mechanical recycling process of PET. Source: Ref. [47]/MDPI.

An alternative PET recycling method is chemical recycling. Here, the materials that were initially used to make PET are reformed at the end of the process. Chemical recycling produces products that can be used to make new PET without any loss in structure or functionality.[48] Therefore, this method of recycling could create a circular economy for PET. However, chemical recycling is much more expensive compared with mechanical recycling. This also requires harsh conditions, such as high temperatures, to achieve depolymerisation. There are several methods of chemical recycling, and these are hydrolysis, methanolysis, glycolysis, ammonolysis and aminolysis.[46] We were particularly interested in hydrolysis as this method is similar to the way PETases break down PET plastic.

When PET is hydrolysed, the ester bonds are broken down to form terephthalic acid (TPA) and ethylene glycol **14**, shown in Scheme 1. Typically, hydrolysis involves the addition of water across the ester bond in either acidic or basic conditions. For PET, quite harsh conditions are required, with temperatures between 200-250 °C and pressures up to 2 MPa.[46–48] Even with these conditions, depolymerisation can take a long time to occur.[48] This is where enzymatic catalysts can be beneficial.

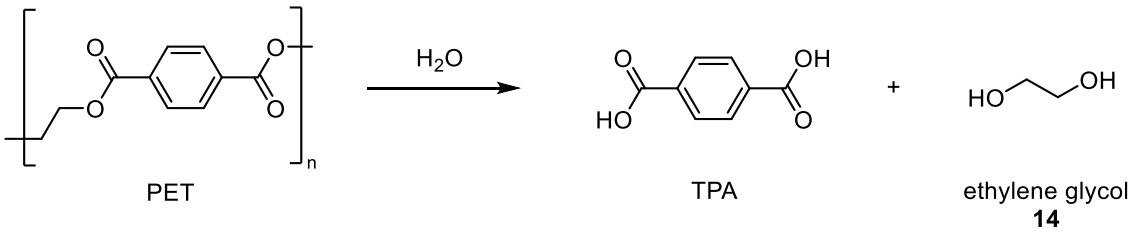

Scheme 1: Hydrolysis of PET.

Two enzymes have been isolated from the bacterium *Ideonella sakaiensis* that are involved in PET hydrolysis.[49] The first is PETase, which is responsible for cleaving PET into bis-hydroxyethyl terephthalate (BHET) and mono-hydroxyethyl terephthalate (MHET). The second is a MHETase enzyme, which can then take the MHET produced from PETase and cleave this into TPA and ethylene glycol **14**, two products that can be used by the bacterium for catabolism.[49] The Ser-His-Asp catalytic triad has been identified in the active site of PETase enzymes.[50] In comparison to other hydrolase enzymes, such as cutinases, the active site of PETase is wider. This wider substrate-binding site is likely an important feature as to why PETase can accommodate the bulky substrate PET. Tryptophan amino acid residues have also been found near the active site in these enzymes. These are thought to aid in substrate binding due to the interactions experienced between aromatic ring structures. Chen et al. proposed a mechanism of action for PETases shown in Figure 25. Here, tryptophan residue 156 adjusts its orientation to help bind the PET substrate through hydrophobic interactions. This positions the carbonyl group of the substrate in the oxyanion hole. We see the same mechanism of action from our catalytic triad that is found in all hydrolase enzymes. The aspartic acid residue forms a hydrogen bond with the histidine residue. The nitrogen in the imidazole ring of the histidine can then deprotonate the serine to form a nucleophile capable of attacking the carbonyl in PET. The ester group is then cleaved, and the remaining benzoic group is then released from the binding site.[50] This reaction mechanism was further analysed by Burgin et al using computational studies. These results supported the mechanism initially proposed by Chen et al.

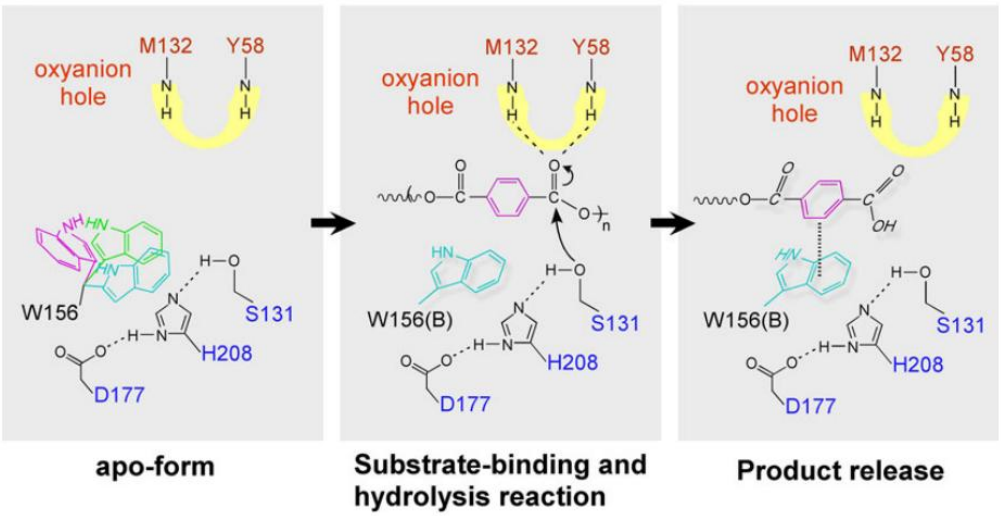

Figure 25: Mechanism of action for PETase enzyme. Source: Adapted from ref. [50] with permission. Copyright (2018) John Wiley and Sons.

Enzymes offer a huge advantage in terms of the efficiency of chemical reactions, as they are such excellent catalysts that function in much milder conditions. Compared to mechanical recycling processes, PETases can selectively degrade PET, removing any impurities at the same time.[51] Enzymes also use less energy and produce less waste than mechanical recycling methods.[51] However, they have several drawbacks previously discussed that prevent these from being used on an industrial scale, including their stability, narrow operating conditions, reuse, and health and safety risks of the enzyme. If we could develop an artificial PETase, we could overcome both the limitations of native enzymes and the limitations of current mechanical PET recycling methods to create an alternative method to tackle PET recycling.

An example of this would be the binuclear catalyst designed by Zhang et al., which was found not only to catalyse the degradation of PET but could be used to demonstrate closed-loop recycling of bottle-grade PET. Inspired by native hydrolase examples of binuclear metalloenzymes, Zhang et al. designed a binuclear catalytic system utilising two Zn^{2+} metal ions for catalysis (Figure 26). This catalyst (Zn_2/C) was found to completely depolymerise PET into its monomers within 10 weeks at pH 8 and 40 °C, with conventional hydrolysis catalysts zinc acetate and zinc oxide showing no activity under the same conditions (Figure 27).[52] Interestingly, they also investigated closed-loop recycling using the TPA they produced from hydrolysis to make new PET. They found this made PET with similar characteristics to that made from virgin pure TPA, and this

was found to meet bottle grade standards.[52] This is an exciting result as it shows the immense benefits that could be had from creating an artificial PETase, which could revolutionise the PET recycling industry, with the potential for a huge positive environmental impact if PET can be recycled under milder conditions more efficiently.

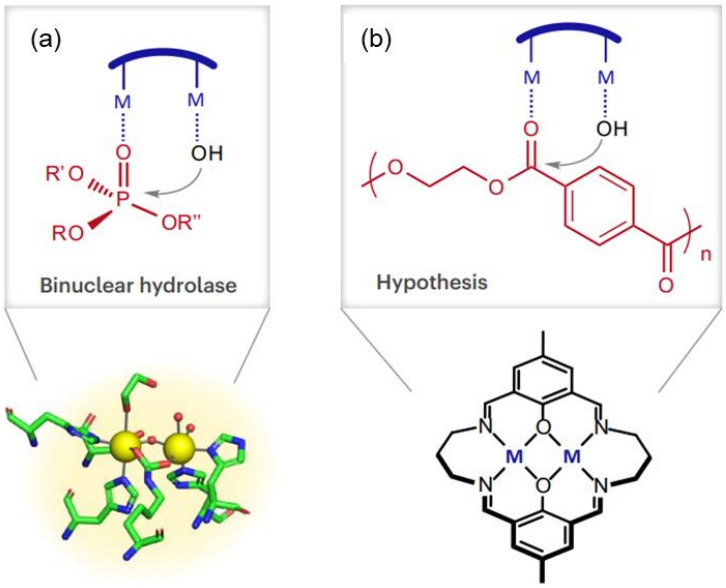

Figure 26: Binuclear metalloenzyme (a) used as inspiration to design a binuclear catalytic system (b) for the hydrolysis of PET. Source: Adapted from ref. [52] with permission. Copyright (2023) Springer Nature.

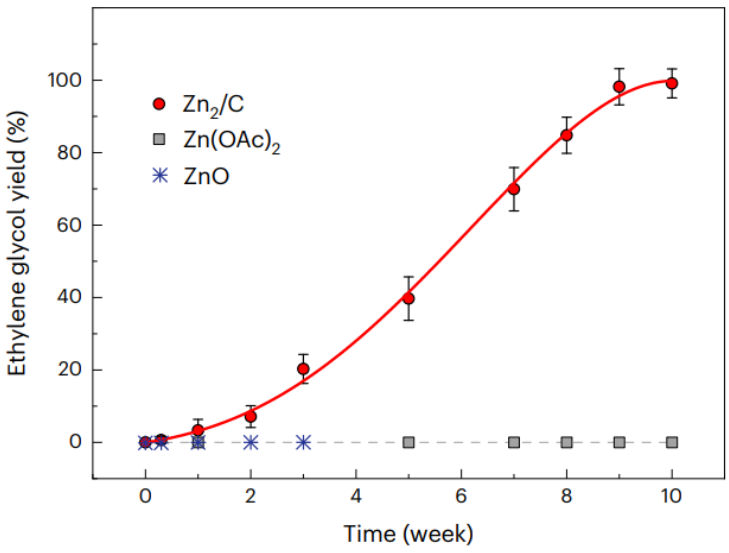

Figure 27: Amount of ethylene glycol produced by artificial PETase (Zn_2/C) compared with traditional hydrolysis catalysts $Zn(OAc)_2$ and ZnO. Source: Adapted from ref. [52] with permission. Copyright (2023) Springer Nature.

1.5 Aims of the thesis

The overarching aim of this thesis was to develop new strategies for constructing modular artificial esterase systems based on self-assembly. This was achieved by functionalising surfactants and small-molecule ligands with catalytic motifs inspired by the active sites of native esterases, as well as by previously reported artificial esterase systems, and subsequently inducing their organisation into vesicular or coordination-polymer architectures capable of catalysis. In contrast to traditional approaches to artificial catalyst design, such as rigid molecular scaffolds or dendrimers, which often require complex multistep syntheses, these modular, self-assembled systems are synthetically accessible and readily tunable. Importantly, their modularity enables rapid optimisation of catalytic performance through straightforward variation of component structure or composition. Moreover, the dynamic and adaptive nature of self-assembled architectures more closely reflects the structural flexibility of native enzymes, offering a promising route towards artificial catalytic systems that can approach enzymatic levels of activity.

Chapter 2 explores the use of self-assembly as a strategy for constructing artificial esterase catalysts. In this chapter, hydrophobic interactions are exploited as the primary driving force for assembly through the design of functionalised surfactants bearing catalytically active headgroups. Upon self-assembly, these headgroups are brought into close proximity, enabling cooperative interactions that give rise to esterase activity. A central objective of this chapter is to demonstrate how modular design principles can be applied to rapidly screen and optimise a wide range of catalytic combinations, thereby providing an efficient and versatile route to the discovery and development of artificial esterases.

Chapter 3 builds upon the initial self-assembled catalytic system by introducing a more rigid, coordination polymer-based architecture while retaining a modular design strategy. This is achieved through the incorporation of catalytic functionalities into thiol-containing ligands, which undergo self-assembly via silver-thiolate coordination to form extended polymeric structures. The aim of this chapter is to demonstrate how increased structural rigidity can enhance catalytic efficiency by enforcing more defined and persistent catalytic environments, while preserving the modularity required for systematic optimisation and rapid tuning of catalytic performance.

Finally, Chapter 4 explores potential future directions and applications arising from the catalytic systems developed in this thesis, with particular emphasis on the extension of these concepts toward more dynamic and adaptive modular architectures. The possibility of catalyst self-selection from combinatorial libraries is proposed as a promising avenue for future research, offering a powerful strategy for the autonomous optimisation of catalytic function. Such systems could enable the identification of the most active catalyst assemblies under given conditions without the need for exhaustive manual screening.

In addition, the most efficient silver-thiolate coordination polymer developed in this work shows potential for application in the catalytic degradation of polyethylene terephthalate (PET), highlighting an exciting opportunity for sustainable plastic recycling. As an extension of the work, the functionalised thiol ligands introduced in Chapter 3 may be repurposed within dynamic molecular scaffold systems, where catalysts are formed *in situ* through reversible disulfide bond formation. This approach could enable the construction of catalytic systems capable of structural reorganisation, adaptability, and self-optimisation, further advancing the development of next-generation artificial catalytic systems.

Chapter 2: Artificial Esterases Formed by Self-Assembly

2.1 Introduction

Self-assembly refers to the spontaneous formation of supramolecular structures from smaller individual units. These structures are typically brought together using hydrogen bonding or hydrophobic interactions. There are several key advantages that self-assembled systems offer compared to more traditional types of artificial catalysts discussed in Chapter 1, including the simplicity, low cost and dynamic nature of the assembled system.[44] The modularity of these systems makes them ideal candidates for catalyst discovery and optimisation, as changes made to the system are less synthetically taxing compared with traditional methods.

2.1.1 Self-assembled artificial esterases reported in the literature

The self-assembly of peptides for catalysis

Peptides have been widely used in the literature to create artificial esterases. The amino acids in the peptides are usually chosen based on their side chain functionalities. These peptides can then be self-assembled into a variety of structures, such as fibrils[53,54], nanofibers[55–58], and nanotubes[44,59]. The key feature all these systems share is that the assembly of the peptides increases the catalysis compared to the individual non-assembled peptides. This positions the catalytic residues close together to facilitate cooperative catalysis, mimicking the positioning of residues as a result of folding in native enzymes.[60]

A photo-switchable peptide designed by Zhao et al. was self-assembled into fibrils that exhibited enhanced catalytic activity when assembled (Figure 28). The irradiation with UV light then disassembled these supramolecular structures, resulting in a decline in catalytic activity, essentially allowing the catalysis to be switched on and off using UV and visible light. The peptide consisted of a photo-switchable azobenzene unit and a catalytic histidine residue, as imidazole functionalities are an essential part of most native hydrolase active sites.[54] The *E*-isomer (trans) azobenzene allows the peptides to self-assemble into fibrous networks for catalysis. Here, they investigated the catalysis using the model substrate *p*-nitrophenyl acetate. The activity of their histamine-containing peptides (Azo-GFGH) was compared to control molecules (Azo-GFG), missing this

histidine residue (Figure 29). Looking at the red bars, we can see that histamine is required to see a great increase in the catalytic activity. They also showed that self-assembly is important, with the self-assembled peptides (filled red bar) having a higher catalytic activity than the disassembled system (filled blue bar). Zhao et al. proposed the mechanism by which catalysis occurs (Figure 30) based on the general acid-base catalysis that histidine facilitates in native enzymes. When in the *E*-conformation, the histidine residues are aligned, resulting in the basicity of the imidazole being enhanced by neighbouring histidine residues.[54] This lowers the pK_a of a bound water molecule, allowing the nitrogen in the imidazole ring to deprotonate the water, leaving a hydroxyl group for nucleophilic attack of the substrate.

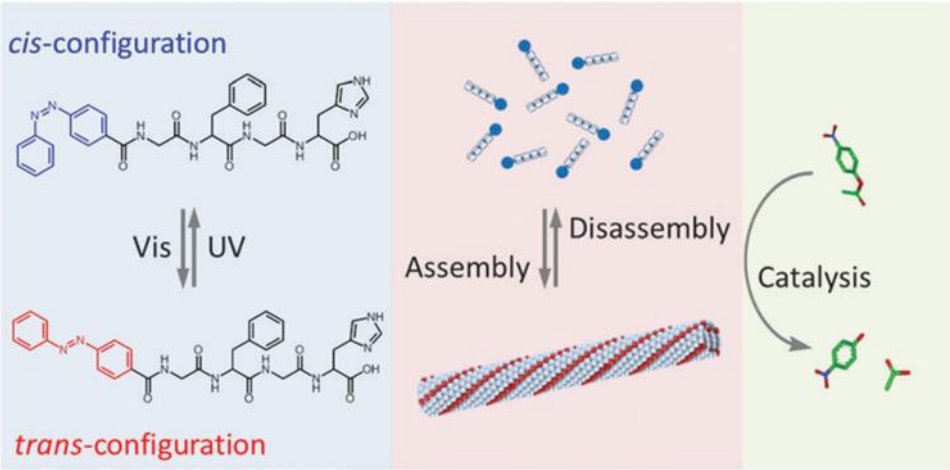

Figure 28: Photo-switchable hydrolase mimic from the self-assembly of peptides. Source: Adapted from ref. [54] with permission. Copyright (2018) Royal Society of Chemistry.

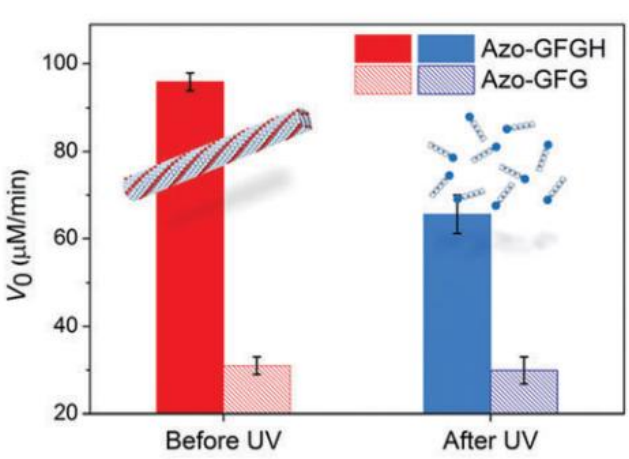

Figure 29: Catalytic activity of histidine-containing peptide (Azo-GFGH) and control peptide (Azo-GFG) before and after being irradiated with UV light. Source: Adapted from ref. [54] with permission. Copyright (2018) Royal Society of Chemistry.

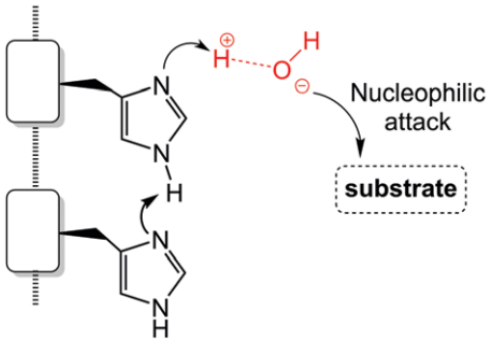

Figure 30: Mechanism for the acid-base catalysis enhanced by neighbouring histidine residues. Source: Adapted from ref. [54] with permission. Copyright (2018) Royal Society of Chemistry.

A nanofiber catalyst formed from self-assembled peptides was found to have both hydrolase and retro-aldolase activity (Figure 31).[58] Here, Ghosh et al. designed 7-residue peptides which could assemble, orienting the catalytic residues, lysine, histidine and tyrosine close together to facilitate cooperative catalysis. All three catalytic units proved to be essential for both hydrolase and retro-aldose activity, with a 280-fold increase seen for the cascade reaction compared with the background.[58]

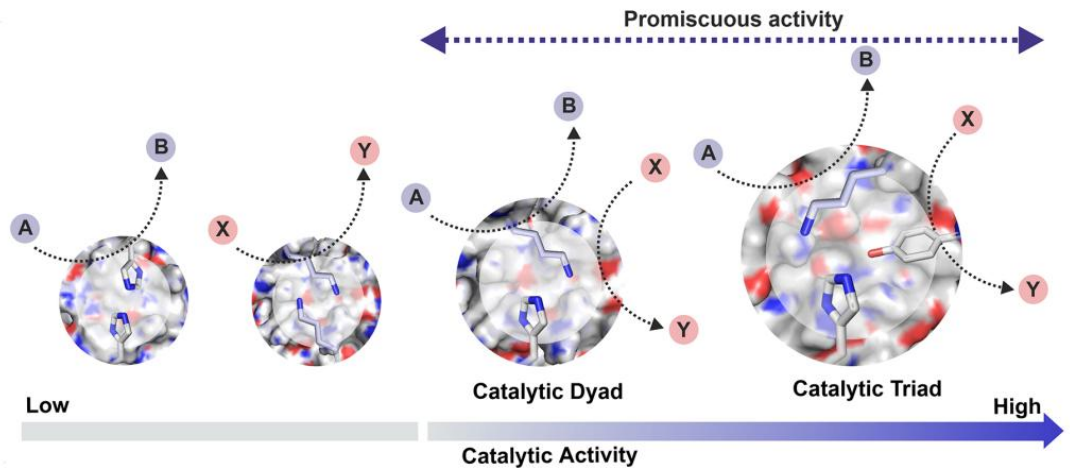

Figure 31: Self-assembled nanofiber catalyst with both hydrolase and retro-aldolase activity. Source: Adapted from ref. [58] with permission. Copyright (2023) American Chemical Society.

Amyloid-forming peptides have been shown to facilitate a zinc-dependent catalytic mechanism similar to that of the native enzyme carbonic anhydrase (Figure 32).[53] The active site of these enzymes consists of Zn^{2+} ions, which lower the pK_a of a bound water molecule, giving a hydroxide ion capable of undergoing nucleophilic attack of the substrate.[53] Histidine residues were incorporated into the peptide due to their ability to bind Zn^{2+} ions for catalysis. Typically, three histidine residues are required to bind Zn^{2+}. Their designed peptides only contained two histidine residues; therefore, the peptides must self-assemble to place three histidine residues close enough to bind a Zn^{2+} ion. Rufo et al. found the activity of their artificial enzyme was Zn-dependent, with no activity seen in the absence of this ion, with their optimised peptide having 100-fold greater catalytic activity in the presence of Zn^{2+}. The self-assembly of these peptides was also enhanced in the presence of Zn^{2+} by a factor of 10.[53]

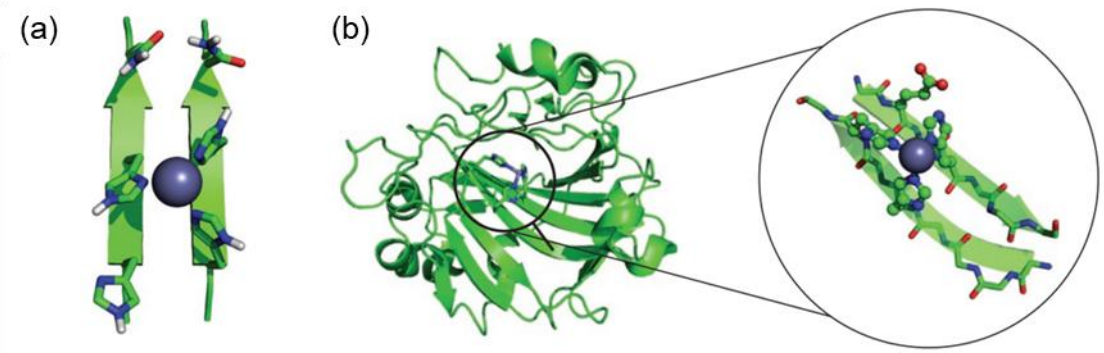

Figure 32: Seven-residue peptide self-assembling to give amyloid fibrils (a) based on the native enzyme carbonic anhydrase (b). Source: Adapted from ref. [53] with permission. Copyright (2014) Springer Nature.

Peptides can also be self-assembled to form nanofibers, fibrous materials with a wide range of potential applications in medicine, electronics, sensors and catalysis.[61] These materials are advantageous for catalysis due to their high surface area to volume ratio.[61]

For example, dipeptides containing histidine and phenylalanine residues have been self-assembled to form nanofibers, which can facilitate ester hydrolysis in a manner similar to the catalytic triad found in the active site of native esterase enzymes (Figure 33).[55] This simple dipeptide also consists of a terminal thiol, which is separated from the amino acid residues via a hydrophobic chain. This hydrophobic chain helps to drive the assembly of the dipeptides, along with the hydrogen bonding that can occur between the histidine and phenylalanine dipeptide heads. All three key features of this catalytic system (histidine, phenylalanine and thiol) were found to be an important part of achieving high catalytic rates.[55] The mechanism of action for this catalyst was proposed by Liu et al. Here, a hydrogen bond is present between the oxygen atom of the carbonylate group in phenylalanine and the hydrogen atom on the nitrogen in the imidazole ring of histidine. This increases the pK_a of the imidazole, resulting in a stronger base.[55] The N atom of the imidazole ring can then deprotonate the thiol from a neighbouring dipeptide to form a nucleophile. The sulphur from the deprotonated thiol can then attack the carbonyl of the ester, resulting in hydrolysis. This mechanism is very similar to that of the catalytic triad found in native esterase enzymes. In the catalytic triad, histidine, aspartic acid, and serine work together for catalysis.[17] In this example by Liu et al., phenylalanine takes the role of aspartic acid, while serine is replaced by the thiol functional group.

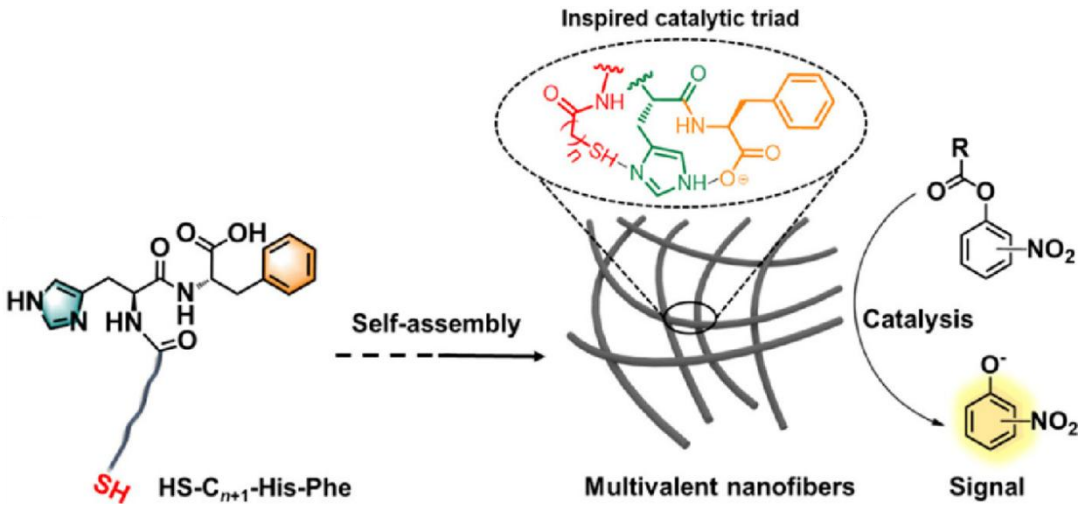

Figure 33: Self-assembly of dipeptides to form nanofibers for esterolysis. Source: Ref. [55]/American Chemical Society.

Molecular imprinting could be used to enhance the catalysis of a self-assembled nanofiber catalyst.[56] Here, peptide monomers consisting of either a serine, histidine or aspartic acid residue were self-assembled to form a nanofiber catalyst (Figure 34). The catalytic centre of this artificial esterase could then be optimised using molecular imprinting. This was achieved by adding an imprinting template, typically a substrate, product, or analogue, to the catalyst and incubating for 24 hours. After which, the template could be removed, leaving behind the optimised catalytic centre. Wang et al. found that molecular imprinting increased the catalysis rate due to the functional groups' preorganisation. It also resulted in higher catalysis for the combination of all three peptides (CoA-HSD$_{max}$) compared to the histidine-containing peptide on its own (SA-H) (Figure 35).[56] This indicated that the catalytic triad has greater activity than histidine on its own when the peptide can be oriented correctly for catalysis via molecular imprinting. When in the correct orientation, these functional groups can facilitate ester hydrolysis via the same mechanism as the catalytic triad found in native enzymes.[56]

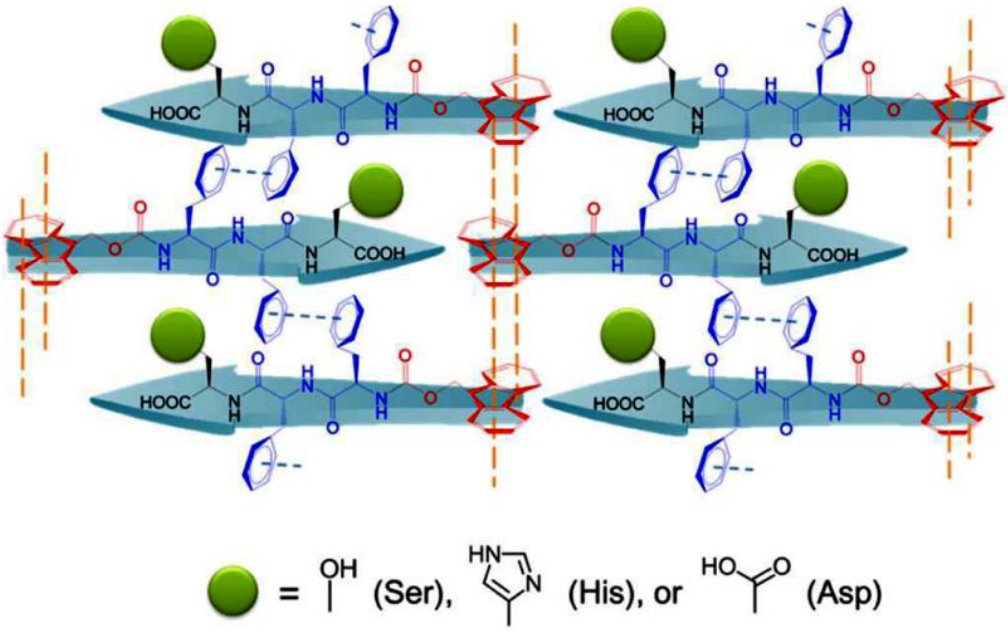

Figure 34: Secondary structure of peptides forming nanofibers. Source: Reprinted from ref. [56] with permission. Copyright (2016) American Chemical Society.

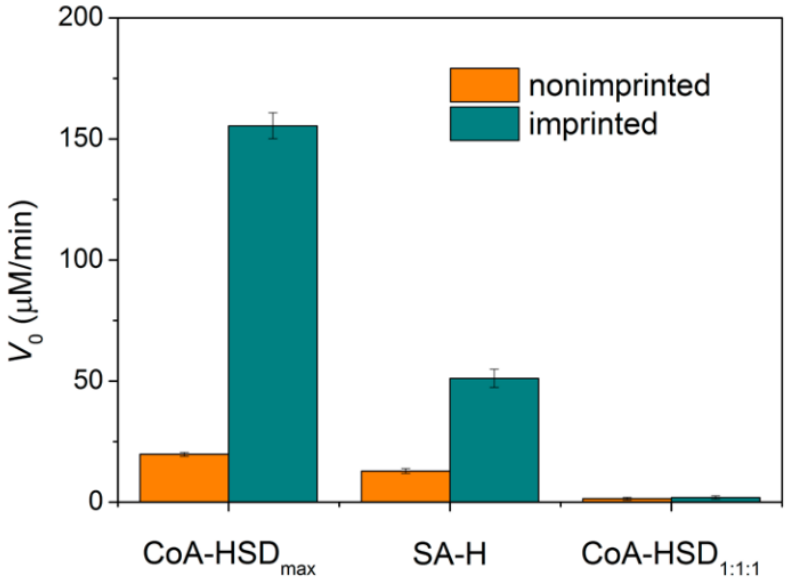

Figure 35: Catalytic rate of molecularly imprinted and nonimprinted peptide-based nanofibers. Source: Adapted from ref. [56] with permission. Copyright (2016) American Chemical Society.

Imidazole and guanidyl functionalities could be incorporated into peptides, which have been shown to self-assemble into both nanofibers[57] and nanotubes[44], exhibiting high catalytic activity. The catalytic mechanism was discussed for both systems, with the imidazole ring deprotonating a water molecule, producing a hydroxide ion for

nucleophilic attack of the substrate *p*-nitrophenyl acetate.[57] This forms a tetrahedral transition state, which is stabilised by the guanidine group binding the oxide ions of the intermediate.[44,57] The C-O bond is then activated for cleavage, releasing *p*-nitrophenol. Figure 36 shows a schematic representation of this mechanism for the nanofiber catalyst. Interestingly, Huang et al. investigated the importance of the guanidines' stabilisation role in their nanotube catalyst. Figure 37 shows that the activity of the co-assembled peptides was greater than that of peptides containing just the imidazole functionality, proving that guanidine does play an important role in the reaction mechanism.[44]

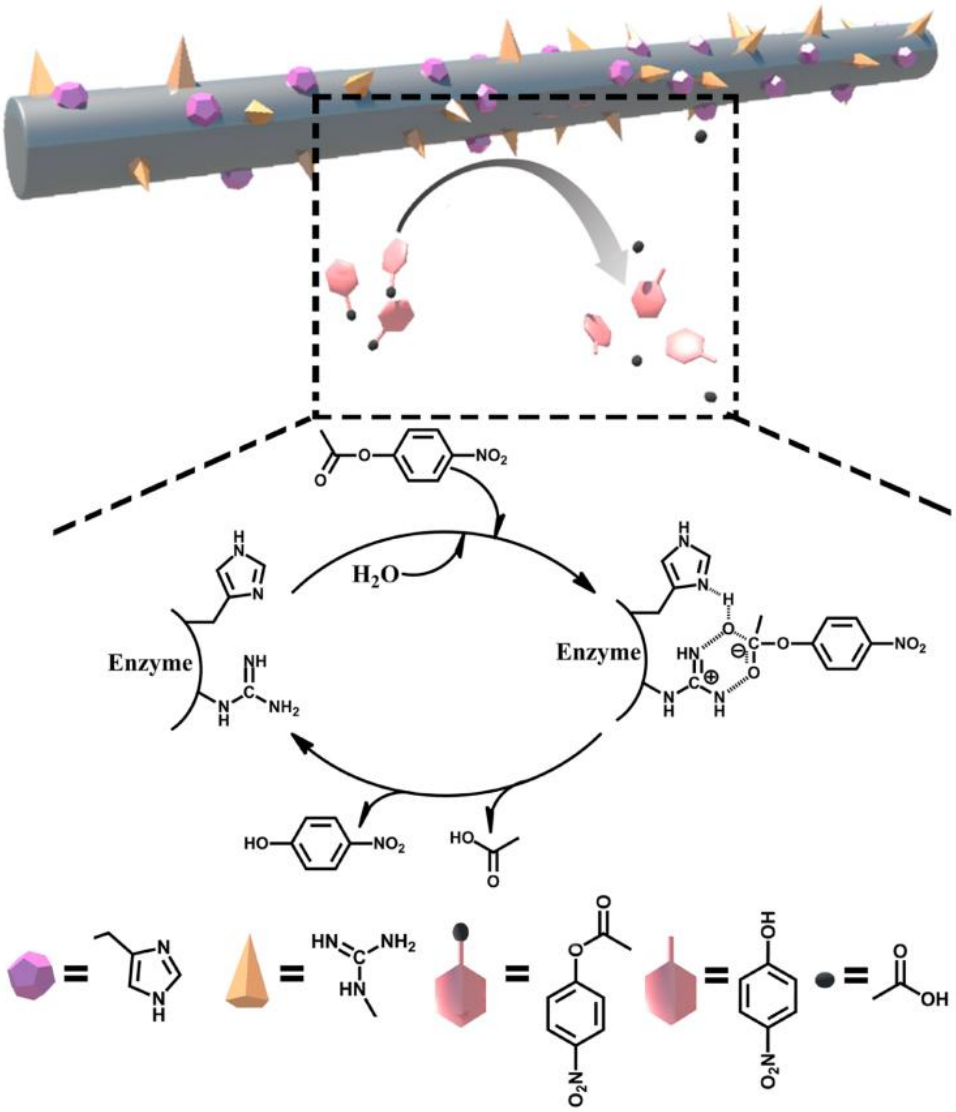

Figure 36: Mechanism of action for self-assembled histidine and guanidine nanofiber catalyst. Source: Reprinted from ref. [57] with permission. Copyright (2014).

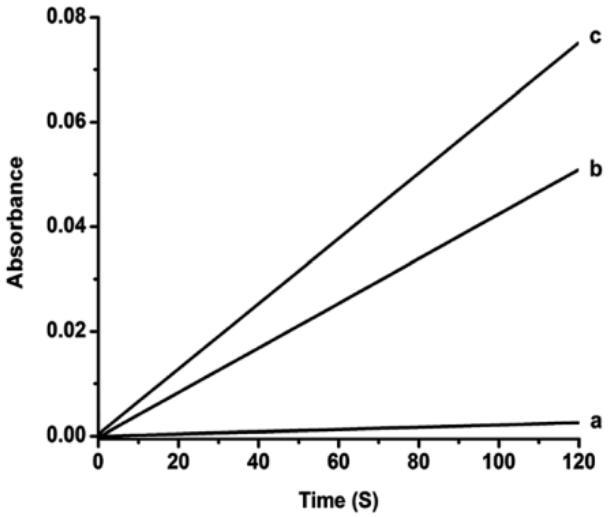

Figure 37: Esterolysis plot for control (a), imidazole-containing peptides (b), and a mix of imidazole and guanidine-containing peptides (c). Source: Reprinted from ref. [44] with permission. Copyright (2013) Royal Society of Chemistry.

A nanotube esterase, which can cleave both activated and non-activated esters, was developed using amine and imidazole functionalities (Figure 38).[59] The imidazole functionality is known to facilitate ester hydrolysis on its own; however, when coupled with the amine, catalysis was enhanced due to the formation of an imine bond with the substrate.[59] This bond is formed between the amine and a ketone functional group in the substrate and, in this way, acts as a binding pocket for the artificial enzyme, orienting the substrate close to the catalytic imidazole group. Peptides were designed with both an imidazole ring and a lysine residue at the *N*-terminal, which would then self-assemble to form nanotube structures. The lysine residue was replaced with an arginine residue, which led to a decrease in catalysis by 1 order of magnitude.[59] This proved the importance of lysine forming the imine bond with the substrate for catalysis.

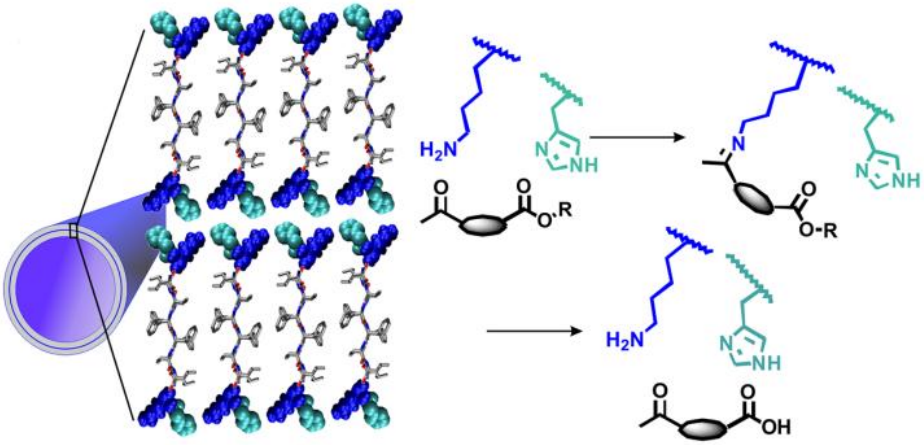

Figure 38: Peptides with terminal lysine residues and imidazole functionalities self-assemble to form nanotubes for catalysis. Source: Adapted from ref. [59] with permission. Copyright (2020) American Chemical Society.

Molecularly imprinted polymers as artificial esterases

Molecularly imprinted polymers (MIPs) are polymers that have been developed using a technique involving templating to form cavities that have particular characteristics based on the template used.[62] The polymer is allowed to self-assemble in the presence of a template molecule and specific cross-linkers. The templates used are often similar in shape and size to the target substrate. After polymerisation, the template molecule is removed, leaving behind a specifically designed cavity which has molecular recognition characteristics for the chosen substrate.[62] In this way, MIPs can mimic enzymes, as this cavity acts like the active site in an enzyme.

Yan Zhao's research group has focused on using MIPs for catalysis. Their work published in 2023 and 2024 focused on creating artificial esterases that can cleave both highly activated *p*-nitrophenyl and non-activated esters.[63,64] Zhao and coworkers start by synthesising their MIPs through the templated polymerisation of cross-linked micelles. For example, their 2018 publication used amines **18a–18d** as templates for *p*-nitrophenyl hexanoate (PNPH) due to their ability to act as ligands for Zn^{2+} complexation and their stability in the presence of Zn^{2+} ions (Figure 39).[65] The use of these templates essentially creates a binding site for the substrate similar to the active site of an enzyme. These binding sites are then able to distinguish between different substrates. For example, their 2018 catalyst was able to pick the desired substrate (PNPH) out from *p*-nitrophenyl acetate, with the rate of catalysis for PNPH being six times that for the acetate substrate.[65]

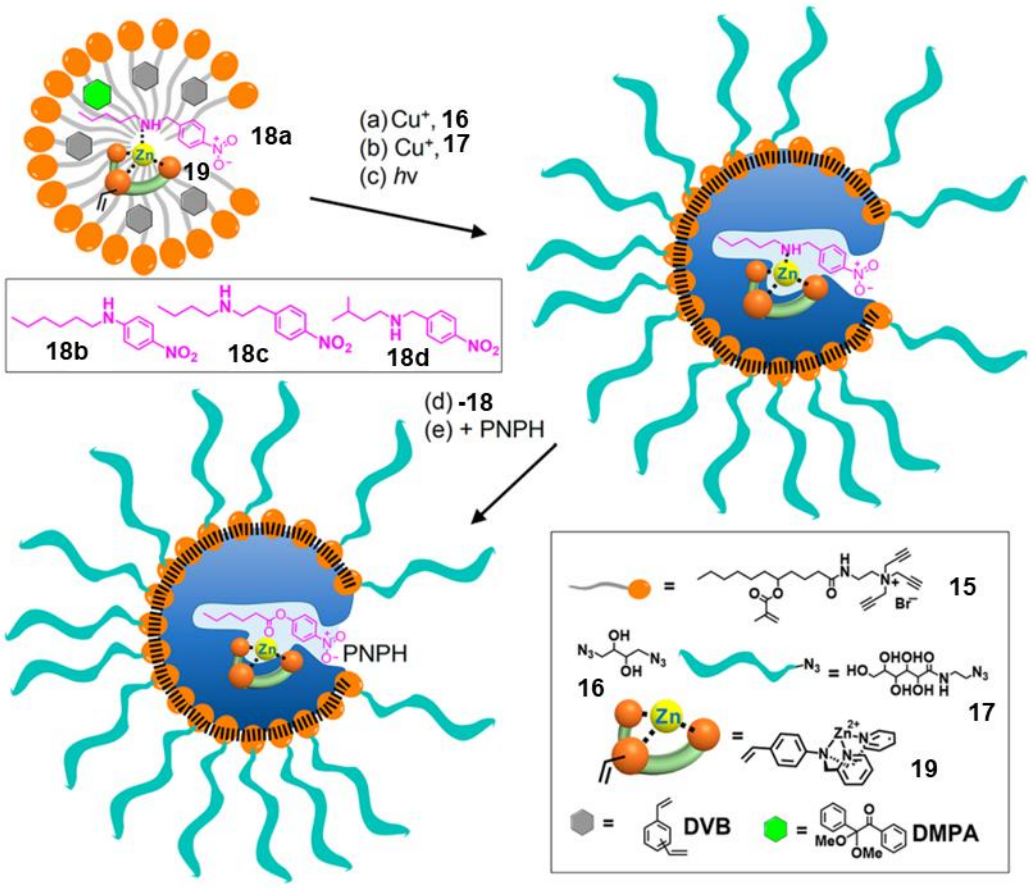

Figure 39: Synthesis of molecularly imprinted polymers for ester hydrolysis. Source: Adapted from ref. [65] with permission. Copyright (2018) American Chemical Society.

The MIPs synthesised by Yan Zhao's group have used a variety of different functional groups for catalysis. These include Zn^{2+} binding groups such as dipicolylamine[63,65], pyridine[64,66], thiouronium[63,64,67], and carboxylic acids[68]. These catalysts compare favourably to other artificial esterases in the literature, with k_{cat}/K_M values of 205 M^{-1} s^{-1} and 379 M^{-1} s^{-1}, which are 5 – 10 times greater than those of other literature examples.[63,64] This suggests that well-defined binding pockets formed from MIPs have significant benefits for catalysis.

Engineered metalloproteins

A metalloprotein was engineered that had a catalytic activity 100-fold less than carbonic anhydrase (the enzyme it was based upon).[69] The catalytic metal site was designed along with the amino acid sequence, which would fold into the three-dimensional structure of the catalyst (Figure 40). The catalytic site of this protein was based around the metal ion Zn^{2+} due to its role in carbonic anhydrase. The peptide was designed to have histidine

residues bind a Zn^{2+} ion for catalysis. In addition to the Zn^{2+} ion, Zastrow and coworkers also used a Hg^{2+} metal centre to help with the stabilisation of the protein. This is the first report of a hydrolytic metalloenzyme that had been engineered to be competitive with carbonic anhydrase, one of the fastest known natural metalloproteins.[69]

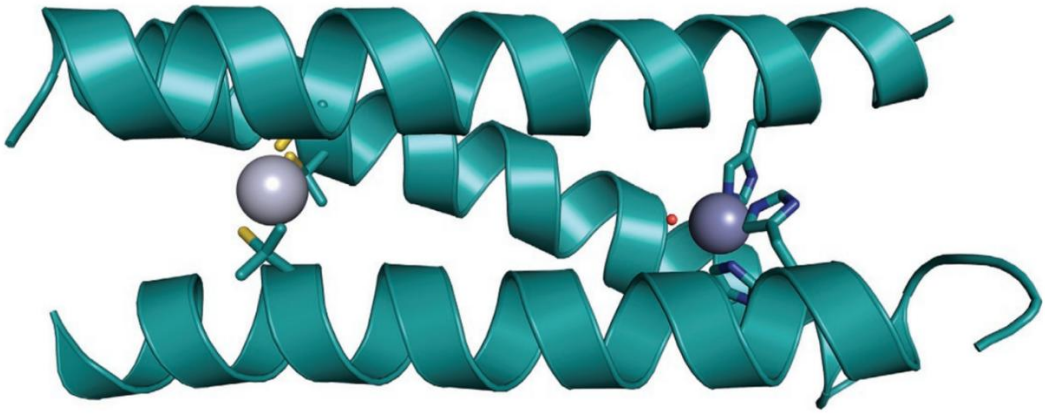

Figure 40: Engineered metalloprotein for ester hydrolysis. Source: Adapted from ref. [69] with permission. Copyright (2011) Springer Nature.

Self-assembly of functionalised surfactants

The self-assembly of functionalised surfactants to form catalytic pockets within micellar or vesicular structures is another exciting method used to develop an artificial catalyst. These structures are formed from the hydrophobic interactions occurring between hydrophobic surfactant chains and are of particular interest in this Chapter. Cooperativity occurs intermolecularly between the functionalised polar head groups of the assembled surfactants. Interestingly, in these systems, enhanced catalytic rates are due to the cooperative effects occurring between the functionalised surfactants, rather than conventional micellar effects such as concentration enhancement and local pH changes.

Micellar structures are formed from the self-assembly of surfactants in aqueous media. This is driven by the interactions between different regions of the amphiphiles, with polar headgroups being exposed to the aqueous environment while hydrophobic tails are hidden within the centre of these self-assembled structures. Micelles have been found to enhance or inhibit a range of chemical reactions compared to the reaction alone in aqueous media.[70] This is due to conventional micellar effects. For example, the collection of hydroxide groups on the surface of the micelle (known as the Stern layer). These ions can interact with the amphiphilic headgroups, resulting in catalysis. This was demonstrated

by Tagaki et al., who used cationic surfactants with imidazole functionalities incorporated into the polar head group. Here, the local pH changes occurring on the micellar surface contribute to the increased rates of catalysis. A positively charged micellar surface causes the ionisation of the imidazole ring, making this the more nucleophilic anion.[71] This can then undergo nucleophilic attack of the *p*-nitrophenyl ester. Hydroxide ions will then concentrate near the positively charged surface of the micelle, promoting the deacylation of the imidazole (Figure 41).[71]

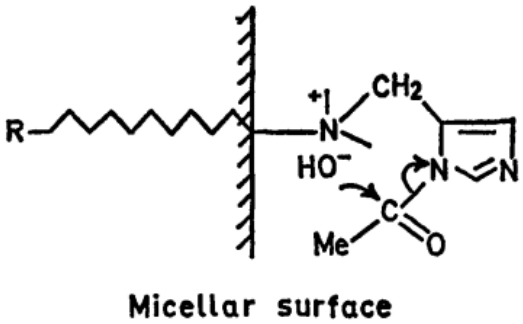

Figure 41: Mechanism for the deacylation of the imidazole as a result of hydroxide ion buildup on the micellar surface. Source: Reprinted from ref. [71] with permission. Copyright (1972) The Society.

Another example found micelles functionalised with imidazole and alcohol groups to undergo a sequential process rather than a cooperative mechanism.[72] This meant that the imidazole functionality would react with the product and form the acetylated intermediate, then the alcohol would react with the imidazole intermediate to form the alcohol acetylated intermediate (Figure 42).[72] This is not a cooperative mechanism as the two functionalities work independently of one another. Instead, Figure 43 shows what would happen for a cooperative mechanism. The alcohol would be activated by the imidazole functionality to make this a better nucleophile.

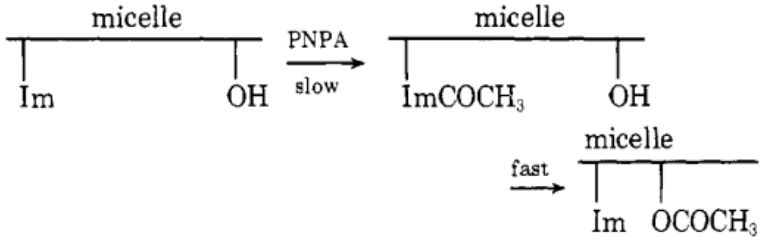

Figure 42: Sequential process for the catalysis of p-nitrophenyl acetate by imidazole and alcohol functionalised micelles. Source: Reprinted from ref. [72] with permission. Copyright (1977) American Chemical Society.

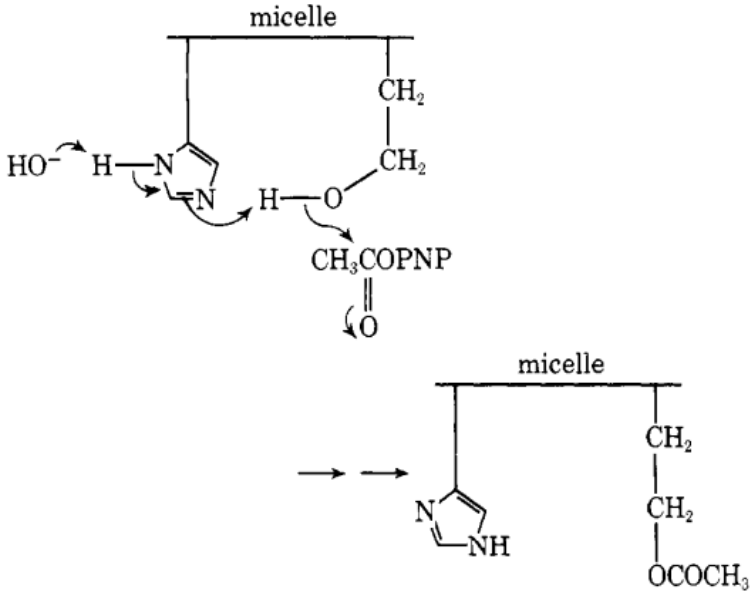

Figure 43: Cooperative catalysis for imidazole and alcohol functionalised micelles. Source: Reprinted from ref. [72] with permission. Copyright (1977) American Chemical Society.

The concentration of reagents in the hydrophobic core for catalysis is another key conventional micellar effect. The hydrophobic interior of micelles can help solubilise substrates that are poorly soluble in aqueous media.[73] This solubility then helps bring the substrate closer to the catalytic sites already solubilised in the micelle. In addition to this, the hydrophobic core can help to stabilise the formation of intermediate species and products.[73] This effect has been utilised in a wide variety of catalytic applications, including Pd-catalysed carbon-carbon bond formation and Cu catalysed click chemistry.[74] Micelles' hydrophobic core can also aid in catalysing oxidation reactions in addition to regioselective and enantioselective reactions.[75]

More recent examples of micellar or vesicular catalysts incorporate cyclen (1,4,7,10-tetraazacyclododecane) functionalities for phosphodiester cleavage.[76,77] Cyclen functionalities can bind Zn^{2+} ions, which can catalyse the hydrolysis of phosphodiester bonds. Gruber and coworkers demonstrated how cyclen units could be assembled to form micelles or be incorporated into vesicles to facilitate catalysis (Figure 44). The self-assembly of these amphiphiles allows for the simple and rapid connection of multiple active sites with minimal synthetic effort.[76] Increased rates of catalysis were attributed to the high local concentration of Zn^{2+} ions coordinated to the cyclen amphiphiles, rather than cooperativity between multiple cyclen-Zn^{2+} units. In contrast to this system, Poznik and König showed that they could see cooperativity occurring between cyclen-Zn^{2+} units and additives added to their membrane catalyst (Figure 45). They investigated a wide range of membrane additives (**25-41**) in combination with their cyclen-Zn^{2+} catalytic units (Figure 46). They found that membrane additives that could form hydrogen bonds had significant rate-enhancing effects, likely due to these aiding in transition state stabilisation. Both membrane and micellar catalysts investigated demonstrated a cooperative hydrolytic effect on phosphodiester cleavage.[76,77]

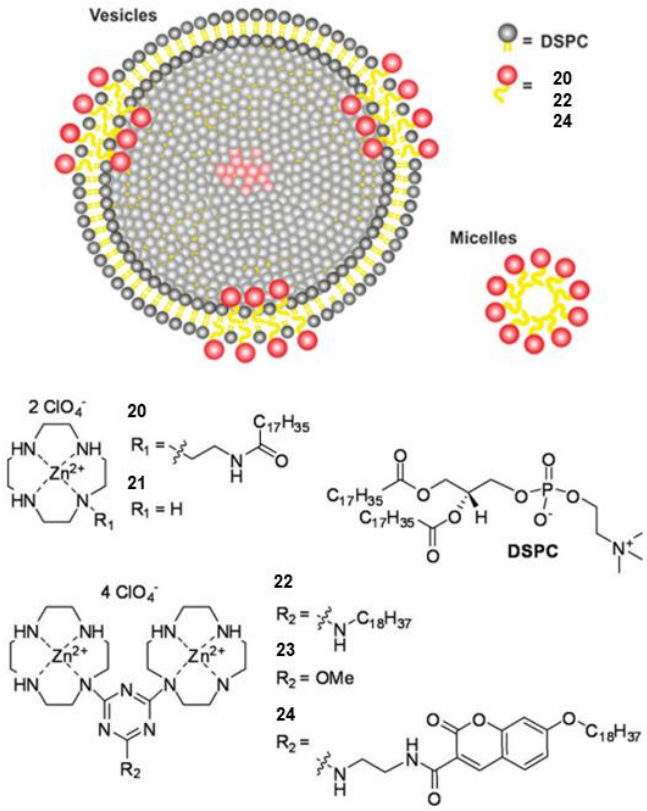

Figure 44: Micelles and vesicle catalysts formed with cyclen-Zn^{2+} catalytic units for phosphodiester cleavage. Source: Adapted from ref. [76] with permission. Copyright (2011) American Chemical Society.

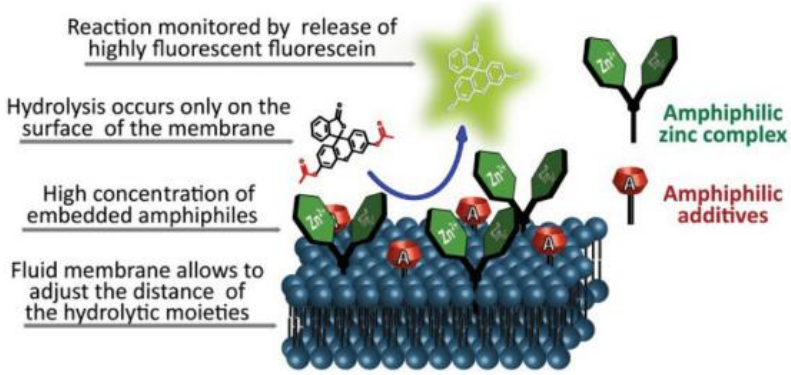

Figure 45: Membrane-based catalysts with cyclen-Zn^{2+}, and additive amphiphiles inserted into the surface. Source: Ref. [77]/Royal Society of Chemistry.

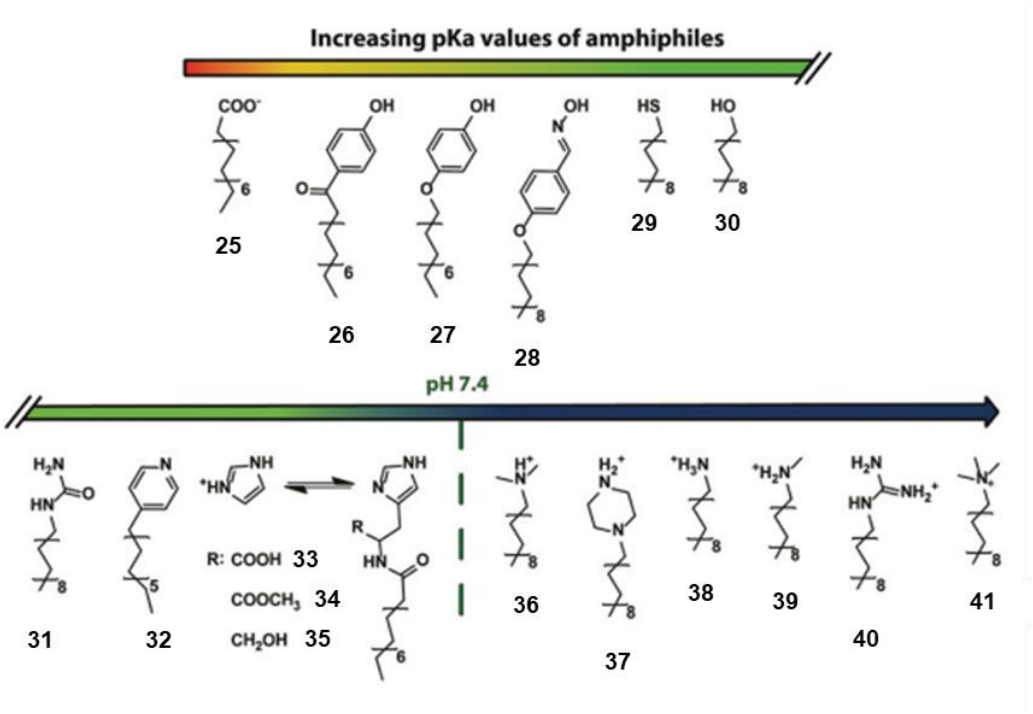

Figure 46: Examples of the additives added to the membrane-based catalyst to enhance catalytic activity. Source: Ref. [77]/Royal Society of Chemistry.

An even more exciting example of a cooperative micellar catalyst was the one designed by Connal and coworkers. This was inspired by the catalytic triad present in native esterase enzymes, which challenged the hydrolysis rates of α-chymotrypsin. Assembly of their catalytic triad amphiphiles **42**, along with guanidine amphiphiles (**G**) and CTAB, positioned the functional groups near one another (Figure 47). This mimics the protein folding of a native enzyme, increasing the rate of catalysis. Their catalytic triad amphiphiles (**42**) contain an imidazole, carboxylic acid and alcohol functional groups, which make up the hydrophilic/catalytic head. **G** was chosen due to its hydrogen bonding ability, which can mimic the oxyanion hole of native enzymes. The addition of CTAB to this system aided in the solubility of the amphiphiles, resulting in a synergistic effect as CTAB is required to increase catalysis by way of solubilising the amphiphiles; however, the CTAB itself is not an active participant in the reaction mechanism. Their research showed that all three catalytic triad functional groups were required for good catalysis. In comparison to the native enzyme, Connal et al. found their micellar catalyst to have a substrate turnover 7 times that of α-chymotrypsin under the same conditions, see Figure 48.[18] However, the substrate used in their kinetic experiments (*p*-nitrophenyl benzoate **43**) is not the natural substrate of α-chymotrypsin which typically cleaves proteins, which

could explain the difference in activity between their micellar catalyst and the native enzyme. Connal and coworkers also discuss how this comparison between enzyme and artificial catalyst is often made in the literature despite the differences in conditions required for enzyme and artificial catalyst optimal performance. This comparison can give an insight into the important roles of supporting environmental effects for optimising the active site chemistry.[18]

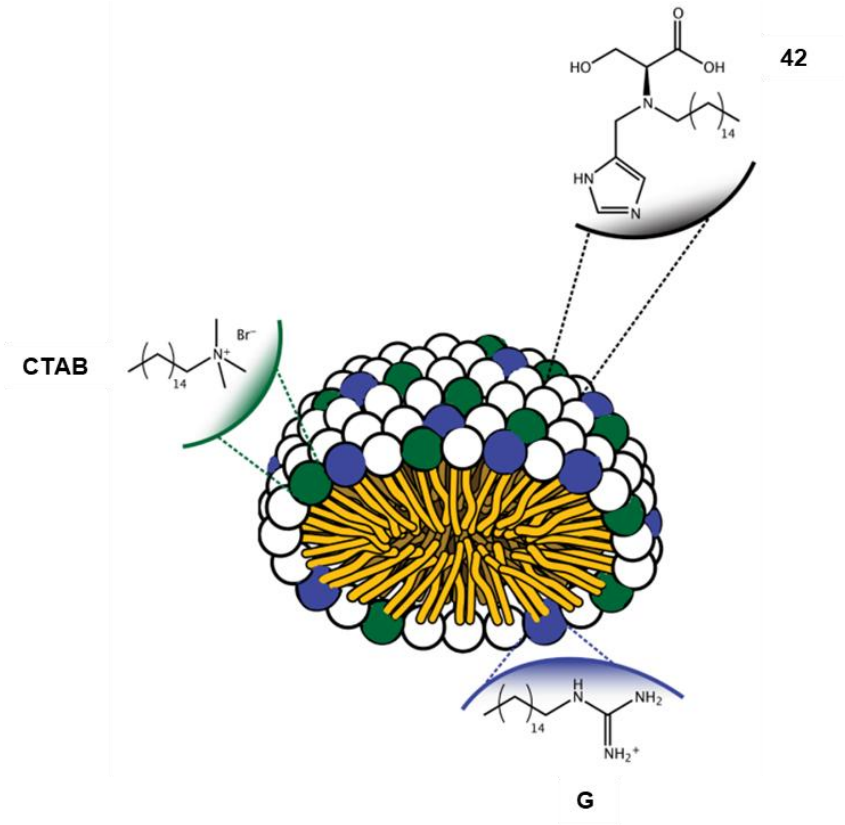

Figure 47: Self-assembled micellar artificial esterase. Source: Adapted from ref. [18]/American Association for the Advancement of Science.

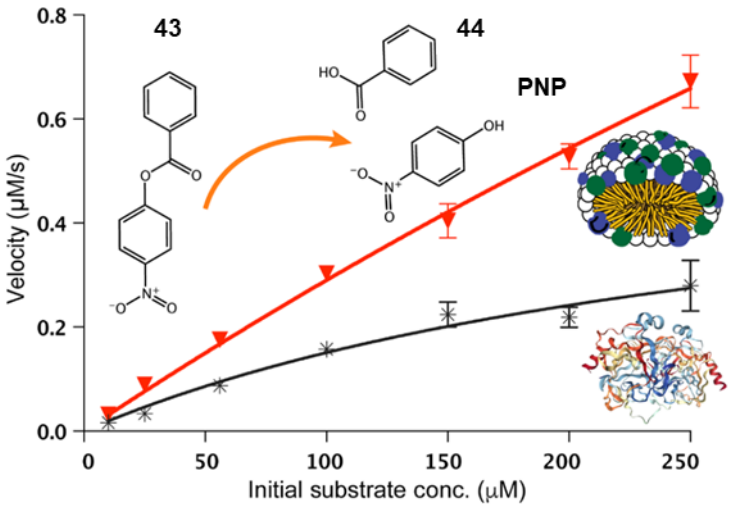

Figure 48: Michaelis-Menten plot of self-assembled micellar catalyst (red) with the native enzyme α-chymotrypsin (black).Source: Adapted from ref. [18]/American Association for the Advancement of Science.

2.1.2 Previous work in the research group

Previously, Jack Chen's research group has demonstrated that they can self-assemble two functionalised surfactants, 1,4,7-triazacyclononane (**TACN**) and guanidine (**G**), to form a transphosphorylation catalyst (Figure 49).[78] **TACN**, in the presence of metal ions such as Cu^{2+} or Zn^{2+}, is capable of facilitating phosphodiester cleavage and has been previously shown by the group to self-assemble into vesicles for catalysis.[79] Ren and coworkers evaluated whether the activity of the catalyst could be enhanced by assembling it with a functional group that would facilitate cooperative catalysis. **G** was chosen as this functional group due to its ability to complement the metal ions' activity through substrate binding and transition-state stabilisation. The substrate used was 2-hydroxypropyl-4-nitrophenol phosphate (HPNPP), as this is a model substrate for RNA cleavage.[78] When cleaved, HPNPP releases cyclic phosphate (cyP) along with *p*-nitrophenolate (PNP), which is yellow and allows the reaction to be monitored using UV-visible spectroscopy.

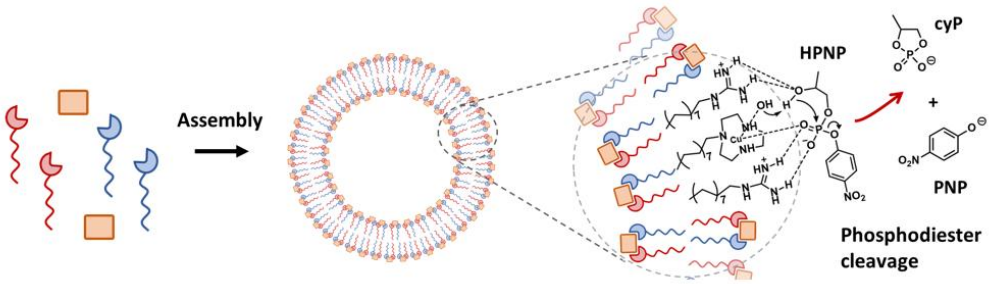

*Figure 49: Representation of the phosphodiesterase formed from the self-assembly of functionalised **TACN** and **G** surfactants. Source: Adapted from ref. [78] with permission. Copyright (2020) American Chemical Society.*

The key result from this research was the synergism demonstrated between the **TACN** and **G** surfactants, shown in Figure 50. This means that the rate of catalysis for the two surfactants combined was greater than that for either **TACN** or **G** on their own. Interestingly, Ren et al also saw that a 1:3 ratio of **TACN**/**G** gave the highest rate of catalysis. This highlights the advantage of a modular system whereby catalysis can be increased simply by altering the proportions of amphiphiles used.

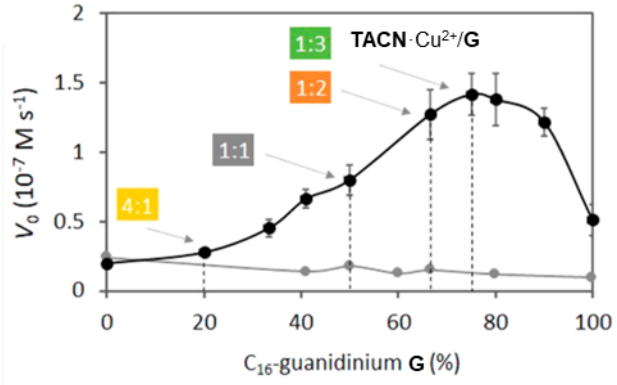

*Figure 50: Initial rates of HPNP cleavage at different **TACN**/**G** ratios. Source: Adapted from ref. [78] with permission. Copyright (2020) American Chemical Society.*

Michaelis-Menten kinetics were used to investigate the activity of this system (Figure 51a). For these experiments, the concentration of substrate (HPNPP) was varied, with the rate of reaction being measured at each concentration. This was conducted for three different catalytic ratios: 1:1, 1:2 and 1:3 **TACN**/**G**. Two key Michaelis-Menten parameters could be calculated from these experiments; these were the K_M and V_{max}. The K_M value defines the binding affinity of the substrate to the catalyst, while the V_{max}

indicates the efficiency of the catalyst. The 1:3 **TACN/G** system was found to have the strongest binding between the catalyst and the substrate, with a significantly lower K_M value compared to the other systems. The $V_{max,}$ however, was highest for the 1:2 system ($7.3 \pm 1.1 \times 10^{-7}$ M s^{-1}), suggesting the formation of different catalytic pockets for each catalytic system. The K_M values calculated were much higher than the concentration of HPNPP used in the initial experiments to investigate the cooperativity of the system. Ideally, for catalysis, we want to have a substrate concentration greater than the K_M value to saturate the surface of the catalyst. Ren and coworkers therefore re-examined the ratios of their amphiphiles at higher concentrations of HPNPP (3 mM) (Figure 51b). Under these new conditions, a 1:2 **TACN/G** system gave the highest rate of catalysis; this was in line with their V_{max} findings.

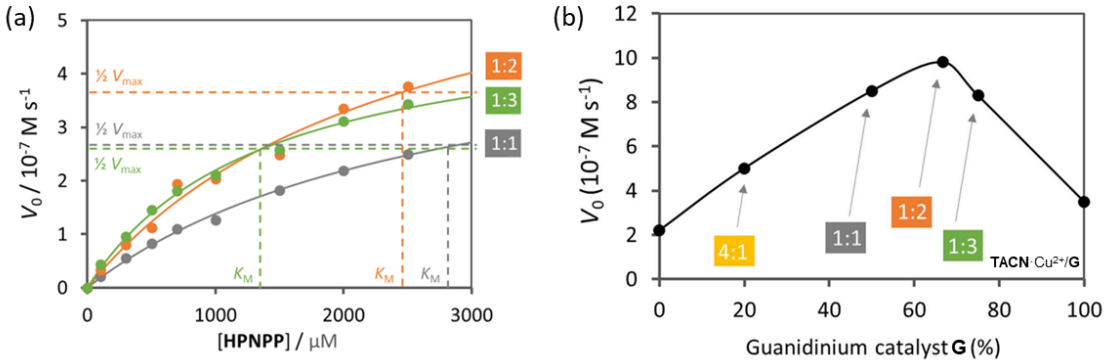

*Figure 51: Michaelis-Menten kinetics at different ratios of **TACN/G** (a) and secondary screen of catalytic ratios with a higher concentration of substrate (b). Source: Adapted from ref. [78] with permission. Copyright (2020) American Chemical Society.*

With this **TACN/G** system, the group also wanted to highlight the dynamic nature of a self-assembled catalyst. This was achieved by modifying the ratio of amphiphiles *in situ*, enabling the up- and down-regulation of catalysis. Figure 52a. shows the up-regulation of catalysis. Here, Ren and coworkers started with a 4:1 **TACN/G** system, which has low catalytic activity. **G** was then added to the system to reach a 1:3 **TACN/G** ratio. This ratio has a much higher catalytic activity, as seen by the green line, compared with the rate of catalysis for the standard 4:1 system shown in yellow. This shows that the system can rapidly reorganise to form a new catalytic system. The down-regulation of catalysis could be seen in Figure 52b where the addition of **TACN** to a 1:3 **TACN/G** system to form a 4:1 **TACN/G** resulted in a decrease in the catalytic rate shown in green. These experiments nicely highlight the dynamic and modular nature of a self-assembled system.

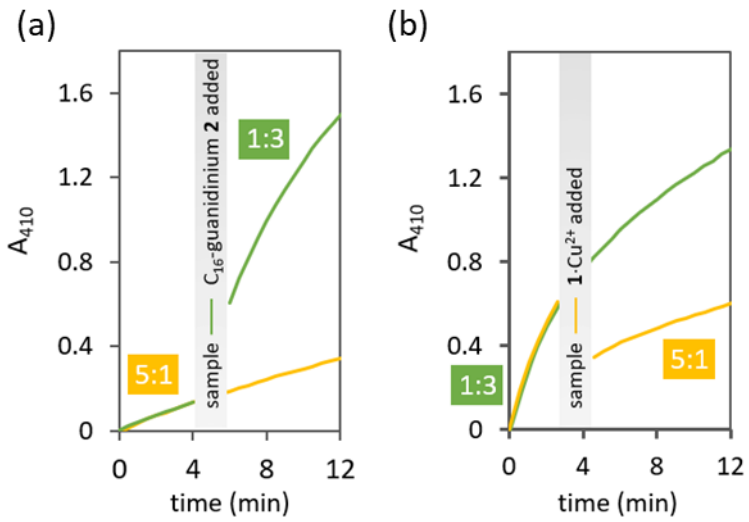

*Figure 52: Up (a) and down-regulation (b) of catalysis for **TACN/G** system. Source: Adapted from ref. [78] with permission. Copyright (2020) American Chemical Society.*

2.1.3 Aim of this chapter

For the start of my PhD project, we wanted to expand upon the work previously carried out by the research group by screening a wider range of functionalised surfactants to develop a self-assembled artificial esterase (Figure 53). A key focus of this research was moving away from systems designed for phosphodiester cleavage, such as the previous self-assembled catalytic work conducted in the group. Instead, we wanted to move towards esterase activity as it has a wider range of potential applications compared to phosphodiester cleavage. Esterase enzymes are becoming more popular in an industrial setting due to their ability to degrade various natural and synthetic substrates.[80,81] In particular, the discovery of PETase enzymes, which can break down PET, offers an exciting new application for artificial esterases.[82]

One key advantage our self-assembled catalytic system offers is its modularity. This means we can rapidly screen a wide range of functionalised surfactants to develop the catalytic system with minimal synthetic effort. This work will also allow us to demonstrate the usefulness of a self-assembled catalytic system in terms of the development and optimisation process.

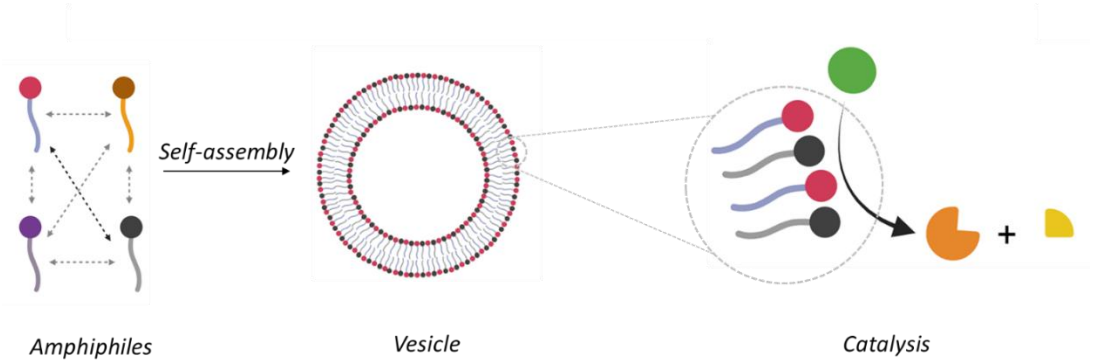

Figure 53: Plan for this chapter.

2.2 Design of amphiphiles for catalysis

To begin, we needed to determine which functionalities we wanted to investigate and convert these into amphiphilic molecules by incorporating a long chain into the molecule. Functional groups we were interested in investigating included those found in the catalytic triad of native esterase enzymes: imidazole, alcohol and carboxylic acid. In addition to this, we also wanted to investigate the guanidine functional group, which has previously been used in a variety of different artificial esterase systems.[18,44,57] Amine functionalities were also of interest due to their ability to act as nucleophilic catalysts. The amphiphiles investigated are shown below in Figure 54. Some of these amphiphiles were commercially available, while others were synthesised.

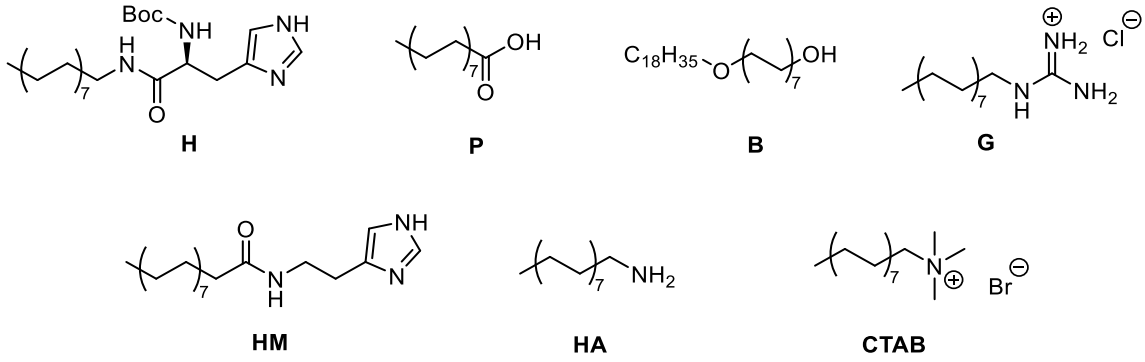

Figure 54: Structure of amphiphiles for catalysis.

2.2.1 Histidine

We were interested in imidazole functionalities as this is the key component of the histidine amino acid, typically found in the active site of esterase enzymes.[17] The role of the imidazole ring in the active site of these enzymes is to deprotonate a neighbouring

serine residue, which then undergoes nucleophilic attack of the substrate.[17] Research has also found that imidazole functionalities are capable of facilitating catalysis on their own. Catalysis can either proceed via general base catalysis, whereby one of the nitrogens in the imidazole ring **45** can form a partial bond with a proton from a water molecule, increasing the nucleophilicity of the oxygen (Scheme 2a), or via nucleophilic catalysis where one of the nitrogens in the imidazole ring acts as a nucleophile (Scheme 2b).[83]

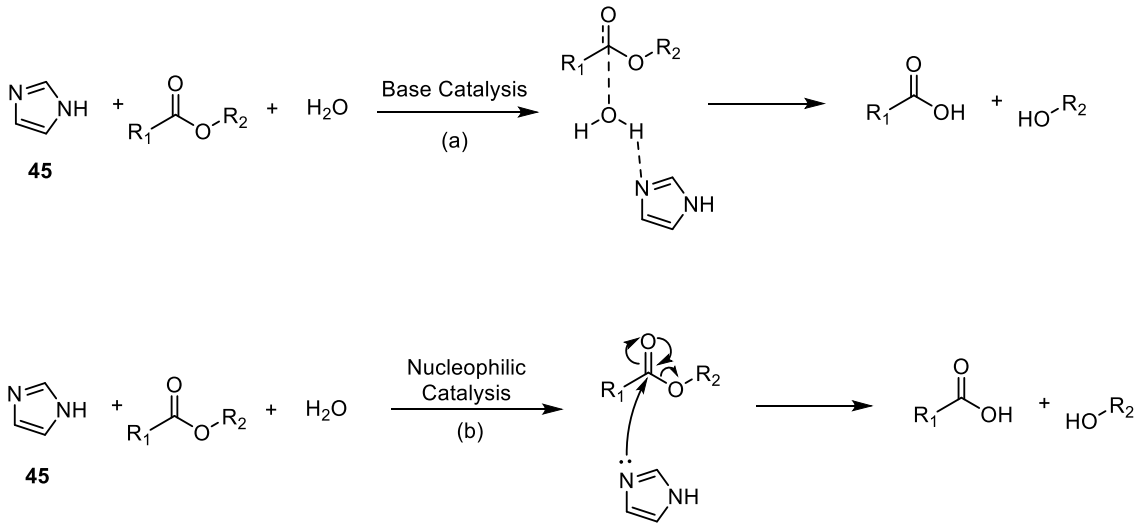

Scheme 2: Imidazole mechanism for catalysis via either base catalysis (a) or nucleophilic catalysis (b).

The imidazole functionality is a very popular choice with artificial esterase reported in the literature. They can be used in combination with alcohol and carboxylic acid functional groups to mimic the catalytic triad[17,18,56], or they can be used in combination with other functionalities such as phenol[55] or guanidine[44,57,84] units. There are also reports of these functionalities working by themselves[54] or binding Zn^{2+} ions[53,65,69] for catalysis.

Synthesis of histidine amphiphile and control molecule

Two histidine-based compounds were synthesised. One contains a C16 alkyl chain to make our histidine amphiphile (**H**), and the other a control molecule containing a C4 alkyl chain (**C4-H**). Both were synthesised using the same reaction conditions discussed below.

The first step involved an amide coupling with Boc-His(BzI)-OH (**46**) and the chosen alkylamine (**47** or **HA**) using HBTU and DIPEA (Scheme 3). The mechanism for this reaction is depicted in Scheme 4. The carboxylic acid is deprotonated by DIPEA, allowing the negative charge on the oxygen to then attack the imine functional group in HBTU.

The molecule then rearranges to lose the benzotriazole. The negatively charged oxygen on this triazole can then attack the newly formed carbonyl, resulting in the loss of a urea by-product **50**.[85] Our activated carbonyl has now been formed, allowing the lone pair on the nitrogen of the amine to attack, losing the triazole **51**, to form our amide. This step was mildly successful for the C4 alkyl chain **48** with a 44% yield. A much greater success was had with the C16 alkyl chain **49**, with a yield of 95%. Both the C4 and C16 histidine protected products (**48** and **49**) could be confirmed by ^{1}H NMR, due to the appearance of aromatic peaks for both the imidazole (two singlet 1 H peaks) and benzyl (5 H seen as either a multiplet or as a multiplet and a doublet of doublets) aromatic peaks.

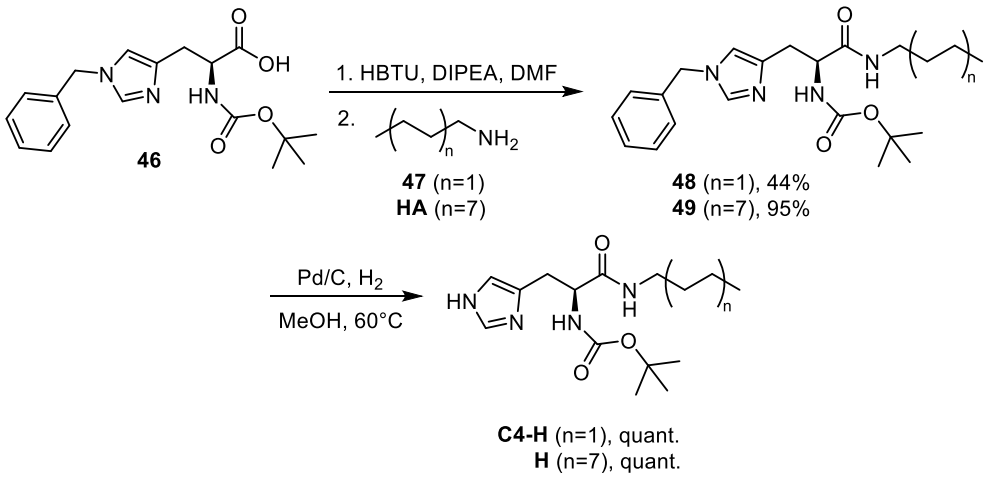

Scheme 3: Synthesis of histidine amphiphile and control molecule.

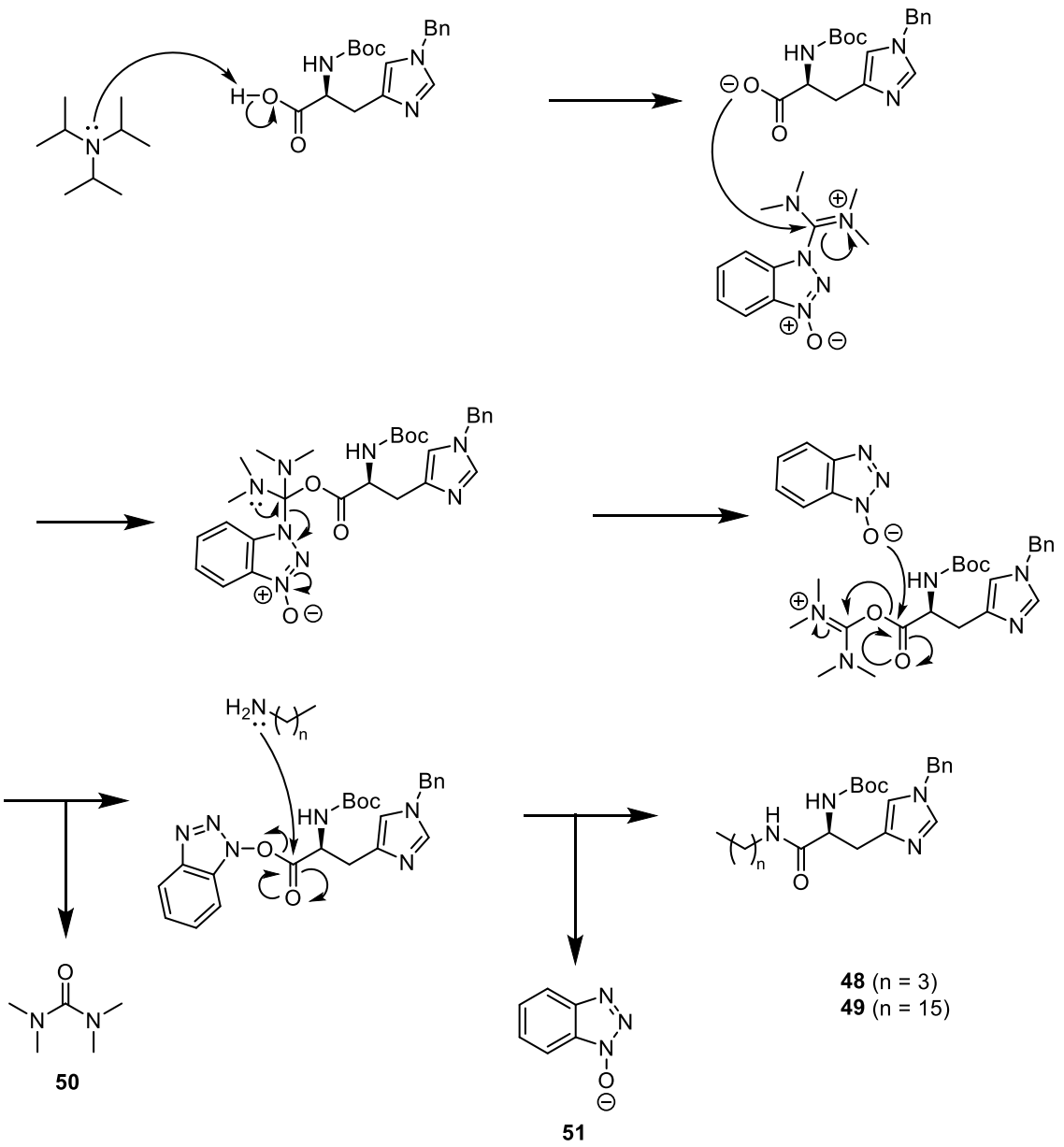

Scheme 4: Amide coupling mechanism.

The second step in this synthesis is to remove the benzyl-protecting group on the nitrogen in the imidazole ring via hydrogenation to give the desired products **C4-H** and **H**. This reaction was successful for both C4 and C16 compounds, with a quantitative yield being obtained. The imidazole nitrogen is now free to facilitate catalysis. The Boc protecting group on the α-amino group remained intact to further mimic the amino acid histidine, whereby this amino group would form an amide bond with the next amino acid in the polypeptide chain of the native enzyme.

2.2.2 Palmitic acid and Brij® O10

Palmitic acid (**P**) and Brij® O10 (**B**) were both commercially available, with the former providing a carboxylic acid functionality while the latter contained a hydroxyl group for catalysis. Both functional groups are found in the catalytic triad and have been previously used in artificial esterases, such as the self-assembled micellar catalyst developed by Nothling et al.[18] In the catalytic triad, the carboxylic acid contains a negatively charged oxygen, which can deprotonate a neighbouring imidazole ring. This results in the movement of electrons, allowing the imidazole to deprotonate the alcohol functional group, forming a negatively charged oxygen capable of undergoing nucleophilic attack of the carbonyl group in the ester (Scheme 5).[17]

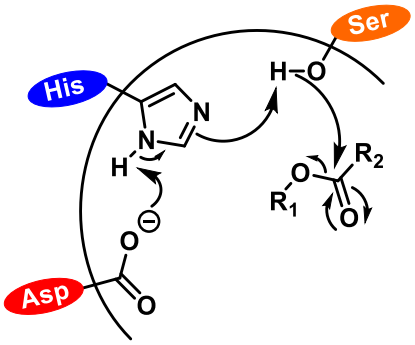

Scheme 5: Mechanism of action for the catalytic triad.

2.2.3 Guanidine

The guanidine functional group was chosen due to its ability to mimic the oxyanion hole found in native esterase enzymes such as serine proteases.[18] The two NH groups in guanidine are capable of hydrogen bonding, which can therefore stabilise the transition state of the ester substrate by binding the carbonyl oxygen (Scheme 6).[44,86] These functional groups have been used in a wide range of catalysts due to their hydrogen-bonding capability. For example, they have been used in the development of phosphodiesterase and hydrogenase[87] enzymes. Guanidine functional groups are present in the amino acid arginine and therefore are found to have this stabilisation effect in native enzymes as well.[88] These amino acids can play an important part in the active site due to their hydrogen-bonding ability. Quite often, these residues directly participate in substrate binding.[88] In addition to this, arginine has also been found to have a catalytic role in enzymes such as serine recombinase, xanthine dehydrogenase and GTPases.[88]

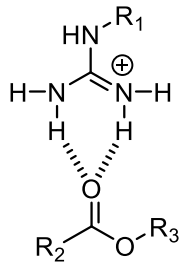

Scheme 6: Hydrogen bonding of guanidine to ester transition state.

Synthesis of guanidine amphiphile and control molecule

Synthesis of the guanidine amphiphile (**G**) followed the experimental conditions previously reported by the research group (Scheme 7).[78] Here, an electrophilic source of guanidine (*N,N′*-Bis-Boc-1-guanylpyrazole (**52**)) is coupled with hexadecylamine (**HA**) to form our protected guanidine (**53**). The mechanism of this step (Scheme 8) involves the lone pair on the hexadecylamine nitrogen attacking the guanidine group of *N,N′*-bis-Boc-1-guanylpyrazole, with the pyrazole acting as our leaving group. The nitrogen from our original amine will then lose a proton to give our Boc-protected guanidine.

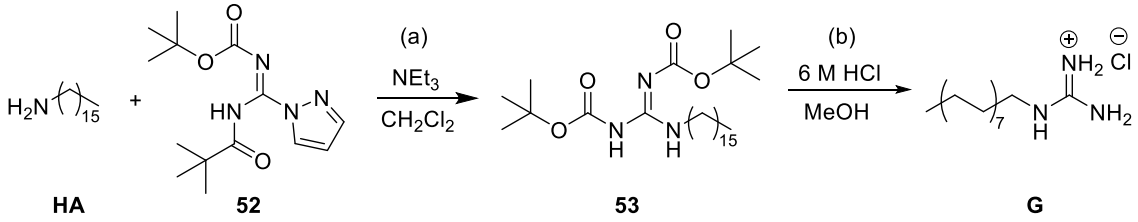

Scheme 7: Synthesis of guanidine.

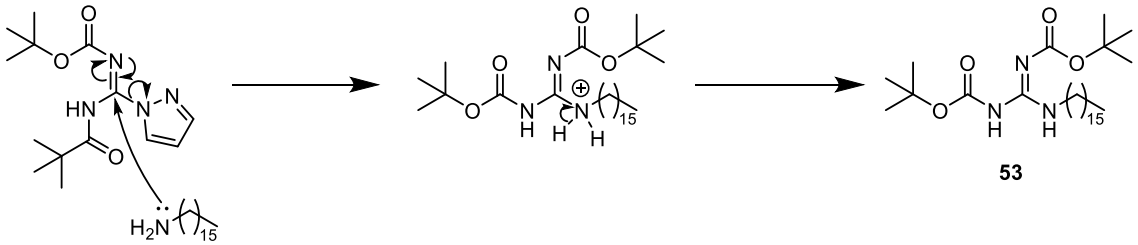

Scheme 8: Mechanism for guanidinylation.

HCl was then used to remove the Boc protecting groups to give our guanidine amphiphile (**G**). Scheme 9 depicts the general reaction mechanism with the oxygen in the carbamate being protonated initially. This allows the *tert*-butyl group to leave as a carbocation,

which is then deprotonated to form isobutylene (**54**). The carbamic acid formed then undergoes proton transfer, followed by decarboxylation where CO_2 is lost, and the deprotected amine is formed.

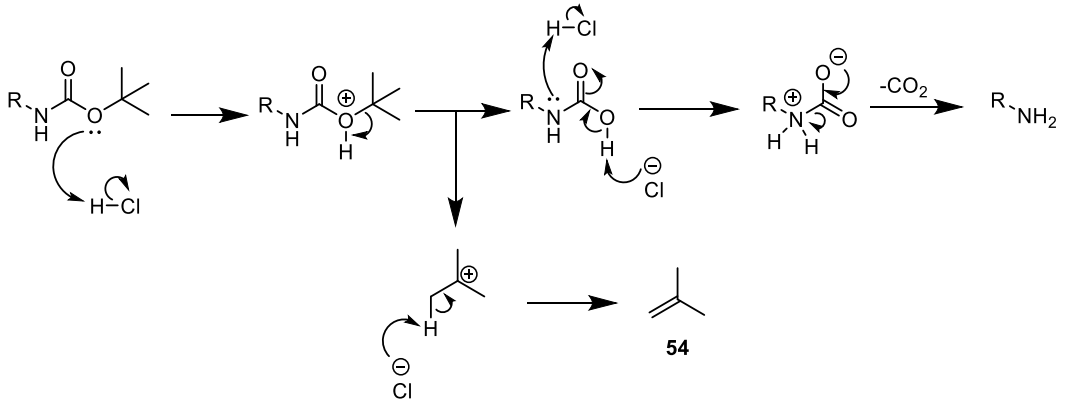

Scheme 9: General Boc-deprotection mechanism.

For the initial guanidinylation step (Scheme 7, a.) we used *N,N′*-bis-Boc-1-guanylpyrazole **52** as our guanidinylation agent as opposed to 1,3-di-Boc-2-(trifluoromethylsulfonyl)guanidine **55** (Figure 55) used in the procedure previously reported by the group.[78] Both triflyl guanidine and pyrazole carboximidamides similarly undergo guanidinylation via chemical transformation.[89] Triflyl guanidines are more reactive guanidinylation reagents due to the nucleofugality of the triflyl group,[90] however, since we had previously reported the success of this reagent for synthesising C16 and C4 guanidine compounds[78] we wanted to try out a more cost-effective reagent, *N,N′*-bis-Boc-1-guanylpyrazole **52**. We saw that the yield for use of the pyrazole carboximidamide (94%) was comparable to that previously reported in the research group with the triflyl guanidine (94%).[78]

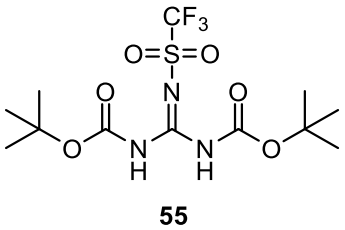

*Figure 55: Guanidinylation reagent 1,3-di-Boc-2-(trifluoromethylsulfonyl)guanidine (**55**).*

A C4 version of our guanidine amphiphile (**C4-G**) had been previously synthesised by the research group[78], and could be used as a control molecule.

2.2.4 Histamine

The histamine amphiphile (**HM**) was synthesised via an amide coupling of palmitic acid (**P**) with histamine dihydrochloride (**56**) (Scheme 10). This procedure used the same conditions as the histidine amide coupling mentioned earlier. Both **HM** and **H** contain the imidazole functionality for catalysis; however, the **HM** version is missing the Boc-protected amine in between the ring and the amide bond. Instead, **HM** simply contains two carbons between these two functionalities. This means we can investigate the role the Boc-protected amine present in our **H** amphiphile has on catalysis.

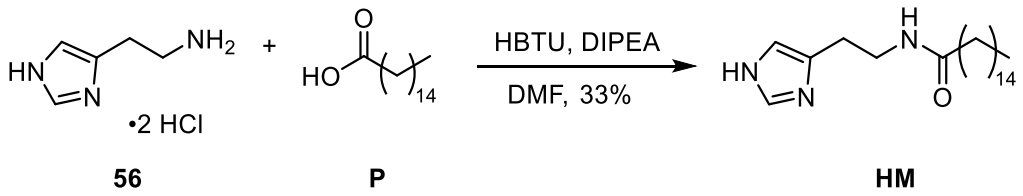

*Scheme 10: Synthesis of **HM**.*

2.2.5 Hexadecylamine and CTAB

The final two amphiphiles in Figure 54, hexadecylamine (**HA**) and cetyltrimethylammonium bromide (**CTAB**), were both commercially available. Hexadecylamine allowed us to investigate the role of a free amine on catalysis, while CTAB had been previously used in self-assembled esterase systems, aiding in solubilising the amphiphiles.[18]

2.3 Reaction used for catalysis

2.3.1 Substrate selection

Selecting the substrate used for catalysis is another key element of designing our catalytic system. We wanted to start with a substrate that was relatively easy to cleave but had minimal background hydrolysis. We also needed a way to monitor the rate of reaction. Many artificial esterase examples use *p*-nitrophenyl derivatives as these produce *p*-nitrophenol (PNP) when cleaved which is yellow (Scheme 11), allowing the reaction to be monitored spectroscopically via the absorbance at 405 nm.[91] The most common

derivatives used are *p*-nitrophenyl acetate[53–56,92] and *p*-nitrophenyl butyrate (PNPB)[17,55,93]. Both are simple esters, which are relatively easy to cleave. However, the acetate is much more susceptible to background hydrolysis compared with PNPB.[17] It is for this reason that we chose PNPB as our substrate, as it is more stable in assay conditions.[17]

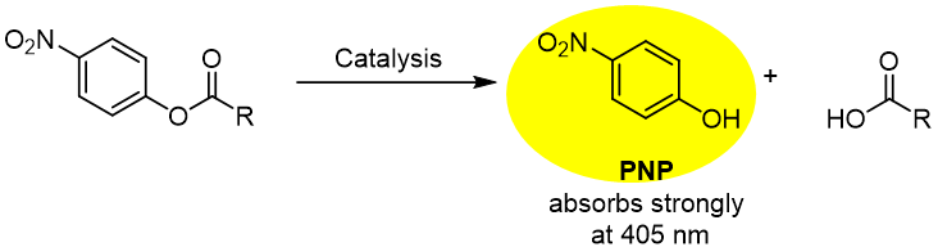

Scheme 11: Esterolysis of p-nitrophenyl derivatives to give PNP.

2.3.2 Molar extinction coefficients determined for rate conversion

Catalysis was measured using the kinetic mode on the UV-visible spectrometer. This plots the absorbance over time for a particular wavelength (for our experiments we used 405 nm). The rate of catalysis calculated from these plots is then in absorbance/minute. We want to convert this rate into the more useful unit M s^{-1}, and this was accomplished using the molar extinction coefficient.

The molar extinction coefficient for PNP was determined in both buffer systems used throughout the thesis (HEPES and Tris buffers). Absorbance was plotted at increasing concentrations of PNP, and the slope was used to determine the molar extinction coefficient, as seen in Figure 56. These molar extinction coefficients could then be used in Equation 4 to give our rate in M s^{-1}. Note that we multiplied the rates by 10^8 to get whole numbers on the scale, hence why the units for the rate of reaction throughout this thesis are reported as 10^8 M s^{-1}.

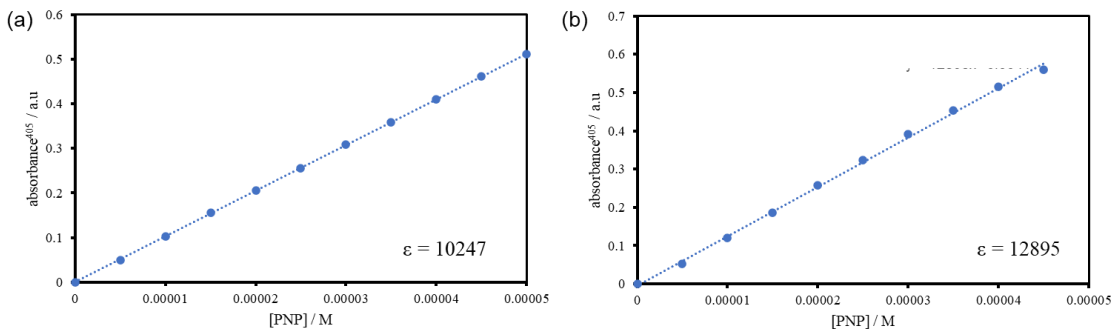

Figure 56: Molar extinction coefficient for PNP in HEPES buffer (5 mM) pH = 7.0 (a) and Tris buffer (5 mM) pH = 7.8 (b). Source: Ref. [94]/Wiley-VCH.

$$M\ s^{-1} = rate\ of\ reaction\ (absorbance/minute)/\varepsilon/60 \quad (4)$$

2.4 Initial screen of amphiphiles to determine the best catalytic combination

We investigated the activity of all our amphiphiles in Figure 54 with excess substrate, PNPB. The selected amphiphile or amphiphilic combination was screened in aqueous solution with HEPES buffer, maintaining a pH of 7. Amphiphiles were combined in equal proportions and all amphiphilic combinations were screened with and without Zn^{2+}. Zn^{2+} has been shown to have a catalytic role in hydrolase enzymes such as carbonic anhydrase.[53] Artificial esterases have also been designed to mimic the active site of carbonic anhydrase, such as the example designed by Rufo et al. whereby three histidine residues are self-assembled to bind a Zn^{2+} ion for catalysis (see Figure 32). The Zn^{2+} ion is capable of stabilising a hydroxyl group, which can undergo nucleophilic attack of the carbonyl position of an ester.[53] Zn^{2+} was added to the system using $Zn(NO_3)_2$, as the NO_3^- counterion will not have an effect on substrate binding or catalysis. The results of this amphiphilic screen are shown below in Figure 57.

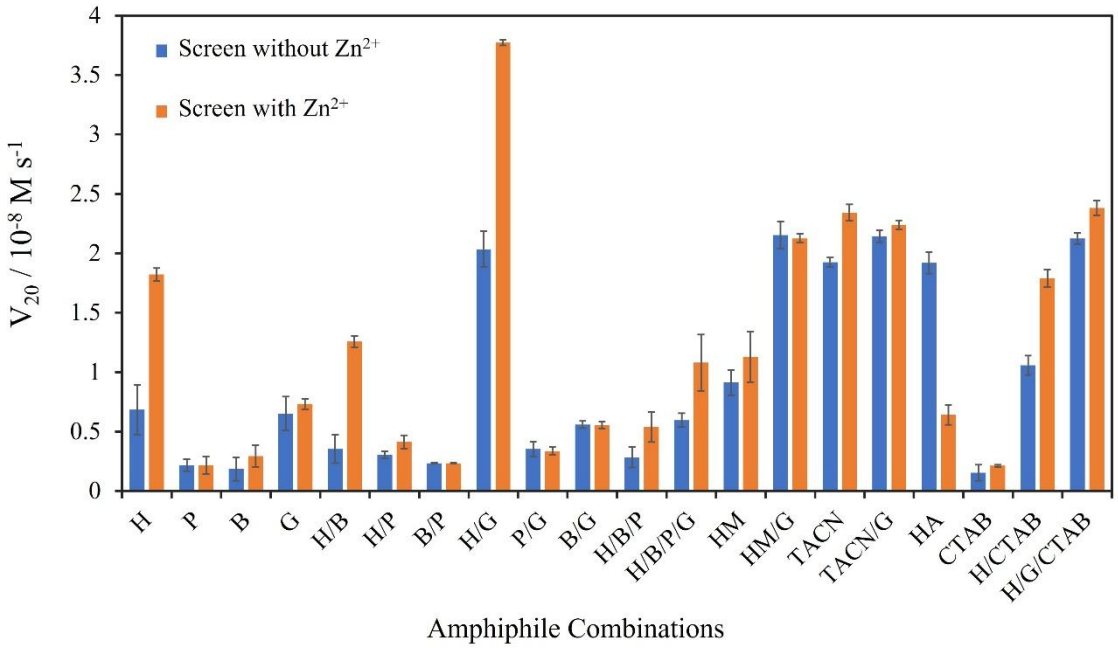

Figure 57: Initial screen of amphiphiles. Experimental conditions: aqueous buffer pH = 7.0 ([HEPES] = 5 mM), [total amphiphile] = 100 μM, [$Zn(NO_3)_2$] = 100 μM, [PNPB] = 500 μM, 40 °C. Amphiphiles were combined in equal proportions. Source: Ref. [94]/Wiley-VCH.

An important note about the results in Figure 57 is that V_{20} was compared as opposed to V_0. This was due to the **H**-only sample needing time to stabilise, as this amphiphile was not completely soluble in the experimental conditions. The cloudy solution then interfered with the absorbance at 405 nm. As time went on, the solution became clear; therefore, *t* = 20 minutes was determined to be a good time to calculate the rate of reaction. In other samples, the solubility of **H** was aided by the presence of other amphiphiles (for example, **H**/**G** was completely soluble due to the presence of **G**).

If we look initially at our amphiphiles inspired by the catalytic triad (**H**, **P**, **B**), our **H** amphiphile can facilitate catalysis with an increase in the catalytic rate seen with the addition of Zn^{2+}. The nucleophilic nature of the imidazole ring in **H** allows this to facilitate catalysis in the absence of Zn^{2+}.[83] However, once Zn^{2+} is present, the increase in catalysis is likely due to the histidine binding Zn^{2+}, similar to the active site of carbonic anhydrase.[53] There are also examples in the literature of self-assembled artificial esterases based on the binding of histidine to Zn^{2+}, for example, the catalyst designed by Rufo et al. discussed earlier. **P** and **B** give minimal activity both with and without Zn^{2+}. The combination of these three amphiphiles to give us our catalytic triad mimic (**H**/**B**/**P**) also

had minimal activity. The activity of this combination is less than that of our **H** amphiphile on its own, which is likely due to the decreased concentration of this in our **H**/**B**/**P** combination. These results were surprising due to the number of examples in the literature using this catalytic triad system. However, these examples typically have the functional groups arranged in such a way that they can facilitate catalysis via the same mechanism as the catalytic triad in native enzymes, whereby the aspartic acid hydrogen bonds to the imidazole ring in histamine, allowing this to deprotonate the serine to form a nucleophile (see Scheme 5).[2] This arrangement can be due to the incorporation of these functional groups all into the same molecule[18] or can be brought about by molecular imprinting[56]. In our system, these functional groups are all incorporated into their own individual amphiphilic structure, which are all then mixed together. The mixing of these amphiphiles in our system is random and may not put these functional groups in the correct orientation to facilitate this mechanism, hence the lower-than-expected catalysis seen. A similar result was seen in Wang et al. system, where molecular imprinting was required to get good catalysis as this placed the functional groups (histidine, serine and aspartic acid) in the correct orientation for catalysis to occur.[56] With molecular imprinting, the addition of serine and aspartic acid to histamine resulted in an increase in catalysis in their system.[56] In contrast, when these functional groups are combined in our system, we see a decrease in the overall rate compared to **H** on its own, potentially due to the absence of preorganisation.

Looking now at our **G** amphiphile, we see moderate activity of this on its own, with no real difference when Zn^{2+} is added. When we have a combination of **H**/**G** we get the highest rate of catalysis of all our screened systems. This system was over two times greater than **H** on its own and more than three times greater than **G**, indicating clear cooperativity between the two amphiphiles. When Zn^{2+} was added to this system, we saw an even greater increase in catalysis, giving the highest rate of catalysis for all screened systems shown in Figure 57. This indicates that Zn^{2+} likely has an important role in this catalytic system.

To help investigate the mechanism of catalysis, we screened another imidazole-containing amphiphile, **HM**. The difference between this amphiphile and our original histidine amphiphile **H** is the absence of the Boc-protected amine between the imidazole and amide bond. We screened the histamine amphiphile **HM** individually and in combination with **G**. The activity of **HM** was comparable to that of **H** when the

amphiphiles were screened individually. Once Zn^{2+} was added, only **H** saw a significant increase in the rate of catalysis. This same effect was seen with the **HM**/**G** combination, where the addition of Zn^{2+} had minimal effect on the catalytic rate. This suggests that the carbamate side chain present in our **H** amphiphile is important in coordinating with Zn^{2+}. Catalysis is enhanced by the activation of a water molecule by the coordinated Zn^{2+} ion, allowing it to act as a nucleophile. In the absence of Zn^{2+}, the imidazole moiety present in both amphiphiles can act as a nucleophilic catalyst. Mass spectrometry data was obtained to support this mechanism, and this will be discussed in detail in Section 2.6.

Hexadecylamine **HA** was another amphiphile investigated due to the primary amine being able to facilitate nucleophilic catalysis. The catalytic activity of **HA** was 2.5 times greater than the rate of histidine in the absence of Zn^{2+}. This is to be expected due to the increased nucleophilicity of the primary amine compared with the imidazole. Figure 58 shows the UV trace of hexadecylamine facilitating catalysis. Here we can see a high initial reaction rate followed by a plateau after 20 minutes, a key sign of an irreversible nucleophilic attack. The addition of Zn^{2+} to this system resulted in a dramatic decrease in the reaction rate, likely due to the coordination of the amines to the Zn^{2+} ions, preventing them from undergoing nucleophilic attack. The nucleophilic nature of this catalytic system could be supported by mass spectrometry. In the absence of Zn^{2+}, Figure 59a. shows evidence of the **HA**-butyrate adduct **57** due to the peak at 312.2, indicating the ability of **HA** to act as a nucleophile with the direct attack on PNPB. When Zn^{2+} is present, this **HA**-butyrate adduct cannot be seen (Figure 59b) likely due to the amphiphile binding Zn^{2+}, preventing the direct nucleophilic attack onto the substrate.

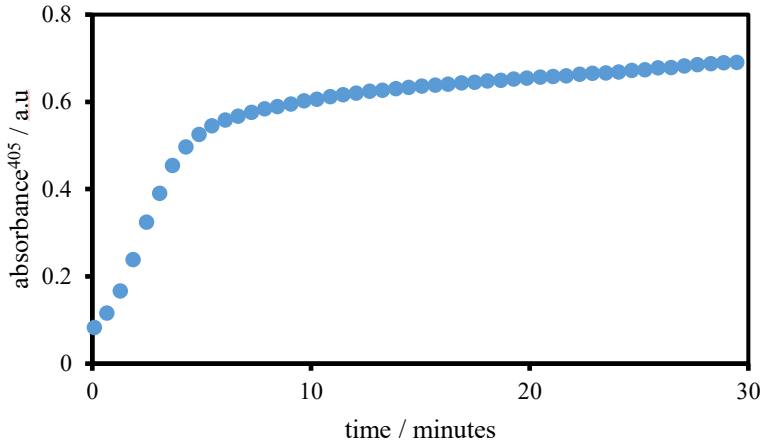

*Figure 58: Representative UV trace for the hexadecylamine catalytic system. Experimental conditions: aqueous buffer pH = 7.0 ([HEPES] = 5 mM), [**HA**] = 100 μM, [PNPB] = 500 μM, 40 °C. Source: Ref. [94]/Wiley-VCH.*

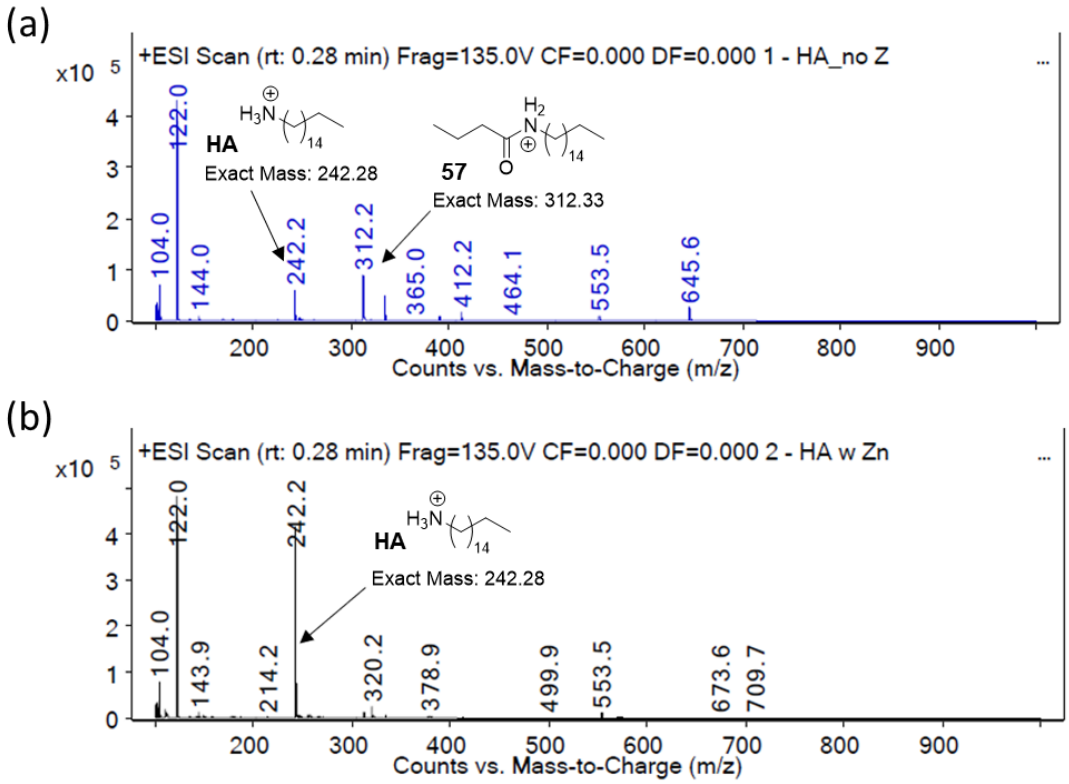

*Figure 59: Mass spectrometry data for **HA** system without Zn^{2+} (a) and with Zn^{2+} (b). Experimental conditions: aqueous buffer pH = 7.0 ([HEPES] = 5 mM), [**HA**] = 100 μM, [Zn^{2+}] = 100 μM, [PNPB] = 500 μM, 40 °C. Source: Ref. [94]/Wiley-VCH.*

The final amphiphile investigated in our initial screen was **CTAB**. This surfactant has been previously shown to enhance the formation of micellar aggregates and aid in the solubility of amphiphilic molecules.[18] Combining **CTAB** with **H** resulted in a significant increase in the rate of reaction, with similar rates observed with now half the **H** concentration. However, adding **CTAB** to our **H**/**G** combination in the presence of Zn^{2+} did not result in a more efficient catalytic system than our **H**/**G** system.

2.5 Examination of the micellar matrix for the H/G combination

The initial screen of amphiphiles showed promising results with cooperativity seen in our 1:1 **H**/**G** system. The main concern with these results was that cooperativity may not be a result of direct synergistic effects between the amphiphiles' catalytic head groups, but rather due to conventional micellar effects such as local concentration effects or local changes in pH. Micelles are spherical structures formed from the self-assembly of amphiphiles, with the hydrophobic tails congregating in the centre of the structure and the hydrophilic head groups surrounding this. The Stern layer then surrounds these hydrophilic groups, consisting of ions and water molecules.[95] The presence of different functional groups in the hydrophilic part of the amphiphile can result in local pH changes in the Stern layer. For example, the presence of positively charged hydrophilic groups would attract negatively charged anions, such as OH^-, into the Stern layer, resulting in an increased local pH. This was discussed earlier with the micellar system by Tagaki et al. Basic conditions can cleave the ester bond in PNPB, so we need to prove that our 1:1 **H**/**G** systems catalysis is due to functional group synergism as opposed to Stern layer effects.

To determine whether this increase in catalysis was due to cooperativity between the two functional groups or if it was due to conventional micellar effects (such as local pH changes), we examined our 1:1 **H**/**G** catalytic system within a range of different micellar matrices. Non-ionic surfactant Brij® O10 (**B**) and cationic surfactant **CTAB** were investigated, with the results shown below in Figure 60. Looking initially at the results with our non-ionic surfactant (blue bars), we see that the catalytic activity of 1:1 **H**/**G** in **B** was significantly higher than that of either **H** or **G** on their own in **B**. This suggests the formation of catalytic pockets between our two catalytic amphiphiles rather than the synergism in the formation of aggregates. The rate of 1:1 **H**/**G** in **B** is significantly lower than the rate of 1:1 **H**/**G** without **B** (orange bar), likely due to the dilution of our

amphiphiles within the micellar matrix, resulting in a lower degree of **H**/**G** intermolecular cooperativity. A decrease in the catalytic activity is observed in the absence of Zn^{2+} in our 1:1 **H**/**G** in the **B** system, once again highlighting the importance of Zn^{2+} in the catalytic mechanism.

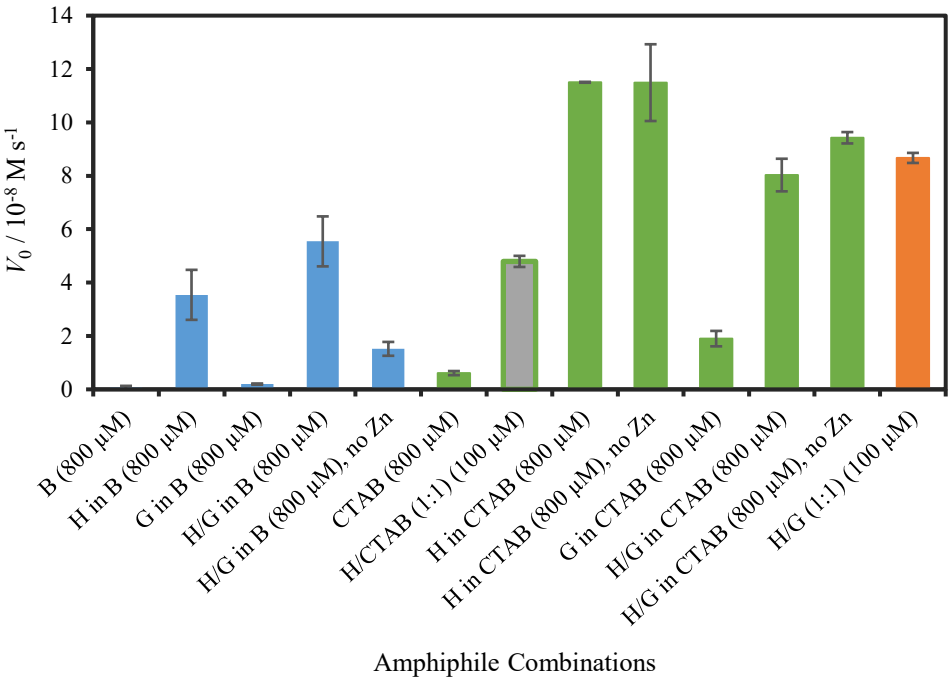

*Figure 60: Esterolysis rate of combinations of **H** and **G** in **B** (800 µM; blue bars), in **CTAB** (800 µM; green bars), and of the 1:1 **H**/**G** system (100 µM) in the absence of **B** or **CTAB** (orange bar). Experimental conditions: aqueous buffer pH = 7.0 ([HEPES] = 5 mM), [**H** and/or **G**] = 100 µM, [**B** or **CTAB**] = 800 µM (0 µM for orange bar), [PNPB] = 500 µM, 40 °C. Source: Ref. [94]/Wiley-VCH.*

Looking now at our cationic surfactant, **CTAB**, we see that **H** on its own in **CTAB** possessed a higher catalytic activity than when we added **G** to the system. It also shows that the addition of Zn^{2+} ions to **H** in **CTAB** did not affect the catalytic rate, which suggests an alternative reaction mechanism occurring as a result of the OH^- ion buildup in the Stern layer from the positively charged surfactant head groups, causing an increase in the local pH.[96,97] The micellar effect, along with the nucleophilicity of our **H** amphiphile are the main drivers of catalysis in this system as there is no benefit observed from the addition of **G**. The presence of Zn^{2+} has no effect on the rate of catalysis suggesting that the increase in local pH from **CTAB** overrides any effect that Zn^{2+} has in

promoting the formation of hydroxyl ions for catalysis. The activity of this **H** in the **CTAB** system is half as much as the activity of our 1:1 **H**/**G** system (in orange). This indicates that the synergistic effect between the **H** and **G** amphiphiles is much greater than the contribution of local pH changes in the Stern layer.

Co-assembling amphiphiles **H** and **G** within a micellar matrix was shown to alleviate any issues with changes in the structure of the self-assembled aggregates. However, moving forward with this research, we decided to forgo the use of these micellar matrices due to the dilution of the intermolecular cooperative effects from the amphiphiles, resulting in decreased rates of catalysis.

2.6 Optimisation of the H/G system

Our **H**/**G** combination could then be further optimised from the initial screen. The ratio of **H** to **G** was examined with and without Zn^{2+}, and the results for this are shown in Figure 61. Looking initially at the results without Zn^{2+} (blue circles), we can see evidence of cooperativity due to the catalytic rate of all the **H**/**G** combinations being greater than that of **H** or **G** alone. If we then add Zn^{2+} to the catalytic system (orange circles), we see a great increase in the rate of catalysis for all our **H**/**G** combinations compared with either **H** or **G** on their own, further supporting cooperative catalysis occurring between the two amphiphiles. Furthermore, when we replace either of our C16 amphiphiles with our C4 control molecules (yellow and grey circles), we see a decrease in the catalytic activity. This is due to the C4 control molecules being unable to form self-assembled structures, which would place the catalytic head groups close to one another for cooperative catalysis to occur. These control experiments also demonstrate how important self-assembly is for catalysis, as when we are no longer able to form these self-assembled structures, we see reduced catalytic activity.

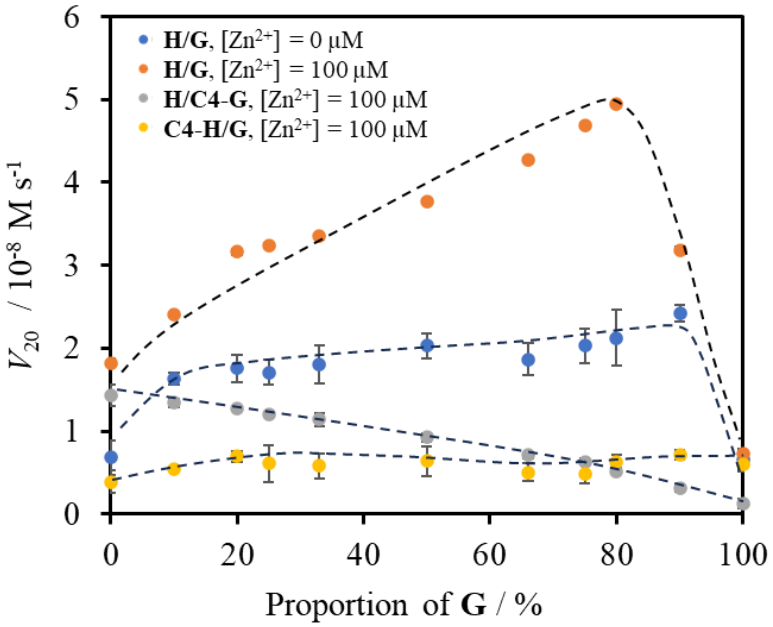

*Figure 61: Esterolysis rate at different ratios of **H**/**G** without Zn^{2+} (blue circles), with Zn^{2+} (orange circles), with **C4-G** control molecule (grey circles) and with **C4-H** control molecule (yellow circles). Experimental conditions: aqueous buffer pH = 7.0 ([HEPES] = 5 mM), [amphiphiles] = 100 µM, [PNPB] = 500 µM, 40 °C. Source: Ref. [94]/Wiley-VCH.*

The other interesting result to come out of these experiments is the distinctive peak seen when we added Zn^{2+} to our system. In the presence of 100 µM Zn^{2+}, our 1:4 **H**/**G** ratio gives us the highest rate of catalysis (Figure 61, orange circles). This result was unexpected as we had predicted that three **H** ligands would stabilise a Zn^{2+} ion, allowing this to bind a hydroxyl group ready for nucleophilic attack. This assumption was based on literature examples where artificial esterases had been designed to have three histidine residues binding a Zn^{2+} ion for catalysis, such as the system from Rufo et al., which was inspired by the native enzyme carbonic anhydrase. In our predicted system, the **G** ligand was expected to activate the carbonyl in the substrate for nucleophilic attack. Again, this was based on a previously reported artificial esterase by Nothling et al., where they added guanidine amphiphiles to their micellar catalyst to mimic the oxyanion hole. Arginine amino acid residues, which contain this guanidine functionality, are also seen in native enzymes' active sites, typically to aid in substrate binding.[88] To further investigate the roles of **H** and **G** in the reaction mechanism we measured the catalytic activity of 1:4 **H**/**G** with increasing concentrations of Zn^{2+}, Figure 62.

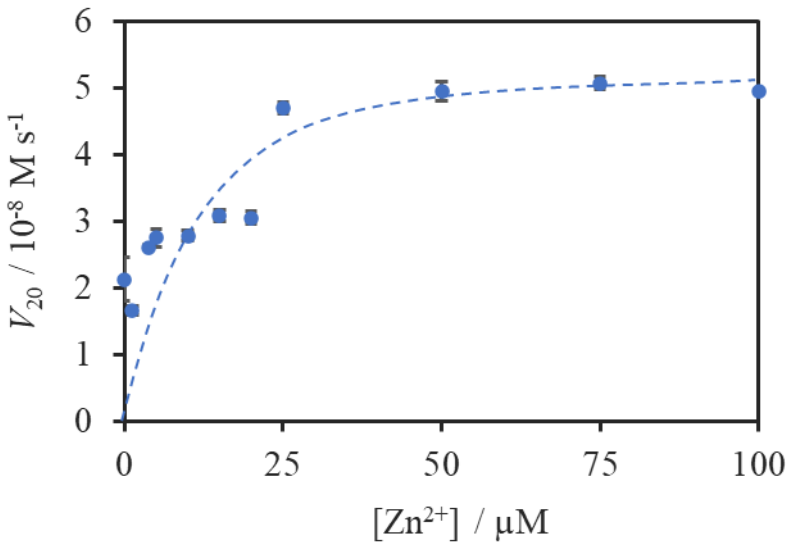

*Figure 62: Esterolysis rate for 1:4 **H**/**G** system at increasing concentrations of Zn^{2+}. Experimental conditions: aqueous buffer pH = 7.0 ([HEPES] = 5 mM), [amphiphiles] = 100 µM, [PNPB] = 500 µM, 40°C. Source: Ref. [94]/Wiley-VCH.*

From Figure 62 we can see that with increasing concentration of Zn^{2+}, we see an increase in the rate of catalysis up to 25 µM Zn^{2+}. After this, any increase in the Zn^{2+} concentration has minimal effect on the rate of reaction. Therefore, our optimised catalytic system is 1:4 **H**/**G** with 1 equivalent Zn^{2+} in relation to **H**. It is worth noting that there is a plateau in the rate of catalysis between 5 and 20 µM Zn^{2+}. The system may be undergoing morphological changes with different Zn^{2+} concentrations. However, using DLS and TEM experiments, we see no difference in the samples with different Zn^{2+} concentrations. SANS/SAXS work may be a better alternative to understand the morphological changes with different Zn^{2+} concentrations and help us relate these to the changes we see with catalytic activity.

To determine how our vesicular system binds Zn^{2+}, we performed titrations of our key amphiphiles and Zn^{2+} in the presence of the colourimetric indicator pyrocatechol violet (PV). PV exhibits a spectral change upon binding with Zn^{2+}, and is commonly used in indicator displacement assays for the detection of phosphates.[98,99] Free PV appears yellow, whereas complexation with ligands bound to Zn^{2+} forms a blue solution, which can be monitored using UV-visible spectroscopy (Figure 63).[98]

Figure 63: Colour change of PV from yellow to blue upon complexation with Zn^{2+}.

Unbound PV has an absorption maximum of 450 nm at pH 7.[100] In the literature, when PV forms a binary metal complex with Zn^{2+} a shift is seen in the absorbance spectra with a new absorption maximum now at 600 nm, when all the PV is bound to Zn^{2+}.[100] For our experiments, increasing amounts of **H** or **G** were added to a mixture of 20 µM PV and 40 µM Zn^{2+}. With increasing concentrations of ligand **H** (Figure 64a) the absorbance at 600 nm increases; concurrently, a new signal at 660 nm is seen to steadily increase, both of which can be attributed to the PV now being bound by **H**. A similar trend is seen for ligand **G**, as seen in Figure 64b. In both cases, the signal intensity at 660 nm begins to decrease above a certain concentration, likely due to the complex precipitating out of solution. The most evident sign of a switch from unbound PV to bound PV was the colour change from yellow to blue, observable with the naked eye. We found that 80 µM of **H** was needed to see this colour change (Figure 65) while only 20 µM of **G** was required to form this blue complex (Figure 66), suggesting that **G** was able to bind Zn^{2+} more efficiently than **H**. Given the 3:1 ratio of **G** and Zn^{2+} as seen in Figure 27, we propose that three **G** amphiphiles form a complex with Zn^{2+} (Scheme 12). This Zn^{2+} complexation has been discussed previously by Stanek et al. in their review article, in which they investigate the formation of metal complexes using guanidine functional groups. The strong donation properties of this functional group allow guanidines to form stable complexes with a wide variety of metals in various oxidation states, including Zn^{2+}.[101] Wittmann et al. also report the synthesis and characterisation of guanidine-based Zn^{2+} complexes.[102] In addition to this, arginine residues have been found to bind cofactors in enzyme active sites,[88] similar to what we are seeing with our 1:4 **H**/**G** system.

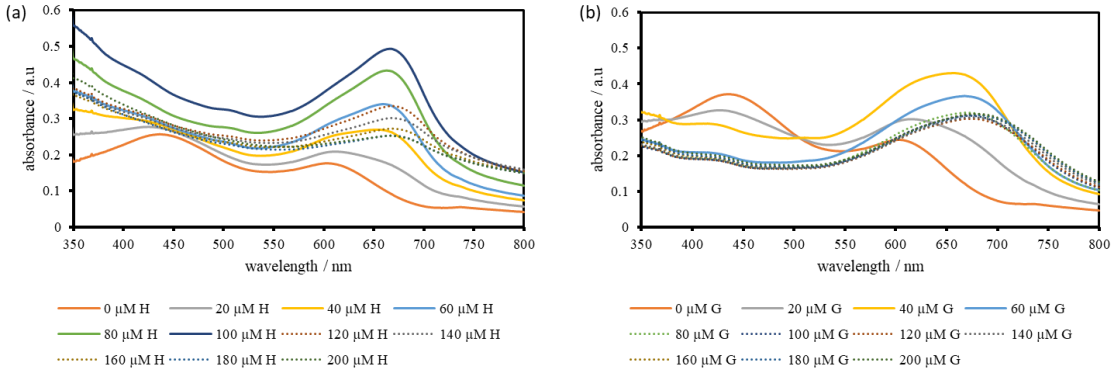

*Figure 64: UV traces showing the addition of ligands **H** (a) and **G** (b) at increasing concentrations to a solution containing PV and Zn^{2+}. Experimental conditions: aqueous buffer pH = 7.0 ([HEPES] = 5 mM), [PV] = 20 µM, [$Zn(NO_3)_2$] = 40 µM, 40 °C. Source: Ref. [94]/Wiley-VCH.*

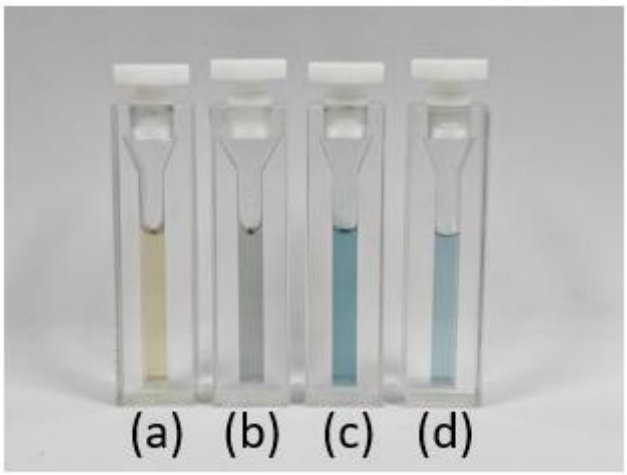

*Figure 65: Colour changes observed following the addition of **H** and **G** into a solution containing PV in the presence of Zn^{2+}. Cuvettes from left to right: PV (20 µM) (a), PV (20 µM) and Zn^{2+} (40 µM) (b), **H** (80 µM) added to PV (20 µM) and Zn^{2+} (40 µM) (c), and **G** (80 µM) added to PV (20 µM) and Zn^{2+} (40 µM) (d). Source: Ref. [94]/Wiley-VCH.*

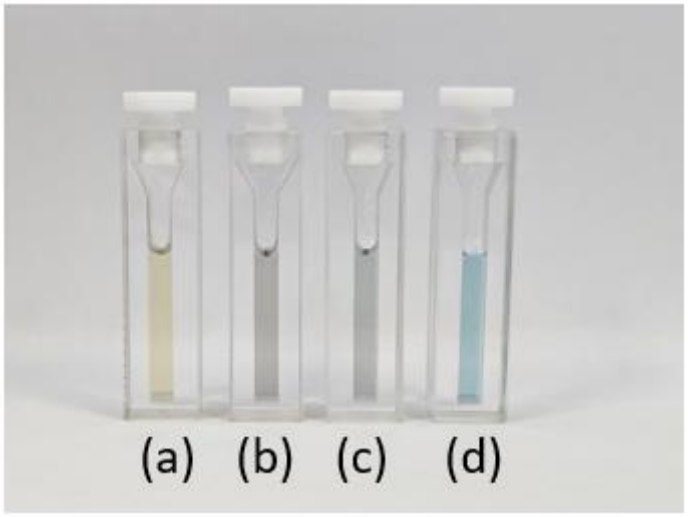

*Figure 66: Colour changes observed following the addition of **H** and **G** into a solution containing PV in the presence of Zn^{2+}. Cuvettes from left to right: PV (20 μM) (a), PV (20 μM) and Zn^{2+} (40 μM) (b), **H** (20 μM) added to PV (20 μM) and Zn^{2+} (40 μM) (c), and **G** (20 μM) added to PV (20 μM) and Zn^{2+} (40 μM) (d). Source: Ref. [94]/Wiley-VCH.*

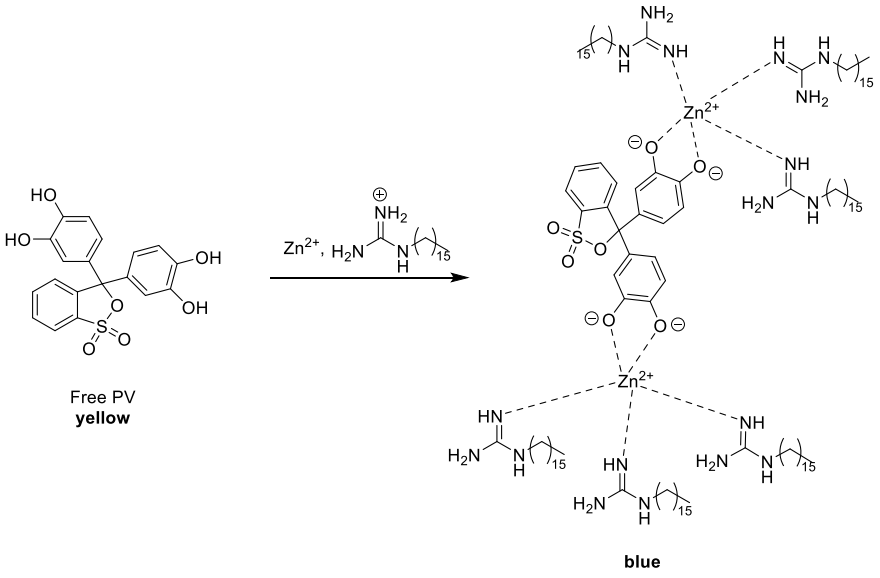

*Scheme 12: Proposed complexation between PV and **G**. Source: Ref. [94]/Wiley-VCH.*

With confirmation that our **G** amphiphile was binding Zn^{2+}, we then started to propose the mechanism by which catalysis was occurring. Figure 67 shows the mechanism that we proposed for our 1:4 **H**/**G** system with 1 equivalent of Zn^{2+}. Here we have 1 equivalent of our **G** amphiphiles acting as an oxyanion hole stabilising the transition state of our substrate PNPB by hydrogen bonding to the carbonyl. Our **H** amphiphile is then able to act as our nucleophilic catalyst with the nitrogen in the imidazole ring attacking the

carbonyl of our substrate. This releases PNP and forms our histidine-butyrate adduct. Using mass spectrometry, we were able to confirm the presence of this **H**-butyrate adduct **58**, seen by the peak in Figure 68 at 549.4. Finally, we have our remaining three **G** amphiphiles forming our metal-ion complex with Zn^{2+}, which stabilises a hydroxyl group, allowing this to undergo nucleophilic attack of our **H**-butyrate adduct to form butyric acid and give us back our amphiphiles, which can then be used as catalysts for another substrate molecule. Therefore, we see a nice straight line for our UV trace now (Figure 69), indicative of a catalytic mechanism, as opposed to the two different slopes we saw earlier for **HA** (Figure 58).

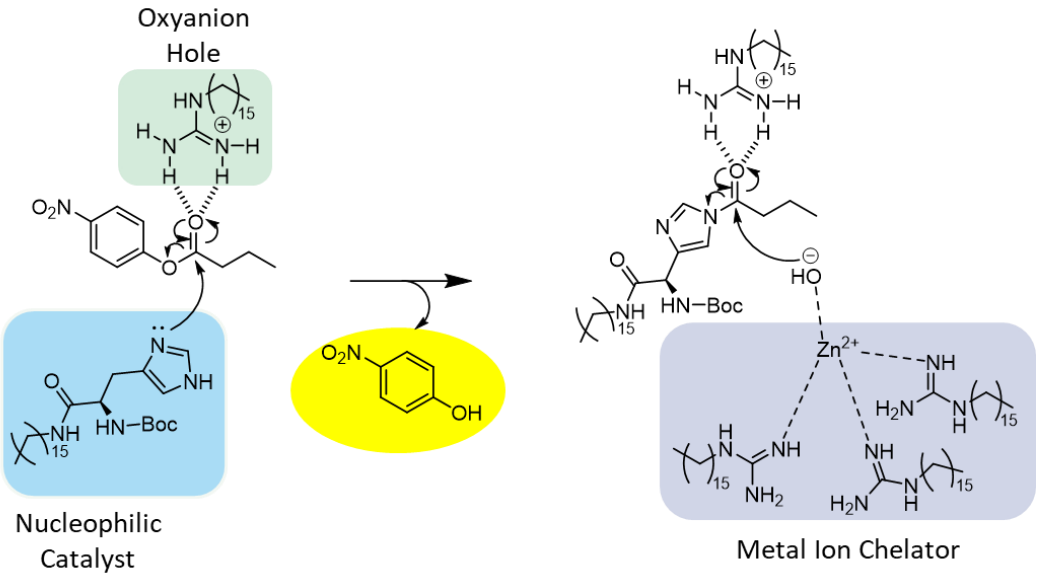

*Figure 67: Proposed mechanism for 1:4 **H**/**G** catalytic system with one equivalent Zn^{2+}.*

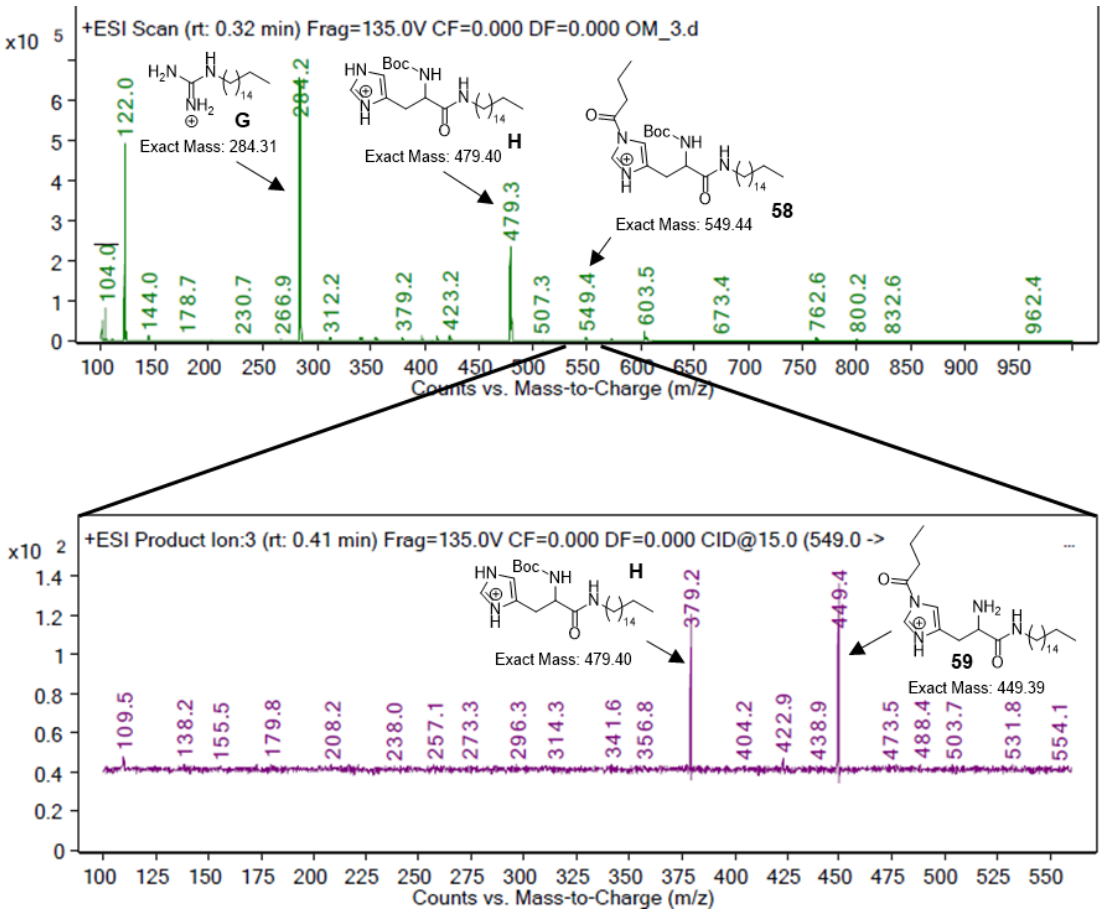

*Figure 68: Mass spectrometry data for 1:4 **H**/**G** system with one equivalent Zn^{2+}, including the MS/MS data. Experimental conditions: aqueous buffer pH = 7.0 ([HEPES] = 5 mM), [amphiphiles] = 100 μM, [$Zn(NO_3)_2$] = 25 μM, [PNPB] = 500 μM, 40 °C. Source: Ref. [94]/Wiley-VCH.*

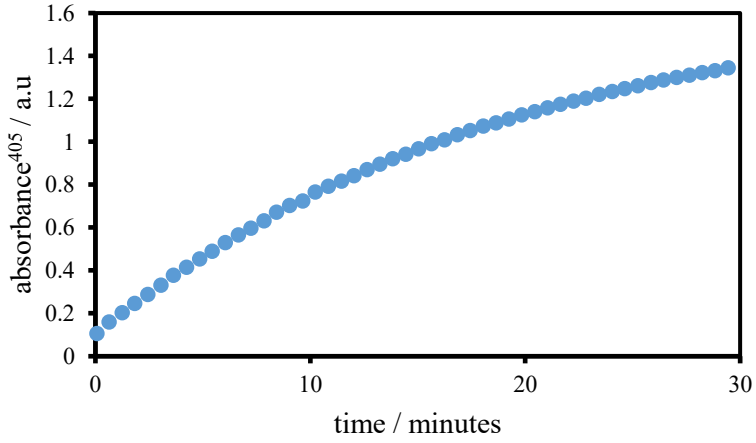

*Figure 69: UV trace of 1:4 **H**/**G** with one equivalent Zn^{2+}. Experimental conditions: aqueous buffer pH = 7.0 ([HEPES] = 5 mM), [amphiphiles] = 100 μM, [$Zn(NO_3)_2$] = 25 μM, [PNPB] = 500 μM, 40 °C. Source: Ref. [94]/Wiley-VCH.*

2.7 Characterisation of the vesicular structures

The self-assembled properties of our lead catalytic system 1:4 **H**/**G** were investigated. We started by determining the critical aggregation concentration (CAC) of our system. This is the minimum concentration of amphiphiles needed in solution to form aggregates. The CAC can be determined by titrating our amphiphiles against a fluorescent dye and monitoring any changes in wavelength maxima or fluorescence intensity. Initially, we tried using the fluorescent dye Nile red, as the method for this had already been established by the group to determine the CAC for various self-assembled systems.[78,79,103] Nile red has poor solubility in water; however, once amphiphiles are added to the solution and start forming aggregates, the Nile red molecules can be solubilised into the hydrophobic regions of these aggregates.[104] When Nile red goes from aqueous environments to being solubilised in non-polar solvents, it experiences a blue shift.[104] This method gave us a CAC just below 200 μM for our 1:4 H/G system, which seemed quite high for our system, as we were expecting a CAC of 100 μM or less based on the CAC we had seen for previous amphiphilic structures in the group.[78,79] We also noticed that increasing the substrate concentration resulted in the same CAC; however, we would have expected this to decrease. The interactions between the substrate (PNPB) and the catalytic head groups can partially neutralise some of the charges of these head groups. This means there is less repulsion between the polar heads of the amphiphiles, allowing them to self-assemble at lower concentrations, decreasing the CAC.

Therefore, we decided to repeat these experiments with a different fluorescent probe to see how these results compare. Our second choice was 1,6-diphenyl-1,3,5-hexatriene (DPH), which is almost insoluble in water, resulting in weak fluorescence.[105] Once DPH is solubilised into hydrophobic environments, the fluorescence intensity increases, allowing us to monitor the formation of aggregates. The CAC for our 1:4 **H**/**G** system using DPH was found to be 95 μM (Figure 70a). The CAC was also found to be dependent on PNPB concentration, indicating that the presence of PNPB promotes the formation of self-assembled structures. The CAC with half the usual amount of substrate (250 μM) was found to be 109 μM (Figure 70b). When the substrate concentration is doubled (1000 μM) compared with the usual substrate concentration, the CAC decreases with this estimated to be 76 μM (Figure 70c). From these results, we concluded that the CAC calculated from the experiments with DPH seemed more realistic than those calculated with Nile red. The CAC using DPH was further supported by a plot of the rate of reaction

vs total amphiphile concentration (Figure 70d). Here, the change in slope was seen at 100 µM total surfactant concentration. A CAC of 100 µM means that we have been working at the CAC for all the previous experiments and can use this concentration of amphiphiles for all systems going forward.

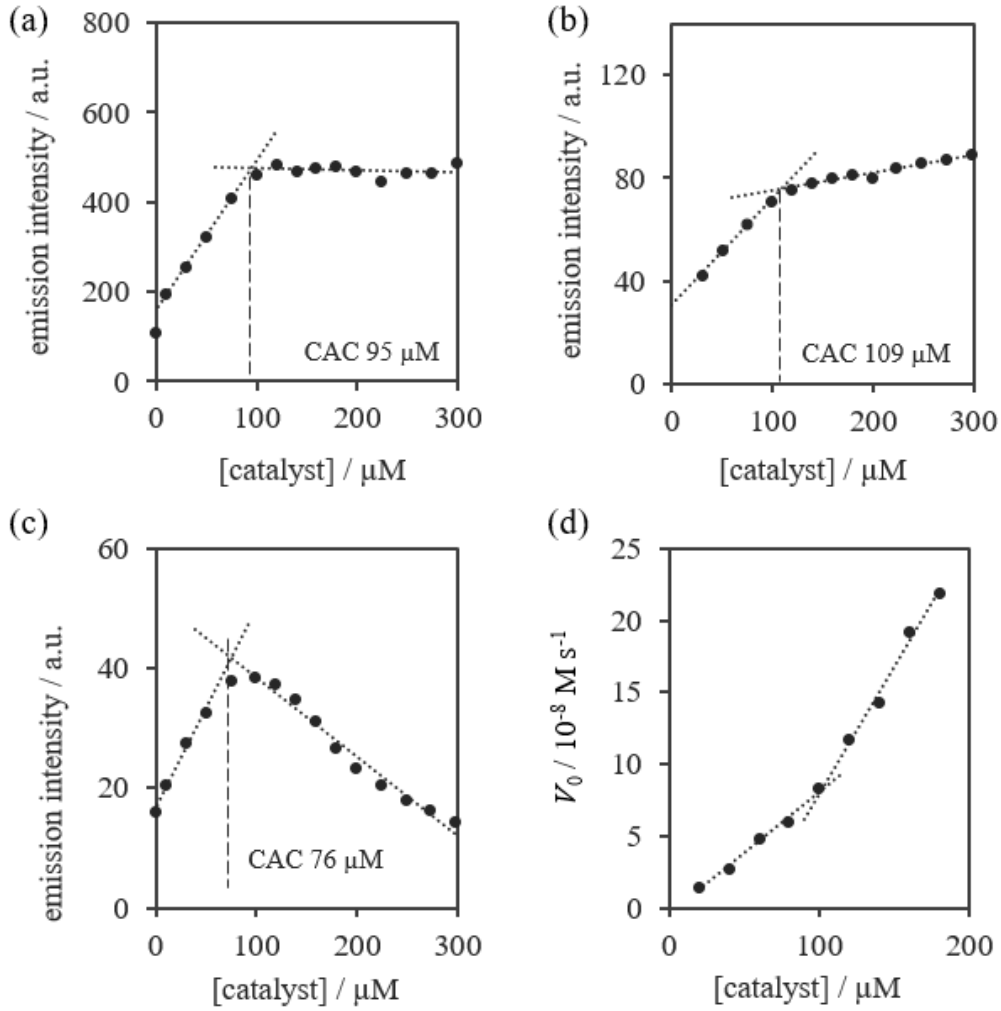

*Figure 70: CAC Determination for 1:4 **H**/**G** system in the presence of Zn^{2+}. Fluorescent titrations using aqueous buffer pH = 7.0 ([HEPES] = 5 mM), [DPH] = 1 µM with 500 µM PNPB (a), 250 µM PNPB (b) and 1000 µM PNPB (c). Esterolysis rate with increasing catalyst concentration in aqueous buffer pH = 7.0 ([HEPES] = 5 mM), [PNPB] = 500 µM, 40 °C (d). Source: Ref. [94]/Wiley-VCH.*

Dynamic light scattering (DLS) was another tool used to characterise the self-assembled properties of our catalytic system. Light scattering techniques such as DLS offer a non-invasive way to measure aggregates in solution.[106] Size information regarding these aggregates is obtained from DLS measurements along with polydispersity information.[106]

The size of the aggregates in our 1:4 **H**/**G** system in the presence of Zn^{2+} was determined to be between 60-70 μM (see Figure 71).

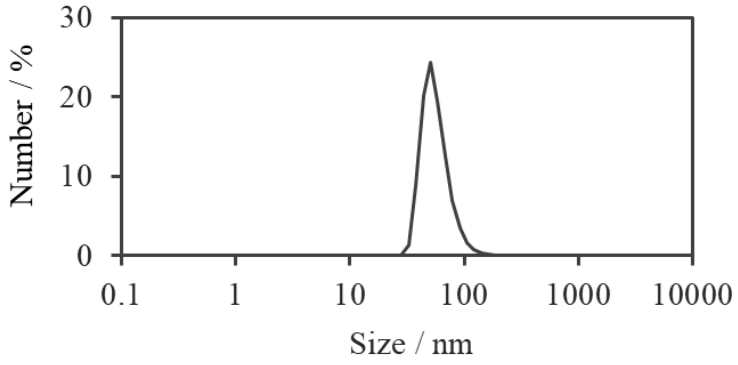

*Figure 71: DLS plot of 1:4 **H**/**G** system with Zn^{2+}. Experimental conditions: aqueous buffer pH = 7.0 ([HEPES] = 5 mM), [amphiphiles] = 100 μM, [$Zn(NO_3)_2$] = 25 μM, [PNPB] = 500 μM. Source: Ref. [94]/Wiley-VCH.*

Transmission electron microscopy (TEM) was used to visualise the aggregates forming in our 1:4 **H**/**G** catalytic system. For this technique, we need to prepare a thin layer of the sample through which a high-energy beam of electrons can pass. The electrons interact with the atoms in the sample, revealing the fine details of the structure.[107] This technique is very popular to aid in the characterisation of self-assembled systems.[108] Figure 72 shows representative TEM images for our 1:4 **H**/**G** catalytic system, with vesicle structures seen in these images.

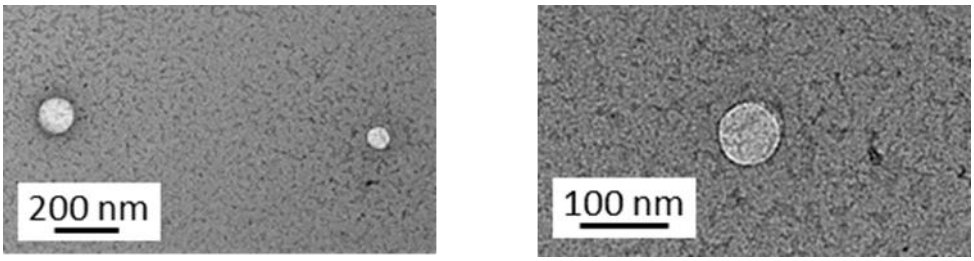

*Figure 72: TEM images of 1:4 **H**/**G** in aqueous buffer pH 7.0 ([HEPES] = 5 mM), [amphiphiles] = 200 μM, [$Zn(NO_3)_2$] = 50 μM, [PNPB] = 500 μM. Source: Ref. [94]/Wiley-VCH.*

2.8 Replacement of G with a stronger metal ion chelator (D2PA)

From the reaction mechanism we proposed for our initial 1:4 **H**/**G** system (Figure 67), we see that three **G** amphiphiles act as a metal ion chelator binding Zn^{2+}, stabilising a hydroxyl group capable of undergoing nucleophilic attack. From this, we predicted that replacing three equivalents of **G** with a stronger Zn^{2+} chelator would further optimise our catalytic system. A secondary screen was then performed using well-known Zn^{2+} chelators 1,4,7-triazacyclononane (**TACN**) and di-(2-picolyl)amine (**D2PA**) (Figure 73), with the results of this screen shown in Figure 74.

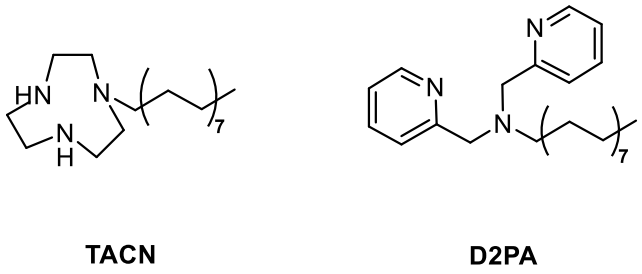

TACN **D2PA**

*Figure 73: Structures of **TACN** and **D2PA** amphiphiles.*

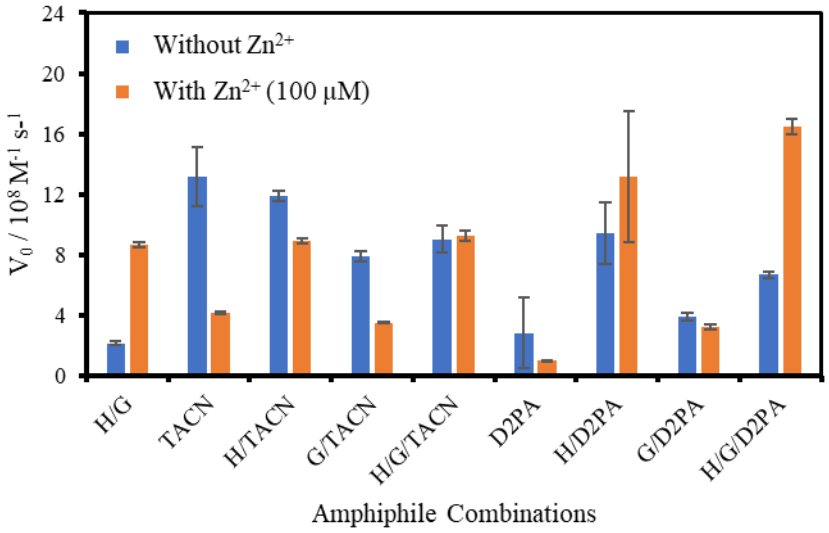

Figure 74: Optimisation screen with stronger Zn^{2+} chelators. Experimental conditions: aqueous buffer pH = 7.0 ([HEPES] = 5 mM), [amphiphiles] = 100 µM, [PNPB] = 500 µM, 40 °C. Amphiphiles were combined in equal proportions. Source: Ref. [94]/Wiley-VCH.

The activity of **TACN** was first investigated on its own, and this was found to have a high initial rate of reaction followed by a plateau after the conversion of approximately 20%

of PNPB (Figure 75a). This UV trace is characteristic of direct nucleophilic attack by the secondary amines present in **TACN**, occurring in a non-catalytic manner. In contrast, when Zn^{2+} is added to **TACN,** we see a decrease in the rate of catalysis. Likely, the secondary amines are now bound to the Zn^{2+} ion and are unable to undergo nucleophilic attack. The UV trace for **TACN** with Zn^{2+} supports this with the presence of just one rate, suggesting that catalysis is occurring because of a hydroxyl group stabilised by a **TACN**·Zn^{2+} complex (Figure 75b). Mass spectrometry was also used to determine the difference between the catalytic mechanisms of **TACN** with and without Zn^{2+} (Figure 76). The mass spectrum of just **TACN** in the presence of PNPB (Figure 76b) shows the formation of **TACN**-butyrate adducts (**60** and **61**), seen by the peaks at 424.4 and 494.4, supporting the direct nucleophilic attack onto PNPB. The mass spectrum for **TACN** with Zn^{2+} (Figure 76c) shows a much smaller peak of the **TACN**-butyrate adduct **61**, with a strong signal from the **TACN** amphiphile itself. The combination of **TACN** with our original **H** or **G** amphiphiles did not result in a significant improvement of the catalytic activity compared with our original 1:4 **H**/**G** system.

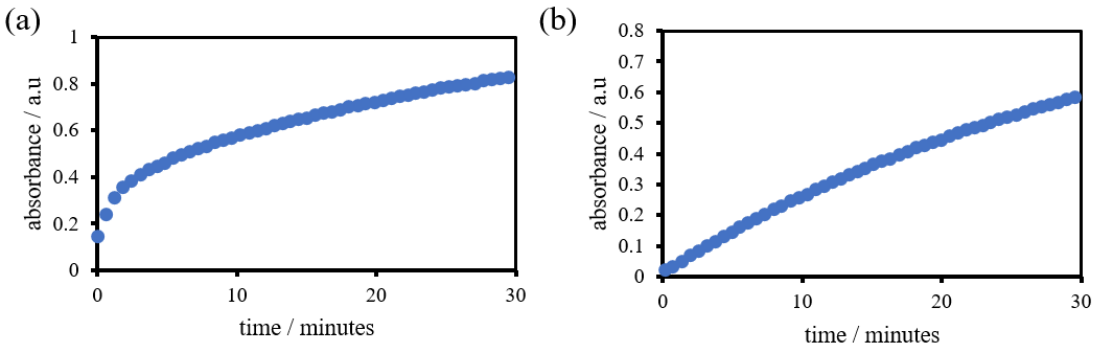

*Figure 75: UV traces for **TACN** without Zn^{2+} (a) and with Zn^{2+} (100 μM) (b). Experimental conditions: aqueous buffer pH = 7.0 ([HEPES] = 5 mM), [**TACN**] = 100 μM, [PNPB] = 500 μM, 40 °C. Source: Ref. [94]/Wiley-VCH.*

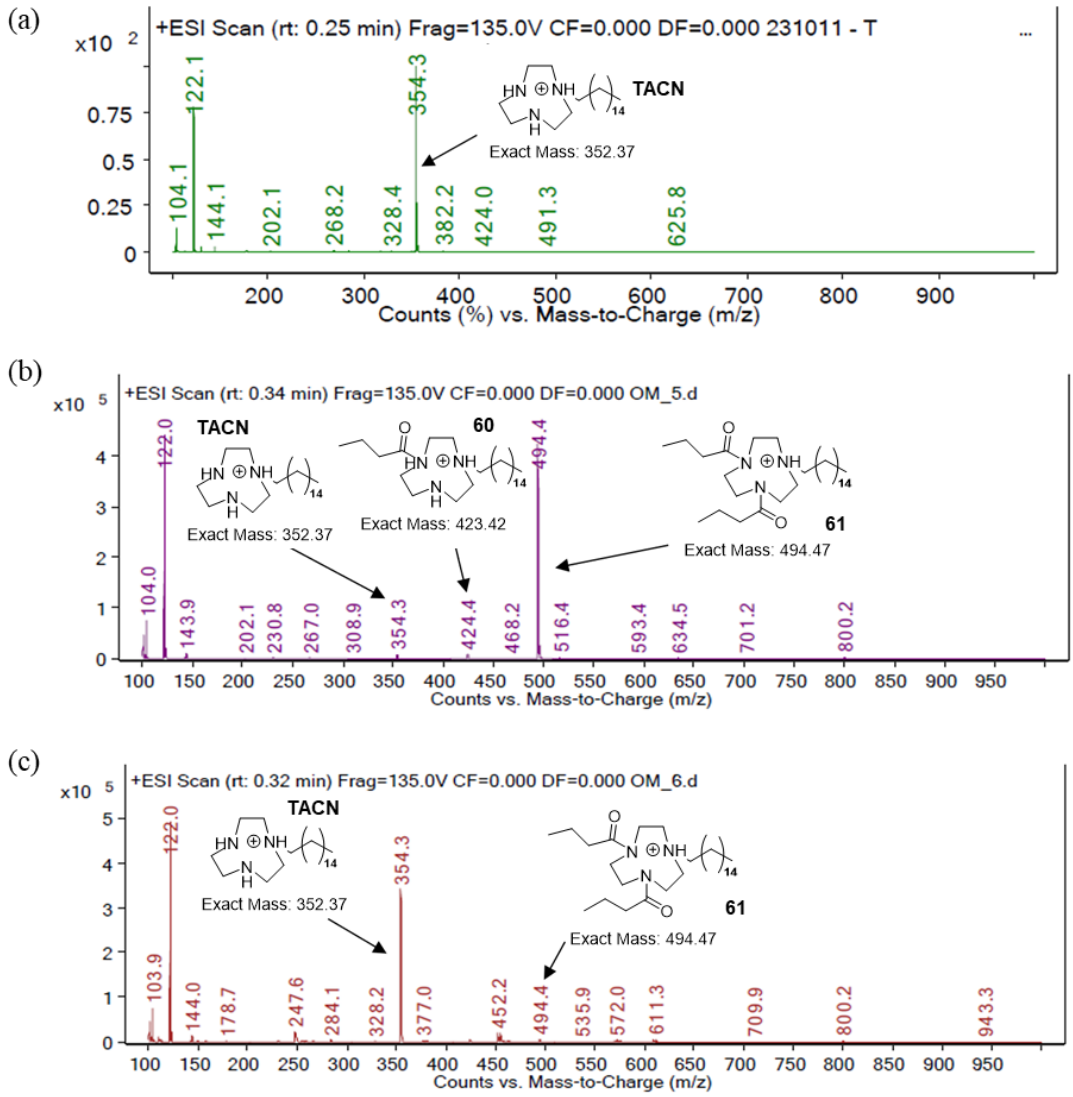

*Figure 76: Mass spectrometry data for the catalysis of PNPB with **TACN** in the absence of Zn^{2+} and PNPB (a), without Zn^{2+} in the presence of PNPB (500 µM) (b), and in the presence of both PNPB (500 µM) and Zn^{2+} (100 µM) (c). Experimental conditions: aqueous buffer pH = 7.0 ([HEPES] = 5 mM), [**TACN**] = 100 µM, 40 °C. Source: Ref. [94]/Wiley-VCH.*

The addition of **D2PA** was shown to improve the rate of catalysis. Firstly, in combination with **H** in a 1:1 ratio in the presence of Zn^{2+} gave higher activity than the original 1:4 **H**/**G** system. The addition of **G** further increased the activity of the 1:1:1 **H**/**G**/**D2PA** system with Zn^{2+}. This reinforces the importance of the **G** amphiphile and its role in the catalytic mechanism, especially since the concentration of ligands is now two-thirds of that in the 1:1 **H**/**D2PA** system. Once again, we can propose a mechanism for catalysis similar to that proposed for the 1:4 **H**/**G** system. Figure 77 shows the proposed mechanism with our **H** amphiphile initially undergoing nucleophilic attack of our substrate, releasing PNP and

forming our **H**-butyrate adduct **58**, which once again could be confirmed using mass spectrometry (Figure 78). Now though, we have our **D2PA** amphiphile acting as our metal ion chelator, forming a complex with Zn^{2+} that can bind a hydroxyl group to undergo nucleophilic attack of the **H**-butyrate adduct to give us back our histidine amphiphile, along with butyric acid. Our **G** amphiphile acts as our oxyanion hole, stabilising our transition state for both nucleophilic attacks.

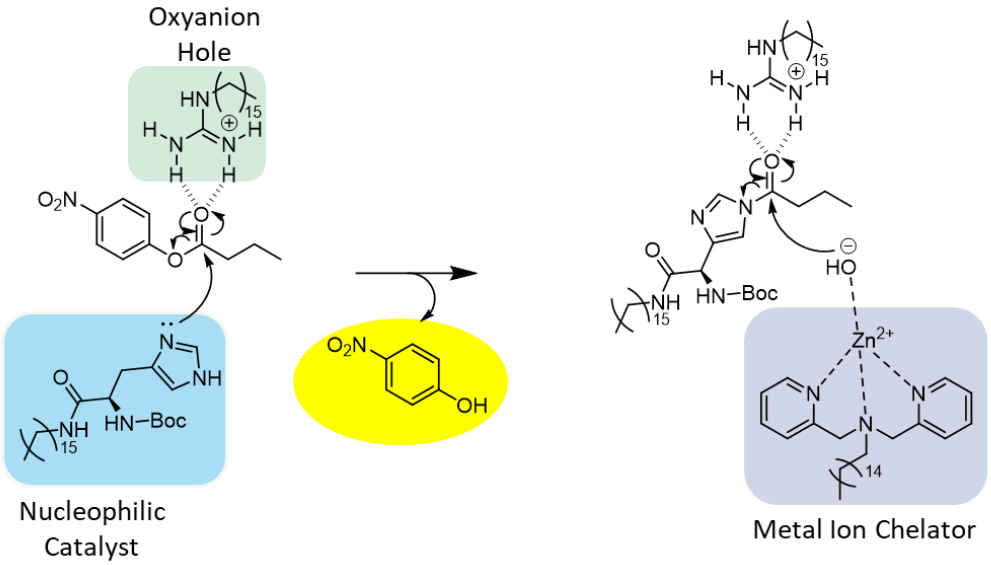

*Figure 77: Mechanism for 1:1:1 **H/G/D2PA** catalytic system in the presence of Zn^{2+}.*

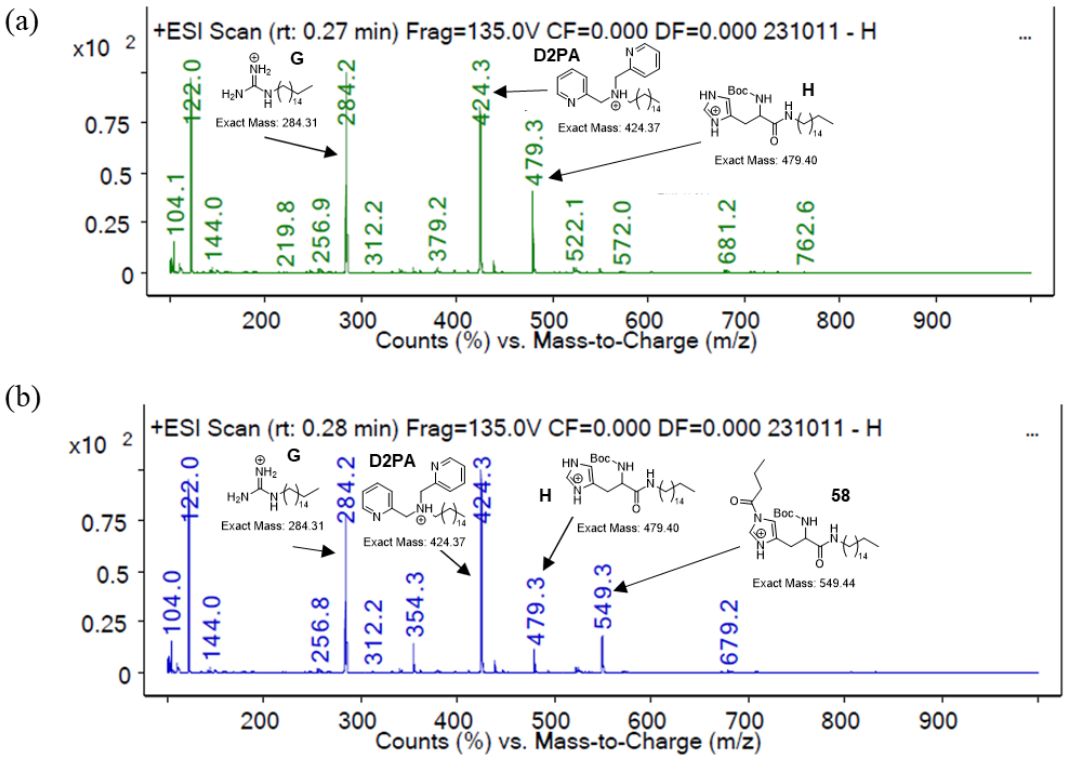

*Figure 78: Mass spectrometry data for 1:1:1 **H**/**G**/**D2PA** system in the absence of PNPB (a) and in the presence of PNPB (500 µM) (b). Experimental conditions: aqueous buffer pH = 7.0 ([HEPES] = 5 mM), [amphiphiles] = 100 µM, [$Zn(NO_3)_2$] = 25 µM, 40 °C. Source: Ref. [94]/Wiley-VCH.*

Interestingly, what we are seeing here is a mix between a cooperative mechanism and a sequential mechanism. Initially, we have our **H** and **G** amphiphiles working cooperatively to facilitate the first nucleophilic attack on the butyrate substrate. This is then followed by the subsequent step, whereby the **D2PA** amphiphile reacts only after the initial nucleophilic attack of the substrate, similar to the mechanism proposed by Moss et al., where the alcohol only attacks the acylated imidazole species (Figure 42). However, the second nucleophilic attack can also be considered a separate cooperative step, as it works in tandem with the **G** amphiphile, which stabilises the transition state in both steps.

2.9 Using Michaelis-Menten kinetics to determine the catalytic efficiency

Michaelis-Menten parameters were used as a tool to compare our two best catalytic systems to those previously reported in the literature. To do this, we first determined these parameters for our system by measuring the initial rates of reaction at increasing

concentrations of substrate (Figure 79). From these plots, we were able to determine the k_{cat} of our catalytic systems. These were determined to be 0.017 ± 0.003 s^{-1} for 1:4 **H/G** and 0.023 ± 0.006 s^{-1} for 1:1:1 **H/G/D2PA**. These k_{cat} values were comparable to those of recently reported artificial esterase examples, which involve rigid, well-defined systems (Table 2). This includes systems by Liu et al., where they designed a self-assembled dipeptide catalyst (Phe-His-C_{16}-SH), which forms nanofibers. Other examples include the catalytic amyloids formed for seven-residue peptides designed by Rufo et al., a catalyst immobilised onto solid-phase supports by Nothling et al. and engineered proteins from Zastrow et al. We also compared the calculated k_{cat} values to the native esterase enzyme α-chymotrypsin. These were comparable to those of our artificial esterase systems.

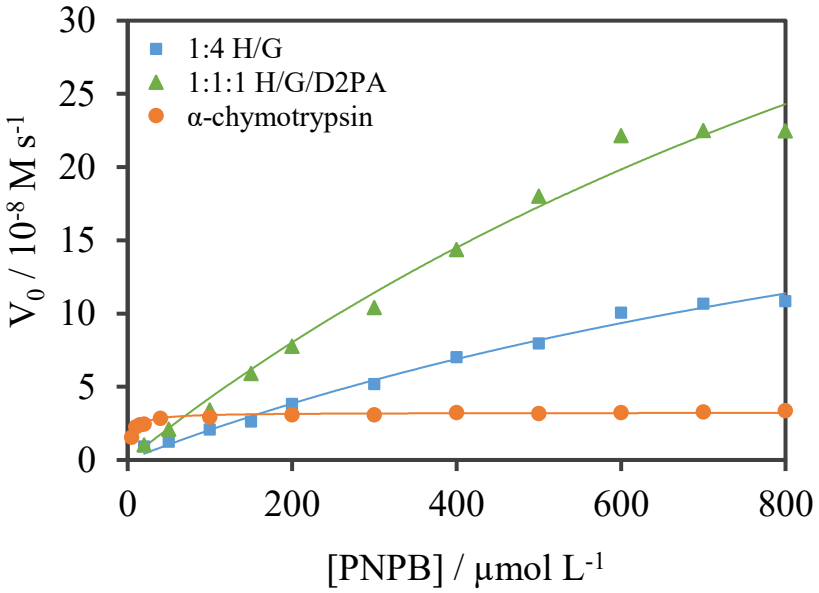

Figure 79: Michaelis-Menten fit for 1:4 ***H/G*** *(100 µM, [$Zn(NO_3)_2$] = 25 µM), 1:1:1* ***H/G/D2PA*** *(100 µM, [$Zn(NO_3)_2$] = 25 µM) and α-chymotrypsin (2 µM, [$CaCl_2$] = 53 mM). Experimental conditions: aqueous buffer pH = 7.8 ([Tris] = 4 mM), 40 °C. Source: Ref. [94]/Wiley-VCH.*

Table 2: Comparison of our best artificial esterase systems to those previously reported in the literature and to the native enzyme α-chymotrypsin. Source: Ref. [94]/Wiley-VCH.

Catalyst system	V_{max} **(10^{-8} M s^{-1})**	k_{cat} **(s^{-1})**	K_M **(mM)**	k_{cat} / K_M **(M^{-1} s^{-1})**
1:4 **H/G**	33 ± 6	0.017 ± 0.003	1.5 ± 0.4	11 ± 5
1:1:1 **H/G/D2PA**	75 ± 20	0.023 ± 0.006	1.7 ± 0.6	14 ± 9
MINP[64]		0.03	0.14	205
Ac-IHIHQI-$CONH_2$[53]		0.026	0.4	62
Phe-His-C_{16}-SH[55]		0.016	1.4	11
Resin-triad[17]		0.027	12	2.3
TRI-peptide-[Zn^{2+}][69]		0.0054	1.7	3.1
α-chymotrypsin	3.20 ± 0.04	0.016 ± 0.002	0.0049 ± 0.0004	3300 ± 300

If we instead compare the catalytic efficiency (k_{cat}/K_M) of our best system (1:1:1 **H/G/D2PA**) to those reported in the literature, we see that this is comparable to systems consisting of rigid, well-organised structures, such as the dipeptides forming nanofibers (Phen-His-C_{16}-SH) from Liu et al. From this, we can conclude that self-assembly can be used as a strategy for the synthesis of an artificial esterase giving similar activity to literature examples featuring highly rigid pockets. However, these systems are not as efficient as catalysts formed from molecularly imprinted polymers, such as the work by Yan Zhao's research group (MINP).[64] This suggests that significant benefits can be had from the generation of highly ordered structures. Comparing our catalyst and the literature examples to the native enzyme α-chymotrypsin, we can see that there is still a lot of work to do to match the catalytic efficiency of the native enzyme, as this is more than 10 times greater than the best artificial esterase system out there.

It is important to note that the curves used to fit the Michaelis-Menten equations are far from saturation. Therefore, their fitting must be conducted with caution. This type of fitting is commonly seen in many artificial esterase systems, including the work by Nothling et al., which is commonly used as a reference. For our system in particular, it is quite hard to reach those high concentrations required to reach saturation. There are several reasons for this. Firstly, the substrate may encounter solubility issues at higher concentrations, whether that be in the cuvette conditions we use for catalysis or in the

more concentrated stock solution. Secondly, the substrate itself can start to interfere with the system by interfering or disrupting vesicle formation at higher concentrations. Therefore, the parameters obtained from the Michaelis-Menten fit are likely affected by large errors resulting from the changing concentrations of the substrate, potentially altering the structure of the aggregates.

2.10 Advantages and limitations of this system

The main advantage of a self-assembled catalytic system is its modularity. This makes the system easy to modify, as changes to the functional groups used and even the proportions in which they are present can be easily varied simply by adding more or less of the desired amphiphile into the system. This allows for the rapid testing of various catalytic systems, a point which was demonstrated in this chapter with the initial screen of potential functional groups for catalysis (Section 2.4), followed by the optimisation of amphiphile concentrations (Section 2.6). Catalysts where the functional groups are immobilised onto a molecular scaffold or surface lack this modularity, requiring total synthesis of the catalyst to make any changes, making these types of systems synthetically taxing.

Self-assembled systems are also highly dynamic, meaning the amphiphiles are not fixed in place with the formation of aggregates such as vesicles. Instead, these are in equilibrium with the bulk. The advantage of this is the ability of the system to dynamically reorganise – something which was previously demonstrated by the research group.[78]

However, from our determination of the catalytic efficiency and comparison with the literature, we can see that self-assembled systems are not always the most efficient option. Artificial esterases consisting of highly organised structures with rigid, well-defined binding pockets resulted in much higher catalytic activity than our best artificial esterase system (over 14 times greater than our best system). This suggests that significant benefits can be had from the generation of these structures.

Self-assembly is therefore a great tool that can be used for the discovery and optimisation of an artificial esterase, due to its rapid and flexible nature. However, in order to generate a more efficient and robust catalyst, some sort of rigidity needs to be introduced into the structure. One approach to achieving this is through catalyst immobilisation, for example onto solid supports such as polymer resins, or through alternative immobilisation

strategies that retain elements of modularity. This concept formed the basis for the next stage of this PhD project. Accordingly, Chapter 3 focuses on the immobilisation of the self-assembled catalytic system to generate a more rigid architecture, while preserving the modular design principles that enable systematic optimisation.

Chapter 3: Silver-Thiol Coordination Polymers

3.1 Introduction

The previous chapter discussed how self-assembly can be utilised as a tool for catalyst discovery and optimisation. The modularity of these systems allows for simple iterative testing of the catalytic system. However, when comparing our self-assembled artificial esterase to examples in the literature, we found that there were still significant benefits to be had from robust, highly ordered catalytic systems. These types of rigid systems with catalytic pockets could give enhanced rates of catalysis compared with the self-assembled system. Therefore, we wanted to adapt our self-assembled catalyst into a more robust catalytic system. Traditional examples of rigid catalytic systems include the immobilisation of catalytic functionalities onto molecular scaffolds or nanoparticles, or the incorporation of these into dendritic structures, all of which have been discussed in detail in Chapter 1. Though these are all great ways to introduce rigidity into a catalytic system, we wanted something that offered a degree of modularity, so we could undergo rapid screening and optimisation in a similar manner to Chapter 2. This then drew us to metal-ligand coordination polymers.

3.1.1 Metal-ligand coordination polymers

Metal-ligand coordination polymers are polymers that are formed via both covalent and non-covalent interactions. The advantage of this is that the polymer can be influenced by external factors, resulting in changes to its properties.[109] These polymers consist of alternating metal ions and organic ligands joined by covalent bonds; see Figure 80, which can then aggregate together due to non-covalent interactions occurring between the ligands in the polymers. The ligands themselves can be modified for a particular function and then incorporated into the polymer with the addition of the desired metal ion. The *in situ* formation of these polymers gives the system some modularity, as the ligands can be varied before polymer formation. This means that changes to the polymer formed require minimal synthetic effort compared to other immobilised systems, such as molecular scaffolds and dendrimers. For this chapter, we wanted to focus on coordination polymers formed from Ag^+ ions and thiol-based ligands.

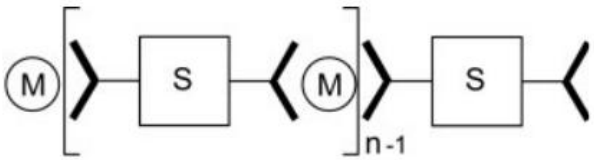

Figure 80: Representation of metal-ligand coordination polymers. Source: Reprinted from ref. [109] with permission. Copyright (2005) John Wiley and Sons.

3.1.2 Silver-thiol coordination polymers

Silver-thiol coordination polymers can form a variety of structures depending on the ligands present. Typically, these are divided into three groups: one-dimensional chains, two-dimensional lamellar structures and three-dimensional metal-organic frameworks.[110] Even with these groups, there is a great variety in the structures seen, with the key factor determining the structure being the functionalisation of the thiol-ligand.

Characterisation of the structures formed by silver-thiol coordination polymers has been reported using a variety of different length alkyl thiols (Figure 81). Here, Parikh et al. found that the layer chain assemblies occurring between the coordination backbone in a double-layer arrangement are all trans-extended chains.[111] In addition to this, the alkyl chains are all oriented perpendicular to the Ag-S bond. Chain organisation of the ligands is determined by the coordination geometry of the Ag-S bond rather than just by van der Waals forces.[111]

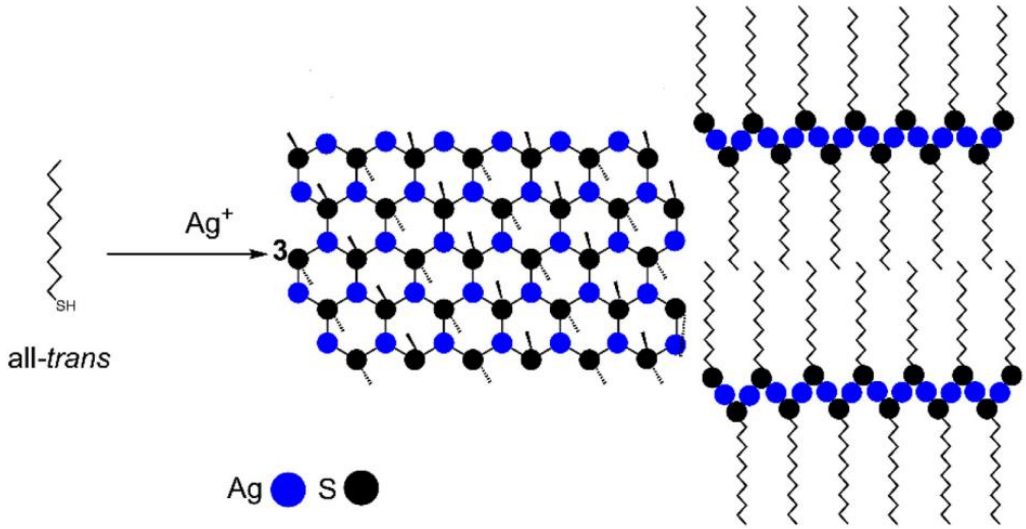

Figure 81: Representation of the structures formed from the assembly of silver-thiol coordination polymers consisting of alkyl-thiol ligands. Source: Adapted from ref. [110] with permission. Copyright (2021) Elsevier.

Casuso and coworkers proposed that different structures of silver-thiol polymer networks form depending on whether the thiol ligand is neutral or acidic. Figure 82 shows the primary structure of the polymers formed from the metal-ligand coordination backbone, with the R groups consisting of one of the neutral or acidic thiol ligands shown in Figure 83. The polymer backbone is stabilised by metallophilic attractions occurring between neighbouring Ag^+ ions.[112] These individual polymer strands then start to assemble, with the microstructure formed being dependent on the functionalisation of the thiol ligand. Those with neutral functionalities (Figure 83a) resulted in fibril structures, while acidic functionalities (Figure 83b) resulted in the formation of sheets.[112] These microstructures were a lot less stable than the coordination backbone, with changes in heat or pH resulting in the breakdown of these structures.[112]

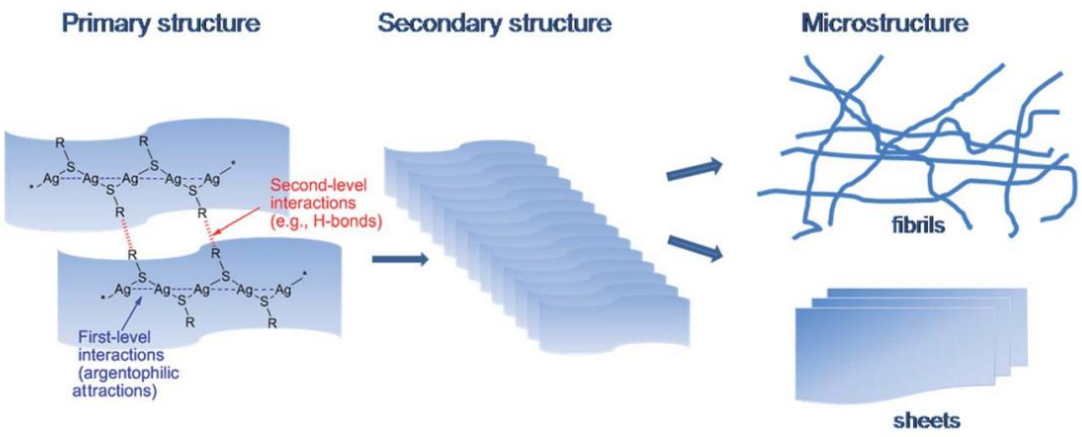

Figure 82: Proposed structures formed from silver-thiol coordination polymers. Source: Reprinted from ref. [112] with permission. Copyright (2011) Royal Society of Chemistry.

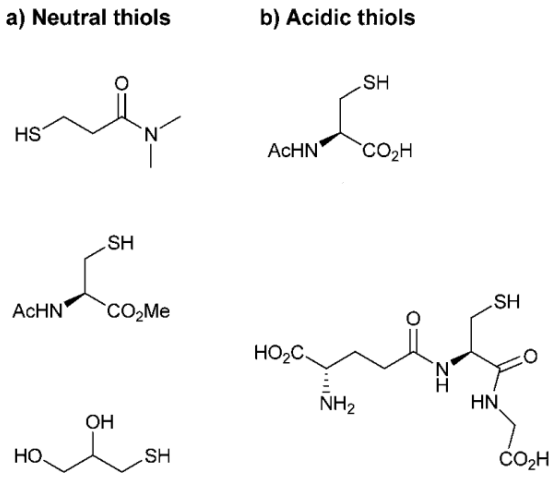

Figure 83: Neutral (a) and acidic (b) R groups for the silver-thiol coordination polymer structures proposed in the figure above. Source: Adapted from ref. [112] with permission. Copyright (2011) Royal Society of Chemistry.

The formation and aggregation of silver-thiol coordination polymers was investigated by Quan and coworkers. Cystine-based thiols were used, and tetraphenylethylene groups were incorporated into these due to their ability to form aggregates and induce emission (Figure 84).[113,114] Tetraphenylethylene groups on their own have weak fluorescent emission; however, when they form aggregates, this emission intensity increases, allowing fluorescence spectroscopy to be used to gain insight into these aggregates.[114] With this, Quan et al. found coordination polymers were able to form in both protic and aprotic solvents. Though the polymers can form in both conditions, the aggregate

structures then formed from these vary depending upon the solvent. In aprotic solvents such as THF, helical fibre structures were seen. As more protic solvents are introduced into the system, such as water, the helical structures transform into nanoparticles, confirmed by SEM.[113] Quan and coworkers also found that aggregates in different solvents had different stabilities, with THF aggregates being more resilient to temperature changes compared to aggregates in THF/water mixtures.[113] This research nicely demonstrated the effect that solvents can have on the structures formed from the aggregation of coordination polymers.

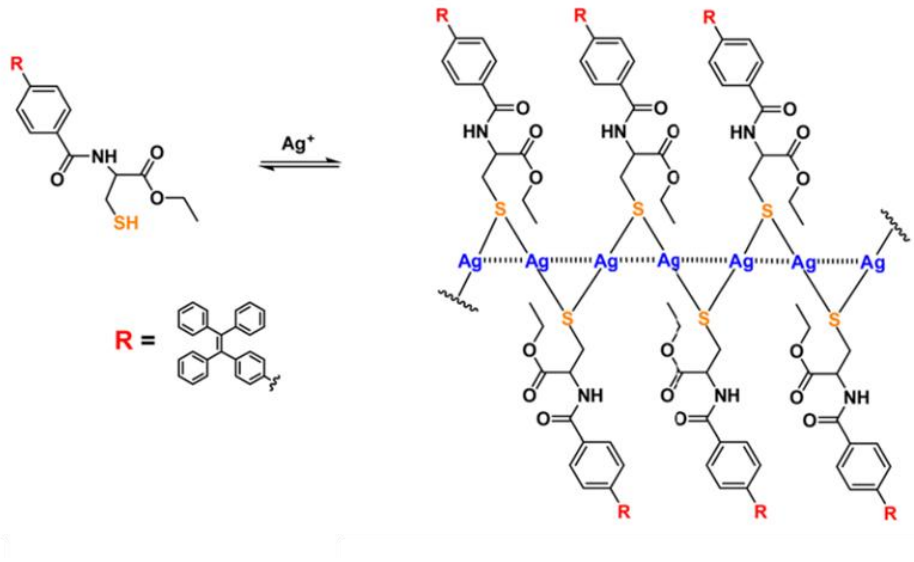

Figure 84: Silver-thiol coordination polymers formed from cystine-based thiols, which incorporate tetraphenylethylene to monitor aggregate formation via induced fluorescent emission. Source: Reprinted from ref. [113] with permission. Copyright (2023) Royal Society of Chemistry.

Silver-thiol coordination polymers have been utilised for a wide range of applications, including non-antibiotic anti-infective coatings for implants[115], hydrogel formation for novel soft materials[112], catalysis[116], and anion sensing[117]. This diverse nature stems from the modification of the organic thiol ligands used in the polymers, rather than the coordination bond itself. For this research, we are interested in using these types of silver-thiol coordination polymers to develop a catalytic system capable of facilitating ester hydrolysis.

Silver-thiol coordination polymers for catalysis

Coordination polymers, formed from the addition of Ag^+ ions to catalytic thiols, have been shown to have phosphodiester activity (Figure 85). These systems have either comparable or higher catalytic activity than micellar, vesicular, dendrimer or nanoparticle-based catalysts reported in the literature, which utilise the same catalytic functionalities.[116] For this system, a series of TACN-based thiols were synthesised. These all consisted of a catalytic TACN group and a thiol separated by different length alkyl chains. Coordination polymers could then be formed *in situ* upon mixing equal amounts of these catalytic thiols with Ag^+. The formation of these polymers brings the catalytic headgroups close together, so once they undergo complexation with Zn^{2+}, they can cooperatively catalyse phosphodiester cleavage.

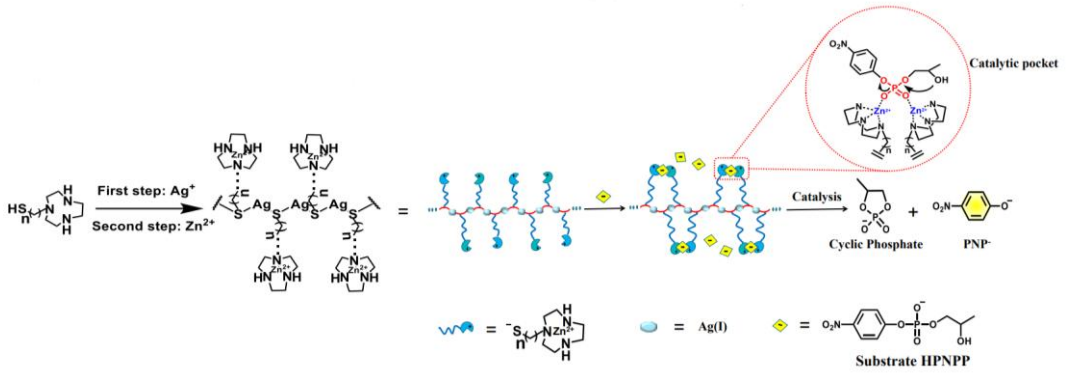

Figure 85: Silver-thiol coordination polymer using TACN catalytic headgroups for phosphodiesterase activity. Source: Adapted from ref. [116] with permission. Copyright (2021) John Wiley and Sons.

Using the model substrate HPNPP, the activity of these polymers could be assessed. Figure 86 shows the determination of metals to use for polymerisation (a) and TACN complexation (b). From this, Cao et al. determined Ag^+ to be the best metal for forming coordination polymers with the catalytic thiols, and Zn^{2+} was found to have the best activity towards phosphodiesters when complexed with TACN.

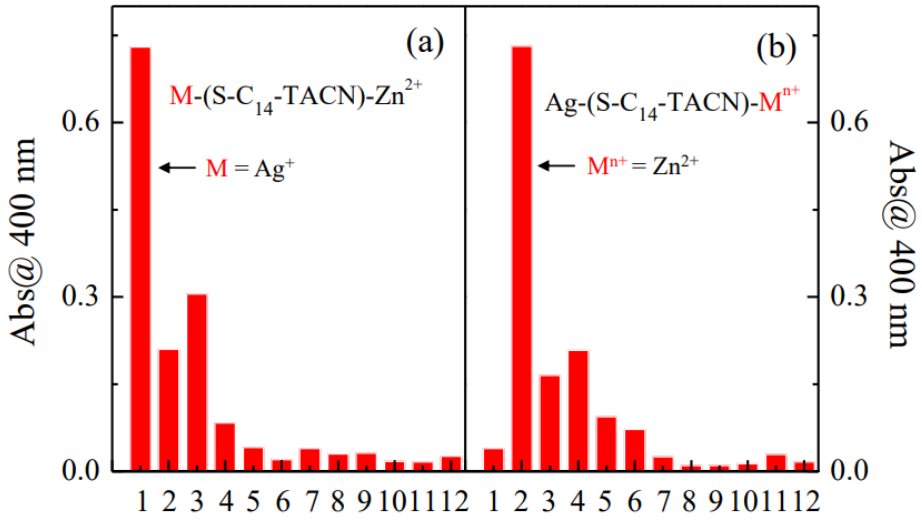

Figure 86: Determination of the ideal metal for coordination polymer formation in the presence of Zn^{2+} complexing TACN (a) and TACN complexation in the presence of Ag^{+} for coordination polymer formation (b). From 1-12, the metal ions used were Ag^{+}, Zn^{2+}, Cd^{2+}, Cu^{2+}, Co^{2+}, Ni^{2+}, Na^{+}, K^{+}, Fe^{3+}, Al^{3+}, Cr^{3+} and Hg^{2+}.Source: Reprinted from ref. [116] with permission. Copyright (2021) John Wiley and Sons.

The other key factor of this system, determined by Cao et al., was the length of the hydrophobic chains in the catalytic thiols. Cao and coworkers reasoned that the length of the alkyl chain needed to be long enough to easily bend, bringing together neighbouring TACN groups, while also creating a hydrophobic environment suspected to enhance reactivity. Cao et al. found that an alkyl chain length of 14 carbons had the highest k_{cat} value of all the chain lengths investigated. It was concluded that this was due to changes in the polarity of the local environment, helping to stabilise the transition state. Interestingly, thiols with alkyl chains greater than 14 (16 or 20) resulted in weaker activity as these longer chains form bulkier polymers, which aggregate together.

3.1.3 Aims of this chapter

In this chapter, we sought to develop a silver-thiolate coordination polymer capable of catalysing ester bond hydrolysis, inspired by the system reported by Cao and co-workers for phosphodiester cleavage. This approach was particularly attractive because it combines the formation of a more robust, polymeric catalytic architecture with a high degree of modularity and tunability. This simply required the initial synthesis of the desired thiol components, then the system could be optimised simply by varying the components to form the coordination polymer *in situ* (Figure 87). We wanted to adapt

this system to use as an artificial esterase, demonstrating that cooperativity could occur in this system between two or more different catalytic functionalities. In addition, we wanted to investigate whether the preorganisation provided by the silver-thiol coordination polymers would enable the formation of catalytic pockets with higher catalytic activity than those in the self-assembled vesicular system.

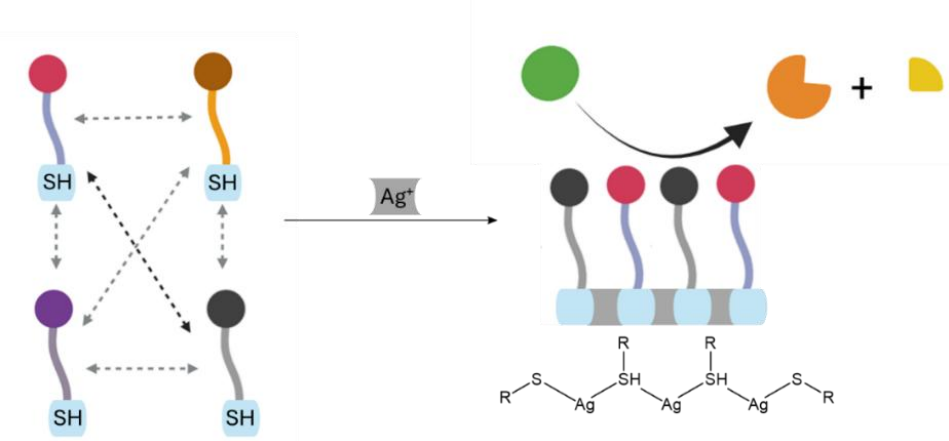

Figure 87: Plan for silver-thiol coordination polymer system.

3.2 Initial synthetic plan

Three important factors needed to be considered when designing the synthetic routes for the thiols for this system: the catalytic functional group, alkyl chain length and thiol protecting group.

We decided to synthesise thiols containing the catalytic functionalities that proved successful in our first system. The plan was to make guanidine, imidazole and di-(2-picolyl)amine containing thiols, to recreate the **H**/**G**/**D2PA** active site of our vesicle system. In our vesicle catalytic system, we discussed the differences between two imidazole-based amphiphiles: histidine (**H**) and histamine (**HM**). We determined that the **H** amphiphile had greater activity in the presence of Zn^{2+}; however, in the absence of this, the two were quite evenly matched (Figure 88). The synthesis of **H** compared with **HM** is slightly more involved (Scheme 13), with **H** requiring two synthetic steps due to the benzyl protecting group on the imidazole N. To optimise the synthesis of our imidazole-containing thiol, we decided to replace the histidine functionality with histamine. Though **HM** had lower catalytic activity compared with **H**, we decided that the simplification of the synthetic route would be worth this slight decrease in activity.

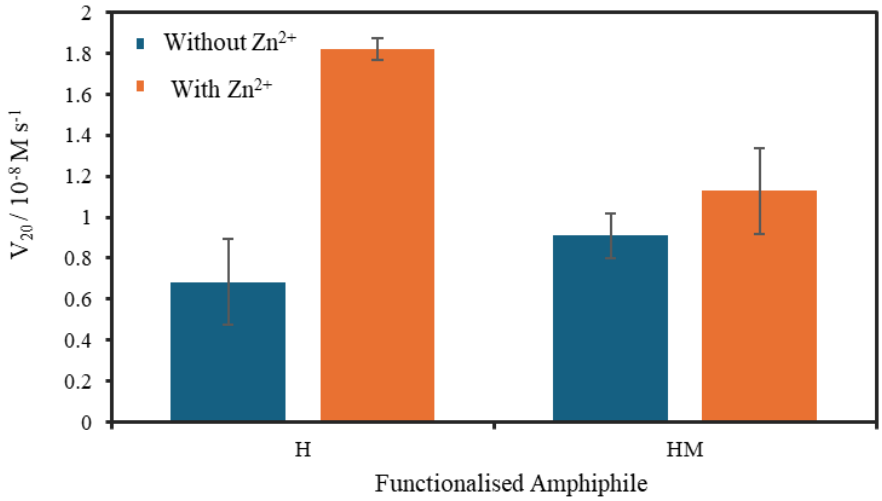

*Figure 88: Comparison of the rates of **H** and **HM** in the self-assembled vesicle system. Experimental conditions: aqueous buffer pH = 7.0 ([HEPES] = 5 mM), [total amphiphile] = 100 μM, [$Zn(NO_3)_2$] = 100 μM, [PNPB] = 500 μM, 40 °C.*

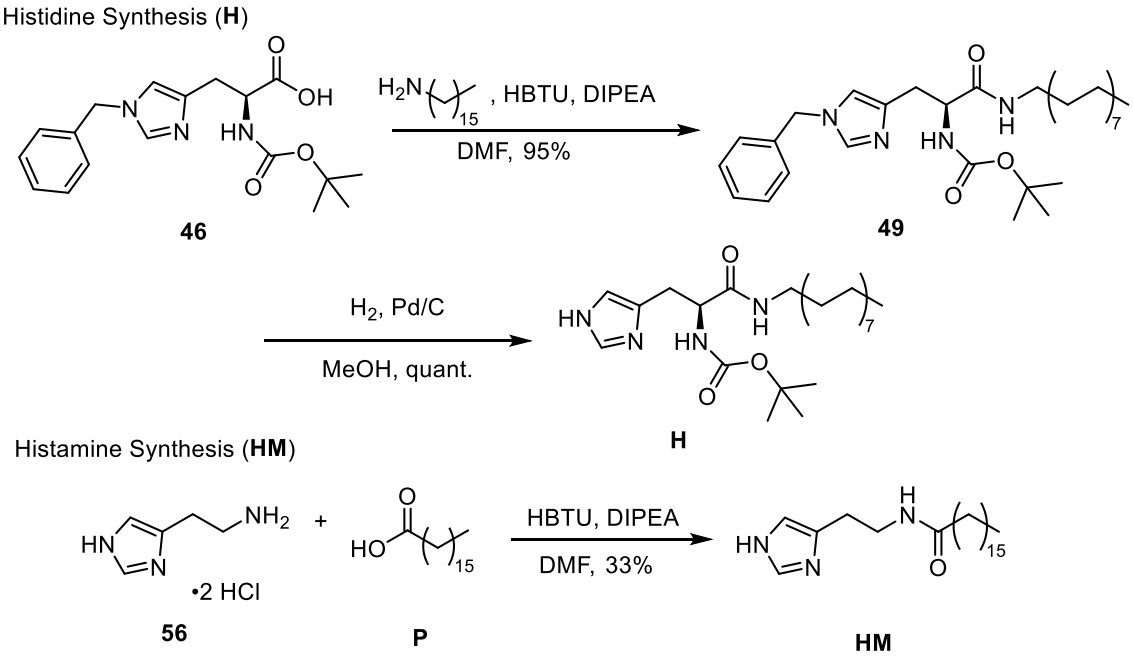

*Scheme 13: Synthesis of histidine (**H**) amphiphile compared to histamine (**HM**).*

In terms of chain length, Cao et al. determined that 14 carbons gave the ideal alkyl chain length for catalysis. However, we were concerned that a long alkyl chain would allow these structures to aggregate in solution. This might mean that any catalysis results we saw could be due to the aggregation of thiols bringing the catalytic groups closer together,

rather than from the formation of polymers. Therefore, we decided to choose an initial chain length that should be unlikely to self-assemble. We settled on a six-carbon chain length. This should be short enough to prevent the assembly of the thiols but hopefully still long enough for the catalytic groups to orient themselves in the correct three-dimensional orientation for catalysis, overcoming any potential repulsions between the catalytic head groups and the silver-thiol polymer chain.

To incorporate the thiol functionality into these molecules, we need to introduce this as a protected thiol to our chosen alkyl chain, preventing this from interfering with the subsequent synthetic steps required to introduce our catalytic functionalities onto the compound. Cao et al. utilised a thioacetate protecting group (Figure 89a) to synthesise their TACN-containing thiols. Though we initially considered this protecting group, we decided instead to use a trityl protecting group (Figure 89b). The concerns we had with using the thioacetate protecting group with our C6 thiol synthesis were to do with the volatility of some of our designed compounds. We were planning to make an alkyl amine (discussed further in Section 3.3.2), which can be quite volatile with a thioacetate functional group and a relatively short carbon chain. The introduction of a trityl protecting group prevented this compound from being so volatile, making it easier to work with. In addition to this, the trityl protecting group had two key advantages. Firstly, the three aromatic rings in this protecting group make it UV active, allowing all reactions to be easily monitored by TLC using a UV lamp to identify the products. Secondly, this protecting group is quite non-polar, so when we start to introduce those quite polar catalytic functionalities onto the compound, the presence of a non-polar protecting group should help with easier purification.

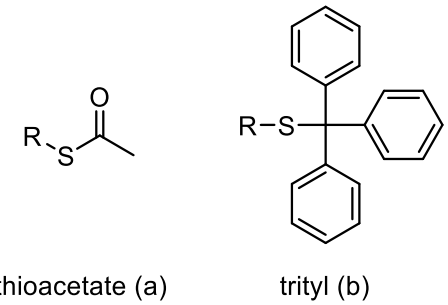

Figure 89: Thioacetate (a) and trityl (b) thiol protecting groups.

3.3 Synthesis of C6 thiols

3.3.1 Synthesis of C6-HM-SH

The synthesis of **C6-HM-SH** is shown in Scheme 14. Starting with 6-bromohexanoic acid (**62**), an esterification reaction was performed using thionyl chloride and MeOH (Scheme 15). Here, the carbonyl oxygen forms a bond with the sulfur in thionyl chloride, resulting in the loss of one of its chlorides. This chloride can then attack the carbonyl carbon, with those electrons moving to neutralise the positive charge on the oxygen. The lone pair of electrons on the oxygen can then reform the carbonyl bond, resulting in the loss of SO_2 and a chloride ion. The lost chloride ion can then deprotonate the carbonyl oxygen to form HCl. This forms our acid chloride (**68**), which can then react to form our ester. The lone pair of electrons on the oxygen in methanol can attack the carbonyl with our chlorine acting as a leaving group, to give our desired ester (**63**). This was obtained in a high yield (92%).

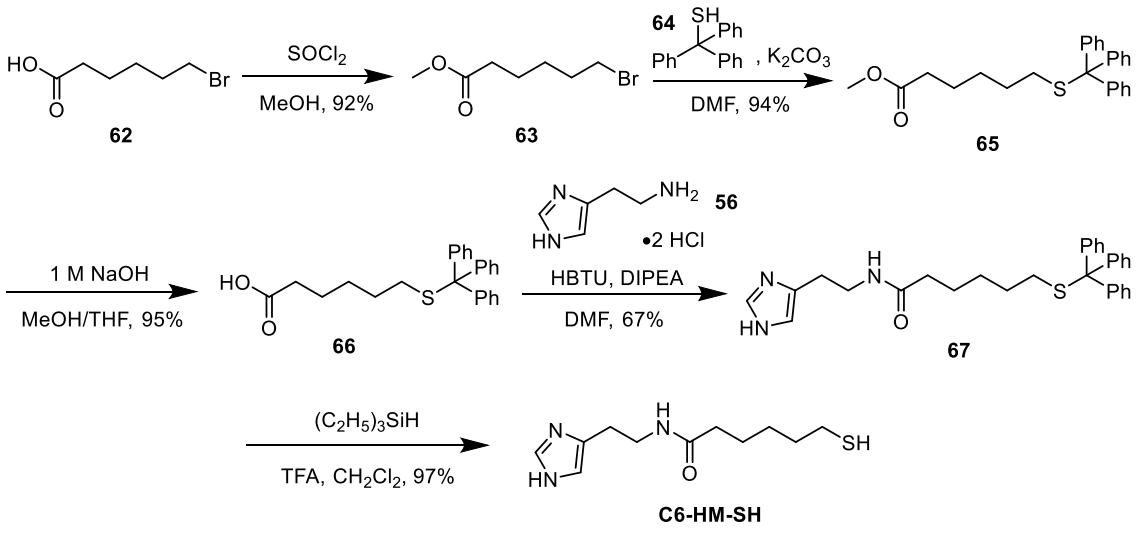

*Scheme 14: Synthesis of **C6-HM-SH**.*

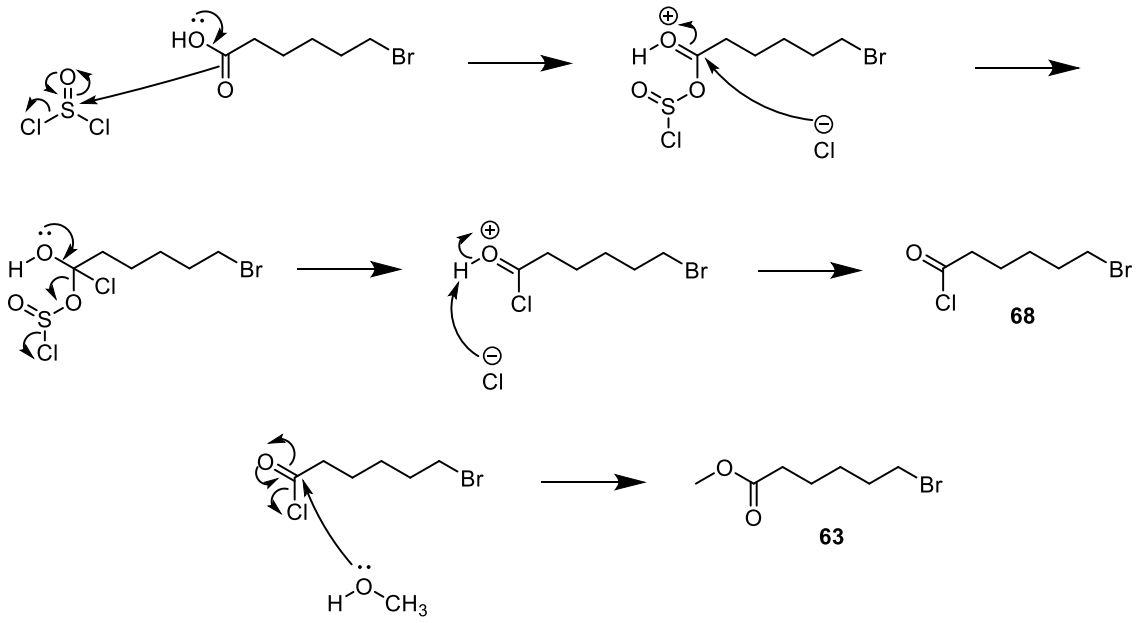

Scheme 15: Mechanism for esterification.

Following esterification, we introduced the thiol into our molecule via an S_N2 reaction between bromide **63** and triphenylmethanethiol (**64**), achieving a 94% yield. The desired final product **65** was confirmed due to the appearance of three multiplet peaks in the aromatic region of the ^{1}H NMR, integrating for a total of 15 H, which was a clear indication that the trityl thiol had been added to the molecule. Compound **65** was then hydrolysed to give the carboxylic acid (**66**). The mechanism for base-catalysed ester hydrolysis is shown in Scheme 16. OH^- acts as a nucleophile attacking the carbonyl of the ester. The OCH_3 species is then eliminated. This species is negatively charged, so it will remove the proton from the carboxylic acid to form the carboxylate ion. The reaction then undergoes an acidic workup (with 1 M HCl) to give carboxylic acid **66** as the product with a yield of 95%. A clear loss of the CH_3 group is seen in the ^{1}H NMR by the disappearance of the singlet peak at 3.64 ppm, confirming the presence of the carboxylic acid functionality in the product.

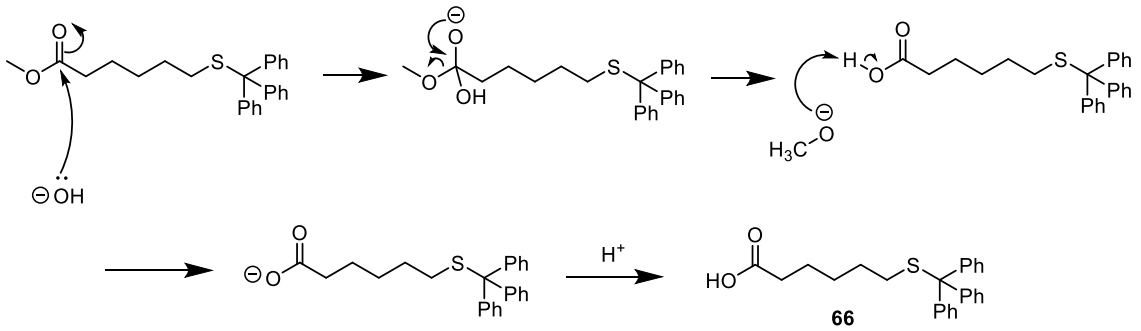

Scheme 16: Mechanism for base-catalysed ester hydrolysis.

Carboxylic acid **66** then underwent an amide coupling with histamine dihydrochloride (**56**) using HBTU and DIPEA. The mechanism for this reaction was previously discussed in Chapter 2, Section 2.2.1. We were able to confirm the presence of the desired product **67** due to the presence of both the imidazole peaks and trityl peaks in the aromatic region of the ^{1}H NMR. Finally, **67** was deprotected to give the free thiol **C6-HM-SH** (Scheme 17). Here, we used TFA and triethylsilane, following a procedure previously reported by Yamada et al. (2017).[118] The lone pair on the thiol takes a proton from TFA, weakening the bond between the thiol and the trityl carbon.[119] This bond breaks, forming our desired thiol along with the trityl carbocation. The triethylsilane then acts as a carbocation scavenger, providing a hydride to neutralise the carbocation to form triphenylmethane (**69**).[119,120]

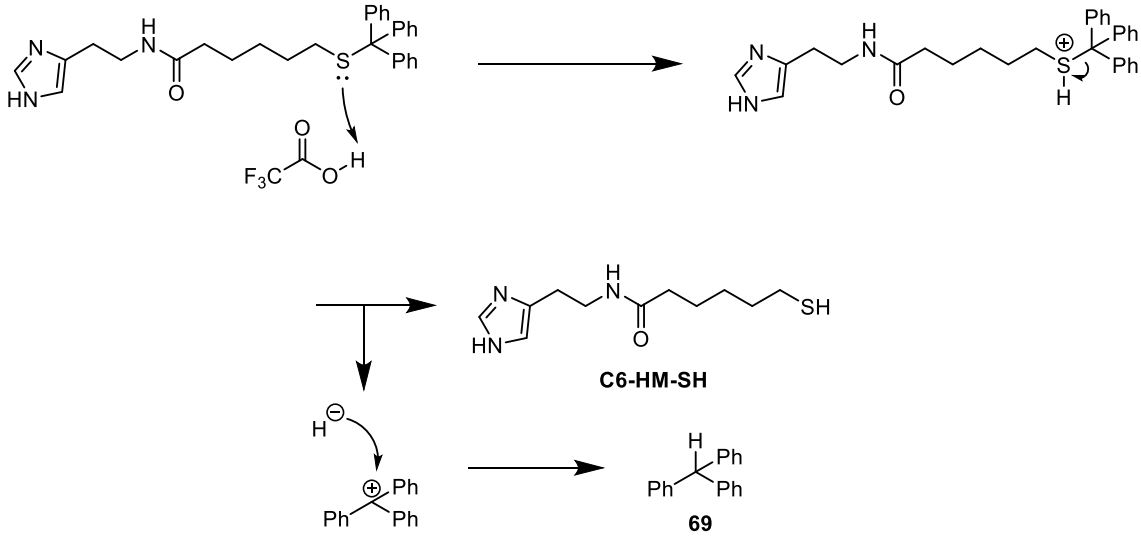

Scheme 17: Trityl deprotection mechanism.

The characterisation of the final compound **C6-HM-SH** could be performed using NMR spectroscopy. The ^{1}H NMR assignment is shown in Figure 90, with the two imidazole peaks assigned to the two singlet peaks above 6.5 ppm. Differentiating between these two imidazole peaks was accomplished using the COSY NMR (Figure 91). The imidazole proton at 6.86 ppm (orange) correlated to an -CH_2 signal, which allowed assignment of the triplets at 2.77 (green) and 3.42 (light blue). The most downfield peak (2.68 ppm) of our now unassigned signals should belong to the -CH_2 next to the thiol (red). From here, we were able to use the COSY correlations to determine the assignment of the remainder of the chain.

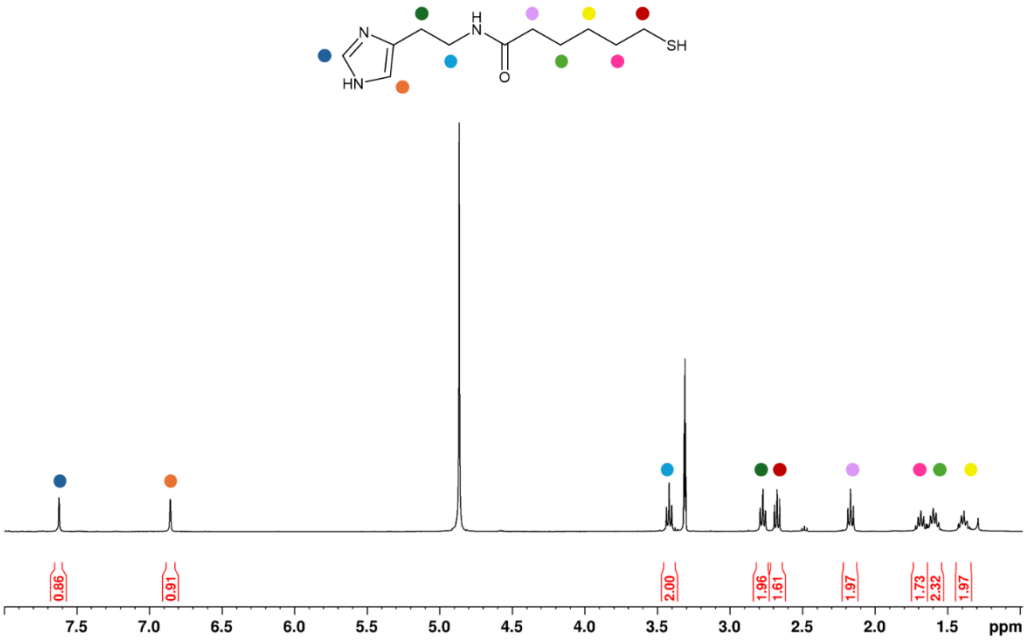

*Figure 90: ^{1}H NMR (400 MHz, CD_3OD) assignment for **C6-HM-SH**.*

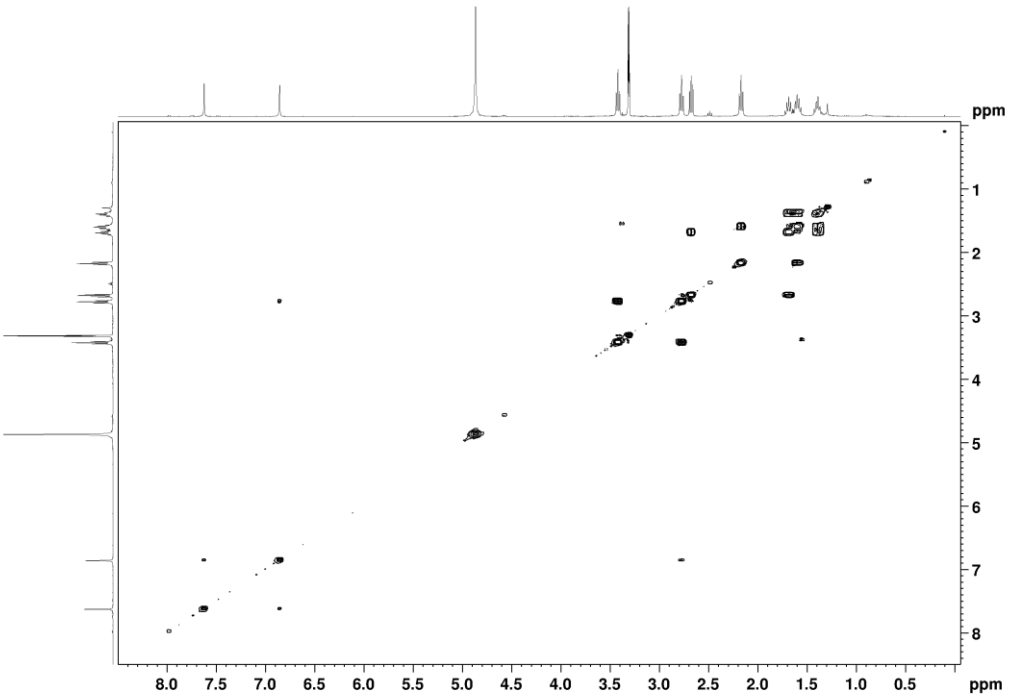

*Figure 91: COSY NMR spectrum for **C6-HM-SH**.*

The ^{13}C NMR (Figure 92) was assigned with the help of the HSQC spectrum (Figure 93). This allows all the carbons that have a proton attached to be assigned due to their correlation to the previously assigned proton signals. This leaves behind two unassigned peaks at 176.1 ppm (purple) and 135.8 ppm (black), which must be quaternary carbons. HMBC data (Figure 94) shows the quaternary at 176.1 ppm correlating to carbons at 40.2 ppm (light blue) and 36.9 ppm (light purple) and was therefore assigned to the carbonyl carbon (dark purple). The remaining quaternary peak at 135.8 ppm was assigned to the quaternary carbon in imidazole (black circle). This can be confirmed by the correlation in the HMBC to the two imidazole proton peaks at 6.85 ppm (orange) and 7.65 ppm (dark blue).

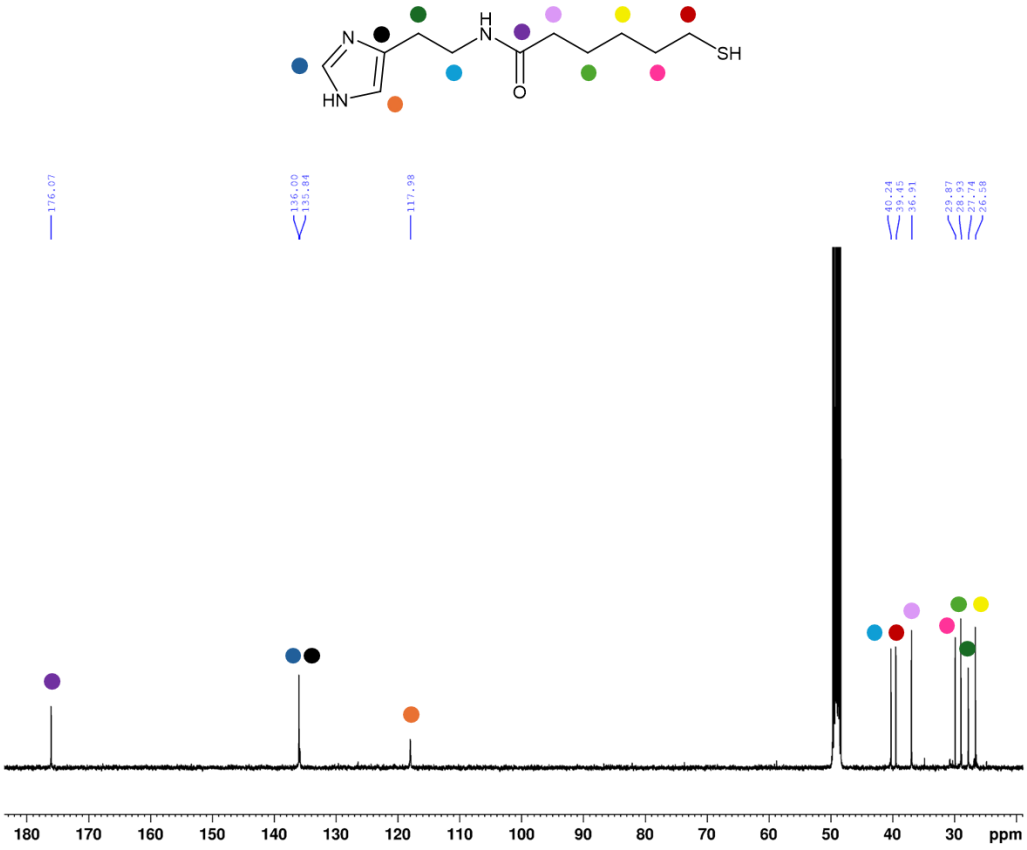

Figure 92: ^{13}C NMR (101 MHz, CD_3OD) assignment for ***C6-HM-SH****.*

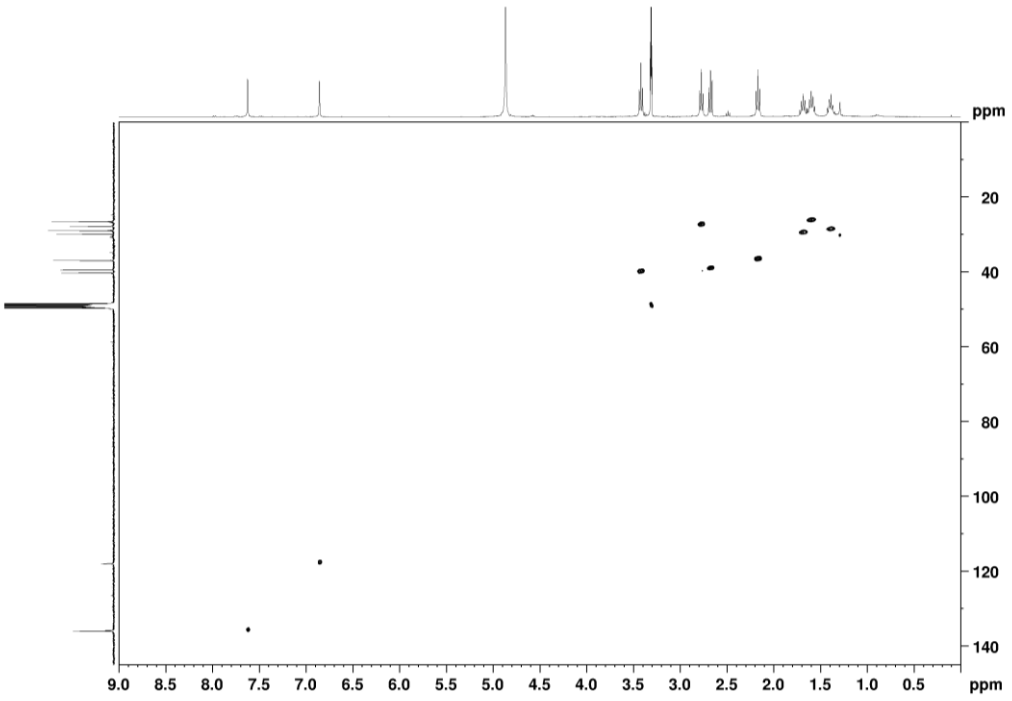

*Figure 93: HSQC NMR spectrum for **C6-HM-SH**.*

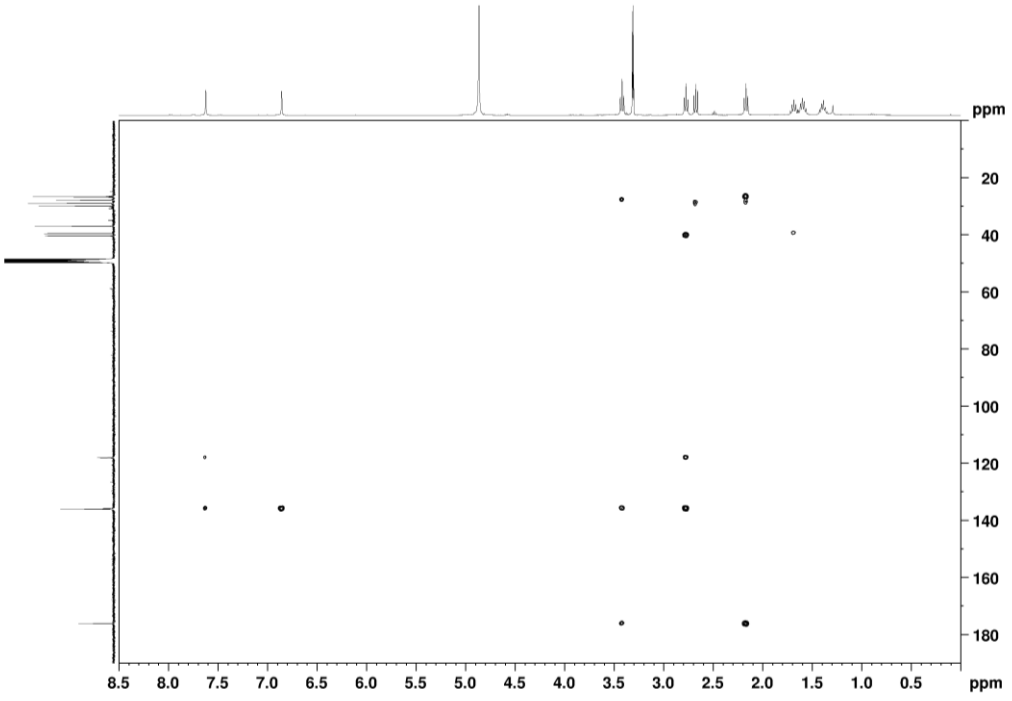

*Figure 94: HMBC NMR spectrum for **C6-HM-SH**.*

3.3.2 Synthesis of C6-G-SH

The synthesis of **C6-G-SH** is shown in Scheme 18. Here we start with *N*-(6-bromohexyl)phthalimide (**70**), which undergoes an S_N2 substitution reaction with triphenyl methanethiol (**64**) to give compound **71**. The presence of our desired product was confirmed using NMR spectroscopy with both the ^{1}H NMR and the ^{13}C NMR matching that previously reported for this compound.[121]

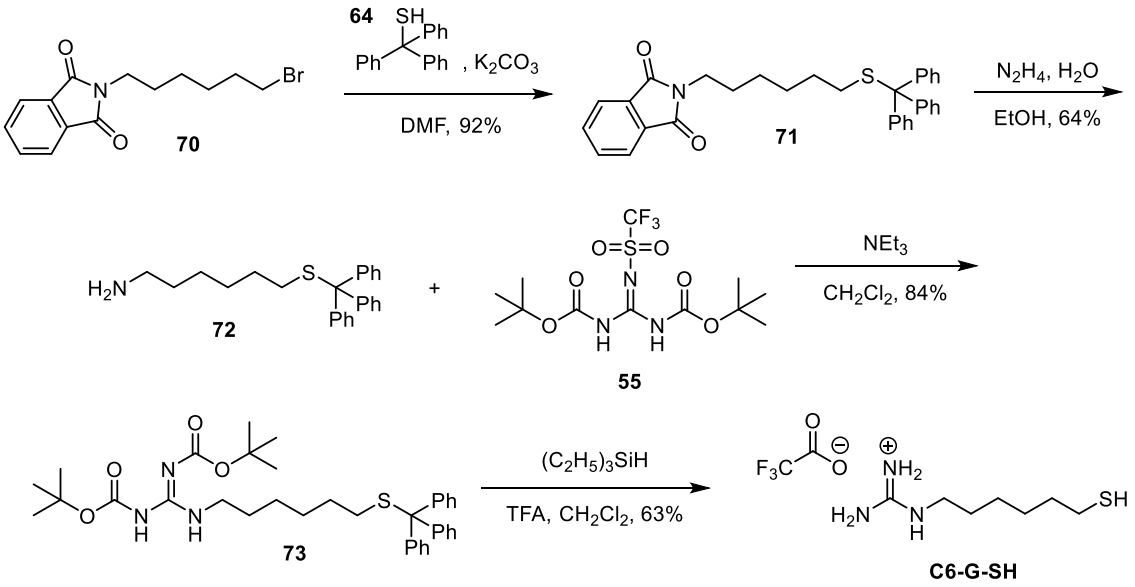

*Scheme 18: Synthesis of **C6-G-SH**.*

The second step involves the liberation of the amine from the phthalimide protecting group to give amine **72**. The mechanism for this reaction is depicted in Scheme 19. Here, one of the nitrogen atoms in hydrazine undergoes a nucleophilic acyl substitution with one of the phthalimide carbonyl groups. A proton is then lost from the hydrazine attached to the carbonyl next to the negatively charged nitrogen. The remaining free amine in hydrazine undergoes a nucleophilic acyl substitution with the previously unreacted carbonyl group, resulting in the amine being released. The amine then takes a proton from the positively charged nitrogen in the phthalimide to give the desired amine **72** along with phthalhydrazide **74**.

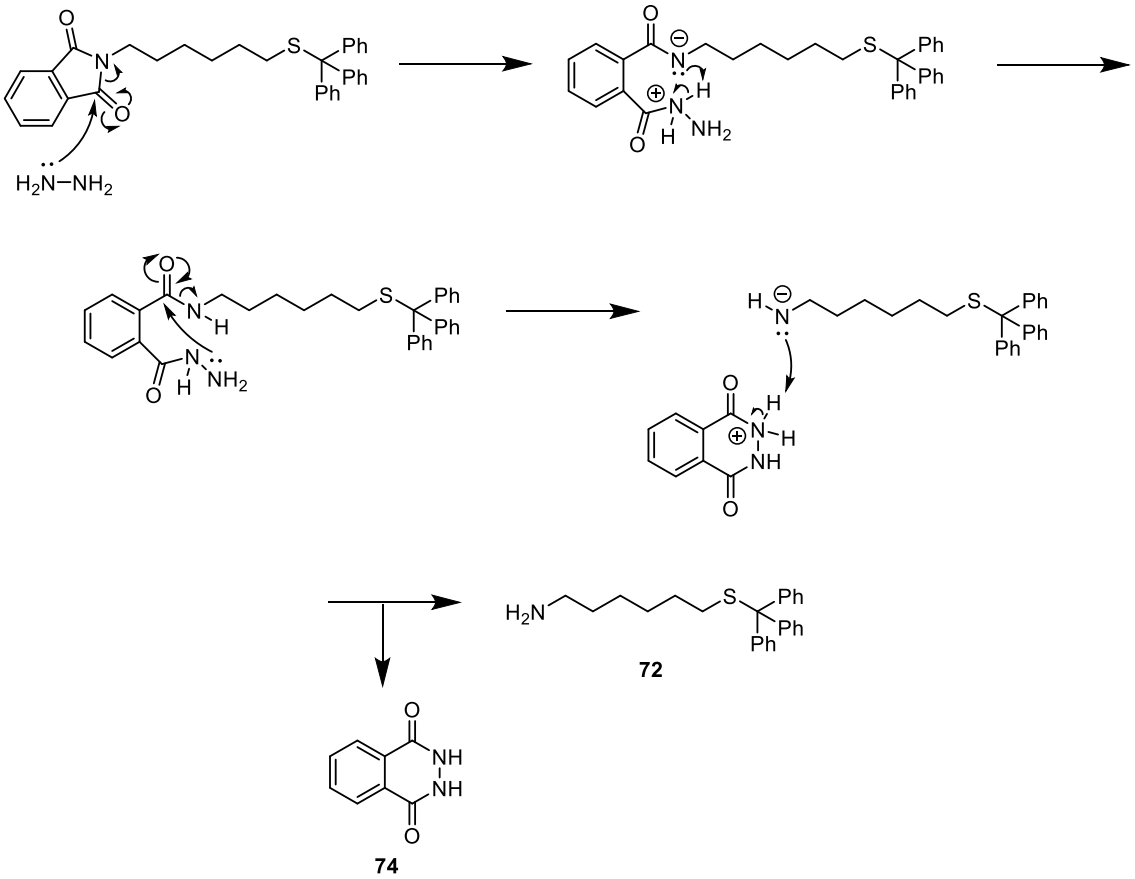

*Scheme 19: Mechanism for **C6-G-SH** hydrazine deprotection.*

With amine **72** in hand, we next performed the guanidinylation reaction. The mechanism for this was discussed previously in Chapter 2, Section 2.2.3. However, for this guanidinylation reaction, we decided to use the more reactive guanidinylation reagent, 1,3-di-Boc-2-(trifluoromethylsulfonyl)guanidine (**55**). The use of this reagent gave us an 84% yield, and successful formation of the product (**73**) was confirmed by the presence of the two singlet peaks in the ^{1}H NMR, each integrating for 9 H, indicating the presence of two Boc protecting groups on our guanidine.

The final step in this synthetic scheme was a global deprotection to give us the final compound **C6-G-SH**. Here, we used TFA and triethylsilane to remove both the trityl protecting group via the mechanism discussed above in Section 3.3.1 and the Boc protecting groups via the mechanism discussed in Chapter 2, Section 2.2.3, the only difference being the acid used for Boc deprotection. The loss of these protecting groups turns a quite non-polar compound into a very polar compound with two amine groups and a free thiol. This means the compound can be extracted into the aqueous layer during the

workup while the organic impurities, such as the triphenylmethane, can be removed. We found that this gave us the product with a few NMR impurities (Figure 95, blue spectra). Unfortunately, the polarity of this deprotected guanidine functionality makes normal phase chromatography unsuitable for purification. Therefore, we decided to use a reversed-phase column for purification as this is better suited for polar compounds. This worked really well using C_{18}-reversed phase silica gel and 40% MeOH/H_2O, with the pure compound being confirmed by NMR (Figure 95, red spectra).

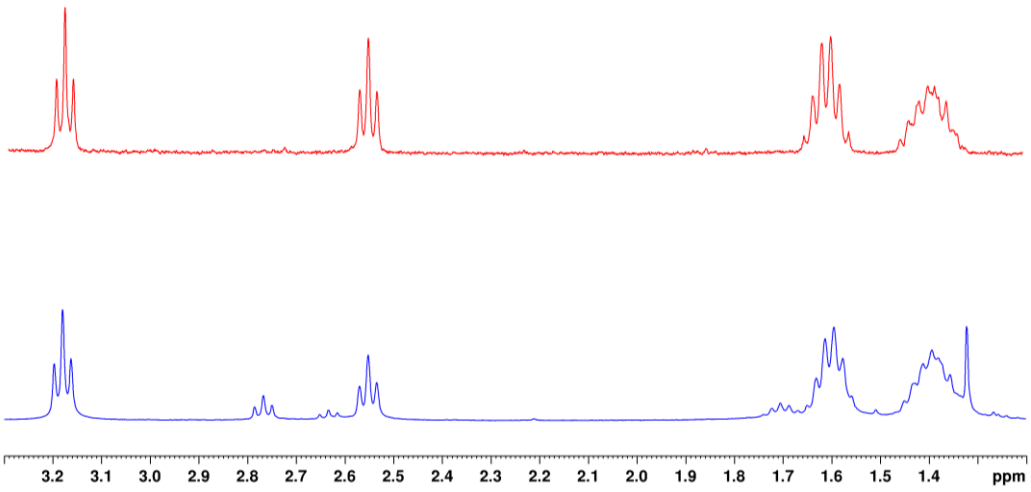

*Figure 95: ^1H NMR (400 MHz, D_2O) of **C6-G-SH** after workup (blue) and following subsequent reversed-phase chromatography (red).*

The final compound **C6-G-SH** was characterised using NMR data. The ^1H NMR assignment (Figure 96) was performed with the assistance of the COSY spectrum (Figure 97). Two triplet peaks integrating for 2 H at 3.18 and 2.55 ppm should be the -CH_2 group next to the NH and next to the thiol. These can be assigned based on the electronegativity of the adjacent atoms. Nitrogen is more electronegative than sulphur, so this will cause the adjacent -CH_2 peak to be more deshielded and therefore the peak will sit further downfield at 3.18 ppm (blue circle). The remaining triplet at 2.55 ppm could then be assigned to the -CH_2 peak adjacent to the thiol (pink circle). The COSY NMR data could then be used to assign the remaining two multiplet peaks, with a correlation from both assigned triplets to the multiplet at 1.65 – 1.55 ppm (orange and red), and from this multiplet to the remaining multiplet at 1.45 – 1.31 ppm (green and purple).

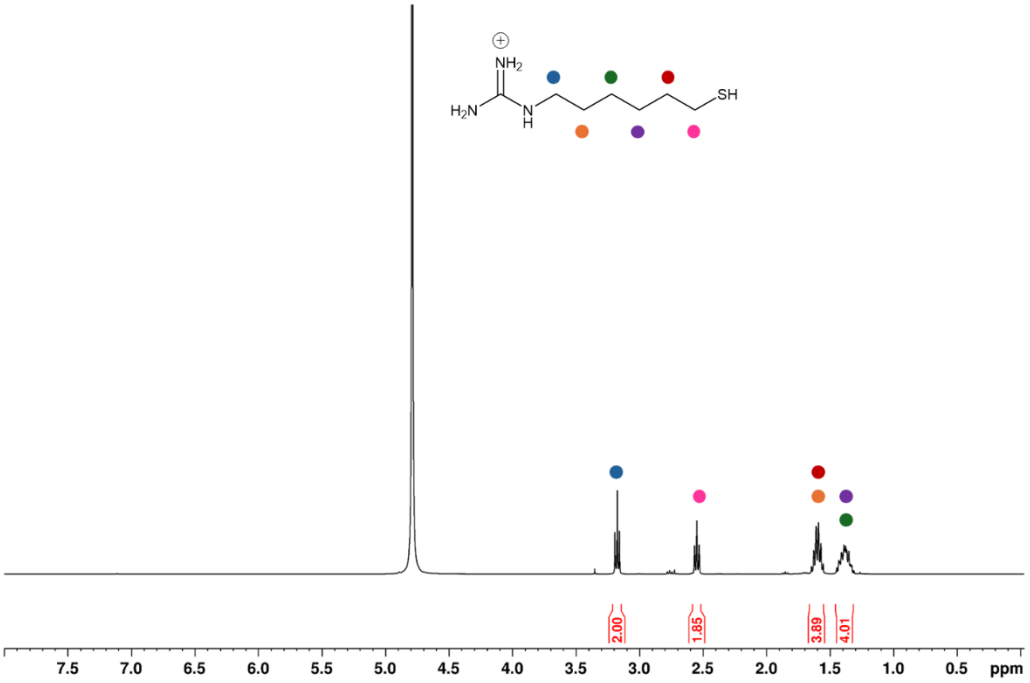

*Figure 96: ^{1}H NMR (400 MHz, D_2O) assignment of **C6-G-SH**.*

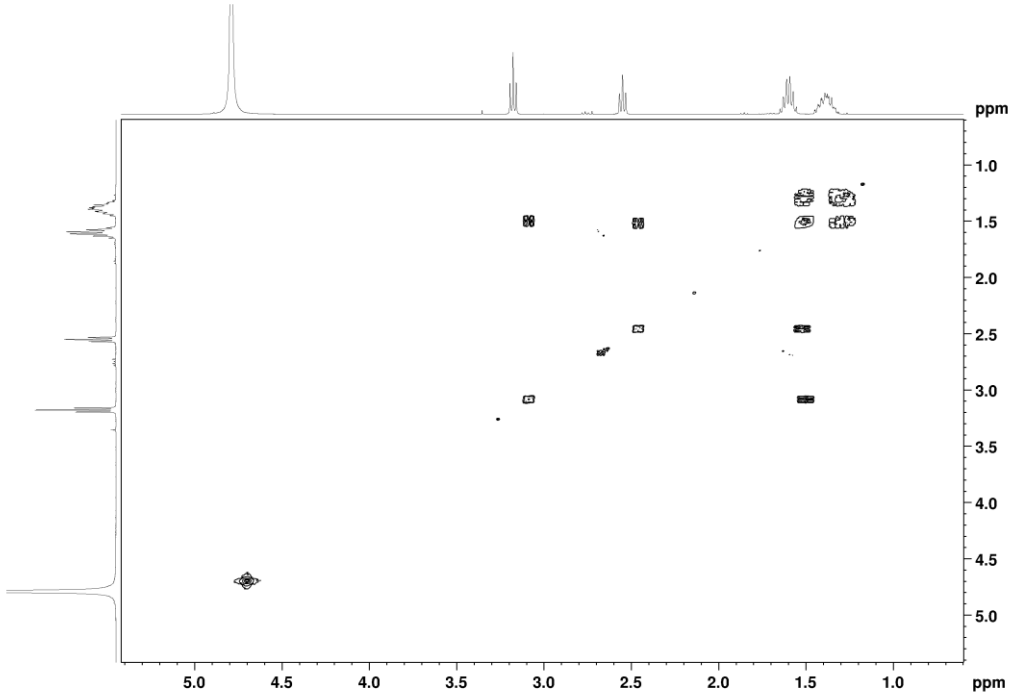

*Figure 97: COSY NMR spectrum for **C6-G-SH**.*

The ^{13}C NMR (Figure 98) could also be assigned using the previously assigned ^{1}H NMR along with HSQC (Figure 99) and HMBC spectra (Figure 100). HSQC allowed for the assignment of 41.0 ppm (blue) and 23.6 ppm (pink). The remaining 4 aliphatic carbon peaks were slightly harder to assign just using the HSQC data, as the one proton peak correlated to two different carbon peaks, though the HMBC spectrum could help with this. The peak at 32.8 ppm (red) correlated to the -CH_2 adjacent to the thiol, while the signal at 27.7 ppm (orange) correlated to the -CH_2 adjacent to the amine. The remaining two carbon peaks 26.9 ppm (purple) and 25.2 ppm (green) could be assigned based on their correlation to that specific half of the chain. The HSQC data was then used to confirm that these assignments of the central 4 carbons matched the direct correlation to the assigned proton peak.

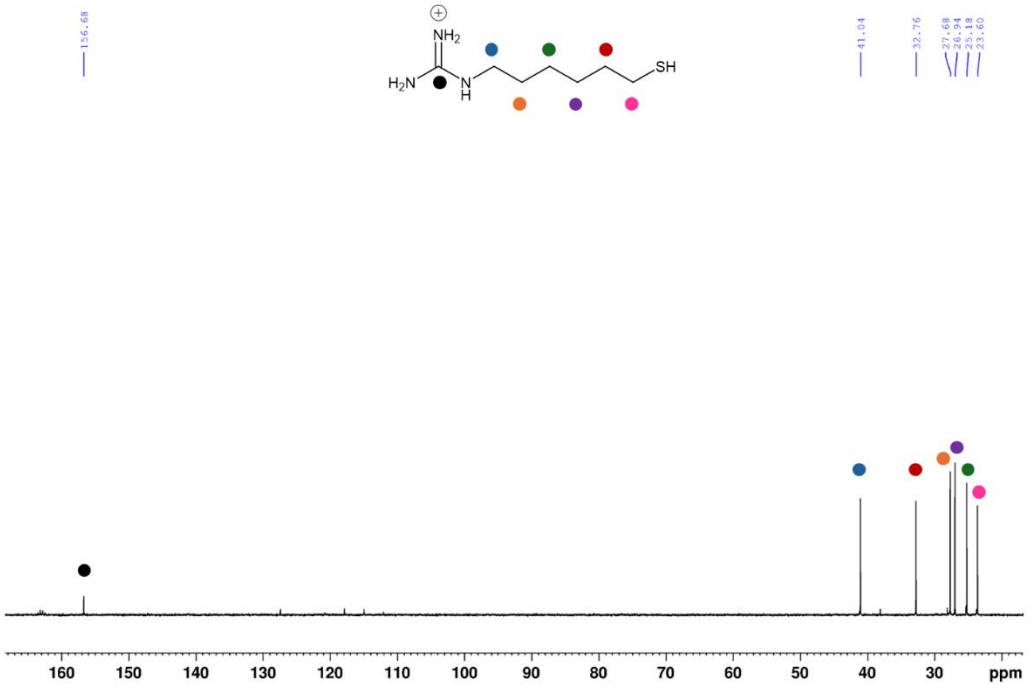

*Figure 98: ^{13}C NMR (101 MHz, D_2O) assignment of **C6-G-SH**.*

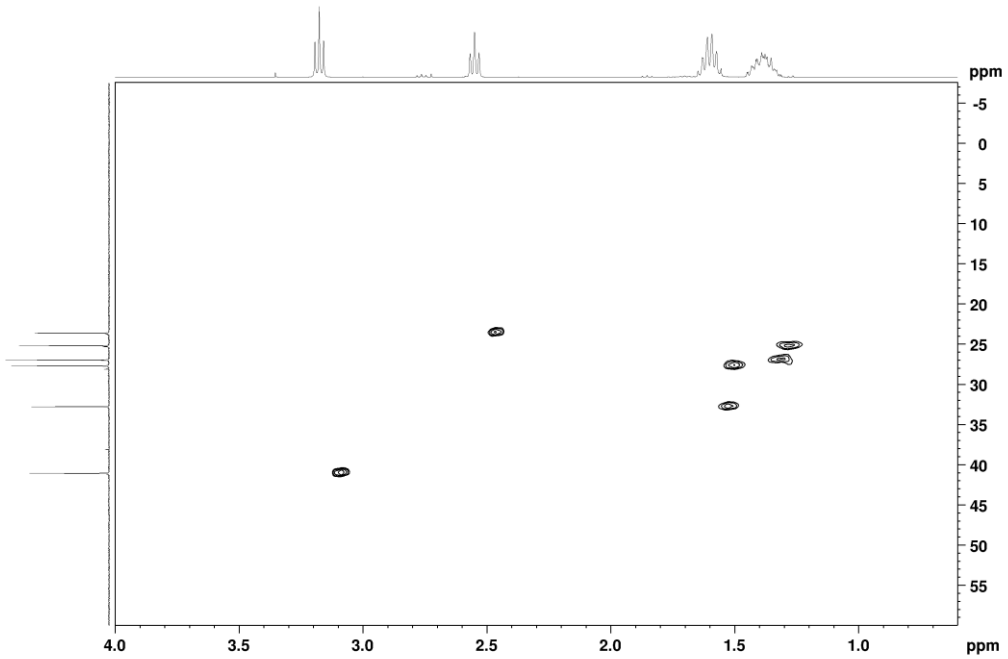

*Figure 99: HSQC NMR spectrum of **C6-G-SH**.*

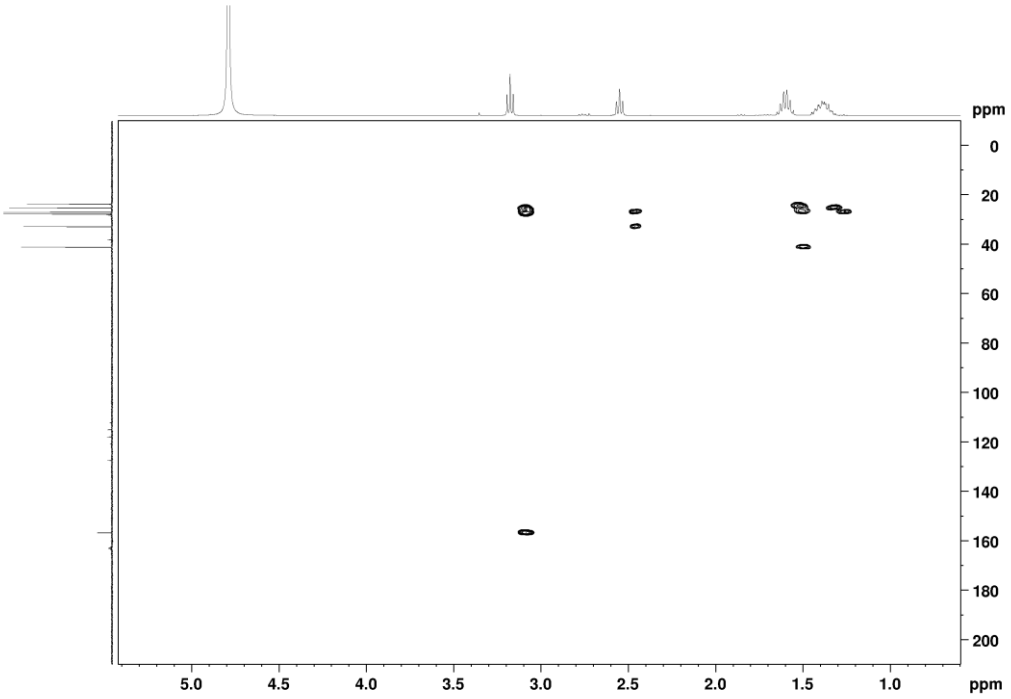

*Figure 100: HMBC NMR spectrum of **C6-G-SH**.*

3.3.3 Synthesis of C6-D2PA-SH

The synthesis of **C6-D2PA-SH** followed a simple two-step procedure, shown in Scheme 20. Here we start with 1,6-dibromohexane (**75**), which is reacted with triphenylmethanethiol (**64**) via an S_N2 reaction to introduce a thiol group onto one end of the C6 chain. Crude product from this first step was then used in a second S_N2 reaction, this time with di-(2-picolyl)amine (**76**) to introduce our catalytic functional group into the molecule. This step was then purified using column chromatography to give **77** with a yield of 61%. The final step was the trityl deprotection using TFA and triethylsilane to give the final compound, **C6-D2PA-SH**, with a yield of 73%. This was characterised using NMR spectroscopy, which matched that previously reported in the literature.[122]

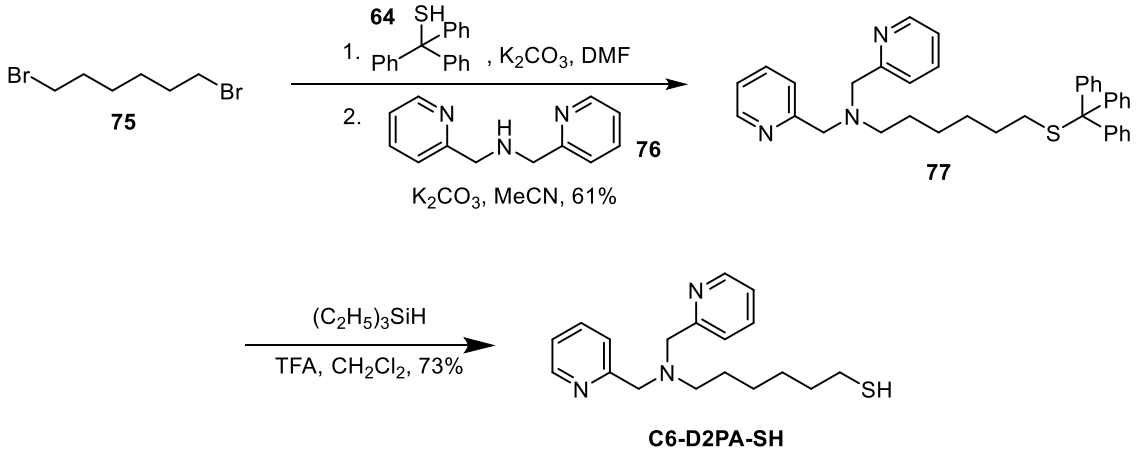

*Scheme 20: Synthesis of **C6-D2PA-SH**.*

3.4 Examination of the silver-thiol polymer system with C6 thiols

3.4.1 Silver-thiol polymer formation with C6-HM-SH

Once our three catalytic thiols had been synthesised, we investigated the catalytic activity of the silver-thiol polymer system. We wanted to start by examining the activity of just one of the thiols on its own, so we could ensure the formation of these polymers, observe esterase activity, and investigate cooperativity between the same catalytic head groups. For this system, we wanted to use the same substrate, *p*-nitrophenyl butyrate (PNPB), as our self-assembled system. This would allow us to directly compare the catalytic activity between the two systems.

The histamine thiol (**C6-HM-SH**) was chosen initially to investigate. This was due to the functional group having been previously shown in the literature to facilitate cooperative catalysis for esterase activity with the same catalytic units.[54] We also saw that this has relatively good activity on its own in our amphiphilic system (see Figure 57)

We investigated the activity of **C6-HM-SH** on its own, and in combination with Ag^+, at increasing concentrations (Figure 101). Here, we see that **C6-HM-SH** on its own has a higher catalytic activity compared with the polymer system at all concentrations. This suggests that the free thiol molecules can bring their catalytic head groups close together to facilitate catalysis in a more effective manner than when these thiols are immobilised in the polymer system. Two key factors could be influencing this. Firstly, the C6 chain length may not be long enough for the catalytic head groups to come in close enough contact to facilitate cooperative catalysis when immobilised on the polymer. Secondly, the C6 thiols may be forming some sort of aggregates in solution in the absence of Ag^+, resulting in the increased catalysis. The free thiols may be able to form disulphide bonds, linking two **C6-HM-SH** units together. These could either fold into a U shape with both catalytic head groups close together for catalysis (Figure 102), or they could potentially self-assemble, as these two linked thiols can now act similarly to bolaamphiphiles.

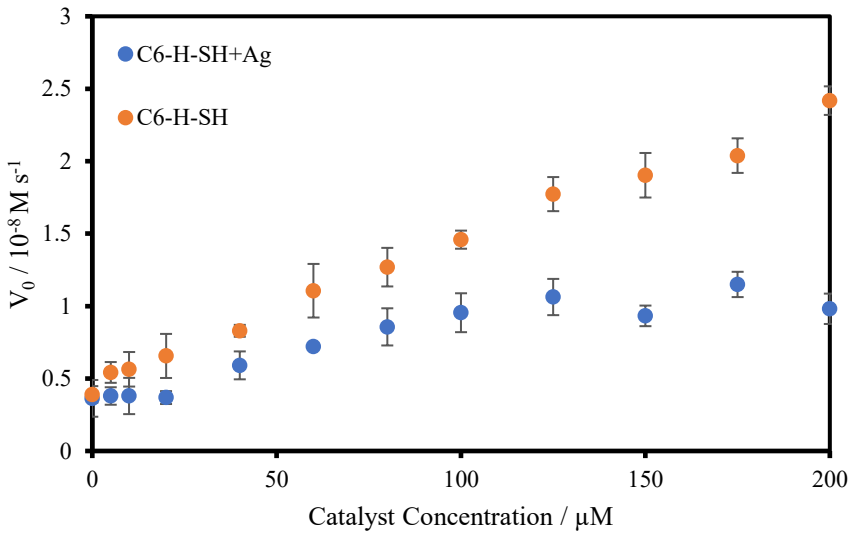

Figure 101: ***C6-HM-SH*** *forming silver-thiol polymers. Experimental conditions: aqueous buffer pH =7.0 ([HEPES] = 5 mM), [PNPB] = 500 µM, 40 °C.*

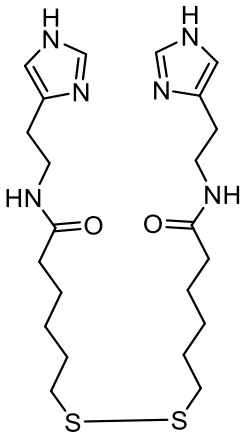

Figure 102: ***C6-HM-SH*** *disulphide folding into a U shape for catalysis.*

Bolaamphiphiles are a type of amphiphilic structure that has two polar headgroups connected through a hydrophobic carbon chain (Figure 103).[123] These types of structures have been found to self-assemble into a wide variety of shapes, including spheres, cylinders, monolayer and bilayer vesicles (Figure 104).[124] The free **C6-HM-SH** units may be assembling in some manner, which results in their increased catalysis. Therefore, the CAC of these thiols could be determined to see if this is indeed the case.

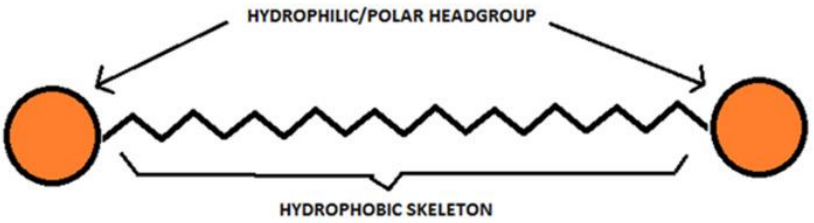

Figure 103: Structure of bolaamphiphiles. Source: Ref. [123]/Advanced Pharmaceutical Bulletin.

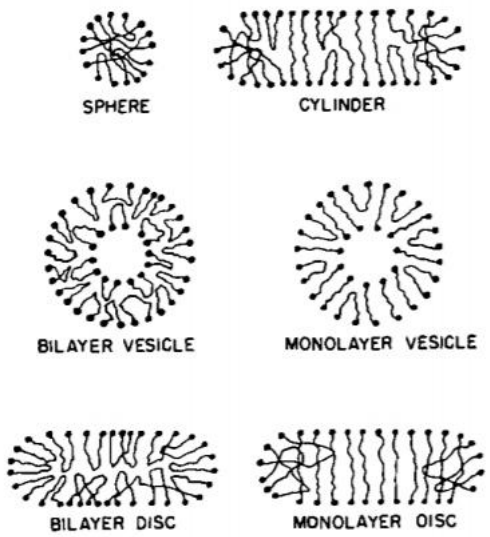

Figure 104: Self-assembled structures formed from bolaamphiphiles. Source: Ref. [124]/Taylor & Francis.

3.4.2 Determination of the CAC for C6-HM-SH

The CAC of **C6-HM-SH** could be determined using the same fluorescence titration with DPH that proved successful with our vesicle system (Chapter 2, Section 2.7). Figure 105 showed that these thiols form aggregates above 128 μM, as seen by the increase in fluorescence intensity of DPH as this is solubilised in the non-polar environments of the aggregates. This assembly of thiols is likely contributing to the increased rate of catalysis we see for the individual thiol system in Figure 101. We see a greater difference between our free thiol system and the polymer system above 100 μM. The assembly of the free thiols allows the imidazole units to come in close enough contact to facilitate cooperative catalysis, enhancing the catalytic rate. Though our fluorescent titration results suggest **C6-HM-SH** is assembling, we cannot determine what kind of structures are being formed, only that this assembly is having a positive effect on catalysis. The confirmation that **C6-HM-SH** is assembling helps to highlight the need for these thiols to come close together for cooperative catalysis to occur.

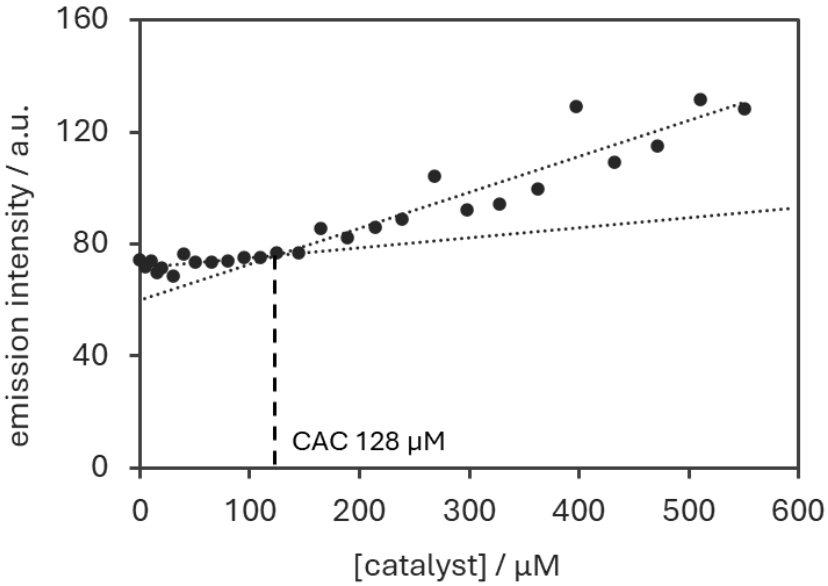

*Figure 105: CAC determination for **C6-HM-SH**. Fluorescent titrations using aqueous buffer pH = 7.0 ([HEPES] = 5 mM), [DPH] = 10 µM, [PNPB] = 500 µM, 40 °C.*

3.4.3 Rethinking the plan for our silver-thiol polymer system

Based on the initial **C6-HM-SH** results, we decided not to proceed with our C6 system. Any cooperative effects from the assembly of **C6-HM-SH** into silver-thiol coordination polymers are overshadowed by the cooperative effects occurring in the absence of Ag^+, by the supposed assembled system. The remaining **C6-G-SH** and **C6-D2PA-SH** thiols were not investigated, as we predicted we would see similar results. Previously, we have seen that these have low activity on their own and only see decent catalysis when they are in combination with imidazole functionalities. Instead, we decided to synthesise much longer catalytic thiols. We decided on a C14 chain length. This should be long enough for our catalytic headgroups to come together to facilitate cooperative catalysis. A potential concern would be the ability for these longer catalytic thiols to self-assemble. However, we thought this could be overcome by working at concentrations below the CAC of our thiols. Cao et al. also had great success with their C14 TACN thiols, with these giving rise to the highest values of k_{cat}. This made us more confident that we would also have similar luck with longer catalytic thiols.

In addition to synthesising our histamine, guanidine and di(2-picolyl)amine based thiols with a C14 chain length, we also wanted to synthesise a couple of other functionalities. This would allow us to screen a library of catalytic functional groups to confirm that the

H/G/D2PA combination from our vesicle system still gives the best catalytic activity. The functional groups we chose to screen were those we initially investigated for the self-assembled system; these include diethylamine, alcohol and carboxylic acid functionalities. This was due to their presence in either existing artificial esterase systems or in the active site of native esterase enzymes. We chose not to re-examine the activity of a free amine, as we found in our previous system that this did not proceed via a catalytic mechanism (see Chapter 2, Section 2.4). Figure 106 shows the structures of all the thiols that we wanted to examine for catalytic activity.

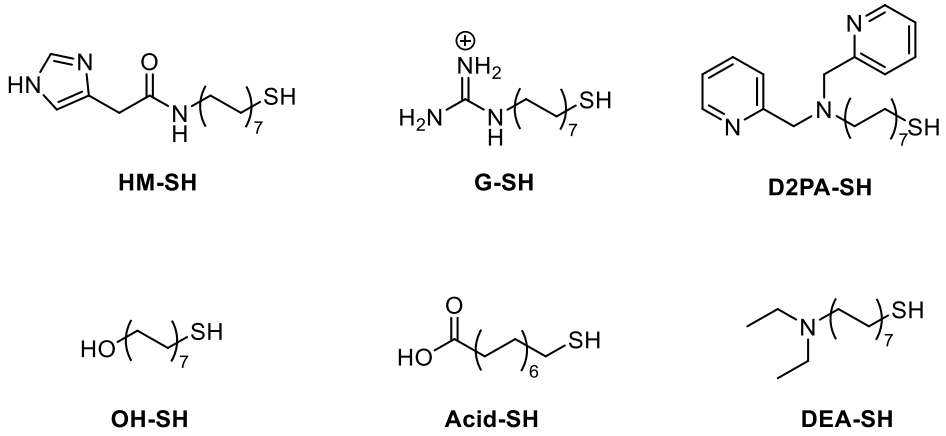

Figure 106: Structures of C14 thiols to synthesise.

3.5 Synthesis of C14 thiols

3.5.1 Initial synthetic plan

To synthesise the compound seen in Figure 106, we derived the following synthetic scheme (Scheme 21) whereby almost all of our desired thiol molecules could be synthesised by the same key building blocks. The idea here was to simplify the synthesis of these thiols, compared with the C6 synthetic routes, by using the same initial synthetic steps to give us five different final compounds. Here, we would start with 14-bromotetradecan-1-ol (**78**) and introduce our thiol into the C14 chain using triphenylmethanethiol (**64**). Immediately, compound (**79**) could be deprotected to give the alcohol containing thiol (**OH-SH**). The remaining compound (**79**) could undergo a tosylation reaction to convert the OH into a good leaving group (compound **80**), allowing this to undergo three different S_N2 reactions: one to form an azide (**83**), one to introduce diethylamine and the other to introduce di-(2-picolyl)amine into the thiol. The diethylamine (**82**) and di-(2-picolyl)amine (**81**) containing thiols could then be

deprotected to give **DEA-SH** and **D2PA-SH**. The C14 trityl-protected azide (**83**) could then be used to synthesise both the histamine and guanidine thiols by first reducing the azide to an amine (**84**). The amine can react with a guanidinylation agent to form our protected guanidine thiol (**85**). The amine can also undergo an amide coupling reaction with 4-imidazole acetic acid hydrochloride to form our protected histamine thiol (**86**). The guanidine and histamine-containing compounds could then undergo a trityl deprotection to give the **G-SH** and **HM-SH-a**.

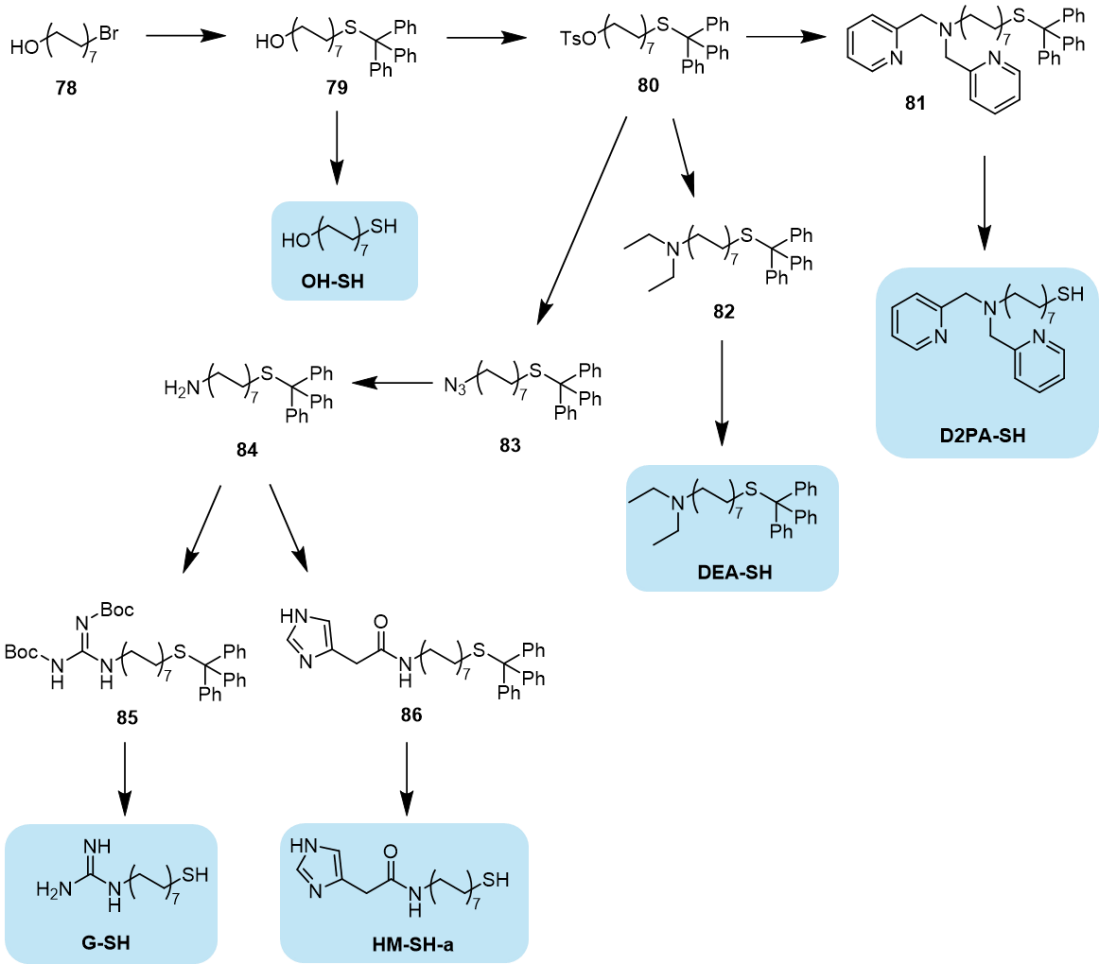

*Scheme 21: Synthetic plan for the synthesis of **OH-SH**, **DEA-SH**, **D2PA-SH**, **G-SH** and **HM-SH-a** thiols.*

The carboxylic acid containing thiol (**Acid-SH**) is the only one unable to be synthesised by Scheme 21. Instead Scheme 22 depicts the plan for this synthesis, with the oxidation of 14-bromotetradecan-1-ol (**78**) needed to introduce the acid group into the molecule. The thiol functionality could then be incorporated using triphenylmethanethiol (**64**). Finally, this can be deprotected to give the acid thiol **Acid-SH**.

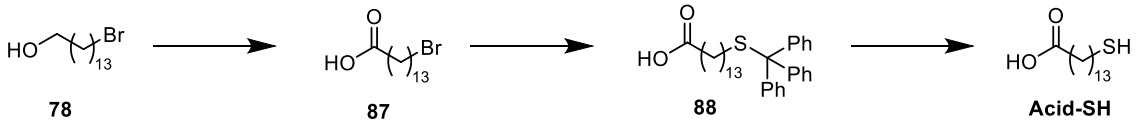

*Scheme 22: Synthesis plan for **Acid-SH**.*

3.5.2 Synthesis of OH-SH

The synthesis of C14 alcohol containing thiol (**OH-SH**) was relatively straightforward (Scheme 23). First, the thiol group is introduced onto 14-bromotetradecan-1-ol (**78**) using triphenylmethanethiol (**64**) via an S_N2 mechanism, using a procedure reported by Tanaka et al.[125] This resulted in a high yield (94%). The alcohol **79** could then undergo a trityl deprotection to give the free thiol **OH-SH**. Characterisation of the final product was achieved using NMR spectroscopy, which found that the ^1H NMR data matched that previously reported in the literature.[126] The HRMS also confirmed the presence of this product.

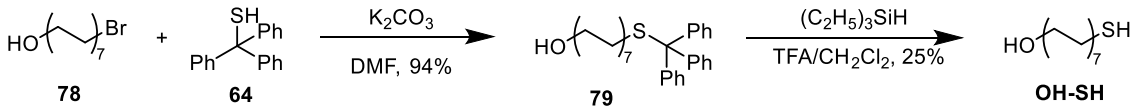

*Scheme 23: Synthesis of **OH-SH**.*

3.5.3 Synthesis of DEA-SH

The synthesis of **DEA-SH**, shown in Scheme 24, proceeds via the same initial step as the **OH-SH** synthesis pathway to give the trityl-protected alcohol (**79**). From here, a tosylation is performed to convert the alcohol into a better leaving group. We adapted a procedure from Borbás et al. using 10 equivalents of tosyl chloride (TsCl) instead of the two equivalents Borbás and coworkers used, along with pyridine acting as both the base and solvent.[127] Our adapted procedure resulted in the reaction finishing within an hour, and a workup to remove both TsCl and pyridine was sufficient to give crude tosyl **80**, which could then undergo the next desired substitution. The mechanism for this tosylation is depicted in Scheme 25, with the alcohol initially undergoing nucleophilic attack of the sulphur in tosyl chloride. This results in the formation of a negative charge on one of the oxygens bound to sulphur. The chlorine can then leave as a result of the oxygen on the sulphur reforming the double bond. Finally, the base, in this case pyridine, can

deprotonate the original alcohol, removing the positive charge on the oxygen, forming our final product.

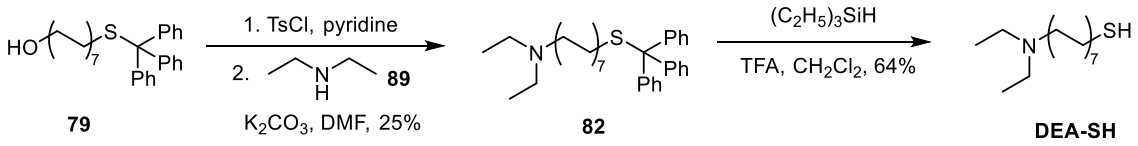

*Scheme 24: Synthesis of **DEA-SH**.*

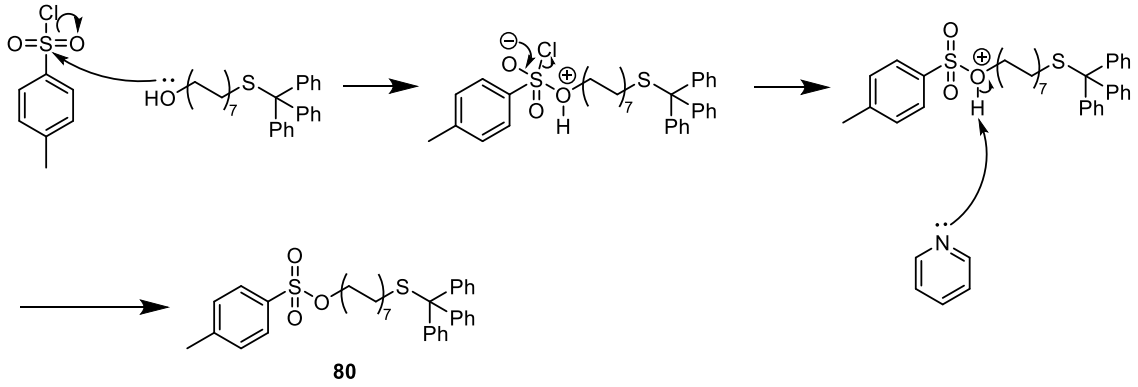

Scheme 25: Mechanism for tosylation.

The tosylation reaction did yield some interesting results with our thiol starting materials. This reaction would always give multiple spots on TLC; however, when these spots were separated using column chromatography and underwent NMR analysis, they all appeared to contain the product. Where these spots would differ would be in the amount of tosyl peaks present in the NMR (see Figure 107). Both an extractive workup and column chromatography were unsuccessful in removing these tosyl impurities from the desired compound. From this, it could be concluded that an inseparable mixture of the desired tosylate and an unidentified species was formed and carried through to the next step. This discrepancy in the amount of tosyl impurity present in the product may account for some of the low yields achieved with the step following this tosylation.

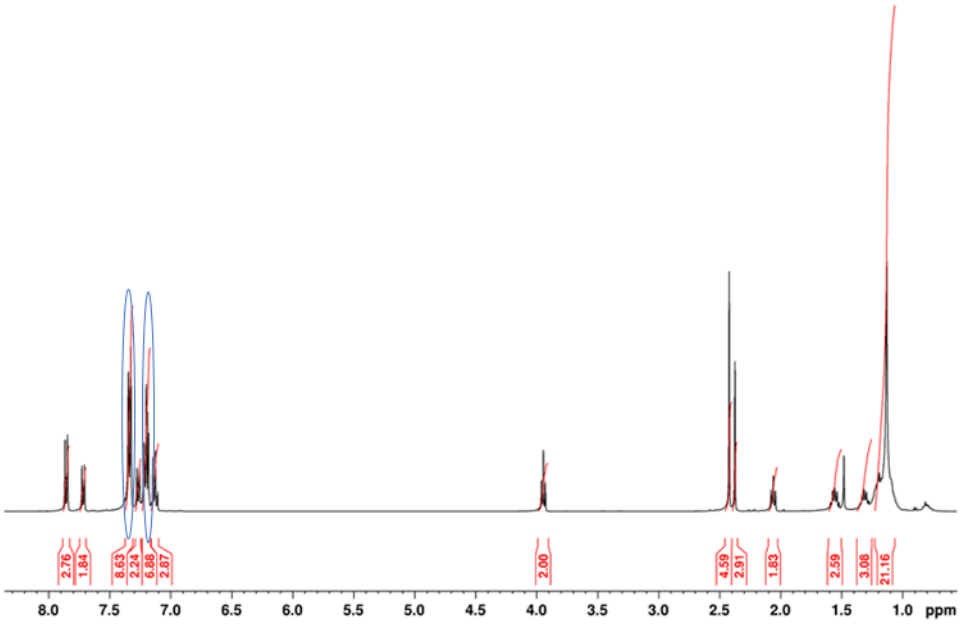

Figure 107: ^{1}H NMR (400 MHz, $CDCl_3$) of tosyl reaction indicates the presence of tosyl impurities (circled in blue) in the product.

The crude tosyl product **80** can then undergo an S_N2 reaction with diethylamine (**89**) to introduce the diethylamine functional group into the thiol molecule. This step is relatively straightforward, though the overall yield is 25% when calculated from the number of moles of **79**, likely due to the tosylation step, resulting in an unknown number of tosyl groups being present in the product, changing the mass of the product. Once made, **82** can simply undergo a trityl deprotection using the same method as for **OH-SH**. This worked better for **DEA-SH**, with a 64% yield achieved.

The ^{1}H NMR (Figure 108) and ^{13}C NMR (Figure 109) for **DEA-SH** were assigned based on the different chemical environments the atoms experience. Those next to the nitrogen should experience a bigger chemical shift than those next to the sulfur. The multiplet at 2.57 – 2.48 ppm (blue) can be assigned to the two CH_2 groups in the diethylamine functionality. The multiplet at 2.44 – 2.36 ppm (orange) can be assigned to the CH_2 next to N in the long chain. The next CH_2 multiplet 1.66 – 1.56 ppm (pink) can be assigned to the CH_2 next to SH, and the two CH_3 groups in diethylamine can be assigned the peak at 1.02 ppm (black). The ^{13}C NMR was slightly harder to assign with arbitrary assignments as follows, with the CH_2 and CH_3 diethylamine peaks being assigned 46.8 ppm (blue) and

23.6 ppm (black). The CH_2 next to the N was assigned 52.2 ppm (black) and the CH_2 next to the thiol assigned 34.9 ppm (pink).

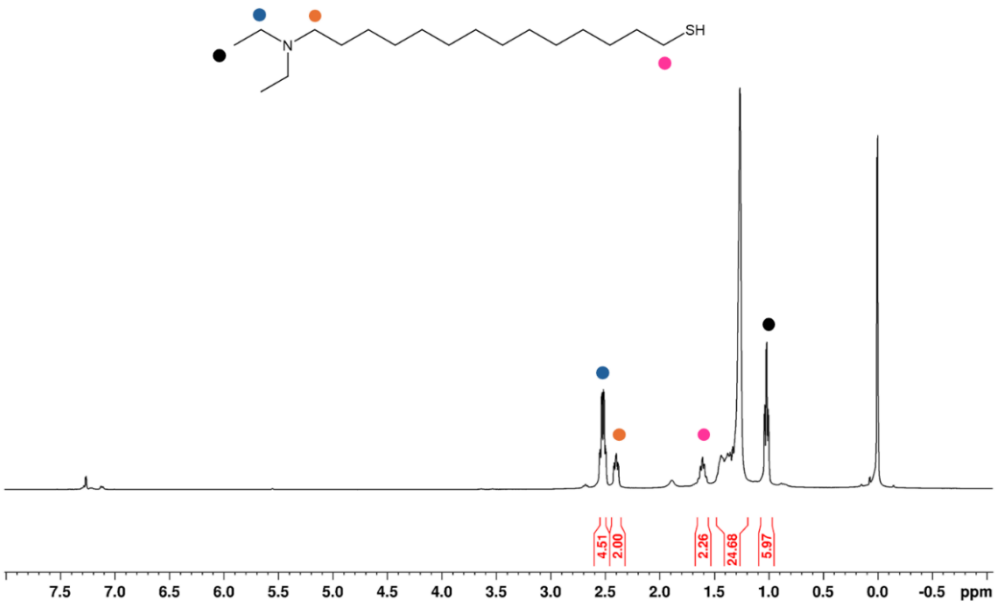

*Figure 108: ^{1}H NMR (400 MHz, $CDCl_3$) assignment of **DEA-SH**.*

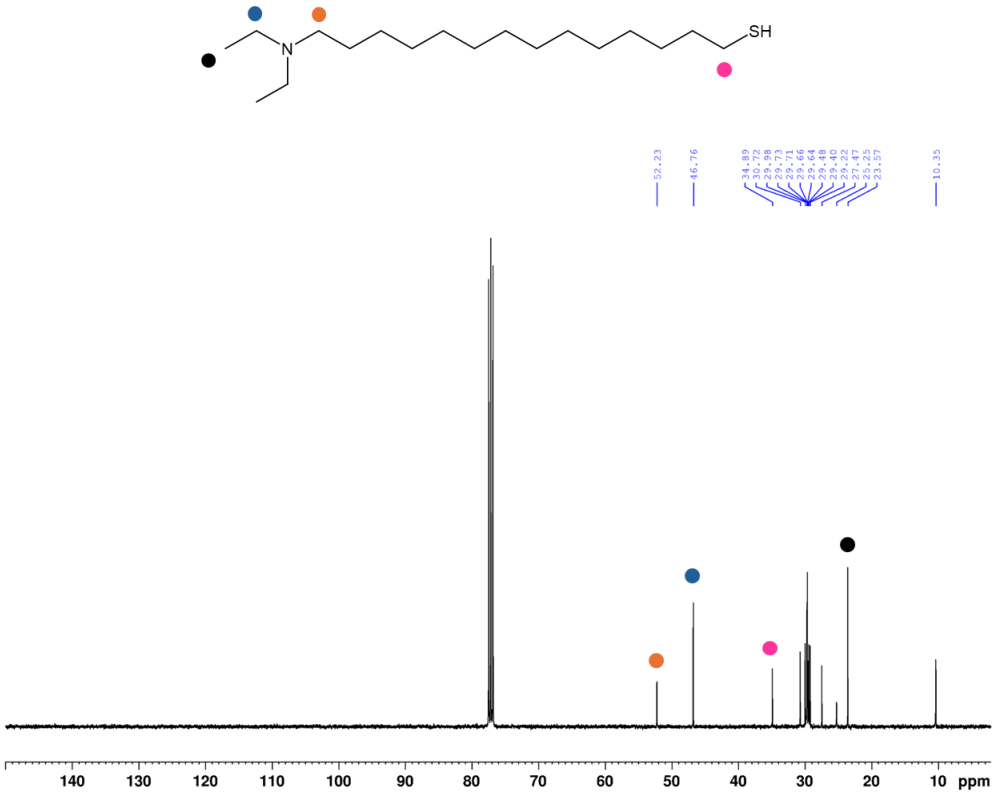

*Figure 109: ^{13}C NMR (101 MHz, $CDCl_3$) assignment of **DEA-SH**.*

3.5.4 Synthesis of D2PA-SH

Alcohol **79** could be used as the starting material to synthesise our **D2PA-SH** molecule (Scheme 26). Similar to the **DEA-SH** synthesis, this could first undergo a tosylation, with the crude product from this then able to undergo a substitution with di-(2-picolyl)amine (**76**), introducing the picolylamine functionality into the thiol molecule. This step did not have a great yield, likely due to the discrepancies in the molar mass of the crude tosyl product used, due to over tosylation. Finally, **81** could undergo a trityl deprotection using the same method as for the previous two compounds to give **D2PA-SH** in a decent yield of 55%.

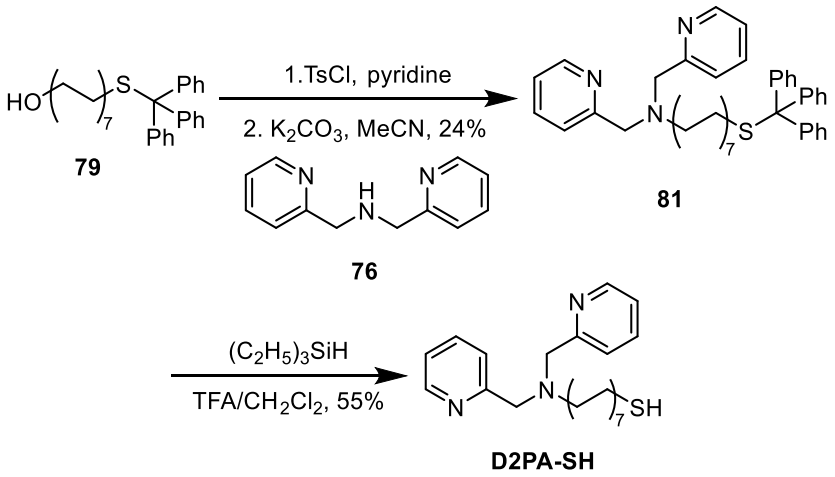

*Scheme 26: Synthesis of **D2PA-SH**.*

The final product could be characterised using NMR spectroscopy. The ^{1}H NMR was assigned in Figure 110 with the aromatic region assigned based on the splitting of the proton peaks and the proximity to the N. The peak at 8.43 ppm (black) is a doublet and is the most downfield peak, indicating that this must be next to the N. The COSY NMR spectra (see appendix) could be used to assign the triplet at 7.80 ppm (dark blue), doublet at 7.64 ppm (light blue) and the multiplet at 7.31 – 7.24 ppm (orange). The two CH_2 groups in the dipicolylamine functionality could be assigned to the singlet peak at 3.78 ppm (yellow). The aliphatic region was assigned to the alkyl chain based on the difference in electronegativity between N and S. An interesting observation here was the splitting of the two CH_2 proton peaks next to the tertiary amine, giving two proton signals integrating for 1 H rather than one signal for 2 H. The ^{13}C NMR (Figure 111) was also assigned using the HSQC and HMBC spectra (see appendix). The quaternary carbon in the pyridine ring was assigned the peak at 161.0 ppm (dark green), and this was confirmed using the

HMBC correlation to the proton peak at 3.78 ppm (yellow). The remaining peaks were all assigned through the HSQC correlation. Note the assignment of the alkyl chain CH_2 peaks are 30.2 ppm (dark green), 29.4 ppm (light purple) and 28.0 ppm (red), as these peaks are very close together in Figure 111.

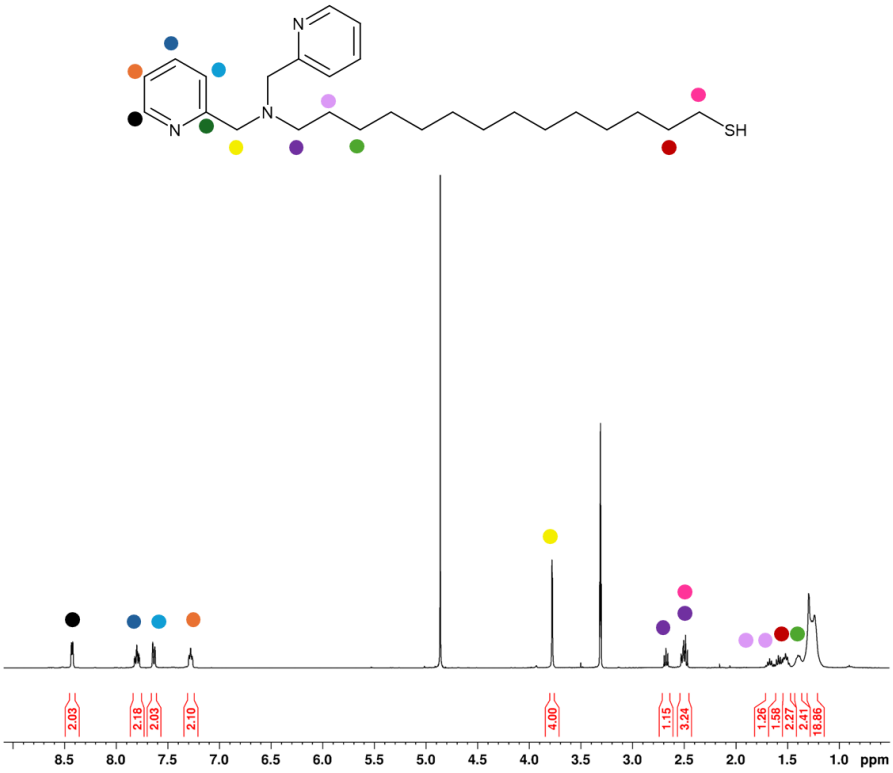

*Figure 110: ^1H NMR (400 MHz, $CDCl_3$) assignment of **D2PA-SH**.*

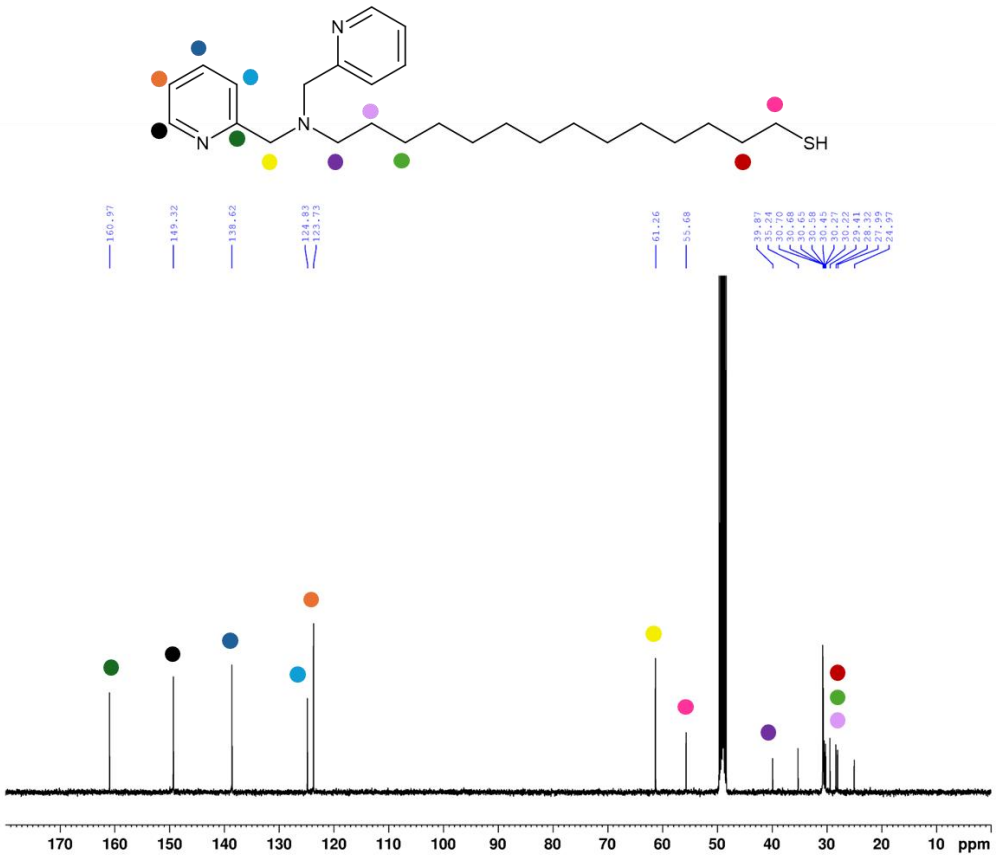

*Figure 111: ^{13}C NMR (101 MHz, $CDCl_3$) assignment for **D2PA-SH**.*

3.5.5 Synthesis of Acid-SH

Synthesis of the acid-containing thiol **Acid-SH** required us to design a whole new synthetic route, shown in Scheme 27. First, we introduced the carboxylic acid group into our starting material, 14-bromotetradecan-1-ol (**78**), using the classical oxidation reagent $KMnO_4$. The procedure we used was adapted from Duffy et al., where they used chromium trioxide to oxidise 9-bromo-1-nonanol.[128] We found this procedure to give us high yields (96%) without the need to purify the compound using flash chromatography.

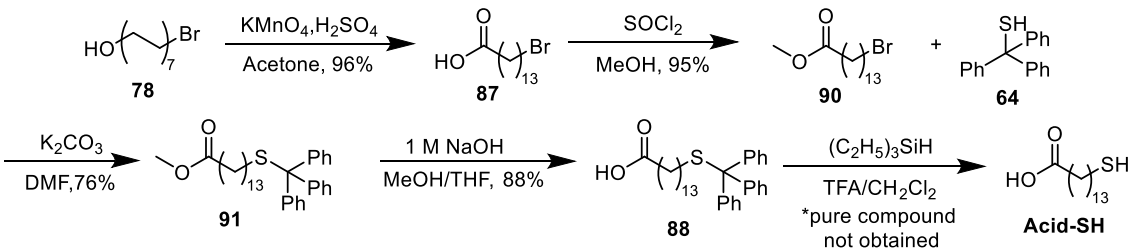

*Scheme 27: Synthesis of **Acid-SH**.*

The mechanism for the oxidation of alcohol to carboxylic acid is depicted in Scheme 28. Here, the lone pair on the oxygen can attack the Mn, forming a bond between the two. This results in the oxygen atom being positively charged as it now has three bonds. One of the negatively charged oxygens on the Mn can then take the proton off the positively charged oxygen, neutralising its charge. A water molecule can then take the proton neighbouring the oxygen from the original alcohol functional group. This results in the formation of our carbonyl group and the release of the manganese as $HMnO_4^-$. At this point, we have formed the aldehyde. A second oxidation must be performed to form the carboxylic acid. This follows a similar mechanism with first a water molecule attacking the carbonyl group, resulting in that oxygen becoming negatively charged. That oxygen will then attack the Mn in a similar fashion to the initial attack of the alcohol. We can then undergo the same steps where one of the negatively charged oxygens on the Mn takes a proton, resulting in the reformation of the carbonyl bond and the loss of the Mn as $HMnO_4^-$. A water molecule can then remove one of the protons on the positively charged oxygen to form the carboxylic acid functionality of the final compound **87**.

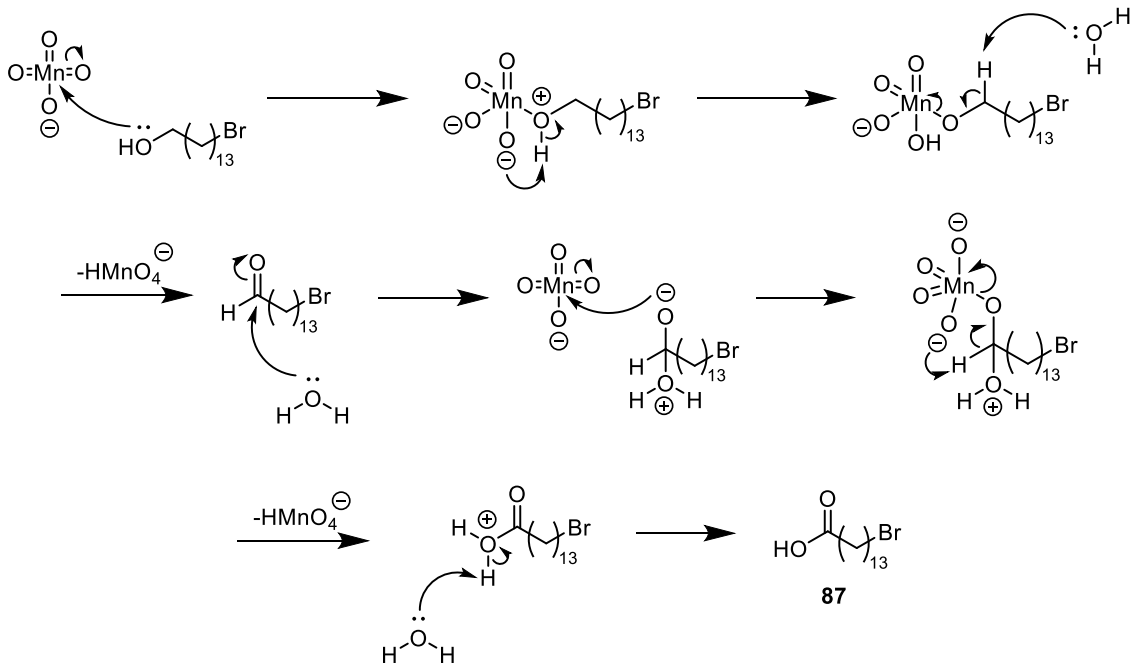

Scheme 28: Mechanism for oxidation of alcohol.

Following the formation of our carboxylic acid group, an esterification reaction was performed to prevent this group from interfering with the thiol formation. The acid group is relatively polar and can cause issues when undergoing purification via column chromatography, with the compound sticking to the silica, resulting in poor yields. To

overcome this, we protect the carboxylic acid with an ester functional group to make the compound easier to column in the subsequent synthetic steps. Esterification of **87** using thionyl chloride and MeOH proceeded very smoothly, with a 95% yield obtained. The mechanism for this was previously discussed in Section 3.3.1. The desired product (**90**) was confirmed using ^{1}H NMR spectroscopy, which showed the appearance of the singlet CH_3 ester peak at 3.66 ppm.

Once the carboxylic acid group has been protected by our ester functional group, we can then introduce the thiol into the molecule. Using the same procedure previously discussed to make **79**, we could form compound **91** with a 76% yield. The characteristic three multiplet aromatic peaks integrating for 15 H total was seen in the ^{1}H NMR, to confirm the presence of the trityl thiol in the product. Once the thiol had been introduced into the molecule, we could then remove both the ester and trityl protecting groups to give **Acid-SH**. We planned to remove these two protecting groups in a stepwise fashion, as the conditions required to cleave the trityl protecting group were not suitable to cleave the ester and vice versa.

Firstly, we remove the ester protecting group to give the free acid (**88**) using 1 M NaOH. The mechanism for base-catalysed ester hydrolysis was previously discussed in Section 3.3.1. This was another very successful reaction with a yield of 88%, with acid **88** being confirmed by the disappearance of the CH_3 ester peak in the ^{1}H NMR.

After this, we could use our trityl deprotection conditions to give the free thiol. This reaction seemed successful as we were able to make the product, which could be confirmed using NMR. However, this compound was very difficult to purify. The ^{1}H NMR shown in Figure 112 shows the absence of the trityl group along with peaks in the aliphatic region which match what we would expect for the product. Though there are many aliphatic impurities present in this NMR which we were unsuccessful in removing. Both column chromatography and trituration were attempted to purify this compound, with no luck. Our theory here was that the acid group was causing the product to stick to the silica in the column, resulting in a very small amount of product being recovered from the column. The product that comes off the column always comes through with these impurities, despite trying different solvent systems and different length columns. Therefore, we determined that column chromatography was not a viable option for the purification of this compound. Trituration was also attempted, though we found the

impurities to have similar solubility to the product, so this was ultimately unsuccessful. Purification of this compound seemed too difficult, so we decided to shift our attention to redesigning the synthetic route.

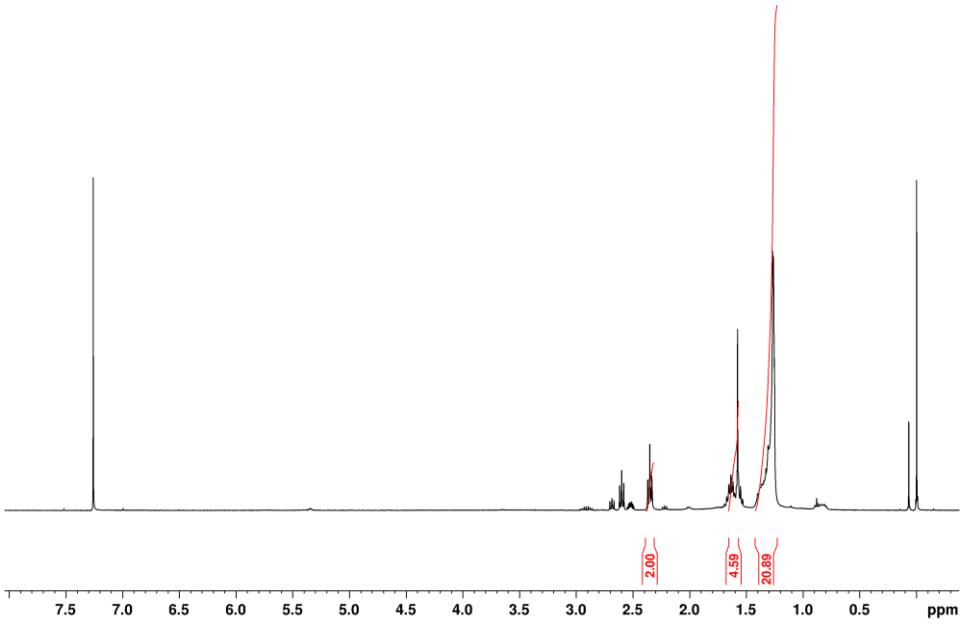

*Figure 112: ^{1}H NMR (400 MHz, $CDCl_3$) of **Acid-SH** after trityl deprotection.*

The main aim we had when redesigning the synthetic route was to use protecting groups that could be removed without the need for difficult purification steps for our final molecule. This brought us back to the thioacetate protecting group used by Cao et al. The deprotection of this protecting group simply required the trityl-protected thiol to be stirred in 3 M HCl at 60 °C for 6 hours, after which evaporation gave the pure compound.[116] This deprotection procedure seemed like a promising alternative to synthesise **Acid-SH**, so we then designed the synthetic route in Scheme 29 to utilise the thioacetate protecting group instead of the trityl protecting group.

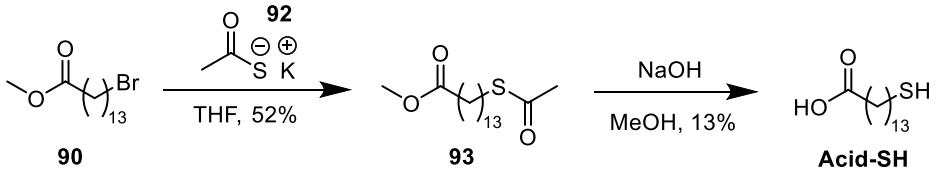

*Scheme 29: Synthesis of **Acid-SH** using the thioacetate protecting group.*

Ester **90** previously synthesised could be used as our starting point for the thioacetate synthetic scheme. Previously, in our research group, students had developed the reaction conditions for the thioacetate substitution using different chain length dibromo starting materials. Here, the research group tried the conditions reported by Cao et al., where the reaction was performed in acetone and stirred at room temperature overnight. They then compared these conditions to using THF and refluxing overnight, of which there are several examples in the literature, including that reported by Shi et al.[129] The research group found that refluxing in THF tended to give a higher yield compared with acetone at room temperature. Therefore, I decided to use the reaction conditions previously developed in our research group, which gave a yield of 52%. This was slightly lower than the students had previously achieved with the dibromo starting materials; however, it gave me enough material to make the **Acid-SH**, so no time was spent trying to further optimise these reaction conditions.

Now that **93** has an ester and thioester group to be removed, we hoped to undergo a global deprotection. The literature reports two key conditions that can be used for this global deprotection, either acidic conditions[8,116] or basic conditions[130]. We attempted both conditions and found that basic conditions using 1 M NaOH at room temperature overnight resulted in the deprotection of both esters, while the acidic conditions only seemed to deprotect one ester. Although the basic conditions resulted in the deprotection of both esters, the product after workup still had some impurities present. This meant we had to perform column chromatography to purify the compound. We found this to work much better for this procedure compared to our trityl deprotection, with the column resulting in pure product (Figure 113). The yield for this reaction, however, was rather low (13%), likely due to the compound getting stuck on the silica due to the polarity of the carboxylic acid functional group. Overall, the change from the trityl-protected thiol to an acetate-protected thiol did not eliminate the need for a tricky purification step, though the column after the acetate deprotection did yield pure **Acid-SH**. The purity of **Acid-SH** was confirmed by comparing the ^{1}H NMR to that which had been previously reported in the literature, the two were in agreement.[131]

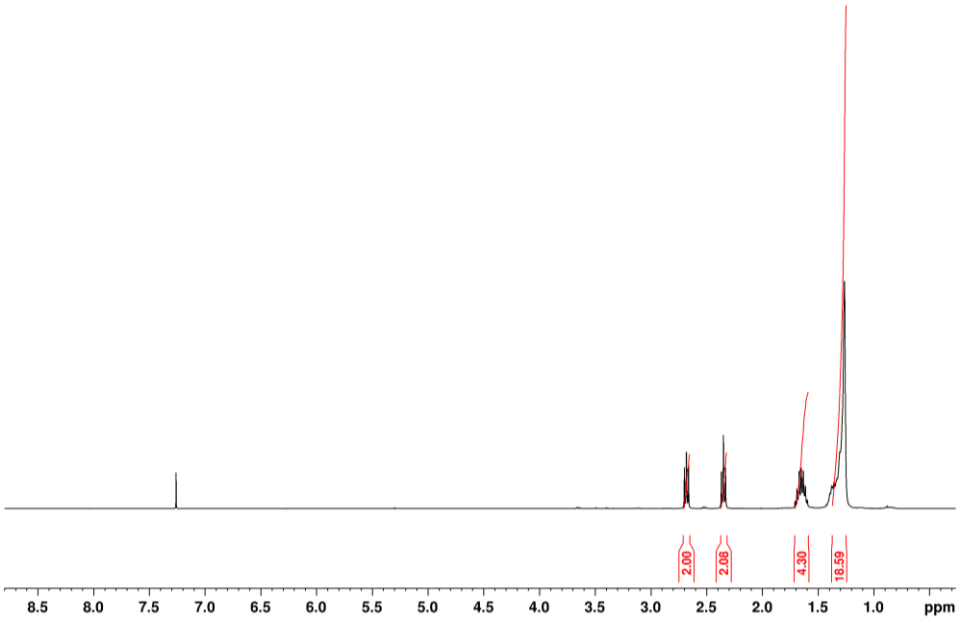

*Figure 113: ^{1}H NMR (400 MHz, $CDCl_3$) of **Acid-SH** after purification following thioacetate deprotection.*

3.5.6 Synthesis of HM-SH

Our initial histamine thiol synthesis plan is depicted below in Scheme 30. Once again, alcohol **79** can undergo a tosylation reaction prior to reacting it with sodium azide to form azide **83**. This reaction gave a moderate yield of 43%. The next step was to reduce azide **83** to an amine using a Staudinger reaction. For this, we used the reducing agent tris(2-carboxyethyl)phosphine (TCEP). TCEP is a water-soluble reducing agent, meaning the reaction simply required an extractive workup- using organic solvent and aqueous washings to remove excess reducing agent and water soluble by products,to give amine **84** in a high yield. The mechanism for this reaction is depicted in Scheme 31. Here, the lone pair on the phosphine can attack the terminal nitrogen in the amine group, moving one of the pairs of electrons in the triple bond onto the middle nitrogen. This forms a linear phosphazide intermediate species.[132] This species can undergo an intramolecular rearrangement. First, the negatively charged nitrogen can then attack the positively charged phosphine, resulting in the formation of a 4-membered ring. The bonds in this 4-membered ring can then break to give an aza-ylide species along with the loss of N_2.[132] In the presence of water, the aza-ylide can undergo hydrolysis to give the desired amine (**84**) and the corresponding phosphine oxide (**95**). This reaction was successful; however,

it did require multiple additions of TCEP for the reaction to reach completion. The likely cause was the use of an old bottle of TCEP reagent where some of the TCEP may have been oxidised. However, since the reaction could reach completion with further additions of TCEP, this was not a significant issue.

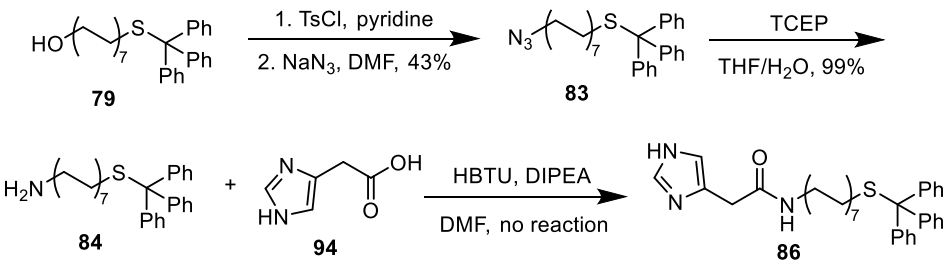

*Scheme 30: Initial **HM-SH** synthesis scheme.*

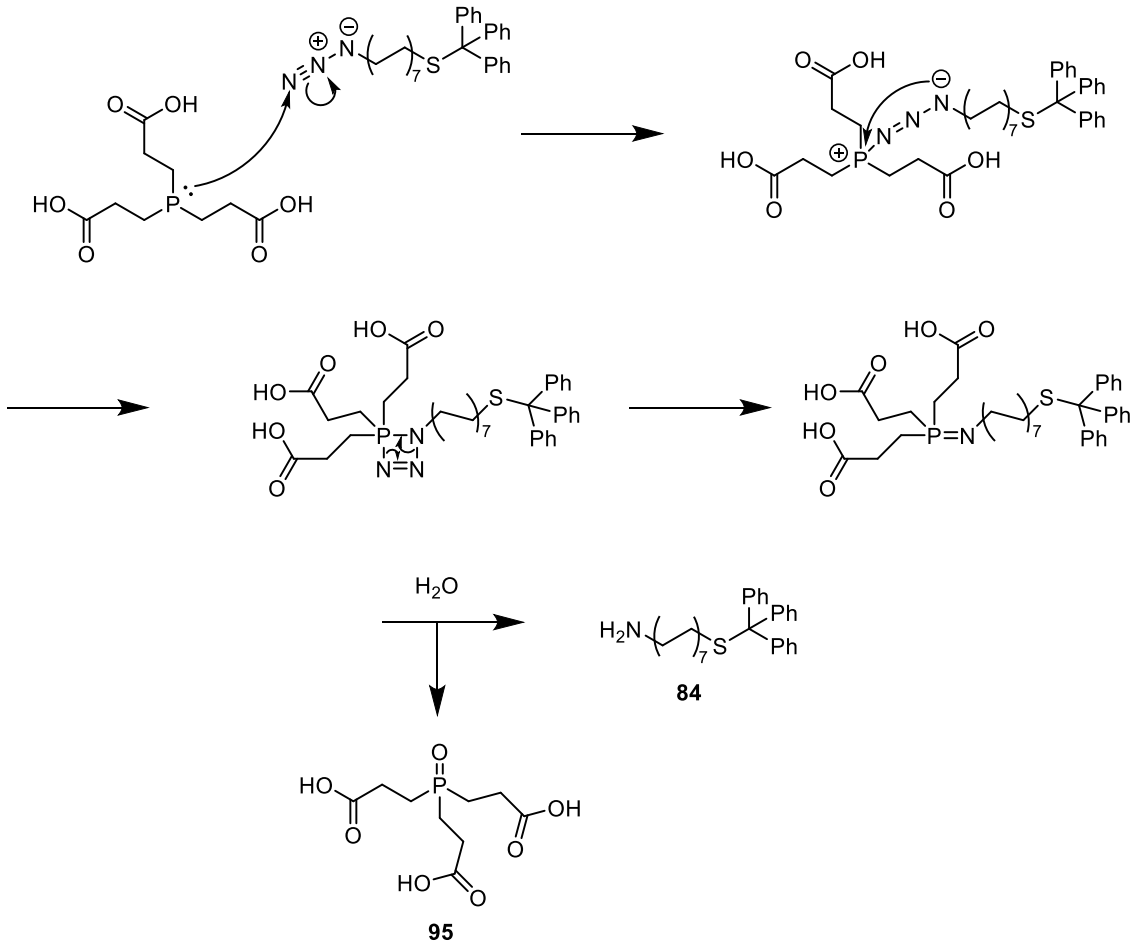

Scheme 31: Mechanism for Staudinger reaction.

The next step was to perform an amide coupling reaction between this amine (**84**) and 4-imidazoleacetic acid (**94**) to introduce the histamine functional group onto the thiol.

Though this step proved quite challenging. For this, the coupling conditions discussed in Chapter 2 to synthesise both our histidine and histamine amphiphiles, as well as to synthesise our **C6-HM-SH** thiol were used. However, the desired product would not form; rather, the starting material remained unreacted. We theorised that the free NH in the imidazole ring was interfering with the reaction. For this particular amide coupling reaction, the imidazole is introduced as the acid rather than the amine. This means the acid is added first, along with HBTU and DIPEA, and left to stir for 15 minutes, allowing for the formation of an activated carbonyl group ready for the amine to attack. Previously, we have performed one reaction where the imidazole was introduced as the carboxylic acid, which was to make histidine amphiphile **H** (Chapter 2, Section 2.2.1). The key difference here was the presence of a benzyl protecting group on the free nitrogen in the imidazole ring, preventing this from interfering in the reaction. Therefore, we predicted the amide coupling reaction would work if the free nitrogen in the imidazole ring was protected.

Instead of using a benzyl protecting group like for the histidine amphiphile synthesis, we decided to use a trityl protecting group. The main advantage this group had was that it would require the same conditions to be cleaved as the trityl thiol protecting group, both of which could be cleaved at the same time to give the final product **HM-SH**. The trityl protection of 4-imidazole acetic acid (**94**) had been previously reported by Meredith et al. Here, imidazole **94** and trityl chloride were dissolved in pyridine and stirred at room temperature for 16 hours (Scheme 32).[133] However, when we attempted this reaction, both TLC and NMR showed no evidence that the trityl group had been added onto our imidazole ring. Thinking now that the acid group could be interfering with this reaction, a new synthesis route was designed (Scheme 33), where acid (**94**) is first converted into an ester (**97**) before introducing the trityl group. Hydrolysis of the ester then gave trityl-protected acid (**96**) ready for amide coupling.

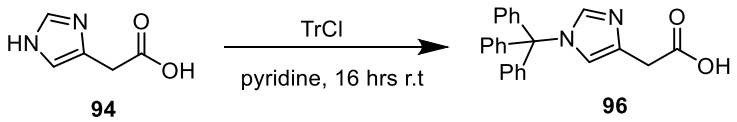

Scheme 32: Synthesis of trityl-protected imidazole using Meredith and coworkers' procedure.[133]

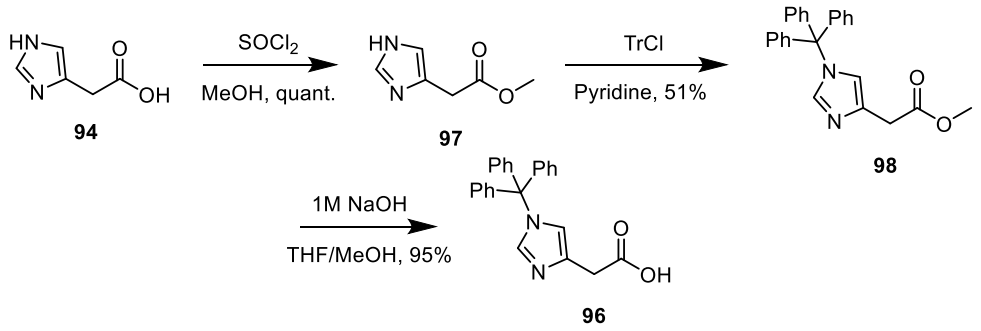

*Scheme 33: Synthesis of trityl-protected imidazole (**96**).*

The initial esterification step proceeded smoothly using our existing procedure to get a quantitative yield. The trityl protection of the imidazole nitrogen was slightly more challenging. Table 3 summarises the reaction conditions tried. The reagents and reaction conditions themselves seemed to work well with the trityl protecting group in slight excess (1.2 eq), using pyridine as our solvent. The main areas of this reaction that underwent optimisation were the extractive workup procedure and the conditions for column chromatography. Initially, we thought that compound **98** may be cleaving on the column to give back starting material **97**, which would remain absorbed on the stationary phase, resulting in a small yield of **98**. Attempting to decrease the column length from attempts 1 to 2 to prevent **98** from reacting with the silica gave a slightly lower yield. Next, we investigated whether the extractive workup was contributing to the low yields rather than the column chromatography step. Initially, 1 M HCl was used to neutralise the pyridine, removing this from the reaction mixture. HCl had been previously used in the workup for other compounds synthesised in this thesis that contained a trityl protecting group. When the first two synthesis attempts both gave such low yields, the workup conditions were re-examined, and it was assumed that the HCl could be cleaving the trityl protecting group. Potentially, the position of this group on the imidazole may make it more susceptible to acid than when this group is bound to the thiol. The optimal approach to confirm this hypothesis was to use a different aqueous phase for our workup. We settled on ammonium chloride, as this is a weak acid which can be used to remove pyridine from solution without cleaving the trityl protecting group. This change in workup procedure had a significant effect on the yield, with this now being 51%. Further optimisation could be achieved by neutralising the silica prior to the column, though this step was never tried as a suitable amount of **96** was produced from the success of attempt 3. The ester

protecting group on the product (**98**) could then be removed using basic conditions to give a 95% yield of trityl-protected imidazole (**96**).

*Table 3: Reaction conditions for the synthesis of imidazole **98**.*

Attempt	**Workup Procedure**	**Column Conditions**	**Yield**
1	1 M HCl / CH_2Cl_2	Regular length 50% EtOAc/hexanes	9%
2	1 M HCl / CH_2Cl_2	Short column 50% EtOAc/hexanes	3%
3	Sat. Ammonium chloride / CH_2Cl_2	Short column 50% EtOAc/hexanes	51%

Now with our trityl-protected imidazole **96** in hand, the amide coupling reaction could be attempted again. Using the previously established amide coupling conditions, two attempts were made to try and synthesise protected histamine thiol **86**, both of which were unsuccessful. Unfortunately, this reaction did not form the desired product; only the amine starting material was able to be isolated from the reaction mixture. Mass spectrometry of the reaction mixture also showed no evidence of product formation. Due to previous success with these amide coupling conditions, the decision was made to investigate an alternative route to synthesise **HM-SH**.

The synthesis scheme was redesigned to use histamine dihydrochloride (**56**) as the reagent to introduce the imidazole structure into the thiol molecule (Scheme 34). This was chosen due to the previous success in amide coupling, where histamine dihydrochloride was coupled to a carboxylic acid for synthesis of both the histamine amphiphile **HM** and

short-chain histamine thiol **C6-HM-SH**. The need for any protecting groups on the imidazole ring is eliminated when it is introduced as the amine rather than the acid in the coupling reaction. For this amide coupling, histamine dihydrochloride (**56**) needs to be coupled with an acid molecule containing a thiol. Fortunately, this molecule had already been synthesised when making **Acid-SH**, therefore acid **88** could directly undergo an amide coupling reaction. Proceeding with the trityl protecting group was decided due to having acid **88** already in hand with the protected thiol and deprotected acid. The thioacetate acid was not suitable as both the acid and thiol protecting groups were removed in the same step. For the amide coupling reaction, the thiol end of the molecule still needed to be protected to prevent this from interfering with the reaction.

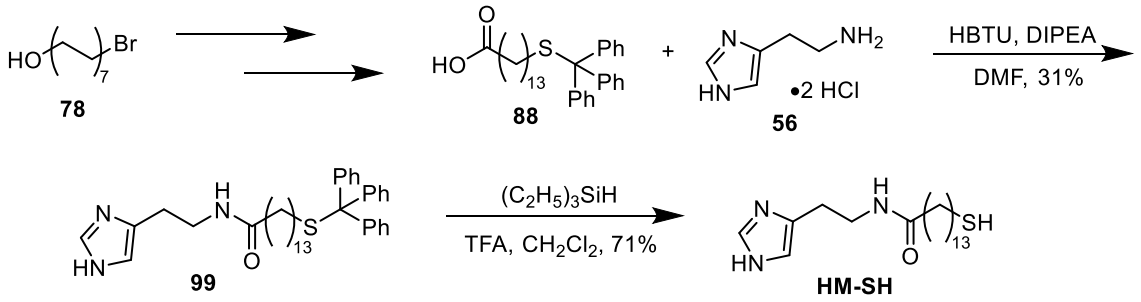

*Scheme 34: New **HM-SH** synthesis scheme based on **C6-HM-SH** synthesis.*

The amide coupling reaction worked with a yield of 31%. The presence of this compound (**99**) on ^{1}H NMR was determined by the presence of two singlet peaks in the aromatic region, both integrating for 1 H and belonging to the imidazole functionality. In addition to this, the characteristic trityl aromatic proton peaks were also seen in this region of the ^{1}H NMR as three multiplets integrating for a total of 15 H. This indicates that we have both the imidazole end and the thiol end present in our compound. The final step, deprotection of the trityl group, gave us a yield of 71%. Overall, the redesign of the **HM-SH** synthetic route was well worth it, given that the amide coupling reaction worked and the trityl deprotection yielded a high amount of product.

Assignment of the **HM-SH** NMR spectra was relatively straightforward, as we could use the **C6-HM-SH** assigned spectra as a guideline for this. The ^{1}H NMR (Figure 114) and ^{13}C NMR (Figure 115) have been assigned below. In addition to the previously assigned **C6-HM-SH** spectra, COSY, HSQC and HMBC spectra were used to confirm these assignments. These additional 2D spectra can be found in the appendix. The -CH_2 peaks in the compound without a colour assigned to them match the peaks in the NMR spectra

without a colour attached to them. These alkyl -CH_2 peaks are harder to identify in long-chain molecules as they tend to overlap.

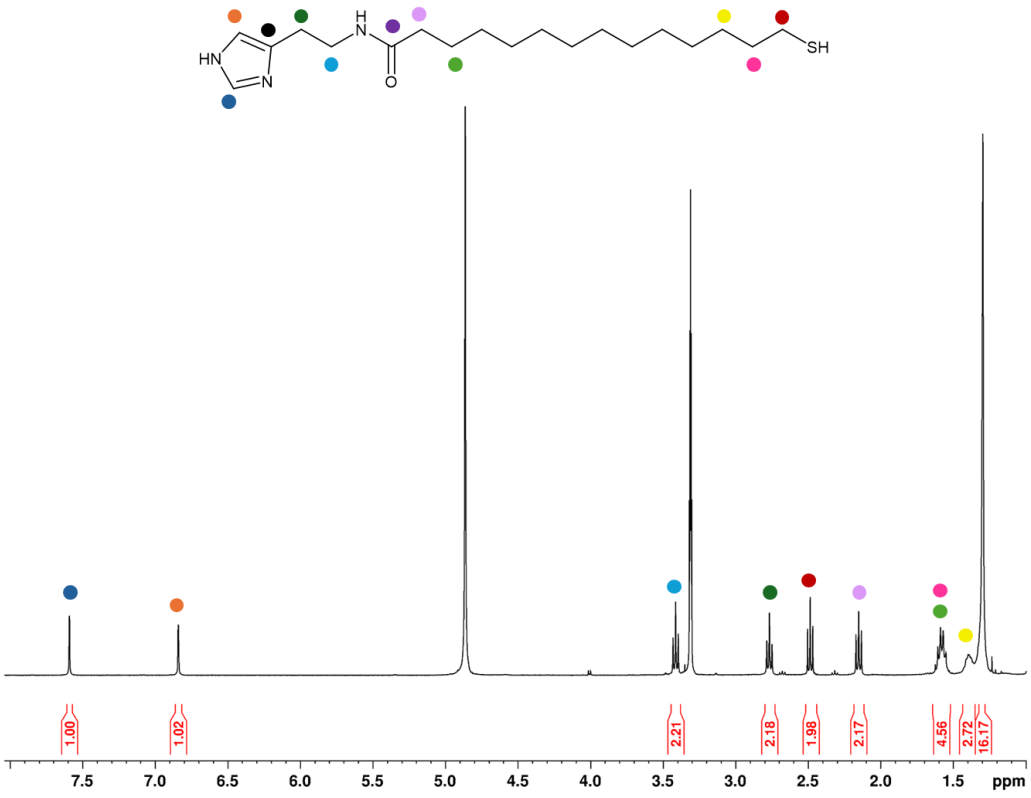

*Figure 114: ^{1}H NMR (400 MHz, CD_3OD) assignment for **HM-SH**.*

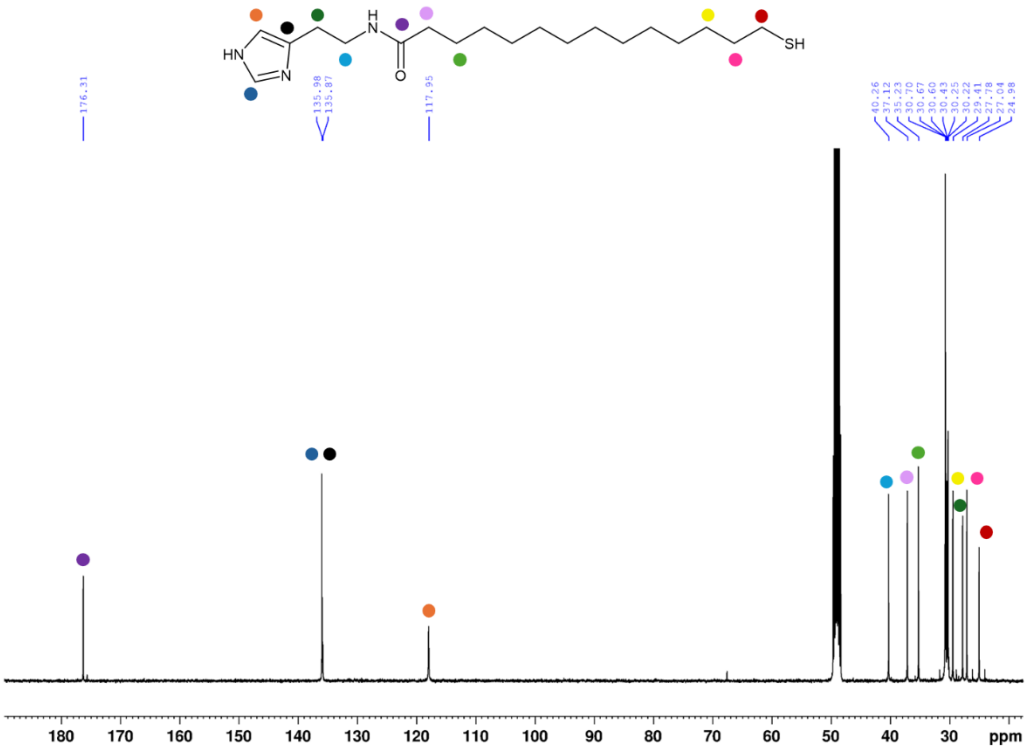

*Figure 115: ^{13}C NMR (101 MHz, CD_3OD) assignment for **HM-SH**.*

3.5.7 Synthesis of G-SH

The original synthetic plan for **G-SH** is depicted in Scheme 35. With amine **84** having been previously synthesised, the next step was to undergo a guanidinylation reaction, the mechanism for which was discussed previously in Chapter 2, Section 2.2.3. However, just like in the **C6-G-SH** synthetic route, we decided to use the more reactive guanidinylation reagent, 1,3-di-Boc-2-(trifluoromethylsulfonyl)guanidine (**55**). The use of 1,3-di-Boc-2-(trifluoromethylsulfonyl)guanidine (**55**) in this reaction gave us a 54% yield, so we were happy with this outcome, though there is potentially room to optimise this reaction to achieve the much higher yields obtained from the guanidinylation with the alkane amine **HA**, and C6 amine **72**.

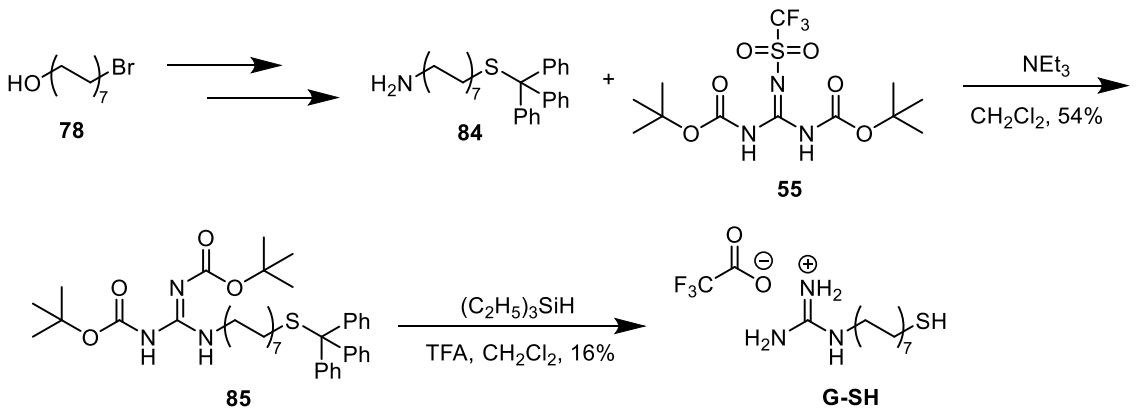

*Scheme 35: Initial synthetic plan for the synthesis of **G-SH**.*

The final step in this synthetic scheme was a global deprotection to give us **G-SH**. Here, we used TFA and triethylsilane to remove both the trityl and Boc protecting groups, the same way we did to yield our **C6-G-SH**. Just like for the C6 analogue, the deprotection results in the formation of a rather polar product. Since this compound contained a significantly longer carbon chain, we thought purification via only the workup might be successful. Triphenylmethane impurities would be extracted into the organic layer, leaving behind **G-SH** in the aqueous layer. Both CH_2Cl_2 and hexanes were trialled for this; however, both resulted in our compound being present in both the organic and aqueous phases. We also found that the small amount of product we could extract into the aqueous phase would come through with a slight impurity, which we could not seem to remove (Figure 116). Reverse-phase chromatography looked to be our only option. Though this worked well for **C6-G-SH**, the process itself is quite tedious and time-consuming; therefore, we wanted to find a simpler alternative to make **G-SH**. This led us to redesign the synthetic route to look at a different protecting group that did not require a workup or column to be removed.

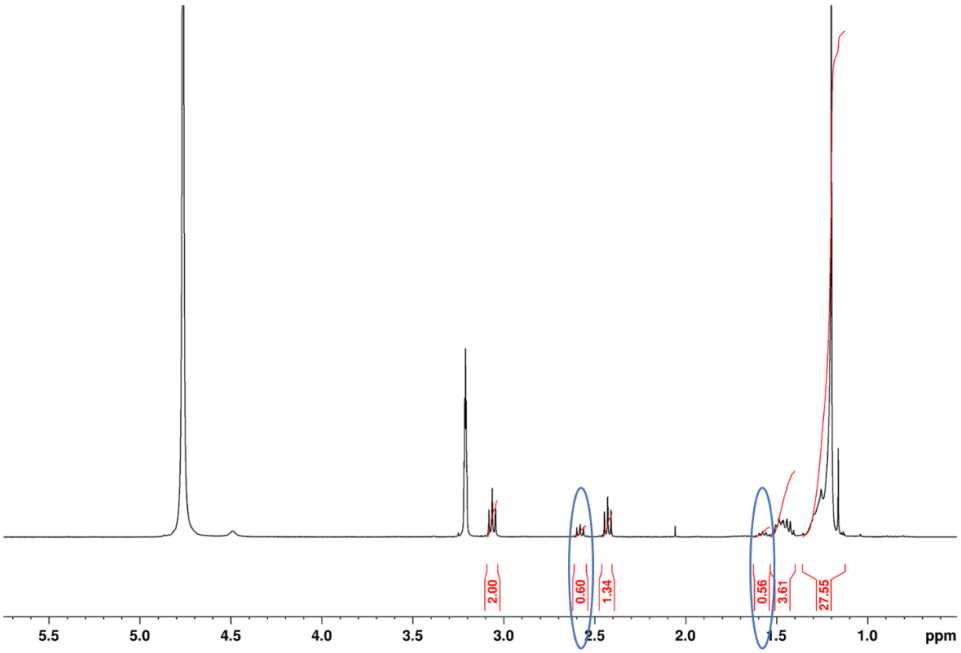

*Figure 116: ^{1}H NMR (400 MHz, CD_3OD) of **G-SH** product with impurities circled in blue.*

The acetate protecting group had proved favourable with our **Acid-SH** synthesis, so we decided to try this for our **G-SH**. The deprotection of the acetate functional group could simply be performed by refluxing the compound with 6 M HCl, then evaporating the solvent to give the desired compound.[116] Therefore, we should have no difficulties with the purification of our final guanidine product (**G-SH**). Scheme 36 depicts our new synthetic route.

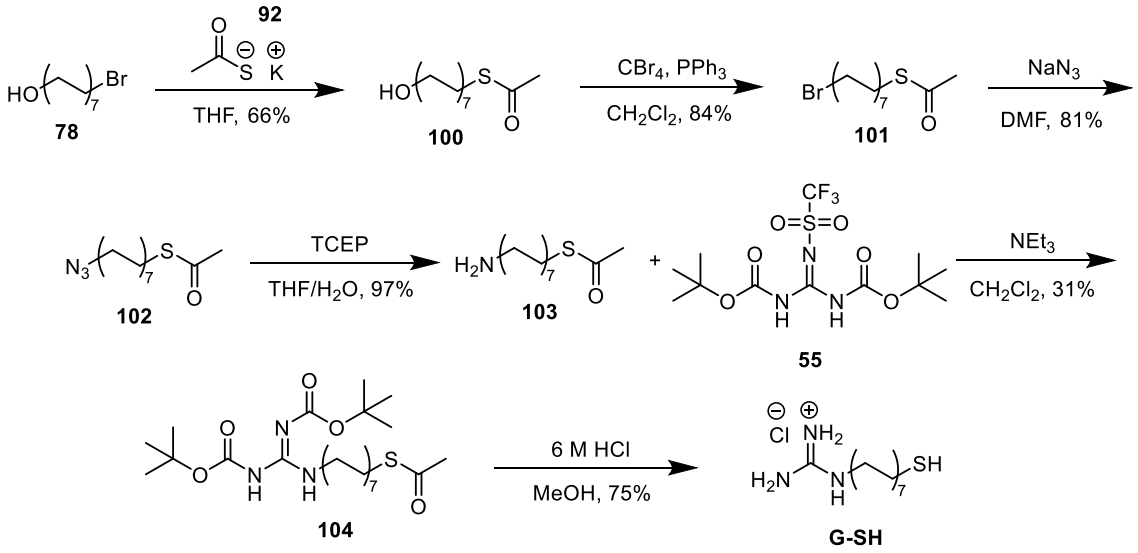

*Scheme 36: New synthetic plan for the synthesis of **G-SH** using an acetate protecting group.*

Starting off with 14-bromotetradecan-1-ol (**78**), we can first introduce our thiol using potassium thioacetate (**92**) via a simple S_N2 reaction with the bromine end of our C14 chain, using the same procedure as for the **Acid-SH** synthesis. The remaining OH could then be converted into a better leaving group. Previously, we have used a tosylation reaction to convert our OH group into a better leaving group. However, we did see some odd results with this (discussed earlier in Section 3.5.3), so we wanted to try a different reaction to see if this would be more straightforward. We decided to convert our alcohol (**100**) into a bromine (**101**) via an Appel Reaction. This reaction was named after Rolf Appel, who did extensive research on the substitution of alcohols to halides using a combination of CX_4 and PPh_3 under mild conditions.[134] The mechanism for this reaction is shown in Scheme 37. Firstly, the triphenylphosphine is activated by an initial reaction with carbon tetrabromide. The lone pair on the phosphorus can take one of the bromines from carbon tetrabromide to form the phosphonium salt. The carbon in carbon tetrabromide is now negatively charged, allowing this to deprotonate the alcohol on compound **100**. The now negatively charged oxygen can attack the positively charged phosphorus, forming a bond between the two. The negatively charged bromine can then come in and attack the carbon bonded to the oxygen. This results in the oxygen-carbon bond breaking with the formation of triphenylphosphine oxide (**105**).

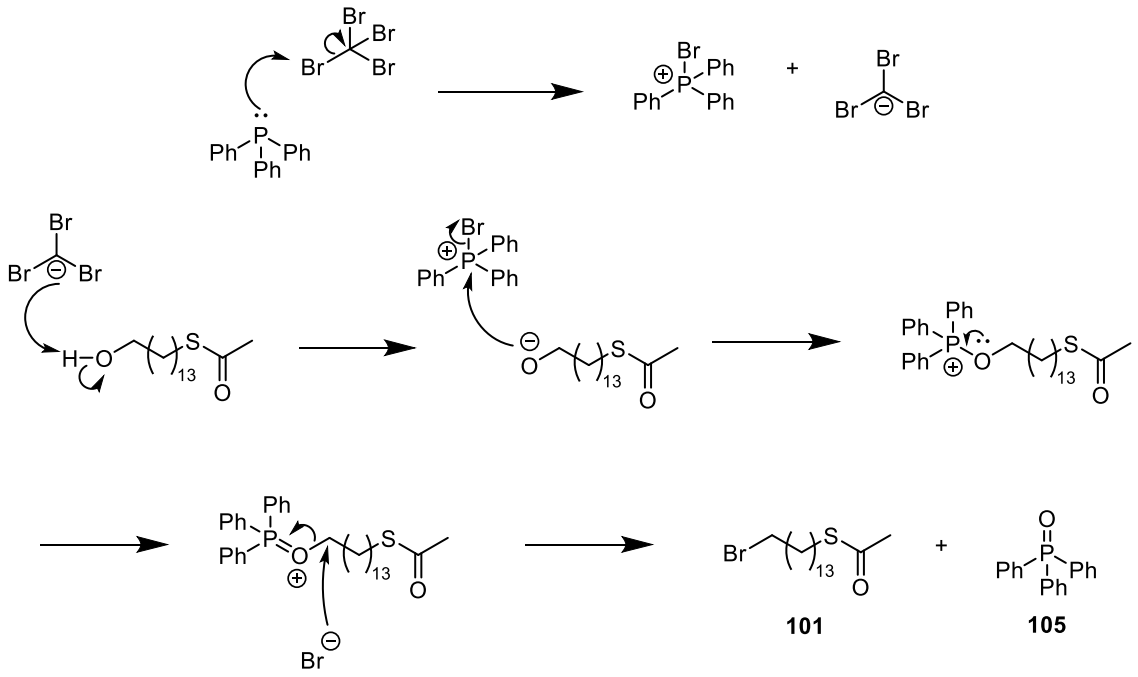

Scheme 37: Mechanism for bromination via an Appel Reaction.

Both tosylation and the Appel reaction were initially trialled on a 10 mg scale with a crude NMR run after the workup. Both the crude tosyl (Figure 117) and bromination product (Figure 118) showed significant impurities on the ^{1}H NMR. However, the bromination impurities were quite clearly a result of leftover triphenyl phosphine, which could be easily removed using column chromatography. The potential ease of removal of the bromination impurities and the previous difficulties we have had with tosylation lead us to proceed with the Appel reaction on a larger scale. This afforded the pure product (**101**) in a 78% yield with NMR data matching that previously reported in the literature.[116]

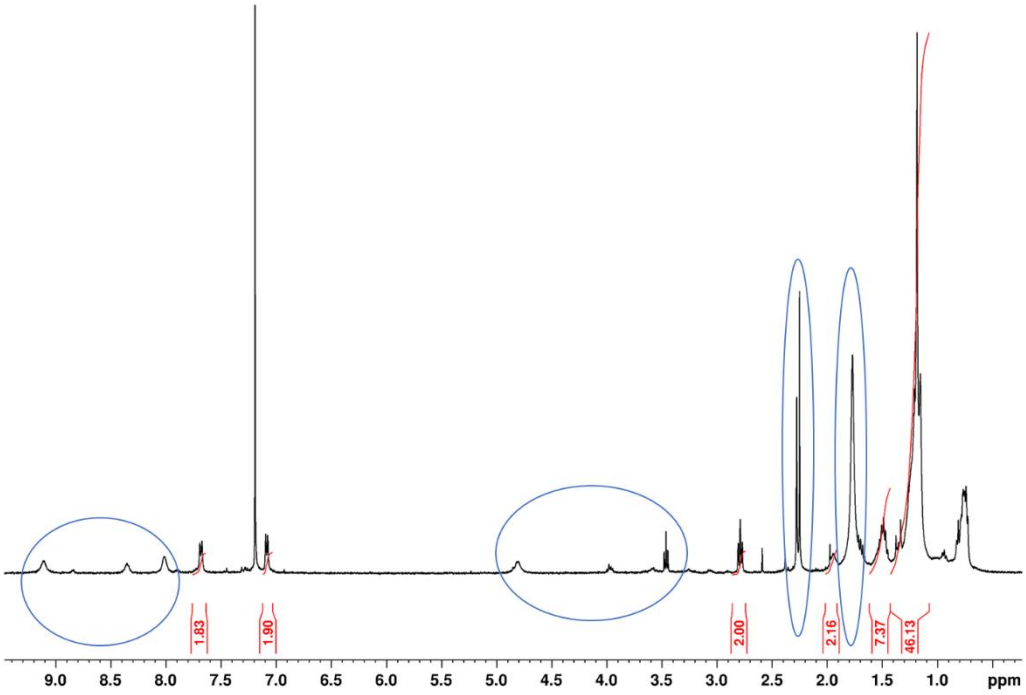

Figure 117: ^{1}H NMR (400 MHz, $CDCl_3$) of crude product from tosylation with impurities circled in blue.

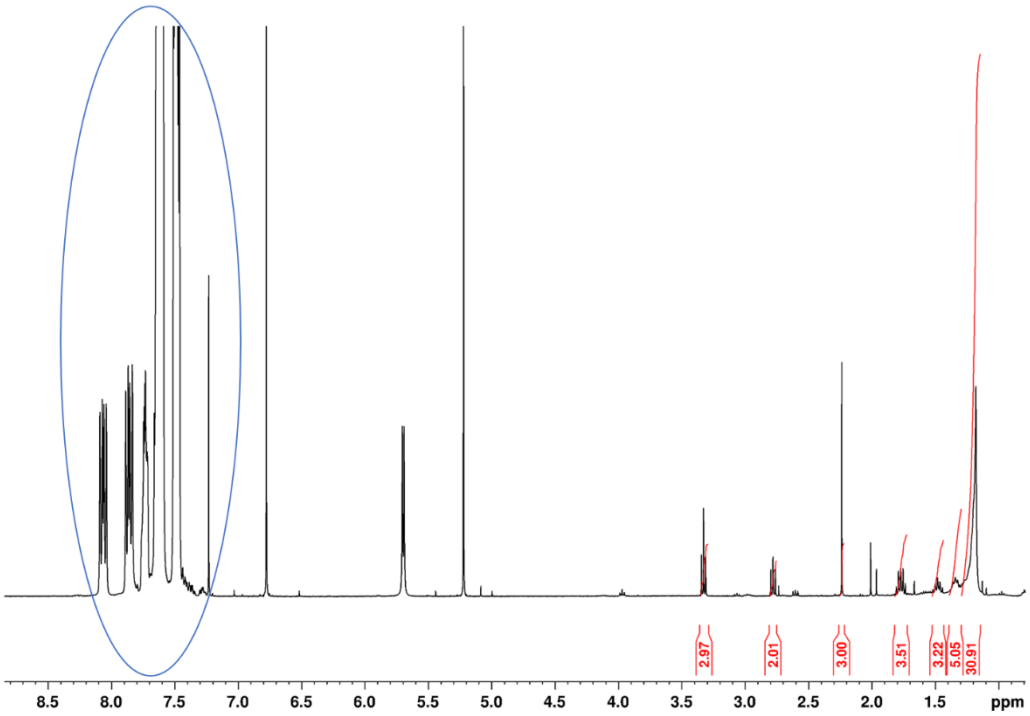

Figure 118: ^{1}H NMR (400 MHz, $CDCl_3$) of crude product from Appel reaction, with triphenyl phosphine impurities circled in blue.

Once we have our bromine (**101**), we can undergo another S_N2 substitution reaction to introduce our azide group into this compound (**102**). The azide group then allows us to form an amine (**103**) via a Staudinger reaction, with the mechanism discussed earlier in Scheme 31. This particular amine needed to be used in the next step relatively soon after being synthesised due to its potential to undergo an intramolecular transacetylation, shown in Scheme 38. The primary amine at one end of the molecule can undergo nucleophilic attack of the carbonyl at the other end of the molecule. This forms a bond between the N and the carbonyl, allowing the S-carbonyl bond to be broken, moving the acetyl group from the thiol to the amine. The acetylated amine (**106**) would be unable to undergo amide coupling in the next step and would be undesirable. However, this reaction does take some time to occur; therefore, if we use the amine relatively quickly after its initial synthesis, we should eliminate any issues that could arise from the potential intramolecular transacetylation. Amine **103** can then react with our guanidinylation reagent **55**, via an S_N2 substitution, to introduce our guanidine functionality into the compound.

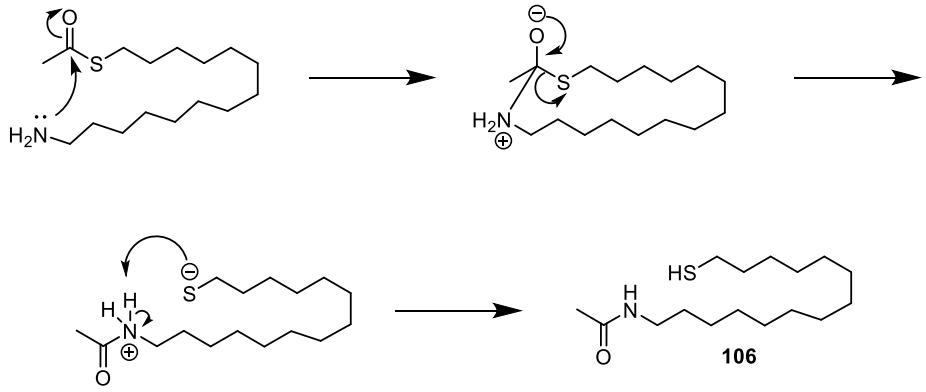

*Scheme 38: Mechanism for the intramolecular transacetylation of compound **103**.*

Finally, we can then undergo a global deprotection to remove both the acetate group on the thiol and the Boc protecting groups on the amines, to get **G-SH**. The general mechanism for the acetate deprotection is depicted in Scheme 39. This is simply acid-catalysed ester hydrolysis. The oxygen is initially protonated under acidic conditions, forming a positive charge on the oxygen. This allows for the nucleophilic addition of water to the carbonyl group. The added oxygen from the water is now positively charged. Proton transfer then occurs, resulting in the thiol taking a proton from the positively charged oxygen. The thiol is now protonated and positively charged. A water molecule can then remove the proton from one of our hydroxyl groups, resulting in the reformation

of our carbonyl group. At the same time, the bond between the carbon and thiol breaks, resulting in the formation of the free thiol along with acetic acid **107**.

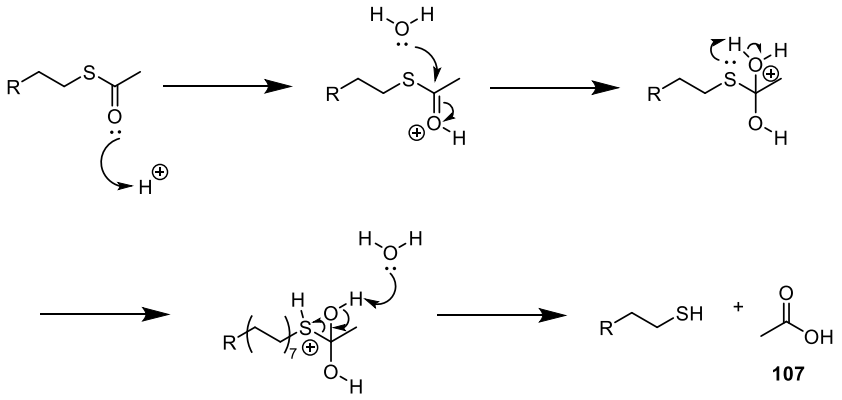

Scheme 39: Mechanism of thioester acid-catalysed hydrolysis.

The global deprotection proceeded smoothly with a yield of 75%. The reaction itself was completed within one hour, followed by evaporation to give the pure product. This was characterised using NMR spectroscopy. The ^{1}H NMR (Figure 119) and ^{13}C NMR (Figure 120) have been assigned using the previous assignment of **C6-G-SH** as a guide. In addition to this, the COSY and HSQC data were used to confirm the assignment. The HMBC spectrum provided little help when assigning this compound. The COSY, HSQC and HMBC spectra are all included in the appendix. Note that the peaks not assigned a coloured circle correspond to the -CH_2 peaks in the alkyl chain that were also not assigned a colour, as the exact position of these groups in the NMR is difficult to determine.

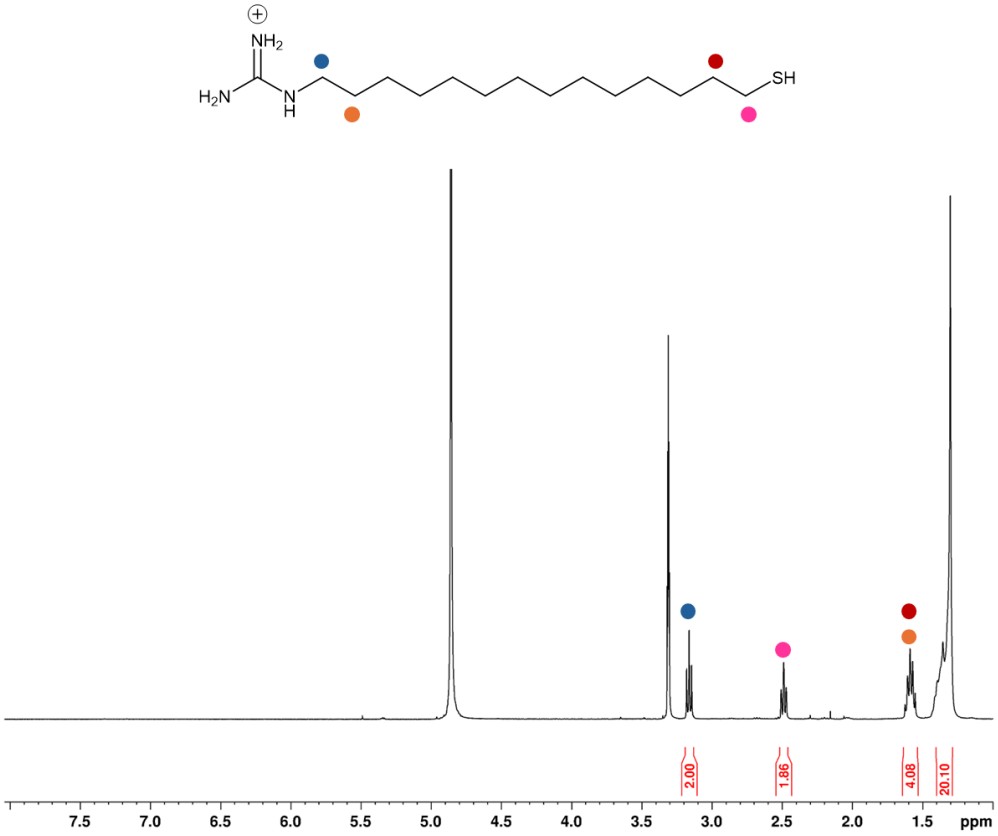

*Figure 119: ^{1}H NMR (400 MHz, CD_3OD) assignment for **G-SH**.*

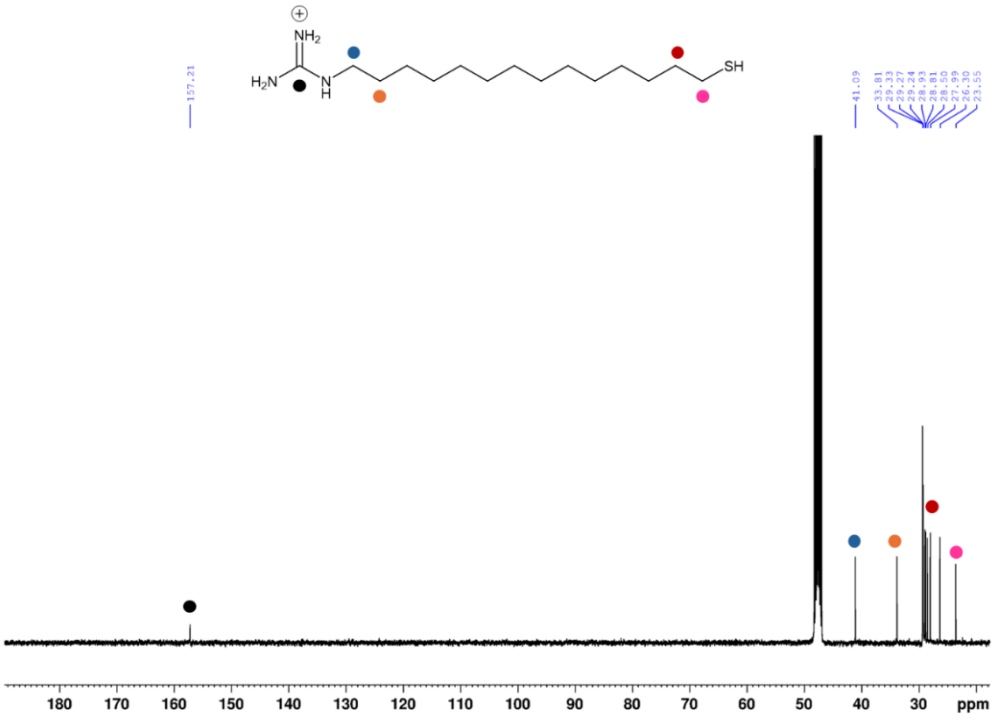

*Figure 120: ^{13}C NMR (400 MHz, CD_3OD) assignment of **G-SH**.*

3.6 Examination of the silver-thiol polymer system with C14 thiols

3.6.1 Silver-thiol polymer formation with HM-SH

The successful synthesis of all the C14 thiols then meant we could start to investigate their activity as silver-thiol polymers. Like for the C6 thiol system, we first wanted to investigate the activity of just our **HM-SH** catalyst to see if the formation of silver-thiol polymers had a positive effect on catalysis.

We investigated the activity of **HM-SH** on its own, and in combination with Ag^{+}, just like for the C6 system. However, this time we also decided to investigate the activity of our **HM-SH** with both Ag^{+} and Zn^{2+}, at increasing concentrations (Figure 121). When we have just the histamine thiol in the catalytic system, the rate of catalysis is fairly low at all concentrations. However, when we add Ag^{+} into the system, we see a dramatic increase in the rate of catalysis, with this getting larger with increasing concentrations of catalyst. This was a very exciting result, suggesting that we are observing polymer formation between the histamine thiol and silver, and that this catalytic system is now more favourable than the **HM-SH** catalyst on its own. The C14 carbon chain is therefore long enough to allow the histamine catalytic groups to be orientated close together, allowing them to facilitate cooperative catalysis. Therefore, the C14 chain length is much more favourable for catalysis in these polymer systems than the shorter C6 system. We also see a much greater rate for catalysis with our **HM-SH** system with Ag^{+} than we did for the free **C6-HM-SH** system, indicating that the formation of these polymers promotes cooperative catalysis.

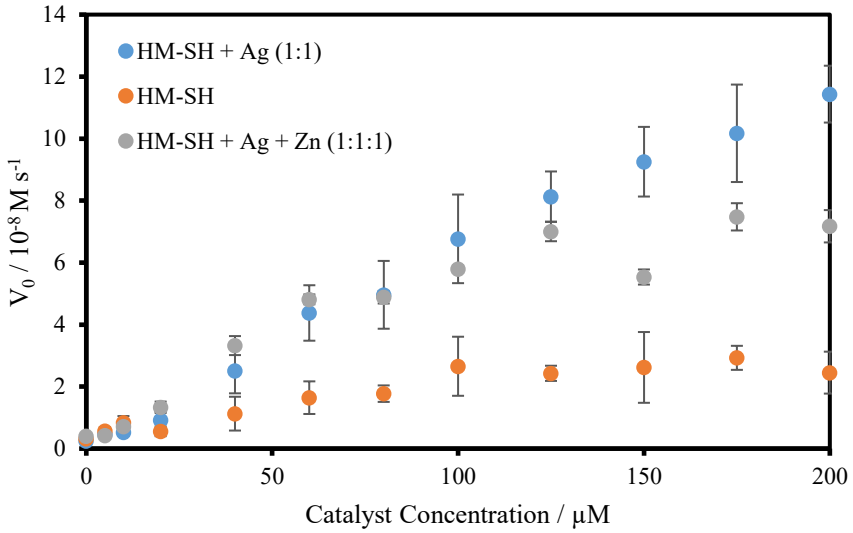

*Figure 121: **HM-SH** forming silver-thiol polymers. Experimental conditions: aqueous buffer pH =7.0 ([HEPES] = 5 mM), [PNPB] = 500 µM, 40 °C.*

Interestingly, the addition of Zn^{2+} into the system had a minimal effect on the rate of catalysis. Previously, with our self-assembled system, the **HM** amphiphile did show a slight increase in the presence of Zn^{2+}, though this was considerably less of an increase compared with our histidine amphiphile (**H**) (Figure 88). When Zn^{2+} is present, three imidazole functionalities will bind the metal ion.[53] This can then stabilise a hydroxyl group, which can undergo nucleophilic attack of the substrate. However, when Zn^{2+} is absent, the imidazole units will undergo a general base mechanism for catalysis whereby the N in the ring can deprotonate a water molecule, forming OH^- for nucleophilic attack of the substrate.[54] This mechanism is aided by the proximity of neighbouring imidazole residues, enhancing the basicity of the ring to then deprotonate the water molecule. The results in Figure 121 suggest that both of these mechanisms (shown in Figure 122) occur at a similar rate, hence why there is minimal difference between the systems with and without Zn^{2+}.

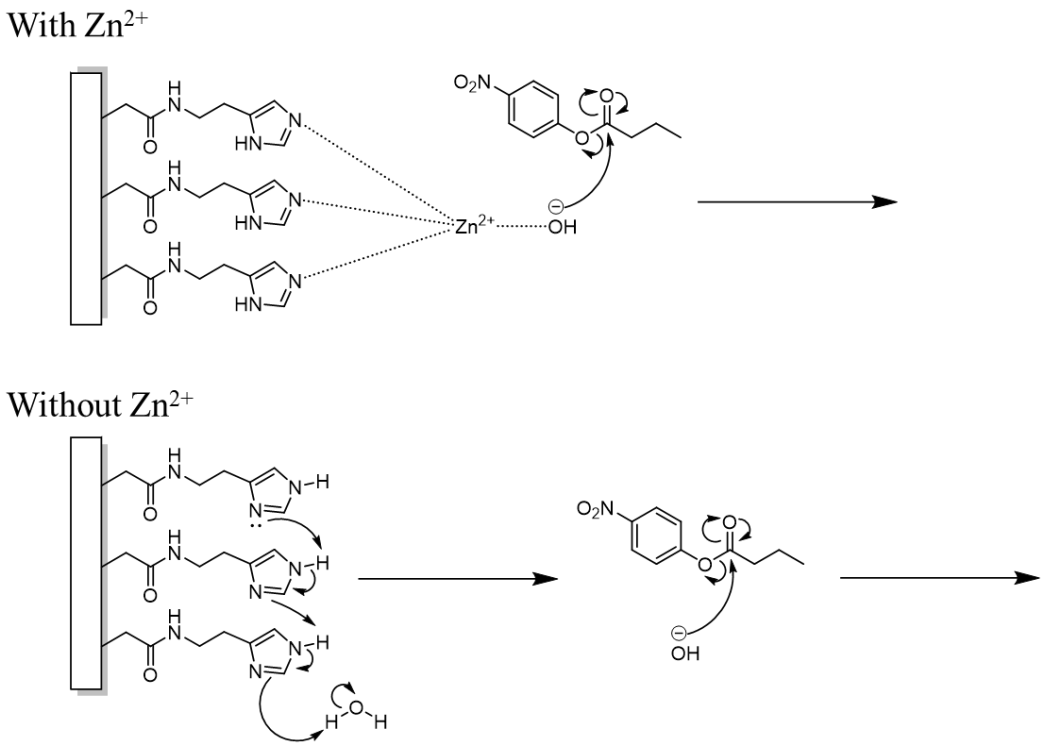

*Figure 122: Mechanism for the catalysis of PNPB with **HM-SH** polymers in the presence and absence of Zn^{2+}.*

3.6.2 Determination of the CAC for HM-SH

Another factor to take into consideration with this system is the potential for the histamine thiol to self-assemble. These compounds have a polar imidazole ring and a polar thiol group separated by a non-polar C14 carbon chain, and now bear the resemblance to bolaamphiphiles. Bolaamphiphiles can self-assemble similarly to amphiphiles, so we want to ensure we are working at concentrations below the CAC to ensure that all the thiols in solution are forming polymers and not self-assembling.

The CAC of **HM-SH** could be determined using the same method used previously for **C6-HM-SH**. Figure 123 shows the CAC to be 122 μM. This means that we want to use a catalyst concentration below 122 μM to investigate our silver-thiol polymer system, as below this, there are not enough of the bolaamphiphiles in solution to self-assemble.

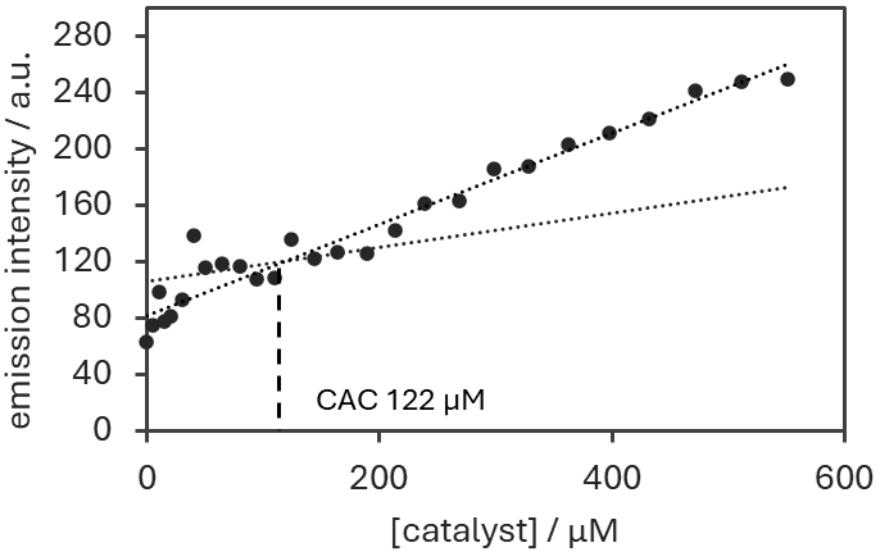

*Figure 123: CAC determination for **HM-SH**. Fluorescent titrations using aqueous buffer pH = 7.0 ([HEPES] = 5 mM), [DPH] = 10 µM, [PNPB] = 500 µM, 40 °C.*

3.6.3 Comparison of the polymer to the initial vesicle system

Now that we can see our silver-thiol polymers are forming and that we have cooperativity occurring between our **HM-SH** catalyst, we can look at comparing this to the initial vesicle system (Figure 124). Here we can see that our **HM-SH** catalyst is far superior to the **HM** vesicle system, with this having more than doubled the rate of catalysis. The **H/G/D2PA** system in the absence of Zn^{2+} results in a very similar rate to our **HM-SH** polymer, though the vesicle system is still far superior when Zn^{2+} is added. These results show promise as the addition of the rigidity to the system in the way of silver-thiol polymers has already had a significant increase in the rate of catalysis. Hopefully, when we start to incorporate our **G-SH** and **D2PA-SH** functionalities into our polymer we will see an increase in the rate of this compared with our optimised vesicular catalyst.

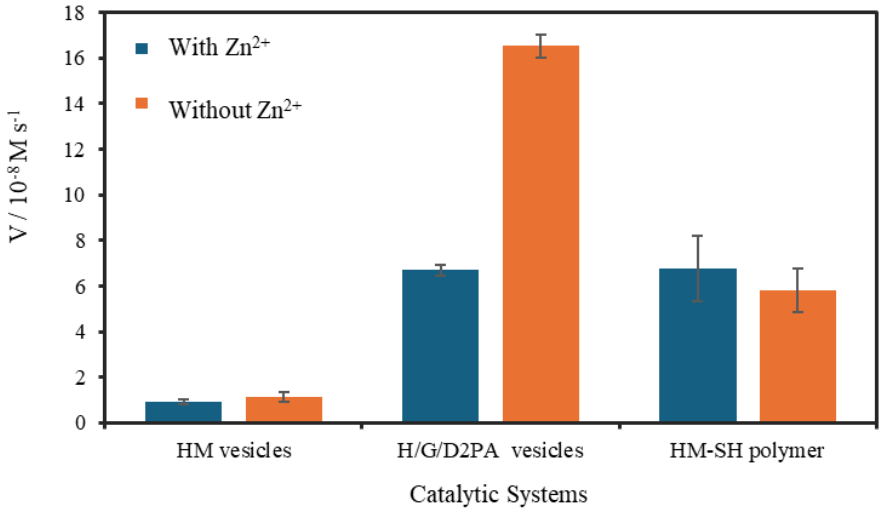

Figure 124: Comparison between the rates of catalysis for the vesicular system and our initial ***HM-SH*** *polymer system. Experimental conditions: aqueous buffer pH = 7.0 ([HEPES] = 5 mM), [total catalyst] = 100 μM, [$Zn(NO_3)_2$] = 100 μM, [PNPB] = 500 μM, 40 °C.*

3.6.4 Characterisation experiments for the system

The formation of these silver-thiol polymers can be visualised using TEM (Figure 125). Similar to Cao and coworkers' system, we observed the aggregate-like morphology of these structures. This suggests that our silver-thiol coordination polymers are forming 2-dimensional structures, similar to those seen previously in the literature.[112,116] Likely, we are forming these kinds of structures due to the basic nature of the HM-SH imidazole ring, similar to how Casuso and coworkers observed different structures with acidic and neutral thiols. Unfortunately, their research did not extend to basic thiols.

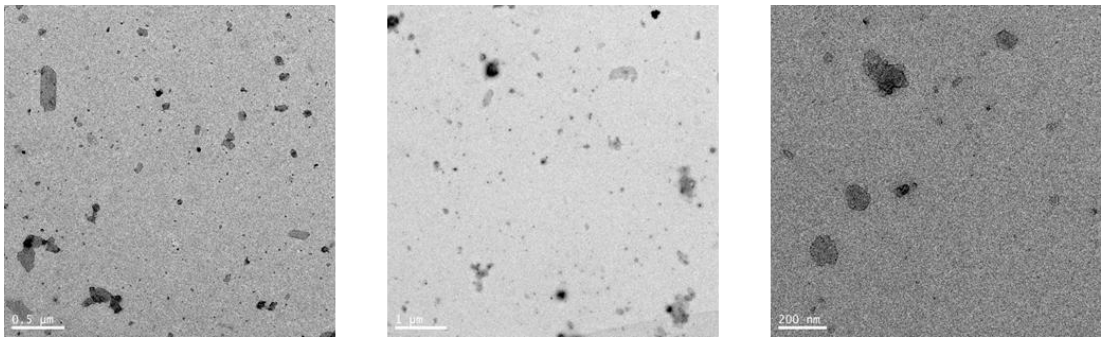

Figure 125: TEM images of ***HM-SH*** *(60 μM) in the presence of Ag^+ (60 μM) with aqueous buffer pH 7.0 ([HEPES] = 5 mM), [PNPB] = 500 μM.*

3.6.5 Screen of functional groups for cooperativity

To expand upon the research conducted by Cao et al. we wanted to see if we could get cooperativity occurring in these silver-thiol polymers between two or more different functional groups, similar to what we have shown for our vesicular system. Figure 126 shows the results of this screen. Despite not seeing much of an increase in activity with our **HM-SH** system in the presence of Zn^{2+}, we still decided to screen all our potential catalytic systems with this. Several artificial esterase examples have been published that utilise Zn^{2+} in the catalytic site.[53,69] In addition to this, our optimised self-assembled catalyst used Zn^{2+} with the **D2PA** amphiphile, so we decided it was still worth screening this metal ion.

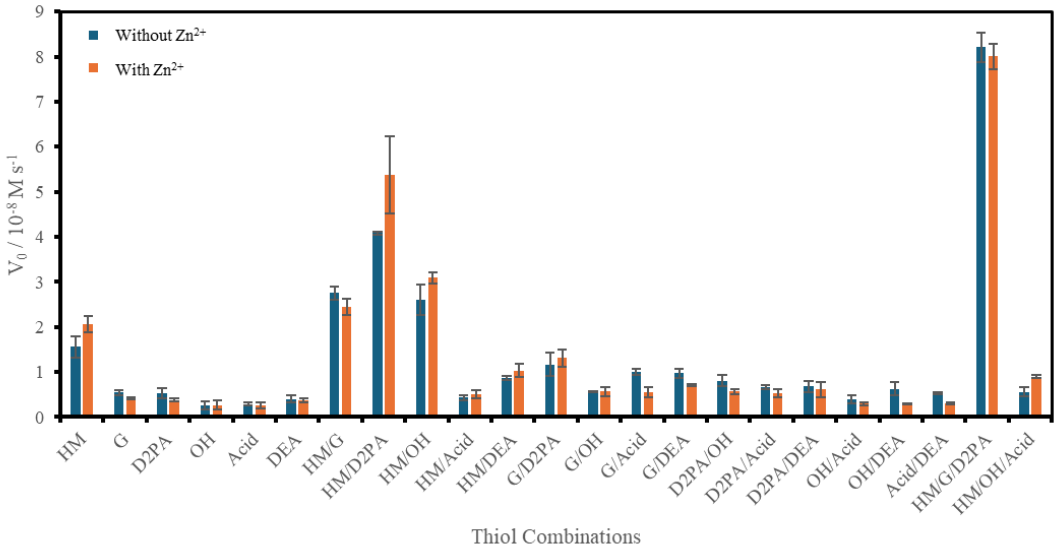

Figure 126: Screen of thiol combinations. Experimental conditions: aqueous buffer pH = 7.0 ([HEPES] = 5 mM), [individual thiol] = 30 μM, [$AgNO_3$] = [total thiol], [$Zn(NO_3)_2$] = [total thiol], [PNPB] = 500 μM, 40 °C. Thiols were combined in equal proportions.

These results are similar to those of our self-assembled system, seen in both our initial screen (Figure 57) and our optimisation of a Zn^{2+} chelator screen (Figure 74). Combinations of note are 1:1 **HM/G-SH**, 1:1 **HM/D2PA-SH** and 1:1:1 **HM/G/D2PA-SH**, which perform well in both the self-assembled and the thiol-polymer system. Interestingly, 1:1 **HM/OH-SH** system is significantly more effective with the silver polymer system. Potentially, the formation of the polymer orients these two functional groups (imidazole ring and alcohol) in a more favourable position to facilitate cooperative catalysis compared to when they are self-assembled together.

The cooperativity of these systems can also be analysed. If cooperative catalysis is occurring, then the catalytic rate of the combined system should be greater than that of the individual components' rates added together. Figure 127 shows the degree of cooperativity for each of our investigated systems. From this, we can see that our four best-performing systems are the only ones that show evidence of cooperativity. What is even more interesting is our 1:1:1 **HM/G/D2PA-SH** combination, which showed the highest rate of catalysis in our initial screen, has the highest degree of cooperativity. This helps emphasise the effect that cooperativity between catalytic functional groups has on the overall rate of reaction.

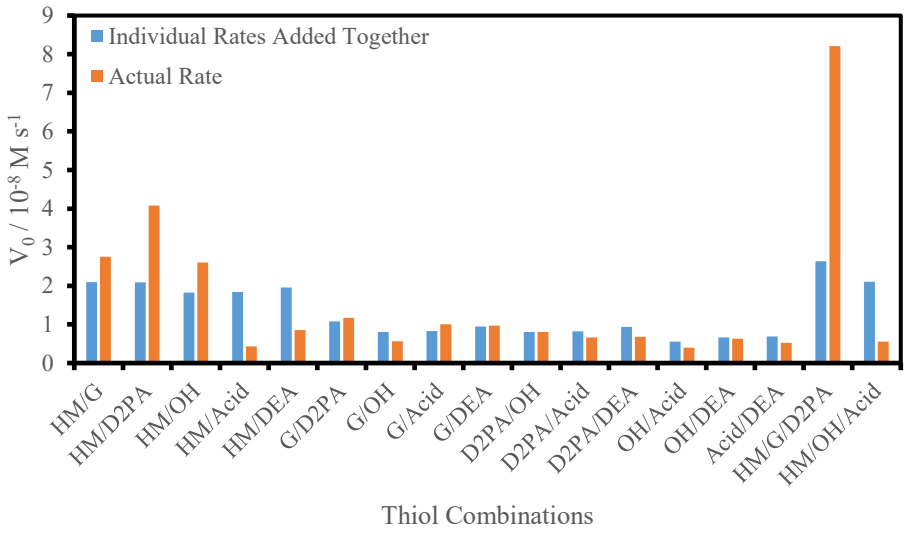

Figure 127: Cooperativity of all our combined catalytic systems. Experimental conditions: aqueous buffer pH = 7.0 ([HEPES] = 5 mM), [individual thiol] = 30 μM, [$AgNO_3$] = [total thiol], [PNPB] = 500 μM, 40 °C. Thiols were combined in equal proportions.

The effect of Zn^{2+} on all these combinations in Figure 126 is very minimal, with only the 1:1 **HM/D2PA-SH** system showing an increase upon the addition of this ion. This was an unexpected result, as previously we had seen the addition of Zn^{2+} increase the rate of catalysis for both our 1:1 **H/G**, 1:4 **H/G** and 1:1:1 **H/G/D2PA** amphiphilic systems. We had also previously determined that the mechanism for these two systems involves a metal chelator for a secondary nucleophilic attack. However, this new silver-thiol polymer system does not appear to need this. Therefore, the next question becomes: what is the mechanism of reaction for these systems? Since our 1:1:1 **HM/G/D2PA-SH** system once

again gives us the highest rate of catalysis, we decided to take this system and try to understand the mechanism of action.

3.6.6 Understanding the HM/G/D2PA-SH system

Screen of different metal ions

The first step in understanding the mechanism for this system was to investigate the chelation effect of the picolylamine thiol. Di(2-picoly)amine is a well-known tridentate ligand capable of binding a variety of different cationic metal centres, including Zn^{2+}.[135] Previously, we had shown that our **D2PA** amphiphile could bind Zn^{2+} ions, resulting in an increased rate of catalysis. Though for our silver-polymer system, the addition of Zn^{2+} had a minimal effect on the rate of reaction. However, Zn^{2+} is not the only metal to which di-(2-picolyl)amine is known to chelate; other metals include Cu^{2+}, Co^{2+}, Ni^{2+}, Mn^{2+}, Fe^{3+}, and Cd^{2+}.[136–140] Of these metals, Cu^{2+}, Co^{2+}, and Ni^{2+} have all been shown to have esterase activity when incorporated into metallomicelles.[141] Therefore, we wondered whether using a different metal would have a positive effect on catalysis.

Figure 128 shows the results of the metal screen. Interestingly, we see a decrease in the catalytic activity when any metal is present compared to the free 1:1:1 **HM/G/D2PA-SH** system. This suggests that the free picolylamine functional group is involved in the catalytic mechanism. When this is then bound to a metal ion, it is no longer available to participate in the catalytic mechanism in the same way; therefore, a decrease in the rate of catalysis is seen. These results also suggest that the reaction mechanism is occurring at a similar rate with and without Zn^{2+}. When Zn^{2+} is present in the system, this is bound by **D2PA-SH**, which allows the Zn^{2+} ion to bind a water molecule, decreasing its pKa to form an OH^- nucleophile. This can then undergo nucleophilic attack of the substrate or intermediate carbonyl group, to then form the product.

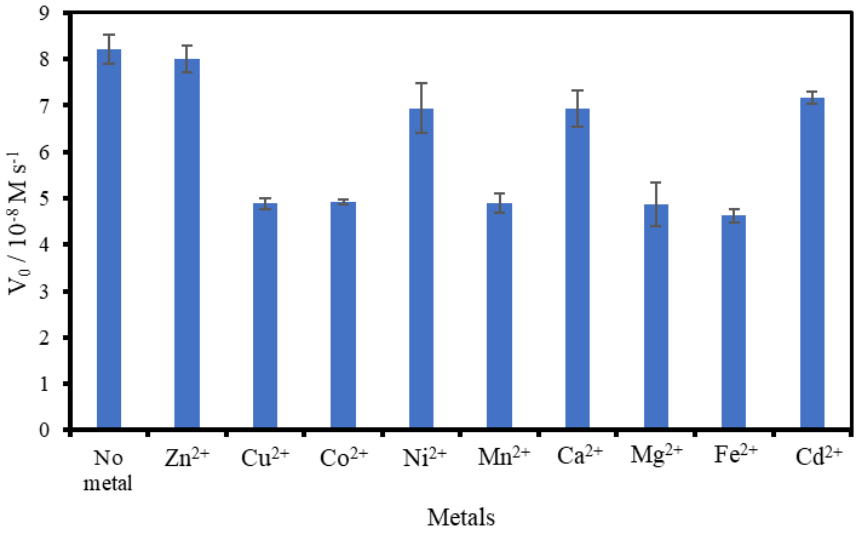

Figure 128: Screen of 1:1:1 ***HM/G/D2PA-SH*** *system with different metals. Experimental conditions: aqueous buffer pH = 7 ([HEPES] = 5 mM), [$AgNO_3$] = 90 µM, [**HM/G/D2PA-SH**] = 90 µM, [metal ion] = 90 µM, [PNPB] = 500 µM, 40 °C.*

The rate of the 1:1:1 **HM/G/D2PA-SH** polymer system could then be compared to the 1:1:1 **H/G/D2PA** vesicle system (Figure 129). Surprisingly, from this comparison, it does not appear that the polymer system offers any advantage compared to the vesicular system. The key reason behind this is that the vesicle system in the presence of Zn^{2+} has a much higher catalytic rate, though in the polymer system, the addition of this metal ion barely has an effect. This indicates that the 1:1:1 **H/G/D2PA** mechanism with Zn^{2+} is far more efficient than the rate of reaction in the absence of Zn^{2+}. However, in the polymer system, the rates of reaction are similar regardless of the presence of Zn^{2+}. A potential factor contributing to this difference in catalytic rate with and without Zn^{2+} in the vesicle system could be the solubility of the aggregates formed. The addition of Zn^{2+} to the vesicle system helps to solubilise the aggregates; without this, these start to precipitate out. Better solubility of the catalyst means it is more likely to come into contact with the soluble substrate, thereby increasing the overall rate. Though this accounts for the difference between the two vesicle systems, it does not account for the vesicle system having a much higher rate than the polymer system. The polymers are soluble regardless of the presence of Zn^{2+} so it is unlikely that solubility is the only factor contributing to these differences.

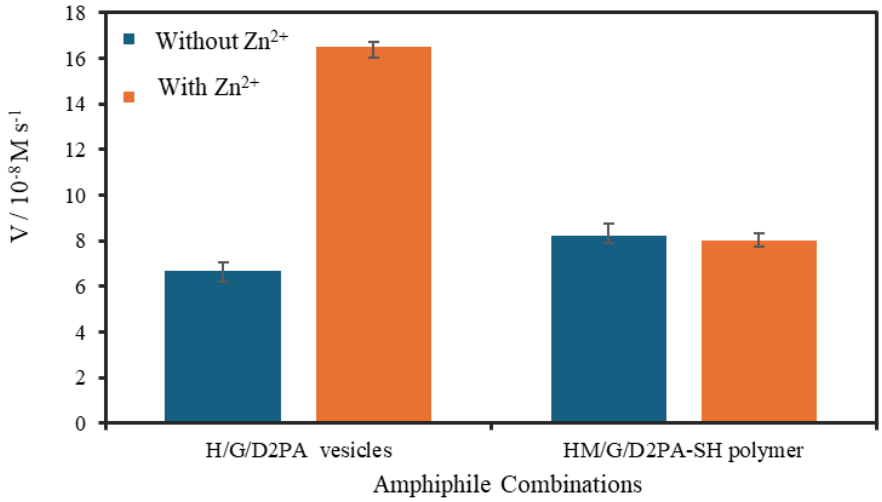

Figure 129: Comparison between the rates of catalysis for the vesicular system (1:1:1 ratio of amphiphiles, 100 μM, [$Zn(NO_3)_2$] = 25 μM) and polymer system (1:1:1 ratio of thiols, 90 μM, [$Zn(NO_3)_2$] = 90 μM). Experimental conditions: aqueous buffer pH = 7.0 ([HEPES] = 5 mM), [PNPB] = 500 μM, 40 °C.

The next question for us to answer was 'what is the picolylamine doing if not acting as a metal ion chelator?' To answer this, we need to re-examine the structure of the di-(2-picolyl)amine functional group, shown in Figure 130. Here, we can see that this contains two pyridine rings in addition to a tertiary amine. All three of these nitrogen atoms could be involved in the reaction mechanism.

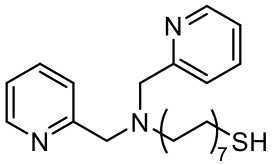

D2PA-SH

*Figure 130: Structure of di-(2-picolyl)amine functional group in **D2PA-SH**.*

Role of the tertiary amine in di-(2-picolyl)amine

To investigate whether the tertiary amine was involved in the reaction mechanism, we could look at substituting our **D2PA-SH** thiol with **DEA-SH**. Now, in our initial screen of functional groups (Figure 126), we did examine **DEA-SH** and saw that this had minimal activity on its own and in combination with our other screened thiols. However, we never directly compared the activity of **DEA-SH** to **D2PA-SH**, and we never looked

at this thiol in combination with **HM/G-SH**. Figure 131 shows the comparison of **DEA-SH** with **D2PA-SH**. We see that while both thiols have comparable activity on their own and in combination with **G-SH**, **D2PA-SH** is far superior when in combination with **HM-SH** (1:1) and **HM/G-SH** (1:1:1). In fact, the addition of **DEA-SH** does not affect the **HM/G-SH** system. This suggests that the tertiary amine is not involved in the catalytic mechanism. Rather, the two pyridine rings present in **D2PA-SH** must be contributing to the high catalytic rate seen in the 1:1:1 **HM/G/D2PA-SH** system. These pyridine rings could potentially be helping through the basicity of the nitrogen in the ring, or the aromaticity between the **D2PA-SH** rings is helping to stack the catalyst and substrate together for catalysis to occur.

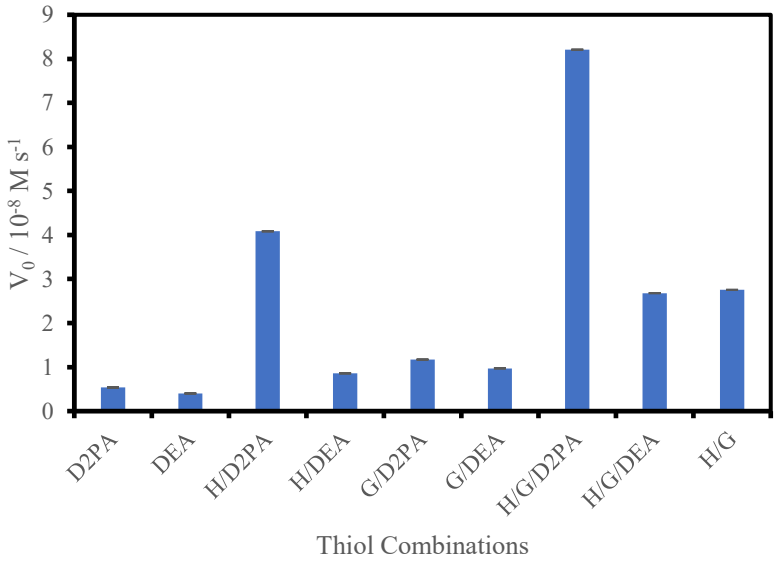

*Figure 131: Comparison between **D2PA-SH** and **DEA-SH**. Experimental conditions: aqueous buffer pH = 7 ([HEPES] = 5 mM), [$AgNO_3$] = [total thiols], [individual thiol] = 30 μM, [PNPB] = 500 μM, 40 °C. Thiols were combined in equal proportions.*

Role of the pyridine ring in di-(2-picolyl)amine

The next point of call was to investigate the reactivity of the pyridine nitrogen in **D2PA-SH**. To do this, we needed to synthesise a new pyridine-based thiol. The original plan was to synthesise compound **110** shown in Scheme 40. This would require a two-step synthesis, using thiol starting materials we already had from synthesising the initial library. However, this synthesis was not straightforward. Here, we wanted to react 4-bromopyridine (**108**) with alcohol **79**. This should react via a nucleophilic aromatic substitution reaction, with the mechanism shown in Scheme 41. The first step involves

the deprotonation of the alkyl alcohol to form the more nucleophilic alkoxide. Once this has formed, it will attack the 4th position carbon on the pyridine ring, resulting in the movement of electrons onto the nitrogen atom. The electrons on the nitrogen can then move back, reforming the aromatic ring, resulting in the bromine leaving to give the final compound.

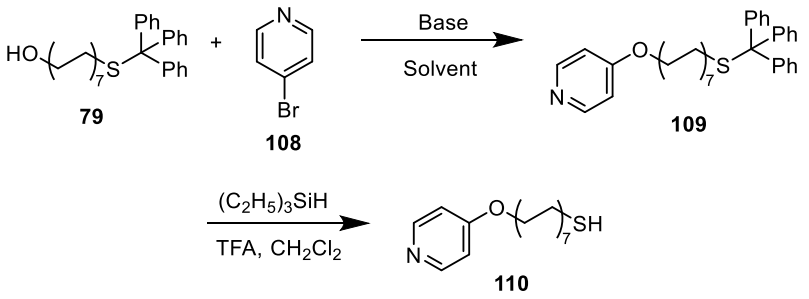

*Scheme 40: Synthesis of pyridine-based thiol **110**.*

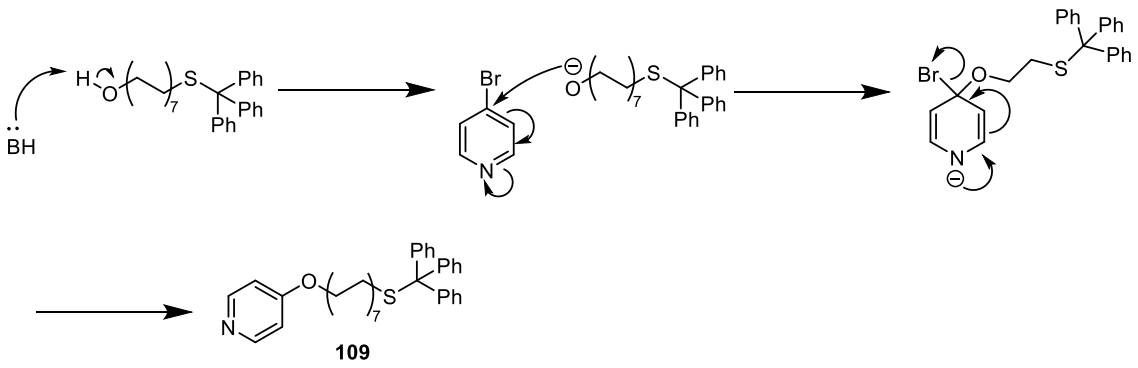

Scheme 41: Nucleophilic aromatic substitution reaction mechanism

For this reaction to be successful, we need to use a base strong enough to deprotonate our alcohol to form our nucleophilic alkoxide species. We tried a variety of different conditions to make this compound, summarised in Table 4. In our initial attempt, we tried using pyridine as our base; however, this is not strong enough to deprotonate our alcohol, so this is likely why the reaction did not work. We then switched out our base to sodium hydride. This is a much stronger base, which should be capable of deprotonating the alcohol; however, we still saw no evidence of a reaction. We then realised that the 4-bromopyridine we were using was the HCl salt. Therefore, we figured that the base may have been used up neutralising this reagent, rather than deprotonating our alcohol. Rethinking our reaction conditions, we instead tried to neutralise the 4-bromopyridine before adding this to the reaction mixture. However, we still found this to be unsuccessful.

We thought harsher experimental conditions (such as pressure or temperature) might help the reaction occur. We then tried the reaction in a pressure vessel at 120 °C for three days. We substituted the base from sodium hydride to potassium *tert*-butoxide, as sodium hydride can potentially produce hydrogen gas, which is unsuitable for a reaction under pressure. Our substituted base, potassium *tert*-butoxide, is also capable of deprotonating the alcohol. We found evidence of the product being formed after three days, using mass spectrometry (Figure 132). However, this was present in such small amounts that it was not visible on NMR. From this, we concluded that this reaction is slow even when using harsh conditions. Therefore, we tried instead to make the pyridine thiol by reacting amine **103** with 4-bromopyridine (**108**).

*Table 4: Conditions for the synthesis of pyridine **109**.*

Equivalents of C14 thiol	**Equivalents of 4-bromopyridine**	**Base Used**	**Solvent**	**Conditions**	**Outcome**
1	1	Pyridine	Pyridine	Pressure vessel, 185 °C, 24 hrs	No reaction
1	1	NaH (1 eq)	MeCN	Rt, 24 hrs	No reaction
1	1 (neutralised first with 1 eq NEt_3)	NaH (1 eq)	MeCN	Rt, 24 hrs	No reaction
1	1	Potassium *tert*-butoxide (6 eq)	MeCN	Pressure vessel, 120 °C, 3 days	Mass spec showed small traces of product

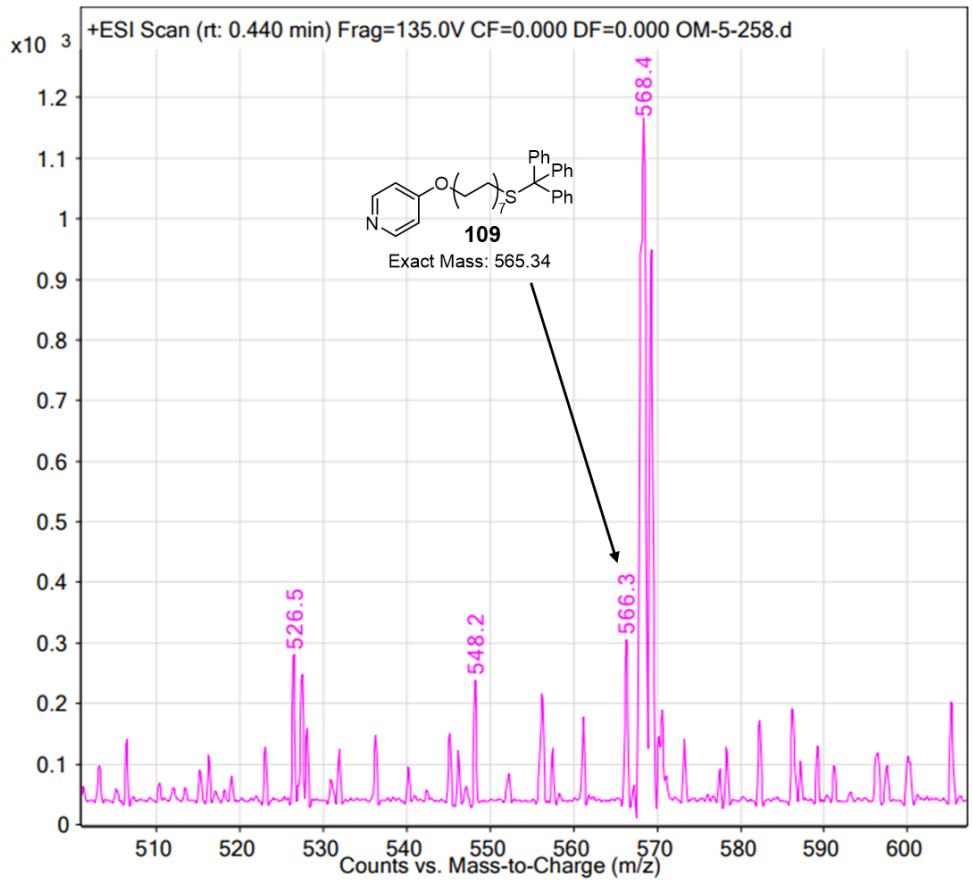

*Figure 132: Mass spectrometry data for pyridine **109** in MeOH.*

Using the thioamine (**103**) starting material instead of the thioalcohol (**79**) should make the reaction easier. The thioamine is a primary amine and therefore can act as a good nucleophile without the need for an initial deprotonation step due to the lone pair on the nitrogen atom. This reaction can then proceed via the same mechanistic pathway as the alcohol previously shown in Scheme 41.

The first step in Scheme 42 was conducted in a pressure vessel and heated at 185 °C for 24 hours. The resulting mixture was then columned, and three fractions were collected. These were then analysed using both NMR and mass spectrometry. The mass spectrometry data showed evidence of the product in all three fractions, seen by the peak at 365.2, which corresponds to the protonated product mass (Figure 133). ^{1}H NMR also suggests that this is the case, though impurities can be seen in each fraction (Figure 134). Therefore, further purification of this compound would be required before this could undergo a deprotection to give **112**.

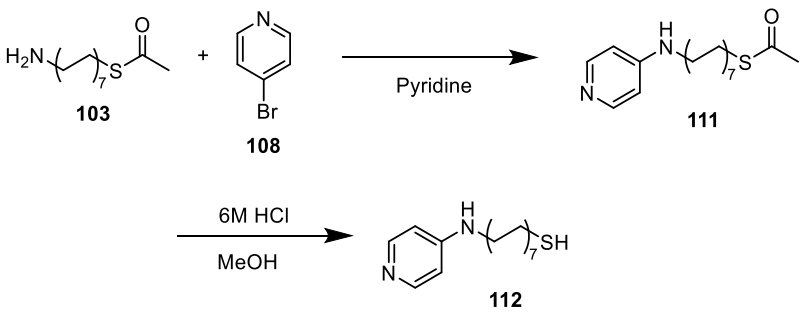

Scheme 42: Synthesis of pyridine-based thiol using thioamine starting material.

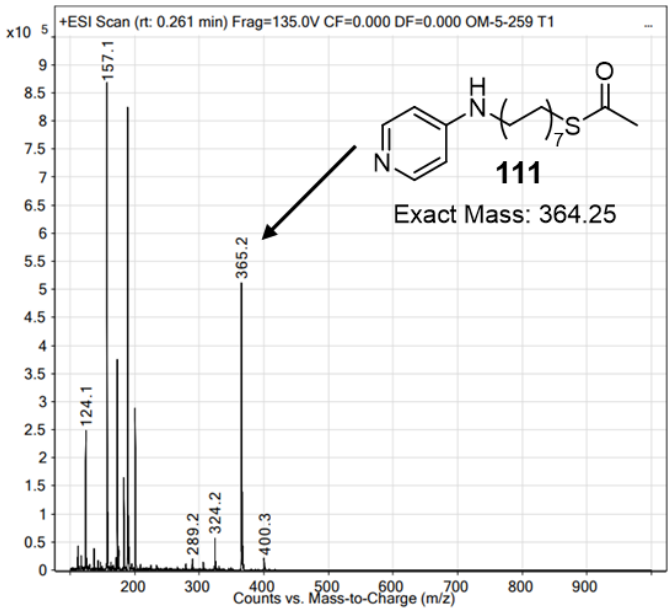

*Figure 133: Mass Spectrometry of pyridine **111** in MeOH.*

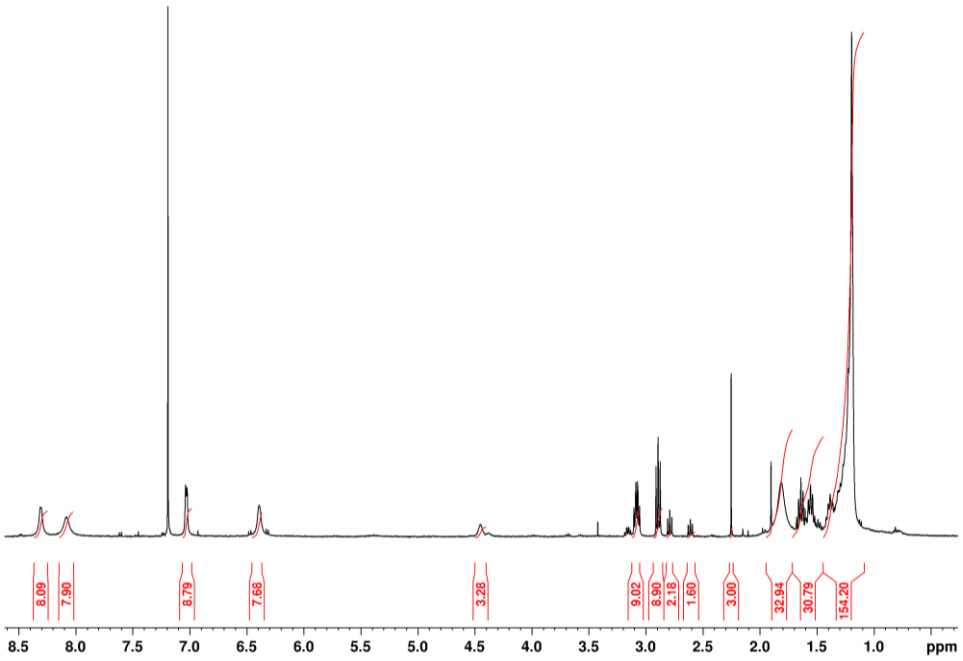

*Figure 134: ^{1}H NMR (400 MHz, $CDCl_3$) of pyridine **111** with impurities.*

Now, around the same time that we were trying to optimise the initial nucleophilic aromatic substitution reaction with the alcohol, we came up with a different pyridine-based molecule to synthesise (**2PA-SH**). This compound, shown in Figure 135, is more like our original di-(2-picolyl)amine thiol (**D2PA-SH**). Now we have just a single 2-picolylamine unit incorporated into the thiol molecule. To synthesise this, we can simply undergo an amide coupling reaction. This is a reaction we have had a lot of success with throughout the synthesis portion of the PhD. Therefore, we figured this synthesis may offer a painless alternative to the nucleophilic aromatic substitution.

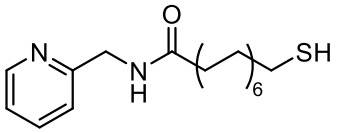

2PA-SH

*Figure 135: Structure of 2-picolylamine base thiol (**2PA-SH**).*

We hypothesised that the incorporation of the amide group instead of an amine between the pyridine and the thiol would not have a huge effect on the reactivity of the pyridine ring. Both functional groups act as electron-donating groups, in addition to the CH_2 directly bound to the pyridine ring so therefore, they should be experiencing similar

electronic effects. They do, however, differ in their ability to form hydrogen bonds. Tertiary amines, like that seen in **D2PA-SH**, can only act as hydrogen bond acceptors, as there are no hydrogen atoms bound to the nitrogen to allow this to act as a donor. Amides, on the other hand, can act as both hydrogen bond donors and acceptors, with the hydrogen bound to the nitrogen acting as the donor and the oxygen in the carbonyl acting as the acceptor.[142,143] This ability may differ in the way the catalytic thiols interact with the substrate. However, if this is an area of concern, a simple solution could be to synthesise the amide version of **D2PA-SH** and compare it with the amine version to see whether this difference in potential hydrogen-bond formation affects the results.

Scheme 43 shows the synthesis of **2PA-SH** using 2-picolylamine (**113**) and our previously synthesised carboxylic acid **88** as our starting materials. Our amide coupling conditions gave us a yield of 51% with the desired compound **114** being confirmed from the presence of both pyridine peaks and trityl peaks in the ^{1}H NMR. The pyridine ring should give four distinct proton peaks; however, these overlapped slightly with the trityl aromatic peaks, though the integration in this region matched the compound. There was also a characteristic doublet peak seen at 4.45 ppm due to the CH_2 substituent on the pyridine ring. This peak is seen as a doublet rather than a singlet, as it is coupling to the NH proton in the amide functional group (seen in the NMR as a singlet at 5.86 ppm). This compound could then be deprotected using our trityl deprotection conditions, to give the final compound **2PA-SH** in a 27 % yield.

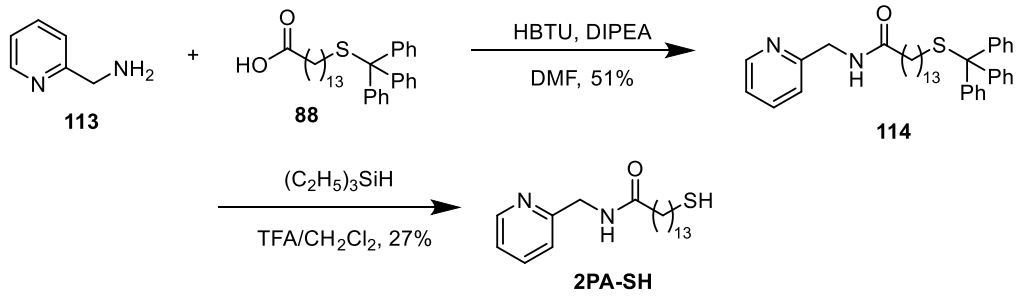

*Scheme 43: Synthesis of **2PA-SH**.*

NMR spectroscopy was used to confirm the final product **2PA-SH**. The ^{1}H NMR could be assigned using the previously assigned NMR for **HM-SH** and **D2PA-SH**, as these had similar structural features to **2PA-SH** (Figure 136). The COSY NMR also aided in the assignment for this structure (Figure 137). The peak at 4.56 ppm (yellow) can be assigned to the -CH_2 peak coming off the pyridine ring, similar to what we see with the **D2PA-SH**

assignment. Interestingly, this peak is now seen as a doublet rather than a singlet due to it coupling to the neighbouring NH proton. COSY correlation then allows the assignment of 6.37 ppm (light pink). The aromatic region can be assigned similarly to **D2PA-SH,** as we expect to see the same peaks with the same splitting, now integrating for 1 H as we only have one pyridine ring. COSY correlation confirms this assignment, though it is important to note that the proton next to the substituent (light blue) is hidden under the $CDCl_3$ solvent peak. The alkyl chain can then be assigned based on the **HM-SH** assignment, as both compounds consist of an alkyl chain with an amide at one end and a thiol at the other. The alkyl peaks in this compound, without a colour assigned to them, belong to the multiplet peak at 1.40 – 1.20 ppm. This is a common trend seen in all our C14 thiols.

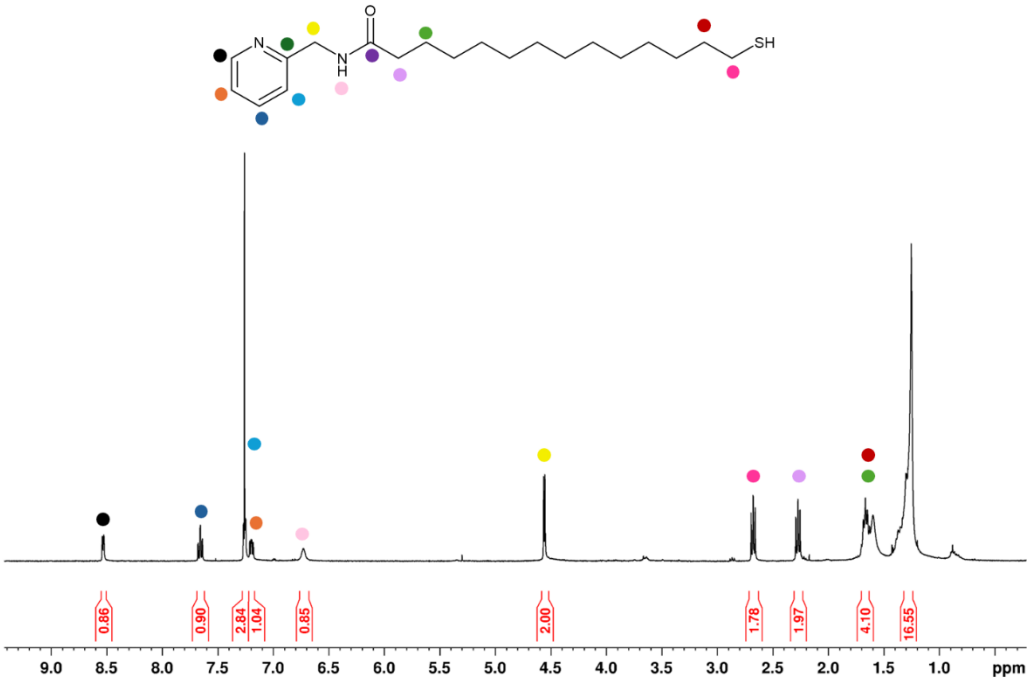

*Figure 136: ^1H NMR (400 MHz, $CDCl_3$) assignment for **2PA-SH**.*

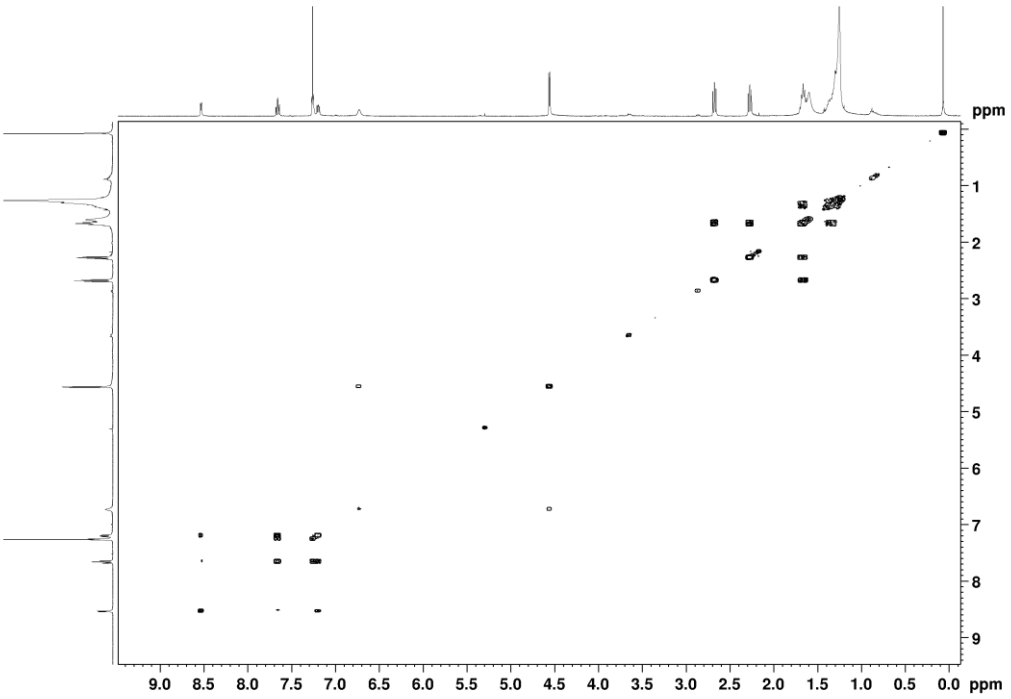

*Figure 137: COSY NMR for **2PA-SH**.*

The ^{13}C NMR for **2PA-SH** (Figure 138) could also be assigned using the aid of **HM-SH** and **D2PA-SH** previously assigned spectra. The HSQC and HMBC spectra could be used to confirm these assignments, with these spectra found in the appendix. A particular assignment to note is that of the -CH_2 group two bonds away from the thiol (red). This assignment simply corresponds to the carbon peak at 29.4 ppm. The remaining carbon peaks in this region are unassigned and belong to the unassigned alkyl chain.

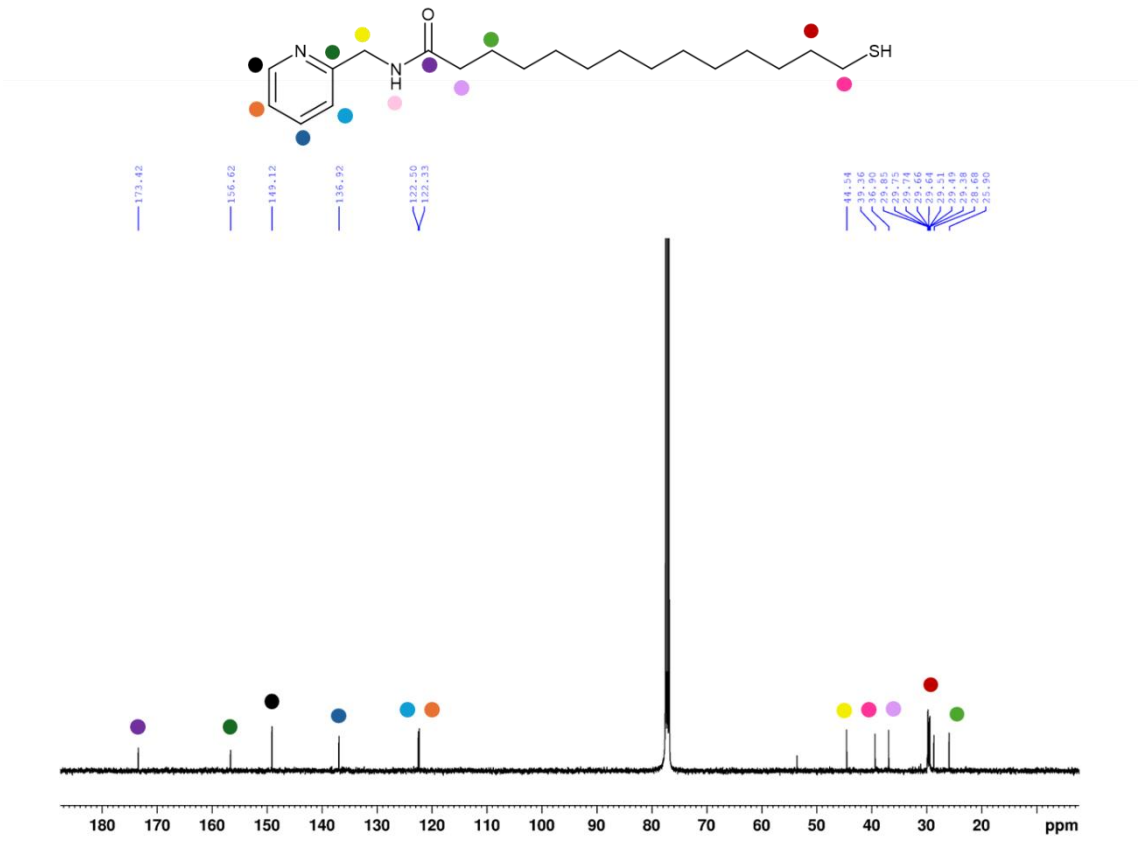

*Figure 138: ^{13}C NMR (101 MHz, $CDCl_3$) assignment for **2PA-SH**.*

Since the synthesis of **2PA-SH** was so successful and straightforward, we decided not to continue with pyridine **111,** as this still needed further optimisation in the purification step. This compound was also less similar to the original **D2PA-SH** structure, whose activity we wanted to examine, hence why we made the shift to **2PA-SH**.

The ease of synthesis of the **2PA-SH** made us decide to also synthesise the 3-picolylamine thiol (**3PA-SH**). The thought here was that in addition to investigating the activity of our pyridine ring, we could also examine the position of substituents on this ring and the relationship between the two nitrogen atoms in the compound. The synthesis of **3PA-SH** is shown in Scheme 44. Here, we follow the same two steps as for the 2-picolyl compound, simply substituting the starting material with 3-picolylamine (**115**). The yields for both reactions were rather high, with 73% for the amide coupling and 89% for the deprotection. This then gave us two different picolylamine-based compounds, which we could investigate.

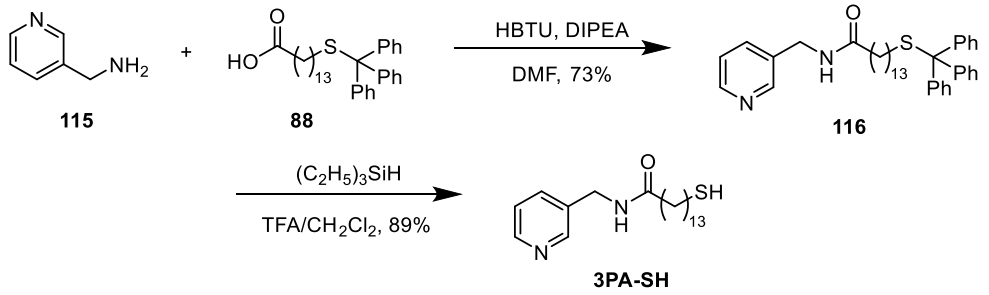

*Scheme 44: Synthesis of **3PA-SH**.*

The NMR of the final compound **3PA-SH** could be assigned to confirm the presence of this product. The ^{1}H NMR was assigned using the **HM-SH** and **2PA-SH** compounds as guides to assigning the alkyl chain (Figure 139). The 3-picolylamine part of the compound was more difficult to assign. This will obviously have a different assignment to **2PA-SH** and **D2PA-SH** as the substituent position on the pyridine ring has moved from the 2 to the 3 position, resulting in different splitting. For **3PA-SH,** we would expect to see four aromatic peaks, a singlet, two doublets and a triplet peak all integrating for 1 H. However, this is not what we see in the NMR. Instead, we see one doublet and two multiplets, one of which integrates for 2 H. We thought the COSY NMR (Figure 140) might be able to shed some light on this, but this was inconclusive as all three aromatic peaks correlate to one another. Therefore, we decided to look at the other 2D spectra, our HSQC (Figure 141) and HMBC (Figure 142). The HMBC seemed like the best place to start, as we should be able to use this to identify our two CH aromatic peaks next to the substituent based on their correlation to the doublet at 4.46 ppm (yellow). From here, we can then work backwards using the HSQC to determine the proton peaks belonging to these carbon peaks. The HSQC shows the 4.46 ppm (yellow) correlating to 149.1 ppm and 134.3 ppm. The HSQC can confirm the assignment of these two peaks based on the splitting observed with the 149.1 ppm peak correlating with the 8.54 – 8.50 ppm multiplet (light blue), and the 134.3 ppm peak correlating with the doublet at 7.63 ppm (dark blue). The remaining aromatic peaks can be assigned based on the structure of the molecule itself. The multiplet at 8.54 – 8.50 ppm integrates for 2 H but has only been assigned 1 H so far (light blue). The second proton assigned to this peak must have a similar chemical environment to result in nearly identical chemical shifts in both spectra. The aromatic protons on both sides of the N in the ring would have the most similar chemical environment, therefore assigning the 8.54 – 8.50 ppm multiplet to two protons (light blue and orange). The multiplet at 7.30 – 7.23 ppm can be assigned to the remaining aromatic

proton (black). The remaining ^{1}H NMR peaks could be assigned using the COSY NMR and the 2PA-SH and D2PA-SH alkyl chain assignment. From this assignment, the ^{13}C NMR (Figure 143) was relatively easy to continue assigning, however the CH_2 groups two bonds away from the thiol (red) and three bonds away from the amide (light green) were unable to be assigned as neither the HSQC nor the HMBC helped to identify which carbon peak belonged to which of these two groups, so they have both been assigned to each possible carbon peak.

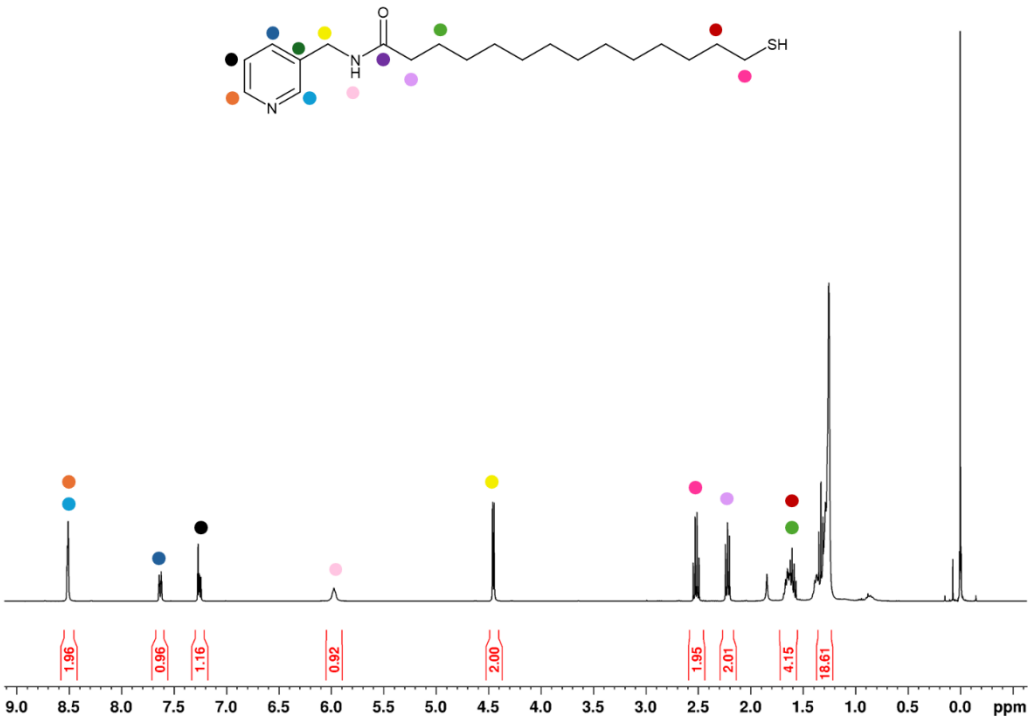

*Figure 139: ^{1}H NMR (400 MHz, $CDCl_3$) assignment of **3PA-SH**.*

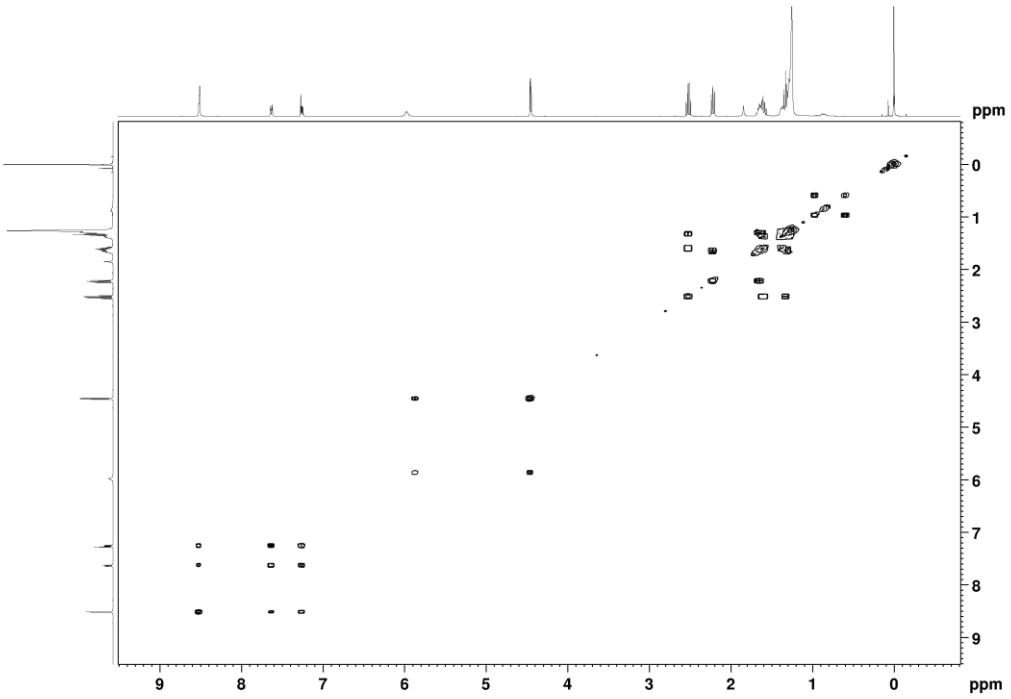

*Figure 140: COSY NMR spectrum for **3PA-SH**.*

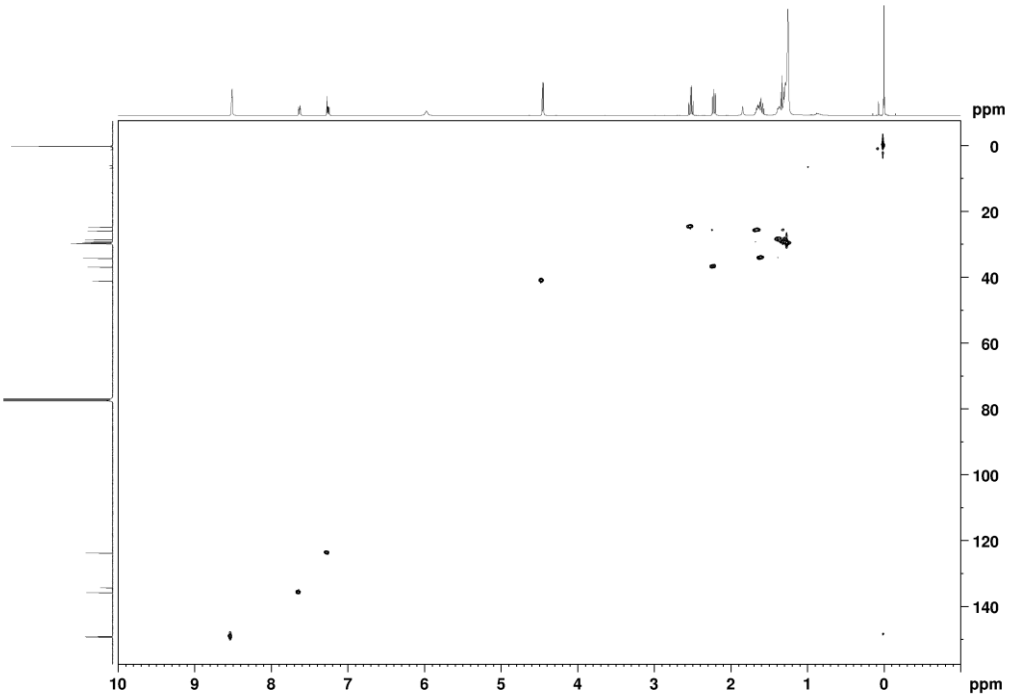

*Figure 141: HSQC NMR spectrum of **3PA-SH**.*

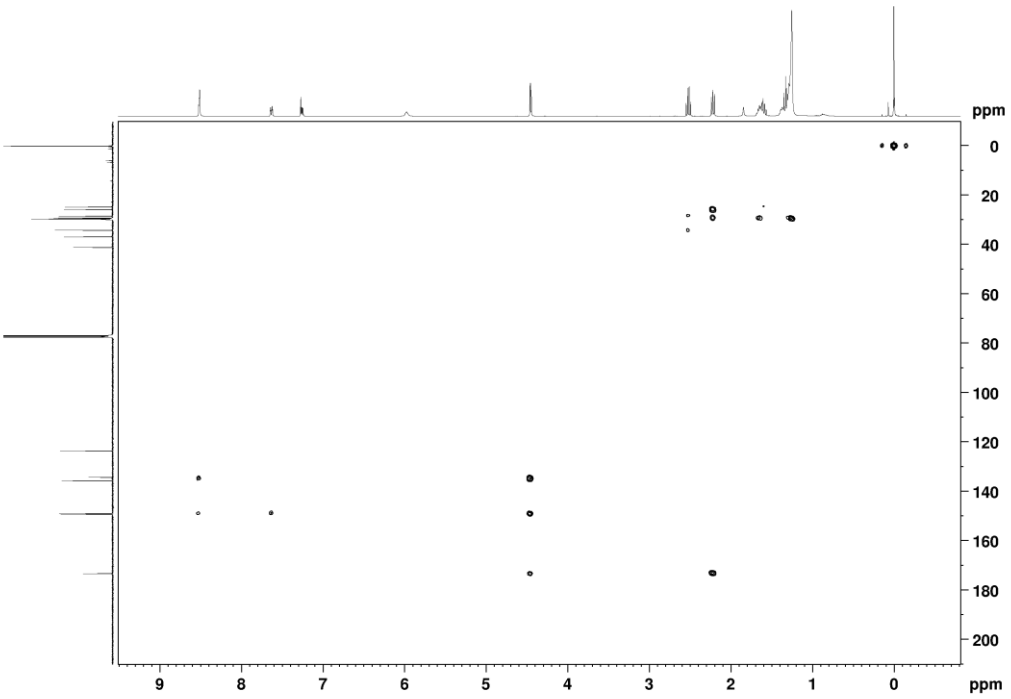

*Figure 142: HMBC NMR spectrum of **3PA-SH**.*

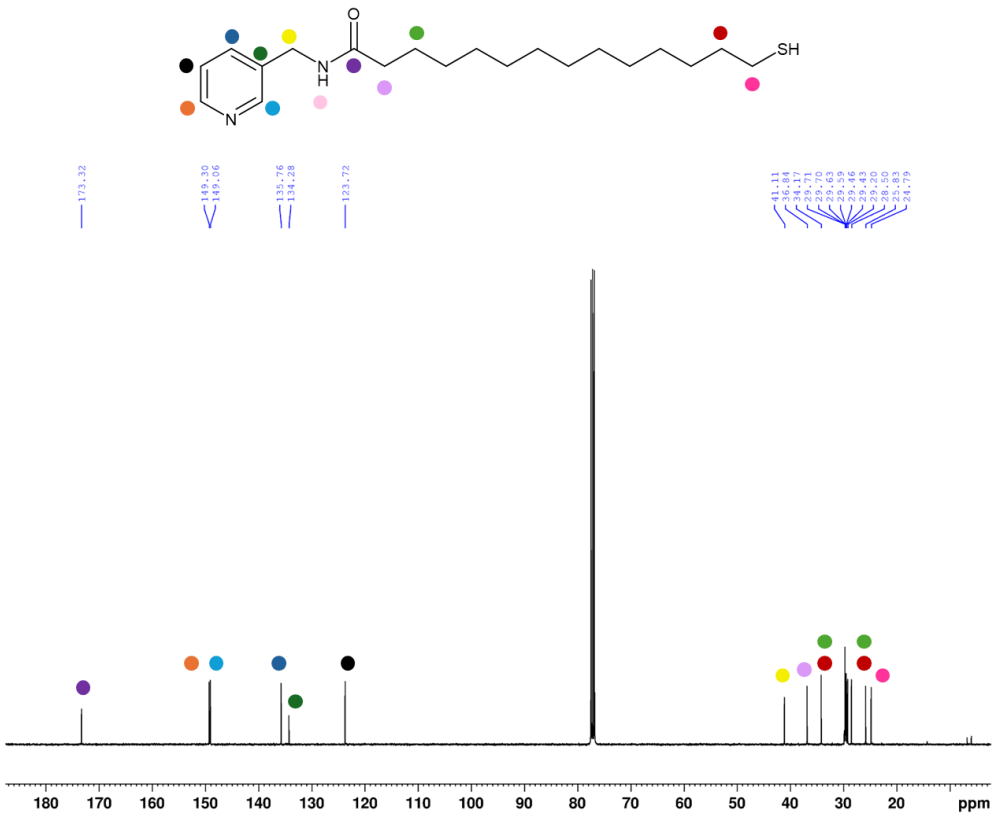

*Figure 143: ^{13}C NMR (101 MHz, $CDCl_3$) assignment for **3PA-SH**.*

Screen with different picolylamine-containing thiols for cooperativity with HM/G-SH

Now that the picolylamine-based thiols have been synthesised, we can assess their catalytic activity. Figure 144 shows the comparison of our three picolylamine-based thiols (di, 2- and 3-picolylamine) with our library of thiols to determine which has the highest rate of catalysis. Our 1:1:1 **HM/G/DPA-SH** system remains superior; however, the 1:1:1 **HM/G/2PA-SH** system also exhibits high catalytic activity, much higher than that of 1:1:1 **HM/G/3PA-SH**. This suggests that the amine substituent is most favourable in the 2-position on the pyridine ring.

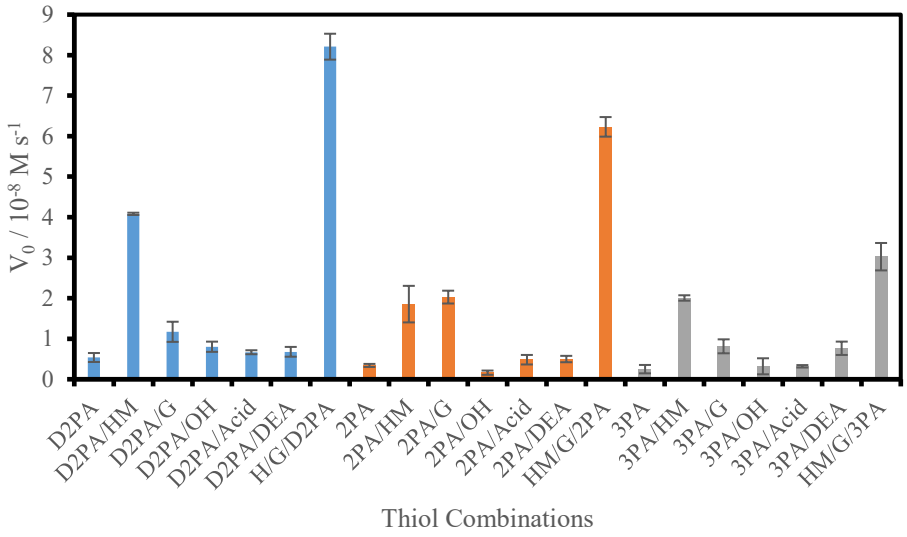

Figure 144: Screen of different picolylamine-based thiols. Experimental Conditions: aqueous buffer pH = 7.0 ([HEPES] = 5 mM), [$AgNO_3$] = [total thiol], [individual thiol] = 30 µM, [PNPB] = 500 µM, 40 °C. Thiols were combined in equal proportions.

These results also indicate that two picolylamine units in the catalytic system are more favourable than one. Therefore, we can look at screening different concentrations of **2PA-SH** in our 1:1:1 **HM/G/2PA-SH** system to see if it is possible to achieve a similar rate to the 1:1:1 **HM/G/D2PA-SH** system if we have double the concentration of **2PA-SH**. However, when we went to investigate different amounts of **2PA-SH** in our system, we found that there was no real difference between the ratios tried (Figure 145). Also, we noticed that the overall activity of our 1:1:1 **HM/G/2PA-SH** system had decreased by half compared to our initial results. This decrease in activity led us to investigate the stability of our **2PA-SH** compound. NMR analysis showed that the compound had indeed degraded, with the aromatic peaks all having shifted, along with the CH_2 peak directly attached to the pyridine ring (Figure 146). The mass spectrometry data was inconclusive as we could not find plausible decomposition products. This compound had only been in solution for a week between the original catalysis results and the newer results with decreased activity. A second attempt was made to synthesise this compound, which yielded similar results in terms of the compound's stability. The short shelf life of this compound, therefore, made it undesirable for our catalytic system.

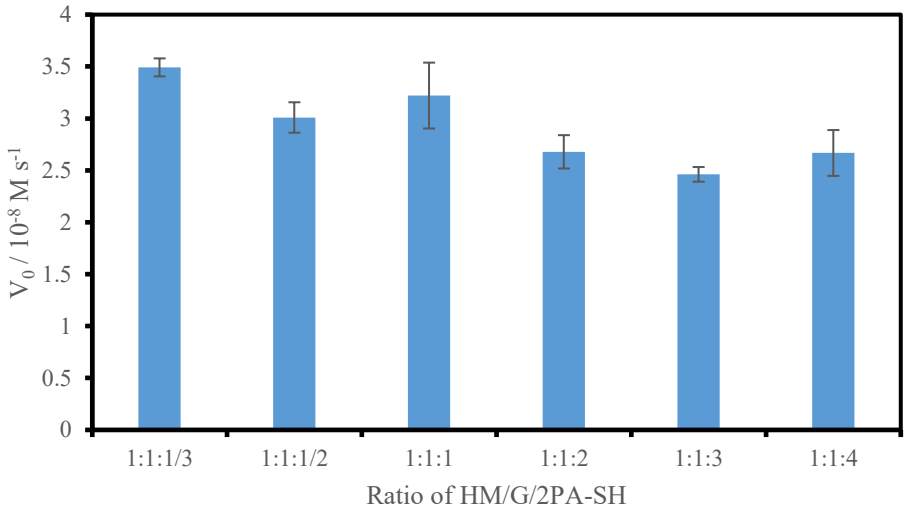

*Figure 145: Varying ratio of **HM/G/2PA-SH**. Experimental conditions: aqueous buffer pH = 7 ([HEPES] = 5 mM), [$AgNO_3$] = [total thiols], [**H-SH**] = 30 µM, [PNPB] = 500 µM, 40°C.*

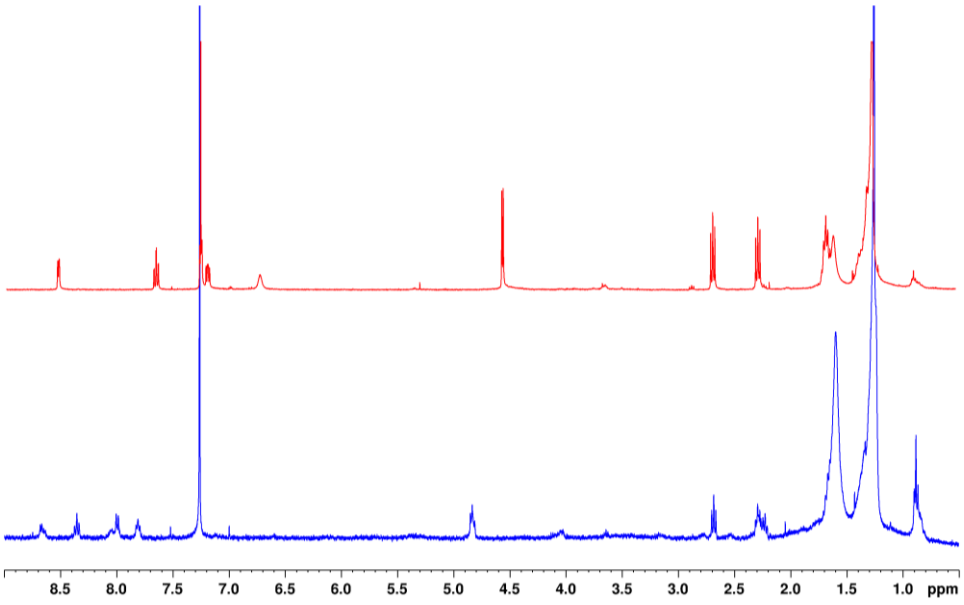

*Figure 146: ^{1}H NMR (400 MHz, $CDCl_3$) analysis of **2PA-SH** with the initial NMR (red) and the degraded NMR (blue).*

We were still interested in trying to understand the role of the pyridine ring in our catalytic systems. The nitrogen in the pyridine ring has been found to facilitate catalysis in either a nucleophilic or basic manner.[144] Going forward, we wanted to find a way to investigate this that was not synthetically taxing.

Screen with free pyridine bases to better understand the mechanism

The best idea we had to assess the basic or nucleophilic activity of the pyridine ring was to try our 1:1 **HM/G-SH** polymer system in the presence of different pyridine bases, shown in Figure 147, essentially, substituting the **D2PA-SH** thiol component with a free base. The use of the free bases allowed us to screen the systems more rapidly, as it did not require any synthetic element. However, because these bases would be floating free in solution, rather than incorporated into the polymer system, we would likely need to use higher equivalents compared with our thiol ligands. Higher concentrations mean a greater chance for these bases to come into close contact with the **HM/G-SH** head groups for cooperative catalysis to occur.

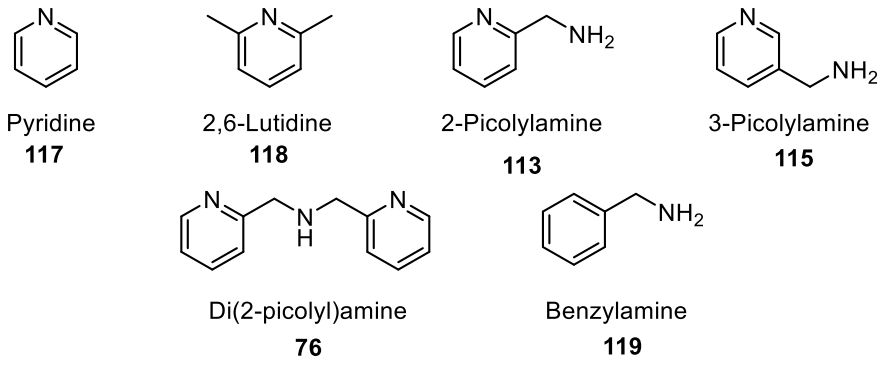

Figure 147: Structures of free bases investigated.

Figure 148 shows the results of this free base screen. In low equivalents (1-5), we can see that the free bases tend to have a slight positive effect on the catalytic rate. Once we start to increase the equivalents, we see two of the free bases stand out: 2-picolylamine (**113**) and 3-picolylamine (**115**). The addition of these to the 1:1 **HM/G-SH** polymer system results in a rate of catalysis up to eight times greater than that of 1:1 **HM/G-SH** on their own. This data fits with what we have seen previously in Figure 144, where the incorporation of **2PA-SH** into **HM/G-SH** has a greater activity than **3PA-SH**. These two free bases have a primary amine present, which could itself be contributing to the catalysis. We saw in the previous chapter with our amphiphilic system that **HA** would facilitate catalysis in a nucleophilic manner to produce the HA-butyrate adduct. Once all the **HA** in solution had reacted with **PNPB**, it was no longer able to act as a catalyst, as all the amine sites were now bound to butyrate. To confirm whether this was giving rise to our high catalytic rates, we investigated the UV traces, compared the activity to

benzylamine (**119**), and underwent some mass spectrometry studies to confirm the presence of any intermediate species.

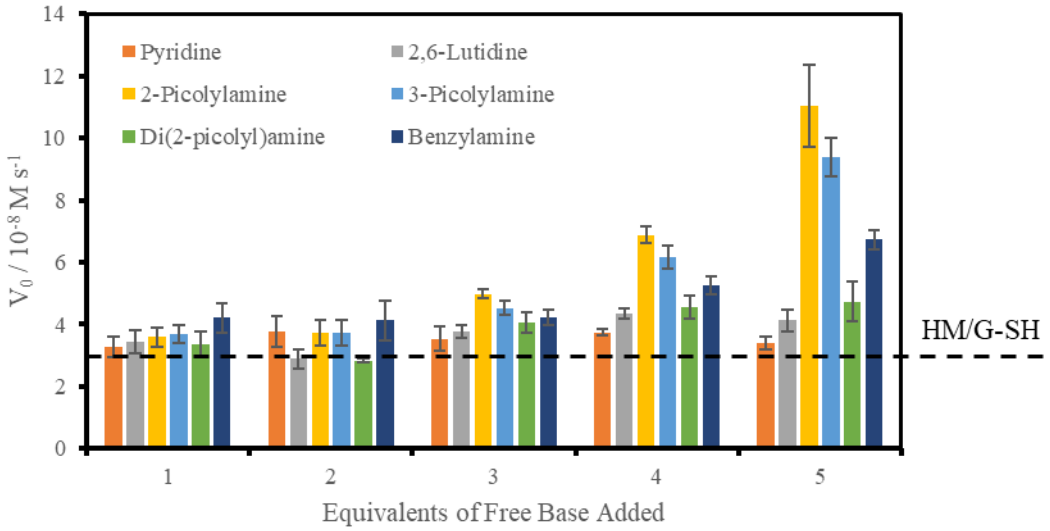

Figure 148: Screen of 1:1 ***HM/G-SH*** *polymer system in combination with free bases. Experimental conditions: aqueous buffer pH = 7 ([HEPES] = 5 mM), [$AgNO_3$] = 60 μM,* ***[HM/G-SH]*** *= 60 μM, [PNPB] = 500 μM, 40 °C.*

Starting with the UV traces shown in Figure 149, we can see that these match that of a catalytic system, as the absorbance is increasing at a similar rate throughout the entire experiment. If instead the two bases (**113** and **115**) were only acting via the primary amine, we would expect the rate of reaction to be initially high, but for this to tail off as the experiment progressed, due to the amine being used up, similar to what we saw for our **HA** amphiphile.

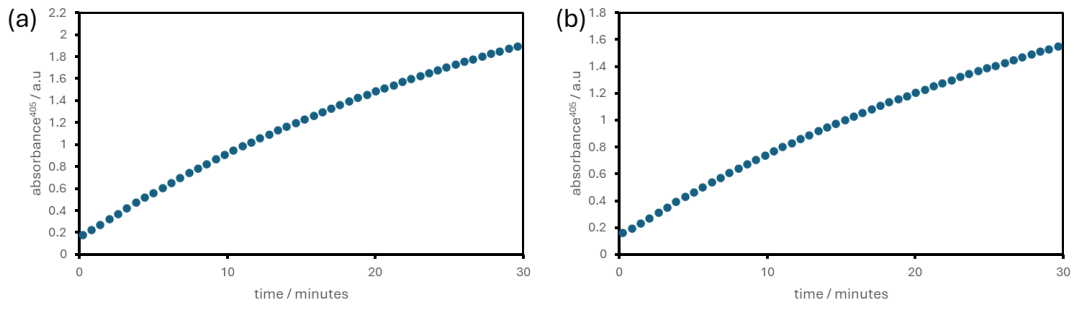

Figure 149: UV trace of 1:1 ***HM/G-SH*** *with 20 eq. of 2-picolylamine (a) and 3-picolylamine (b). Experimental conditions: aqueous buffer pH = 7 ([HEPES] = 5 mM), [$AgNO_3$] =* ***[HM/G-SH]*** *= 60 μM, [picolylamine] = 600 μM, [PNPB] = 500 μM, 40 °C.*

Looking back at Figure 148, we can see that the rates for 2-picolylamine (**113**) and 3-picolylamine (**115**) are much greater than that of benzylamine (**119**). Benzylamine is essentially the same structure as our picolylamines, just without the nitrogen in the ring. Therefore, this should be able to undergo nucleophilic catalysis with the primary amine in a similar manner to 2- and 3-picolylamine (**113** and **115**) . Since both our picolylamine free bases result in a much higher catalytic rate than benzylamine, the nitrogen in the pyridine ring must be having an effect. Mass spectrometry can be used to determine the presence of intermediate species formed from the nucleophilic attack of the free amine. Figure 150 shows that 2-picolylamine, 3-picolylamine and benzylamine all form the butyrate adduct (**120**, **121** and **122,** respectively). However, since the rate of catalysis for our 1:1 **HM/G-SH** system in combination with both picolylamine bases (**113** and **115**) is greater than that of benzylamine, the pyridine nitrogen must be contributing to catalysis. We can assume this effect is cooperative, as the rate of the picolylamine combination is greater than that of pyridine and lutidine. Therefore, a combination of the pyridine ring and its substituent amine must be favourable for cooperative catalysis.

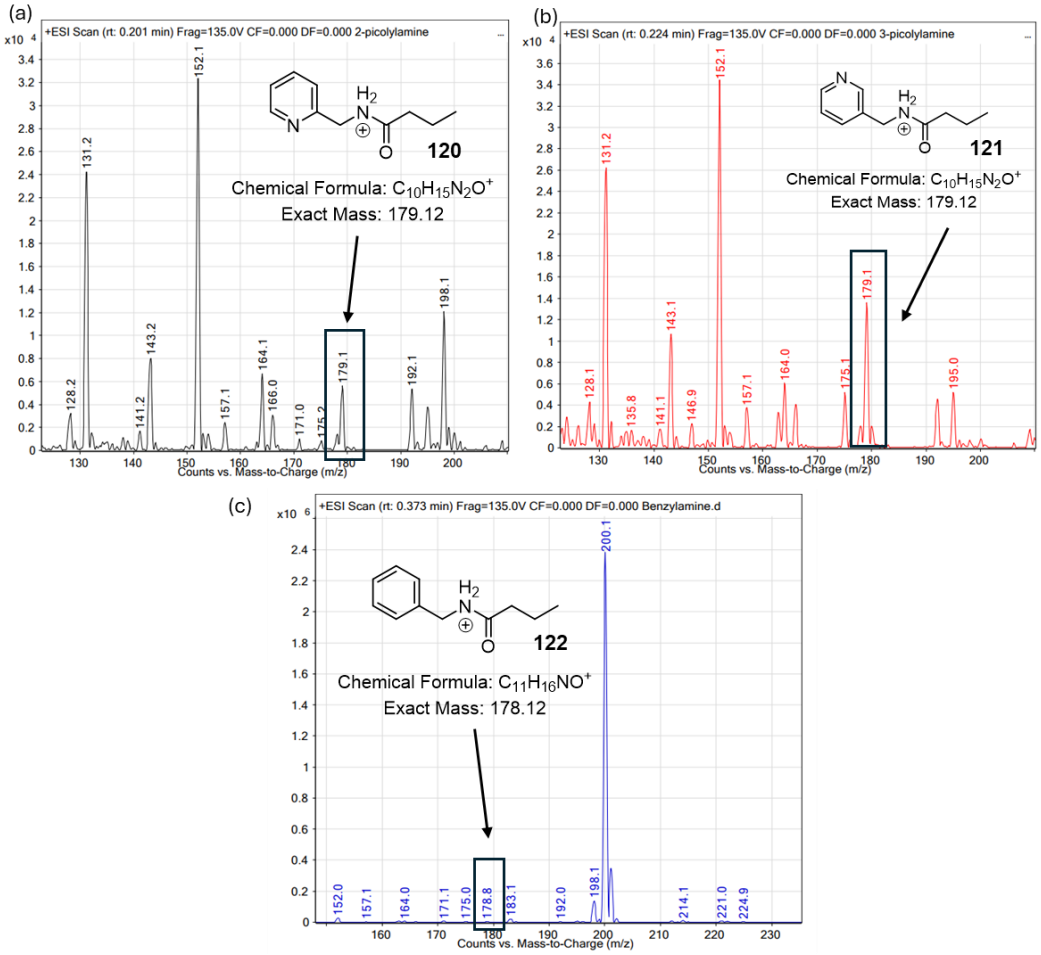

Figure 150: Mass spectrometry to determine the presence of butyrate adducts in the presence of 2-picolylamine (a), 3-picolylamine (b) and benzylamine (c). Experimental conditions: aqueous buffer pH = 7 ([HEPES] = 5 mM), [$AgNO_3$] = 60 μM, [1:1 ***HM/G-SH****] = 60 μM, [free base] = 1.2 mM, [PNPB] = 500 μM, 40 °C.*

Screen of 2-picolylamine alkyl chains compounds for cooperativity with HM/G-SH

We had seen that both **2PA-SH** and the free base can cooperate with 1:1 **HM/G-SH** polymers. However, the instability of the thiol compound and the presence of a primary amine in the free base prevent either from forming an optimised catalytic system. But what if we could meet somewhere in the middle of these two compounds? Our next idea was to synthesise a series of 2-picolylamine compounds with different chain lengths attached, without the presence of a thiol. The thought here was similar to that of the free bases; the 2-picolylamine compounds synthesised should be able to slot themselves into the polymer due to the hydrophobic interactions between the 2-picolylamine carbon chain and the C14 chain of our catalytic thiols. We synthesised 2-picolylamine compounds containing 4, 6, 8 and 12 carbons, each requiring only one synthetic step. The synthesis

scheme and yields for these compounds are shown in Scheme 45. This synthesis was rather straightforward, as we used the same amide coupling procedure as previously discussed. Interestingly, the stability of all these compounds was much greater than that of our **2PA-SH**, likely indicating that the thiol played a role in that compound's degradation.

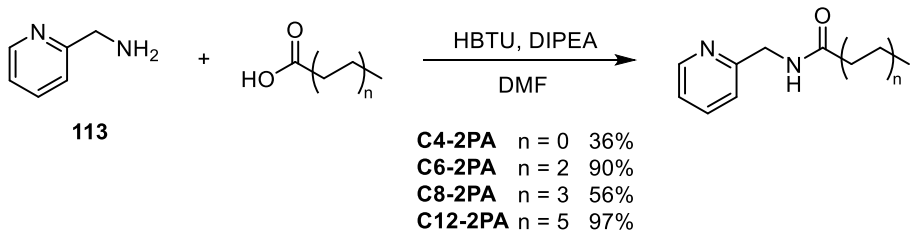

Scheme 45: Synthesis of a series of 2-picolylamine carbon chain containing compounds.

Since these 2-picolylamine compounds will not be bound to the polymer, we need to examine the cooperativity in the presence of excess 2-picolylamine. The results of this screen are shown in Figure 151. Unfortunately, these results were not what we were expecting. The rate of catalysis seems unaffected by the addition of our 2-picolylamine compound, no matter the chain length. No cooperativity is observed between 1:1 **HM/G-SH** and the 2-picolylamine carbon chain compounds. The reason for this may be that they are unable to slot themselves into the polymer and therefore can not get close enough to facilitate cooperative catalysis. The free base catalysts that we examined earlier are a lot smaller, as they do not contain this carbon chain, so it is much easier for them to get close to the **HM/G-SH** catalytic head groups.

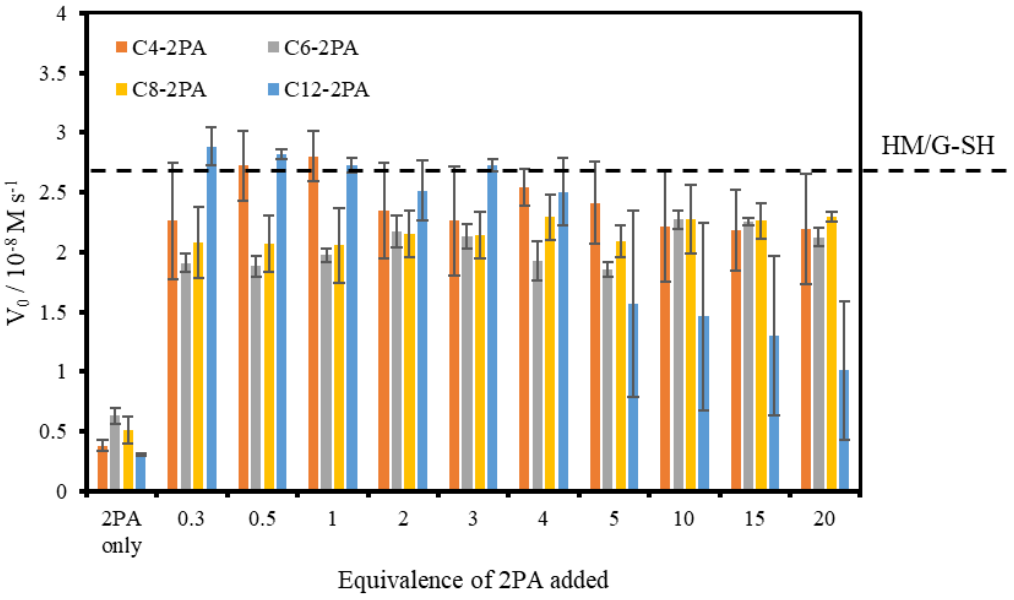

Figure 151: Screen of 1:1 ***HM/G-SH*** *in combination with different length 2-picolylamine chains. Experimental conditions: aqueous buffer pH = 7.0 ([HEPES) = 5 mM, [$AgNO_3$] = 60 µM, [**HM/G-SH**] = 60 µM, [PNPB] = 500 µM, 40 °C.*

An important feature of this catalytic system is the order of addition. Essentially, the different ways you add in the individual catalytic reagents can result in varied rates of catalysis for the same system. We had previously established that for a two or more component system, the best order of addition was to add the silver to the solution first, followed by the thiol catalysts, which had already been premixed (see Chapter 5, Section 5.6 for the general procedure). When adding premixed thiols to silver in solution, this will form polymers that have a random order of the different thiol catalysts along the polymer chain. Therefore, for this new system using our 2-picolylamine carbon chain compounds, we followed the same procedure to first make our polymer system and then add our extra component. Now this process worked well for the free bases but not for the 2-picolylamine carbon chain compounds, likely because these are too big now to insert themselves into the already formed polymer. Therefore, we wanted to investigate different orders of addition, where maybe the polymer is not formed first, to see if we could potentially see some evidence of cooperativity.

For these experiments, **C6-2PA** was chosen to use in 20 eq. This would be the most likely combination to see any cooperativity, as the C6 length seemed short enough to fit within the polymer, but still long enough to have hydrophobic interactions occurring between

the C6 chain and the C14 hydrophobic chains of our catalyst. Figure 152 shows that out of all the orders of addition screened (in orange), none of them offer any cooperativity when compared to the relevant control (in green). This was a disappointing result as it shows that our 2-picolylamine compounds with hydrophobic tails were unable to cooperate with the 1:1 **HM/G-SH** system.

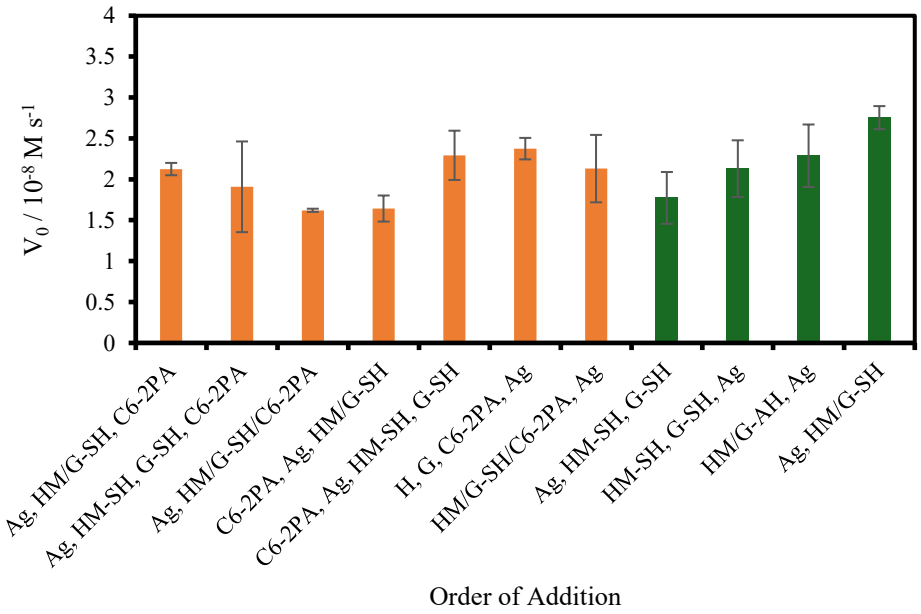

Figure 152: Varying the order of addition for cooperativity. Experimental conditions: aqueous buffer pH = 7.0 ([HEPES) = 5 mM, [$AgNO_3$] = 60 μM, [1:1 ***HM/G-SH****] = 60 μM, [****C6-2PA****] = 1.2 mM, [PNPB] = 500 μM, 40 °C.*

Moving forward, we decided to proceed with our 1:1:1 **HM/G/D2PA-SH** system as we were unable to optimise a system containing a single 2-picolylamine unit. However, these experiments have given us a great insight into the potential mechanism occurring in this system, in the absence of Zn^{2+}.

3.6.7 Proposed mechanism for our HM/G/D2PA-SH system

Though we were unable to further optimise our 1:1:1 **HM/G/D2PA-SH** catalytic system, the experiments in the previous section greatly helped us to understand the catalytic mechanism. In our original vesicle system, we had our **H** amphiphile acting as our nucleophilic catalyst, **G** acting as our oxyanion hole and **D2PA** acting as our metal ion chelator, stabilising a hydroxyl group for secondary nucleophilic attack (Figure 77). For our silver-thiol coordination polymer system, our **D2PA** functionality no longer acts as a

metal ion chelator. Instead, this facilitates catalysis via the nitrogen in the pyridine ring. This nitrogen can act in either a nucleophilic or basic manner.[144] We have proposed a mechanism for both.

Figure 153 has our **D2PA-SH** acting as a general base catalyst. The nitrogen in the pyridine ring can deprotonate a water molecule, forming OH^-, which can act as a nucleophile, attacking the histamine-butyrate adduct to give the final products and reform the catalyst. Figure 154 instead has **D2PA-SH** acting as a nucleophilic catalyst. Here, the nitrogen in the pyridine ring directly attacks the carbonyl of the histamine butyrate adduct. Mass spectrometry experiments showed no evidence of a picolylamine adduct for this mechanism; however, intermediate species are not always detected. Both proposed mechanisms involve a combination of cooperative and sequential mechanistic steps. Similarly to our vesicular system, we start with **HM-SH** and **G-SH** cooperatively facilitating the first nucleophilic attack. This is followed by a sequential step where the pyridine nitrogen in **D2PA-SH** reacts only after the initial nucleophilic attack of the substrate, like both our vesicle system and the mechanism proposed by Moss et al., both discussed in Chapter 2. The second nucleophilic attack with **D2PA-SH** can also be considered as a separate cooperative step as this works in tandem with **G-SH**, which aids in the stabilisation of the transition state in both nucleophilic attacks.

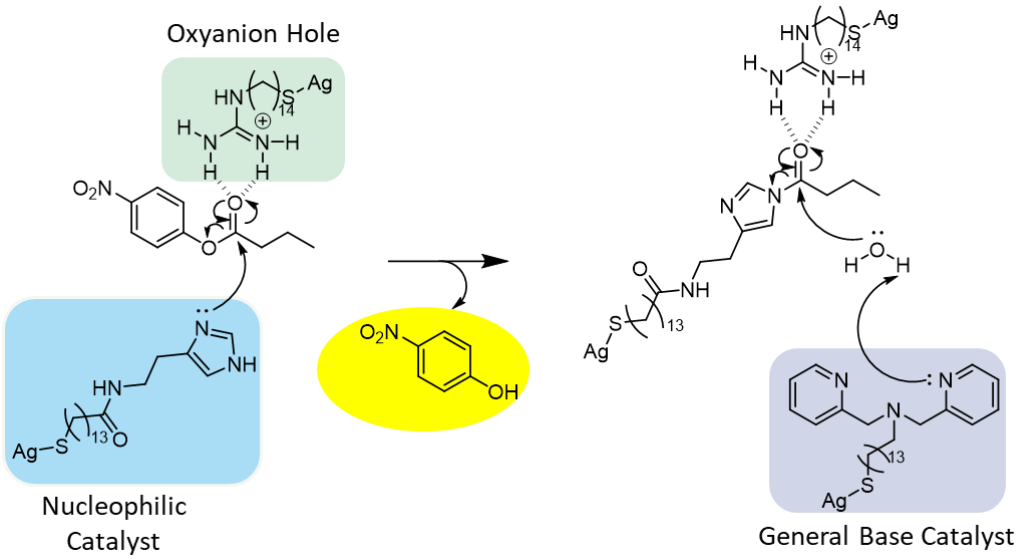

*Figure 153: Proposed mechanism where **D2PA-SH** acts as a general base catalyst.*

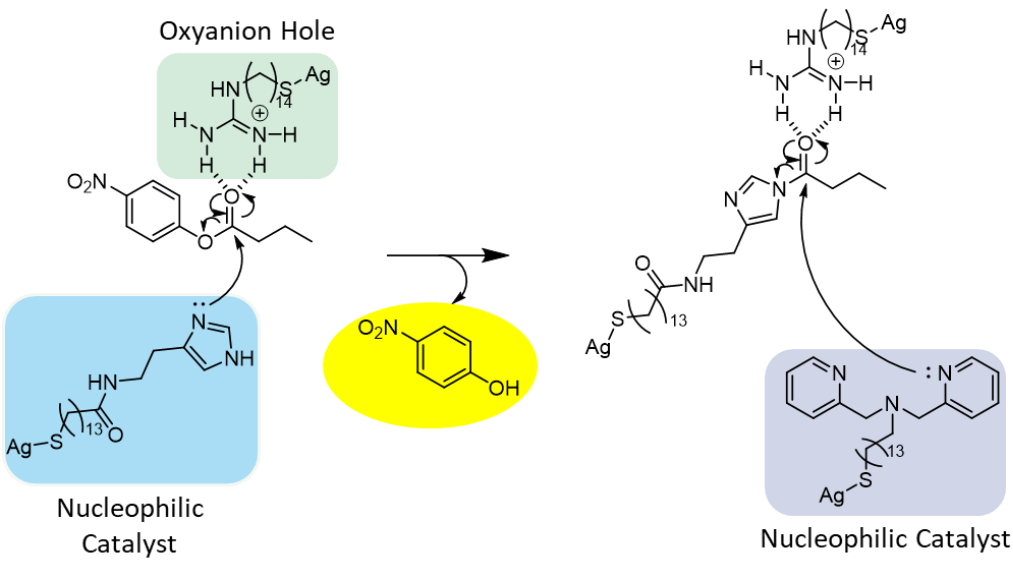

*Figure 154: Proposed mechanism where **D2PA-SH** acts as a nucleophilic catalyst.*

There have been studies previously in the literature to understand the catalysis pathway of pyridine-based molecules. The catalysis of esters by pyridine (**117**) has been found to undergo a nucleophilic pathway.[144,145] However, nucleophilic catalysis by the pyridine nitrogen is inhibited when methyl substituents are present in position 2. Rather, the 2-substituted pyridine (**124**) will undergo a general base pathway (Scheme 46).[144] Pyridines substituted with primary amines instead of methyl groups in position 2 (**125**) are still able to undergo the nucleophilic pathway (Scheme 47).[145] Therefore, we would need to undergo more mechanistic studies to see what effect our substituents have on the activity of the pyridine rings.

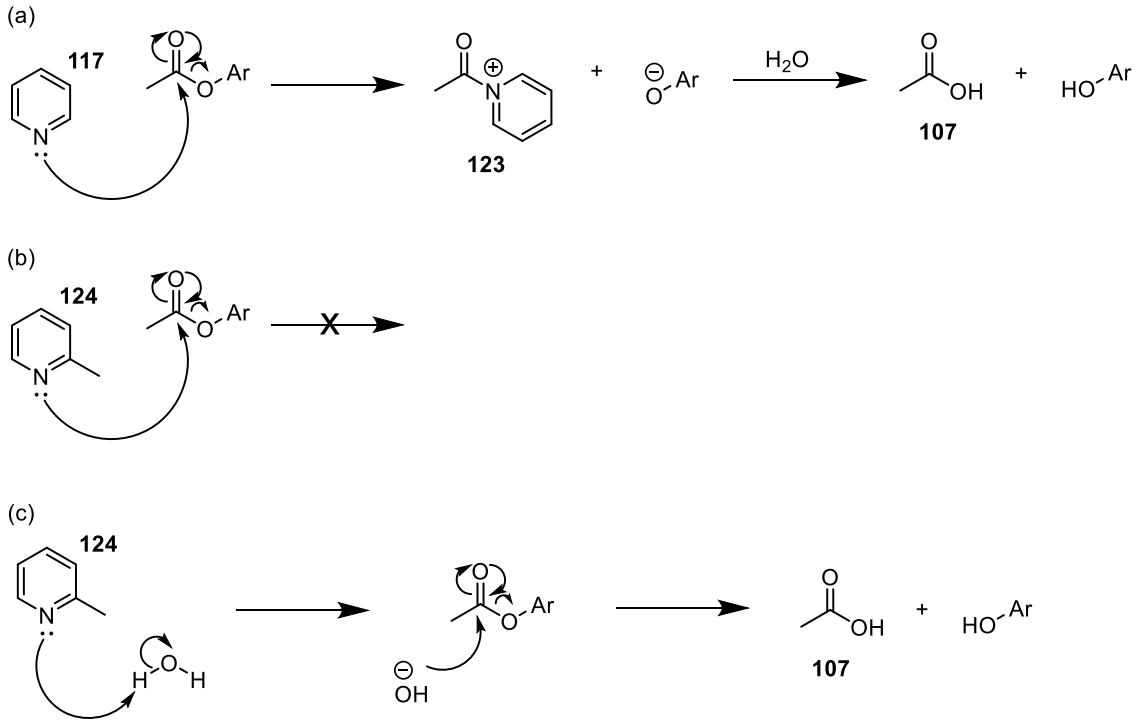

Scheme 46: Mechanistic pathways for the catalysis of aryl esters by pyridine through nucleophilic catalysis (a) and 2-methyl pyridine through nucleophilic (b) and basic (c) catalytic pathways.[144]

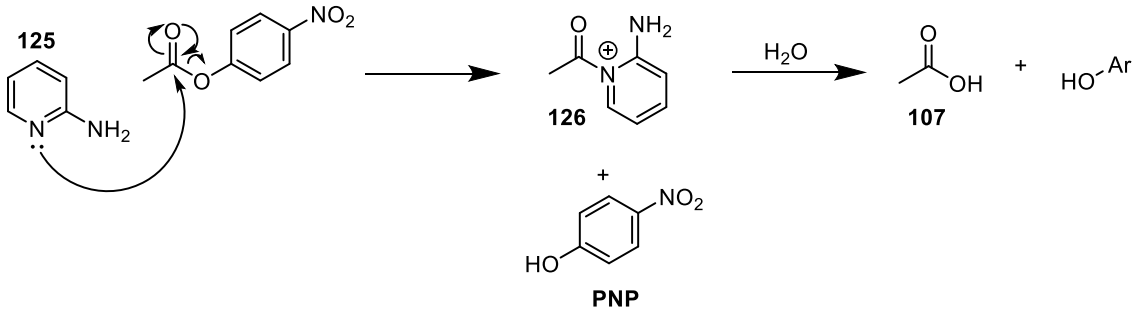

Scheme 47: Mechanistic pathway for the catalysis of p-nitrophenyl acetate by 2-aminopyridine through nucleophilic catalysis.[145]

There is also evidence for the artificial esterases containing pyridine functionalities facilitating catalysis via a general base catalytic mechanism.[64] Bose et al. undertook several mechanistic studies to determine that the pyridine in the active site of their molecularly imprinted micelles (Figure 155) underwent a general base catalytic mechanism. Bose and coworkers analysed both the Hammet σ-ρ relationship and the solvent isotopic effects, both of which gave conclusive results that the pyridine nitrogen was acting as a general base catalyst.[64] This is in contrast to much older mechanistic

studies that suggest 4-substituted pyridines undergo nucleophilic catalysis (whether they are substituted with a methyl or an amine group).[144,145] Therefore, it is likely that we cannot confirm which of the two pathways our mechanism proceeds via unless we undergo much more detailed mechanistic analysis.

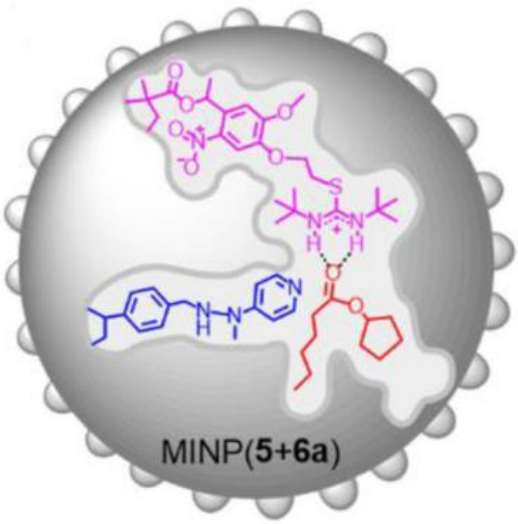

Figure 155: Molecularly imprinted micelle with a pyridine active site in blue and substrate in red. Source: Adapted from ref. [64] with permission. Copyright (2023) Elsevier.

3.6.8 Using Michaelis-Menten kinetics to determine the catalytic efficiency of the system

Michaelis-Menten kinetics can be used to assess the catalytic activity of our silver-thiol coordination polymers. This allows us to directly compare the activity of this new system to our previous vesicular catalyst, other artificial esterases reported in the literature, and to the native esterase enzyme α-chymotrypsin. The Michaelis-Menten parameters were determined by measuring the initial rate of reaction at increasing concentrations of substrate. We decided to assess our optimised 1:1:1 **HM/G/D2PA-SH** system. We did this in the presence and absence of Zn^{2+}, as we thought this could offer more insight into why the addition of Zn^{2+} had a minimal effect on catalysis. Figure 156 shows the results of this. What is particularly interesting with these results is how our 1:1:1 **HM/G/D2PA-SH** without Zn^{2+} perfectly fits the Michaelis-Menten model. We saw in the previous chapter that neither of our vesicle conditions showed this distinctive Michaelis-Menten curve (Figure 79). Though the addition of Zn^{2+} to our 1:1:1 **HM/G/D2PA-SH** system seems to lose this perfect curve. This difference in curve is reflected in the Michaelis-Menten constant K_M, seen in Table 5. The K_M for 1:1:1 **HM/G/D2PA-SH** without Zn^{2+}

is much smaller than that with $Zn^{2+,}$ indicating that the system without Zn^{2+} has much more efficient binding to the substrate. 1:1:1 **HM/G/D2PA-SH** without Zn^{2+} also has much more efficient substrate binding than our vesicular 1:1:1 **H/G/D2PA** system. The π-π interactions occurring between the substrate PNPB and the free **D2PA-SH** unit likely aid in the system's ability to better bind the substrate. Examples of this have been seen in the literature where the affinity of benzene-containing substrates has been greater towards molecular scaffold artificial catalysts due to their π-π interactions occurring between the substrate and aromatic cavity, compared with acetate-containing substrates.[146]

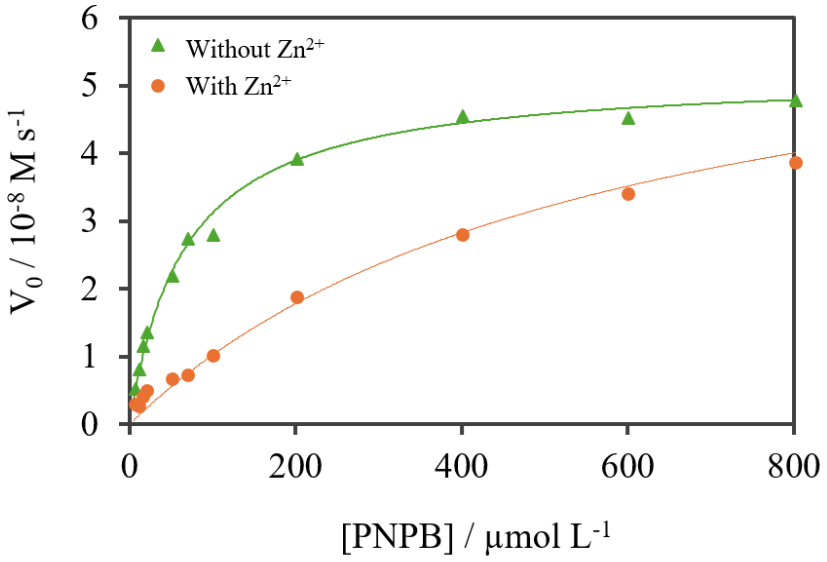

Figure 156: Michaelis-Menten fit for 1:1:1 ***HM/G/D2PA-SH*** *with and without* Zn^{2+}*. (Experimental conditions: aqueous buffer pH = 7.0 ([HEPES] = 5 mM),* $[AgNO_3]$ *= 60 µM,* ***[HM/G/D2PA-SH]*** *= 60 µM,* $[Zn(NO_3)_2]$ *= 60 µM. 40 °C.*

Table 5: Comparison of our best silver-thiol coordination polymers to our previous vesicular catalyst, previously reported artificial esterases and native enzyme α-chymotrypsin.

Catalyst system	V_{max} **(10^{-8} M s^{-1})**	k_{cat} **(s^{-1})**	K_M **(mM)**	k_{cat} / K_M **(M^{-1} s^{-1})**
1:1:1 **H/G/D2PA**	75 ± 20	0.023 ± 0.006	1.7 ± 0.6	14 ± 9
1:1:1 **HM/G/D2PA-SH** without Zn^{2+}	5.2 ± 0.1	0.0026 ± 0.00005	0.066 ± 0.006	39 ± 4
1:1:1 **HM/G/D2PA-SH** with Zn^{2+}	6.9 ± 0.6	0.0034 ± 0.0003	0.57 ± 0.099	6.0 ± 1.5
MINP[64]		0.03	0.14	205
Ac-IHIHQI-$CONH_2$[53]		0.026	0.4	62
Phe-His-C_{16}-SH[55]		0.016	1.4	11
α-chymotrypsin	3.20 ± 0.04	0.016 ± 0.002	0.0049 ± 0.0004	3300 ± 300

Interestingly, the V_{max} of the 1:1:1 **HM/G/D2PA-SH** system with Zn^{2+} is higher than that of the system without Zn^{2+}. This means that at higher concentrations of substrate, we would see better rates of catalysis with our Zn^{2+} system. From this, it appears that an alternative mechanism takes place involving Zn^{2+} that proceeds via a different transition state than in the absence of this ion. When Zn^{2+} is present, the system has high catalytic activity but poor binding to the substrate (due to the larger K_M).

Looking now to compare the catalytic efficiencies (k_{cat}/K_M) of our two different catalytic systems, we see that our 1:1:1 **HM/G/D2PA-SH** system is superior. The level of rigidity and organisation introduced to the system via the formation of coordination polymers increases catalytic efficiency. This is now greater than that of Liu and coworkers' system, where they used a self-assembled dipeptide catalyst (Phen-His-C_{16}-SH). However, we still have quite a way to go to reach the catalytic efficiency of native enzymes. Though we have approached the efficiency of some of the more rigid, well-organised artificial esterases reported in the literature.[53,64] For example, the system by Rufo and coworkers (Ac-IHIHQI-$CONH_2$), where they use catalytic amyloids formed from seven-residue peptides, is only slightly more efficient than our 1:1:1 **HM/G/D2PA-SH** system. This system is comprised of short individual peptides that self-assemble in the presence of Zn^{2+}. The peptides that Rufo and coworkers add together to form this catalyst are

structurally more rigid than our thiol ligands, which we add to form our catalyst. The additional incorporation of rigidity in the building blocks of Rufo and coworkers' catalyst may contribute to the slightly higher catalytic efficiency when compared to our system.

Molecularly imprinted polymers formed by Bose et al. are still far superior to our optimised silver-thiol polymer catalyst. Therefore, the generation of highly ordered structures still has significant benefits to be had. The use of molecular imprinting greatly increases the efficiency of the catalyst, likely due to the catalytic functionalities being oriented in the correct conformation before catalysis through the formation of a rigid well-defined binding pocket.

3.6.9 Switching catalysis on and off using KI

Coordination polymers for catalysis were formed in situ upon the addition of the catalytic thiols to a solution containing Ag^+. Therefore, we wondered if it was possible to control the catalysis by controlling the formation and breakdown of these polymers. A literature search revealed we may be able to achieve this through the addition of iodine.

The reversible nature of these silver-thiol coordination polymers has been demonstrated by Shen et al. A reversible transition between their hydrogel and solution state occurred when iodine was added to the solution (Figure 157). Iodine can react with the silver to form AgI. The bond formed between Ag^+ and I^- is stronger than that between Ag^+ and the thiol, allowing I^- to displace the thiols, resulting in depolymerisation.[117] Once the polymer had been broken, 1 eq of Ag^+ could be added to reform the polymer. This transition could be completed at least three times by alternatively adding I^- and Ag^+.[117] In this research, Shen and coworkers were using hydrogels as a sensor for anions, specifically to detect iodine, based on the state change. However, we figured that we could apply this concept to our catalytic system, using this principle to switch on and off catalysis.

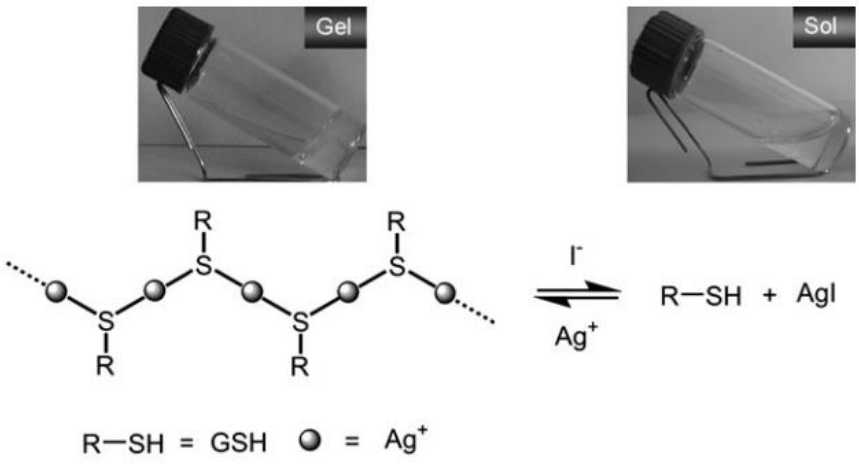

Figure 157: Reversible transition between gel and solution state of silver-thiol coordination polymer via the addition of either I^- or Ag^+. Source: Reprinted from ref. [117] with permission. Copyright (2009) Royal Society of Chemistry.

Initially, we wanted to try the switching of our 1:1:1 **HM/G/D2PA-SH** system in a single cuvette. For these experiments, we started by adding our individual thiol components to the solution, followed by PNPB. This was left to react for 5 minutes to obtain the rate of catalysis. 1 eq of Ag^+ was then added; this should form the coordination polymers, increasing the rate of catalysis. After 5 minutes, 1 eq KI was then added to the system. This will react with the Ag^+ to form AgI, essentially breaking the polymers. As a result, the rate should decrease. The system should then be able to cycle through the high and low catalysis states simply by the addition of Ag^+ and KI.

Figure 158 shows our initial attempt at switching. The first addition of Ag^+ has a high rate of reaction as the coordination polymers are formed. The rate is then decreased following the first addition of KI. However, after this, no real change is seen in the rate of catalysis despite adding Ag^+ to reform the polymer. The substrate concentration may be getting depleted relatively quickly, so it is less likely to come into contact with the catalyst, resulting in a lower rate of catalysis. Higher concentrations of PNPB were trialled. Double the PNPB concentration had no effect, and anything higher than this resulted in the substrate precipitating out of solution.

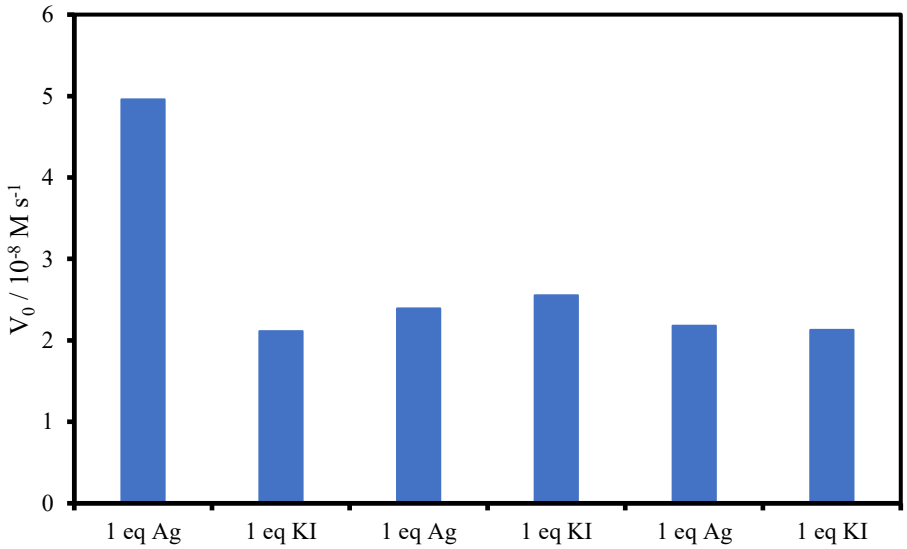

Figure 158: Switching in a single cuvette. Experimental conditions: aqueous buffer pH = 7.0 ([HEPES] = 5 mM), [1:1:1 ***HM/G/D2PA-SH****] = 60 µM, [PNPB] = 500 µM, 40 °C.*

A potential way to overcome this is to add more substrate with each Ag^+ and KI addition to help top up the concentration. Adding smaller amounts at a time should prevent any issues with insolubility, as we are not saturating the solution. This method has had great results in the past for the research group when investigating the switching on and off of azobenzene-based catalysts for phosphodiester cleavage.[103] Figure 159 shows the results of this new method. Here we see a similar result to Figure 158, where we can initially switch off the system, but subsequent additions of Ag^+ have no effect. It now seemed we were getting batch product inhibition. 4-Nitrophenolate produced from the cleavage of PNPB could be binding to the catalytic site, preventing these from being available to the substrate. The way to overcome this batch product inhibition was to conduct our switching in separate cuvettes.

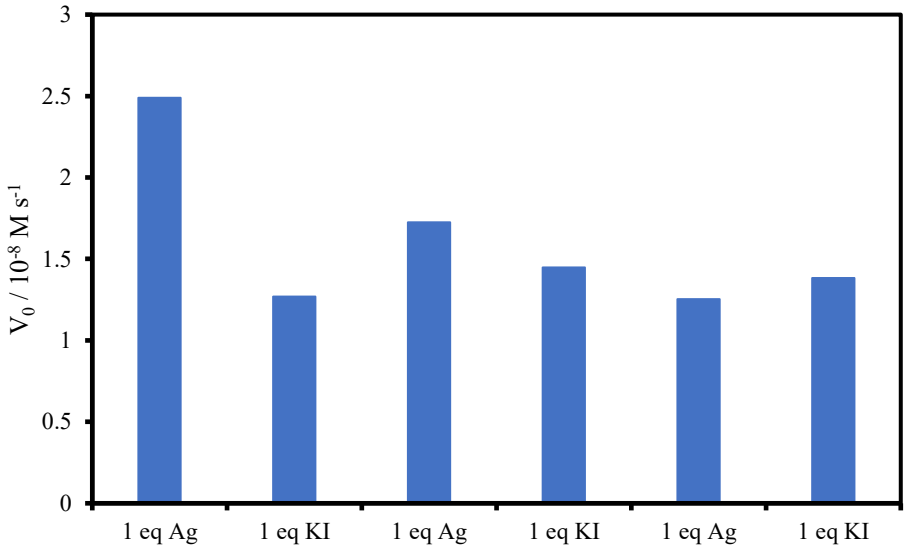

Figure 159: Switching in single cuvette with PNPB (100 µM) added each switch. Experimental conditions: aqueous buffer pH = 7.0 ([HEPES] = 5 mM), [1:1:1 ***HM/G/D2PA-SH****] = 60 µM, [initial addition PNPB] = 500 µM, 40 °C.*

Switching in separate cuvettes allows us to eliminate any issues we might be having with substrate or product buildup. For this, we will have a series of cuvettes. The first will contain our catalytic thiols and Ag^+, then PNPB will be added. The second cuvette will have the thiols, Ag^+ and then after 5 minutes, KI will be added to switch the solution. This will be followed by the addition of PNPB. Consecutive switches can be completed by waiting 5 minutes between each Ag^+/KI addition, then adding PNPB at the end of the cycle. Essentially, PNPB is added after all the desired switches for that cuvette have occurred. Figure 160 shows that this works much better than in the single cuvette. In this case, we can actually see catalysis increasing with every Ag^+ addition. Therefore, the low rates from the previous experiments can be attributed to product inhibition. Though these results are promising, the second and third additions of Ag^+ do not match the activity of the first Ag^+ addition. Perhaps more than 1 eq Ag^+ is required to reform our coordination polymers. Further optimisation of these switching experiments will be required to truly show how important the silver-thiol coordination bond is for catalysis.

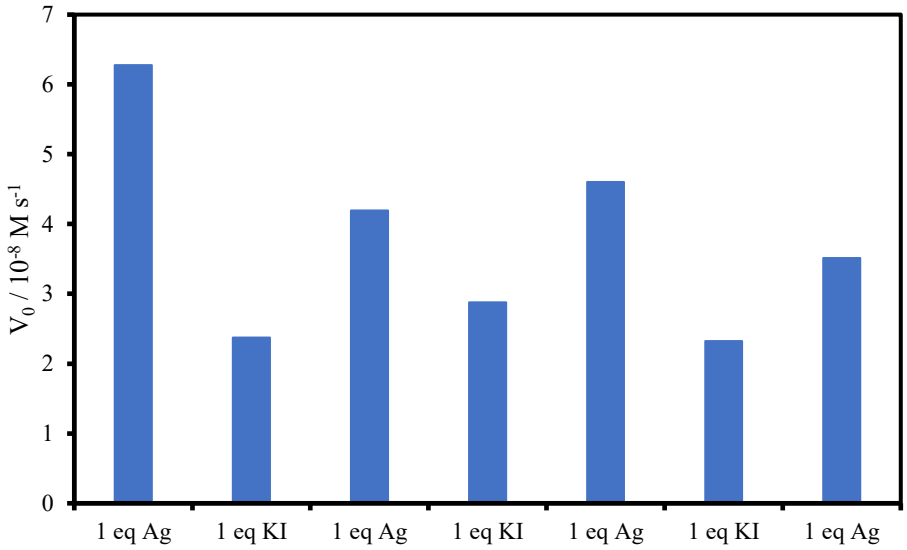

Figure 160: Switching in separate cuvettes. Experimental conditions: aqueous buffer pH = 7.0 ([HEPES] = 5 mM), [1:1:1 ***HM/G/D2PA-SH****] = 60 μM, [PNPB] = 500 μM, 40 °C.*

Optimisation of switching experiments

The use of KI to switch on and off catalysis showed promising results; however, this requires further optimisation to see a greater difference between the on and off states to indicate how crucial polymer formation is for the catalyst. For these experiments, we used 60 μM of our catalyst. Though this is below the CAC of **HM-SH** (122 μM) we have yet to determine the CAC of our 1:1:1 **HM/G/D2PA-SH** system. If this is around 60 μM, chances are the free thiols can start to assemble, and this could be contributing to the small difference we see between the switched-on and off states. To really see the effect of the polymer formation, we would want to be working at concentrations below the CAC to prevent any assembly and limit any catalysis occurring in the absence of our polymers. Once we have determined the ideal concentration for these experiments, we can also play around with the equivalents of Ag^+ and KI added for each switch. So far, we have only tried 1 eq each addition, but maybe the addition of more (1.5 or 2 eq) will result in more of a difference between the two catalytic states.

3.7 Conclusions for Chapter 3

In this Chapter, we successfully synthesised a silver-thiol coordination polymer capable of catalysing ester hydrolysis. We demonstrated how we could achieve cooperativity between multiple functionalities, with our 1:1:1 **HM/G/D2PA-SH** showing the highest catalysis rate and the highest degree of cooperativity. This system was found to work

similarly with and without Zn^{2+}, a contrast to what we saw for our vesicular catalyst in Chapter 2. Therefore, we conducted a series of experiments to determine the role of **D2PA-SH** in the absence of Zn^{2+}. From this, we proposed a couple of mechanistic pathways in which the pyridine nitrogen in **D2PA-SH** acts as either a base or a nucleophile in catalysis. Importantly, the incorporation of rigidity into this compound increased the catalytic efficiency (k_{cat}/K_M) of our silver-thiol polymer compared with our vesicular catalyst. The role of polymer formation was further probed through the addition of KI, which disrupted Ag-S coordination and resulted in diminished catalytic performance. Collectively, these results demonstrate that introducing rigidity into modular catalytic systems can substantially improve catalytic efficiency while preserving cooperative behaviour.

Chapter 4: Conclusions and Future Work

4.1 Overall conclusions for the thesis

One of the key aims of this thesis was to develop artificial esterases using modular catalytic systems. Modularity of the catalytic system makes it easier to optimise, as changes to the individual catalytic components can be made simply by adjusting their concentrations. This eliminates the synthetic strain inherent to more rigid catalytic systems, such as molecular scaffolds, dendrimers, or nanoparticles, as changes to the modular catalyst do not require total synthesis.

In this thesis, I have developed two modular catalytic systems that can function as artificial esterases. The first focused on the self-assembly of functionalised surfactants, driven by hydrophobic interactions. A series of functionalised surfactants was initially screened for esterase activity both individually and in combination with one another. They were also screened in the presence and absence of Zn^{2+}. This found a 1:1 **H/G** combination with Zn^{2+} to have the highest rate of catalysis. We then took this combination through an optimisation process where we altered the ratio of our two amphiphiles and the concentration of Zn^{2+} to give a 1:4 **H/G** system with 1 eq Zn^{2+} as our optimised system. With the aid of colourimetric titrations to determine the amphiphiles' binding to Zn^{2+}, and mass spectrometry data to determine the presence of any intermediate species, we could propose the mechanism for this system. Our **H** amphiphile acts as a nucleophilic catalyst with 1 eq **G** stabilising the transition state. The remaining 3 eq **G** then act as Zn^{2+} chelators, allowing the metal ion to bind a hydroxide ion for secondary nucleophilic attack. This insight into the mechanism enabled us to further optimise the catalyst by replacing 3 eq **G** with a stronger metal-ion chelator. **D2PA** was found to work the best, giving an optimised catalytic system of 1:1:1 **H/G/D2PA** with 1 eq Zn^{2+}. The mechanism was determined to proceed via a similar pathway, with **D2PA** now taking the role of the metal ion chelator. The catalytic efficiency of this system could be determined and compared to artificial esterases previously reported in the literature and to the native enzyme α-chymotrypsin. Our vesicular catalyst was comparable to systems comprising rigid, well-organised structures, such as dipeptides that form nanofibers.[55] Though highly ordered structures made from molecular imprinted polymers were over 14 times more efficient than our 1:1:1 **H/G/D2PA** vesicular catalyst, suggesting that the formation of highly rigid binding pockets greatly increases efficiency. However, the native enzyme α-

chymotrypsin greatly outperformed the artificial esterases, being more than 10 times as efficient as the best artificial esterase system.

This system also demonstrated how self-assembly can be used as a tool for the rapid discovery and optimisation of an artificial catalyst. Changes to the functional groups used, and even the proportions in which they are present in the catalyst, can be easily varied with minimal to no synthetic effort. This is in contrast to traditional artificial esterase systems on molecular scaffolds or nanoparticles, which would require total synthesis to undergo such modifications to the catalytic system.

Though the dynamic nature of our self-assembled system is advantageous for catalyst optimisation, it can also limit the use of this type of system. The assembled vesicular catalyst is susceptible to environmental changes, such as changes in concentration, which could cause the catalyst concentration to fall below the CAC, preventing assembly. Any changes that affect the self-assembly of the system will also negatively affect its catalytic efficiency. Therefore, we looked at pivoting from a modular self-assembled system to a modular system that did not rely solely on hydrophobic interactions.

Comparing catalytic efficiencies between the literature and our vesicular catalytic system, we found that incorporating more rigid, well-defined structures led to more efficient catalysts. Therefore, we wanted to incorporate a level of rigidity into our catalytic system while still maintaining the modularity of our first system to facilitate rapid optimisation. This was achieved through silver-thiol coordination polymers, with the tunability of the system resulting from the *in situ* formation of these polymers. Our catalytic functionalities from our vesicle catalyst (imidazole ring, guanidine and di-(2-picolylamine) were incorporated into the thiol ligands, initially using a 6-carbon chain to separate the thiol and the catalytic unit. However, initial tests with **C6-HM-SH** showed that the free thiol had greater activity on its own than in the polymer system. The short length of the carbon chain was thought to be the contributing factor, potentially preventing the **C6-HM-SH** catalytic headgroups from coming close enough to facilitate cooperative catalysis. Therefore, we synthesised longer catalytic thiols consisting of a 14-carbon chain. **HM-SH** demonstrated much higher activity in the polymer than for the free thiol, indicating that the longer length carbon chains were required to bring the catalytic units close enough for cooperative catalysis. Our series of long thiols was screened in combination with one another. This proved that a combination of 1:1:1 **HM/G/D2PA-SH** functionalities,

similar to those seen in the vesicular catalyst, gave rise to the highest rate of catalysis and the highest degree of cooperativity. Demonstrating that we can have cooperativity occurring between different catalytic functionalities in the silver-thiol coordination polymer. However, the addition of Zn^{2+} to this system had a minimal effect on the rate of catalysis. This was surprising as **D2PA-SH** is a well-known metal-ion chelator. Therefore, we wanted to determine the role of this functional group in the reaction mechanism in the absence of Zn^{2+}. A series of experiments was conducted to determine the role of both the tertiary amine and the pyridine nitrogen. The pyridine nitrogen was found to be the contributing factor for catalysis. An attempt to optimise this system using a single 2-picolylamine functionality instead of the two present in **D2PA-SH** was ultimately unsuccessful. The **2PA-SH** ligand synthesised was relatively unstable; the 2-picolylamine base could also undergo nucleophilic attack via the amine, which was undesirable, and incorporation of 2-picolylamine compounds consisting of various length carbon chains had minimal effect on the catalysis of the 1:1 **HM/G-SH** system. Therefore, our 1:1:1 **HM/G/D2PA-SH** combination remained our best system with two potential mechanisms proposed based on the pyridine nitrogen acting as either a nucleophile or a base. The catalytic efficiency of this system was compared to our initial vesicle system, with our silver-thiol polymer being more than double that of our vesicle system. The introduction of rigidity into this system improved catalytic efficiency, demonstrating its importance in artificial catalysts.

Once again, the modularity of the silver-thiol coordination polymers proved advantageous in terms of catalyst optimisation. It allowed for the investigation of the 1:1:1 **HM/G/D2PA-SH** system with minimal synthetic effort, as only new structures that we wished to incorporate into the system needed to be synthesised. Total synthesis is typically required for traditional immobilised catalytic systems (such as molecular scaffolds) to incorporate new functionalities.

4.2 Substrate-induced formation of catalyst

The development of modular artificial esterase systems in this thesis has inspired us to investigate catalyst self-selection as an area of research for a future project. Starting with a series of catalytic functionalities in solution (10-20 building blocks), the substrate can be added to drive self-assembly or the formation of coordination polymers (Figure 161). This formed catalyst can then be removed from the catalytic library, and through a process

of elimination, the components of the catalyst can be determined. This self-selection of a catalyst has been previously demonstrated by Otto and coworkers using a transition state analogue to select the catalyst from a dynamic combinatorial library of interconnecting structures (Figure 162). A Diels-Alder catalyst was selected from a dynamic combinatorial library of **127**-**129**, using the product of the reaction **130** as a transition state analogue. In the presence of compound **130**, macrocycles **131** and **132** were selected from the combinatorial mixture, of which only macrocycle **132** was catalytically active.

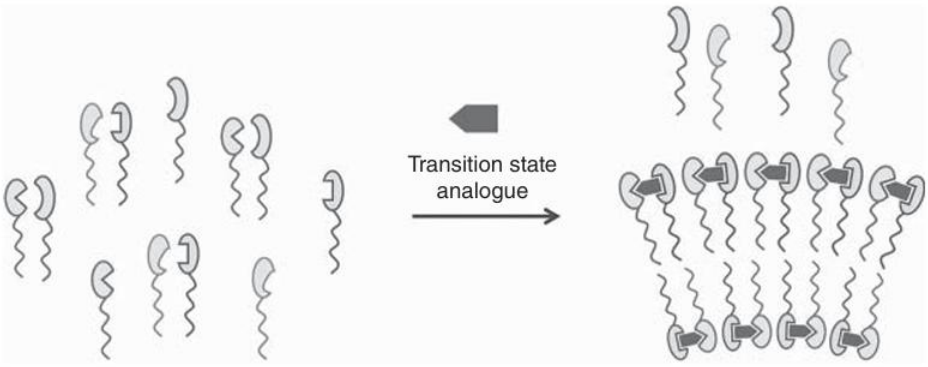

Figure 161: Self-selection of a catalyst from a dynamic combinatorial library by the addition of a transition state analogue. Source: Reprinted from ref. [147] with permission. Copyright (2023) John Wiley and Sons.

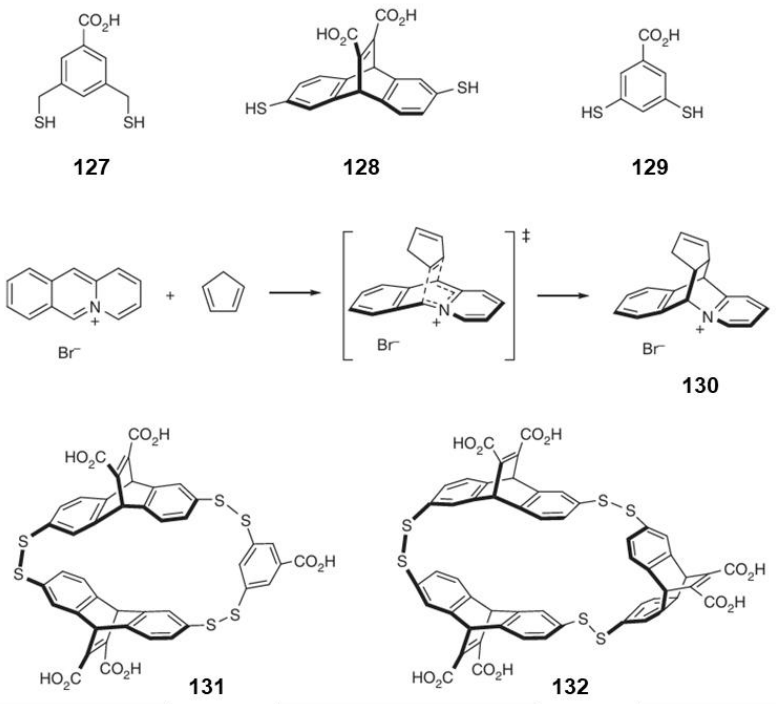

*Figure 162: Dynamic combinatorial library formed using dithiols **127-129**, where the addition of transition state analogue **130** promotes the formation of **131** and **132**. Source: Reprinted from ref. [147] with permission. Copyright (2023) John Wiley and Sons.*

The self-selection of the catalyst would reduce the time spent optimising a modular catalyst. The optimal catalyst is selected in a single step, rather than the functional group screens we conducted throughout the thesis, which required a separate experiment for each catalytic combination investigated. It would also eliminate the need for further optimisation steps to determine the ideal ratio of components, as this would also be determined in the initial self-selection step. The ability to self-select a catalyst would enable rapid development of artificial enzymes.

4.3 PETase activity

In this PhD, I have demonstrated that we can engineer an artificial esterase capable of hydrolysing the model esterase substrate PNPB. One of the long-term goals of this research was to design an artificial esterase capable of breaking down PET plastic. PET is a polymer consisting of ester bonds linking together the monomeric units, TPA and ethylene glycol **14**. It is much harder to break down than PNPB. PNPB contains an activated ester, which makes it more susceptible to nucleophilic attack due to the presence of an electron-withdrawing group (-NO_2), making it easier to degrade. Since we have

shown that our artificial esterase systems are capable of breaking down the ester bond in PNPB, we wanted to look at cleaving the more challenging and ultimately more relevant substrate PET. There are already examples now of both native[45] and artificial[52] enzymes that can break down PET, previously discussed in Chapter 1.

We have conducted some preliminary experiments using our optimised 1:1:1 **HM/G/D2PA-SH** silver-thiol coordination polymers, which have shown promising results. Here we were looking to see if our catalyst could break down BHET rather than PET itself. BHET is a monomeric version of PET, which can be hydrolysed to give TPA and ethylene glycol (Scheme 48). This should cleave slightly more easily than PET.

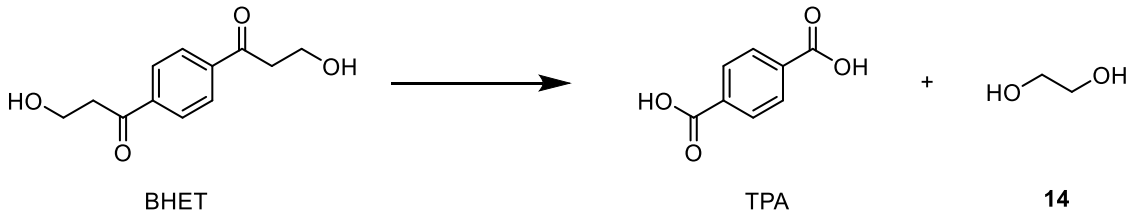

Scheme 48: Hydrolysis of BHET.

For this substrate, we employed a different method to monitor catalysis than for PNPB, as the hydrolysis products were no longer visible using the UV-vis spectrometer. Zhang et al. report using ^{1}H NMR to monitor the amount of ethylene glycol produced from the hydrolysis of PET.[52] We employed a modified method where we compared our ethylene glycol NMR peak to that of a known internal standard (maleic acid). Using Equation 5, we can determine the molar concentration of ethylene glycol. For this equation, I refers to the integration, N the number of protons corresponding to the peak, and M the molar concentration. The same research paper by Zhang et al. gave us a starting point for the conditions for catalysis. In their research, Zhang and coworkers made a binuclear complex featuring Zn-Zn active sites for PET catalysis. The conditions they used for successful catalysis include pH 8 at 40 °C and pH 13 at 90 °C.[52] Zhang et al. also reported that complete depolymerisation occurred in 10 weeks.

$$M_{analyte} = \frac{I_{analyte}}{I_{standard}} \frac{N_{standard}}{N_{analyte}} M_{standard} \quad (5)$$

For our experiments, we decided to try our 1:1:1 **HM/G/D2PA-SH** polymers at both 60 °C and 90 °C for 12 weeks, using Tris buffer at pH 9. DMSO (5%) was also added to

these experiments to help solubilise the substrate (BHET). The results of these experiments are shown in Figure 163. At both temperatures, we observe that our 1:1:1 **HM/G/D2PA-SH** catalyst has higher activity than the controls, with the 90 °C experiments yielding much higher ethylene glycol production than the 60 °C experiments. However, the controls for both experiments are higher than we would like.

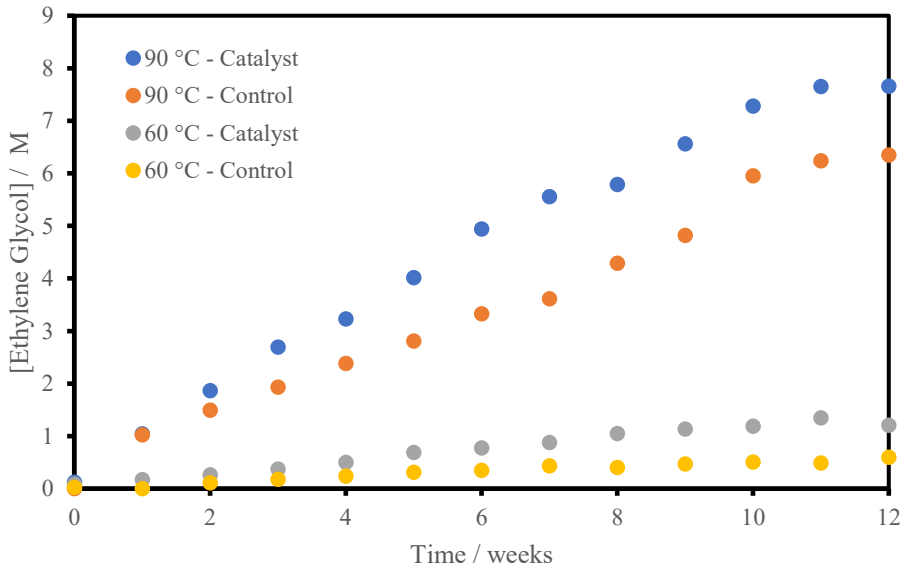

*Figure 163: Hydrolysis of PET to produce ethylene glycol (**14**) at 60 °C and 90 °C. Experimental conditions: 5 % DMSO.d6 in D_2O, aqueous buffer pH = 9 ([tris buffer] = 5 mM), [$AgNO_3$] = 60 μM, [1:1:1 **HM/G/D2PA-SH**] = 60 μM, [maleic acid] = 7.457 mM, [BHET] = 1 mM.*

Going forward, we would want to adjust the experimental conditions to see a greater difference between the catalyst and the control. The activity of the controls may be decreased by lowering the temperature or the pH. In addition to reducing the activity of the control, we also want to optimise our artificial catalyst to be more effective against the BHET substrate. The key here might be to investigate adding aromatic groups to aid substrate binding, rather than optimising the existing catalytic head groups. The active site of native PETase enzymes contain a tryptophan residue to help bind the PET substrate through hydrophobic interactions.[50] Tryptophan itself is an aromatic amino acid consisting of an indole side chain, allowing it to interact with aromatic structures through hydrophobic interactions such as π-π stacking. Since our target substrate, BHET, also has an aromatic ring at its core, the addition of aromatic thiols to the silver-thiol polymer could help bring this substrate closer to the catalytic functionalities, enhancing the rate of

catalysis. The addition of hydrophobic groups to artificial esterases has already proved favourable, as shown by Connal and coworkers' previous work, in which they incorporated hydrophobic resins into their artificial esterase to aid substrate binding (Figure 164). The catalytic triad was created by incorporating alcohol, imidazole, and carboxylic acid functionalities into a single molecule, which was then immobilised onto a solid-phase support resin. The resin itself was then modified with C16 alkyl chains to tune the hydrophobicity of the local environment, to mimic the hydrophobic pocket found in native esterase enzymes. Modified resin had a catalytic rate 50 times greater than that of the same resin without this modification.[17] Connal et al. proposed that the reason for this enhancement was due to the increased affinity between the modified resin catalyst and the substrate. Although the substrate investigated was PNPB, which is much easier to cleave than BHET due to its activated ester, the impact of incorporating hydrophobicity into the design of the artificial catalyst on reaction rate is clear.

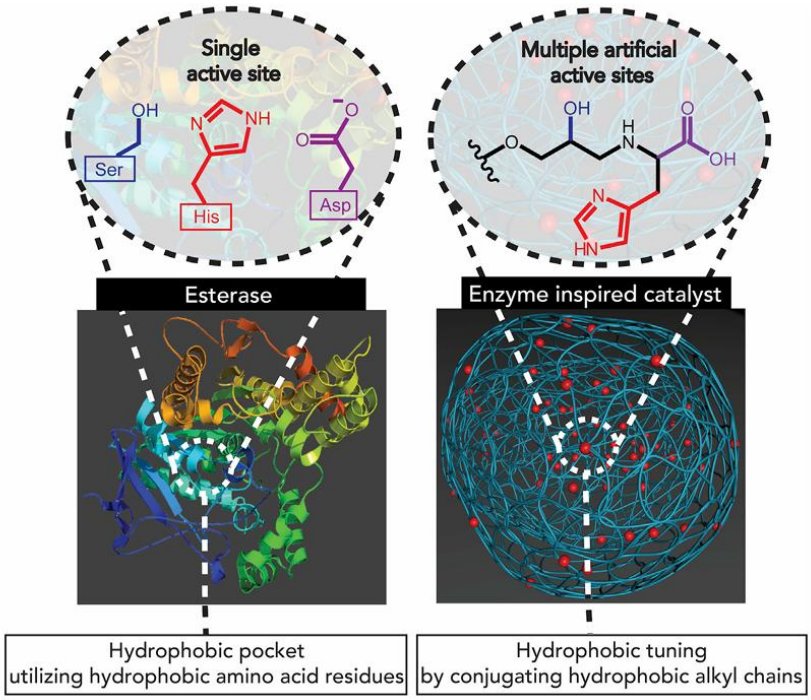

Figure 164: Artificial esterase consisting of catalytic triad immobilised on hydrophobic modified resin to mimic the hydrophobic pocket in native enzymes. Source: Reprinted from ref. [17] with permission. Copyright (2017) Elsevier.

Therefore, we could look at synthesising thiol ligands functionalised with aromatic groups to see if these would increase the catalytic rate through improved substrate binding. Figure 165 shows some proposed functionalities we could consider

incorporating, such as benzene **133**, indole **134**, and naphthalene **135**. The modularity of the silver-thiol polymer system means that we can simply incorporate our aromatic thiols once synthesised in different equivalents to see if these have a positive effect on catalysis.

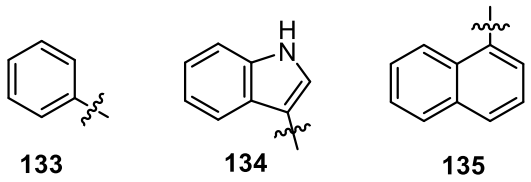

Figure 165: Proposed aromatic functionalities which we could look at incorporating into thiol ligands to aid in substrate binding.

Once our BHET catalyst conditions have been optimised, we could then look at catalysing actual PET. The idea here would be to make PET nanoparticles to then add to the system with our catalyst to see if this can be broken down into its monomers. The use of PET nanoparticles is quite popular to monitor PETase activity in native enzymes[149–151] due to the environmental concern of microplastics and nanoplastics.[152] Therefore, native enzymes are screened to break down plastics of similar sizes, which cannot be treated by traditional recycling methods due to their small size. There are a few methods described in the literature to synthesise PET nanoparticles. One utilises laser ablation of polymer films in water to produce nanoparticles with a controlled size distribution.[153] Another utilises mechanical milling to resize PET into nanoparticles.[152] The type of method we would likely use to synthesise PET nanoparticles would involve the precipitation of nanoparticles from solution. This type of nanoparticle synthesis has been used previously in the research group to synthesise cellulose-based nanoparticles.[154,155] Therefore, the group already has the knowledge and methods for nanoparticle synthesis using precipitation that could be modified and applied to PET. A good starting point for this modification could be the research done by Rodríguez-Hernández and coworkers, where they looked at undergoing large-scale precipitation of PET nanoparticles for them to then be used in toxicological and environmental studies.[156] Once PET nanoparticles had been synthesised, the same ^{1}H NMR method could likely be used to monitor catalysis.

Ultimately, the use of artificial esterases to break down PET plastic is a very exciting field for the research group to continue exploring. Despite the challenges that will arise with trying to catalyse a much harder esterase substrate, the future impact of this research is significant. The development of an artificial esterase that can break down PET into its

monomeric components can allow PET to exist in a circular economy, whereby the monomeric components produced from recycling can be reused to make new PET products. This will alleviate the environmental concerns regarding the disposal of PET through more efficient recycling and reuse of this polymer. Allowing PET to still be utilised in society in a greener way.

4.4 Using thiol compounds for modular molecular scaffolds

In Chapter 3, we saw how a series of thiol-based molecules can be assembled to form coordination polymers. These polymers offer more rigidity and stability compared to the vesicular system described in Chapter 2, with the thiol component providing some form of tunability in the polymer system. With our key catalytic thiols already synthesised, we can look to repurpose these building blocks to form other types of rigid, modular catalytic systems.

The system we had in mind is a modular molecular scaffold. Here, instead of using thiol-silver bonds to bring together our catalytic groups, we would use disulfide bonds to attach our thiols to a molecular scaffold. For this system, we wanted to use benzene-based molecular scaffolds with thiol substituents. We were particularly interested in a tri-substituted benzene (1,3,5-benzenetrithiol) as this would allow us to recreate our 1:1:1 **HM/G/D2PA-SH** catalyst (Figure 166). Since the thiols had already been synthesised and we had used them for one catalytic system, we figured this system would be relatively easy to start investigating. However, this system proved much more complex than we had envisioned.

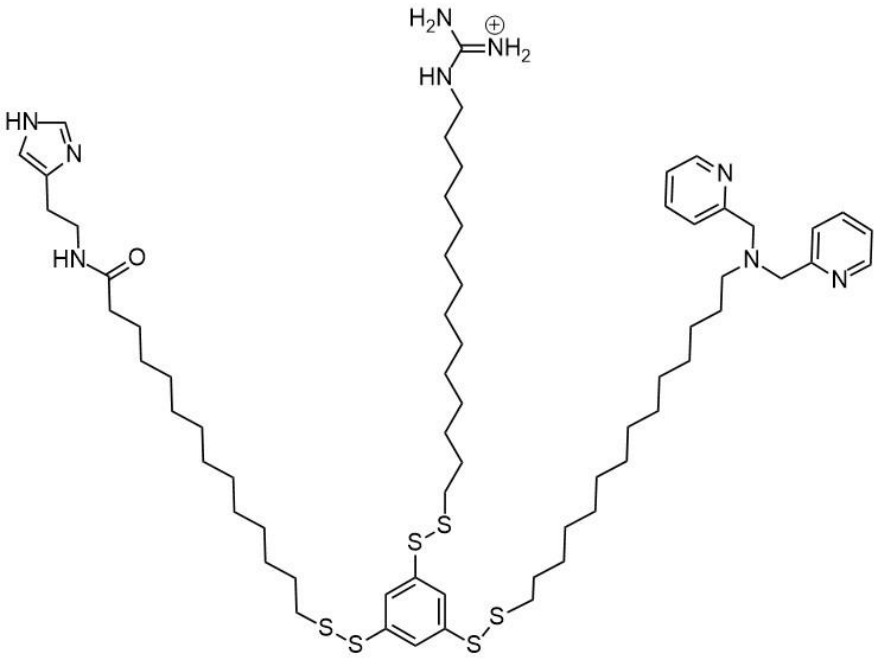

*Figure 166: Idea for molecular scaffold catalytic system with **HM/G/D2PA-SH** catalyst combination.*

Starting simple, we wanted to show that we could form a molecular scaffold system with just our **HM-SH** thiol, which catalysed ester hydrolysis at a higher rate than the thiols alone. A molecular scaffold with three imidazole functionalities should be able to promote cooperative catalysis. The basicity of the imidazole nitrogen is enhanced by neighbouring functionalities. This imidazole can then deprotonate a water molecule, forming a hydroxide ion ready to undergo nucleophilic attack on the substrate. We chose to use our C14 thiols for this system rather than the C6 thiols, as we have previously observed that the longer length is beneficial for cooperativity. Figure 167 shows that the catalytic rate increases slightly when the scaffold is present compared to HM-SH alone. This seemed promising, as it appears we are forming molecular scaffolds with our HM-SH thiols, though we need to perform more thorough mass spectrometry experiments to confirm that our **HM-SH** ligands are bound to the scaffold.

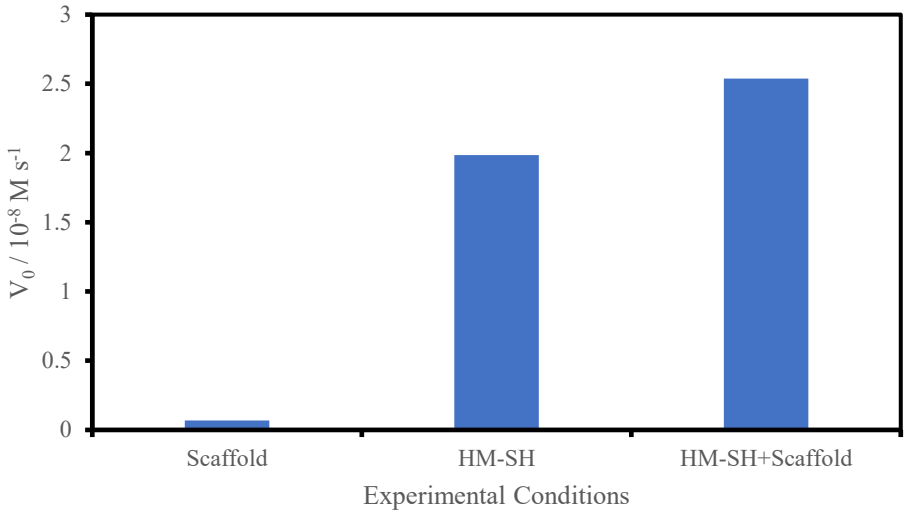

*Figure 167: **HM-SH** forming molecular scaffolds with a benzene trithiol scaffold. Experimental conditions: aqueous buffer pH = 7.0 ([HEPES] = 5 mM), [1,3,5-benzenetrithiol] = 30 µM, [**HM-SH**] = 90 µM, [PNPB] = 500 µM, 40 °C.*

The next step was to investigate the formation of 1:1:1 **HM/G/D2PA-SH** molecular scaffolds and to confirm the presence of cooperativity in these systems. The challenge here is that there is no way for us to ensure we are getting one of each of our catalytic thiols bound to our molecular scaffold. Chances are we will be forming a mix of molecular scaffolds which could contain one, two or all three catalytic functionalities. In addition to this, the scaffold and ligands may bind to themselves rather than to each other. There are examples in the literature of disubstituted thiobenzenes forming bonds with each other to make massive ring structures (Figure 168).[157,158] These structures are then capable of stacking together. It is possible that our system could be forming something similar as well, though the ability to form massive ring structures seems unlikely, as these can take several days to form.[157] This uncertainty as to what our system is forming is reflected in our preliminary results (Figure 169). Here, we see some odd results: our **G-SH** system shows a high catalysis rate, while our 1:1:1 **HM/G/D2PA-SH** system shows a lower rate than expected. The most likely cause of these unexpected results is the variability in what can form in our solution.

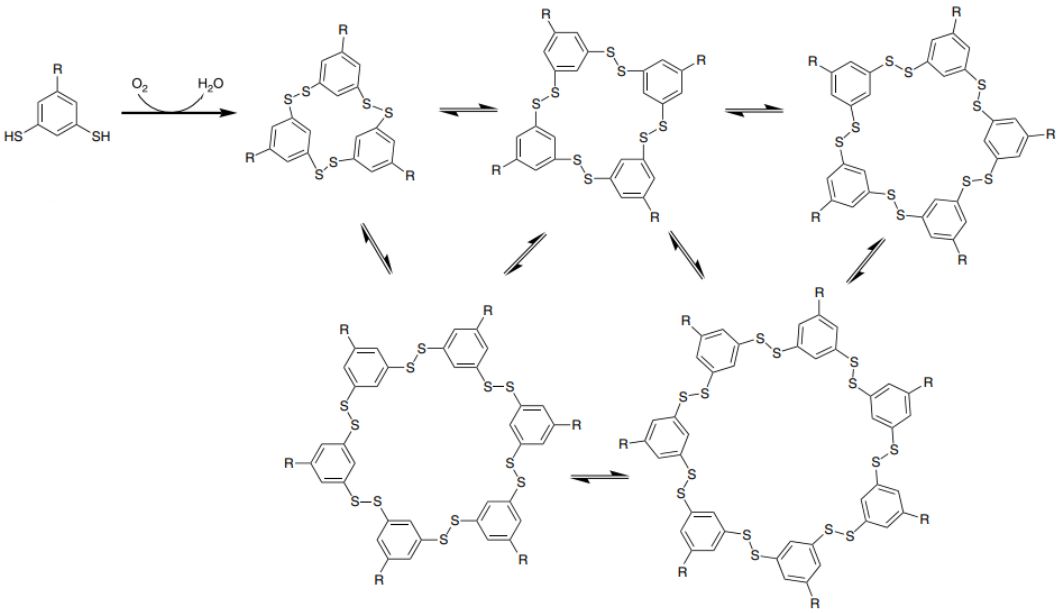

Figure 168: Example of disubstituted thiol benzenes forming ring structures. Source: Ref. [158]/Springer Nature.

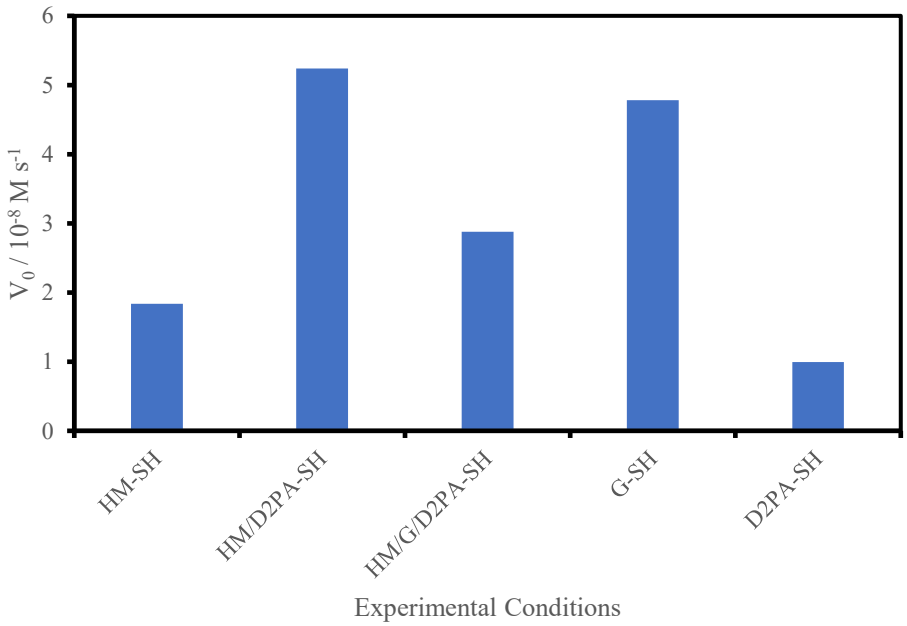

*Figure 169: Preliminary experiment to see if we can get cooperativity occurring between our **HM/G/D2PA-SH** system. Experimental conditions: aqueous buffer pH = 7.0 ([HEPES] = 5 mM), [1,3,5-benzenetrithiol] = 10 µM, [total thiols] = 30 µM, [PNPB] = 500 µM, 40 °C. Thiols were combined in equal proportions.*

Moving forward with this system, the biggest area of optimisation required is the formation of these scaffold structures. We plan to use mass spectrometry to confirm that the catalytic ligands bind to the scaffolds. This should also provide an indication of which ligands are binding to the scaffold in our more complex two- and three-component systems. In addition to this, we want to try adding an oxidant to the system to help with the formation of the disulfide bonds. Potentially, adding the oxidant after the ligands and scaffold are in solution could facilitate bond formation between the two. Another interesting factor to consider would be the order of addition. One possible strategy would be to introduce the substrate first, followed by the catalytic thiol ligands, allowing favourable catalyst-substrate interactions to form prior to scaffold assembly. Subsequent addition of the scaffold could then promote binding of the catalytic ligands in an optimised spatial arrangement, potentially leading to enhanced cooperativity in catalysis. To reduce system complexity in the initial stages, a two-component system could be investigated first, employing a dithiol scaffold rather than a trithiol analogue. In this context, the original 1:1 **H/G** catalytic combination developed for the vesicular system represents a promising starting point for translating this approach to a scaffold-based architecture.

If successfully realised, this approach would provide an exciting new strategy for constructing molecular scaffold-based catalytic systems. Conventional scaffold architectures are typically highly rigid, offer little structural flexibility, and often require extensive total synthesis to implement even minor structural modifications. The proposed thiol-based molecular scaffold system has the potential to overcome many of these limitations. Because the catalyst is formed *in situ*, the catalytic ligands and the scaffold can be modified independently, significantly reducing the overall synthetic burden. In addition, this system offers tunability analogous to that observed for the silver-thiol coordination polymers described in Chapter 3. Importantly, the development of new catalytic variants would require only the synthesis of alternative thiol components, rather than complete reconstruction of the scaffold. While immobilisation of the catalytic ligands on the scaffold introduces an element of rigidity, this is expected to be beneficial, as increased rigidity has been shown to enhance catalytic efficiency. It would therefore be of considerable interest to compare the performance of this molecular scaffold system with both the vesicular catalysts and the silver-thiol coordination polymers explored in this thesis.

Chapter 5: Experimental

5.1 General details

All fine chemicals were purchased from commercial suppliers such as Sigma-Aldrich and AK Scientific and used directly without purification. NMR solvents, including deuterated methanol-d4, deuterium oxide, dimethyl sulfoxide-d6 and deuterated chloroform, were purchased from Eurisotop. Anhydrous solvents DMF, MeCN, methanol and toluene were purchased from Merck. Anhydrous magnesium sulfate was purchased from Scharlau. Palladium on carbon (10 wt.% loading, matrix activated carbon support) and Celite® 545 was purchased from Sigma Aldrich.

Organic compounds were synthesised and characterised by ^{1}H, ^{13}C NMR, IR and HRMS (ESI), and the data was compared to literature values where available. Flash column chromatography was performed using silica gel 60 (Aldrich) or basic alumina gel and a suitable eluent. Reverse phase chromatography was performed using C18-silica with a suitable eluent. Analytical TLC was performed on aluminium-backed plates pre-coated (0.25 mm) with Merck Silica Gel 60 F_{254} or alumina oxide 60 F_{254} neutral with a suitable solvent system. These were visualised using UV fluorescence (254 nm) and/or developed with ninhydrin, vanillin, phosphomolybdic acid, bromocresol green, or potassium permanganate.

4-(2-Hydroxyethyl)-1-piperazineethanesulfonic acid (HEPES) and Trizma® hydrochloride were purchased from Sigma-Aldrich and used without further purification. The pH of buffer solutions was determined at room temperature using a Metrohm-632 pH-meter equipped with an Ag/AgCl/KCl reference electrode. In all cases, stock solutions were prepared using deionised water filtered with a MilliQ water purifier (Millipore) and stored at 4 °C. α-Chymotrypsin from bovine pancreas was purchased from Sigma Aldrich, and a solution was made following the Sigma quality control test procedure for the enzymatic assay of chymotrypsin.

^{1}H, and ^{13}C NMR spectra were recorded using a Bruker Ascend 400 NMR spectrometer operating at 400 MHz for ^{1}H nuclei and 101 MHz for ^{13}C nuclei. Chemical shifts (δ) are quoted in parts per million (ppm) and coupling constants (*J*) are in Hertz (Hz). Residual solvent peaks were used as the internal reference for ^{1}H and ^{13}C NMR. Abbreviations for

multiplicity are as follows: s = singlet, d = doublet, t = triplet, q = quartet, m = multiplet, dd = doublet of doublet, etc.

Infrared (IR) spectra were recorded using a Nicolet iS10 spectrometer (Thermo Fisher Scientific Inc.) with the absorption peaks expressed in wavenumbers (cm^{-1}) and recorded using a range of 450 to 4000 cm^{-1}. IR spectra were analysed using OMNIC 9.2.86. High resolution mass spectrometry (HRMS) measurements were obtained using a ThermoFisher Orbitrap Exploris 240 with a Vanquish Flex UHPLC system at a nominal resolution of 5000 to 10000 as appropriate.

UV-visible spectroscopy was conducted using a Cary 100 UV-vis spectrophotometer (Agilent Technologies, model number: G9821A), equipped with a Cary temperature controller (Agilent Technologies, model number: G9844A). UV-vis spectra were recorded using Cary WinUV 4.20(468). Fluorescence measurements were recorded on a Varian Cary Eclipse Fluorescence spectrophotometer equipped with a thermostatted cell holder.

Standard TEM images were recorded on a FEI Tecnai FEG20 or a FEI Tecnai 12 with Gatan cold stages and a Gatan Ultrascan 100 4 Mpixel digital camera. DLS analyses were performed on a Malvern Zetasizer Nano-S instrument using milli-Q water and buffer solution.

5.2 Synthesis of amphiphiles for Chapter 2

5.2.1 1-Benzyl-*N*-(*tert*-butoxycarbonyl)-L-histidine hexadecyl amide (49)

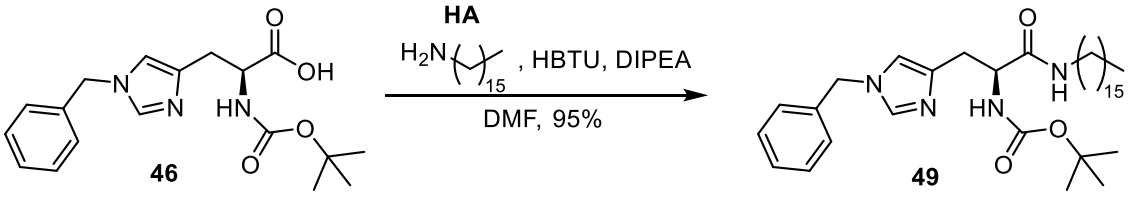

To a solution of Boc-His(Bzl)-OH (**46**) (0.500 g, 1.59 mmol) in anhydrous DMF (2 mL) was added HBTU (0.758 g, 1.91 mmol). DIPEA (1.11 mL, 6.36 mmol) was slowly added. The reaction was stirred for 15 minutes before adding hexadecylamine (**HA**) (0.461 g, 1.91 mmol). This was stirred for 24 hours at room temperature. The crude product was purified by flash chromatography on silica gel using a gradient of solvents starting with

hexanes, followed by 50% EtOAc/hexanes, and CH_2Cl_2, then finally 10% MeOH/CH_2Cl_2 was used to obtain the *title compound* (0.709 g, 1.25 mmol, 78%) as a yellow solid.

^{1}H NMR (400 MHz, CD_3OD): δ (ppm) 8.83 (s, 1H), 7.37 (s, 5H), 7.28 (s, 1H), 5.34 (s, 2H), 4.30 (s, 1H), 3.28 (s, 1H), 3.20 – 3.04 (m, 4H), 1.68 – 1.53 (m, 2H), 1.32 (s, 9H), 1.27 – 1.23 (m, 24 H), 0.86 (t, J = 6.2 Hz, 3H). **^{13}C NMR** (101 MHz, CD_3OD): δ (ppm) 172.7, 163.1, 157.4, 136.1, 135.6, 132.9, 130.3, 130.2, 129.5, 120.9, 80.8, 55.0, 53.7, 46.3, 40.5. 40.1, 33.0, 30.9, 30.8, 30.6, 30.4 (2 x CH_2), 30.3, 28.9, 28.6 (2 x CH_2), 27.9, 27.8, 23.7, 14.5. **IR** ν_{max}(film)/cm^{-1}: 2924, 2852, 1667, 1499, 1386, 1166, 1091, 837, 753, 658. **HRMS** found (ESI): MH$^+$, 569.4423, $C_{34}H_{57}N_4O_3$, 569.4425.

5.2.2 *N*-(*tert*-Butoxycarbonyl)-L-histidine hexadecyl amide (H)

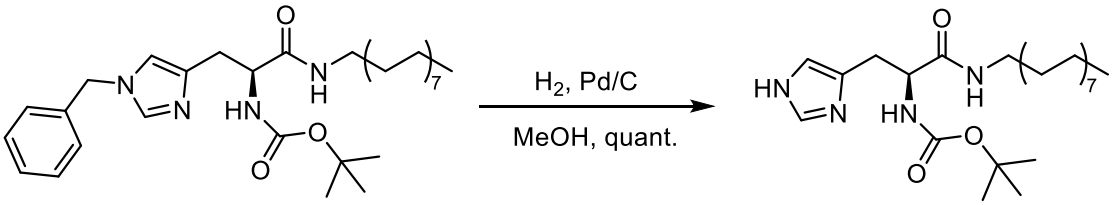

49 **H**

A solution of 1-benzyl-*N*-(*tert*-butoxycarbonyl)-L-histidine hexadecyl amide (**49**) (0.541 g, 0.951 mmol) in MeOH (40 mL) was flushed with nitrogen to keep inert atmosphere, followed by adding palladium on carbon (10 wt%, 0.050 g). The reaction was heated to 50 °C and then flushed with hydrogen for three hours. The reaction mixture was filtered through Celite® and the solvent was removed under reduced pressure to give the *title compound* (0.455 g, 0.951 mmol, quant.) as a white solid.

^{1}H NMR (400 MHz, $CDCl_3$): δ (ppm) 7.55 (s, 1H), 6.94 (s, 1H), 6.81 (s, 1H), 5.83 (s, 1H), 4.38 (s, 1H), 3.22 – 3.06 (m, 3H), 3.03 – 2.90 (m, 1H), 1.42 (s, 9H), 1.23 (d, J = 5.6 Hz, 28H), 0.87 (t, J = 6.6 Hz, 3H). **^{13}C NMR** (101 MHz, $CDCl_3$): δ (ppm) 172.0, 156.1, 135.1, 80.48, 54.1, 39.7, 32.1, 29.8 (4 x CH_2), 29.8 (3 x CH_2), 29.7, 29.7, 29.5 (2 x CH_2), 29.4, 28.9, 28.5 (2 x CH_2), 26.9, 22.8, 14.3. **IR** ν_{max}(film)/cm^{-1}: 3392, 2919, 2850, 1699, 1640, 1518, 1366, 1245, 1172, 827. **HRMS** found (ESI): MH$^+$, 479.3956, $C_{27}H_{51}N_4O_3$, 479.3956.

5.2.3 1-Benzyl-*N*-(*tert*-butoxycarbonyl)-L-histidine butyl amide (48)

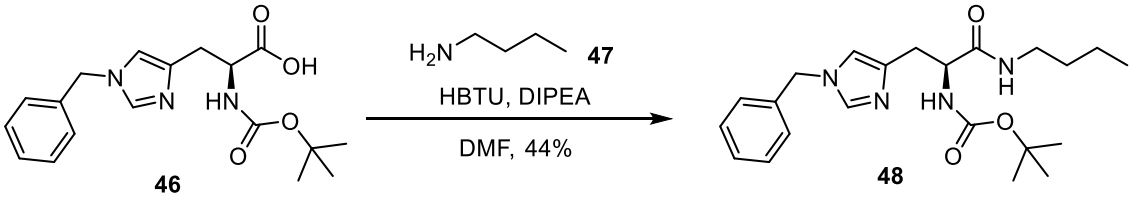

To a solution of Boc-His(Bzl)-OH (**46**) (0.100 g, 0.290 mmol) in anhydrous DMF (0.5 mL) was added HBTU (0.131 g, 0.347 mmol). DIPEA (0.201 mL, 1.16 mmol) was slowly added. The reaction was stirred for 15 minutes before adding *n*-butylamine (**47**) (0.0340 mL, 0.350 mmol). This was stirred for 24 hours at room temperature. The crude product was purified by flash chromatography on silica gel using a gradient of solvents starting with hexanes, followed by 50% EtOAc/hexanes, then CH_2Cl_2, and finally 10% MeOH/CH_2Cl_2 to obtain the *title compound* (0.0511 g, 0.128 mmol, 44%) as a yellow solid.

^{1}H NMR (400 MHz, $CDCl_3$): δ (ppm) 7.42 (s, 1H), 7.37 – 7.30 (m, 3H), 7.12 (dd, J = 7.9, 2.1 Hz, 2H), 6.80 (s, 1H), 6.72 (s, 1H), 6.28 (d, J = 6.5 Hz, 1H), 5.02 (s, 2H), 4.35 (s, 1H), 3.19 – 3.03 (m, 3H), 2.87 (dd, J = 15.3, 6.1 Hz, 1H), 1.43 (s, 9H), 1.39 – 1.29 (m, 2H), 1.29 – 1.17 (m, 2H), 0.86 (t, J = 7.3 Hz, 3H).**^{13}C NMR** (101 MHz, $CDCl_3$): δ (ppm) 171.6, 155.8, 138.8, 136.7,136.0, 129.1, 128.5, 127.5, 117.4, 54.8, 51.0, 39.1, 31.5, 31.0, 30.5, 28.5, 20.0, 13.8. **IR** ν_{max}(film)/cm^{-1}: 3305, 2960, 2930, 2872, 1656, 1497, 1365, 1246, 1164, 750. **HRMS** found (ESI): MH^+, 401.2548, $C_{22}H_{33}N_4O_3$, 401.2547. **m.p**: 82 – 84 °C.

5.2.4 *N*-(*tert*-Butoxycarbonyl)-L-histidine butyl amide (C4-H)

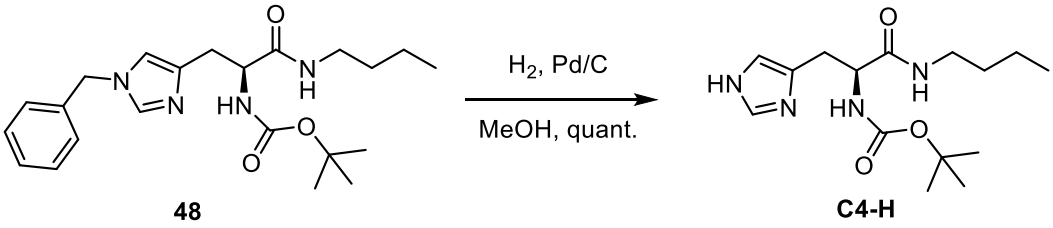

A solution of 1-benzyl-*N*-(*tert*-butoxycarbonyl)-L-histidine butyl amide (**48**) (0.141 g, 0.325 mmol) in MeOH (8 mL) was flushed with nitrogen to keep an inert atmosphere, followed by adding palladium on carbon (10 wt%). The reaction was flushed with hydrogen at 50 °C for three hours. The reaction mixture was filtered through Celite®, and

the solvent was removed under reduced pressure to give the *title compound* (0.101 g, 0.325 mmol, quant.) as a white solid.

^{1}H NMR (400 MHz, $CDCl_3$): δ (ppm) 7.53 (s, 1H), 6.87 (s, 1H), 6.81 (s, 1H), 5.84 (s, 1H), 4.37 (s, 1H), 3.24 – 3.07 (m, 3H), 2.95 (dd, J = 15.1, 6.2 Hz, 1H), 1.50 – 1.32 (m, 11H), 1.28 – 1.19 (m, 2H), 0.86 (t, J = 7.3 Hz, 3H).**^{13}C NMR** (101 MHz, $CDCl_3$): δ (ppm) 172.1, 156.1, 135.2, 80.4, 77.2, 54.3, 39.3, 31.5, 29.8*, 29.1*, 28.4, 20.0, 13.8. **IR** ν_{max}(film)/cm^{-1}: 3282, 2960, 2931, 2872, 1645, 1515, 1365, 1246, 1164, 661. **HRMS** found (ESI): MH^+, 311.2080, $C_{15}H_{27}N_4O_3$, 311.2078.

*Peaks due to the presence of rotamers.

5.2.5 *N*-[2-(1*H*-Imidazol-4-yl)ethyl]hexadecanamide (HM)

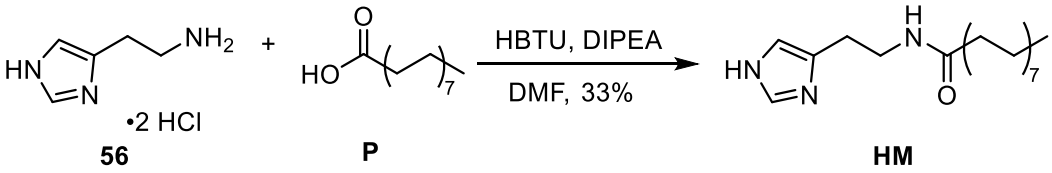

To a solution of palmitic acid (**P**) (0.230 g, 0.897 mmol) in anhydrous DMF (1 mL) was added HBTU (0.408 g, 1.08 mmol). DIPEA (0.940 mL, 5.40 mmol) was slowly added. The reaction was stirred for 15 minutes before adding histamine dihydrochloride (**56**) (0.0997 g, 0.897 mmol). This was stirred for 24 hours at room temperature. The crude product was purified by flash chromatography on silica gel using a gradient of solvents starting with hexanes, followed by 50% EtOAc/hexanes, then CH_2Cl_2, and finally 10% MeOH/CH_2Cl_2 to obtain the *title compound* (0.110 g, 0.300 mmol, 33%) as a white solid.

^{1}H NMR (400 MHz, CD_3OD): δ (ppm) 8.82 (s, 1H), 7.35 (s, 1H), 3.50 (t, J = 6.7 Hz, 2H), 2.92 (t, J = 6.7 Hz, 2H), 2.18 (t, J = 7.6 Hz, 2H), 1.64 – 1.50 (m, 2H), 1.36 – 1.21 (m, 24H), 0.90 (t, J = 6.8 Hz, 3H) **^{13}C NMR** (101 MHz, CD_3OD): δ (ppm) 176.7, 134.9, 132.8, 117.6, 39.0, 36.9, 34.8, 33.0, 30.7, 30.7, 30.6, 30.5, 30.4, 30.4, 30.3, 30.3, 30.2, 27.0, 26.0, 25.8, 23.7, 14.4. **IR** ν_{max}(film)/cm^{-1}: 3325, 2955, 2914, 2849, 1732, 1643, 1552, 1467, 1246, 720. **HRMS** found (ESI): MH^+, 364.33, $C_{22}H_{42}N_3O$, 364.32. **m.p**: 110 – 112 °C

5.2.6 *N,N'*-Bis(*tert*-butoxycarbonyl)-*N''*-hexadecylguanidine (53)

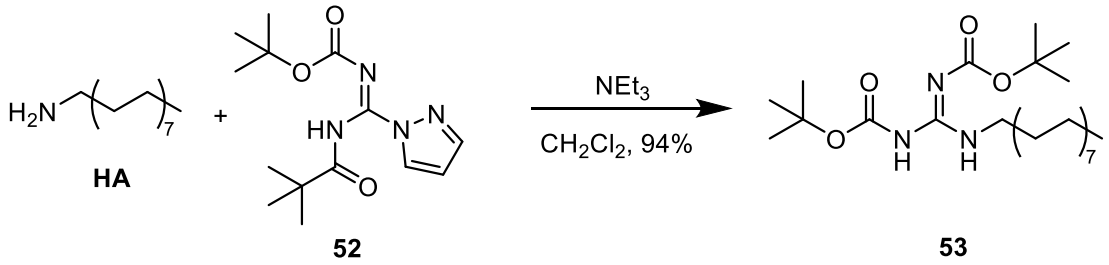

To a solution of *N,N'*-bis-Boc-1-guanylpyrazole (**52**)(1.54 g, 4.97 mmol) in anhydrous CH_2Cl_2 (15 mL) was added hexadecylamine (**HA**) (1.00 g, 4.14 mmol) and triethylamine (0.58 mL, 4.1 mmol). The reaction was stirred at room temperature for 24 hours. Water (20 mL) was then added, and the reaction was stirred for a further 30 minutes. Product was extracted with CH_2Cl_2 (3 x 20 mL) and dried over $MgSO_4$. The compound was purified using flash chromatography on silica gel with 10% EtOAc/hexanes to give the title compound (1.88 g, 4.12 mmol, 94%) as a white solid.

^{1}H NMR (400 MHz, $CDCl_3$): δ (ppm) 11.50 (s, 1H), 8.29 (s, 1H), 3.43 (m, 2H), 1.59-1.53 (m, 2H), 1.50 (s, 9H), 1.49 (s, 9H), 1.29-1.21 (m, 26H). **^{13}C NMR** (101 MHz, $CDCl_3$): δ (ppm) 163.8, 156.2, 153.5, 83.1, 79.3, 41.1, 32.1, 29.8, 29.8, 29.8, 29.7, 29.6, 29.5, 29.4, 29.1, 28.5, 28.2, 27.0, 22.8, 14.3.

The NMR data reported above are in line with literature data previously published by the research group.[78]

5.2.7 1-Hexadecylguanidinium chloride (G)

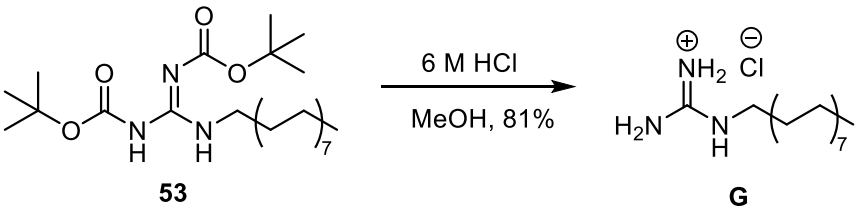

To a solution of *N,N*'-bis(*tert*-butoxycarbonyl)-*N*''-hexadecylguanidine (**53**) (0.050 g, 0.10 mmol) in MeOH (3 mL) was added 6 M HCl (10 mL). The reaction was refluxed at 60 °C for three hours. The solvent was then removed *in vacuo* to give the title compound (0.026 g, 0.081 mmol, 81%) as a white solid.

^{1}H NMR (400 MHz, CD_3OD) 3.17 (t, J = 7.1 Hz, 2H), 1.64-1.54 (m, 2H), 1.41-1.24 (m, 26H), 0.89 (t, J = 7.0 Hz, 3H). **^{13}C NMR** (101 MHz, CD_3OD) 158.6, 42.5, 33.1, 30.8 (4 x CH_2), 30.8 (2 x CH_2), 30.7, 30.7, 30.5, 30.3, 29.9, 27.7, 23.7, 14.5.

The NMR data reported above is in line with literature data previously published by the research group.[78]

5.2.8 Hexadecyl bis(2-pyridylmethyl)amine (D2PA)

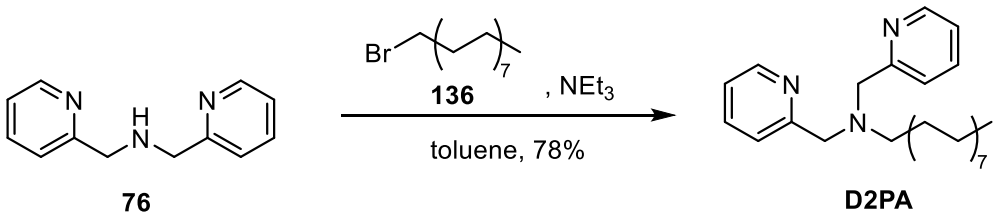

76 **D2PA**

To a solution of di-(2-picolyl)amine (**76**) (0.156 g, 0.786 mmol) in toluene (7 mL) was added 1-bromohexadecane (**136**) (0.200 g, 0.655 mmol), and NEt_3 (0.272 mL, 1.97 mmol). The reaction was refluxed for three days. The toluene was removed *in vacuo,* and the product was extracted into $CHCl_3$ (3 x 15 mL) and washed with water (3 x 15 mL), before being dried over $MgSO_4$. Flash chromatography on silica gel was used to purify the product. $CHCl_3$ was initially used as the eluent until the first band was eluted, then a MeOH/$CHCl_3$ eluent system was used with varying polarity from 2% to 4% MeOH. This gave the title compound (0.209 g, 0.510 mmol, 78%) as a brown oil.

^{1}H NMR (400 MHz, $CDCl_3$): δ (ppm) 8.51 (d, J = 4.7 Hz, 2H), 7.65 (t, J = 7.6 Hz, 2H), 7.54 (d, J = 7.7 Hz, 2H), 7.13 (t, J = 5.8 Hz, 2H), 3.81 (s, 4H), 2.53 (t, J = 7.3 Hz, 2H), 1.53 (quintet, J = 6.8 Hz, 2H), 1.15 – 1.32 (m, 26H), 0.87 (t, J = 6.6 Hz, 3H). **^{13}C NMR** (101 MHz, $CDCl_3$): δ (ppm) 160.2, 149.1, 136.4, 123.0, 121.9, 60.6, 54.7, 32.0, 29.8, 29.8, 29.8, 29.6, 29.5, 27.5, 22.8, 14.2. **IR** ν_{max}(film)/cm^{-1}: 2918, 2849, 2810, 1589, 1567, 1469, 1433, 1092, 779, 756. **HRMS** found (ESI): MNa^+, 446.3496, $C_{28}H_{45}N_3Na$, 446.3506.

Note that 6 fewer signals are observed on the ^{13}C NMR than expected for the molecule due to the signals corresponding to the carbons in the long hydrophobic chain overlapping.

The ^{1}H NMR data matches that previously reported in the literature.[159,160]

5.3 General procedure for UV experiments in Chapter 2

The kinetic UV experiments were conducted as follows:

Water was added to the cuvette, followed by the buffer. The catalytic amphiphiles were then added sequentially. If Zn^{2+} was used in the system, this was then added and the cuvette was mixed. This was placed in the UV and allowed 5 minutes to warm to 40 °C. The substrate PNPB was then added, and the cuvette was mixed again before being placed back in the UV to begin recording measurements. The UV recorded the absorbance at 405 nm every 0.6 minutes for a total of 40 minutes.

The wavescan UV experiments were conducted as follows:

Water was added to the cuvette, followed by the buffer. PV was added and the wavescan run. Zn^{2+} was then added, mixed and the wavescan run. A known concentration of surfactant was then added to the cuvette, mixed and another wavescan was run. This process could be repeated until the total concentration of surfactant was ~200 μM.

The stock solutions for these experiments were:

[HEPES, pH = 7.0] = 100 mM in milli-Q water, [**H**] = 20 mM in MeOH, [**P**] = 20 mM in MeOH, [**B**] = 20 mM in MeOH, [**G**] = 20 mM in milli-Q water, [**HM**] = 20 mM in MeOH, [**HA**] = 20 mM in MeOH, [**CTAB**] = 20 mM in milli-Q water, [**PNPB**] = 50 mM in DMSO, [$Zn(NO_3)_2$] = 20 mM in milli-Q water, [PV] = 20 mM in milli-Q water, [**TACN**] = 20 mM in milli-Q water, [**D2PA**] = 20 mM in MeOH, [Tris, pH = 7.8] = 100 mM in milli-Q water, [α-chymotrypsin] = 2 μM in 1 mM HCl.

5.4 General procedure for CAC determining experiments in Chapters 2 and 3

The fluorescent experiments were conducted as follows:

Water was added to the cuvette, followed by the buffer. The substrate PNPB was added, followed by the fluorescent probe. This was then mixed, and the initial fluorescent measurement was run. A known concentration of surfactant was then added to the cuvette, mixed and another fluorescent measurement was run. This process could be repeated until the total concentration of surfactant was ~500 μM. Measurements on the fluorimeter were

recorded using an excitation wavelength of 350 nm, recording the emission value at 450 nm for the fluorescent probe DPH.

The stock solutions for these experiments were:

[HEPES, pH = 7.0] = 100 mM in milli-Q water, [**PNPB**] = 50 mM in DMSO, [DPH] = 1 mM in THF, [$Zn(NO_3)_2$] = 20 mM in milli-Q water, [**H**] = 20 mM in MeOH, [**G**] = 20 mM in milli-Q water, [**C6-HM-SH**] = 20 mM in MeOH, [**HM-SH**] = 20 mM in MeOH

5.5 Synthesis of thiols for Chapter 3

5.5.1 Methyl 6-bromohexanoate (63)

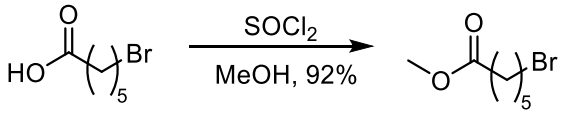

62 **63**

A solution of 6-bromohexanoic acid (**62**) (2.00 g, 10.3 mmol) in anhydrous MeOH (15 mL) was cooled on ice. $SOCl_2$ (1.12 mL, 15.4 mmol) was then added dropwise. This was allowed to warm to room temperature and stirred for 24 hours. The reaction was evaporated in vacuo, MeOH was added, and the mixture was evaporated *in vacuo* three times to give the title compound (1.98 g, 9.47 mmol, 92%) as a colourless oil.

^{1}H NMR (400 MHz, $CDCl_3$): δ (ppm) 3.66 (s, 3H), 3.40 (t, J = 6.6 Hz, 2H), 2.32 (t, J = 7.2 Hz, 2H), 1.87 (quint, J = 7.1 Hz, 2H), 1.65 (quint, J = 7.2 Hz, 2H), 1.52-1.41 (m, 2H).**^{13}C NMR** (101 MHz, $CDCl_3$): δ (ppm) 173.9, 51.6, 33.8, 33.4, 32.4, 27.7, 24.1.

The NMR data match what was previously reported in the literature.[161–163]

5.5.2 Methyl 6-(tritylthio)hexanoate (65)

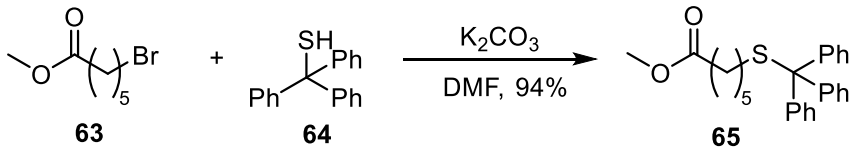

63 **64** **65**

To a solution of methyl 6-bromohexanoate (**63**) (0.468 g, 2.23 mmol) in anhydrous DMF (1 mL) was added triphenylmethanethiol (**64**) (0.616 g, 2.23 mmol), and K_2CO_3 (0.462 g, 3.35 mmol). The reaction mixture was stirred at room temperature for 24 hours. 1 M

HCl (15 mL) was added, and the product was extracted with CH_2Cl_2 (3 x 15 mL). This was dried over $MgSO_4$ and purified via flash chromatography on silica gel using 2% EtOAc/hexanes to give the *title compound* (0.850 g, 2.10 mmol, 94%) as a white solid.

^{1}H NMR (400 MHz, $CDCl_3$): δ (ppm) 7.44 – 7.38 (m, 6H), 7.32 – 7.24 (m, 6H), 7.23 – 7.17 (m, 3H), 3.64 (s, 3H), 2.21 (t, J = 7.5 Hz, 2H), 2.14 (t, J = 7.3 Hz, 2H), 1.49 (quint, J = 7.5 Hz, 2H), 1.43 – 1.34 (m, 2H), 1.32 – 1.21 (m, 2H). **^{13}C NMR** (101 MHz, $CDCl_3$): δ (ppm) 174.2, 145.1, 129.7, 128.0, 126.7, 66.6, 51.6, 34.0, 31.9, 28.6, 28.4, 24.6. **IR** ν_{max}(film)/cm^{-1}: 2954, 2938, 2854, 1739, 1591, 1439, 1265, 1163, 697. **HRMS** found (ESI): MNa^+, 427.1701, $C_{26}H_{28}O_2S$, 427.17022.

5.5.3 6-(Tritylthio)hexanoic acid (66)

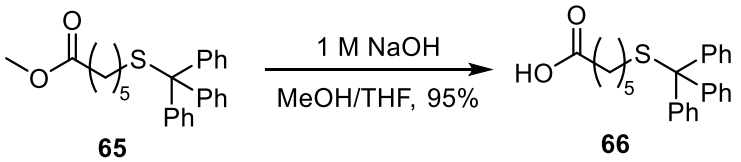

65 66

To a solution of methyl 6-(tritylthio)hexanoate (**65**) (0.482 g, 1.19 mmol) in a 1:1 mixture of MeOH and THF (10 mL) was added 1 M NaOH (5 mL). The reaction mixture was stirred at 60 °C for 1 hour. THF was evaporated *in vacuo* prior to the workup. 1 M HCl (10 mL) was added to the solution. The product was extracted into CH_2Cl_2 (3 x 10 mL) and dried over $MgSO_4$ to give the title compound (0.440 g, 1.13 mmol, 95%) as a white solid.

^{1}H NMR (400 MHz, $CDCl_3$): δ (ppm) 7.44 – 7.37 (m, 6H), 7.31 – 7.24 (m, 6H), 7.24 – 7.17 (m, 3H), 2.25 (t, J = 7.2 Hz, 2H), 2.14 (t, J = 7.1 Hz, 2H), 1.54 – 1.44 (m, 2H), 1.44 – 1.33 (m, 2H), 1.33 – 1.23 (m, 2H). **^{13}C NMR** (101 MHz, $CDCl_3$): δ (ppm) 179.4, 145.1, 129.7, 128.0, 126.7, 66.6, 33.9, 31.9, 28.5, 28.4, 24.4.

The NMR data matches that which has been previously reported in the literature.[164]

5.5.4 *N*-[2-(1*H*-Imidazol-4-yl)ethyl]-6-(tritylthio)hexanamide (67)

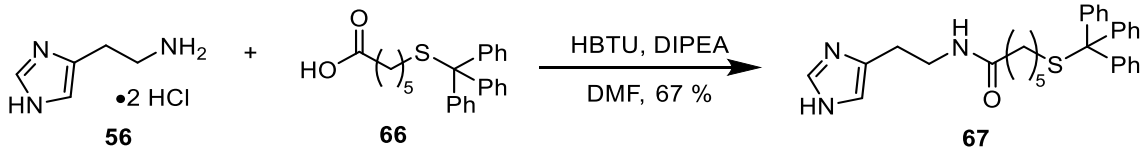

56 **66** **67**

To a solution of 6-(tritylthio)hexanoic acid (**66**) (0.440 g, 1.13 mmol) in anhydrous DMF (2 mL) was added HBTU (0.510 g, 1.35 mmol). DIPEA (1.2 mL, 6.8 mmol) was slowly added. The reaction was stirred for 15 minutes before adding histamine dihydrochloride (**56**) (0.125 g, 1.13 mmol). This was stirred at room temperature for 24 hours. Reaction was then purified via flash chromatography on alumina gel using 10% MeOH/CH_2Cl_2 to give the *title compound* (0.37 g, 0.76 mmol, 67%) as a white solid.

^{1}H NMR (400 MHz, CD_3OD): δ (ppm) 7.74 (s, 1H), 7.40 – 7.35 (m, 6H), 7.30 – 7.23 (m, 6H), 7.23 – 7.17 (m, 3H), 6.89 (s, 1H), 3.40 (t, J = 7.2 Hz, 2H), 2.77 (t, J = 7.2 Hz, 2H), 2.13 (t, J = 7.3 Hz, 2H), 2.07 (t, J = 7.4 Hz, 2H), 1.48 – 1.39 (m, 2H), 1.39 – 1.31 (m, 2H), 1.26 – 1.17 (m, 2H). **^{13}C NMR** (101 MHz, CD_3OD): δ (ppm) 176.0, 146.4, 136.0, 131.3, 128.8, 127.7, 118.0, 67.6, 40.2, 36.8, 32.8, 29.5, 29.4, 27.7, 26.5. **IR** ν_{max}(film)/cm^{-1}:3018, 2924, 2896, 1634, 1575, 1489, 1454, 1274, 985, 837, 698. **HRMS** found (ESI): MH^+, 484.2418, $C_{30}H_{34}ON_3S$, 484.24171. **m.p:** 146 – 148 °C

5.5.5 *N*-[2-(1*H*-Imidazol-4-yl)ethyl]-6-mercaptohexanamide (C6-HM-SH)

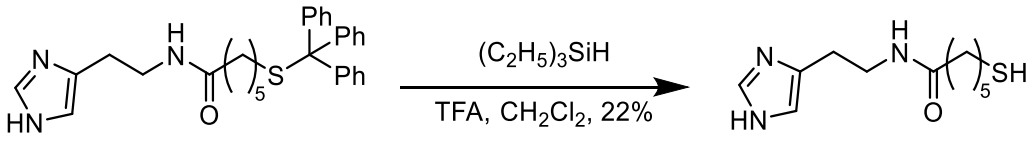

67 **C6-HM-SH**

A solution of *N*-[2-(1*H*-imidazol-4-yl)ethyl]-6-(tritylthio)hexanamide (**67**) (0.10 g, 0.21 mmol) in anhydrous CH_2Cl_2 (2 mL) and cooled on ice. TFA (2 mL) was added followed by triethylsilane (0.033 mL, 0.21 mmol). This was stirred for 1 hour, after which CH_2Cl_2 (5 mL) was added and the product was extracted into H_2O. The aqueous layer was evaporated to dryness. The product was purified via flash chromatography on alumina gel using 5% MeOH/CH_2Cl_2 to give the *title compound* (0.071 g, 0.20 mmol, 97%) as a white solid.

^{1}H NMR (400 MHz, CD_3OD): δ (ppm) 7.62 (s, 1H), 6.86 (s, 1H), 3.42 (t, J = 7.2 Hz, 2H), 2.77 (t, J = 7.2 Hz, 2H), 2.68 (t, J = 7.2 Hz, 2H), 2.17 (t, J = 7.4 Hz, 2H), 1.74 – 1.64 (m, 2H), 1.64 – 1.54 (m, 2H), 1.44 – 1.34 (m, 2H). **^{13}C NMR** (101 MHz, CD_3OD): δ (ppm) 176.1, 136.0, 135.8, 118.0, 40.2, 39.4, 36.9, 29.9, 28.9, 27.7, 26.6. **IR** ν_{max}(film)/cm^{-1}: 2930, 2858, 1628, 1549, 1434, 1198, 1129, 830, 719. **HRMS** found (ESI): MH^+, 242.1321, $C_{11}H_{20}ON_3S$, 242.13216.

5.5.6 2-[6-[(Tritylthio)]hexyl]-1*H*-isoindole-1,3(2*H*)-dione (71)

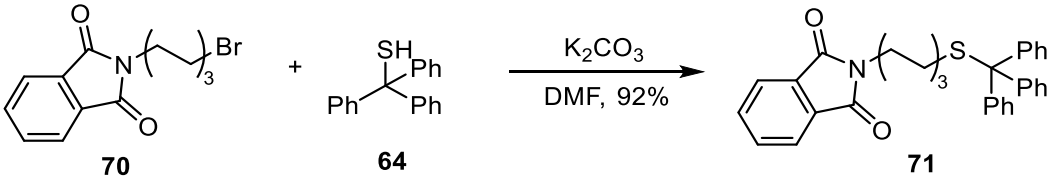

To a solution of *N*-(6-bromohexyl)phthalimide (**70**) (1.23 g, 3.98 mmol) in anhydrous DMF (7 mL) was added triphenylmethanethiol (**64**) (1.00 g, 3.62 mmol) and K_2CO_3 (0.750 g, 5.43 mmol). The reaction mixture was stirred at room temperature for 24 hours. Reaction was neutralised with 1 M HCl (20 mL), product extracted with CH_2Cl_2 (3 x 20 mL) and dried over $MgSO_4$. The crude was purified using flash chromatography on silica gel with a gradient of solvents starting with hexanes and increasing to 10% EtOAc/hexanes to give the title compound (1.68 g, 3.32 mmol, 92%) as a white solid.

^{1}H NMR (400 MHz, $CDCl_3$): δ (ppm) 7.86 – 7.80 (m, 2H), 7.74 – 7.67 (m, 2H), 7.45 – 7.37 (m, 6H), 7.31 – 7.23 (m, 6H), 7.23 – 7.16 (m, 3H), 3.62 (t, J = 7.3 Hz, 2H), 2.12 (t, J = 7.2 Hz, 2H), 1.64 – 1.54 (m, 2H), 1.42 – 1.33 (m, 2H), 1.32 – 1.25 (m, 2H), 1.24 – 1.15 (m, 2H). **^{13}C NMR** (101 MHz, $CDCl_3$): δ (ppm) 168.6, 145.2, 134.0, 132.3, 129.7, 127.9, 126.6, 123.3, 66.6, 38.05, 32.0, 28.6, 28.5, 27.9, 26.5.

The NMR data matches that pervious reported in the literature.[121]

5.5.7 6-(Tritylthio)hexan-1-amine (72)

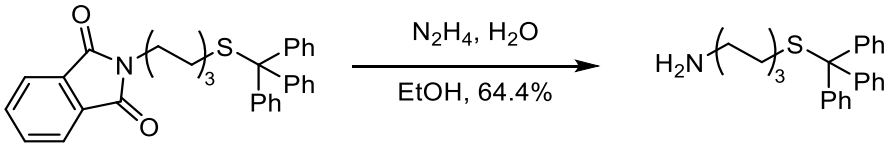

71 72

To a solution of 2-[6-[(tyritylthio)]hexyl]-1*H*-isoindole-1,3(2*H*)-dione (**71**) (0.600 g, 1.19 mmol) in EtOH (8 mL) was added hydrazine monohydrate (0.416 g, 8.31 mmol). The reaction mixture was refluxed for 24 hours. EtOH was then evaporated *in vacuo*. Water (15 mL) was added, and CH_2Cl_2 (3 x 10 mL) was used to extract the product. This was dried over $MgSO_4$. The crude was purified via flash chromatography on silica gel using 10% MeOH/CH_2Cl_2 + 1% NEt_3 to give the title compound (0.290 g, 0.772 mmol, 64%) as a white solid.

^{1}H NMR (400 MHz, $CDCl_3$): δ (ppm) 7.43 – 7.39 (m, 6H), 7.30 – 7.23 (m, 6H), 7.22 – 7.16 (m, 3H), 2.65 (t, J = 7.2 Hz, 2H), 2.13 (t, J = 7.3 Hz, 2H), 1.46 – 1.34 (m, 4H), 1.30 – 1.15 (m, 4H). **^{13}C NMR** (101 MHz, $CDCl_3$): δ (ppm) 145.1, 129.7, 127.9, 127.9, 126.6, 66.5, 41.9, 33.0, 32.0, 28.8, 28.6, 26.5.

There are slight discrepancies in the ^{1}H NMR compared with the literature. However, the ^{13}C NMR matches perfectly.[121]

5.5.8 *N*,*N*'Bis(tert-butoxylcarbonyl)-*N*''-6-(tritylthio)hexylguanidine (73)

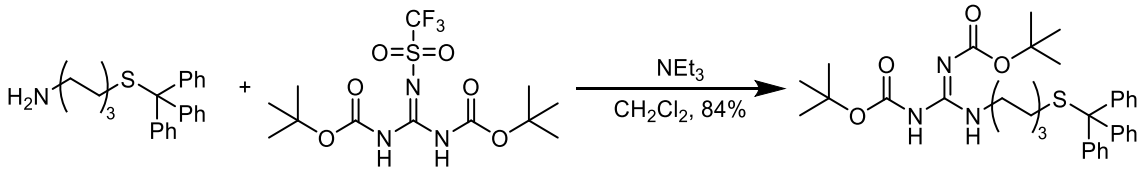

72 55 73

To a solution of 6-(tritylthio)hexan-1-amine (**72**) (0.290 g, 0.772 mmol) in anhydrous CH_2Cl_2 (7 mL) was added 1,3-di-Boc-2-(trifluoromethyl sulfonyl) guanidine (**55**) (0.362 g, 0.926 mmol) and NEt_3 (0.12 mL, 0.77 mmol). The reaction mixture was stirred at room temperature for 24 hours. Water (10 mL) was then added to the reaction and allowed to stir for 30 minutes. The product was then extracted with CH_2Cl_2 (3 x 10 mL) and dried over $MgSO_4$. Flash chromatography on silica gel using 10% EtOAc/hexanes gave the title compound (0.400 g, 0.647 mmol, 84%) as a white solid.

^{1}H NMR (400 MHz, $CDCl_3$): δ (ppm) 11.50 (s, 1H), 8.26 (s, 1H), 7.43 – 7.37 (m, 6H), 7.30 – 7.24 (m, 6H), 7.23 – 7.17 (m, 3H), 3.34 (q, J = 6.6 Hz, 2H), 2.13 (t, J = 7.3 Hz, 2H), 1.50 (s, 9H), 1.49 (s, 9H), 1.48 – 1.42 (m, 2H), 1.42 – 1.32 (m, 2H), 1.30 – 1.17 (m, 4H). **^{13}C NMR** (101 MHz, $CDCl_3$): δ (ppm) 156.2, 153.4, 145.2, 129.7, 127.9, 126.6, 83.2, 79.4, 66.6, 41.0, 32.0, 28.9, 28.7, 28.6, 28.4, 28.2, 26.5. **IR** ν_{max}(film)/cm^{-1}:3333, 2976, 2929, 2856, 1717, 1636, 1328, 1128, 1050, 698. **HRMS** found (ESI): MH^+, 618.3351, $C_{36}H_{48}O_4N_3S$, 618.33600.

5.5.9 *N*-(6-Mercaptohexyl)guanidine (C6-G-SH)

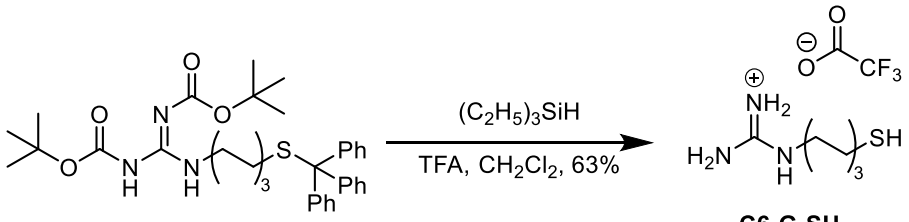

73 **C6-G-SH**

A solution of *N,N*'-Bis(*tert*-butoxylcarbonyl)-*N*''-6-(tritylthio)hexylguanidine (**73**) (0.10 g, 0.16 mmol) in anhydrous CH_2Cl_2 (2 mL) was cooled on ice. TFA (2 mL) was added, followed by triethylsilane (0.026 mL, 0.16 mmol). This was stirred for 1 hour, after which CH_2Cl_2 (10 mL) was added and the product extracted in water (3 x 10 mL). The compound was purified using C_{18}-reverse phase silica gel and 40% MeOH/H_2O to give the *title compound* (0.018 g, 0.10 mmol, 63%) as a colourless oil.

^{1}H NMR (400 MHz, D_2O): δ (ppm) 3.18 (t, J = 6.9 Hz, 2H), 2.55 (t, J = 7.2 Hz, 2H), 1.65 – 1.55 (m, 4H), 1.45 – 1.31 (m, 4H). **^{13}C NMR** (101 MHz, D_2O): δ (ppm) 156.7, 41.0, 32.8, 27.7, 26.9, 25.2, 23.6. **IR** ν_{max}(film)/cm^{-1}: 3288, 2939, 2862, 2344, 1661, 1615, 1181, 1135. **HRMS** found (ESI): MH^+, 176.1216, $C_7H_{18}N_3S$, 176.12159.

5.5.10 1-(Bis(pyridine-2-yl)methyl-6-(tritylthio)hexanamine (77)

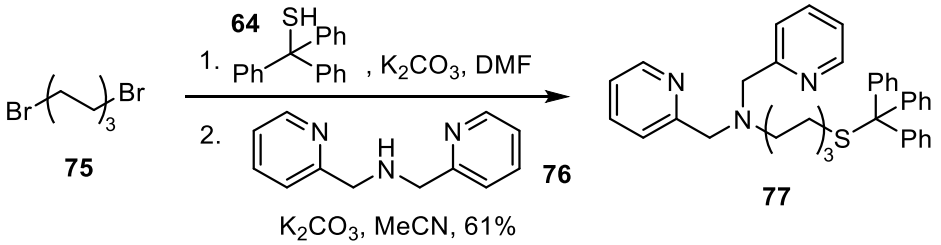

To a solution of 1,6-dibromohexane (**75**) (1.77 g, 7.24 mmol) in anhydrous DMF (0.8 mL) was added triphenylmethanethiol (**64**) (1.00 g, 3.62 mmol) and K_2CO_3 (0.750 g, 5.43 mmol). The reaction mixture was stirred at room temperature for 24 hours. 1 M HCl (10 mL) was added to the reaction mixture, and the product was extracted with CH_2Cl_2 (3 x 15 mL) and dried over $MgSO_4$. The crude product (1.28 g) was then used in the next step without further purification.

To a solution of crude product (1.28 g) in anhydrous MeCN (7 mL) was added di-(2-picolyl)amine (**76**) (0.386 mL, 1.94 mmol) and K_2CO_3 (0.804 g, 5.82 mmol). The reaction mixture was refluxed for 24 hours. 1 M HCl (10 mL) was added to the reaction mixture. Product was extracted with CH_2Cl_2 (3 x 15 mL) and dried over $MgSO_4$. Flash chromatography on silica gel using CH_2Cl_2 to remove impurities then increasing to 10% MeOH/CH_2Cl_2 to give the *title compound* (0.663 g, 1.18 mmol, 61%) as a brown oil.

*Note: yield has been calculated using the amount of di-(2-picolyl)amine (**76**).

^{1}H NMR (400 MHz, $CDCl_3$): δ (ppm) 8.52 (d, J = 4.7 Hz, 2H), 7.64 (t, J = 7.6 Hz, 2H), 7.57 (d, J = 7.7 Hz, 2H), 7.41 – 7.37 (m, 6H), 7.28 – 7.24 (m, 6H), 7.22 – 7.13 (m, 5H), 3.94 (s, 4H), 2.61 (s, 2H), 2.09 (t, J = 7.3 Hz, 2H), 1.55 – 1.48 (m, 2H), 1.38 – 1.30 (m, 2H), 1.19 – 1.10 (m, 4H).**^{13}C NMR** (101 MHz, $CDCl_3$): δ (ppm) 149.2, 145.1, 136.7, 129.7, 127.9, 126.6, 123.5, 122.4, 66.5, 60.1, 54.2, 32.0, 28.8, 28.6, 26.8. **IR** ν_{max}(film)/cm^{-1}:3054, 2927, 2853, 1589, 1487, 1433, 1033, 995, 741, 698. **HRMS** found (ESI): MH^+, 558.2933, $C_{37}H_{40}N_3S$, 558.29375.

5.5.11 1-(Bis(pyridin-2-ylmethyl)amino)hexane-6-thiol (C6-D2PA-SH)

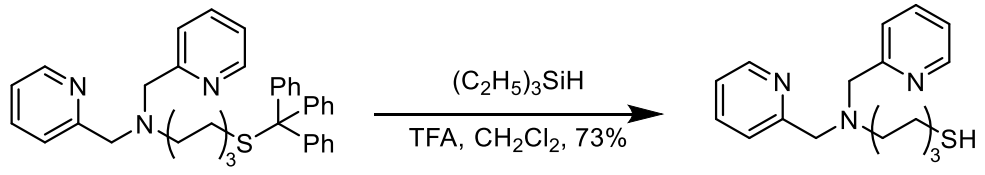

77 **C6-D2PA-SH**

A solution of 1-(bis(pyridine-2-yl)methyl-6-(tritylthio)hexanamine (**77**) (0.050 g, 0.090 mmol) in anhydrous CH_2Cl_2 (1 mL) was cooled on ice. TFA (1 mL) was added, followed by triethylsilane (0.014 mL, 0.090 mmol). This was stirred for 1 hour, after which the solvent was removed *in vacuo*. The product was purified via flash chromatography on alumina gel using CH_2Cl_2 to remove the impurity and 10% MeOH/CH_2Cl_2 to give the title compound (0.020 g, 0.063 mmol, 73%) as a brown oil.

^{1}H NMR (400 MHz, $CDCl_3$): δ (ppm) 8.52 (d, J = 4.1 Hz, 2H), 7.64 (td, J = 7.6, 1.8 Hz, 2H), 7.52 (d, J = 7.8 Hz, 2H), 7.13 (dd, J = 7.4, 4.8 Hz, 2H), 3.80 (s, 4H), 2.56 – 2.42 (m, 4H), 1.59 – 1.48 (m, 4H), 1.33 – 1.21 (m, 4H). **^{13}C NMR** (101 MHz, $CDCl_3$): δ (ppm) 159.4, 149.1, 136.6, 123.3, 122.2, 60.4, 54.4, 39.1, 29.8, 29.2, 28.4, 27.0, 26.8. **IR** ν_{max}(film)/cm^{-1}: 2925, 2853, 1667, 1590, 1569, 1472, 1433, 757. **HRMS** found (ESI): MH^+, 629.3455, $C_{36}H_{49}N_6S_2$, 629.34546.

Note: the dimer was observed in the HRMS.

The NMR data matches that previously reported in the literature.[122]

5.5.12 14-(Tritylthio)tetradecane-1-ol (79)

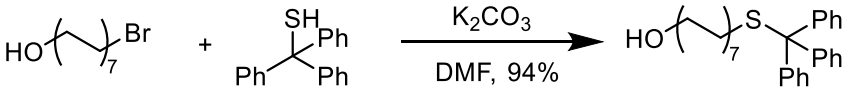

78 **64** **79**

To a solution of 14-bromotetradecan-1-ol (**78**) (0.500 g, 1.70 mmol) in anhydrous DMF (5 mL) was added triphenylmethanethiol (**64**) (0.565 g, 2.05 mmol) and K_2CO_3 (0.352 g, 2.55 mmol). The reaction mixture was stirred at room temperature for 24 hours. 1 M HCl (20 mL) was added to the reaction. The product was extracted using CH_2Cl_2 (3 x 20 mL) and dried over $MgSO_4$. Flash chromatography on silica gel using 20% EtOAc/hexanes gave the *title compound* (0.777 g, 1.59 mmol, 94%) as a white solid.

^{1}H NMR (400 MHz, $CDCl_3$): δ (ppm) 7.46 – 7.38 (m, 6H), 7.30 – 7.25 (m, 6H), 7.24 – 7.17 (m, 3H), 3.64 (t, J = 6.6 Hz, 2H), 2.13 (t, J = 7.3 Hz, 2H), 1.60 – 1.52 (m, 2H), 1.43 – 1.10 (m, 22H). **^{13}C NMR** (101 MHz, $CDCl_3$): δ (ppm) 145.2, 130.3, 127.9, 126.6, 66.5, 63.3, 33.0, 32.2, 29.8 (4 x CH_2), 29.7, 29.6 (2 x CH_2), 29.3, 29.2, 28.7, 25.9. **IR** ν_{max}(film)/cm^{-1}: 3345, 3062, 2918, 2849, 1594, 1441, 1181, 1035, 740, 698. **HRMS** found (ESI): MH^+, 511.3005, $C_{33}H_{44}ONaS$, 511.30051.

5.5.13 14-Mercapto-1-tetradecanol (OH-SH)

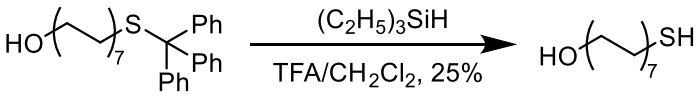

79 **OH-SH**

A solution of 14-(tritylthio)tetradecane-1-ol (**79**) (50 mg, 0.102 mmol) in anhydrous CH_2Cl_2 (1 mL) was cooled on ice. TFA (1 mL) was added, followed by triethylsilane (0.016 mL, 0.102 mmol). The reaction was stirred for 35 minutes. Flash chromatography was used to purify the compound on silica gel using 20% EtOAc/petroleum ether to obtain the title compound (6.3 mg, 0.026 mmol, 25%) as a white solid.

^{1}H NMR (400 MHz, $CDCl_3$): δ (ppm) 3.64 (t, J = 6.7 Hz, 2H), 2.52 (dd, J = 7.5, 7.3 Hz, 2H), 1.64-1.52 (m, 4H), 1.37-1.25 (m, 20H).**^{13}C NMR** (101 MHz, $CDCl_3$): δ (ppm) 63.2, 34.2, 33.0, 29.8 (3 x CH_2), 29.7 (2 x CH_2), 29.7, 29.6, 29.2, 28.5, 25.9, 24.8. **IR** ν_{max}(film)/cm^{-1}: 3272, 2917, 2848, 1472, 1461, 1260, 1070, 1023, 802, 731. **HRMS** found (ESI): M^-, 245.1943, $C_{14}H_{29}OS$, 245.19336.

The ^{1}H NMR data match that previously reported in the literature.[126]

5.5.14 *N,N*-Diethyl-14-(tritylthio)-1-tetradecanamine (82)

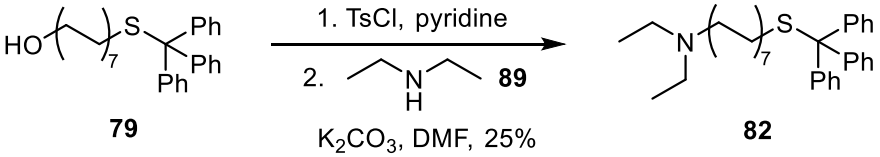

79 **82**

To a solution of 14-(tritylthio)tetradecane-1-ol (**79**) (0.500 g, 1.02 mmol) in anhydrous pyridine (10 mL) was added 4-toluenesulfonyl chloride (1.95 g, 10.2 mmol). The reaction mixture was stirred for one hour at room temperature. CH_2Cl_2 (20 mL) was added to the reaction and washed with 3% $CuSO_4$ (3 x 20 mL). This was dried over $MgSO_4$ and

evaporated *in vacuo* to give the crude tosyl product, which was then used without further purification in the next step.

To a solution of crude tosyl in anhydrous DMF (5 mL) was added diethylamine (**89**) (0.116 mL, 1.12 mmol) and K_2CO_3 (0.141 g, 1.02 mmol) were added. The reaction was stirred at room temperature for seven days. Ice water (15 mL) was added to the reaction mixture, and CH_2Cl_2 (3 x 15 mL) was used to extract the product. This was dried over Na_2SO_4. Flash chromatography on alumina gel using 5% EtOAc/petroleum ether gave the *title compound* (0.139 g, 0.256 mmol, 25%) as a colourless oil.

*Note: yield has been calculated using the amount of 14-(tritylthio)tetradecane-1-ol (**79**).

^{1}H NMR (400 MHz, $CDCl_3$): δ (ppm) 7.43 – 7.39 (m, 6H), 7.29 – 7.24 (m, 6H), 7.22 - 7.17 (m, 3H), 2.52 (q, J = 7.2 Hz, 4H), 2.44 – 2.37 (m, 2H), 2.13 (t, J = 7.4 Hz), 1.49 – 1.33 (m, 4H), 1.29 – 1.09 (m, 20H), 1.02 (t, J = 7.2 **^{13}C NMR** (101 MHz, $CDCl_3$): δ (ppm) 145.2, 129.8, 127.9, 126.6, 66.5, 53.1, 47.0, 32.2, 29.8 (4 x CH_2), 29.7, 29.7, 29.6, 29.3, 29.2, 28.7, 27.9, 27.0, 11.8. **IR** ν_{max}(film)/cm^{-1}: 2922, 2851, 1595, 1489, 1444, 1369, 1201, 1081, 764, 697. **HRMS** found (ESI): MH^+, 544.3972, $C_{37}H_{54}NS$, 544.39715.

5.5.15 *N,N*-Diethyl-14-mercapto-1-tetradecanamine (DEA-SH)

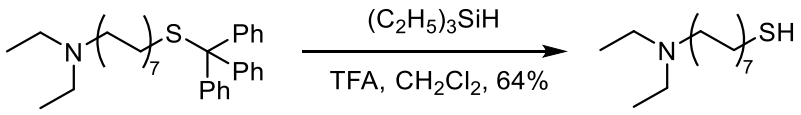

82 **DEA-SH**

A solution of *N,N*-diethyl-14-(tritylthio)-1-tetradecanamine (**82**) (0.077 g, 0.14 mmol) in anhydrous CH_2Cl_2 (2 mL) was cooled on ice. TFA (2 mL) was added, followed by triethylsilane (0.023 mL, 0.14 mmol). This was stirred for one hour. The solvent was then removed *in vacuo*. Flash chromatography on alumina gel using 50% EtOAc/petroleum ether gave the *title compound* (0.038 g, 0.091 mmol, 64%) as a colourless oil.

^{1}H NMR (400 MHz, $CDCl_3$): δ (ppm) 2.57 – 2.48 (m, 4H), 2.44 – 2.36 (m, 2H), 1.66 – 1.56 (m, 2H), 1.48 – 1.20 (m, 24H), 1.02 (td, J = 7.2, 2.8 Hz, 6H). **^{13}C NMR** (101 MHz, $CDCl_3$): δ (ppm) 52.2, 46.8, 34.9, 30.7, 30.0, 29.7, 29.7, 29.7, 29.6, 29.5, 29.4, 29.2, 27.5, 25.2, 23.6, 10.4. **IR** ν_{max}(film)/cm^{-1}: 2967, 2922, 2852, 2798, 1465, 1382, 1202, 1069, 721. **HRMS** found (ESI): MH_2^{2+}, 301.2799, $C_{36}H_{78}N_2S_2$, 301.27977.

Note: the dimer is observed in the HRMS as the title compound does not ionise well.

5.5.16 1-(Bis(pyridine-2-yl)methyl-14-(tritylthio)tetradecanamine (81)

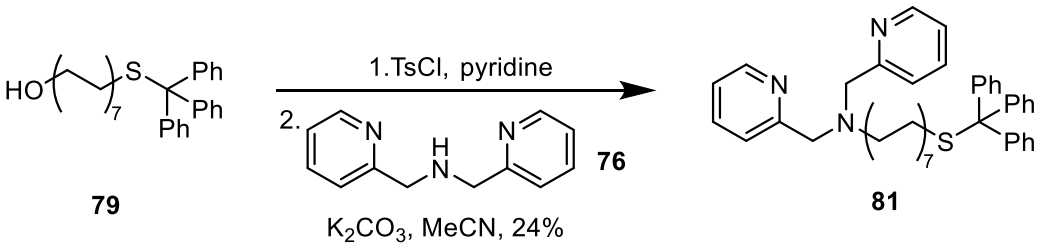

To a solution of 14-(tritylthio)tetradecane-1-ol (**79**) (1.15 g, 2.35 mmol) in anhydrous pyridine (10 mL) was added 4-toluenesulfonyl chloride (4.48 g, 23.5 mmol). The reaction mixture was stirred at room temperature for one hour. CH_2Cl_2 (20 mL) was added to the reaction and washed with 3% $CuSO_4$ (3 x 30 mL). This was dried over $MgSO_4$. The crude tosyl product was then used without further purification in the next step.

To a solution of crude tosyl product in anhydrous MeCN (10 mL) was added di-(2-picolyl)amine (**76**) (0.313 g, 1.57 mmol) and K_2CO_3 (0.6496 g, 4.70 mmol). The reaction was refluxed for 20 hours. 1 M HCl (15 mL) was added, and the product was extracted into CH_2Cl_2 (3 x 20 mL) before being dried over $MgSO_4$. Flash chromatography on alumina gel initially using CH_2Cl_2, followed by 5% MeOH/CH_2Cl_2 gave the *title compound* (0.3818 g, 0.570 mmol, 24%) as a brown oil.

*Note: yield has been calculated using the amount of 14-(tritylthio)tetradecane-1-ol (**79**).

^{1}H NMR (400 MHz, $CDCl_3$): δ (ppm) 8.51 (d, J = 4.7 Hz, 2H), 7.63 (t, J = 7.6 Hz, 2H), 7.54 (d, J = 7.8 Hz, 2H), 7.42 – 7.39 (m, 6H), 7.29 – 7.25 (m, 6H), 7.22 - 7.17 (m, 3H), 7.15 – 7.10 (m, 2H), 3.80 (s, 4H), 2.52 (t, J = 7.3 Hz, 2H), 2.13 (t, J = 7.3 Hz, 2H), 1.57 – 1.48 (m, 2H), 1.43 – 1.33 (m, 2H), 1.25 – 1.13 (m, 20H). **^{13}C NMR** (101 MHz, $CDCl_3$): δ (ppm) 160.4, 149.1, 145.2, 136.4, 129.8, 127.9, 126.6, 122.9, 121.9, 66.5, 60.7, 54.7, 32.2, 29.8 (3 x CH_2), 29.7, 29.6, 29.6, 29.3, 29.2, 28.7, 27.5, 27.3. **IR** ν_{max}(film)/cm^{-1}: 3056, 2922, 2851, 1589, 1468, 1433, 1034, 742, 698. **HRMS** found (ESI): MH^+, 670.4191, $C_{45}H_{56}N_3S$, 670.41895.

5.5.17 1-(Bis(pyridin-2-ylmethyl)amino)tetradecane-14-thiol (D2PA-SH)

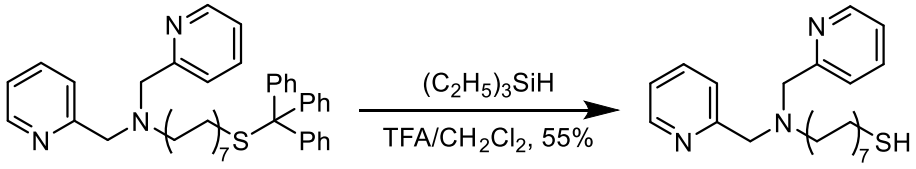

81 **D2PA-SH**

A solution of 1-(bis(pyridine-2-yl)methyl-14-(tritylthio)tetradecanamine (**81**) (0.060 g, 0.090 mmol) in anhydrous CH_2Cl_2 (1 mL) was cooled on ice. TFA (1 mL) was added, followed by triethylsilane (0.014 mL, 0.090 mmol). The reaction was stirred for 45 minutes. Flash chromatography was used to purify the compound on alumina gel, running initially in CH_2Cl_2 then increasing to 2% MeOH/CH_2Cl_2 to obtain the *title compound* (0.021 g, 0.049 mmol, 55%) as an orange oil.

^{1}H NMR (400 MHz, CD_3OD): δ (ppm) 8.43 (d, J = 5.0 Hz, 2H), 7.80 (t, J = 7.9 Hz, 2H), 7.64 (d, J = 7.9 Hz, 2H), 7.31 – 7.24 (m, 2H), 3.78 (s, 4H), 2.68 (t, J = 7.3 Hz, 1H), 2.54 – 2.45 (m, 3H), 1.72 – 1.63 (m, 1H), 1.63 – 1.54 (m, 1H), 1.54 – 1.47 (m, 2H), 1.43 – 1.36 (m, 2H), 1.34 – 1.17 (m, 18H). **^{13}C NMR** (101 MHz, CD_3OD): δ (ppm) 161.0, 149.3, 138.6, 124.9, 124.8, 123.7, 61.3, 55.7, 39.9, 35.2, 30.7, 30.7, 30.6, 30.6, 30.5, 30.3, 30.2, 29.4, 28.3, 28.0, 25.0. **IR** ν_{max}(film)/cm^{-1}: 2922, 2851, 1589, 1465, 1433, 1362, 1147, 1046, 995, 756. **HRMS** found (ESI): M^+, 427.3009, $C_{26}H_{41}N_3S$, 427.30157.

5.5.18 14-Bromotetradecanoic acid (87)

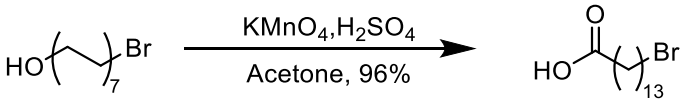

78 **87**

A solution of $KMnO_4$ (0.404 g, 2.56 mmol) in water (1 mL) was cooled on ice. Concentrated H_2SO_4 (0.182 mL, 3.40 mmol) was added, followed by more water (4 mL) and stirred for 5 minutes. A solution of 14-bromotetradecan-1-ol (**78**) (0.500 g, 1.70 mmol) in acetone (10 mL) was added dropwise. Reaction was stirred at 0 °C for 2 hours, warmed to room temperature and stirred for a further 20 hours. Water (10 mL) was added, and the product was extracted with CH_2Cl_2 (3 x 15 mL). This was dried over $MgSO_4$ and evaporated *in vacuo* to give the title compound (0.500 g, 1.63 mmol, 96%) as a white solid.

^{1}H NMR (400 MHz, $CDCl_3$): δ (ppm) 3.41 (t, J = 6.7 Hz, 2H), 2.35 (t, J = 7.4 Hz, 2H), 1.89 – 1.80 (m, 2H), 1.67 – 1.58 (m, 2H), 1.46 – 1.37 (m, 2H), 1.36 – 1.23 (m, 16H). **^{13}C NMR** (101 MHz, $CDCl_3$): δ (ppm) 178.3, 34.2, 33.9, 33.0, 29.7, 29.7, 29.7, 29.6, 29.6, 29.4, 29.2, 28.9, 28.3, 24.8. **IR** ν_{max}(film)/cm^{-1}: 2916, 2850, 1694, 1472, 1214, 914, 716. **HRMS** found (ESI): MH^+, 307.1269, $C_{14}H_{28}O_2{}^{79}Br$, 307.12672.

The characterisation data is in agreement with literature values.[165]

5.5.19 Methyl 14-bromotetradecanoate (90)

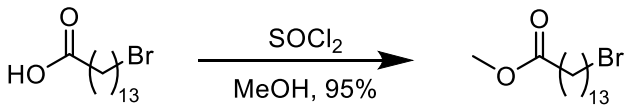

87 **90**

A solution of 14-bromotetradecanoic acid (**87**) (0.176 g, 0.572 mmol) in anhydrous MeOH (5 mL) was cooled on ice. Thionyl chloride (0.062 mL, 0.858 mmol) was added dropwise and the reaction was stirred at room temperature for 24 hours. Reaction was evaporated *in vacuo*, MeOH was added and evaporated *in vacuo* three times to give the *title compound* (0.174 g, 0.540 mmol, 95%) as a yellow oil.

^{1}H NMR (400 MHz, $CDCl_3$): δ (ppm) 3.66 (s, 3H), 3.41 (t, J = 6.88 Hz, 2H), 2.30 (t, J = 7.56 Hz, 2H), 1.90 – 1.81 (m, 2H), 1.66 – 1.59 (m, 2H), 1.46 – 1.37 (m, 2H), 1.32 – 1.24 (m, 16H). **^{13}C NMR** (101 MHz, $CDCl_3$): δ (ppm) 174.5, 51.6, 34.3, 34.2, 33.0, 29.7, 29.7, 29.7, 29.6 (2 x CH_2), 29.4, 29.3, 28.9, 28.3, 25.1. **IR** ν_{max}(film)/cm^{-1}: 2922, 2852, 1738, 1463, 1436, 1250, 1196, 1169, 722. **HRMS** found (ESI): MH^+, 321.1424, $C_{15}H_{30}O_2{}^{79}Br$, 321.14237.

5.5.20 Methyl 14-(tritylthio)tetradecanoate (91)

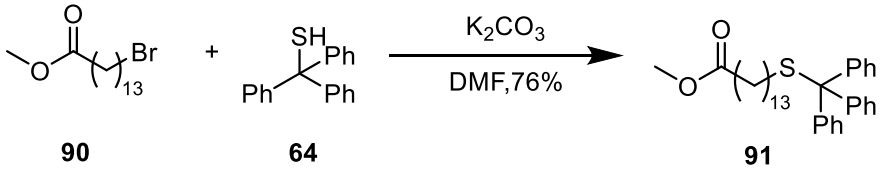

90 **64** **91**

To a solution of methyl 14-bromotetradecanoate (**90**) (2.15 g, 6.69 mmol) in DMF was added triphenylmethanethiol (**64**) (2.22 g, 8.03 mmol) and K_2CO_3 (1.39 g, 10.0 mmol). The reaction mixture was stirred at room temperature for 24 hours. 1 M HCl (20 mL) was added to the reaction, and CH_2Cl_2 (3 x 20 mL) was used to extract the product. The

organic phase was dried over $MgSO_4$. Flash chromatography on silica gel initially using 2% diethyl ether/hexanes to remove the initial impurities, followed by 5% diethyl ether/hexanes to get the *title compound* (2.63 g, 5.07 mmol, 76%) as a white solid.

^{1}H NMR (400 MHz, $CDCl_3$): δ (ppm) 7.47 – 7.38 (m, 6H), 7.30 – 7.24 (m, 6H), 7.24 – 7.17 (m, 3H), 3.66 (s, 3H), 2.30 (t, J = 7.6 Hz, 2H), 2.13 (t, J = 7.4 Hz, 2H), 1.68 – 1.57 (m, 2H), 1.43 – 1.33 (m, 2H), 1.31 – 1.11 (m, 18H). **^{13}C NMR** (101 MHz, $CDCl_3$): δ (ppm) 174.5, 145.2, 129.8, 127.9, 126.6, 66.5, 51.6, 34.3, 32.2, 29.7, 29.7, 29.7, 29.6, 29.6, 29.4, 29.3, 29.3, 29.2, 28.7, 25.1. **IR** ν_{max}(film)/cm^{-1}: 2918, 2849, 1742, 1439, 1166, 740, 698. **HRMS** found (ESI): MNa^+, 539.2954, $C_{34}H_{44}O_2NaS$, 539.29542.

5.5.21 14-(Tritylthio)tetradecanoic acid (88)

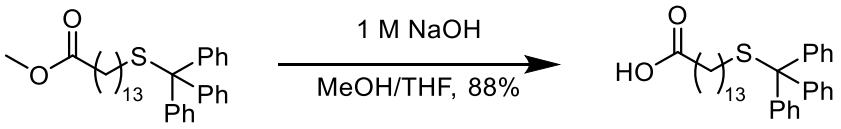

91 **88**

To a solution of methyl 14-(tritylthio)tetradecanoate (**91**) (1.00 g, 1.94 mmol) in a 1:1 mixture of MeOH and THF (30 mL) was added 1 M NaOH (15 mL). The reaction was stirred at 60 °C for three hours. THF was evaporated *in vacuo* prior to the workup. 1 M HCl (20 mL) was added, the product was extracted into CH_2Cl_2 (3 x 20 mL) and dried over $MgSO_4$ to give the *title compound* (0.839 g, 1.71 mmol, 88%) as a yellow oil.

^{1}H NMR (400 MHz, $CDCl_3$): δ (ppm) 7.43-7.37 (m, 6H), 7.29-7.23 (m, 6H), 7.22-7.16 (m, 3H), 2.37-2.24 (m, 2H), 2.12 (t, J = 7.3 Hz, 2H), 1.68-1.53 (m, 2H), 1.42-1.07 (m, 20H). **^{13}C NMR** (101 MHz, $CDCl_3$): δ (ppm) 145.2, 129.7, 127.9, 126.6, 66.5, 32.2, 29.8, 29.7 (4 x CH_2), 29.6 (2 x CH_2), 29.6, 29.5, 29.4 (2 x CH_2), 29.2, 28.7. **IR** ν_{max}(film)/cm^{-1}: 2923, 2852, 1706, 1489, 1443, 1216, 1034, 908, 741, 697. **HRMS** found (ESI): MNa^+, 525.2789, $C_{33}H_{42}O_2NaS$, 525.27977.

5.5.22 Methyl 14-(acetylthio)tetradecanoate (93)

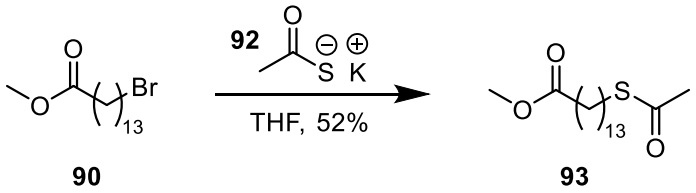

90 **93**

To a solution of methyl 14-bromotetradecanoate (**90**) (0.193 g, 0.601 mmol) in anhydrous THF (10 mL) was added potassium thioacetate (**92**) (0.206 g, 1.80 mmol). The reaction was refluxed at 70 °C for 24 hours. The solvent was then removed *in vacuo*. CH_2Cl_2 (20 mL) was added to the reaction and washed with water (3 x 30 mL). This was dried over Na_2SO_4. Flash chromatography on silica gel using 2% EtOAc/petroleum ether gave the *title compound* (0.0986 g, 0.314 mmol, 52%) as a yellow solid.

^{1}H NMR (400 MHz, $CDCl_3$): δ (ppm) 3.66 (s, 3H), 2.86 (t, J = 7.3 Hz, 2H), 2.34 – 2.27 (m, 5H), 1.65 – 1.51 (m, 4H), 1.38 – 1.22 (m, 18H). **^{13}C NMR** (101 MHz, $CDCl_3$): δ (ppm) 196.2, 174.5, 51.6, 34.2, 30.8, 29.7 (2 x CH_2), 29.7, 29.6, 29.6, 29.6, 29.4, 29.3 (2 x CH_2), 29.2, 28.9, 25.1. **IR** ν_{max}(film)/cm^{-1}: 2916, 2849, 1735, 1689, 1467, 1169, 1113, 955, 720. **HRMS** found (ESI): MH^+, 303.1989, $C_{16}H_{31}O_3S$, 303.19884.

5.5.23 14-Mercaptotetradecanoic acid (Acid-SH)

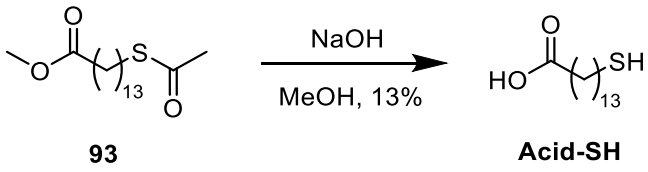

93 **Acid-SH**

A solution of methyl 14-(acetylthio)tetradecanoate (**93**) (0.10 g, 0.32 mmol) in anhydrous MeOH (8 mL) was cooled on ice. 2 M NaOH (0.95 mL, 1.9 mmol) was added dropwise to the solution. The reaction was then warmed to room temperature and stirred for 24 hours. The solvent was removed *in vacuo*. Water (10 mL) was added to the reaction flask. The solution was then acidified to pH 1 using 1 M HCl. EtOAc (3 x 15 mL) was used to extract the product. This was then dried over Na_2SO_4. Flash chromatography on silica gel using 8% MeOH/CH_2Cl_2 gave the title compound (0.011 g, 0.042 mmol, 13%) as a white solid.

^{1}H NMR (400 MHz, $CDCl_3$): δ (ppm) 2.68 (t, J = 7.3 Hz, 2H), 2.35 (t, J = 7.4 Hz, 2H), 1.71 – 1.59 (m, 4H), 1.40 – 1.24 (m, 18H). **^{13}C NMR** (101 MHz, $CDCl_3$): δ (ppm) 179.8,

39.5, 34.1, 29.9, 29.7, 29.6 (2 x CH_2), 29.6, 29.4 (2 x CH_2), 29.3, 29.0, 28.6, 24.8. **IR** ν_{max}(film)/cm^{-1}: 2915, 2848, 1690, 1471, 1218, 946, 718. **HRMS** found (ESI): MH^-, 517.3389, $C_{28}H_{53}O_4S_2$, 517.33798.

Note: the dimer is observed in the HRMS as the title compound doesn't ionise well.

The ^{1}H NMR data is in line with that previously reported in the literature.[131]

5.5.24 14-(Tritylthio)-1-azotetradecane (83)

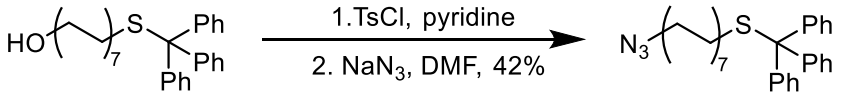

79 **83**

To a solution of 14-(tritylthio)tetradecane-1-ol (**79**) (1.15 g, 2.35 mmol) in anhydrous pyridine (10 mL) was added 4-toluenesulfonyl chloride (4.48 g, 23.5 mmol). The reaction mixture was stirred at room temperature for one hour. CH_2Cl_2 (20 mL) was added to the reaction and washed with 3% $CuSO_4$ (3 x 20 mL). This was dried over $MgSO_4$ and evaporated *in vacuo* to give the crude tosyl product, which was then used without further purification in the next step.

To a solution of crude tosyl product in anhydrous DMF (5 mL) was added sodium azide (0.458 g, 7.05 mmol). The reaction was stirred at room temperature for 24 hours. Ice water (15 mL) was added to the reaction. The product was then extracted into CH_2Cl_2 (3 x 10 mL) before being dried over $MgSO_4$. Flash chromatography on silica gel using 2% EtOAc/petroleum ether gave the *title compound* (0.5104 g, 0.993 mmol, 42%) as a white solid.

*Note: yield has been calculated using the amount of 14-(tritylthio)tetradecane-1-ol (**79**).

^{1}H NMR (400 MHz, $CDCl_3$): δ (ppm) 7.47 – 7.36 (m, 6H), 7.33 – 7.23 (m, 6H), 7.23 – 7.15 (m, 3H), 3.25 (t, J = 7.0 Hz, 2H), 2.13 (t, J = 7.4 Hz, 2H), 1.63 – 1.53 (m, 2H), 1.43 – 1.33 (m, 4H), 1.33 – 1.09 (m, 18 H). **^{13}C NMR** (101 MHz, $CDCl_3$): δ (ppm) 145.2, 129.7, 127.9, 126.6, 66.5, 51.6, 32.2, 29.7 (2 x CH_2), 29.7 (2 x CH_2), 29.6, 29.5, 29.3, 29.3, 29.2, 29.0, 28.7, 26.9. **IR** ν_{max}(film)/cm^{-1}: 2917, 2850, 2091, 1485, 1468, 1440, 1261, 1180, 1034, 742, 698. **HRMS** found (ESI): MNa^+, 536.3071, $C_{33}H_{43}N_3NaS$, 536.30699. **m.p**. 87 – 89 °C.

5.5.25 14-(Tritylthio)-1-tetradecanamine (84)

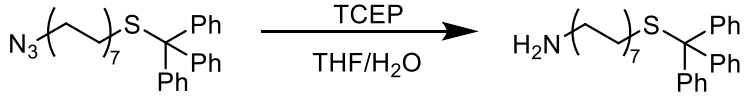

83 **84**

To a solution of 14-(tritylthio)-1-azotetradecane (**83**) (0.510 g, 0.993 mmol) in a 1:1 mixture of THF and water (8 mL) was added TCEP (1.14 g, 3.97 mmol). The reaction mixture was stirred at room temperature for 24 hours. A second addition of TCEP (1.14 g, 3.97 mmol) was required, followed by a further 24 hours of stirring. The THF was then evaporated *in vacuo* before the product was extracted with CH_2Cl_2 (20 mL) and washed with brine (3 x 15 mL). This was dried over $MgSO_4$ and evaporated *in vacuo.* The crude compound was used in the next step without further purification.

5.5.26 Methyl 2-(1*H*-imidazol-4-yl)acetate hydrochloride (97)

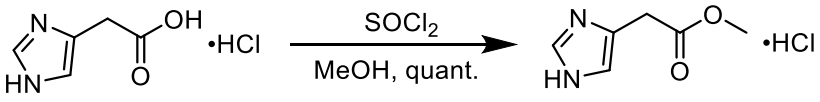

94 **97**

A solution of 4-imidazole acetic acid hydrochloride (**94**) (0.500 g, 3.08 mmol) in anhydrous MeOH (10 mL) was cooled on ice. $SOCl_2$ (1.12 mL, 15.4 mmol) was added dropwise. The reaction was then warmed to room temperature and left to stir for 24 hours. Reaction was evaporated *in vacuo*, MeOH was added and evaporated *in vacuo* three times to give the title compound (0.544 g, 3.08 mmol, quant.) as a white solid.

^{1}H NMR (400 MHz, CD_3OD): δ (ppm) 8.88 (s, 1H), 7.47 (s, 1H), 3.91 (s, 2H), 3.76 (s, 3H) **^{13}C NMR** (101 MHz, CD_3OD): δ (ppm) 170.6, 135.3, 128.3, 119.0, 53.1, 30.6. **IR** ν_{max}(film)/cm^{-1}: 3123, 2939, 2725, 2597, 1735, 1623, 1365, 1181, 852, 792. **HRMS** found (ESI): MH^+, 141.0658, $C_6H_9O_2N_2$, 141.06585. **m.p**. 120 – 122 °C

The ^{1}H NMR data match that previously reported in the literature.[166]

5.5.27 Methyl 2-(1-trityl-1*H*-imidazol-4-yl)acetate (98)

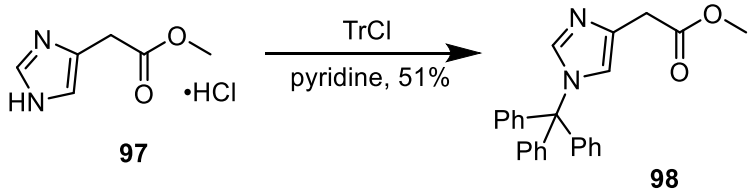

To a solution of methyl 2-(1*H*-imidazol-4-yl)acetate hydrochloride (**97**) (0.544 g, 3.08 mmol) in anhydrous pyridine (3 mL) was added trityl chloride (1.03 g, 3.70 mmol). The reaction mixture was stirred at room temperature for 20 hours. Saturated ammonium chloride (20 mL) was added, and CH_2Cl_2 (3 x 20 mL) was used to extract the product. This was dried over $MgSO_4$ before being purified using flash chromatography on silica gel using 50% EtOAc/hexanes to give the title compound (0.600 g, 1.57 mmol, 51%) as a white solid.

^{1}H NMR (400 MHz, $CDCl_3$): δ (ppm) 7.37 (d, J = 1.39 Hz, 1H), 7.36 – 7.30 (m, 10H), 7.17 – 7.11 (m, 5H), 6.78 – 6.76 (m, 1H), 3.96 (s, 3H), 3.62 (s, 2H). **^{13}C NMR** (101 MHz, $CDCl_3$): δ (ppm) 171.8, 142.6, 138.7, 134.0, 129.9, 128.2, 119.9, 75.5, 52.1, 34.6. **IR** ν_{max}(film)/cm^{-1}: 2917, 2849, 1746, 1490, 1201, 1158, 1127, 978, 764, 703. **HRMS** found (ESI): MH^+, 383.1753, $C_{25}H_{23}O_2N_2$, 383.17540. **m.p**. 134 – 136 °C.

The NMR data matches that previously reported in the literature.[167]

5.5.28 2-(1-Trityl-1*H*-imidazol-4-yl)acetic acid (96)

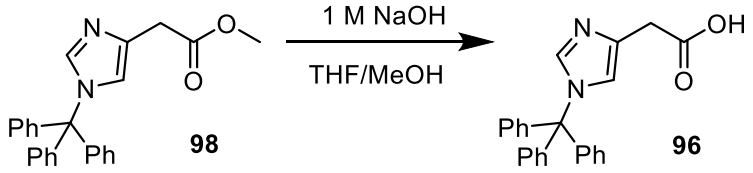

To a solution of methyl 2-(1-trityl-1*H*-imidazol-4-yl)acetate (**98**) (0.231 g, 0.604 mmol) in a 1:1 mixture of THF and MeOH (4 mL) was added 1 M NaOH (2 mL) was added. The reaction was stirred at 60 °C for one hour. THF was evaporated prior to the workup. 1 M HCl (10 mL) was added to the reaction mixture, the product was extracted with CH_2Cl_2 (3 x 10 mL) and dried over $MgSO_4$. The crude compound was used in the next step without purification.

5.5.29 *N*-[2-(1*H*-Imidazol-4-yl)ethyl]-14-(tritylthio)tetradecanamide (99)

56 **88** **99**

To a solution of methyl 14-(tritylthio)tetradecanoic acid (**88**) (0.056 g, 0.11 mmol) in anhydrous DMF (1 mL) was added HBTU (0.051 g, 0.13 mmol). DIPEA (0.12 mL, 0.67 mmol) was slowly added, and the reaction was stirred for 15 minutes. Histamine dihydrochloride (**56**) (0.012 g, 0.11 mmol) was added, and the reaction was stirred at room temperature for 24 hours. The crude product was then purified via flash chromatography on alumina gel using 2% MeOH/CH_2Cl_2 to remove initial impurities, followed by 5% MeOH/CH_2Cl_2 to give the *title compound* (0.020 g, 0.034 mmol, 31%) as a white solid.

^{1}H NMR (400 MHz, $CDCl_3$): δ (ppm) 7.56 (s, 1H), 7.46 – 7.38 (m, 6H), 7.31 – 7.24 (m, 6H), 7.23 – 7.17 (m, 3H), 6.81 (s, 1H), 6.35 (s, 1H), 3.54 (q, J = 6.2 Hz, 2H), 2.81 (t, J = 6.5 Hz, 2H), 2.20 – 2.10 (m, 4H), 1.64 – 1.54 (m, 2H), 1.43 – 1.34 (m, 2H), 1.30 – 1.11 (m, 18H). **^{13}C NMR** (101 MHz, $CDCl_3$): δ (ppm) 173.8, 145.2 (2 x CH), 134.9, 130.3, 129.7, 127.9, 126.6, 66.5, 39.3, 37.0, 32.2, 29.7 (2 x CH_2), 29.7, 29.6, 29.5, 29.5, 29.4, 29.3, 29.1, 28.7, 27.1, 25.9. **IR** ν_{max}(film)/cm^{-1}: 3054, 2921, 2850, 1636, 1573, 1444, 1256, 1090, 982, 740, 697. **HRMS** found (ESI): MH^+, 596.3669, $C_{38}H_{50}ON_3S$, 596.36691.

5.5.30 *N*-[2-(1*H*-Imidazol-4-yl)ethyl]-14-mercaptotetradecanamide (HM-SH)

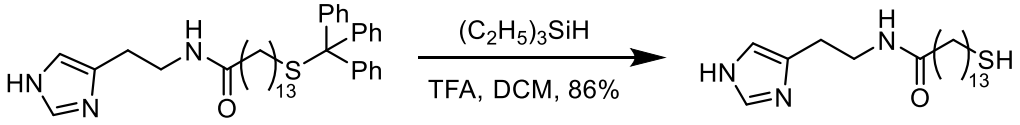

99 **HM-SH**

A solution of *N*-[2-(1H-imidazol-4-yl)ethyl]-14-(tritylthio)tetradecanamide (**99**) (0.04 g, 0.067 mmol) in anhydrous CH_2Cl_2 (1 mL) was cooled on ice. TFA (1 mL) was added, followed by triethylsilane (0.012 mL, 0.067 mmol). This was stirred for 1 hour, after which the solvent was removed *in vacuo*. The crude product was purified via flash chromatography on alumina gel using CH_2Cl_2 to remove initial impurities and 5% MeOH/CH_2Cl_2 to give the *title compound* (0.011 g, 0.046 mmol, 86%) as a white solid.

^{1}H NMR (400 MHz, CD_3OD): δ (ppm) 7.59 (s, 1H), 6.84 (s, 1H), 3.41 (t, J = 7.2 Hz, 2H), 2.77 (t, J = 7.1 Hz, 2H), 2.49 (t, J = 7.2 Hz, 2H), 2.15 (t, J = 7.4 Hz, 2H), 1.65 – 1.52 (m, 4H), 1.43 – 1.35 (m, 2H), 1.34 – 1.25 (m, 16H). **^{13}C NMR** (101 MHz, $CDCl_3$): δ (ppm) 176.3, 136.0, 135.9, 118.0, 40.3, 37.1, 35.2, 30.7 (2 x CH_2), 30.7, 30.6, 30.4, 30.3, 30.2, 29.4, 27.8, 27.0, 25.0. **IR** ν_{max}(film)/cm^{-1}: 3137, 2915, 2849, 1636, 1575, 1455, 1091, 986, 834. **HRMS** found (ESI): M^+, 353.2490, $C_{19}H_{35}N_3OS$, 353.24953.

5.5.31 *N,N'*-Bis(*tert*-butoxycarbonyl)-*N''*-14-(tritylthio)tetradecylguanidine (85)

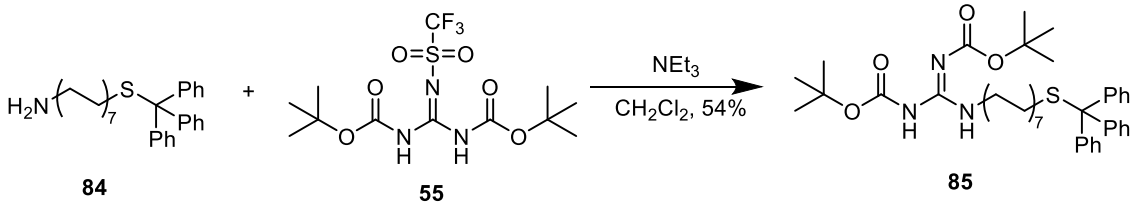

To a solution of crude 14-(tritylthio)-1-tetradecanamine (**84**) (0.220 g, 0.451 mmol) in anhydrous CH_2Cl_2 (5 mL) was added 1,3-di-Boc-2-(trifluromethyl sulfonyl) guanidine (**55**) (0.211 g, 0.542 mmol) and NEt_3 (0.063 mL, 0.45 mmol). The reaction was stirred at room temperature for 24 hours. Water (10 mL) was added, and the reaction was stirred for 10 minutes before being extracted with CH_2Cl_2. This was dried over $MgSO_4$. Flash chromatography on silica gel was used to purify the crude product with a solvent system of 5% EtOAc/hexanes, to give the *title compound* (0.117 g, 0.160 mmol, 54%) as a yellow oil.

^{1}H NMR (400 MHz, $CDCl_3$): δ (ppm) 11.51 (s, 1H), 8.34 (s, 1H), 7.44 – 7.38 (m, 6H), 7.32 – 7.23 (m, 6H), 7.22 – 7.17 (m, 3H), 3.46 – 3.37 (m, 2H), 2.13 (t, J = 7.5 Hz, 2H), 1.61 – 1.53 (m, 2H), 1.51 (s, 9H), 1.49 (s, 9H), 1.43 – 1.10 (m, 22H). **^{13}C NMR** (101 MHz, $CDCl_3$): δ (ppm) 163.8, 156.2, 153.5, 145.2, 129.8, 127.9, 126.6, 83.1, 79.3, 66.5, 41.1, 32.2, 29.8, 29.7, 29.6, 29.6, 29.4, 29.3, 29.2, 29.1, 28.7, 28.5, 28.2. **IR** ν_{max}(film)/cm^{-1}: 3333, 2923, 2852, 1718, 1637, 1366, 1329, 1129, 1052, 698. **HRMS** found (ESI): MH^+, 730.4606, $C_{44}H_{64}O_4N_3S$, 730.46120.

5.5.32 *S*-(14-Hydroxytetradecyl) ethanethioate (100)

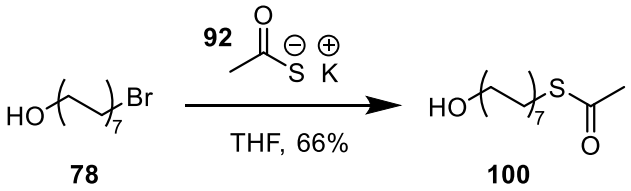

To a solution of 14-bromotetradecan-1-ol (**78**) (0.200 g, 0.682 mmol) in anhydrous THF (10 mL) was added potassium thioacetate (**92**) (0.234 g, 2.05 mmol). The reaction was refluxed at 70 °C for 24 hours. The solvent was then removed *in vacuo*. CH_2Cl_2 (20 mL) was added to the reaction flask to dissolve the product. This was then washed with water (3 x 30 mL) before being dried over Na_2SO_4. Flash chromatography on silica gel using 10% EtOAc/petroleum ether gave the *title compound* (0.131 g, 0.454 mmol, 66%) as an orange solid.

^{1}H NMR (400 MHz, $CDCl_3$): δ (ppm) 3.64 (t, J = 6.6 Hz, 2H), 2.86 (t, J = 7.3 Hz, 2H), 2.32 (s, 3H), 1.61 – 1.52(m, 4H), 1.37 – 1.24 (m, 20H). **^{13}C NMR** (101 MHz, $CDCl_3$): δ (ppm) 196.3, 63.3, 33.0, 30.8, 29.7 (3 x CH_2), 29.7, 29.7, 29.6, 29.6, 29.6, 29.3, 29.3, 29.0, 25.9. **IR** ν_{max}(film)/cm^{-1}: 3284, 2913, 2849, 1691, 1472, 1058, 716. **HRMS** found (ESI): MH^+, 289.2195, $C_{16}H_{33}O_2S$, 289.21958.

5.5.33 *S*-(14-Bromotetradecyl) ethanethioate (101)

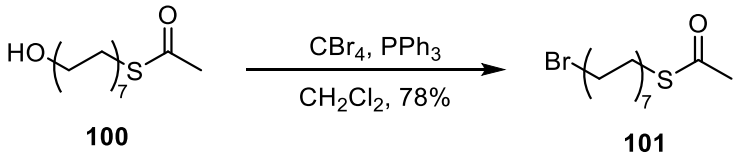

To a solution of *S*-(14-hydroxytetradecyl) ethanethioate (**100**) (1.07 g, 3.69 mmol) in anhydrous CH_2Cl_2 (20 mL) was added tetrabromomethane (4.90 g, 14.8 mmol). The reaction was cooled on ice for 10 minutes. Triphenylphosphine (3.88 g, 14.8 mmol) was slowly added to the reaction and stirred for 20 minutes before warming to room temperature and stirring for 24 hours. The solvent was removed *in vacuo,* and the crude product was purified using flash chromatography on silica gel using 2% diethyl ether/hexanes to give the title compound (1.01 g, 2.86 mmol, 78%) as a white solid.

^{1}H NMR (400 MHz, $CDCl_3$): δ (ppm) 3.41 (t, J = 6.9 Hz, 2H), 2.86 (t, J = 7.3 Hz, 2H), 2.32 (s, 3H), 1.90 – 1.81 (m, 2H), 1.60 – 1.51 (m, 2H), 1.46 – 1.38 (m, 2H), 1.37 – 1.23

(m, 18H). **^{13}C NMR** (101 MHz, $CDCl_3$): δ (ppm) 196.3, 34.2, 33.0, 30.8, 29.7 (2 x CH_2), 29.7, 29.7, 29.6, 29.6, 29.6, 29.3, 29.3, 29.0, 28.9, 28.3. **IR** ν_{max}(film)/cm^{-1}: 2915, 2849, 1685, 1470, 1119, 960, 718. **HRMS** found (ESI): MH^+, 351.1352, $C_{16}H_{32}O^{79}BrS$, 351.13518.

The NMR data is in agreement with the literature.[116]

5.5.34 *S*-(14-Azidotetradecyl) ethanethioate (102)

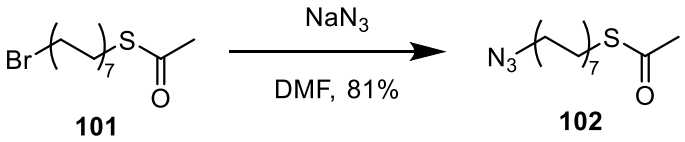

101 **102**

To a solution of *S*-(14-bromotetradecyl) ethanethioate (**101**) (0.118 g, 0.335 mmol) in anhydrous DMF (1 mL) was added sodium azide (0.0650 g, 1.00 mmol). The reaction was stirred at room temperature overnight. Ice water (10 mL) was then added to the reaction mixture, and the product was extracted using CH_2Cl_2 (3 x 15 mL). This was then dried over Na_2SO_4 and evaporated *in vacuo* to give the *title compound* (0.0846 g, 0.270 mmol, 81%) as a yellow oil.

^{1}H NMR (400 MHz, $CDCl_3$): δ (ppm) 3.25 (t, J = 7.0 Hz, 2H), 2.86 (t, J = 7.3 Hz, 2H), 2.32 (s, 3H), 1.62 – 1.54 (m, 4H), 1.37 – 1.25 (m, 20H). **^{13}C NMR** (101 MHz, $CDCl_3$): δ (ppm) 196.3, 51.6, 30.8, 29.7 (2 x CH_2), 29.7, 29.7, 29.6 (2 x CH_2), 29.6, 29.3 (2 x CH_2), 29.3, 29.0, 29.0, 26.9. **IR** ν_{max}(film)/cm^{-1}: 2923, 2852, 2092, 1682, 1465, 1352, 1255, 1133, 951. **HRMS** found (ESI): MNa^+, 336.2079, $C_{16}H_{31}ON_3NaS$, 336.20800.

5.5.35 *N,N'*-Bis(*tert*-butoxycarbonyl)-*N''*-14-(acetylthio)tetradecylguanidine (104)

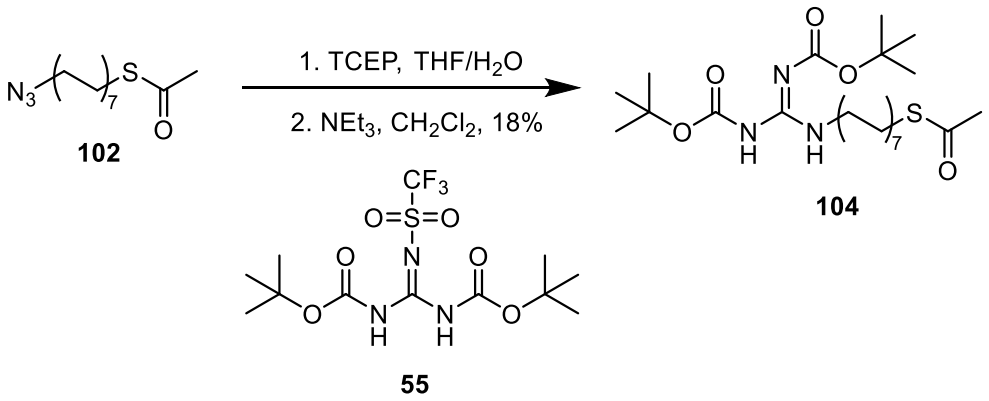

To a solution of *S*-(14-azidotetradecyl) ethanethioate (**102**) (0.0846 mg, 0.270 mmol) in a 5:3 mixture of THF and water (8 mL) was added TCEP (0.310 g, 1.08 mmol). The reaction mixture was stirred at room temperature for 24 hours. A second addition of TCEP (0.310 g, 1.08 mmol) followed by the reaction being stirred for a further 24 hours. A third addition of TCEP (0.310 g, 1.08 mmol) followed by the reaction being stirred for a further 24 hours. The THF was then evaporated *in vacuo* before the product was extracted with CH_2Cl_2 (20 mL) and washed with brine (3 x 15 mL). This was dried over Na_2SO_4 and evaporated *in vacuo* to give crude amine product

To a solution of crude amine (45 mg) in anhydrous CH_2Cl_2 (7 mL) was added 1,3-di-Boc-2-(trifluromethyl sulfonyl) guanidine (**55**) (74 mg, 0.19 mmol) and anhydrous NEt_3 (0.02 mL, 0.16 mmol). The reaction mixture was stirred at room temperature for 24 hours. Water (7 mL) was added, and the reaction was stirred for 15 minutes before being extracted with CH_2Cl_2 (3 x 10 mL). This was dried over Na_2SO_4. Flash chromatography on silica gel was used to purify the compound with a solvent system of 5% EtOAc/petroleum ether, to give the *title compound* (26 mg, 0.049 mmol, 18 %) as a white solid.

*Note that the yield has been calculated using the amount of *S*-(14-azidotetradecyl) ethanethioate (**102**).

^{1}H NMR (400 MHz, $CDCl_3$): δ (ppm) 11.50 (s, 1H), 8.29 (s, 1H), 3.40 (q, J = 6.4 Hz, 2H), 2.86 (t, J = 7.4 Hz, 2H), 2.32 (s, 3H), 1.58 – 1.53 (m, 4H), 1.50 (s, 9H), 1.49 (s, 9H), 1.35 – 1.23 (m, 20H). **^{13}C NMR** (101 MHz, $CDCl_3$): δ (ppm) 196.2, 163.8, 156.2, 153.5, 83.1, 79.3, 41.1, 30.8, 29.7, 29.7, 29.6, 29.6, 29.4, 29.3, 29.2, 29.1, 28.9, 28.4, 28.2, 27.0.

IR ν_{max}(film)/cm^{-1}: 3334, 2977, 2918, 2850, 1722, 1637, 1128. **HRMS** found (ESI): MH$^+$, 330.2574, $C_{17}H_{36}N_3OS$, 330.25736.

5.5.36 *N*-(14-Mercaptotetradecyl)guanidine (G-SH)

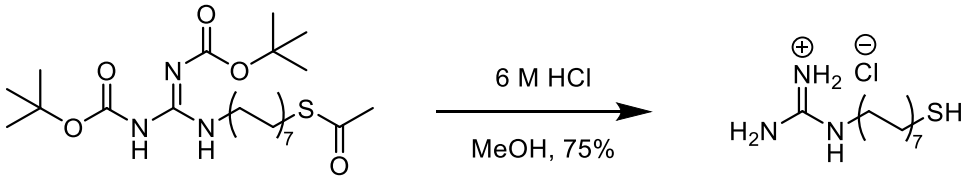

104 **G-SH**

To a solution of *N,N'*-Bis(tert-butoxycarbonyl)-*N*''-14-(acetylthio)tetradecylguanidine (**104**) (26 mg, 0.049 mmol) in MeOH (3 mL) was added 6 M HCl. The reaction mixture was refluxed at 60 °C for one hour. The solvent was then removed *in vacuo* to give the *title compound* (12 mg, 0.036 mmol, 75%) as a yellow oil.

^{1}H NMR (400 MHz, CD_3OD): δ (ppm) 3.16 (t, J = 7.1 Hz, 2H), 2.49 (t, J = 7.1 Hz, 2H), 1.64 – 1.54 (m, 4H), 1.41 – 1.29 (m, 20H). **^{13}C NMR** (101 MHz, CD_3OD): δ (ppm) 157.2, 41.1, 33.8, 29.3 (3 x CH_2), 29.3 (2 x CH_2), 29.2, 28.9, 28.8, 28.5, 28.0, 26.3, 23.6. **IR** ν_{max}(film)/cm^{-1}: 3323, 3143, 2921, 2849, 2482, 1651, 1609, 1469. **HRMS** found (ESI): M$^+$, 288.2468, $C_{15}H_{34}N_3S$, 288.24680.

5.5.37 *N*-[(Pyridin-2-yl)methyl]-14-(tritylthio)tetradecanamide (114)

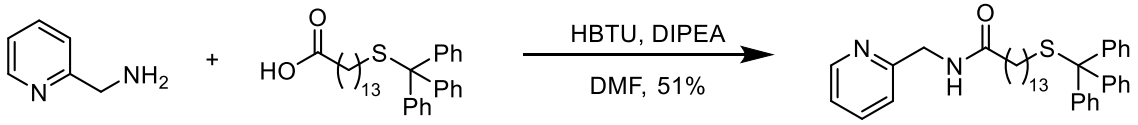

113 **88** **114**

To a solution of methyl 14-(tritylthio)tetradecanoate (**88**) (0.100 g, 0.204 mmol) in anhydrous DMF (0.5 mL) was added HBTU (0.464 g, 1.22 mmol). DIPEA (0.213 mL, 1.22 mmol) was slowly added, and the reaction was stirred for 15 minutes. 2-Picolylamine (**133**) (0.021 mL, 0.204 mmol) was added, and the reaction was stirred at room temperature for 24 hours. Reaction was then purified via flash chromatography on alumina gel using CH_2Cl_2 to give the *title compound* (0.0611 g, 0.103 mmol, 51%) as a yellow oil.

^{1}H NMR (400 MHz, $CDCl_3$): δ (ppm) 8.56 – 8.45 (m, 2H), 7.64 (d, J = 7.82 Hz, 1H), 7.45 – 7.34 (m, 6H), 7.31 – 7.23 (m, 7H), 7.23 – 7.16 (m, 3H), 5.86 (s, 1H), 4.45 (d, J =

6.0 Hz, 2H), 2.21 (t, J = 7.6 Hz, 2H), 2.13 (t, J = 7.4 Hz, 2H), 1.69 – 1.59 (m, 2H), 1.43 – 1.34 (m, 2H), 1.31 – 1.15 (m, 18H). **^{13}C NMR** (101 MHz, $CDCl_3$): δ (ppm) 173.4, 156.6, 149.1, 145.2, 136.9, 129.8, 127.9, 126.6, 122.5, 122.3, 66.5, 44.5, 36.9, 32.2, 29.7 (2 x CH_2), 29.7, 29.6, 29.6, 29.5, 29.5, 29.3, 29.2, 28.7, 25.9. **IR** ν_{max}(film)/cm^{-1}: 3295, 2921, 2851, 1651, 1592, 1437, 1033, 741, 698. **HRMS** found (ESI): MH$^+$, 593.3558, $C_{39}H_{49}ON_2S$, 593.35601.

5.5.38 *N*-[(Pyridin-2-yl)methyl]-14-mercaptotertadecanamide (2PA-SH)

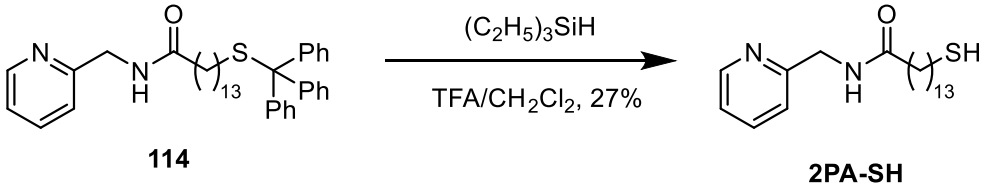

114 **2PA-SH**

N-[(Pyridin-2-yl)methyl]-14-(tritylthio)tetradecanamide (**114**) (0.061 g, 0.10 mmol) was dissolved in anhydrous CH_2Cl_2 (1 mL) and cooled on ice. TFA (1 mL) was added, followed by triethylsilane (0.016 mL, 0.10 mmol). This was stirred for 15 minutes, after which the solvent was removed *in vacuo*. The product was purified via flash chromatography on alumina gel using CH_2Cl_2 to remove initial impurities and 2% MeOH/CH_2Cl_2 to give the *title compound* (0.0098 g, 0.028 mmol, 27%) as a yellow solid.

^{1}H NMR (400 MHz, $CDCl_3$): δ (ppm) 8.53 (d, J = 4.9 Hz, 1H), 7.66 (td, J = 7.7, 1.8 Hz, 1H), 7.28 – 7.23 (m, 2H), 7.20 (t, J = 6.2 Hz, 1H), 4.56 (d, J = 4.89, 2H), 2.68 (t, J = 7.4 Hz, 2H), 2.27 (t, J = 7.7 Hz, 2H), 1.70 – 1.63 (m, 4H), 1.40 – 1.20 (m, 16H). **^{13}C NMR** (101 MHz, $CDCl_3$): δ (ppm) 173.4, 156.6, 149.1, 136.9, 122.5, 122.3, 53.6, 44.5, 39.4, 36.9, 29.8, 29.8, 29.7, 29.7, 29.6, 29.5, 29.5, 29.4, 28.7, 25.9. **IR** ν_{max}(film)/cm^{-1}: 3300, 2917, 2849, 1644, 1544, 1471, 1260, 1088, 1019, 799. **HRMS** found (ESI): M$^+$, 350.2386, $C_{20}H_{34}N_2OS$, 350.23864.

5.5.39 *N*-[(Pyridin-3-yl)methyl]-14-(tritylthio)tetradecanamide (116)

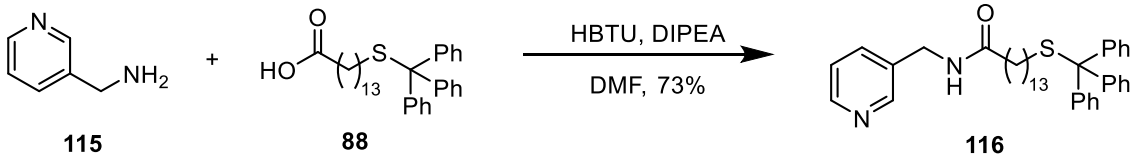

115 88 116

To a solution of methyl 14-(tritylthio)tetradecanoate (**88**) (0.100 g, 0.204 mmol) in anhydrous DMF (0.5 mL) was added HBTU (0.464 g, 1.22 mmol). DIPEA (0.213 mL, 1.22 mmol) was slowly added, and the reaction was stirred for 15 minutes. 3-Picolylamine (**115**) (0.021 mL, 0.204 mmol) was added, and the reaction was stirred at room temperature for 24 hours. Reaction was then purified via flash chromatography on alumina gel using CH_2Cl_2 to give the *title compound* (0.0880 g, 0.148 mmol, 73%) as a yellow oil.

^{1}H NMR (400 MHz, $CDCl_3$): δ (ppm) 8.55 – 8.49 (m, 2H), 7.64 (d, J = 7.9 Hz, 1H), 7.46 – 7.38 (m, 6H), 7.30 – 7.24 (m, 7H), 7.22 – 7.17 (m, 3H), 5.86 (s, 1H), 4.45 (d, J = 6.0 Hz, 2H), 2.21 (t, J = 7.6 Hz, 2H), 2.13 (t, J = 7.3 Hz, 2H), 1.65 (quint, J = 7.1 Hz, 2H), 1.44 – 1.34 (m, 2H), 1.32 – 1.12 (m, 18H). **^{13}C NMR** (101 MHz, $CDCl_3$): δ (ppm) 173.3, 149.2, 148.9, 145.2, 135.9, 129.7, 127.9, 126.6, 123.8, 66.5, 41.1, 36.8, 32.2, 29.8, 29.7 (2 x CH_2), 29.7, 29.6, 29.5, 29.5, 29.4, 29.3, 29.1, 28.7, 25.8. **IR** ν_{max}(film)/cm^{-1}: 3277, 2921, 2850, 1645, 1544, 1443, 1259, 1029, 796. **HRMS** found (ESI): MH^+, 593.3560, $C_{39}H_{49}ON_2S$, 593.35601.

5.5.40 *N*-[(Pyridin-3-yl)methyl]-14-mercaptotertadecanamide (3PA-SH)

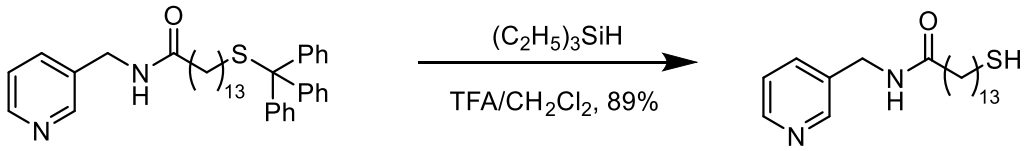

116 3PA-SH

A solution of *N*-[(pyridin-3-yl)methyl]-14-(tritylthio)tetradecanamide (**116**) (0.16 g, 0.27 mmol) was dissolved in anhydrous CH_2Cl_2 (2 mL) and cooled on ice. TFA (2 mL) was added, followed by triethylsilane (0.043 mL, 0.27 mmol). This was stirred for 30 minutes, after which the solvent was removed *in vacuo*. The product was purified via flash chromatography on alumina gel using $CHCl_3$ to give the *title compound* (0.083 g, 0.24 mmol, 89%) as a white solid.

^{1}H NMR (400 MHz, $CDCl_3$): δ (ppm) 8.54 – 8.50 (m, 2H), 7.63 (d, J = 7.8 Hz, 1H), 7.30 – 7.23 (m, 1H), 5.87 (s, 1H), 4.46 (d, J = 5.9 Hz, 2H), 2.52 (q, J = 7.3 Hz, 2H), 2.22 (t, J = 7.4 Hz, 2H), 1.69 – 1.56 (m, 4H), 1.42 – 1.21 (m, 18H). **^{13}C NMR** (101 MHz, $CDCl_3$): δ (ppm) 173.3, 149.3, 149.1, 135.8, 134.3, 123.7, 41.1, 36.8, 34.2, 29.8, 29.7, 29.7, 29.6, 29.6, 29.5, 29.4, 29.2, 28.5, 25.8, 24.8. **IR** ν_{max}(film)/cm^{-1}: 3295, 2917, 2850, 1637, 1540, 1471, 1426, 1222, 714. **HRMS** found (ESI): MH^+, 351.2464, $C_{20}H_{35}ON_2S$, 351.24646.

5.5.41 *N*-(pyridine-2-ylmethyl)butanamide (C4-2PA)

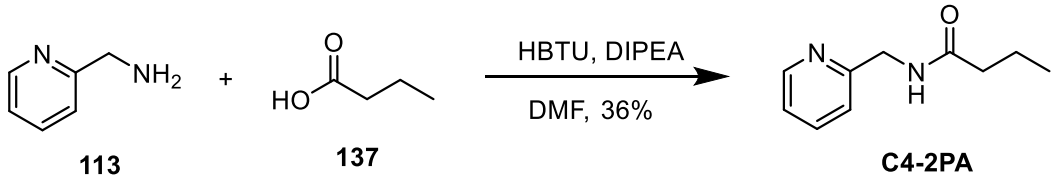

113 **137** **C4-2PA**

To a solution of butyric acid (**137**) (0.200 g, 2.27 mmol), in anhydrous DMF (4 mL) was added HBTU (2.58 g, 6.81 mmol). DIPEA (2.37 mL, 13.6 mmol) was slowly added, and the reaction was stirred for 15 minutes. 2-Picolylamine (**113**) (0.234 mL, 2.27 mmol) was added, and the reaction was stirred at room temperature for 24 hours. CH_2Cl_2 (20 mL) was added to the reaction before being washed with 5% LiCl (3 x 50 mL) to remove DMF. Reaction was then purified via flash chromatography on alumina gel using 20% EtOAc/petroleum ether initially, followed by 50% EtOAc/petroleum ether to give the *title compound* (0.147 g, 0.826 mmol, 36%) as a yellow oil.

^{1}H NMR (400 MHz, $CDCl_3$): δ (ppm) 8.53 (d, J = 4.6 Hz, 1H), 7.66 (t, J = 7.7 Hz, 1H), 7.26 (d, J = 7.6 Hz, 1H), 7.20 (t, J = 6.1 Hz, 1H), 4.57 (d, J = 5.1 Hz, 2H), 2.26 (t, J = 7.5 Hz, 2H), 1.71 (sextet, J = 7.5 Hz, 2H), 0.96 (t, J = 7.4 Hz, 3H). **^{13}C NMR** (101 MHz, $CDCl_3$): δ (ppm) 173.3, 156.7, 149.0, 136.9, 122.5, 122.3, 44.5, 38.7, 19.3, 13.9. **IR** ν_{max}(film)/cm^{-1}:3285, 3066, 2962, 2931, 2872, 1645, 1539, 1436, 1208, 751. **HRMS** found (ESI): MH^+, 179.1179, $C_{10}H_{15}ON_2$, 179.11789.

5.5.42 *N*-(pyridine-2-ylmethyl)hexanamide (C6-2PA)

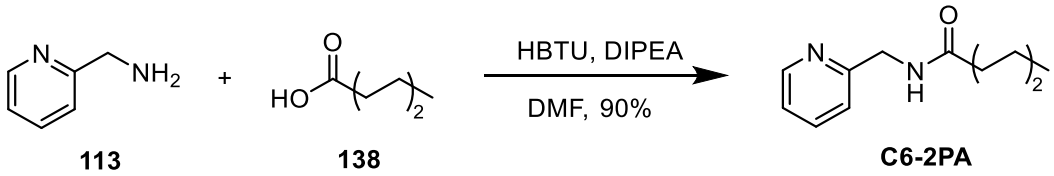

113 138 C6-2PA

To a solution of hexanoic acid (**138**) (0.200 g, 1.72 mmol), in anhydrous DMF (4 mL) was added HBTU (3.91 g, 10.3 mmol). DIPEA (1.80 mL, 10.3 mmol) was slowly added, and the reaction was stirred for 15 minutes. 2-Picolylamine (**113**) (0.177 mL, 1.72 mmol) was added, and the reaction was stirred at room temperature for 24 hours. CH_2Cl_2 (20 mL) was added to the reaction before being washed with 5% LiCl (3 x 50 mL) to remove DMF. Reaction was then purified via flash chromatography on alumina gel using 20% EtOAc/petroleum ether initially, followed by 50% EtOAc/petroleum ether to give the title compound (0.321 g, 1.56 mmol, 90%) as a yellow oil.

^{1}H NMR (400 MHz, $CDCl_3$): δ (ppm) 8.53 (d, J = 4.8 Hz, 1H), 7.66 (t, J = 7.8 Hz, 1H), 7.27 (d, J = 8.0 Hz, 1H), 7.20 (d, J = 6.1 Hz, 1H), 6.81 (s, 1H), 4.56 (d, J = 4.88 Hz, 2H), 2.27 (t, J = 7.6 Hz, 2H), 1.68 (quint, J = 7.3 Hz, 2H), 1.41 – 1.26 (m, 4H), 0.89 (t, J = 6.5 Hz, 3H). **^{13}C NMR** (101 MHz, $CDCl_3$): δ (ppm) 173.4, 156.7, 149.1, 136.9, 122.5, 122.3, 44.5, 36.8, 31.6, 25.5, 22.5, 14.0.

The NMR data matches that which has been previously reported in the literature.[168]

5.5.43 *N*-(pyridine-2-ylmethyl)octanamide (C8-2PA)

113 139 C8-2PA

To a solution of octanoic acid (**139**) (0.22 mL, 1.4 mmol), in anhydrous DMF (4 mL) was added HBTU (3.16 g, 8.34 mmol). DIPEA (1.45 mL, 8.34 mmol) was slowly added, and the reaction was stirred for 15 minutes. 2-Picolylamine (**113**) (0.14 mL, 1.4 mmol) was added, and the reaction was stirred at room temperature for 24 hours. CH_2Cl_2 (20 mL) was added to the reaction before being washed with 5% LiCl (3 x 50 mL) to remove DMF. Reaction was then purified via flash chromatography on alumina gel using 20%

EtOAc/petroleum ether initially, followed by 50% EtOAc/petroleum ether to give the *title compound* (0.182 g, 0.778 mmol, 56 %) as a yellow oil.

^{1}H NMR (400 MHz, $CDCl_3$): δ (ppm) 8.54 (d, J = 5.0 Hz, 1H), 7.66 (td, J = 7.7, 1.7 Hz, 1H), 7.26 (d, J = 7.7 Hz, 1H), 7.20 (t, J = 6.2 Hz, 1H), 6.73 (s, 1H), 4.56 (d, J = 4.9 Hz, 2H), 2.28 (t, J = 7.6 Hz, 2H), 1.71 – 1.62 (m, 2H), 1.38 – 1.20 (m, 8H), 0.87 (t, J = 6.6 Hz, 3H). **^{13}C NMR** (101 MHz, $CDCl_3$): δ (ppm) 173.4, 156.6, 149.1, 136.9, 122.5, 122.3, 44.5, 36.9, 31.8, 29.4, 29.1, 25.9, 22.7, 14.2. **IR** ν_{max}(film)/cm^{-1}: 3286, 3067, 2924, 2855, 1645, 1540, 1436, 1234, 1028, 750. **HRMS** found (ESI): MH^+, 235.1803, $C_{14}H_{23}ON_2$, 235.18049.

5.5.44 *N*-(Pyridin-2-ylmethyl)dodecanamide (C12-2PA)

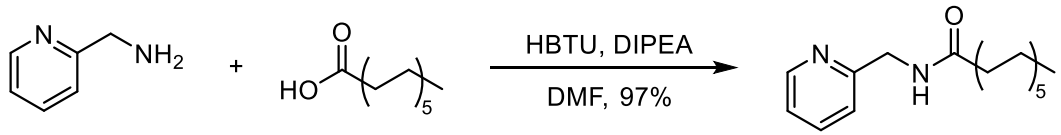

113 **140** **C12-2PA**

To a solution of dodecanoic acid (**140**) (0.100 g, 0.499 mmol) in anhydrous DMF (1 mL) was added HBTU (1.135 g, 2.99 mmol). DIPEA (0.522 mL, 2.99 mmol) was slowly added, and the reaction was stirred for 15 minutes. 2-Picolylamine (**113**) (0.051 mL, 0.499 mmol) was added, and the reaction was stirred at room temperature for 24 hours. Reaction was then purified via flash chromatography on alumina gel using $CHCl_3$ to give the title compound (0.141 g, 0.485 mmol, 97%) as a white solid.

^{1}H NMR (400 MHz, $CDCl_3$): δ (ppm) 8.54 (d, J = 4.9 Hz, 1H), 7.66 (td, J = 7.7, 1.8 Hz, 1H), 7.29 – 2.25 (m, 1H), 7.20 (t, J = 6.3 Hz, 1H), 6.71 (s, 1H), 4.57 (d, J = 4.79 Hz, 2H), 2.28 (t, J = 7.6 Hz, 2H), 1.71 – 1.61 (m, 2H), 1.37 – 1.21 (m, 16H), 0.88 (t, J = 6.8 Hz, 3H). **^{13}C NMR** (101 MHz, $CDCl_3$): δ (ppm) 173.4, 156.6, 149.1, 136.9, 122.5, 122.4, 44.5, 36.9, 32.1, 29.7 (2 x CH_2), 29.6, 29.5 (2 x CH_2), 29.5, 25.9, 22.8, 14.3.

The NMR data match that which has been previously reported in the literature.[168]

5.6 General procedure for UV experiments in Chapter 3

The UV experiments were conducted as follows:

Water was added to the cuvette, followed by the buffer. Ag^{+} was added to the cuvette, followed by the catalytic thiols. If there was more than one catalytic thiol being added, these were premixed prior to addition. The cuvette was then mixed. If Zn^{2+} was used in the system, it was then added, and the cuvette was mixed. This was placed in the UV and allowed 5 minutes to warm to 40 °C. The substrate PNPB was then added, and the cuvette was mixed again before being placed back in the UV to begin recording measurements. The UV recorded the absorbance at 405 nm every 0.6 minutes for a total of 40 minutes.

The stock solutions for these experiments were:

[HEPES, pH = 7.0] = 100 mM in milli-Q water, [**C6-HM-SH**] = 20 mM in MeOH, [$AgNO_3$] = 20 mM in milli-Q water, [**PNPB**] = 50 mM in DMSO, [**HM-SH**] = 20 mM in MeOH, [**G-SH**] = 20 mM in MeOH, [**D2PA-SH**] = 20 mM in MeOH, [**OH-SH**] = 20 mM in MeOH, [**Acid-SH**] = 20 mM in DMSO, [**DEA-SH**] = 20 mM in MeOH, [$Zn(NO_3)_2$] = 20 mM in milli-Q water, [$CuSO_4$] = 20 mM in milli-Q water, [$CoSO_4$] = 20 mM in milli-Q water, [$NiCl_2$] = 20 mM in milli-Q water, [$MnSO_4$] = 20 mM in milli-Q water, [$CaCl_2$] = 20 mM in milli-Q water, [$MgSO_4$] = 20 mM in milli-Q water, [$FeCl_3$] = 20 mM in milli-Q water , [$CdCl_2$] = 20 mM in milli-Q water, [**2PA-SH**] = 20 mM in MeOH, [**3PA-SH**] = 20 mM in MeOH, [pyridine **117**] = 20 mM in MeOH, [2,6-lutidine **118**] = 20 mM in MeOH, [2-picolylamine **113**] = 20 mM in MeOH, [3-picolylamine **115**] = 20 mM in MeOH, [di-(2-picolyl)amine **76**] = 20 mM in MeOH, [benzylamine **119**] = 20 mM in MeOH, [**C4-2PA]** = 20 mM in MeOH, [**C6-2PA]** = 20 mM in MeOH, [**C8-2PA]** = 20 mM in MeOH, [**C12-2PA]** = 20 mM in MeOH, [KI] = 20 mM in milli-Q water.

References

(1) Dong, Z.; Luo, Q.; Liu, J. Artificial Enzymes Based on Supramolecular Scaffolds. *Chem. Soc. Rev.* **2012**, *41* (23), 7890–7908. https://doi.org/10.1039/C2CS35207A.

(2) Reetz, M. T. What Are the Limitations of Enzymes in Synthetic Organic Chemistry? *Chem. Rec.* **2016**, *16* (6), 2449–2459. https://doi.org/10.1002/tcr.201600040.

(3) Mashuri, S. I. S.; Ibrahim, M. L.; Kasim, M. F.; Mastuli, M. S.; Rashid, U.; Abdullah, A. H.; Islam, A.; Mijan, N. A.; Tan, Y. H.; Mansir, N.; Kaus, N. H. M.; Hin, T.-Y. Y. Photocatalysis for Organic Wastewater Treatment: From the Basis to Current Challenges for Society. *Catalysts* **2020**, *10*, 1260. https://doi.org/doi:10.3390/catal10111260.

(4) Roduner, E. Understanding Catalysis. *Chem Soc Rev* **2014**, *43* (24), 8226–8239. https://doi.org/10.1039/C4CS00210E.

(5) Soleymani, F.; Paquet, E.; Viktor, H.; Michalowski, W.; Spinello, D. Protein–Protein Interaction Prediction with Deep Learning: A Comprehensive Review. *Comput. Struct. Biotechnol. J.* **2022**, *20*, 5316–5341. https://doi.org/10.1016/j.csbj.2022.08.070.

(6) Kuah, E.; Toh, S.; Yee, J.; Ma, Q.; Gao, Z. Enzyme Mimics: Advances and Applications. *Chem. – Eur. J.* **2016**, *22* (25), 8404–8430. https://doi.org/10.1002/chem.201504394.

(7) Ringe, D.; Petsko, G. A. How Enzymes Work. *Science* **2008**, *320* (5882), 1428–1429. https://doi.org/10.1126/science.1159747.

(8) Smith, A. J. T.; Müller, R.; Toscano, M. D.; Kast, P.; Hellinga, H. W.; Hilvert, D.; Houk, K. N. Structural Reorganization and Preorganization in Enzyme Active Sites: Comparisons of Experimental and Theoretically Ideal Active Site Geometries in the Multistep Serine Esterase Reaction Cycle. *J. Am. Chem. Soc.* **2008**, *130* (46), 15361–15373. https://doi.org/10.1021/ja803213p.

(9) Kahraman, A.; Thornton, J. M. Methods to Characterize the Structure of Enzyme Binding Sites. In *Computational Structural Biology*; WORLD SCIENTIFIC, 2008; pp 189–221. https://doi.org/10.1142/9789812778789_0008.

(10) Broderick, J. B. Coenzymes and Cofactors. In *Encyclopedia of Life Sciences*; Wiley, 2001. https://doi.org/10.1038/npg.els.0000631.

(11) Callender, R.; Dyer, R. B. The Dynamical Nature of Enzymatic Catalysis. *Acc. Chem. Res.* **2015**, *48* (2), 407–413. https://doi.org/10.1021/ar5002928.

(12) Boehr, D. D.; Nussinov, R.; Wright, P. E. The Role of Dynamic Conformational Ensembles in Biomolecular Recognition. *Nat. Chem. Biol.* **2009**, *5* (11), 789–796. https://doi.org/10.1038/nchembio.232.

(13) Choi, B.; Rempala, G. A.; Kim, J. K. Beyond the Michaelis-Menten Equation: Accurate and Efficient Estimation of Enzyme Kinetic Parameters. *Sci. Rep.* **2017**, *7* (1), 17018. https://doi.org/10.1038/s41598-017-17072-z.

(14) Wang, Y.; Wang, G.; Moitessier, N.; Mittermaier, A. K. Enzyme Kinetics by Isothermal Titration Calorimetry: Allostery, Inhibition, and Dynamics. *Front. Mol. Biosci.* **2020**, *7*. https://doi.org/10.3389/fmolb.2020.583826.

(15) Garrido-González, J. J.; Iglesias Aparicio, M. M.; García, M. M.; Simón, L.; Sanz, F.; Morán, J. R.; Fuentes de Arriba, Á. L. An Enzyme Model Which Mimics Chymotrypsin and N-Terminal Hydrolases. *ACS Catal.* **2020**, *10* (19), 11162–11170. https://doi.org/10.1021/acscatal.0c02121.

(16) Nothling, M. D.; Xiao, Z.; Bhaskaran, A.; Blyth, M. T.; Bennett, C. W.; Coote, M. L.; Connal, L. A. Synthetic Catalysts Inspired by Hydrolytic Enzymes. *ACS Catal.* **2019**, *9* (1), 168–187. https://doi.org/10.1021/acscatal.8b03326.

(17) Nothling, M. D.; Ganesan, A.; Condic-Jurkic, K.; Pressly, E.; Davalos, A.; Gotrik, M. R.; Xiao, Z.; Khoshdel, E.; Hawker, C. J.; O'Mara, M. L.; Coote, M. L.; Connal, L. A. Simple Design of an Enzyme-Inspired Supported Catalyst Based on a Catalytic Triad. *Chem* **2017**, *2* (6), 893–894. https://doi.org/10.1016/j.chempr.2017.05.015.

(18) Nothling, M. D.; Xiao, Z.; Hill, N. S.; Blyth, M. T.; Bhaskaran, A.; Sani, M.-A.; Espinosa-Gomez, A.; Ngov, K.; White, J.; Buscher, T.; Separovic, F.; O'Mara, M. L.; Coote, M. L.; Connal, L. A. A Multifunctional Surfactant Catalyst Inspired by Hydrolases. *Sci. Adv.* **2020**, *6* (14), eaaz0404. https://doi.org/10.1126/sciadv.aaz0404.

(19) Fojan, P.; Jonson, P. H.; Petersen, M. T. N.; Petersen, S. B. What Distinguishes an Esterase from a Lipase: A Novel Structural Approach. *Biochimie* **2000**, *82* (11), 1033–1041. https://doi.org/10.1016/S0300-9084(00)01188-3.

(20) Oh, C.; Kim, T. D.; Kim, K. K. Carboxylic Ester Hydrolases in Bacteria: Active Site, Structure, Function and Application. *Crystals 9* (11), 597. https://doi.org/10.3390/cryst9110597.

(21) Chapman, J.; Ismail, A. E.; Dinu, C. Z. Industrial Applications of Enzymes: Recent Advances, Techniques, and Outlooks. *Catalysts* **2018**, *8* (6). https://doi.org/10.3390/catal8060238.

(22) Victorino da Silva Amatto, I.; Gonsales da Rosa-Garzon, N.; Antônio de Oliveira Simões, F.; Santiago, F.; Pereira da Silva Leite, N.; Raspante Martins, J.; Cabral, H. Enzyme Engineering and Its Industrial Applications. *Biotechnol. Appl. Biochem.* **2022**, *69* (2), 389–409. https://doi.org/10.1002/bab.2117.

(23) Shamim, S.; Liaqat, U.; Rehman, A. Microbial Lipases and Their Applications – a Review. **2018**.

(24) Hasan, F.; Shah, A. A.; Hameed, A. Industrial Applications of Microbial Lipases. *Enzyme Microb. Technol.* **2006**, *39* (2), 235–251. https://doi.org/10.1016/j.enzmictec.2005.10.016.

(25) Raveendran, S.; Parameswaran, B.; Ummalyma, S. B.; Abraham, A.; Mathew, A. K.; Madhavan, A.; Rebello, S.; Pandey, A. Applications of Microbial Enzymes in Food Industry. *Food Technol. Biotechnol.* **2018**, *56* (1). https://doi.org/10.17113/ftb.56.01.18.5491.

(26) Choi, J.-M.; Han, S.-S.; Kim, H.-S. Industrial Applications of Enzyme Biocatalysis: Current Status and Future Aspects. *Biotechnol. Adv.* **2015**, *33* (7), 1443–1454. https://doi.org/10.1016/j.biotechadv.2015.02.014.

(27) DiCosimo, R.; McAuliffe, J.; Poulose, A. J.; Bohlmann, G. Industrial Use of Immobilized Enzymes. *Chem. Soc. Rev.* **2013**, *42* (15), 6437. https://doi.org/10.1039/c3cs35506c.

(28) Wang, Y.; Xue, P.; Cao, M.; Yu, T.; Lane, S. T.; Zhao, H. Directed Evolution: Methodologies and Applications. *Chem. Rev.* **2021**, *121* (20), 12384–12444. https://doi.org/10.1021/acs.chemrev.1c00260.

(29) Dalby, P. A. Strategy and Success for the Directed Evolution of Enzymes. *Curr. Opin. Struct. Biol.* **2011**, *21* (4), 473–480. https://doi.org/10.1016/j.sbi.2011.05.003.

(30) Chica, R. A.; Doucet, N.; Pelletier, J. N. Semi-Rational Approaches to Engineering Enzyme Activity: Combining the Benefits of Directed Evolution and Rational Design. *Curr. Opin. Biotechnol.* **2005**, *16* (4), 378–384. https://doi.org/10.1016/j.copbio.2005.06.004.

(31) Solís-Muñana, P.; Salam, J.; Ren, C. Z.-J.; Carr, B.; Whitten, A. E.; Warr, G. G.; Chen, J. L.-Y. An Amphiphilic (Salen)Co Complex – Utilizing Hydrophobic

Interactions to Enhance the Efficiency of a Cooperative Catalyst. *Adv. Synth. Catal.* **2021**, *363* (13), 3207–3213. https://doi.org/10.1002/adsc.202100494.

(32) Breslow, R.; Dong, S. D. Biomimetic Reactions Catalyzed by Cyclodextrins and Their Derivatives. *Chem. Rev.* **1998**, *98* (5), 1997–2012. https://doi.org/10.1021/cr970011j.

(33) Del Valle, E. M. M. Cyclodextrins and Their Uses: A Review. *Process Biochem.* **2004**, *39* (9), 1033–1046. https://doi.org/10.1016/S0032-9592(03)00258-9.

(34) Zhang, B.; Breslow, R. Ester Hydrolysis by a Catalytic Cyclodextrin Dimer Enzyme Mimic with a Metallobipyridyl Linking Group. *J. Am. Chem. Soc.* **1997**, *119* (7), 1676–1681. https://doi.org/10.1021/ja963769d.

(35) Lagona, J.; Mukhopadhyay, P.; Chakrabarti, S.; Isaacs, L. The Cucurbit[n]Uril Family. *Angew. Chem. Int. Ed.* **2005**, *44* (31), 4844–4870. https://doi.org/10.1002/anie.200460675.

(36) Pemberton, B. C.; Raghunathan, R.; Volla, S.; Sivaguru, J. From Containers to Catalysts: Supramolecular Catalysis within Cucurbiturils. *Chem. – Eur. J.* **2012**, *18* (39), 12178–12190. https://doi.org/10.1002/chem.201202083.

(37) Klöck, C.; Dsouza, R. N.; Nau, W. M. Cucurbituril-Mediated Supramolecular Acid Catalysis. *Org. Lett.* **2009**, *11* (12), 2595–2598. https://doi.org/10.1021/ol900920p.

(38) Assaf, K. I.; Nau, W. M. Cucurbiturils: From Synthesis to High-Affinity Binding and Catalysis. *Chem. Soc. Rev.* **2014**, *44* (2), 394–418. https://doi.org/10.1039/C4CS00273C.

(39) Gissot, A.; Rebek, J. A Functionalized, Deep Cavitand Catalyzes the Aminolysis of a Choline Derivative. *J. Am. Chem. Soc.* **2004**, *126* (24), 7424–7425. https://doi.org/10.1021/ja049074r.

(40) Soberats, B.; Sanna, E.; Martorell, G.; Rotger, C.; Costa, A. Programmed Enzyme-Mimic Hydrolysis of a Choline Carbonate by a Metal-Free 2-Aminobenzimidazole-Based Cavitand. *Org. Lett.* **2014**, *16* (3), 840–843. https://doi.org/10.1021/ol403612e.

(41) Darbre, T.; Reymond, J.-L. Peptide Dendrimers as Artificial Enzymes, Receptors, and Drug-Delivery Agents. *Acc. Chem. Res.* **2006**, *39* (12), 925–934. https://doi.org/10.1021/ar050203y.

(42) Pengo, P.; L, B.; Pasquato, L.; P, S. Substrate Modulation of the Activity of an Artificial Nanoesterase Made of Peptide-Funtionalized Gold Nanoparticles. **2007**. https://doi.org/10.1002/anie.200602581.

(43) Pasquato, L.; Rancan, F.; Scrimin, P.; Mancin, F.; Frigeri, C. N-Methylimidazole-Functionalized Gold Nanoparticles as Catalysts for Cleavage of a Carboxylic Acid Ester. *Chem. Commun.* **2000**, No. 22, 2253–2254. https://doi.org/10.1039/b005244m.

(44) Huang, Z.; Guan, S.; Wang, Y.; Shi, G.; Cao, L.; Gao, Y.; Dong, Z.; Xu, J.; Luo, Q.; Liu, J. Self-Assembly of Amphiphilic Peptides into Bio-Functionalized Nanotubes: A Novel Hydrolase Model. *J. Mater. Chem. B* **2013**, *1* (17), 2297. https://doi.org/10.1039/c3tb20156b.

(45) Cruz, J. N.; Martínez, K. D.; Zavariz, Á. D.; Hernández, I. P. Review of the Thermochemical Degradation of PET: An Alternative Method of Recycling. *J. Ecol. Eng.* **2022**, *Vol. 23* (nr 9). https://doi.org/10.12911/22998993/151766.

(46) Bartolome, L.; Imran, M.; Gyoo, B.; A., W.; Hyun, D. Recent Developments in the Chemical Recycling of PET. In *Material Recycling - Trends and Perspectives*; Achilias, D., Ed.; InTech, 2012. https://doi.org/10.5772/33800.

(47) Wu, H.-S.; Damayanti. Strategic Possibility Routes of Recycled PET. *Polymers* **2021**, *13* (9), 1475. https://doi.org/10.3390/polym13091475.

(48) Siddiqui, M. N.; Redhwi, H. H.; Al-Arfaj, A. A.; Achilias, D. S. Chemical Recycling of PET in the Presence of the Bio-Based Polymers, PLA, PHB and PEF: A Review. *Sustainability* **2021**, *13* (19), 10528. https://doi.org/10.3390/su131910528.

(49) Burgin, T.; Pollard, B. C.; Knott, B. C.; Mayes, H. B.; Crowley, M. F.; McGeehan, J. E.; Beckham, G. T.; Woodcock, H. L. The Reaction Mechanism of the Ideonella Sakaiensis PETase Enzyme. *Commun. Chem.* **2024**, *7* (1), 65. https://doi.org/10.1038/s42004-024-01154-x.

(50) Chen, C.-C.; Han, X.; Ko, T.-P.; Liu, W.; Guo, R.-T. Structural Studies Reveal the Molecular Mechanism of PETase. *FEBS J.* **2018**, *285* (20), 3717–3723. https://doi.org/10.1111/febs.14612.

(51) Muringayil Joseph, T.; Azat, S.; Ahmadi, Z.; Moini Jazani, O.; Esmaeili, A.; Kianfar, E.; Haponiuk, J.; Thomas, S. Polyethylene Terephthalate (PET) Recycling: A Review. *Case Stud. Chem. Environ. Eng.* **2024**, *9*, 100673. https://doi.org/10.1016/j.cscee.2024.100673.

(52) Zhang, S.; Hu, Q.; Zhang, Y.-X.; Guo, H.; Wu, Y.; Sun, M.; Zhu, X.; Zhang, J.; Gong, S.; Liu, P.; Niu, Z. Depolymerization of Polyesters by a Binuclear Catalyst

for Plastic Recycling. *Nat. Sustain.* **2023**, *6* (8), 965–973. https://doi.org/10.1038/s41893-023-01118-4.

(53) Rufo, C. M.; Moroz, Y. S.; Moroz, O. V.; Stöhr, J.; Smith, T. A.; Hu, X.; DeGrado, W. F.; Korendovych, I. V. Short Peptides Self-Assemble to Produce Catalytic Amyloids. *Nat. Chem.* **2014**, *6* (4), 303–309. https://doi.org/10.1038/nchem.1894.

(54) Zhao, Y.; Lei, B.; Wang, M.; Wu, S.; Qi, W.; Su, R.; He, Z. A Supramolecular Approach to Construct a Hydrolase Mimic with Photo-Switchable Catalytic Activity. *J. Mater. Chem. B* **2018**, *6* (16), 2444–2449. https://doi.org/10.1039/C8TB00448J.

(55) Liu, N.; Li, S.-B.; Zheng, Y.-Z.; Xu, S.-Y.; Shen, J.-S. Minimalistic Artificial Catalysts with Esterase-Like Activity from Multivalent Nanofibers Formed by the Self-Assembly of Dipeptides. *ACS Omega* **2023**, *8* (2), 2491–2500. https://doi.org/10.1021/acsomega.2c06972.

(56) Wang, M.; Lv, Y.; Liu, X.; Qi, W.; Su, R.; He, Z. Enhancing the Activity of Peptide-Based Artificial Hydrolase with Catalytic Ser/His/Asp Triad and Molecular Imprinting. *ACS Appl. Mater. Interfaces* **2016**, *8* (22), 14133–14141. https://doi.org/10.1021/acsami.6b04670.

(57) Zhang, C.; Xue, X.; Luo, Q.; Li, Y.; Yang, K.; Zhuang, X.; Jiang, Y.; Zhang, J.; Liu, J.; Zou, G.; Liang, X.-J. Self-Assembled Peptide Nanofibers Designed as Biological Enzymes for Catalyzing Ester Hydrolysis. *ACS Nano* **2014**, *8* (11), 11715–11723. https://doi.org/10.1021/nn5051344.

(58) Ghosh, C.; Menon, S.; Bal, S.; Goswami, S.; Mondal, J.; Das, D. Emergence of Catalytic Triad by Short Peptide Based Nanofibrillar Assemblies. *Nano Lett.* **2023**, *23* (12), 5828–5835. https://doi.org/10.1021/acs.nanolett.3c01852.

(59) Sarkhel, B.; Chatterjee, A.; Das, D. Covalent Catalysis by Cross β Amyloid Nanotubes. *J. Am. Chem. Soc.* **2020**, *142* (9), 4098–4103. https://doi.org/10.1021/jacs.9b13517.

(60) Hamley, I. W. Biocatalysts Based on Peptide and Peptide Conjugate Nanostructures. *Biomacromolecules* **2021**, *22* (5), 1835–1855. https://doi.org/10.1021/acs.biomac.1c00240.

(61) Guerrero-Pérez, M. O. Research Progress on the Applications of Electrospun Nanofibers in Catalysis. *Catalysts* **2021**, *12* (1), 9. https://doi.org/10.3390/catal12010009.

(62) *Molecularly Imprinted Polymers in Biotechnology*; Mattiasson, B., Ye, L., Eds.; Advances in Biochemical Engineering/Biotechnology; Springer International Publishing: Cham, 2015; Vol. 150. https://doi.org/10.1007/978-3-319-20729-2.

(63) Lakavathu, M.; Zhao, Y. Direct Synthesis of Artificial Esterase through Molecular Imprinting Using a Substrate-Mimicking Acylthiourea Template. *J. Org. Chem.* **2024**, *89* (20), 15336–15340. https://doi.org/10.1021/acs.joc.4c01789.

(64) Bose, I.; Bahrami, F.; Zhao, Y. Artificial Esterase for Cooperative Catalysis of Ester Hydrolysis at pH 7. *Mater. Today Chem.* **2023**, *30*, 101576. https://doi.org/10.1016/j.mtchem.2023.101576.

(65) Arifuzzaman, M.; Zhao, Y. Artificial Zinc Enzymes with Fine-Tuned Active Sites for Highly Selective Hydrolysis of Activated Esters. *ACS Catal.* **2018**, *8* (9), 8154–8161. https://doi.org/10.1021/acscatal.8b02292.

(66) Hu, L.; Zhao, Y. Molecularly Imprinted Artificial Esterases with Highly Specific Active Sites and Precisely Installed Catalytic Groups. *Org. Biomol. Chem.* **2018**, *16* (31), 5580–5584. https://doi.org/10.1039/C8OB01584H.

(67) Hu, L.; Zhao, Y. A Bait-and-Switch Method for the Construction of Artificial Esterases for Substrate-Selective Hydrolysis. *Chem. – Eur. J.* **2019**, *25* (32), 7702–7710. https://doi.org/10.1002/chem.201900560.

(68) Bose, I.; Zhao, Y. Selective Hydrolysis of Aryl Esters under Acidic and Neutral Conditions by a Synthetic Aspartic Protease Mimic. *ACS Catal.* **2021**, *11* (7), 3938–3942. https://doi.org/10.1021/acscatal.1c00371.

(69) Zastrow, M. L.; Peacock, A. F. A.; Stuckey, J. A.; Pecoraro, V. L. Hydrolytic Catalysis and Structural Stabilization in a Designed Metalloprotein. *Nat. Chem.* **2012**, *4* (2), 118–123. https://doi.org/10.1038/nchem.1201.

(70) Dwars, T.; Paetzold, E.; Oehme, G. Reactions in Micellar Systems. *Angew. Chem. Int. Ed.* **2005**, *44* (44), 7174–7199. https://doi.org/10.1002/anie.200501365.

(71) Tagaki, W.; Chigira, M.; Amada, T.; Yano, Y. Catalysis in Ester Hydrolysis by a Cationic Detergent Containing an Imidazole Group at the Polar Head. *J. Chem. Soc. Chem. Commun.* **1972**, No. 4, 219–220. https://doi.org/10.1039/C39720000219.

(72) Moss, R. A.; Nahas, R. C.; Ramaswami, S. Sequential Bifunctional Micellar Catalysis. *J. Am. Chem. Soc.* **1977**, *99* (2), 627–629. https://doi.org/10.1021/ja00444a062.

(73) Polarz, S.; Jaschke, M.; Siroky, S.; Kalies, S.; Weber, N.; Heisterkamp, A. Micellar (Photo−)Catalysis Driven by IR-Active Semiconductor Surfactants. *ChemCatChem* **2024**, *16* (22), e202400661. https://doi.org/10.1002/cctc.202400661.

(74) Lipshutz, B. H.; Ghorai, S.; Cortes-Clerget, M. The Hydrophobic Effect Applied to Organic Synthesis: Recent Synthetic Chemistry "in Water." *Chem. – Eur. J.* **2018**, *24* (26), 6672–6695. https://doi.org/10.1002/chem.201705499.

(75) Acharjee, A.; Rakshit, A.; Chowdhury, S.; Saha, B. Micelle Catalysed Conversion of 'on Water' Reactions into 'in Water' One. *J. Mol. Liq.* **2021**, *321*, 114897. https://doi.org/10.1016/j.molliq.2020.114897.

(76) Gruber, B.; Kataev, E.; Aschenbrenner, J.; Stadlbauer, S.; König, B. Vesicles and Micelles from Amphiphilic Zinc(II)–Cyclen Complexes as Highly Potent Promoters of Hydrolytic DNA Cleavage. *J. Am. Chem. Soc.* **2011**, *133* (51), 20704–20707. https://doi.org/10.1021/ja209247w.

(77) Poznik, M.; König, B. Cooperative Hydrolysis of Aryl Esters on Functionalized Membrane Surfaces and in Micellar Solutions. *Org Biomol Chem* **2014**, *12* (20), 3175–3180. https://doi.org/10.1039/C4OB00247D.

(78) Ren, C. Z.-J.; Solís-Muñana, P.; Warr, G. G.; Chen, J. L.-Y. Dynamic and Modular Formation of a Synergistic Transphosphorylation Catalyst. *ACS Catal.* **2020**, *10* (15), 8395–8401. https://doi.org/10.1021/acscatal.0c01321.

(79) Solís Muñana, P.; Ragazzon, G.; Dupont, J.; Ren, C. Z.-J.; Prins, L. J.; Chen, J. L.-Y. Substrate-Induced Self-Assembly of Cooperative Catalysts. *Angew. Chem. Int. Ed Engl.* **2018**, *57* (50), 16469–16474. https://doi.org/10.1002/anie.201810891.

(80) Kirk, O.; Borchert, T. V.; Fuglsang, C. C. Industrial Enzyme Applications. *Curr. Opin. Biotechnol.* **2002**, *13* (4), 345–351. https://doi.org/10.1016/S0958-1669(02)00328-2.

(81) Bajpai, P. Chapter 8 - Industrial Applications of Thermophilic/Hyperthermophilic Enzymes. In *Developments and Applications of Enzymes from Thermophilic Microorganisms*; Bajpai, P., Ed.; Progress in Biochemistry and Biotechnology; Academic Press, 2023; pp 105–284. https://doi.org/10.1016/B978-0-443-19197-8.00016-5.

(82) Mrigwani, A.; Thakur, B.; Guptasarma, P. Enhancing High-Temperature Degradation of Polyethylene Terephthalate through a Synergistic Division of Enzyme Labour between a Solid-Degrading Thermostable Cutinase and a Reaction

Intermediate-Degrading Thermostable Carboxylesterase. bioRxiv February 3, 2022, p 2022.02.02.478778. https://doi.org/10.1101/2022.02.02.478778.

(83) Lombardo, A. Kinetics of Imidazole Catalyzed Ester Hydrolysis: Use of Buffer Dilutions to Determine Spontaneous Rate, Catalyzed Rate, and Reaction Order. *J. Chem. Educ.* **1982**, *59* (10), 887. https://doi.org/10.1021/ed059p887.

(84) Javor, S.; Delort, E.; Darbre, T.; Reymond, J.-L. A Peptide Dendrimer Enzyme Model with a Single Catalytic Site at the Core. *J. Am. Chem. Soc.* **2007**, *129* (43), 13238–13246. https://doi.org/10.1021/ja074115f.

(85) Montalbetti, C. A. G. N.; Falque, V. Amide Bond Formation and Peptide Coupling. *Tetrahedron* **2005**, *61* (46), 10827–10852. https://doi.org/10.1016/j.tet.2005.08.031.

(86) Broo, K. S.; Nilsson, H.; Nilsson, J.; Flodberg, A.; Baltzer, L. Cooperative Nucleophilic and General-Acid Catalysis by the HisH+─His Pair and Arginine Transition State Binding in Catalysis of Ester Hydrolysis Reactions by Designed Helix−Loop−Helix Motifs. *J. Am. Chem. Soc.* **1998**, *120* (17), 4063–4068. https://doi.org/10.1021/ja9737580.

(87) Dutta, A.; Roberts, J. A. S.; Shaw, W. J. Arginine-Containing Ligands Enhance H2 Oxidation Catalyst Performance. *Angew. Chem.* **2014**, *126* (25), 6605–6609. https://doi.org/10.1002/ange.201402304.

(88) Gupta, M. N.; Uversky, V. N. Biological Importance of Arginine: A Comprehensive Review of the Roles in Structure, Disorder, and Functionality of Peptides and Proteins. *Int. J. Biol. Macromol.* **2024**, *257*, 128646. https://doi.org/10.1016/j.ijbiomac.2023.128646.

(89) Campo-Balguerías, A. del; Parra-Cadenas, B.; Nieto-Jimenez, C.; Bravo, I.; Ripoll, C.; Poyatos-Racionero, E.; Gancarski, P.; Carrillo-Hermosilla, F.; Alonso-Moreno, C.; Ocaña, A. Guanylation Reactions for the Rational Design of Cancer Therapeutic Agents. *Int. J. Mol. Sci.* **2023**, *24* (18), 13820. https://doi.org/10.3390/ijms241813820.

(90) Shainyan, B. A.; Tolstikova, L. L.; Schilde, U. Simple Methods for the Preparation of *N*-Triflyl Guanidines and the Structure of Compounds with the CF3SO2NCN Fragment. *J. Fluor. Chem.* **2012**, *135*, 261–264. https://doi.org/10.1016/j.jfluchem.2011.12.004.

(91) Fanjul-Bolado, P.; González-García, M. B.; Costa-García, A. Flow Screen-Printed Amperometric Detection of p-Nitrophenol in Alkaline Phosphatase-Based Assays.

Anal. Bioanal. Chem. **2006**, *385* (7), 1202–1208. https://doi.org/10.1007/s00216-006-0367-8.

(92) Overberger, C. G.; Salamone, J. C.; Yaroslavsky, Samuel. Cooperative Effects in the Esterolytic Action of Synthetic Macromolecules Containing Imidazole and Hydroxyl Functions. *J. Am. Chem. Soc.* **1967**, *89* (24), 6231–6236. https://doi.org/10.1021/ja01000a043.

(93) Yang, H.; Sherman, J. C. Ester Hydrolysis by a Histidine-Containing Cavitein. *Bioorg. Med. Chem. Lett.* **2013**, *23* (6), 1752–1753. https://doi.org/10.1016/j.bmcl.2013.01.063.

(94) Matich, O.; Naiya, M. M.; Salam, J.; Tiban Anrango, B. A.; Chen, J. L.-Y. Modular Assembly and Optimization of an Artificial Esterase from Functionalised Surfactants. *ChemCatChem* **2024**, *16* (20), e202400945. https://doi.org/10.1002/cctc.202400945.

(95) Kundu, A.; Verma, P. K.; Cho, M. Water Structure and Dynamics in the Stern Layer of Micelles: Femtosecond Mid-Infrared Pump-Probe Spectroscopy Study. *J. Phys. Chem. B* **2019**, *123* (25), 5238–5245. https://doi.org/10.1021/acs.jpcb.9b03183.

(96) Schwert, G. W.; Neurath, H.; Kaufman, S.; Snoke, J. E. The Specific Esterase Activity Of Trypsin. *J. Biol. Chem.* **1948**, *172* (1), 221–239. https://doi.org/10.1016/S0021-9258(18)35631-X.

(97) Anoardi, L.; Fornasier, R.; Tonellato, U. Functional Micellar Catalysis. Part 4. Catalysis of Activated Ester Hydrolysis by Surfactant Systems as Chymotrypsin Models. *J. Chem. Soc. Perkin Trans. 2* **1981**, No. 2, 260. https://doi.org/10.1039/p29810000260.

(98) Han, Min Su. Visual Detection of Di-and Tri-Phosphates in Aqueous Solution of Neutral pH. *Bull. Korean Chem. Soc.* **2004**, *25* (8), 1151–1155. https://doi.org/10.5012/BKCS.2004.25.8.1151.

(99) Liu, X.; Ngo, H. T.; Ge, Z.; Butler, S. J.; Jolliffe, K. A. Tuning Colourimetric Indicator Displacement Assays for Naked-Eye Sensing of Pyrophosphate in Aqueous Media. *Chem. Sci.* **2013**, *4* (4), 1680. https://doi.org/10.1039/c3sc22233k.

(100) Ivanov, V. M.; Kochelayeva, G. A. Pyrocatechol Violet in Spectrophotometric and Novel Optical Methods. *Russ. Chem. Rev.* **2006**, *75* (3), 255–266.

(101) Stanek, J.; Rösener, T.; Metz, A.; Mannsperger, J.; Hoffmann, A.; Herres-Pawlis, S. Guanidine Metal Complexes for Bioinorganic Chemistry and Polymerisation Catalysis. In *Guanidines as Reagents and Catalysts II*; 2017; pp 95–164.

(102) Wittmann, H.; Raab, V.; Schorm, A.; Plackmeyer, J.; Sundermeyer, J. Complexes of Manganese, Iron, Zinc, and Molybdenum with a Superbasic Tris(Guanidine) Derivative of Tris(2-Ethylamino)Amine (Tren) as a Tripod Ligand. *Eur. J. Inorg. Chem.* **2001**, *2001* (8), 1937–1948. https://doi.org/10.1002/1099-0682(200108)2001:8%3C1937::AID-EJIC1937%3E3.0.CO;2-I.

(103) Ren, C. Z.-J.; Solís Muñana, P.; Dupont, J.; Zhou, S. S.; Chen, J. L.-Y. Reversible Formation of a Light-Responsive Catalyst by Utilizing Intermolecular Cooperative Effects. *Angew. Chem. Int. Ed Engl.* **2019**, *58* (43), 15254–15258. https://doi.org/10.1002/anie.201907078.

(104) Stuart, M.; van de Pas, J.; Engberts, J.; Pas, J. C. van de. The Use of Nile Red to Monitor the Aggregation Behavior in Ternary Surfactant-Water-Organic Solvent Systems. *J. Phys. Org. Chem.* **2005**, *18* (9), 929–934. https://doi.org/10.1002/poc.919.

(105) Dutta, P.; Dey, J.; Ghosh, G.; Nayak, R. R. Self-Association and Microenvironment of Random Amphiphilic Copolymers of Sodium *N*-Acryloyl-l-Valinate and *N*-Dodecylacrylamide in Aqueous Solution. *Polymer* **2009**, *50* (6), 1516–1525. https://doi.org/10.1016/j.polymer.2008.12.049.

(106) Pencer, J.; Hallett, F. R. Effects of Vesicle Size and Shape on Static and Dynamic Light Scattering Measurements. *Langmuir* **2003**, *19* (18), 7488–7497. https://doi.org/10.1021/la0345439.

(107) Pascucci, L.; Scattini, G. Imaging Extracelluar Vesicles by Transmission Electron Microscopy: Coping with Technical Hurdles and Morphological Interpretation. *Biochim. Biophys. Acta BBA - Gen. Subj.* **2021**, *1865* (4), 129648. https://doi.org/10.1016/j.bbagen.2020.129648.

(108) Friedrich, H.; Frederik, P. M.; de With, G.; Sommerdijk, N. A. J. M. Imaging of Self-Assembled Structures: Interpretation of TEM and Cryo-TEM Images. *Angew. Chem. Int. Ed.* **2010**, *49* (43), 7850–7858. https://doi.org/10.1002/anie.201001493.

(109) Dobrawa, R.; Würthner, F. Metallosupramolecular Approach toward Functional Coordination Polymers. *J. Polym. Sci. Part Polym. Chem.* **2005**, *43* (21), 4981–4995. https://doi.org/10.1002/pola.20997.

(110) Wang, Q.; Dong, S.-L.; Tao, D.-D.; Li, Z.; Jiang, Y.-B. Ag(I)-Thiolate Coordination Polymers: Synthesis, Structures and Applications as Emerging Sensory Ensembles. *Coord. Chem. Rev.* **2021**, *432*, 213717. https://doi.org/10.1016/j.ccr.2020.213717.

(111) Parikh, A. N.; Gillmor, S. D.; Beers, J. D.; Beardmore, K. M.; Cutts, R. W.; Swanson, B. I. Characterization of Chain Molecular Assemblies in Long-Chain, Layered Silver Thiolates: A Joint Infrared Spectroscopy and X-Ray Diffraction Study. *J. Phys. Chem. B* **1999**, *103* (15), 2850–2861. https://doi.org/10.1021/jp983938b.

(112) Casuso, P.; Carrasco, P.; Loinaz, I.; Cabañero, G.; Grande, H. J.; Odriozola, I. Argentophilic Hydrogels: Elucidating the Structure of Neutral versus Acidic Systems. *Soft Matter* **2011**, *7* (7), 3627–3633. https://doi.org/10.1039/C0SM01217C.

(113) Quan, J.-J.; Wang, Q.; Li, Z.; Jiang, Y.-B. Aggregated Coordination Polymers of Ag^+ with a Cysteine Derivative Ligand Containing an AIEgen. *Chem. Commun.* **2023**, *59* (29), 4320–4323. https://doi.org/10.1039/D3CC00474K.

(114) Qi, C.; Li, Q.; Wei, K.; Zhao, W.; Zhang, W.; Chen, M.-M.; Zhang, X.; Feng, H.-T. Tetraphenylethylene Based Chiral AIEgen for Enantioselective Detection of Chiral Acids. *Dyes Pigments* **2025**, *239*, 112781. https://doi.org/10.1016/j.dyepig.2025.112781.

(115) Gordon, O.; Vig Slenters, T.; Brunetto, P. S.; Villaruz, A. E.; Sturdevant, D. E.; Otto, M.; Landmann, R.; Fromm, K. M. Silver Coordination Polymers for Prevention of Implant Infection: Thiol Interaction, Impact on Respiratory Chain Enzymes, and Hydroxyl Radical Induction. *Antimicrob. Agents Chemother.* **2010**, *54* (10), 4208–4218. https://doi.org/10.1128/AAC.01830-09.

(116) Cao, Y.-J.; Yao, M.-X.; Prins, L. J.; Ji, R.-X.; Liu, N.; Sun, X.-Y.; Jiang, Y.-B.; Shen, J.-S. Self-Assembled Multivalent Ag-SR Coordination Polymers with Phosphatase-Like Activity. *Chem. – Eur. J.* **2021**, *27* (28), 7646–7650. https://doi.org/10.1002/chem.202100368.

(117) Shen, J.-S.; Li, D.-H.; Cai, Q.-G.; Jiang, Y.-B. Highly Selective Iodide-Responsive Gel–Sol State Transition in Supramolecular Hydrogels. *J. Mater. Chem.* **2009**, *19* (34), 6219. https://doi.org/10.1039/b908755a.

(118) Yamada, T.; Miki, S.; Ul'Husna, A.; Michikawa, A.; Nakatani, K. Synthesis of Naphthyridine Carbamate Dimer (NCD) Derivatives Modified with Alkanethiol

and Binding Properties of G–G Mismatch DNA. *Org. Lett.* **2017**, *19* (16), 4163–4166. https://doi.org/10.1021/acs.orglett.7b01632.

(119) Sidoryk, K.; Michalak, O.; Kubiszewski, M.; Leś, A.; Cybulski, M.; Stolarczyk, E. U.; Doubsky, J. Synthesis of Thiol Derivatives of Biological Active Compounds for Nanotechnology Application. *Molecules* **2020**, *25* (15), 3470. https://doi.org/10.3390/molecules25153470.

(120) Mehta, A.; Jaouhari, R.; Benson, T. J.; Douglas, K. T. Improved Efficiency and Selectivity in Peptide Synthesis: Use of Triethylsilane as a Carbocation Scavenger in Deprotection of t-Butyl Esters and t-Butoxycarbonyl-Protected Sites. *Tetrahedron Lett.* **1992**, *33* (37), 5441–5444. https://doi.org/10.1016/S0040-4039(00)79116-7.

(121) Raghunand, N.; Jagadish, B.; Trouard, T. P.; Galons, J.-P.; Gillies, R. J.; Mash, E. A. Redox-Sensitive Contrast Agents for MRI Based on Reversible Binding of Thiols to Serum Albumin. *Magn. Reson. Med.* **2006**, *55* (6), 1272–1280. https://doi.org/10.1002/mrm.20904.

(122) Li, M.; Zhou, H.; Shi, L.; Li, D.-W.; Long, Y.-T. Ion-Selective Gold–Thiol Film on Integrated Screen-Printed Electrodes for Analysis of Cu(II) Ions. *The Analyst* **2014**, *139* (3), 643–648. https://doi.org/10.1039/C3AN01860A.

(123) Fariya, M.; Jain, A.; Dhawan, V.; Shah, S.; Nagarsenker, M. S. Bolaamphiphiles: A Pharmaceutical Review. *Adv. Pharm. Bull.* **2014**, *4* (Suppl 2), 483. https://doi.org/10.5681/apb.2014.072.

(124) Nagarajan, R. Self-Assembly Of Bola Amphiphiles. *Chem. Eng. Commun.* **1987**, *55* (1–6), 251–273. https://doi.org/10.1080/00986448708911931.

(125) Tanaka, M.; Sawaguchi, T.; Hirata, Y.; Niwa, O.; Tawa, K.; Sasakawa, C.; Kuraoka, K. Properties of Modified Surface for Biosensing Interface. *J. Colloid Interface Sci.* **2017**, *497*, 309–316. https://doi.org/10.1016/j.jcis.2017.02.070.

(126) Yue, H.; Waldeck, D. H.; Schrock, K.; Kirby, D.; Knorr, K.; Switzer, S.; Rosmus, J.; Clark, R. A. Multiple Sites for Electron Tunneling between Cytochrome c and Mixed Self-Assembled Monolayers. *J. Phys. Chem. C* **2008**, *112* (7), 2514–2521. https://doi.org/10.1021/jp076769g.

(127) Bege, M.; Bereczki, I.; Herczeg, M.; Kicsák, M.; Eszenyi, D.; Herczegh, P.; Borbás, A. A Low-Temperature, Photoinduced Thiol–Ene Click Reaction: A Mild and Efficient Method for the Synthesis of Sugar-Modified Nucleosides. *Org. Biomol. Chem.* **2017**, *15* (43), 9226–9233. https://doi.org/10.1039/C7OB02184D.

(128) Duffy, P. E.; Quinn, S. M.; Roche, H. M.; Evans, P. Synthesis of *Trans*-Vaccenic Acid and *Cis*-9-*Trans*-11-Conjugated Linoleic Acid. *Tetrahedron* **2006**, *62* (20), 4838–4843. https://doi.org/10.1016/j.tet.2006.03.006.

(129) Shi, L.; Jing, C.; Ma, W.; Li, D.-W.; Halls, J. E.; Marken, F.; Long, Y.-T. Plasmon Resonance Scattering Spectroscopy at the Single-Nanoparticle Level: Real-Time Monitoring of a Click Reaction. *Angew. Chem. Int. Ed.* **2013**, *52* (23), 6011–6014. https://doi.org/10.1002/anie.201301930.

(130) Yusof, Y.; Tan, D. T. C.; Arjomandi, O. K.; Schenk, G.; McGeary, R. P. Captopril Analogues as Metallo-β-Lactamase Inhibitors. *Bioorg. Med. Chem. Lett.* **2016**, *26* (6), 1589–1593. https://doi.org/10.1016/j.bmcl.2016.02.007.

(131) Wu, X.; Wang, P.; Liu, R.; Zeng, H.; Chao, F.; Liu, H.; Xu, C.; Hou, H.; Yao, Q. Development of 11C-Labeled ω-Sulfhydryl Fatty Acid Tracer for Myocardial Imaging with PET. *Eur. J. Med. Chem.* **2018**, *143*, 1657–1666. https://doi.org/10.1016/j.ejmech.2017.10.062.

(132) Lin, F. L.; Hoyt, H. M.; Van Halbeek, H.; Bergman, R. G.; Bertozzi, C. R. Mechanistic Investigation of the Staudinger Ligation. *J. Am. Chem. Soc.* **2005**, *127* (8), 2686–2695. https://doi.org/10.1021/ja044461m.

(133) Meredith, E. L.; Ksander, G.; Monovich, L. G.; Papillon, J. P. N.; Liu, Q.; Miranda, K.; Morris, P.; Rao, C.; Burgis, R.; Capparelli, M.; Hu, Q.-Y.; Singh, A.; Rigel, D. F.; Jeng, A. Y.; Beil, M.; Fu, F.; Hu, C.-W.; LaSala, D. Discovery and in Vivo Evaluation of Potent Dual CYP11B2 (Aldosterone Synthase) and CYP11B1 Inhibitors. *ACS Med. Chem. Lett.* **2013**, *4* (12), 1203–1207. https://doi.org/10.1021/ml400324c.

(134) Kalkeren, H. A. van; Delft, F. L. van; Rutjes, F. P. J. T. Catalytic Appel reactions. *Pure Appl. Chem.* **2012**, *85* (4), 817–828. https://doi.org/10.1351/PAC-CON-12-06-13.

(135) Routasalo, T.; Helaja, J.; Kavakka, J.; Koskinen, A. M. P. Development of Bis(2-Picolyl)Amine–Zinc Chelates for Imidazole Receptors. *Eur. J. Org. Chem.* **2008**, *2008* (18), 3190–3199. https://doi.org/10.1002/ejoc.200700926.

(136) Götzke, L.; Gloe, K.; Jolliffe, K. A.; Lindoy, L. F.; Heine, A.; Doert, T.; Jäger, A.; Gloe, K. Nickel(II) and Zinc(II) Complexes of *N*-Substituted Di(2-Picolyl)Amine Derivatives: Synthetic and Structural Studies. *Polyhedron* **2011**, *30* (5), 708–714. https://doi.org/10.1016/j.poly.2010.12.005.

(137) Škalamera, Đ.; Sanders, E.; Vianello, R.; Maršavelski, A.; Pevec, A.; Turel, I.; Kirin, S. I. Synthesis and Characterization of **ML** and $\mathbf{ML_2}$ Metal Complexes with Amino Acid Substituted Bis(2-Picolyl)Amine Ligands. *Dalton Trans.* **2016**, *45* (7), 2845–2858. https://doi.org/10.1039/C5DT03387J.

(138) Song, Y.; Nayab, S.; Jeon, J.; Park, S. H.; Lee, H. Cadmium(II) Complexes Containing N′-Substituted N,N-Di(2-Picolyl)Amine: The Formation of Monomeric versus Dimeric Complexes Is Affected by the N′-Substitution Group on the Amine Moiety. *J. Organomet. Chem.* **2015**, *783*, 55–63. https://doi.org/10.1016/j.jorganchem.2015.02.011.

(139) Zhou, D.-F.; Chen, Q.-Y.; Qi, Y.; Fu, H.-J.; Li, Z.; Zhao, K.-D.; Gao, J. Anticancer Activity, Attenuation on the Absorption of Calcium in Mitochondria, and Catalase Activity for Manganese Complexes of N-Substituted Di(Picolyl)Amine. *Inorg. Chem.* **2011**, *50* (15), 6929–6937. https://doi.org/10.1021/ic200004y.

(140) Kong, M.-Y.; Wang, L.; Chen, Q.-Y.; Xu, X.-L.; Lu, W.-L. Study on the Interaction of Fe(III) Complex of BODIPY Appended Di(Picolyl)Amine with Water and HeLa Cells. *Spectrochim. Acta. A. Mol. Biomol. Spectrosc.* **2015**, *151*, 790–795. https://doi.org/10.1016/j.saa.2015.07.038.

(141) Bhattacharya, S.; Kumari, N. Metallomicelles as Potent Catalysts for the Ester Hydrolysis Reactions in Water. *Coord. Chem. Rev.* **2009**, *253* (17–18), 2133–2149. https://doi.org/10.1016/j.ccr.2009.01.016.

(142) Goswami, S.; Das, N. K.; Sen, D.; Hazra, G.; Goh, J. H.; Sing, Y. C.; Fun, H.-K. Recognition of Acids Involved in Krebs Cycle by 9-Anthrylmethyl-Di(6-Acetylamino-2-Picolyl)Amine: A Case of Selective Fluorescence Enhancement for Maleic Acid. *New J. Chem.* **2011**, *35* (12), 2811–2819. https://doi.org/10.1039/C1NJ20339H.

(143) Hamoudi, H.; Döring, K.; Chesneau, F.; Lang, H.; Zharnikov, M. Self-Assembly of Pyridine-Substituted Alkanethiols on Gold: The Electronic Structure Puzzle in the Ortho- and Para-Attachment of Pyridine to the Molecular Chain. *J. Phys. Chem. C* **2012**, *116* (1), 861–870. https://doi.org/10.1021/jp2089643.

(144) Butler, A. R.; Robertson, I. H. Nucleophilic and General Base Catalysis by Pyridine and Methylpyridines in the Hydrolysis of Aryl Acetates. *J. Chem. Soc. Perkin Trans. 2* **1975**, No. 6, 660. https://doi.org/10.1039/p29750000660.

(145) Deady, L.; Finlayson, W. The Aminolysis of P-Nitrophenyl Acetate by Aminopyridines. Mechanisms in Aqueous and Aprotic Solvents. *Aust. J. Chem.* **1980**, *33* (11), 2441–2446. https://doi.org/10.1071/CH9802441.

(146) Cevasco, G.; Galatini, A.; Pirinççioğlu, N.; Thea, S.; Williams, A. A Study on a Primitive Artificial Esterase Model: Reactivity of a Calix[4]Resorcinarene Bearing Carboxyl Groups. *J. Phys. Org. Chem.* **2008**, *21* (6), 498–504. https://doi.org/10.1002/poc.1371.

(147) Lo, S.; Ren, C. Z.-J.; Solís-Muñana, P.; Chen, J. L.-Y. Dynamic Self-Assembled Supramolecular Catalysts. In *Supramolecular Nanotechnology*; John Wiley & Sons, Ltd, 2023; pp 469–493. https://doi.org/10.1002/9783527834044.ch17.

(148) Fanlo-Virgós, H.; Alba, A.-N. R.; Hamieh, S.; Colomb-Delsuc, M.; Otto, S. Transient Substrate-Induced Catalyst Formation in a Dynamic Molecular Network. *Angew. Chem. Int. Ed.* **2014**, *53* (42), 11346–11350. https://doi.org/10.1002/anie.201403480.

(149) Wei, R.; Oeser, T.; Barth, M.; Weigl, N.; Lübs, A.; Schulz-Siegmund, M.; Hacker, M. C.; Zimmermann, W. Turbidimetric Analysis of the Enzymatic Hydrolysis of Polyethylene Terephthalate Nanoparticles. *J. Mol. Catal. B Enzym.* **2014**, *103*, 72–78. https://doi.org/10.1016/j.molcatb.2013.08.010.

(150) Chaves, M.; Lima, M.; Malafatti-Picca, L.; De Angelis, D.; De Castro, A.; Valoni, É.; Marsaioli, A. A Practical Fluorescence-Based Screening Protocol for Polyethylene Terephthalate Degrading Microorganisms. *J. Braz. Chem. Soc.* **2017**. https://doi.org/10.21577/0103-5053.20170224.

(151) Pirillo, V.; Pollegioni, L.; Molla, G. Analytical Methods for the Investigation of Enzyme-Catalyzed Degradation of Polyethylene Terephthalate. *FEBS J.* **2021**, *288* (16), 4730–4745. https://doi.org/10.1111/febs.15850.

(152) Lionetto, F.; Corcione, C. E.; Rizzo, A.; Maffezzoli, A. Production and Characterization of Polyethylene Terephthalate Nanoparticles. *Polymers* **2021**, *13* (21), 3745. https://doi.org/10.3390/polym13213745.

(153) Magrì, D.; Sánchez-Moreno, P.; Caputo, G.; Gatto, F.; Veronesi, M.; Bardi, G.; Catelani, T.; Guarnieri, D.; Athanassiou, A.; Pompa, P. P.; Fragouli, D. Laser Ablation as a Versatile Tool To Mimic Polyethylene Terephthalate Nanoplastic Pollutants: Characterization and Toxicology Assessment. *ACS Nano* **2018**, *12* (8), 7690–7700. https://doi.org/10.1021/acsnano.8b01331.

(154) Tiban Anrango, B. A.; Naiya, M. M.; Van Dongen, J.; Matich, O.; Whitby, C. P.; Chen, J. L.-Y. Nanoprecipitation to Produce Hydrophobic Cellulose Nanospheres for Water-in-Oil Pickering Emulsions. *Cellulose* **2024**, *31* (10), 6225–6239. https://doi.org/10.1007/s10570-024-05983-w.

(155) Tiban Anrango, B. A.; Naiya, M. M.; Van Dongen, J.; Matich, O.; Whitby, C. P.; Chen, J. L. Y. Synthesis of Hydrophobically Modified Cellulose Nanospheres and Their Application as Water-in-Oil Pickering Emulsifiers. Social Science Research Network: Rochester, NY February 7, 2024. https://doi.org/10.2139/ssrn.4719653.

(156) G. Rodríguez-Hernández, A.; Alejandro Muñoz-Tabares, J.; Cristobal Aguilar-Guzmán, J.; Vazquez-Duhalt, R. A Novel and Simple Method for Polyethylene Terephthalate (PET) Nanoparticle Production. *Environ. Sci. Nano* **2019**, *6* (7), 2031–2036. https://doi.org/10.1039/C9EN00365G.

(157) Carnall, J. M. A.; Waudby, C. A.; Belenguer, A. M.; Stuart, M. C. A.; Peyralans, J. J.-P.; Otto, S. Mechanosensitive Self-Replication Driven by Self-Organization. *Science* **2010**, *327* (5972), 1502–1506. https://doi.org/10.1126/science.1182767.

(158) Colomb-Delsuc, M.; Mattia, E.; Sadownik, J. W.; Otto, S. Exponential Self-Replication Enabled through a Fibre Elongation/Breakage Mechanism. *Nat. Commun.* **2015**, *6* (1), 7427. https://doi.org/10.1038/ncomms8427.

(159) Feng, R.; Xu, Y.; Zhao, H.; Duan, X.; Sun, S. A Novel Platform Self-Assembled from Squaraine-Embedded Zn(II) Complexes for Selective Monitoring of ATP and Its Level Fluctuation in Mitotic Cells. *Analyst* **2016**, *141* (11), 3219–3223. https://doi.org/10.1039/C6AN00646A.

(160) Fonge, H.; Jin, L.; Cleynhens, J.; Bormans, G.; Verbruggen, A. 99mTc-Tricarbonyl Labeled Agents for Cell Labeling: Development, Biodistribution in Normal Mice and Preliminary in Vitro Evaluation. *Bioorg. Med. Chem.* **2010**, *18* (1), 396–402. https://doi.org/10.1016/j.bmc.2009.10.045.

(161) Shukla, P.; Sharma, A.; Pallavi, B.; Cheng, C. H. Nickel-Catalyzed Reductive Heck Type Coupling of Saturated Alkyl Halides with Acrylates and Oxabenzonorbornadiene. *Tetrahedron* **2015**, *71* (15), 2260–2266. https://doi.org/10.1016/j.tet.2015.02.067.

(162) Groendyke, B. J.; Modak, A.; Cook, S. P. Fenton-Inspired C–H Functionalization: Peroxide-Directed C–H Thioetherification. *J. Org. Chem.* **2019**, *84* (20), 13073–13091. https://doi.org/10.1021/acs.joc.9b01979.

(163) Von Delius, M.; Geertsema, E. M.; Leigh, D. A. A Synthetic Small Molecule That Can Walk down a Track. *Nat. Chem.* **2010**, *2* (2), 96–101. https://doi.org/10.1038/nchem.481.

(164) Moreno, A. Y.; Mayorov, A. V.; Janda, K. D. Impact of Distinct Chemical Structures for the Development of a Methamphetamine Vaccine. *J. Am. Chem. Soc.* **2011**, *133* (17), 6587–6595. https://doi.org/10.1021/ja108807j.

(165) Greaves, J.; Munro, K. R.; Davidson, S. C.; Riviere, M.; Wojno, J.; Smith, T. K.; Tomkinson, N. C. O.; Chamberlain, L. H. Molecular Basis of Fatty Acid Selectivity in the zDHHC Family of S-Acyltransferases Revealed by Click Chemistry. *Proc. Natl. Acad. Sci. U. S. A.* **2017**, *114* (8), E1365–E1374. https://doi.org/10.1073/pnas.1612254114.

(166) Bouchet, M. J.; Rendon, A.; Wermuth, C. G.; Goeldner, M.; Hirth, C. Aryl Diazo Compounds and Diazonium Salts as Potential Irreversible Probes of the GABA Receptor. *J. Med. Chem.* **1987**, *30* (12), 2222–2227. https://doi.org/10.1021/jm00395a008.

(167) Krall, J.; Brygger, B. M.; Sigurðardóttir, S. B.; Ng, C. K. L.; Bundgaard, C.; Kehler, J.; Nielsen, B.; Bek, T.; Jensen, A. A.; Frølund, B. Discovery of α-Substituted Imidazole-4-Acetic Acid Analogues as a Novel Class of P1 γ-Aminobutyric Acid Type A Receptor Antagonists with Effect on Retinal Vascular Tone. *ChemMedChem* **2016**, *11* (20), 2299–2310. https://doi.org/10.1002/cmdc.201600356.

(168) García, F. F.; Musikant, D.; Escalona, J. L.; Edreira, M. M.; Liñares, G. G. Lipase-Catalyzed Synthesis and Biological Evaluation of *N* -Picolineamides as *Trypanosoma Cruzi* Antiproliferative Agents. *ACS Med. Chem. Lett.* **2023**, *14* (1), 59–65. https://doi.org/10.1021/acsmedchemlett.2c00425.

Appendix

NMR Spectra for Synthesis of Amphiphiles for Self-Assembled Artificial Esterase

1-Benzyl-*N*-(*tert*-butoxycarbonyl)-L-histidine hexadecyl amide (49)

^{1}H NMR (400 MHz, CD_3OD)

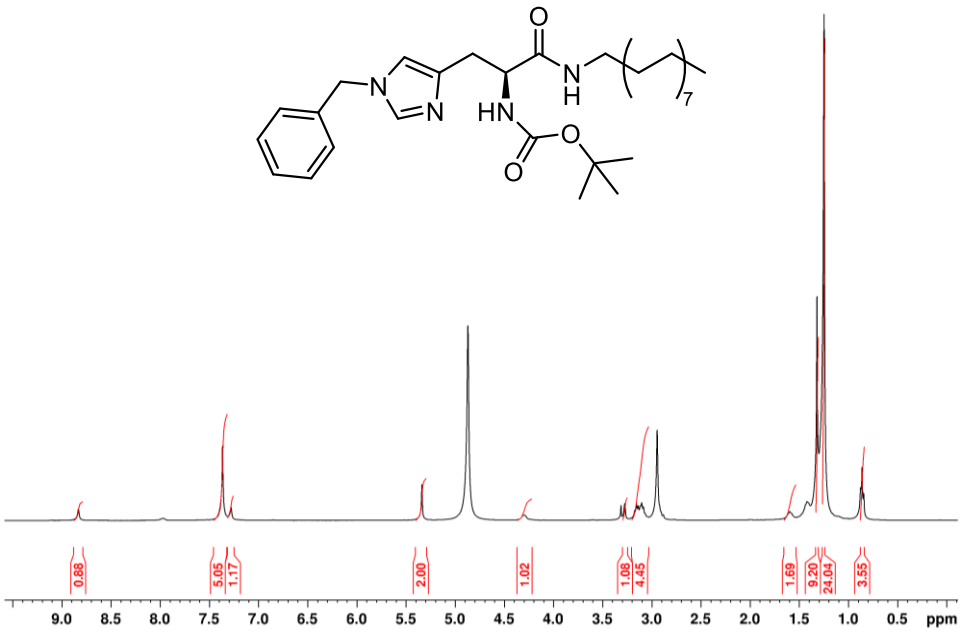

^{13}C NMR (101 MHz, CD_3OD)

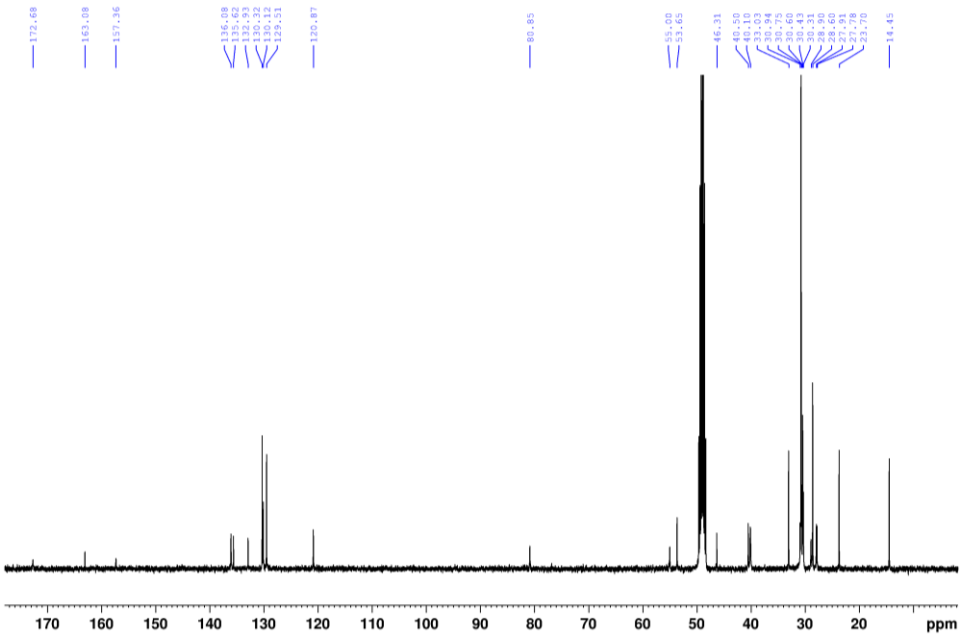

_N_-(_tert_-Butoxycarbonyl)-L-histidine hexadecyl amide (H)

^{1}H NMR (400 MHz, $CDCl_3$)

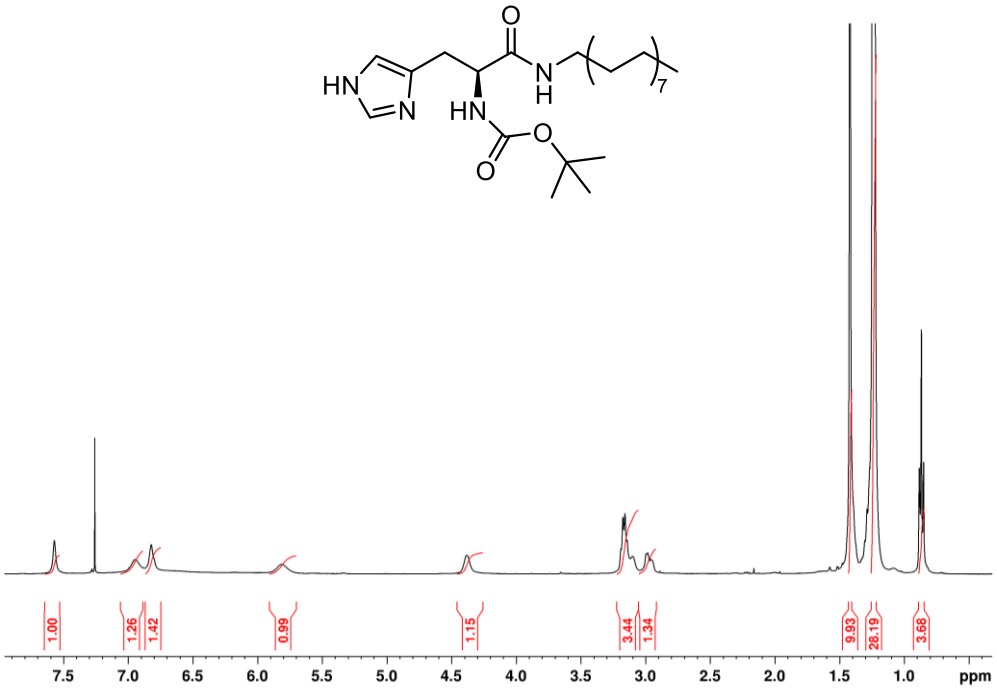

^{13}C NMR (101 MHz, $CDCl_3$)

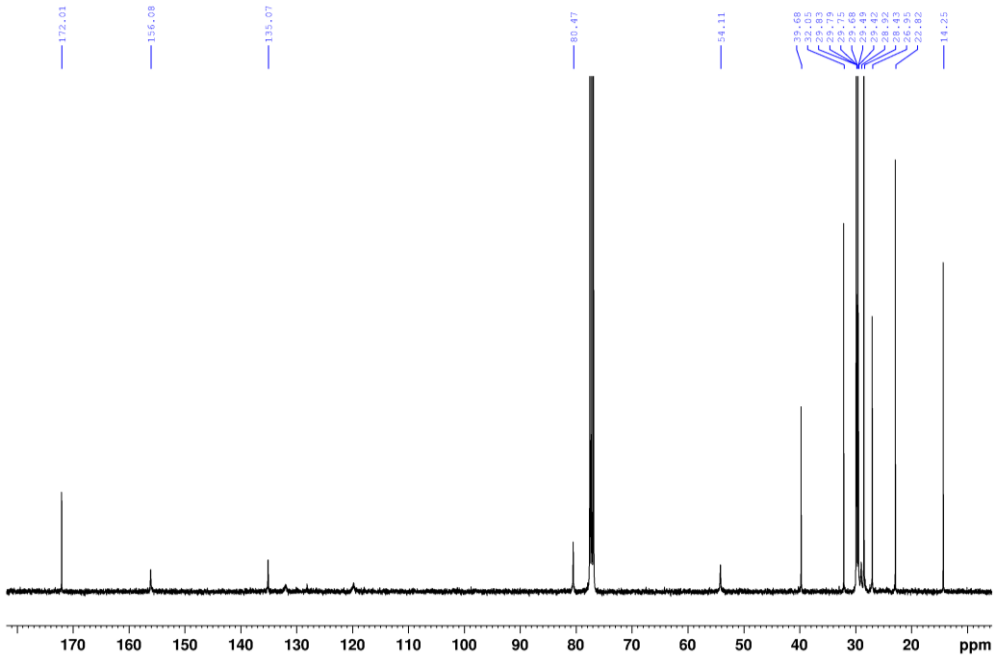

1-Benzyl-*N*-(*tert*-butoxycarbonyl)-L-histidine butyl amide (48)

^{1}H NMR (400 MHz, $CDCl_3$)

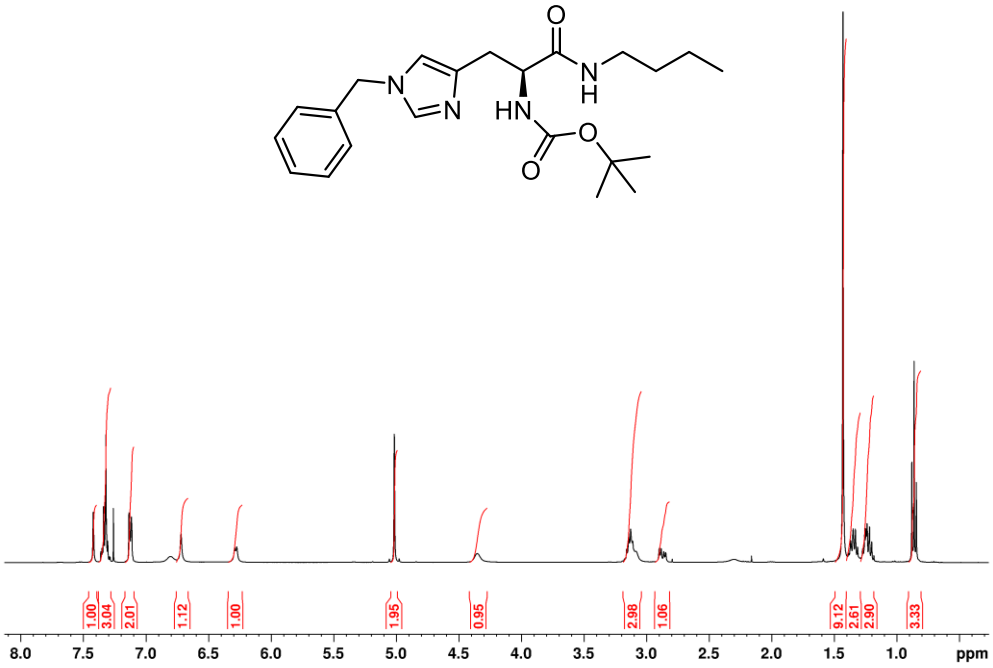

^{13}C NMR (101 MHz, $CDCl_3$)

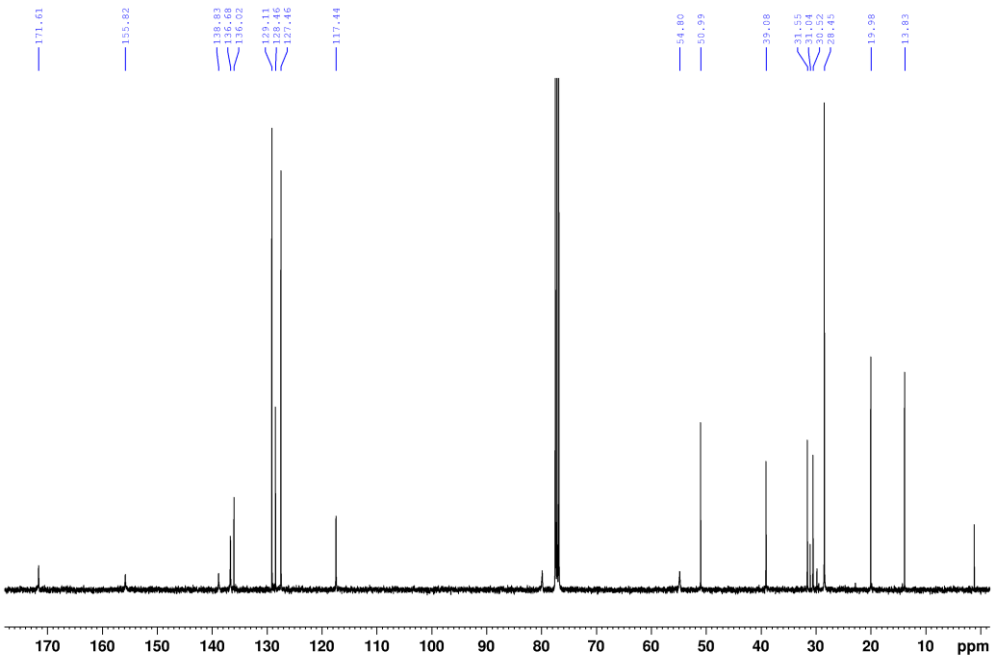

_N_-(_tert_-Butoxycarbonyl)-L-histidine butyl amide (C4-H)

^{1}H NMR (400 MHz, $CDCl_3$)

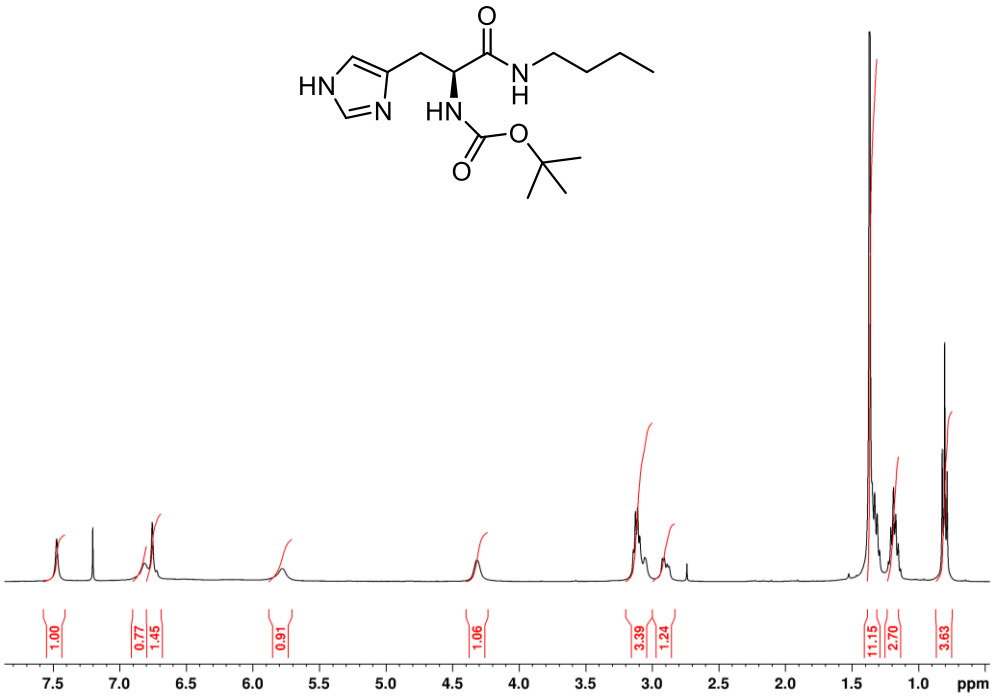

^{13}C NMR (101 MHz, $CDCl_3$)

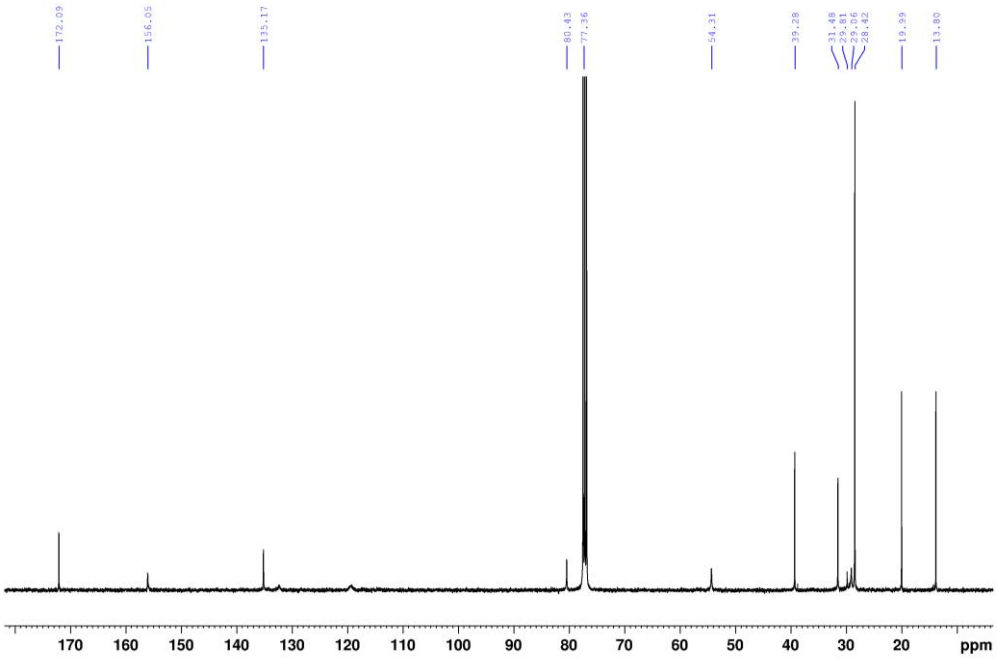

***N*-[2-(1*H*-Imidazol-5-yl)ethyl]heptadecanamide (HM)**

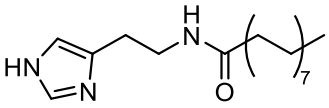

^{1}H NMR (400 MHz, CD_3OD)

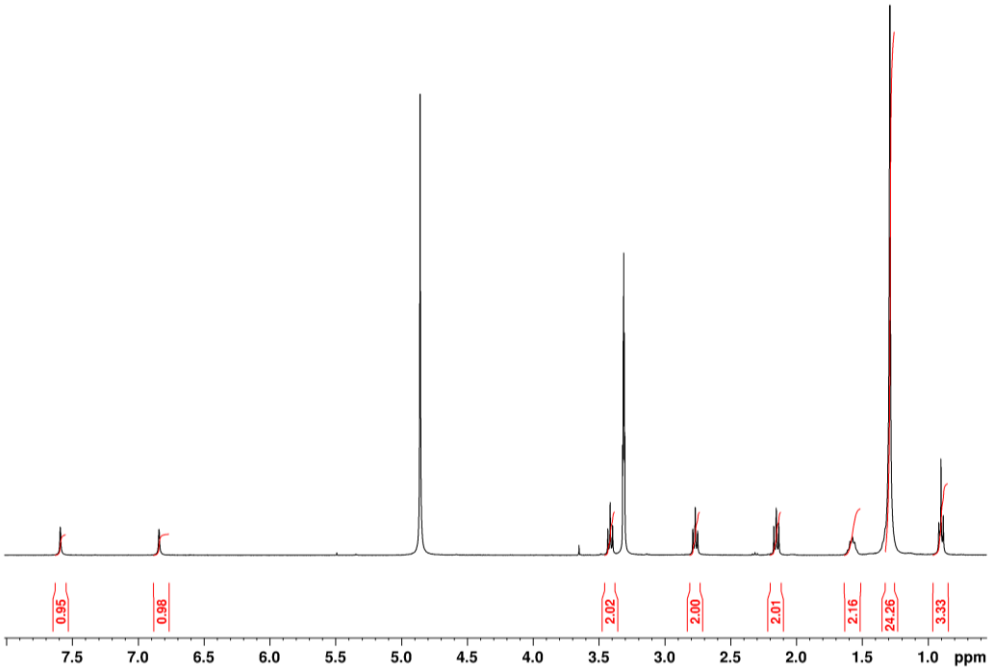

^{13}C NMR (101 MHz, CD_3OD)

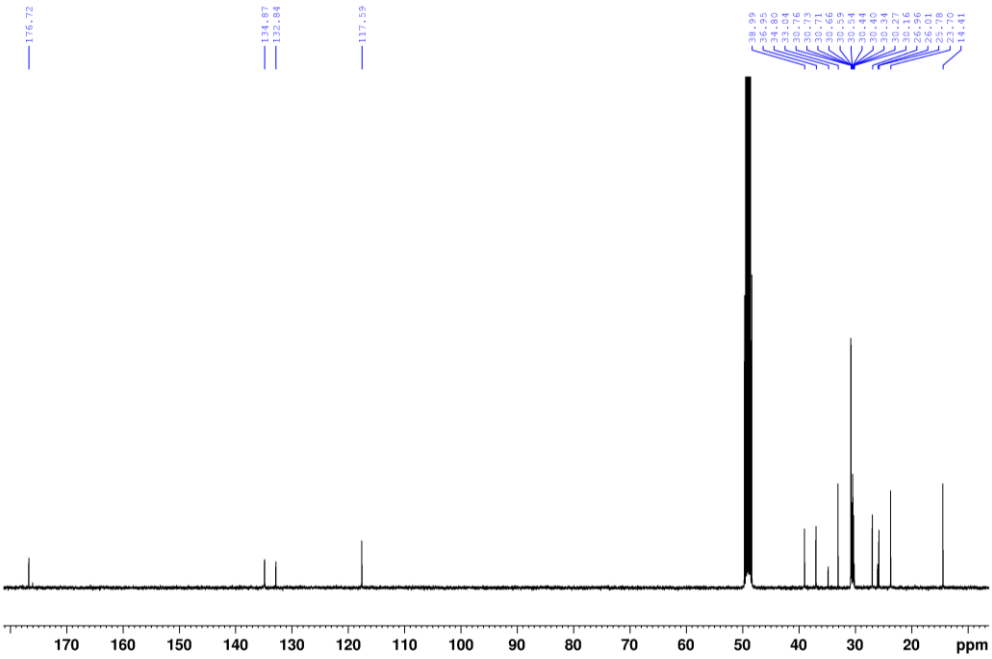

NMR Spectra for Synthesis of Thiols for Silver-Thiol Coordination Polymers

Methyl 6-(tritylthio) hexanoate (65)

^{1}H NMR (400 MHz, $CDCl_3$)

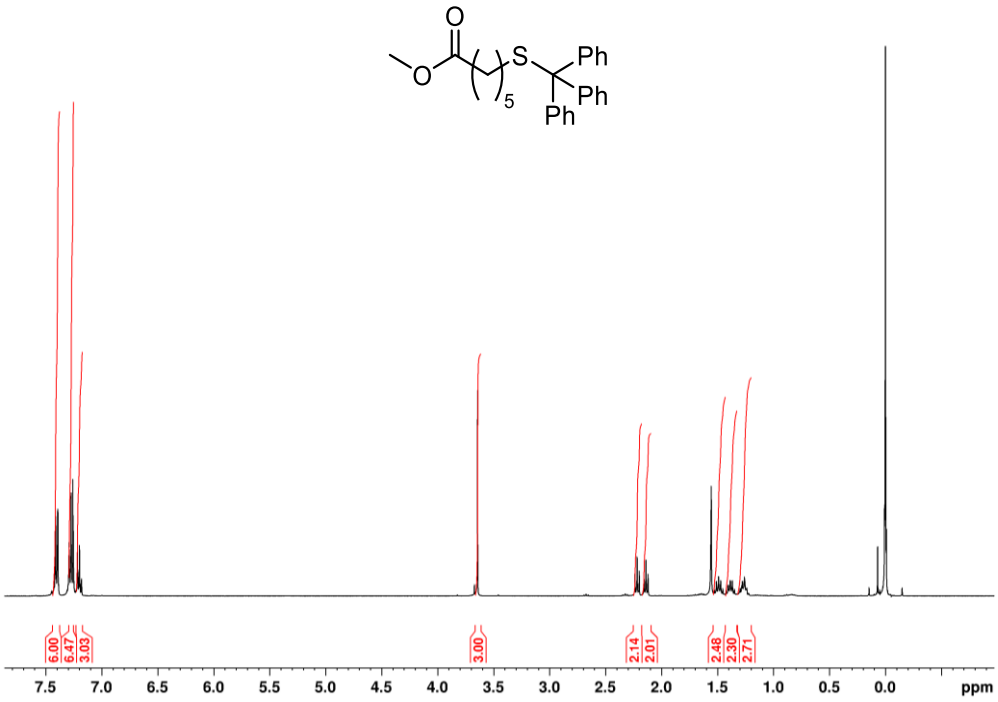

^{13}C NMR (101 MHz, $CDCl_3$)

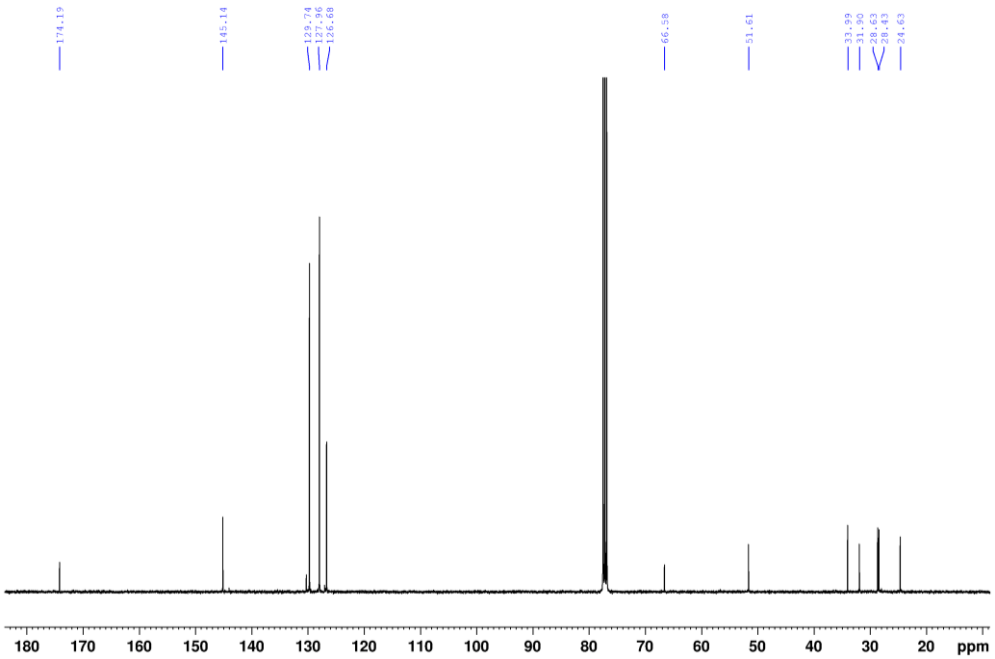

_N_-[2-(1_H_-Imidazol-4-yl)ethyl]-6-(tritylthio)hexanamide (67)

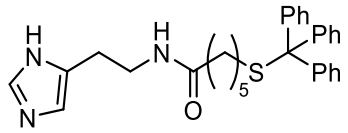

^{1}H NMR (400 MHz, CD_3OD)

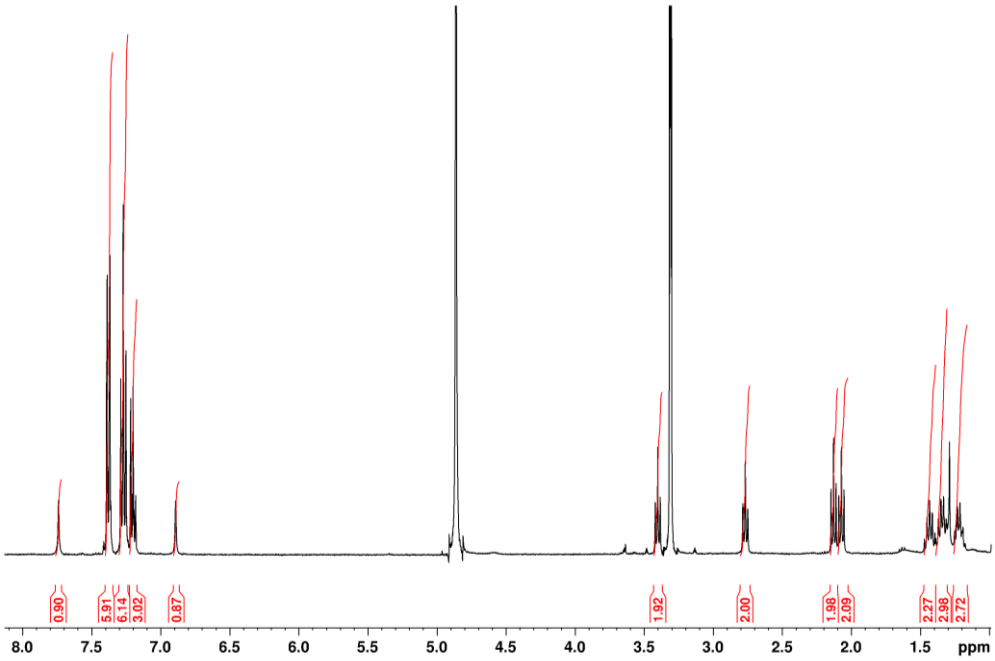

^{13}C NMR (101 MHz, CD_3OD)

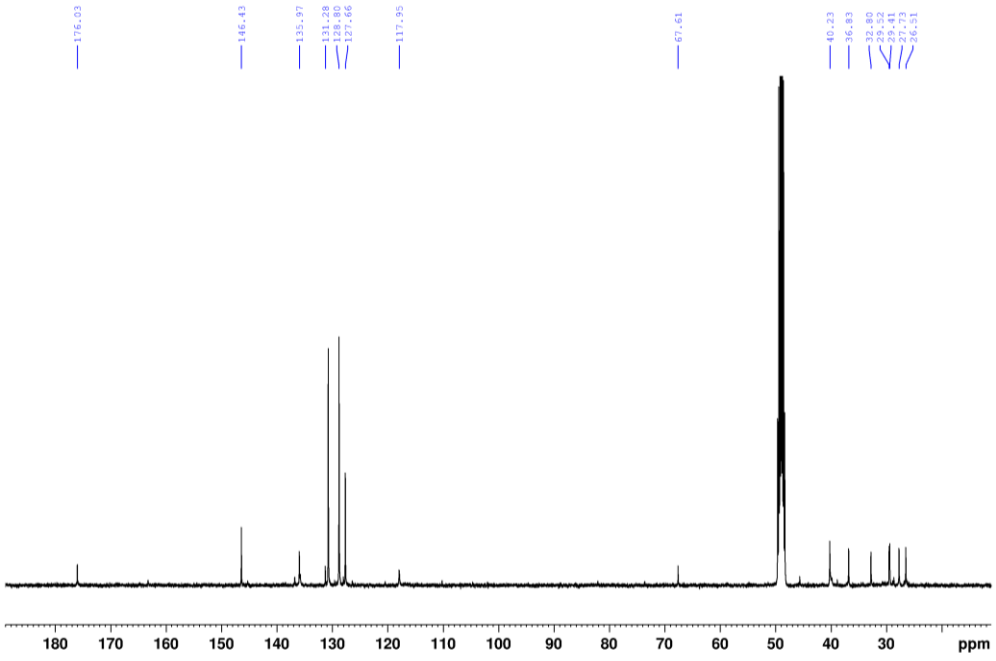
176.03
146.43
135.97
131.28
129.60
128.80
127.66
117.95
67.61
40.23
36.83
32.80
30.52
29.41
27.73
26.51
180
170
160
150
140
130
120
110
100
90
80
70
60
50
40
30
ppm

***N*-[2-(1*H*-Imidazol-4-yl)ethyl]-6-mercaptohexanamide (C6-HM-SH)**

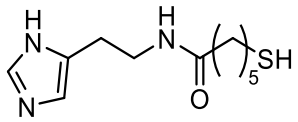

^{1}H NMR (400 MHz, CD_3OD)

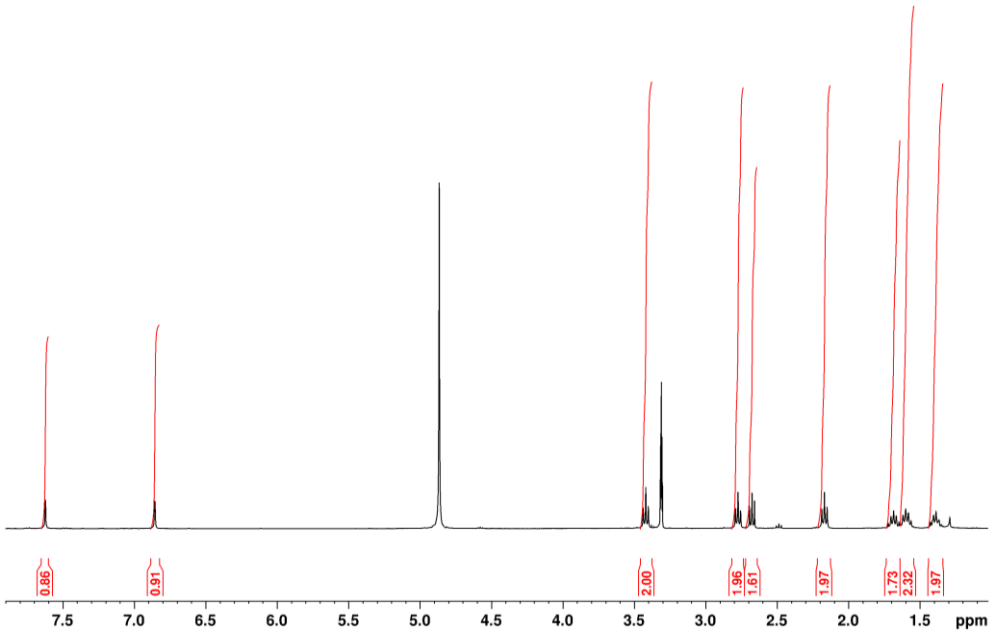

^{13}C NMR (101 MHz, CD_3OD)

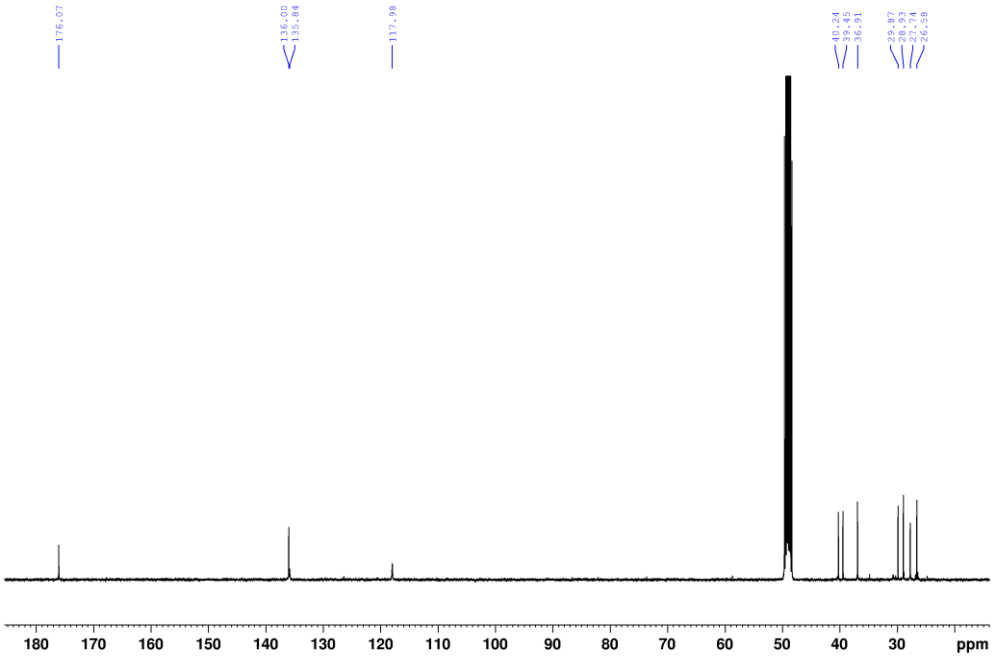

***N*,*N*'Bis(tert-butoxylcarbonyl)-*N*''-6-(tritylthio)hexylguanidine (73)**

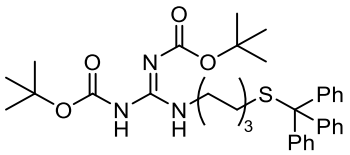

^{1}H NMR (400 MHz, $CDCl_3$)

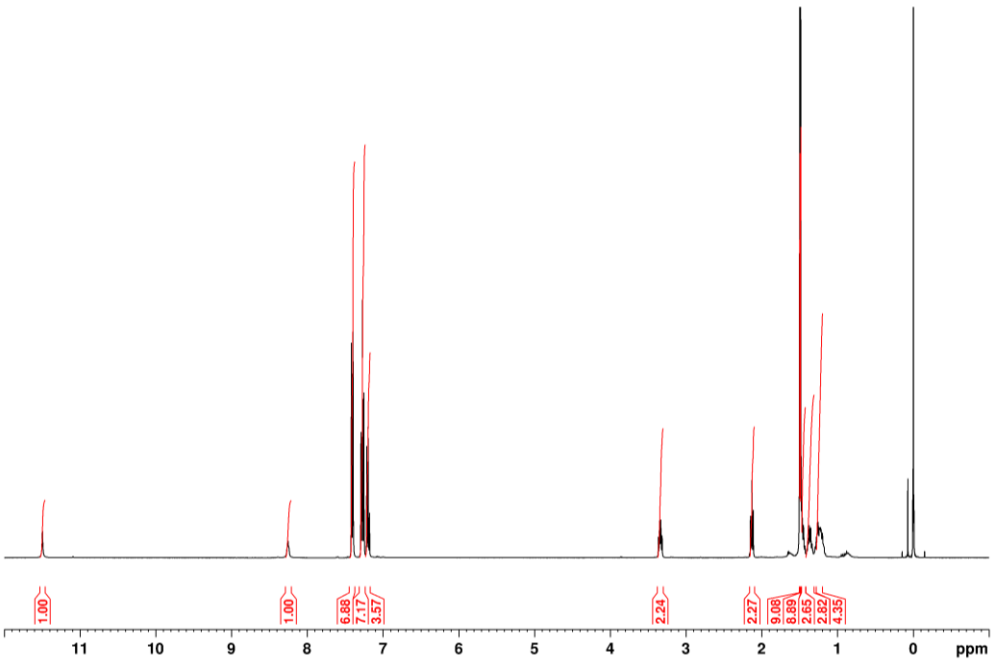

^{13}C NMR (101 MHz, $CDCl_3$)

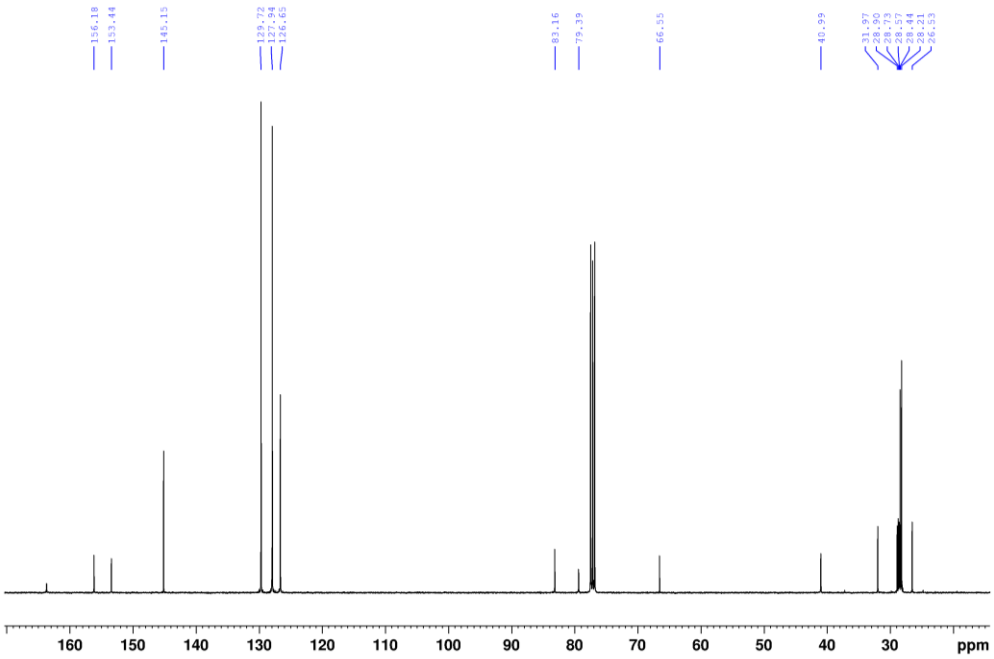

***N*-(6-Mercaptohexyl)guanidine (C6-G-SH)**

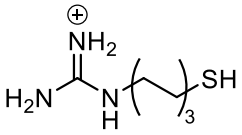

^{1}H NMR (400 MHz, D_2O)

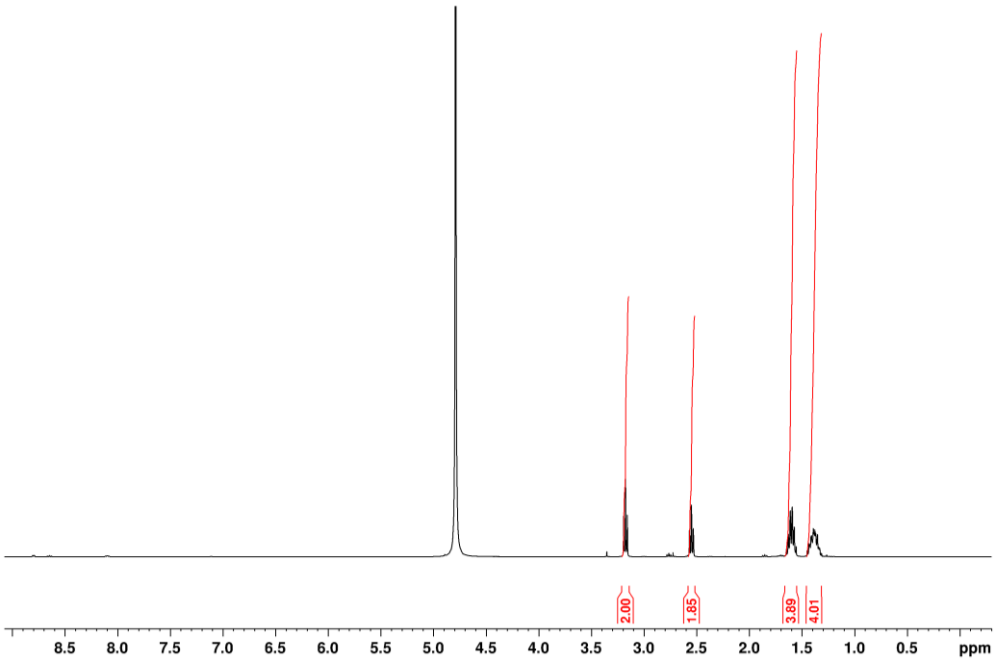

^{13}C NMR (101 MHz, D_2O)

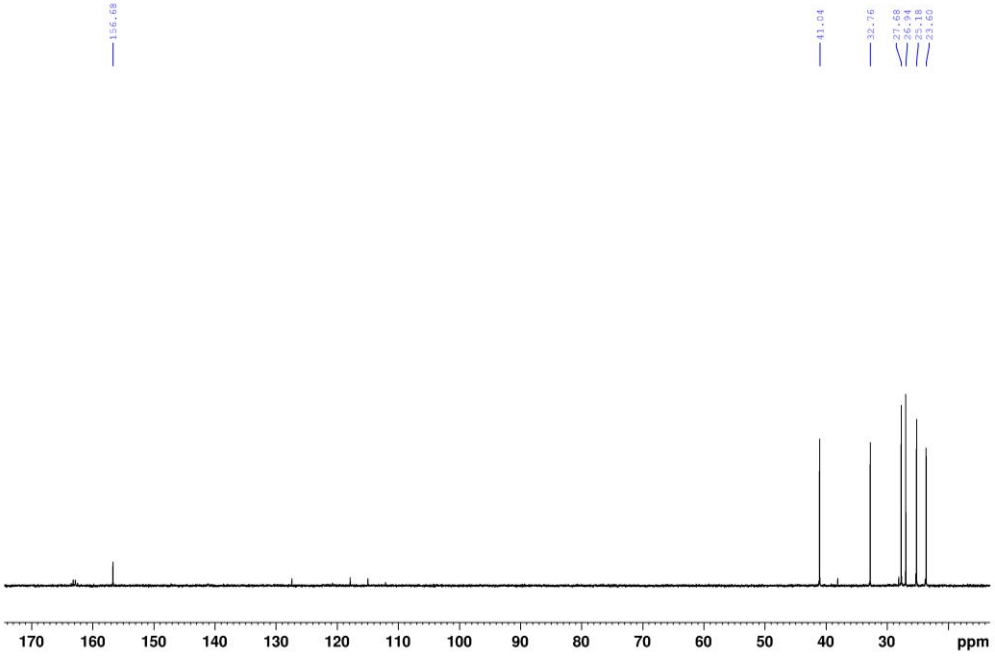

Bis[(pyridine-2-yl)methyl][6-(tritylthio)hexane]amine (77)

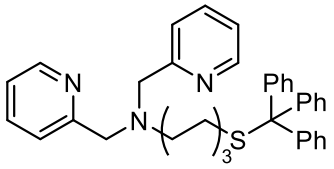

^{1}H NMR (400 MHz, $CDCl_3$)

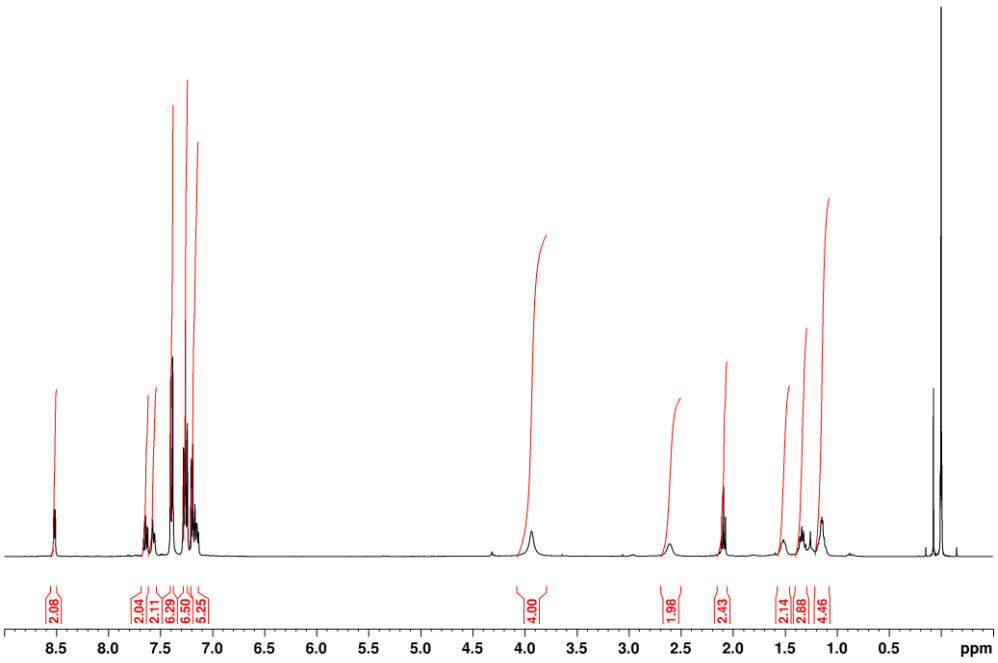

^{13}C NMR (101 MHz, $CDCl_3$)

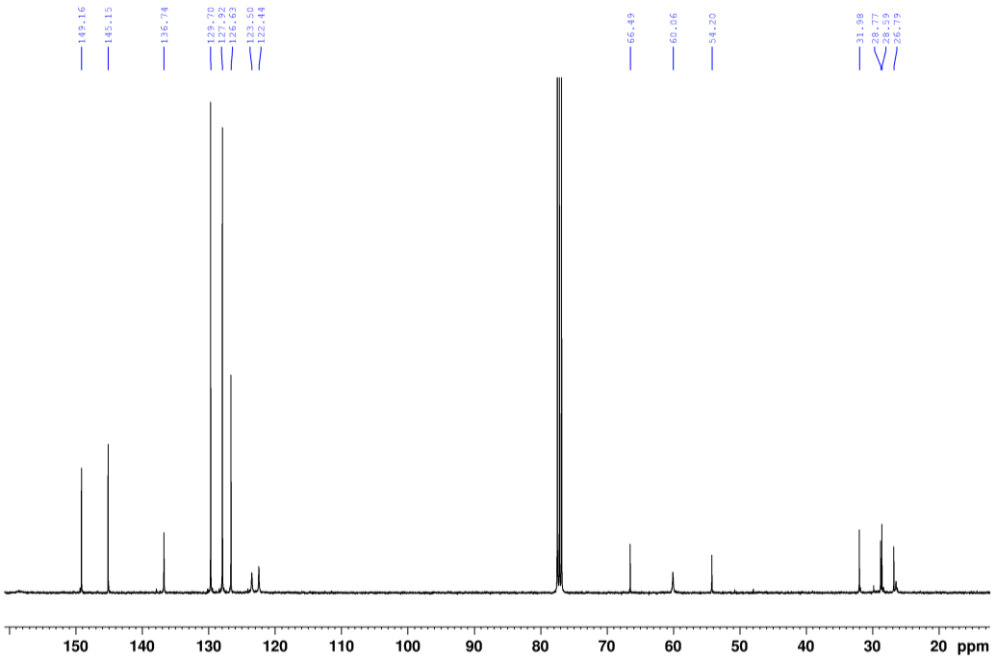

14-(Tritylthio)tetradecane-1-ol (79)

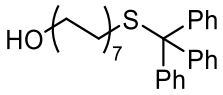

^{1}H NMR (400 MHz, $CDCl_3$)

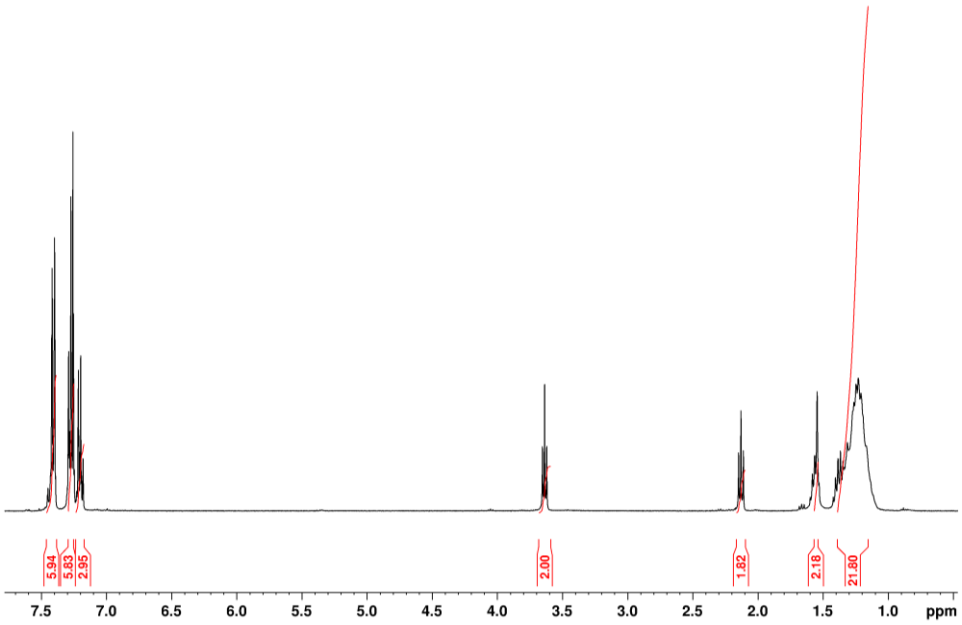

^{13}C NMR (101 MHz, $CDCl_3$)

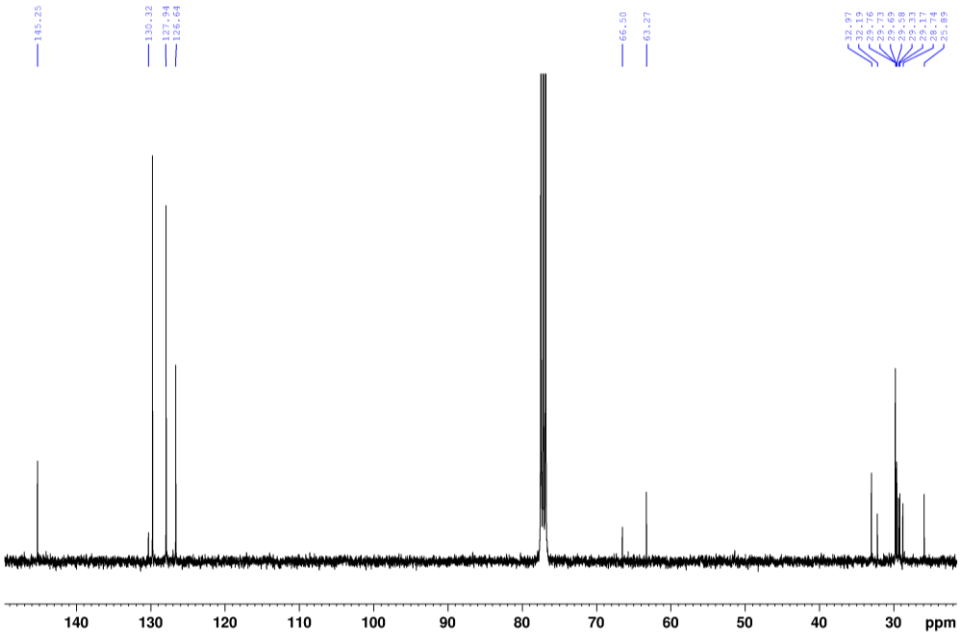

***N,N*-Diethyl-14-(tritylthio)-1-tetradecanamine (82)**

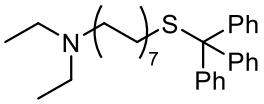

^{1}H NMR (400 MHz, $CDCl_3$)

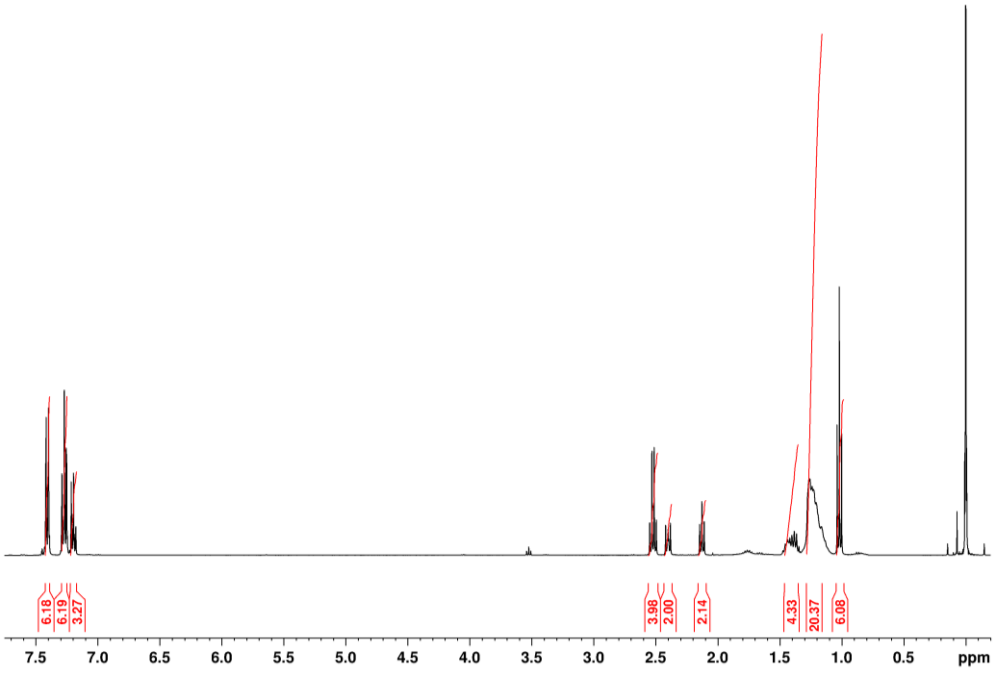

^{13}C NMR (101 MHz, $CDCl_3$)

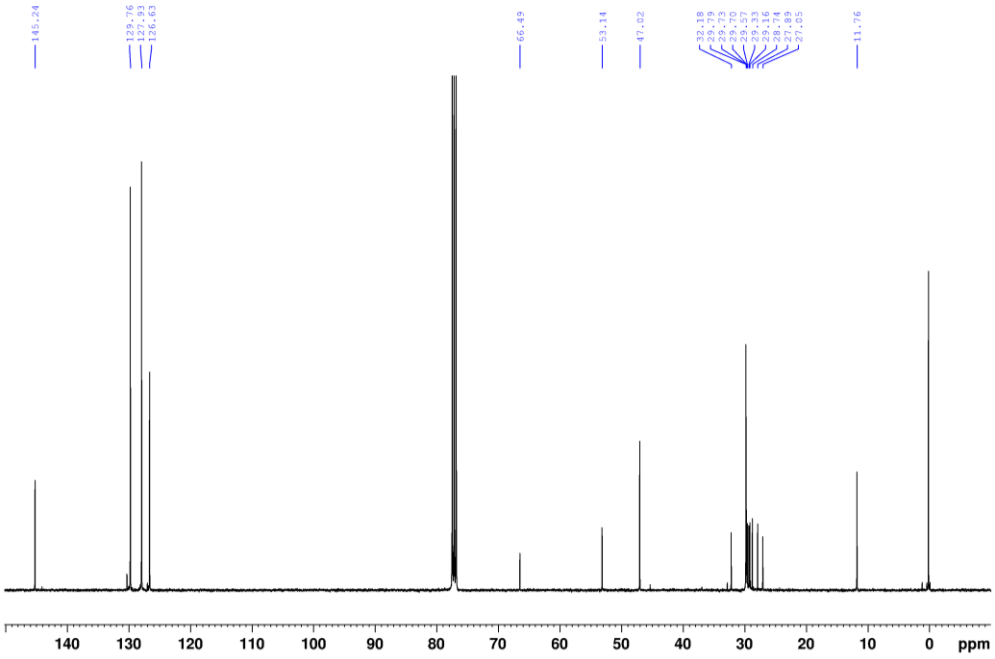

***N,N*-Diethyl-14-mercapto-1-tetradecanamine (DEA-SH)**

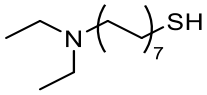

^{1}H NMR (400 MHz, $CDCl_3$)

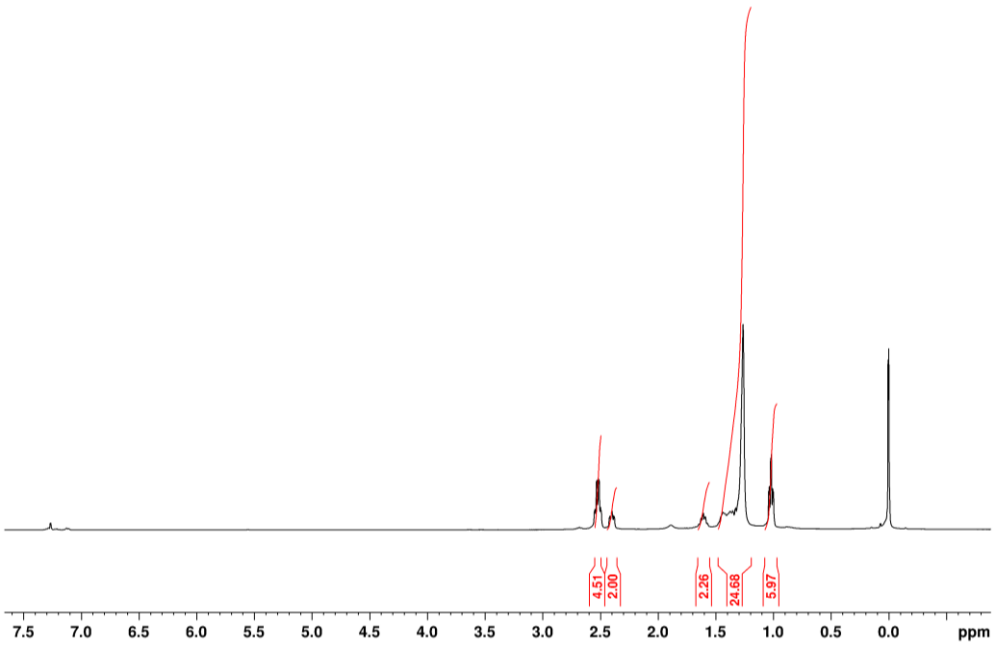

^{13}C NMR (101 MHz, $CDCl_3$)

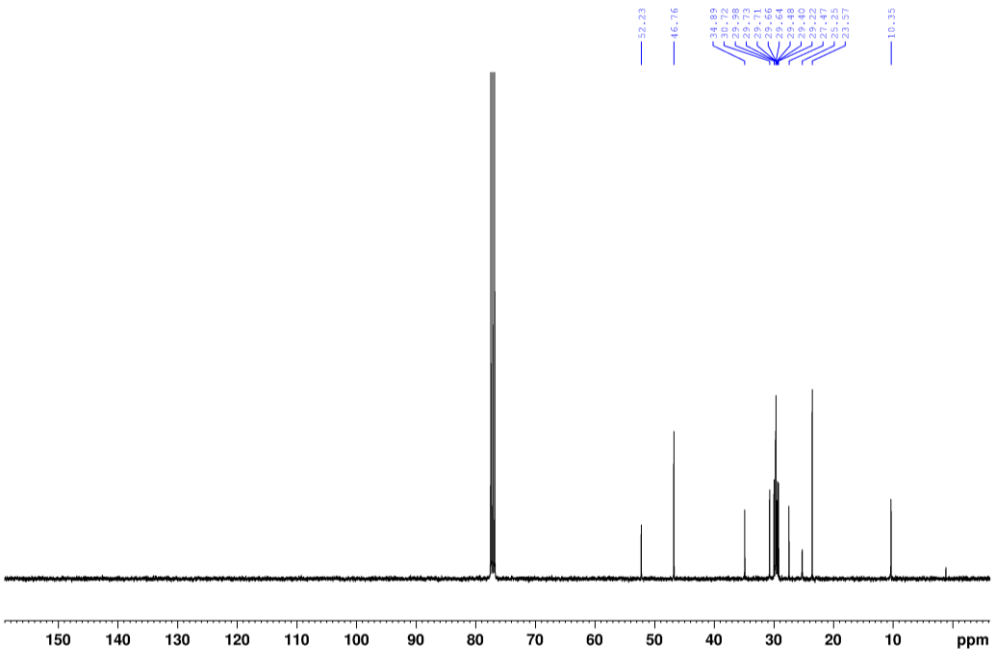

Bis[(pyridine-2-yl)methyl][14-(tritylthio)tetradecane]amine (81)

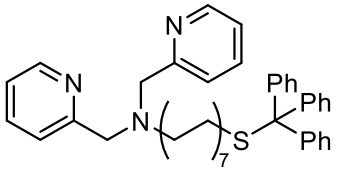

^{1}H NMR (400 MHz, $CDCl_3$)

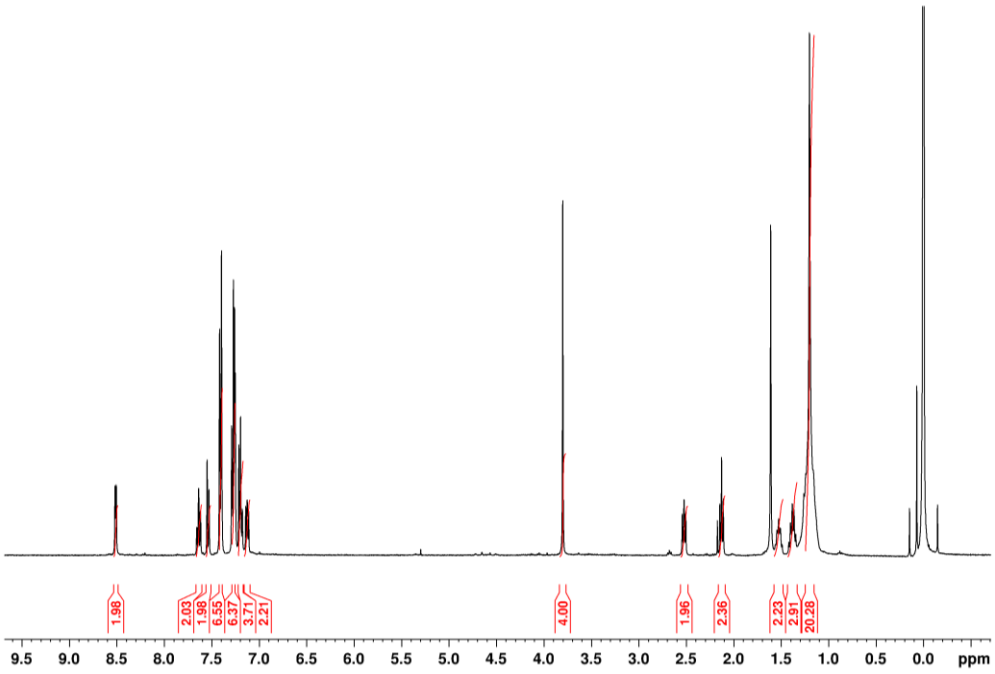

^{13}C NMR (101 MHz, $CDCl_3$)

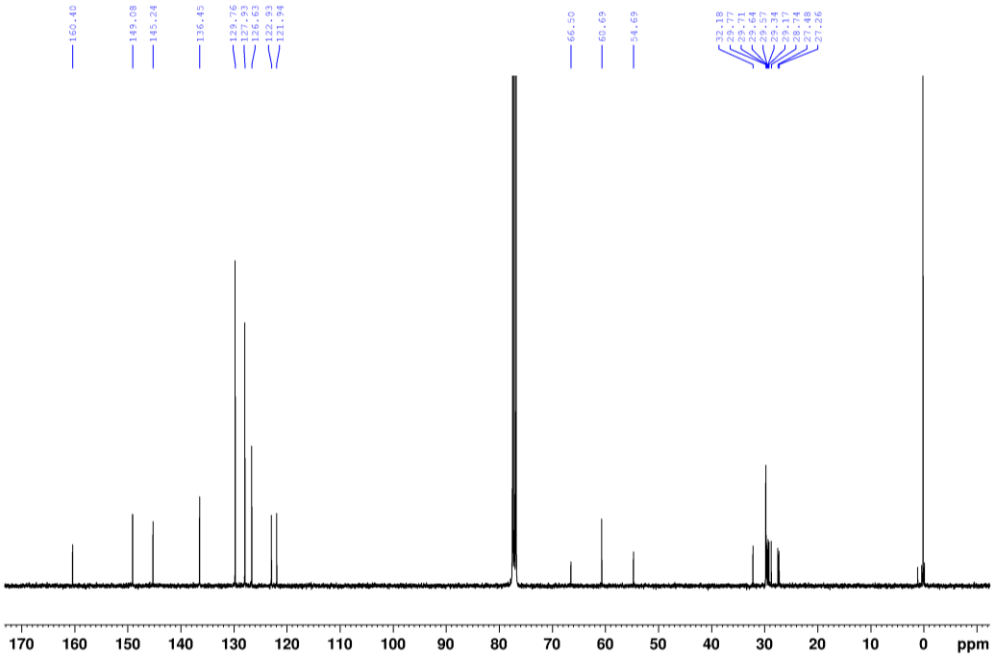

14-{Bis[(pyridine-2-yl)methyl]amino}tetradecane-1-thiol (D2PA-SH)

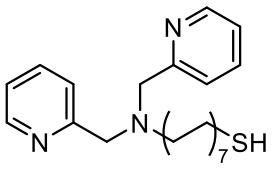

^{1}H NMR (400 MHz, CD_3OD)

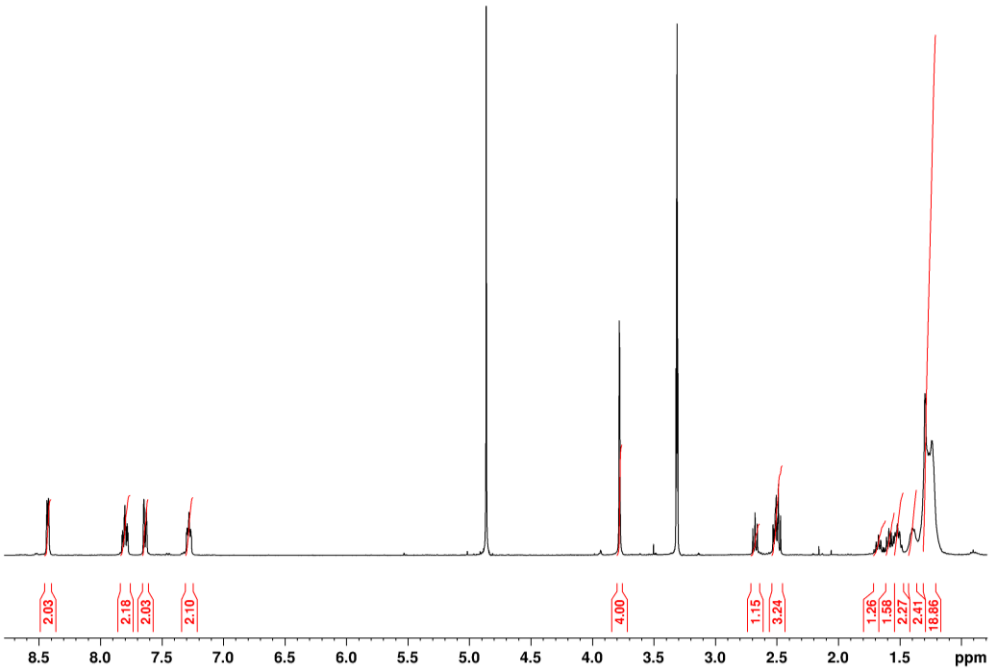

^{13}C NMR (101 MHz, CD_3OD)

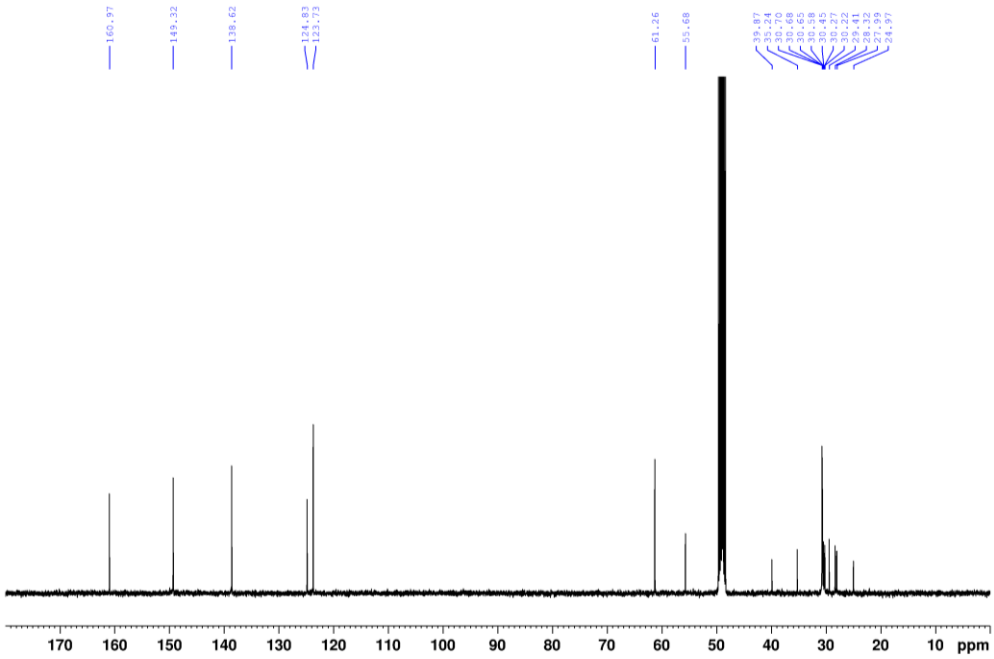

COSY NMR

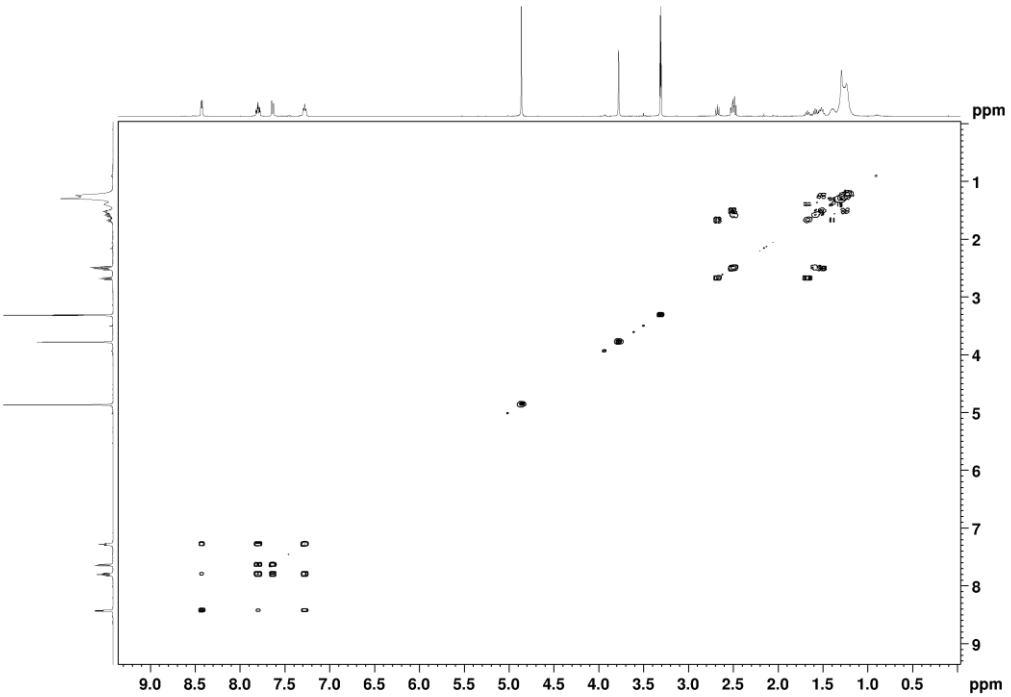

HSQC NMR

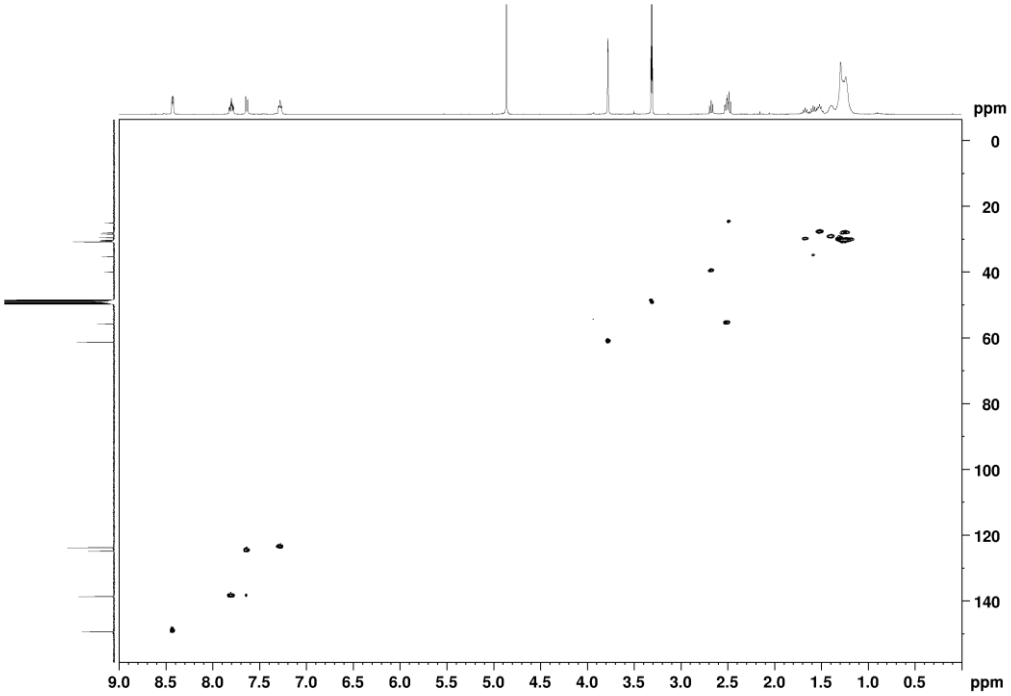

HMBC NMR

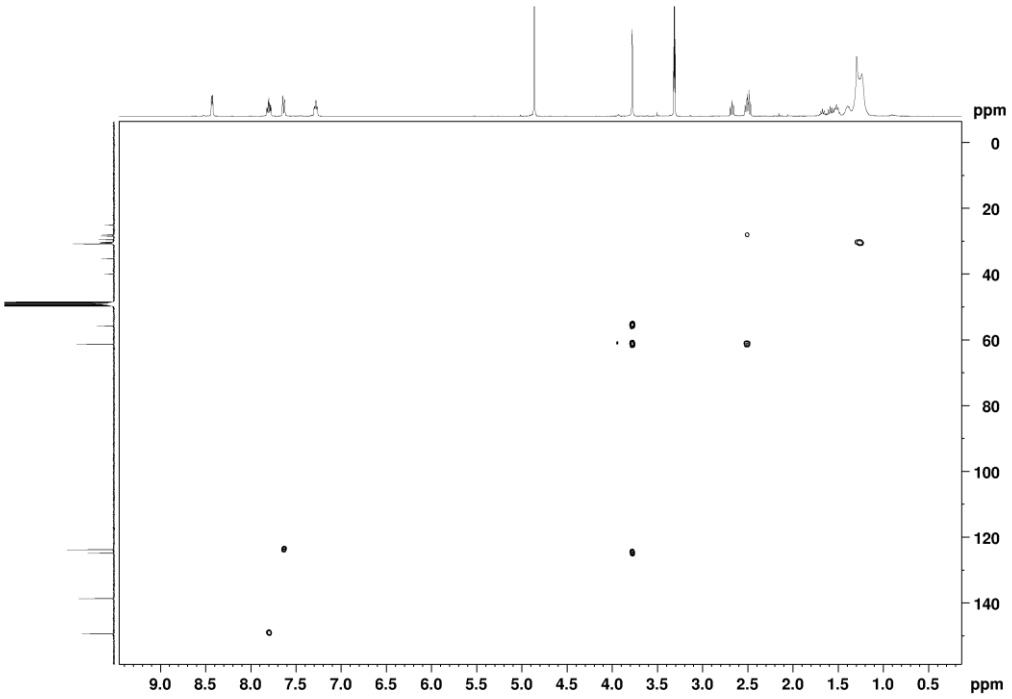
ppm
0
20
40
60
80
100
120
140
9.0
8.5
8.0
7.5
7.0
6.5
6.0
5.5
5.0
4.5
4.0
3.5
3.0
2.5
2.0
1.5
1.0
0.5
ppm

Methyl 14-bromotetradecanoate (90)

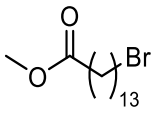

^{1}H NMR (400 MHz, $CDCl_3$)

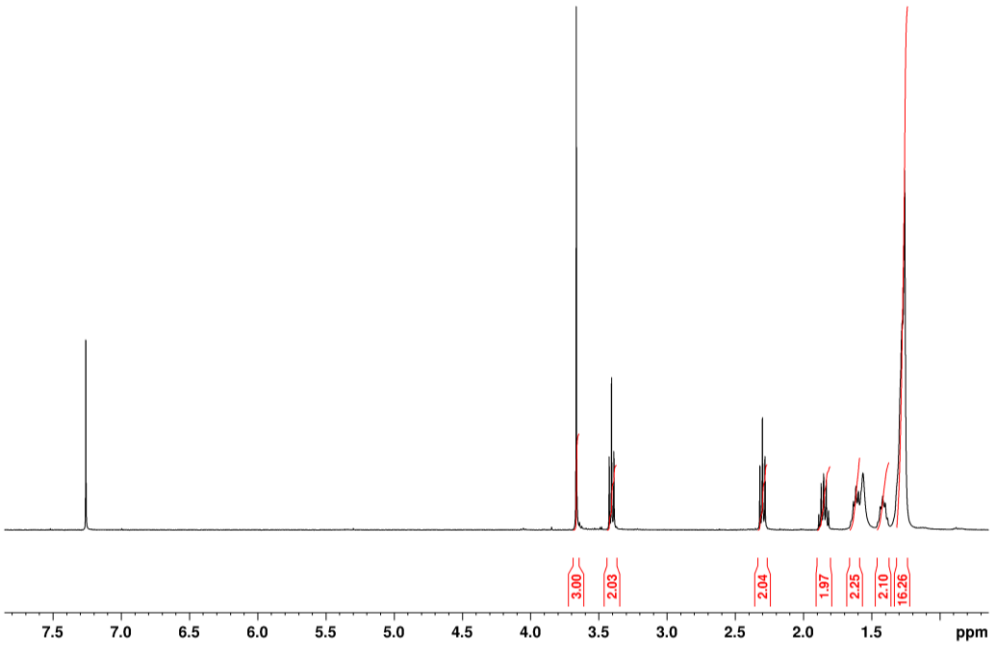

^{13}C NMR (101 MHz, $CDCl_3$)

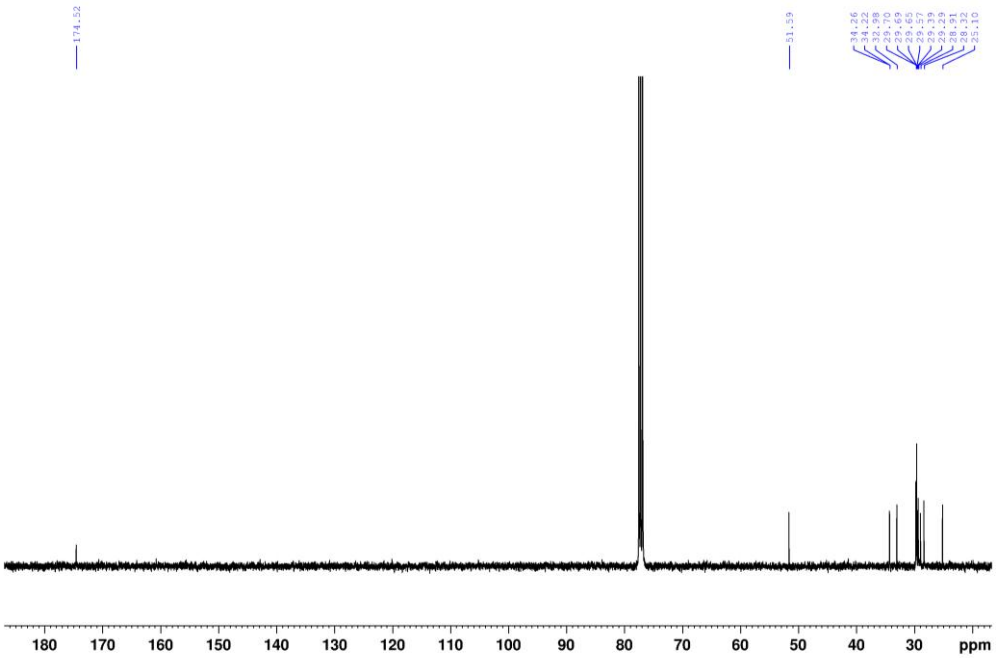

Methyl 14-(tritylthio) tetradecanoate (91)

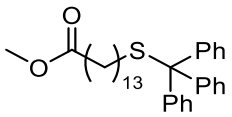

^{1}H NMR (400 MHz, $CDCl_3$)

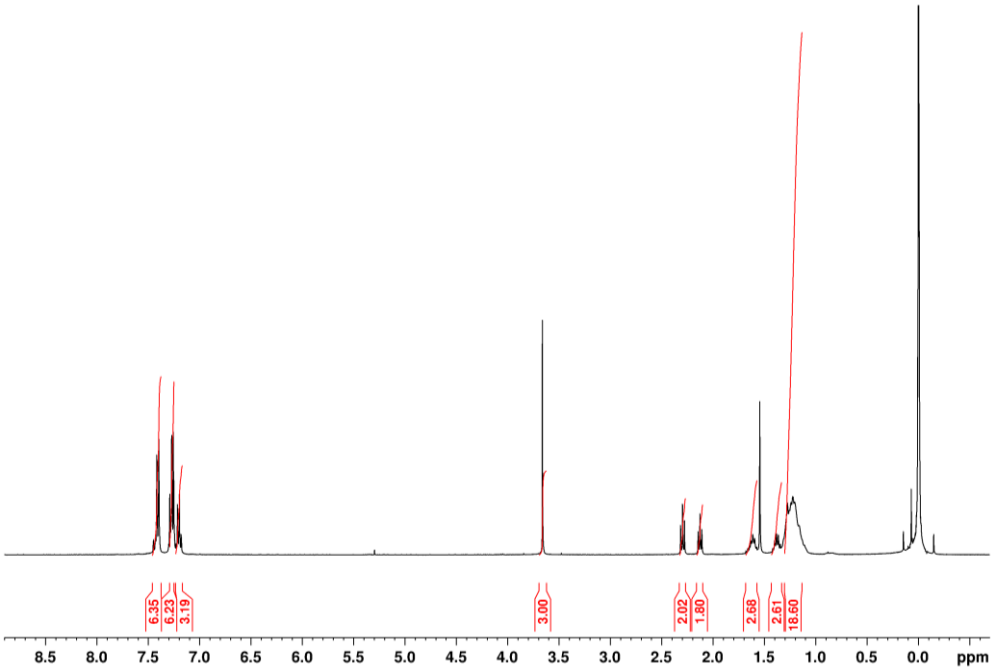

^{13}C NMR (101 MHz, $CDCl_3$)

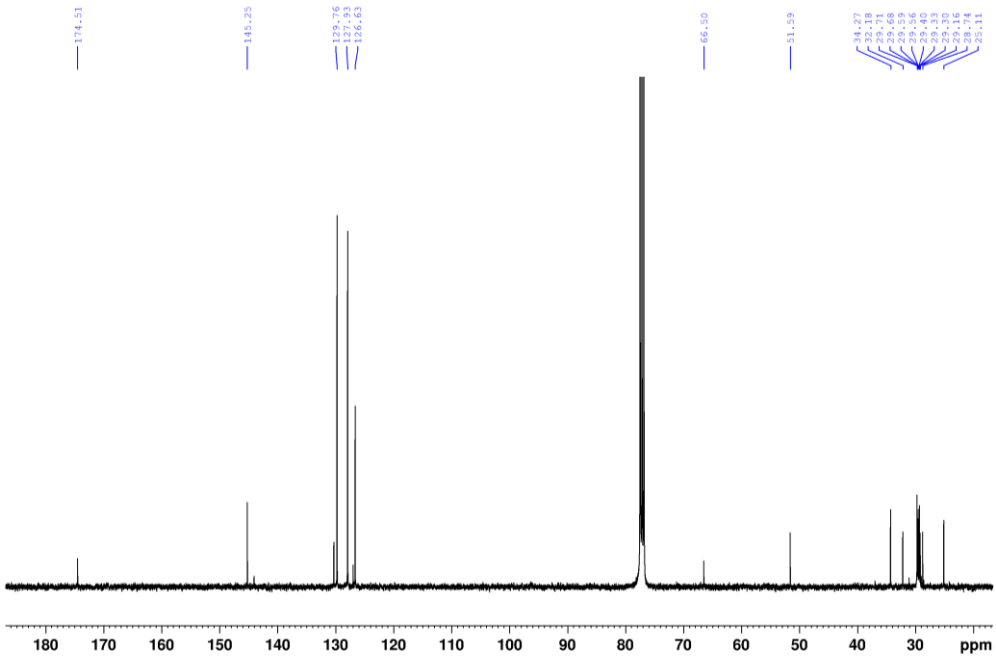

14-(Tritylthio) tetradecanoic acid (88)

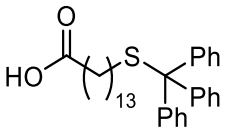

^{1}H NMR (400 MHz, $CDCl_3$)

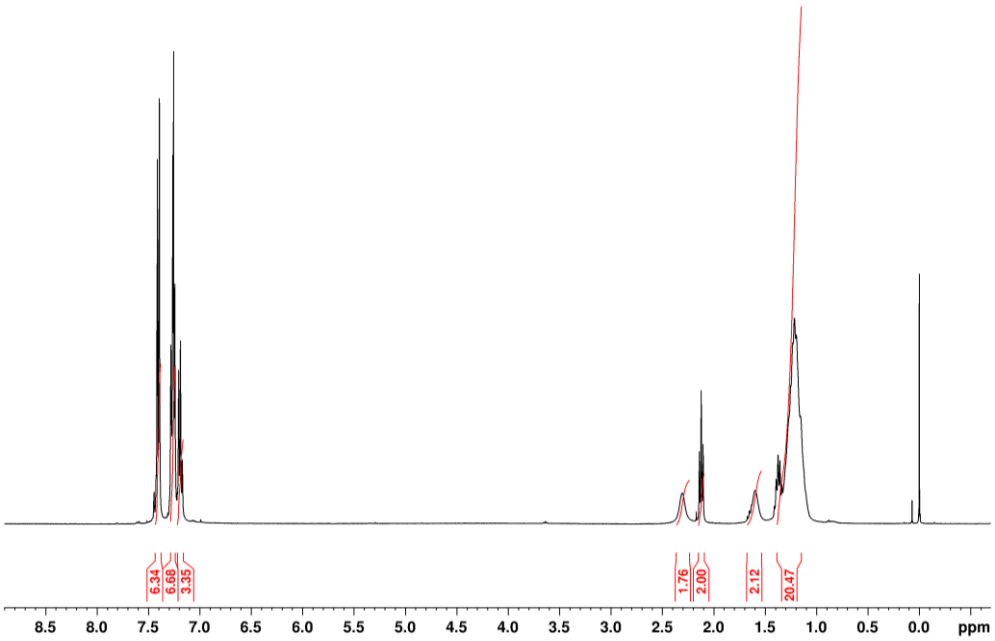

^{13}C NMR (101 MHz, $CDCl_3$)

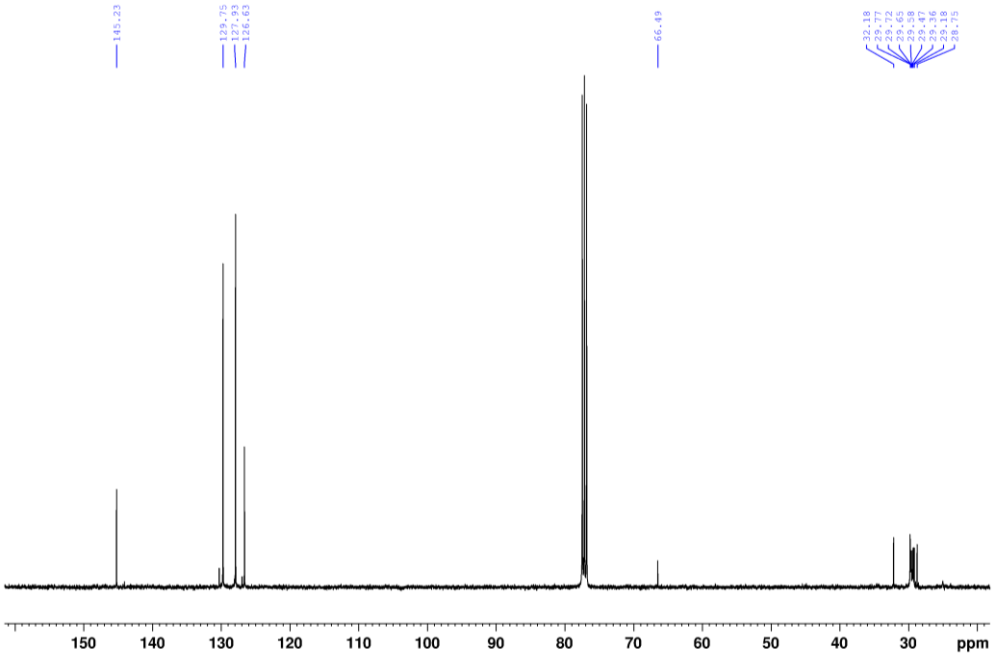

Methyl 14-(acetylthio)tetradecanoate (93)

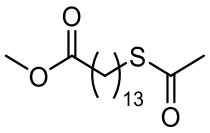

^{1}H NMR (400 MHz, $CDCl_3$)

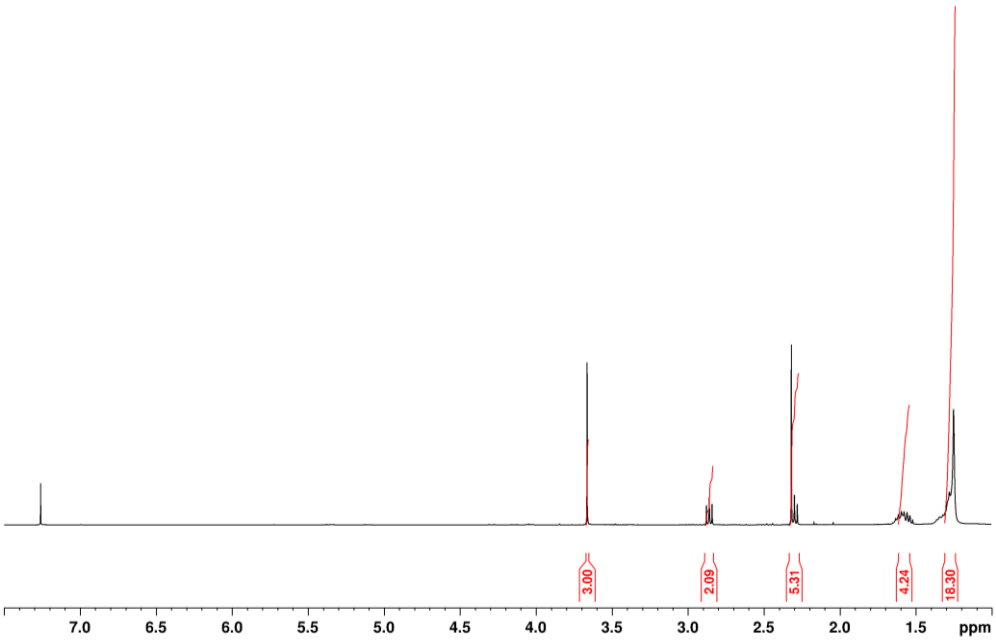

^{13}C NMR (101 MHz, $CDCl_3$)

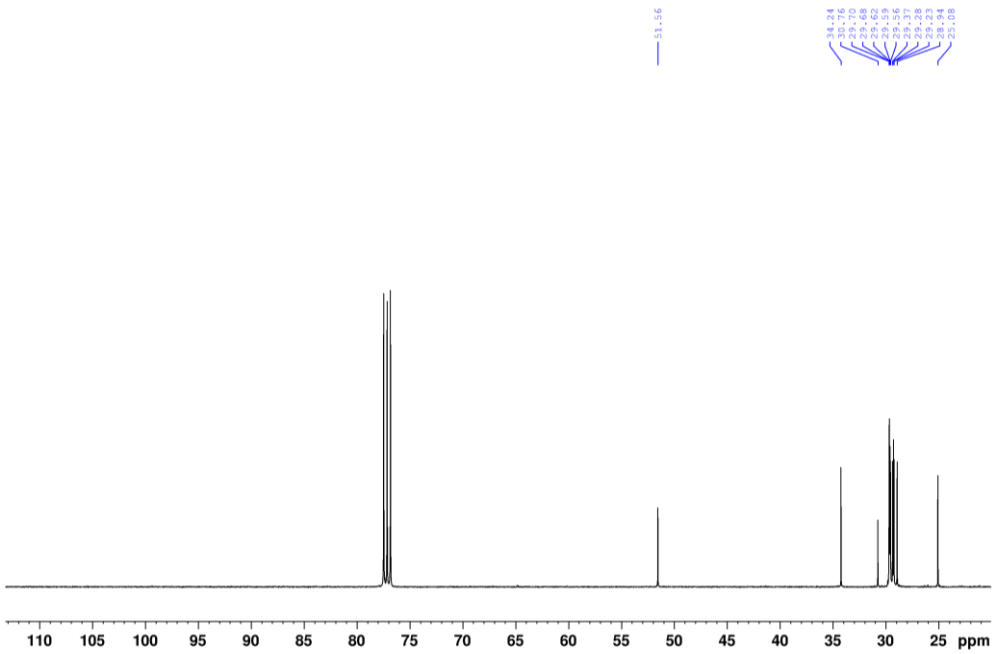

14-(Tritylthio)-1-azotetradecane (83)

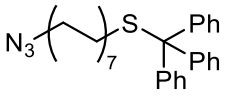

^{1}H NMR (400 MHz, $CDCl_3$)

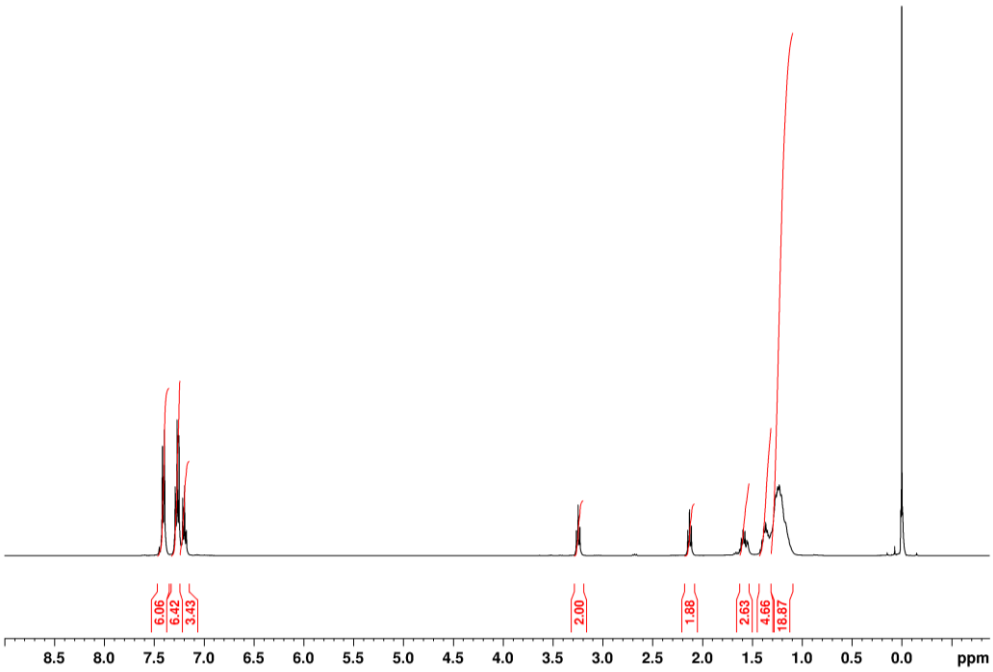

^{13}C NMR (101 MHz, $CDCl_3$)

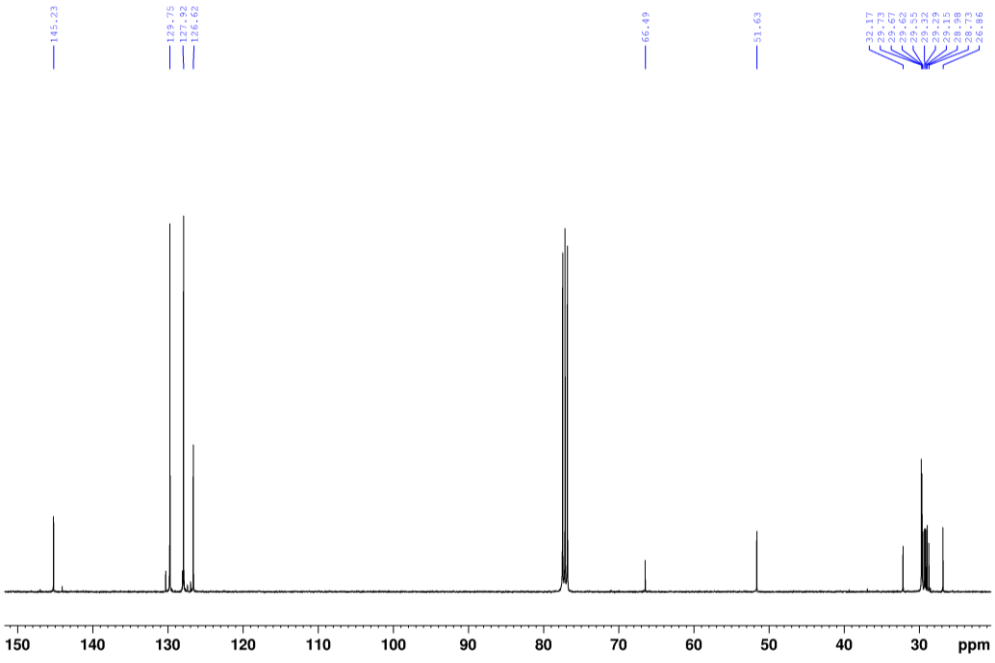

_N_-[2-(1_H_-Imidazol-4-yl)ethyl]-14-(tritylthio)tetradecanamide (99)

^{1}H NMR (400 MHz, $CDCl_3$)

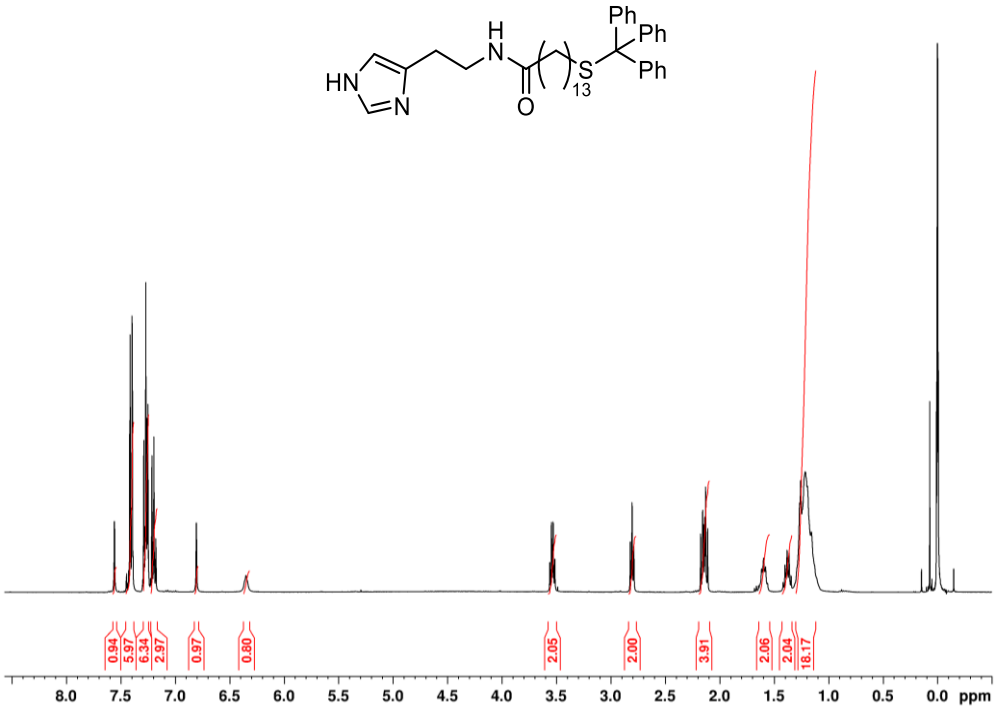

^{13}C NMR (101 MHz, $CDCl_3$)

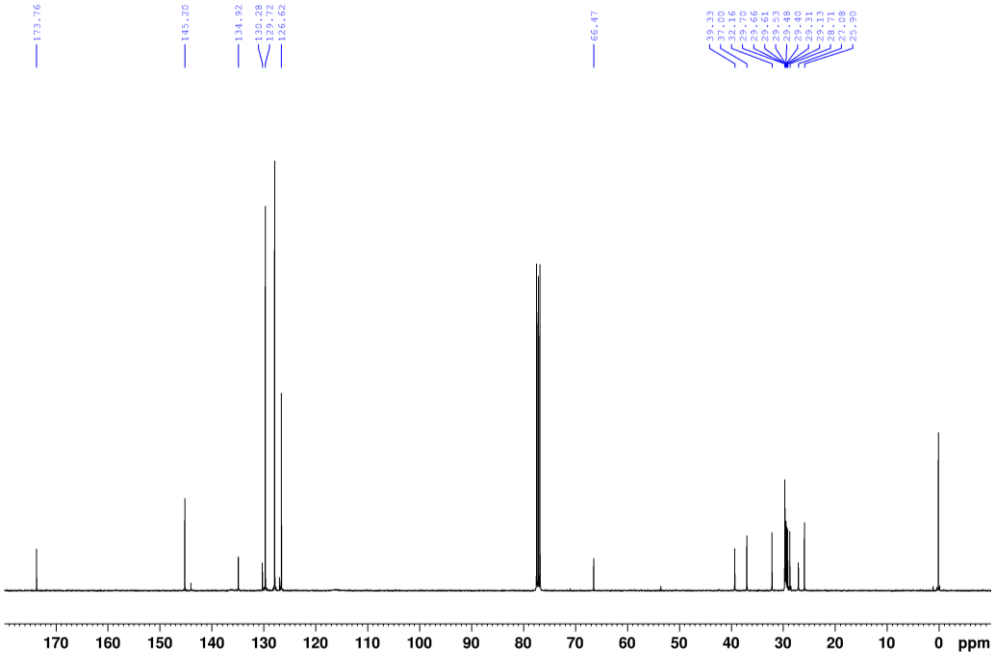

***N*-[2-(1*H*-Imidazol-4-yl)ethyl]-14-mercaptotetradecanamide (HM-SH)**

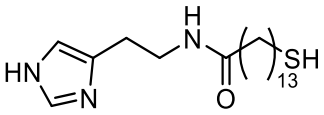

^{1}H NMR (400 MHz, CD_3OD)

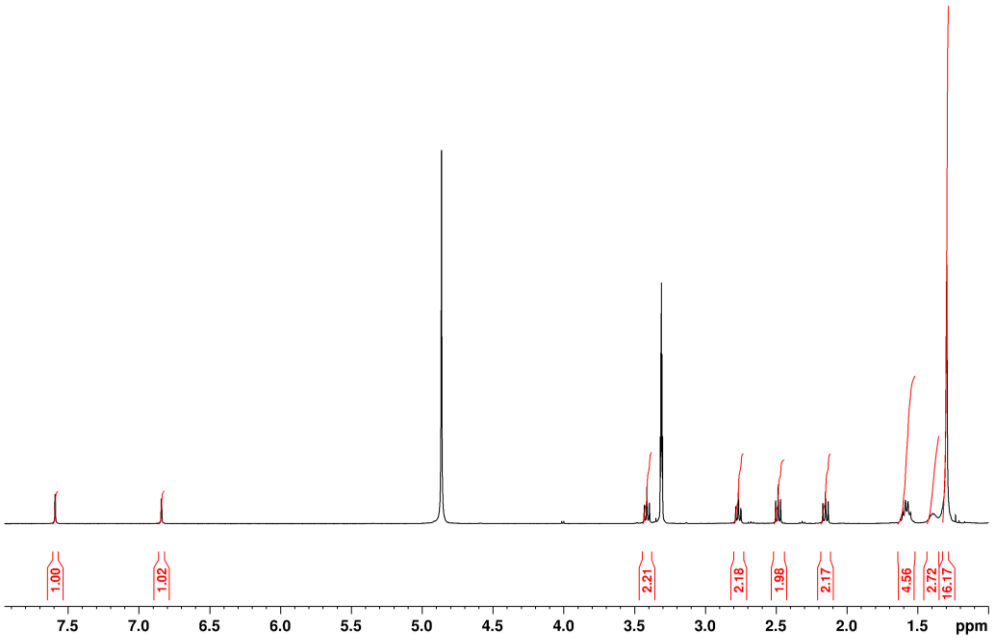

^{13}C NMR (101 MHz, CD_3OD)

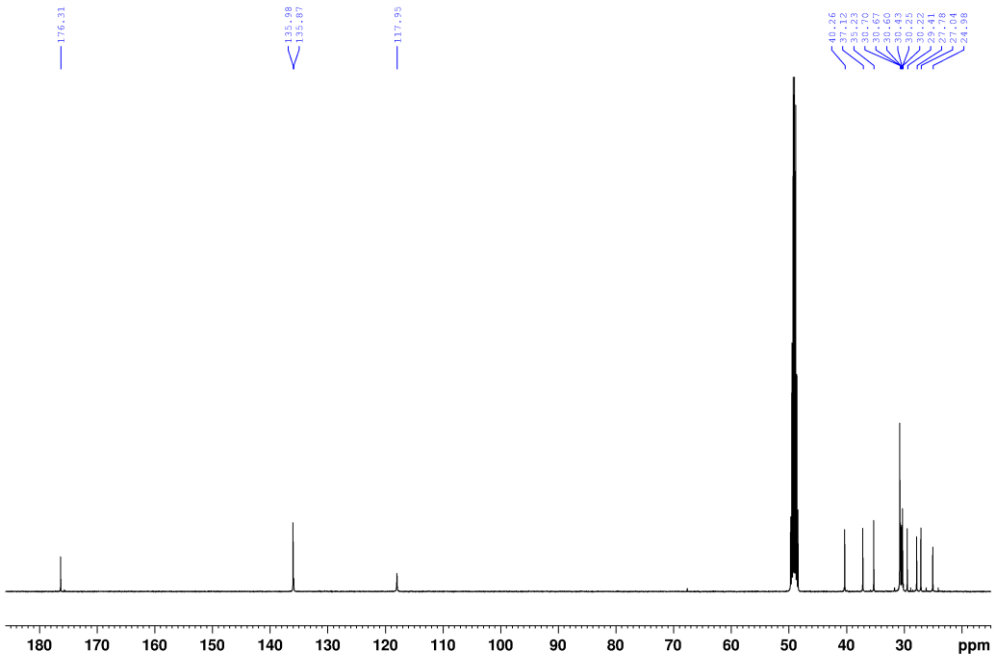

COSY NMR

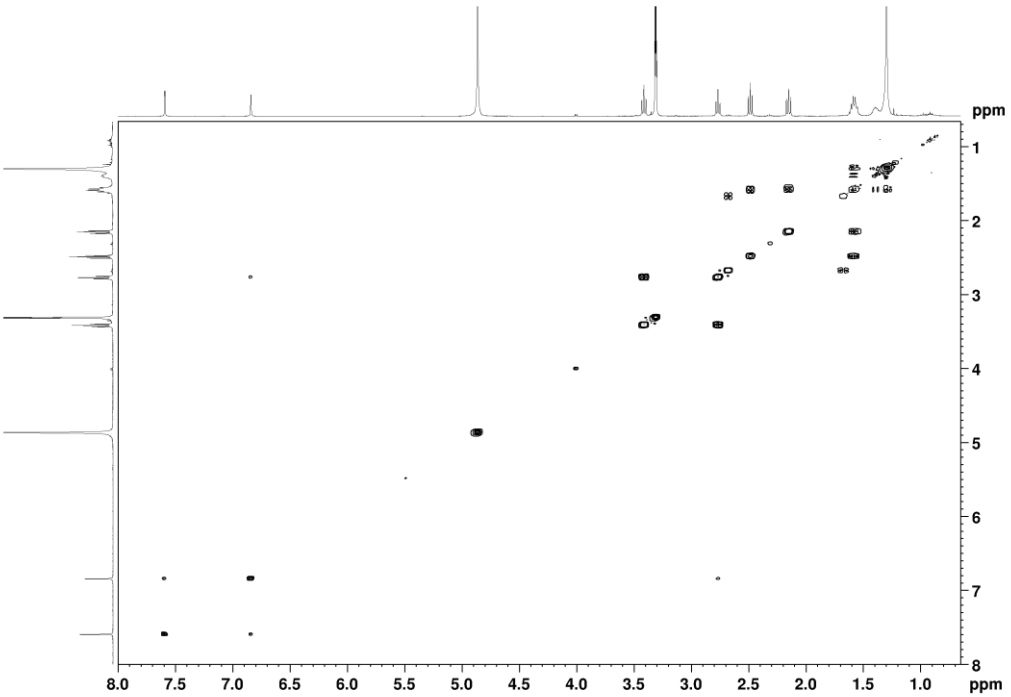

HSQC NMR

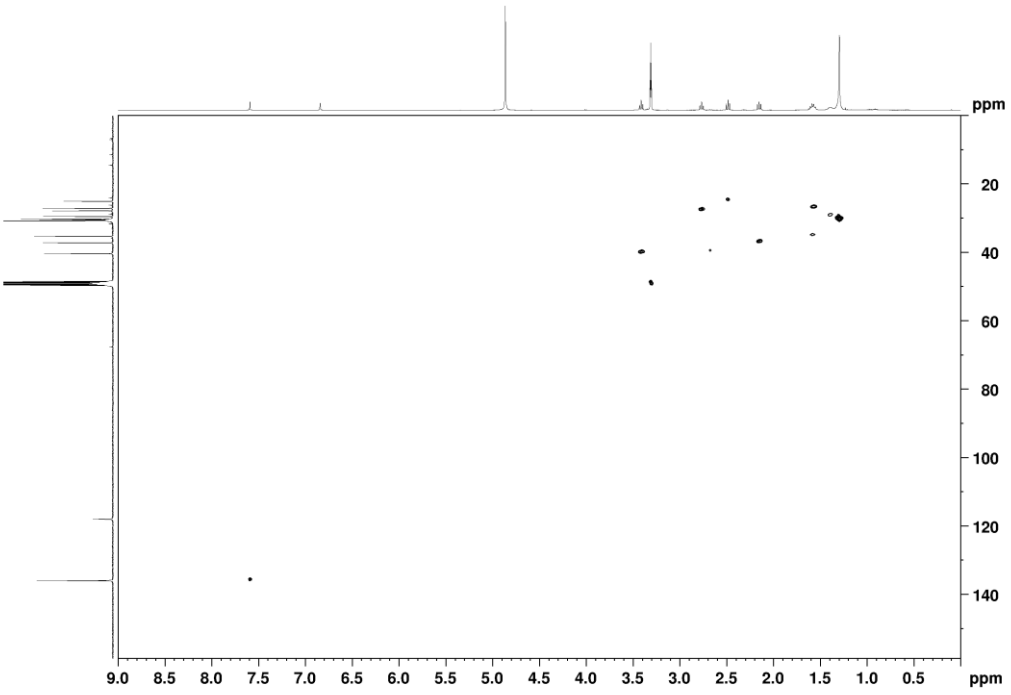

HMBC NMR

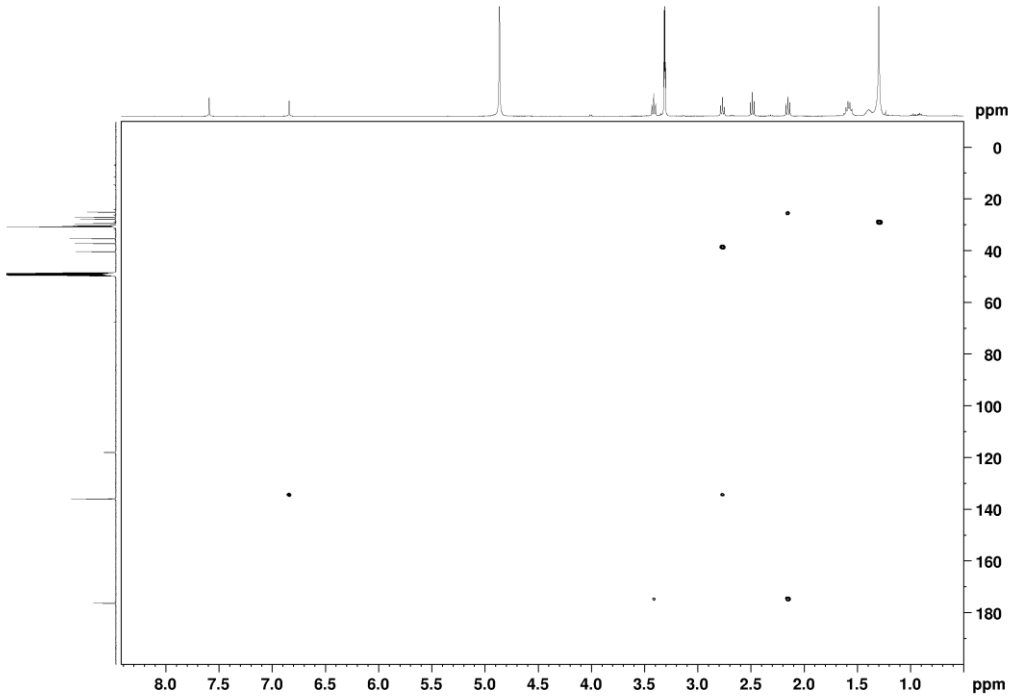
ppm
0
20
40
60
80
100
120
140
160
180
8.0
7.5
7.0
6.5
6.0
5.5
5.0
4.5
4.0
3.5
3.0
2.5
2.0
1.5
1.0
ppm

***N,N'*-Bis(tert-butoxycarbonyl)-*N''*-14-(tritylthio)tetradecylguanidine (85)**

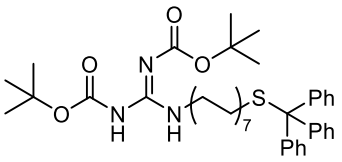

^{1}H NMR (400 MHz, $CDCl_3$)

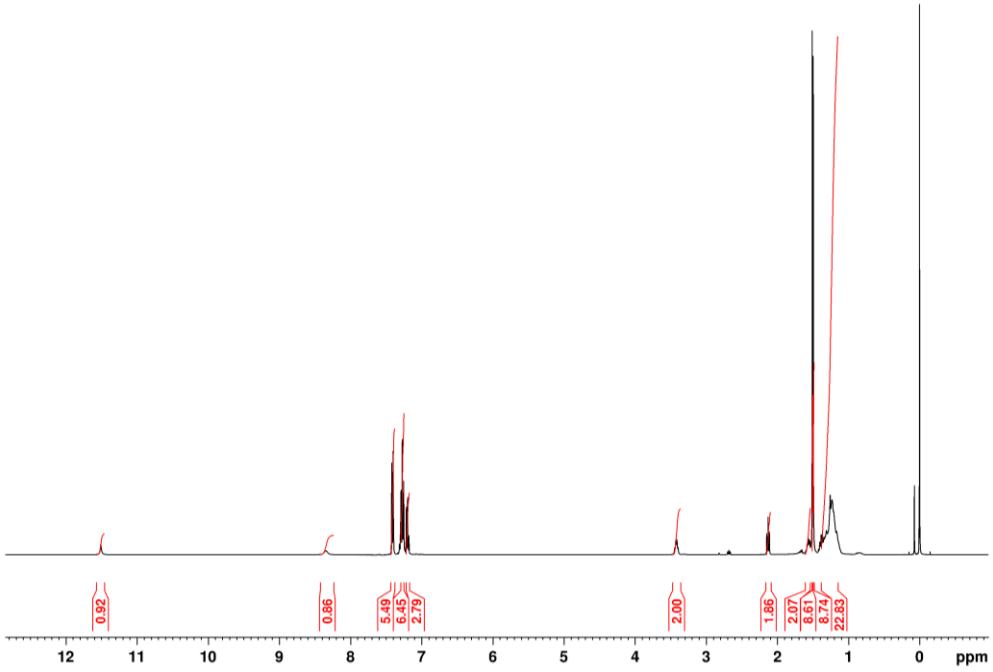

^{13}C NMR (101 MHz, $CDCl_3$)

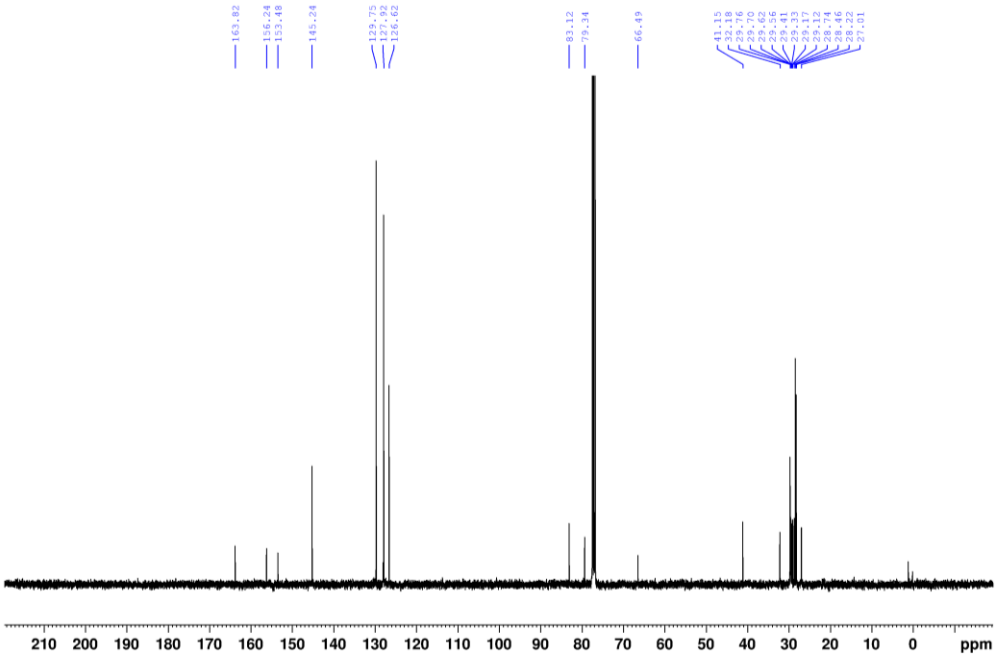

_S_-(14-Hydroxytetradecyl) ethanethioate (100)

^{1}H NMR (400 MHz, $CDCl_3$)

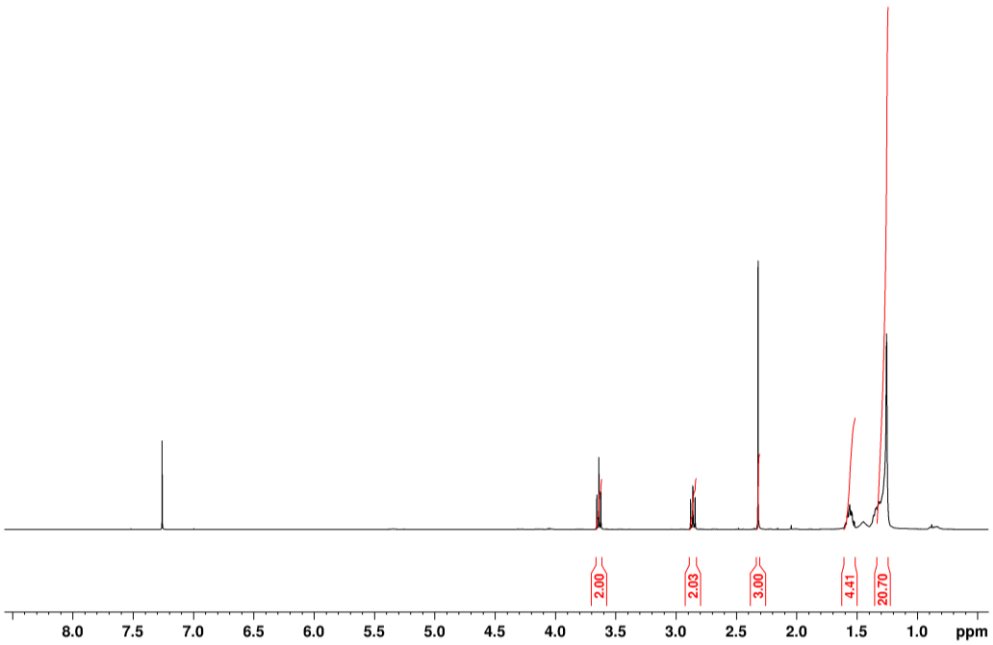

^{13}C NMR (101 MHz, $CDCl_3$)

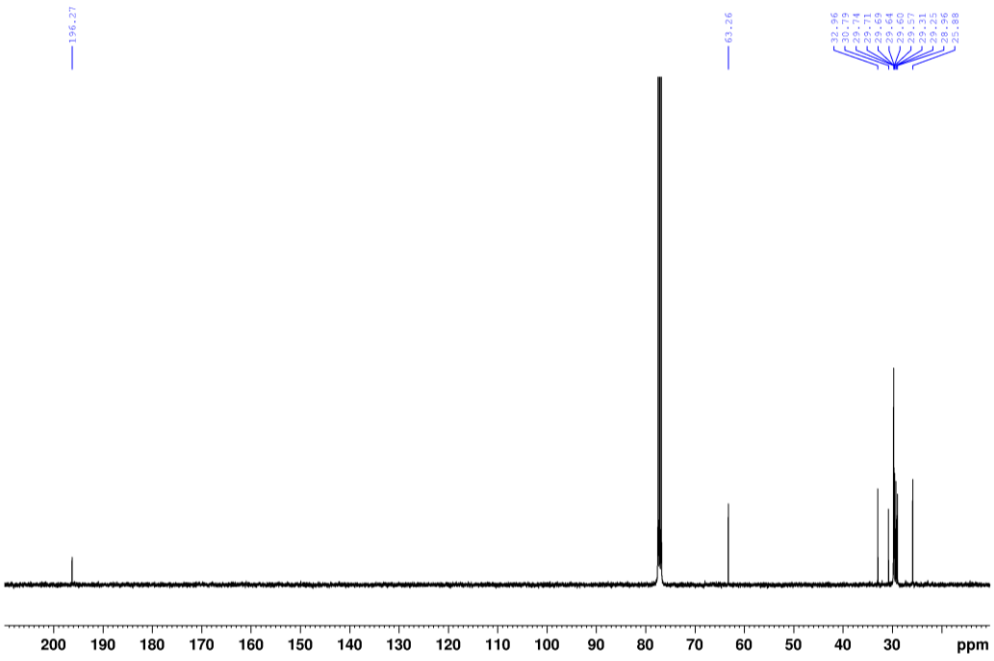

***S*-(14-Azidotetradecyl) ethanethioate (102)**

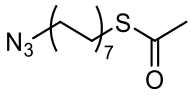

^{1}H NMR (400 MHz, $CDCl_3$)

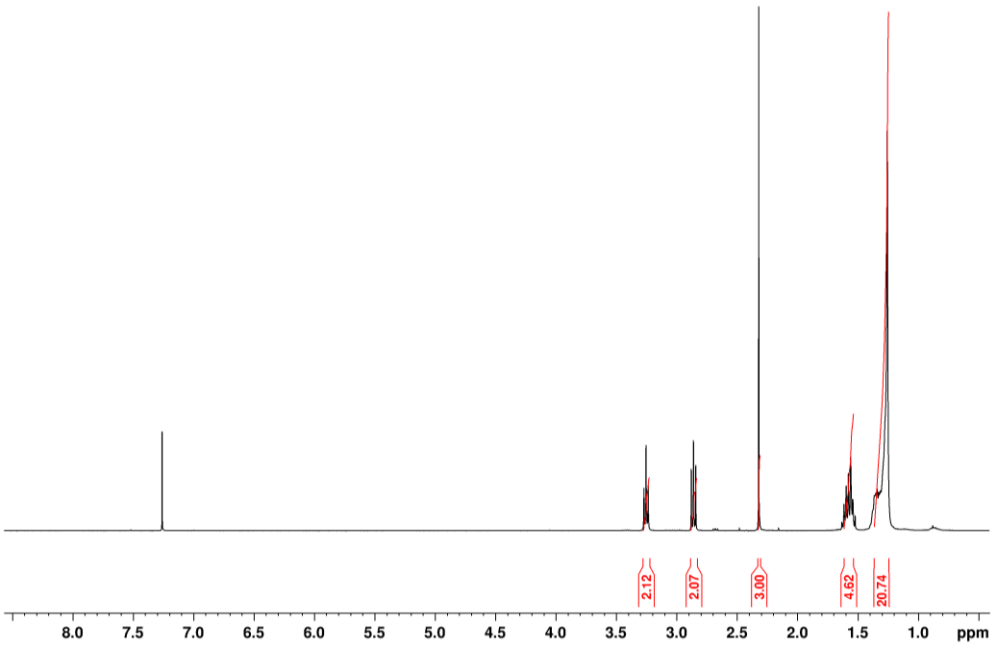

^{13}C NMR (101 MHz, $CDCl_3$)

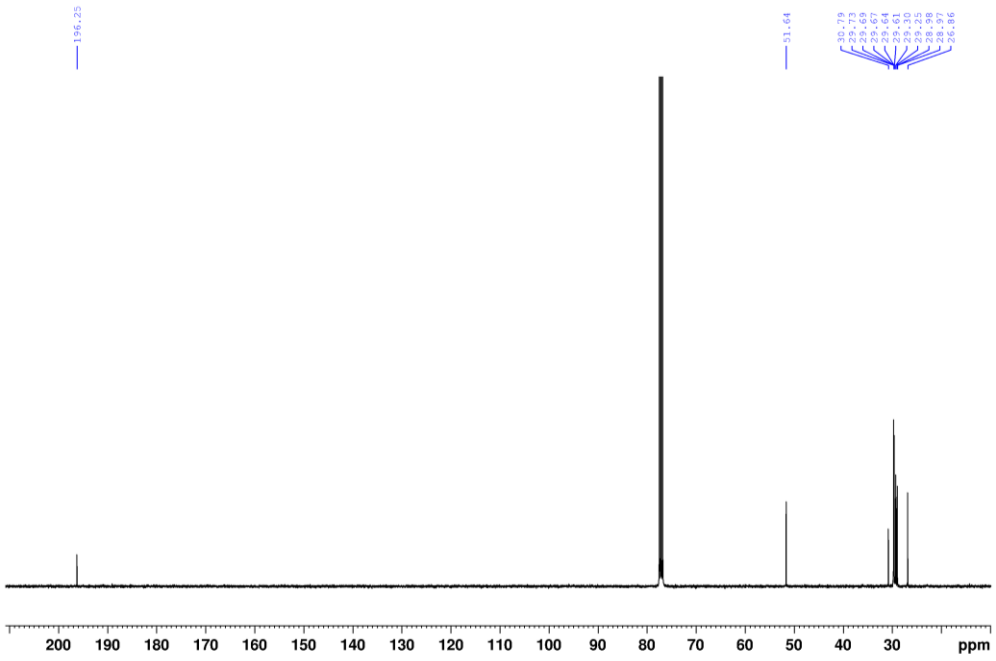

***N*,*N*'-Bis(tert-butoxycarbonyl)-*N*''-14-(acetylthio)tetradecylguanidine (104)**

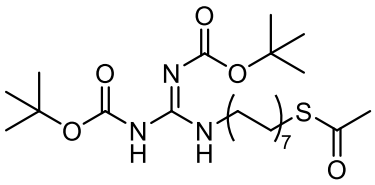

^{1}H NMR (400 MHz, $CDCl_3$)

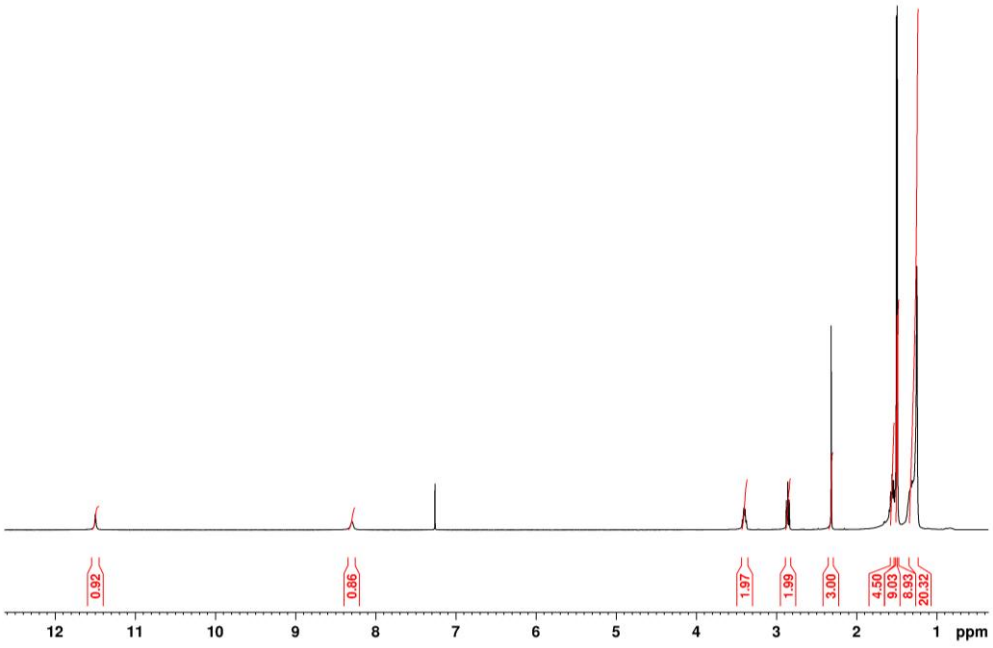

^{13}C NMR (101 MHz, $CDCl_3$)

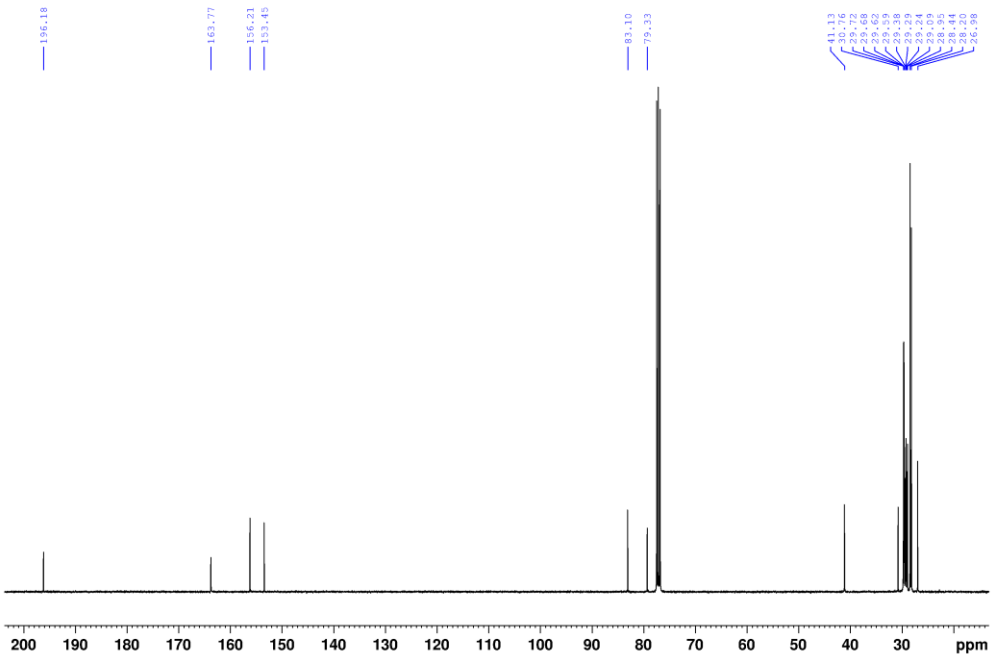

***N*-(14-Mercaptotetradecyl)guanidine (G-SH)**

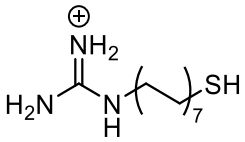

^{1}H NMR (400 MHz, CD_3OD)

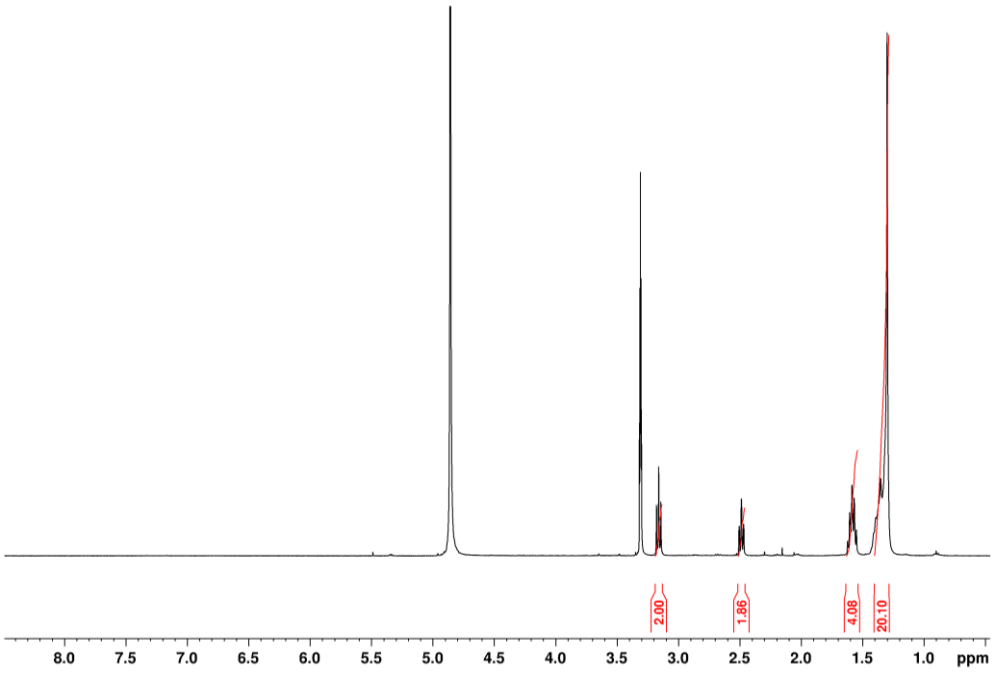

^{13}C NMR (101 MHz, CD_3OD)

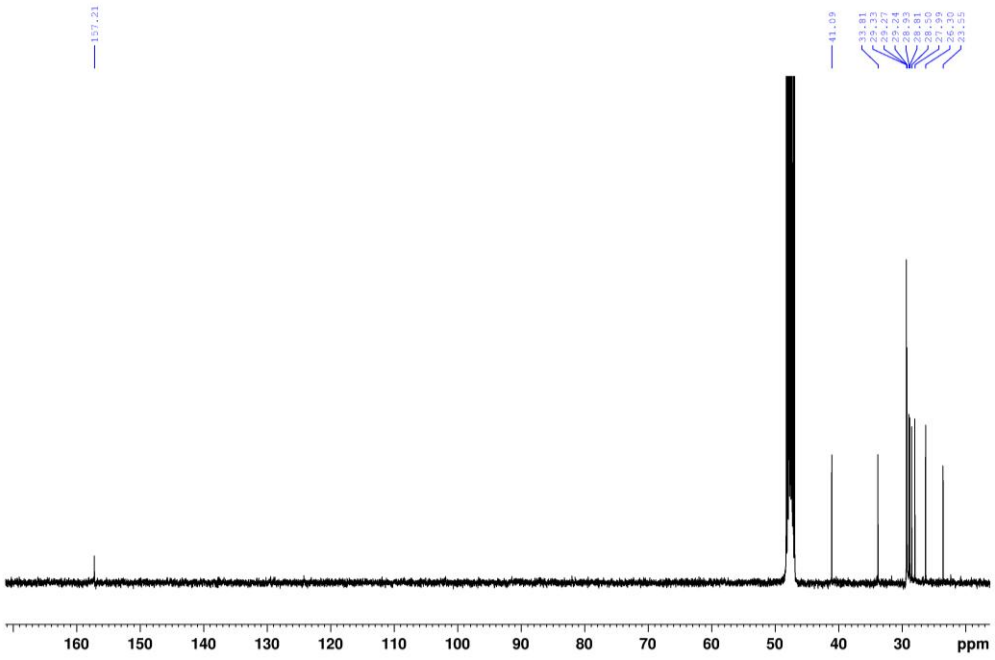

COSY NMR

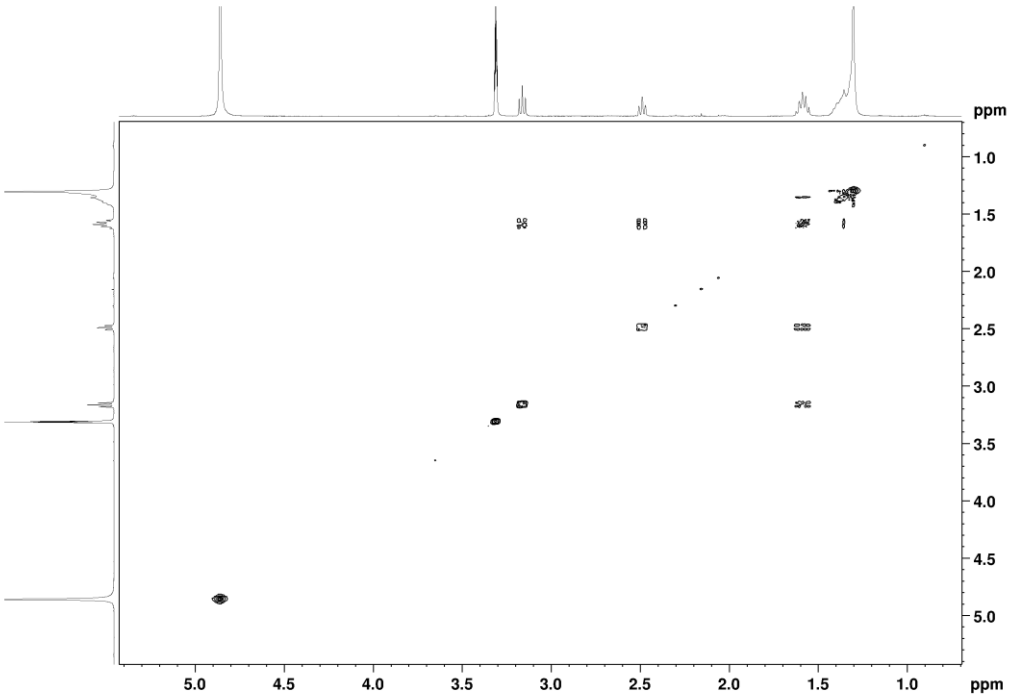

HSQC NMR

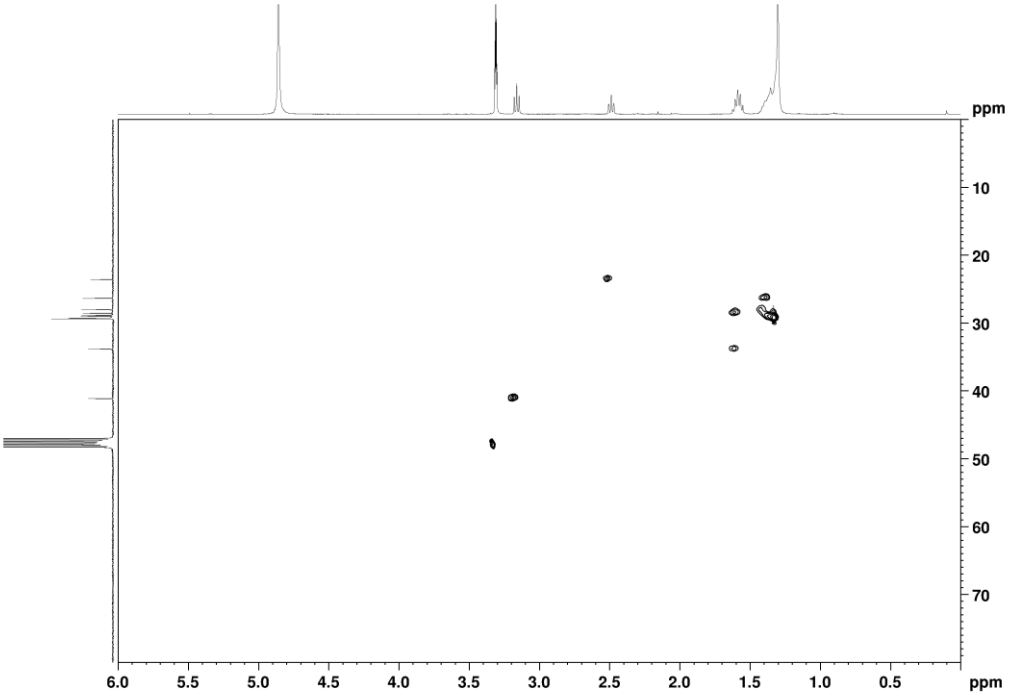

HMBC NMR

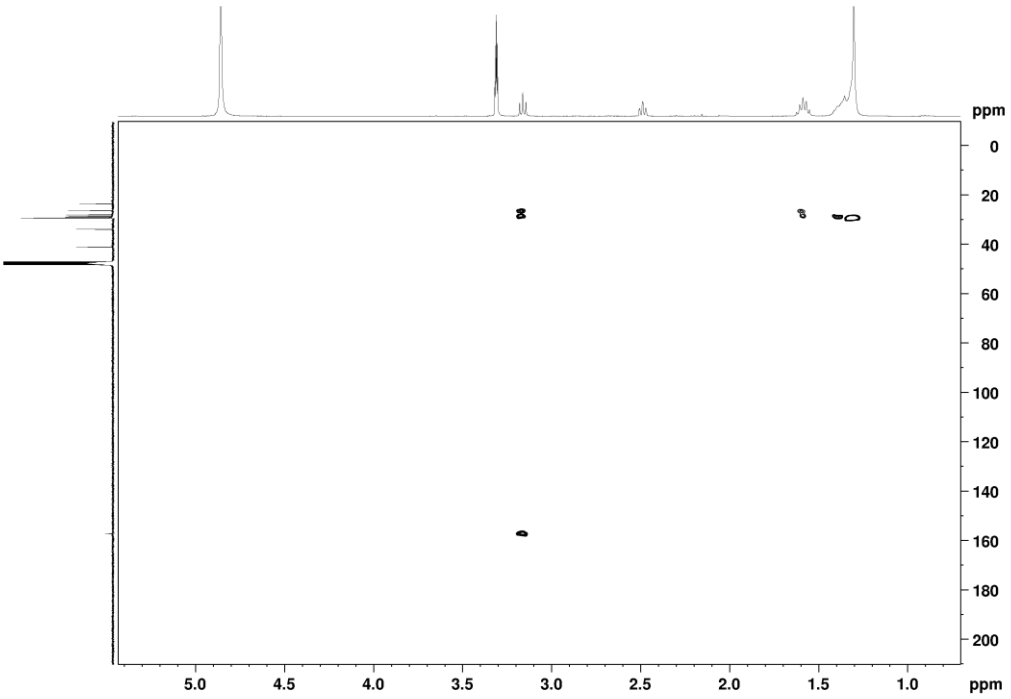
ppm
0
20
40
60
80
100
120
140
160
180
200
5.0
4.5
4.0
3.5
3.0
2.5
2.0
1.5
1.0
ppm

_N_-[(Pyridin-2-yl)methyl]-14-(tritylthio)tetradecanamide (114)

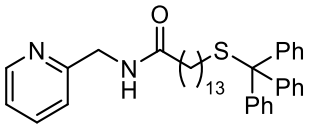

^{1}H NMR (400 MHz, $CDCl_3$)

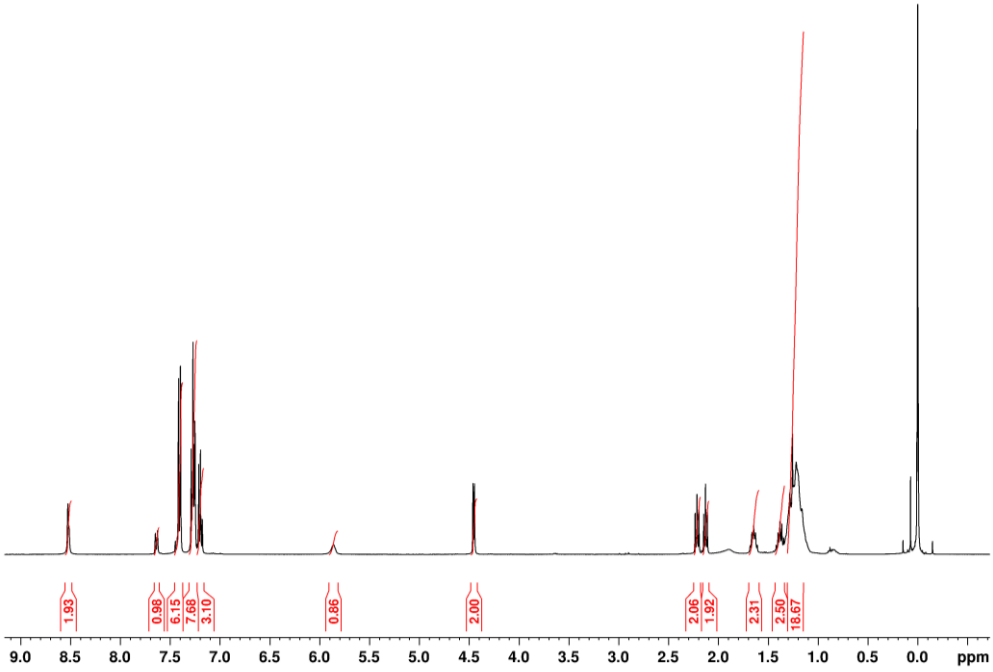

^{13}C NMR (101 MHz, $CDCl_3$)

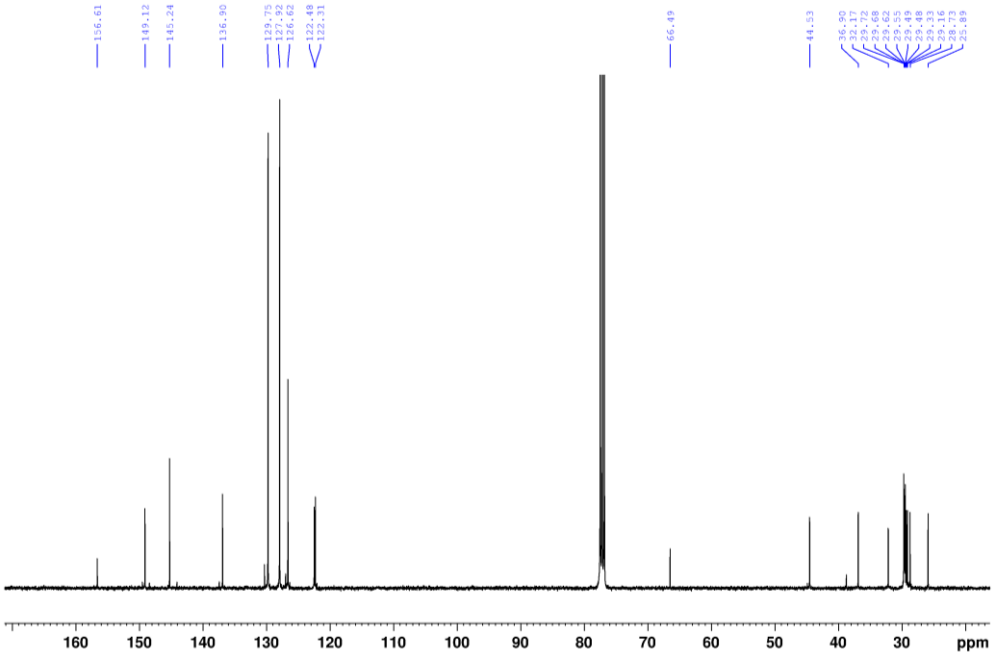

***N*-[(Pyridin-2-yl)methyl]-14-mercaptotertadecanamide (2PA-SH)**

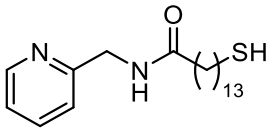

^{1}H NMR (400 MHz, $CDCl_3$)

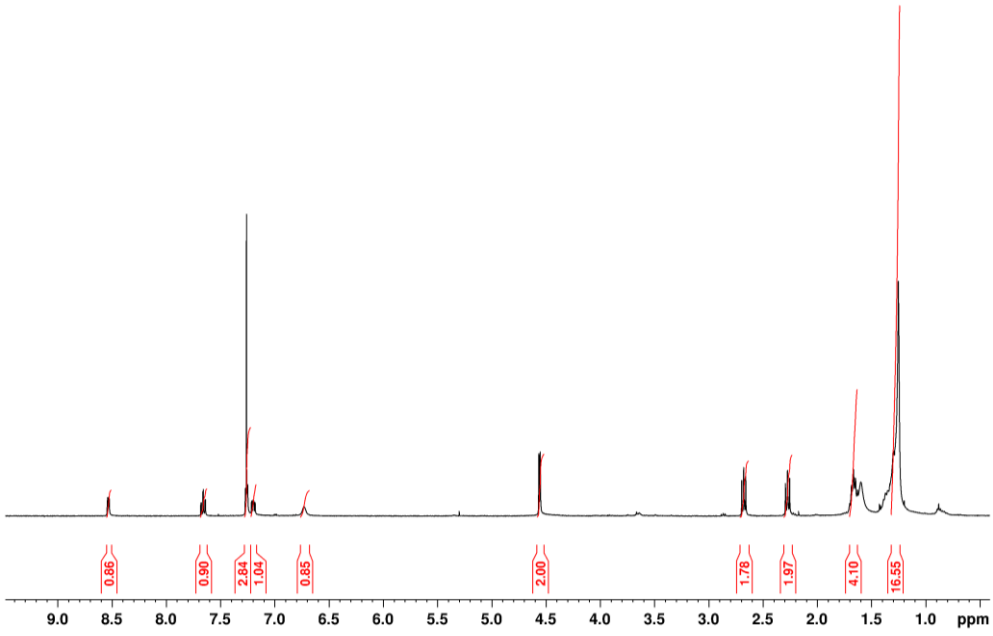

^{13}C NMR (101 MHz, $CDCl_3$)

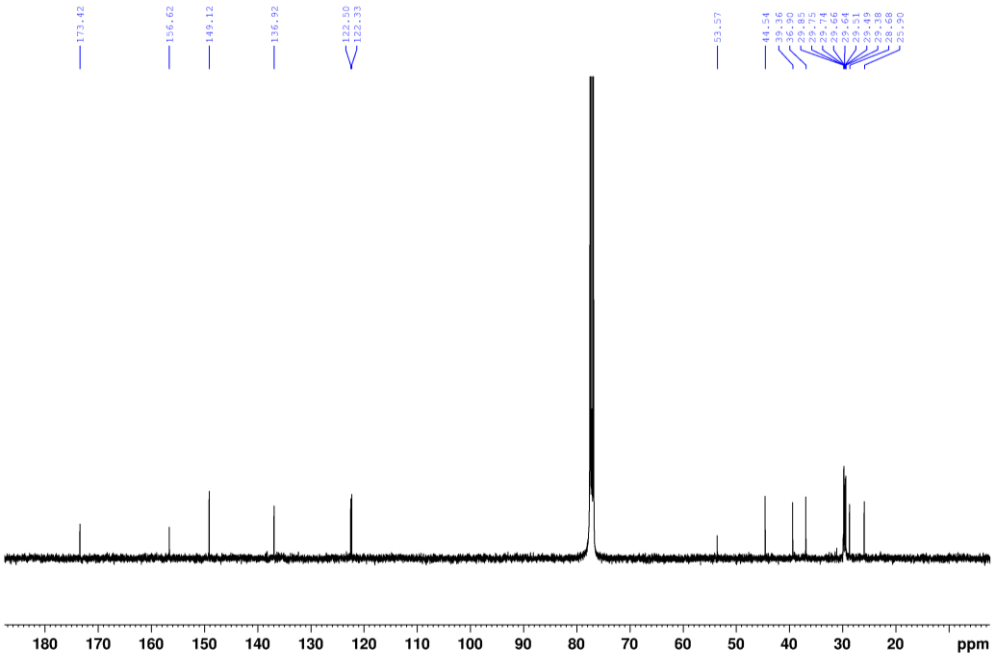

HSQC NMR

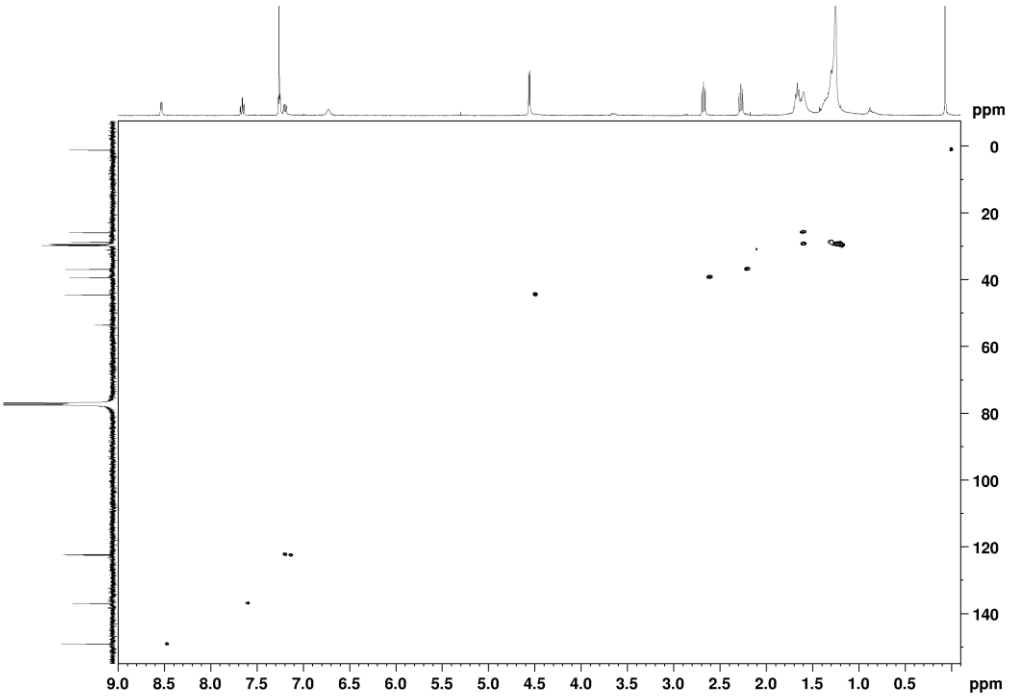

HMBC NMR

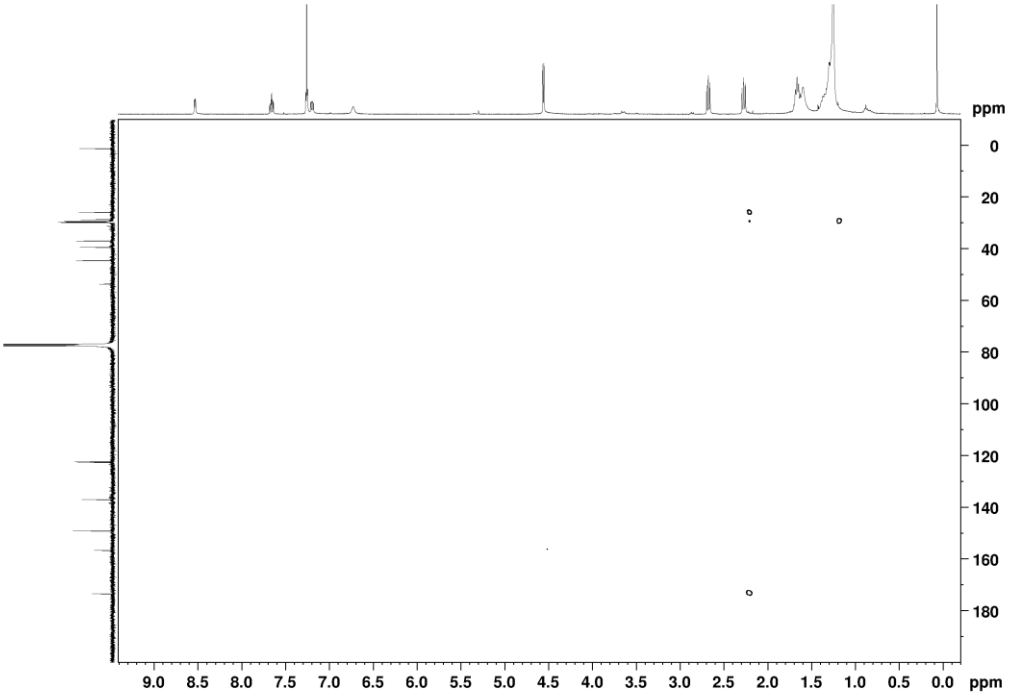

***N*-[(Pyridin-3-yl)methyl]-14-(tritylthio)tetradecanamide (116)**

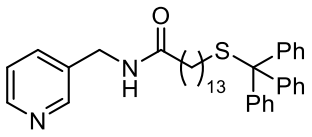

^{1}H NMR (400 MHz, $CDCl_3$)

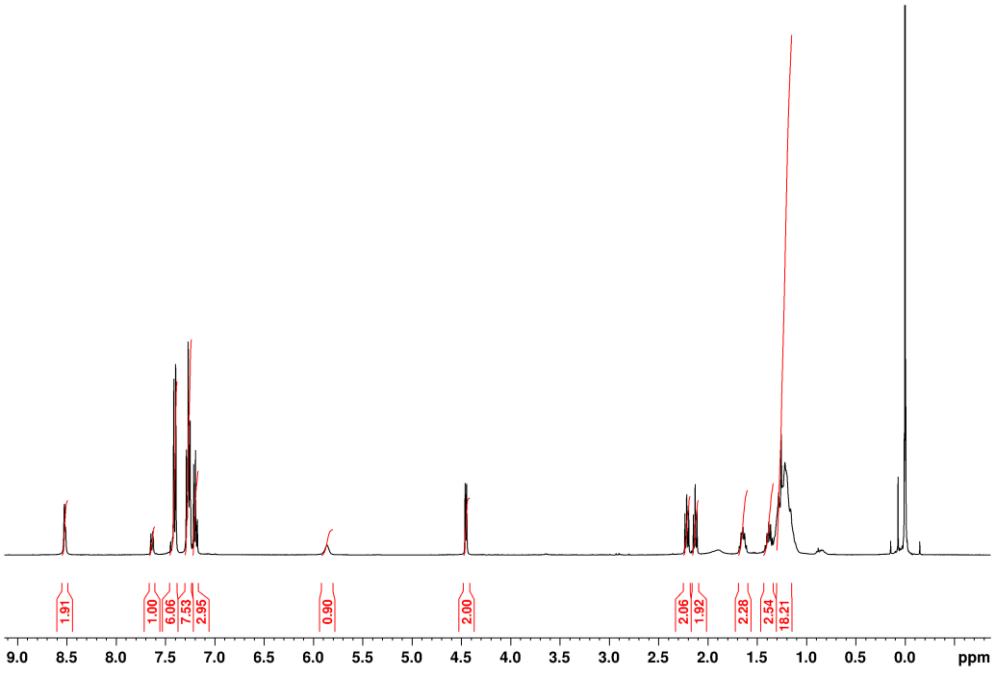

^{13}C NMR (101 MHz, $CDCl_3$)

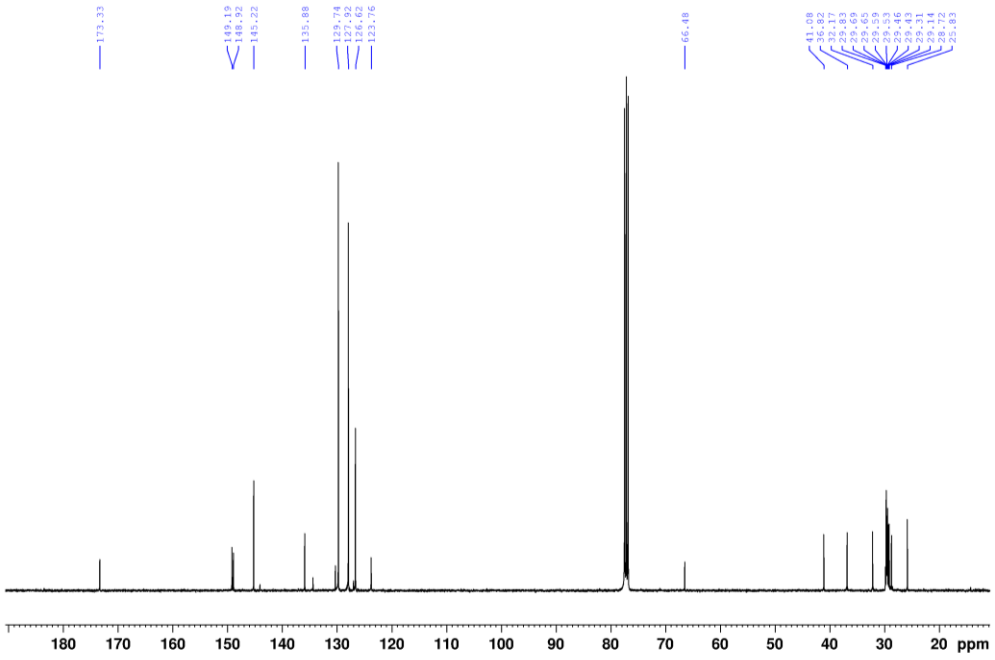

***N*-[(Pyridin-3-yl)methyl]-14-mercaptotertadecanamide (3PA-SH)**

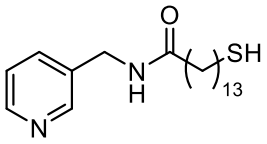

^{1}H NMR (400 MHz, $CDCl_3$)

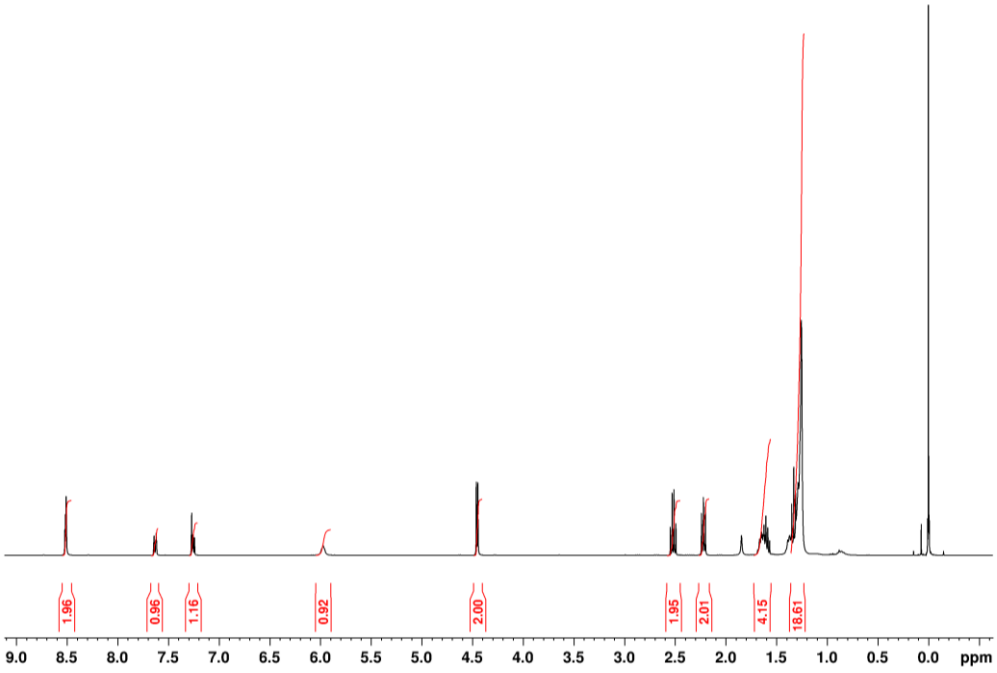

^{13}C NMR (101 MHz, $CDCl_3$)

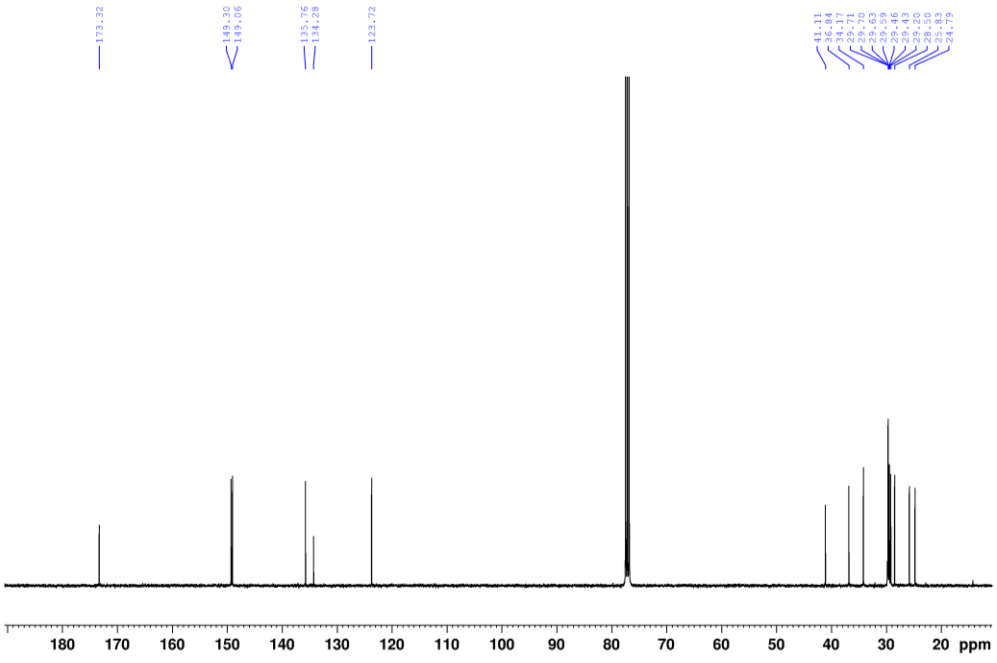

***N*-(Pyridine-2-ylmethyl)butanamide (C4-2PA)**

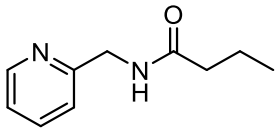

^{1}H NMR (400 MHz, $CDCl_3$)

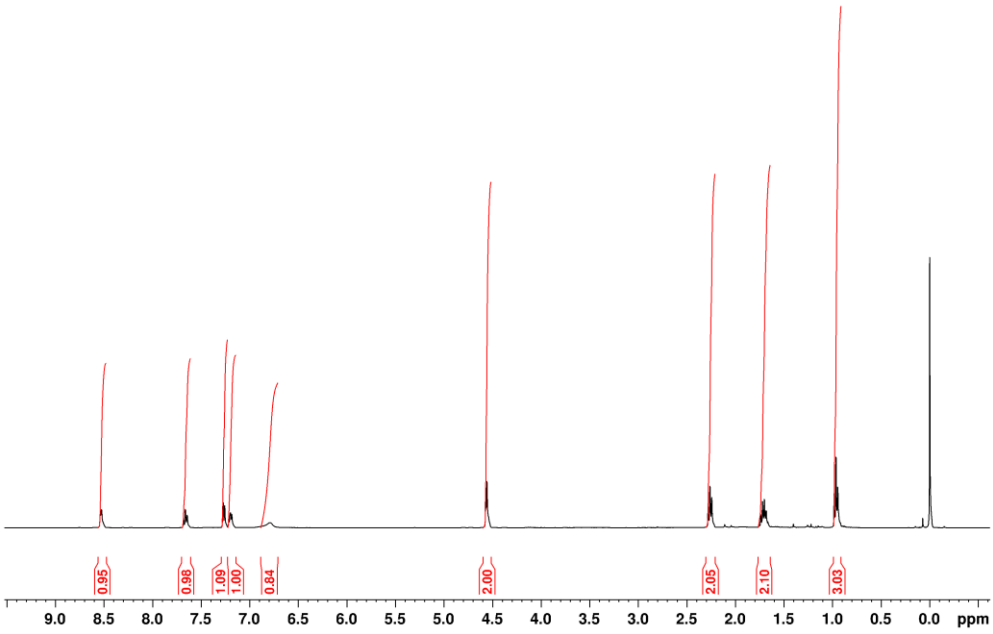

^{13}C NMR (101 MHz, $CDCl_3$)

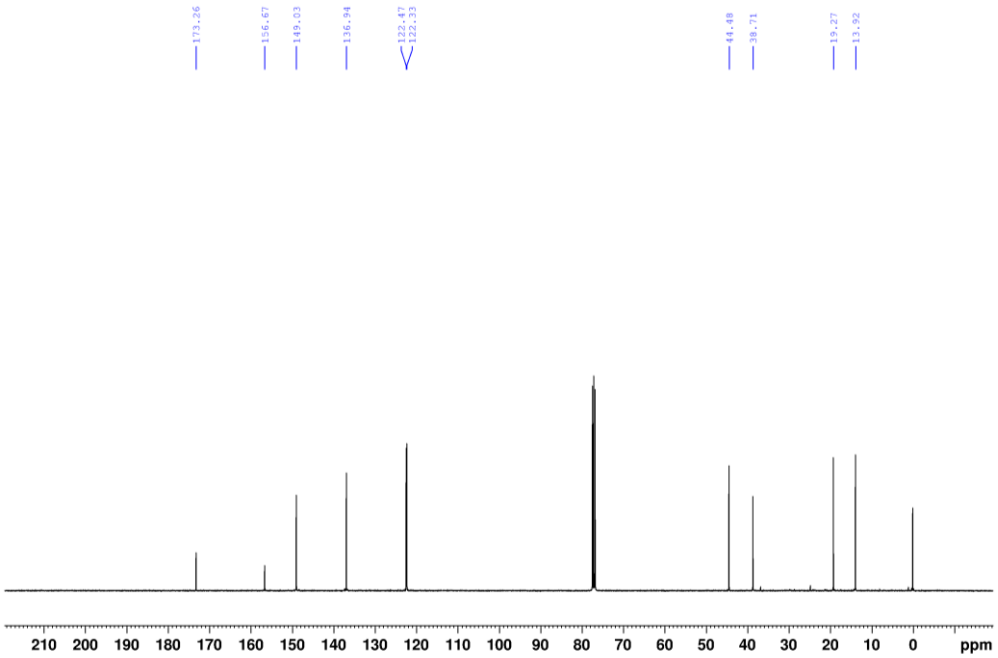

***N*-(Pyridine-2-ylmethyl)octanamide (C8-2PA)**

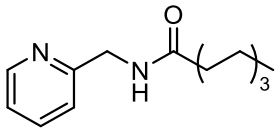

^{1}H NMR (400 MHz, $CDCl_3$)

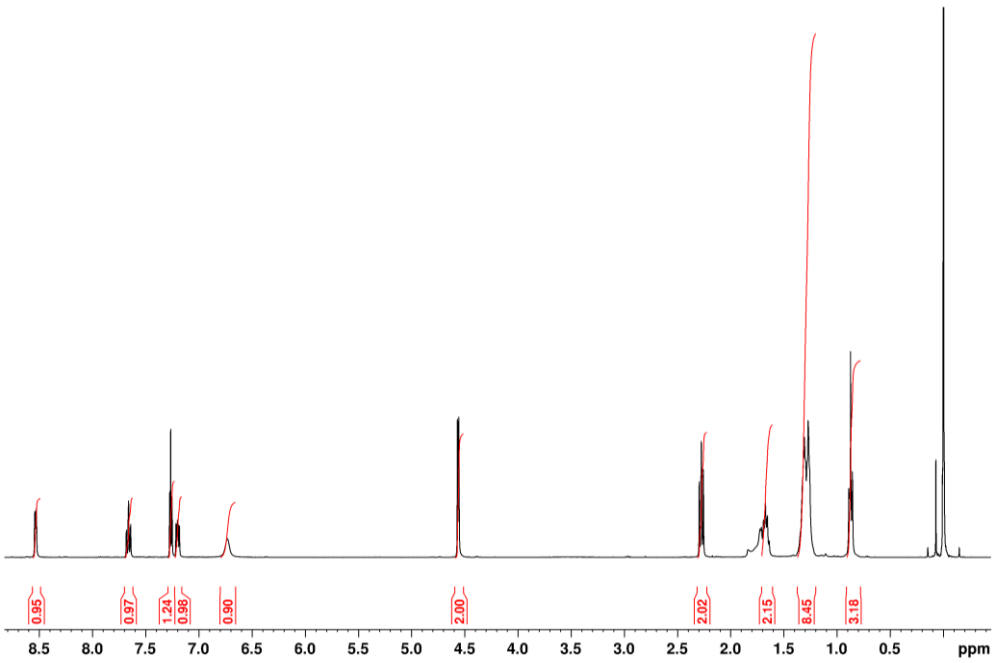

^{13}C NMR (101 MHz, $CDCl_3$)